HAL
open science

The Anatomy of Electro-Weak Symmetry Breaking. I: The Higgs boson in the Standard Model

Abdelhak Djouadi

To cite this version:

Abdelhak Djouadi. The Anatomy of Electro-Weak Symmetry Breaking. I: The Higgs boson in the Standard Model. 2005. hal-00004502v2

HAL Id: hal-00004502

https://hal.science/hal-00004502v2

Preprint submitted on 3 May 2005

HAL is a multi-disciplinary open access archive for the deposit and dissemination of scientific research documents, whether they are published or not. The documents may come from teaching and research institutions in France or abroad, or from public or private research centers.

L'archive ouverte pluridisciplinaire **HAL**, est destinée au dépôt et à la diffusion de documents scientifiques de niveau recherche, publiés ou non, émanant des établissements d'enseignement et de recherche français ou étrangers, des laboratoires publics ou privés.

LPT–Orsay–05–17
March 2005

The Anatomy of Electro–Weak Symmetry Breaking

Tome I: The Higgs boson in the Standard Model

Abdelhak DJOUADI

Laboratoire de Physique Théorique d'Orsay, UMR8627–CNRS,
Université Paris–Sud, Bât. 210, F–91405 Orsay Cedex, France.

Laboratoire de Physique Mathématique et Théorique, UMR5825–CNRS,
Université de Montpellier II, F–34095 Montpellier Cedex 5, France.

E–mail : `Abdelhak.Djouadi@cern.ch`

ccsd-00004502, version 2 - 3 May 2005

Abstract

This review is devoted to the study of the mechanism of electroweak symmetry breaking and this first part focuses on the Higgs particle of the Standard Model. The fundamental properties of the Higgs boson are reviewed and its decay modes and production mechanisms at hadron colliders and at future lepton colliders are described in detail.

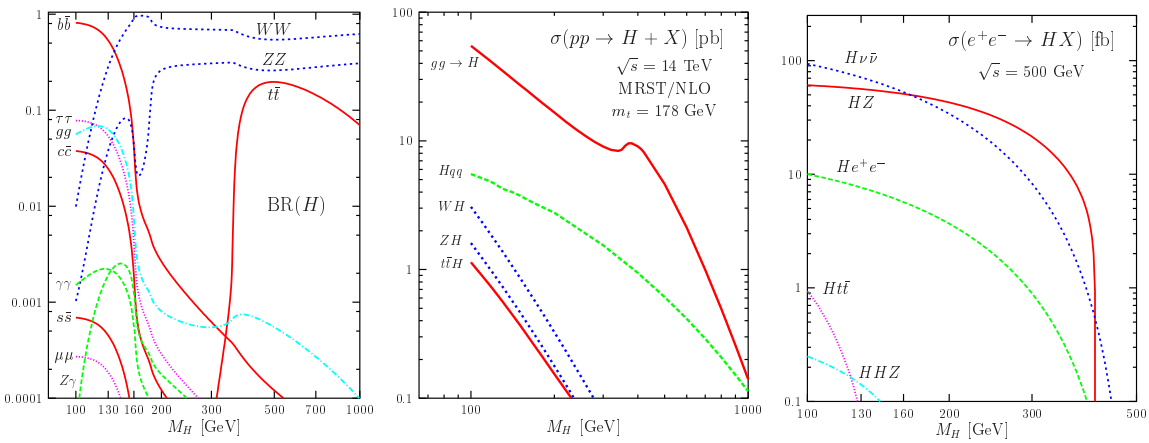

The decay branching ratios of the Standard Model Higgs boson and its production cross sections in the main channels at the LHC and at a 500 GeV e^+e^- collider.

Contents

Préambule **5**

1 The Higgs particle in the SM **13**
1.1 The SM of the strong and electroweak interactions . . . 13
1.1.1 The SM before electroweak symmetry breaking . . . 13
1.1.2 The Higgs mechanism . . . 16
1.1.3 The SM Higgs particle and the Goldstone bosons . . . 21
1.1.4 The SM interactions and parameters . . . 25
1.2 High–precision tests of the SM . . . 31
1.2.1 Observables in Z boson decays . . . 32
1.2.2 The electroweak radiative corrections . . . 35
1.2.3 Observables in W boson production and decay . . . 39
1.2.4 Approximating the radiative corrections . . . 43
1.2.5 The electroweak precision data . . . 46
1.3 Experimental constraints on the Higgs boson mass . . . 50
1.3.1 Constraints from high precision data . . . 50
1.3.2 Constraints from direct searches . . . 54
1.4 Theoretical constraints on the Higgs boson mass . . . 59
1.4.1 Constraints from perturbativity and unitarity . . . 59
1.4.2 Triviality and stability bounds . . . 64
1.4.3 The fine–tuning constraint . . . 69

2 Decays of the SM Higgs boson **73**
2.1 Decays to quarks and leptons . . . 74
2.1.1 The Born approximation . . . 74
2.1.2 Decays into light quarks and QCD corrections . . . 75
2.1.3 The case of the top quark . . . 76
2.1.4 Distinction between scalar and pseudoscalar Higgs bosons . . . 79
2.2 Decays into electroweak gauge bosons . . . 82
2.2.1 Two body decays . . . 82
2.2.2 Three body decays . . . 83
2.2.3 Four body decays . . . 84
2.2.4 CP properties and comparison with the CP–odd case . . . 85
2.3 Loop induced decays into $\gamma\gamma, \gamma Z$ and gg . . . 88
2.3.1 Decays into two photons . . . 89
2.3.2 Decays into a photon and a Z boson . . . 92
2.3.3 Decays into gluons . . . 94

2.4 The electroweak corrections and QCD improvements 97
2.4.1 The low energy theorem 99
2.4.2 EW corrections to decays into fermions and massive gauge bosons . . 100
2.4.3 NNLO QCD and EW corrections to the loop induced decays 104
2.4.4 Summary of the corrections to hadronic Higgs decays 108
2.5 The total decay width and the Higgs branching ratios 110

3 Higgs production at hadron colliders 115
3.1 Higgs bosons at hadron machines 115
3.1.1 Generalities about hadron colliders 115
3.1.2 Higgs production at hadron machines 117
3.1.3 The higher–order corrections and the K–factors 118
3.1.4 The scale dependence 119
3.1.5 The parton distribution functions 120
3.2 The associated production with W/Z bosons 123
3.2.1 The differential and total cross sections at LO 123
3.2.2 The QCD radiative corrections 125
3.2.3 The electroweak radiative corrections 129
3.2.4 The total cross section and the PDF uncertainties 131
3.3 The vector boson fusion processes 133
3.3.1 The differential and total cross sections at LO 133
3.3.2 The cross section at NLO 135
3.3.3 Kinematics of the process 137
3.3.4 Dependence on the scale and on the PDFs at NLO 140
3.3.5 The effective longitudinal vector boson approximation 143
3.4 The gluon–gluon fusion mechanism 145
3.4.1 The production cross section at LO 145
3.4.2 The cross section at NLO 146
3.4.3 The cross section beyond NLO in the heavy top quark limit 151
3.4.4 The distributions and Higgs + n jet production 157
3.5 Associated Higgs production with heavy quarks 161
3.5.1 The cross sections at the tree level 161
3.5.2 The ttH cross section at NLO 164
3.5.3 The case of the bbH process 169
3.5.4 Associated Higgs production with a single top quark 170
3.6 The higher–order processes 172
3.6.1 Higgs boson pair production 172
3.6.2 Higgs production in association with gauge bosons 176

3.6.3 More on higher–order processes . . . 179
3.6.4 Diffractive Higgs boson production . . . 181
3.7 Detecting and studying the Higgs boson . . . 184
3.7.1 Summary of the production cross sections . . . 184
3.7.2 Higgs signals and backgrounds at the Tevatron and the LHC . . . 188
3.7.3 Discovery expectations at the Tevatron and the LHC . . . 195
3.7.4 Determination of the Higgs properties at the LHC . . . 199
3.7.5 Higher luminosities and higher energies . . . 205

4 Higgs production at lepton colliders 209
4.1 Lepton colliders and the physics of the Higgs boson . . . 209
4.1.1 Generalities about e^+e^- colliders . . . 209
4.1.2 The photon colliders . . . 212
4.1.3 Future muon colliders . . . 215
4.1.4 Higgs production processes in lepton collisions . . . 217
4.2 The dominant production processes in e^+e^- collisions . . . 219
4.2.1 The Higgs–strahlung mechanism . . . 219
4.2.2 The WW fusion process . . . 224
4.2.3 The electroweak radiative corrections . . . 226
4.3 The subleading production processes in e^+e^- collisions . . . 230
4.3.1 The ZZ fusion mechanism . . . 230
4.3.2 Associated production with heavy fermion pairs . . . 233
4.3.3 Higgs boson pair production . . . 237
4.3.4 Other subleading processes in e^+e^- collisions . . . 241
4.4 Higgs studies in e^+e^- collisions . . . 247
4.4.1 Higgs boson signals . . . 247
4.4.2 Precision measurements for a light Higgs boson . . . 253
4.4.3 Combined measurements and the determination of the couplings . . . 263
4.4.4 Measurements at higher and lower energies . . . 265
4.5 Higgs production in $\gamma\gamma$ collisions . . . 269
4.5.1 Higgs boson production as an s–channel resonance . . . 269
4.5.2 Measuring the CP–properties of the Higgs boson . . . 275
4.5.3 Other Higgs production mechanisms . . . 279
4.6 Higgs production at muon colliders . . . 283
4.6.1 Higgs production in the s–channel . . . 283
4.6.2 Determination of the properties of a light Higgs boson . . . 288
4.6.3 Study of the CP properties of the Higgs boson . . . 291

References 295

Préambule

A short praise of the Standard Model

The end of the last millennium witnessed the triumph of the Standard Model (SM) of the electroweak and strong interactions of elementary particles [1, 2]. The electroweak theory, proposed by Glashow, Salam and Weinberg [1] to describe the electromagnetic [3] and weak [4] interactions between quarks and leptons, is based on the gauge symmetry group $\mathrm{SU(2)_L} \times \mathrm{U(1)_Y}$ of weak left–handed isospin and hypercharge. Combined with Quantum Chromo–Dynamics (QCD) [2], the theory of the strong interactions between the colored quarks based on the symmetry group $\mathrm{SU(3)_C}$, the model provides a unified framework to describe these three forces of Nature. The theory is perturbative at sufficiently high energies [2] and renormalizable [5], and thus describes these interactions at the quantum level.

A cornerstone of the SM is the mechanism of spontaneous electroweak symmetry breaking (EWSB) proposed forty years ago by Higgs, Brout, Englert, Guralnik, Hagen and Kibble [6] to generate the weak vector boson masses in a way that is minimal and, as was shown later, respects the requirements of renormalizability [5] and unitarity [7]. An SU(2) doublet of complex scalar fields is introduced and its neutral component develops a non–zero vacuum expectation value. As a consequence, the electroweak $\mathrm{SU(2)_L} \times \mathrm{U(1)_Y}$ symmetry is spontaneously broken to the electromagnetic $\mathrm{U(1)_Q}$ symmetry. Three of the four degrees of freedom of the doublet scalar field are absorbed by the $W^{\pm}$ and Z weak vector bosons to form their longitudinal polarizations and to acquire masses. The fermion masses are generated through a Yukawa interaction with the same scalar field and its conjugate field. The remaining degree of freedom corresponds to a scalar particle, the Higgs boson. The discovery of this new type of matter particle is unanimously considered as being of profound importance.

The high–precision measurements of the last decade [8, 9] carried out at LEP, SLC, Tevatron and elsewhere have provided a decisive test of the Standard Model and firmly established that it provides the correct effective description of the strong and electroweak interactions at present energies. These tests, performed at the per mille level accuracy, have probed the quantum corrections and the structure of the $\mathrm{SU(3)_C} \times \mathrm{SU(2)_L} \times \mathrm{U(1)_Y}$ local symmetry. The couplings of quarks and leptons to the electroweak gauge bosons have been measured precisely and agree with those predicted by the model. The trilinear couplings among electroweak vector bosons have also been measured and agree with those dictated by the $\mathrm{SU(2)_L} \times \mathrm{U(1)_Y}$ gauge symmetry. The $\mathrm{SU(3)_C}$ gauge symmetric description of the strong interactions has also been thoroughly tested at LEP and elsewhere. The only sector of the model which has not yet been probed in a satisfactory way is the scalar sector. The missing and most important ingredient of the model, the Higgs particle, has not been observed [9, 10] and only indirect constraints on its mass have been inferred from the high–precision data [8].

Probing electroweak symmetry breaking: a brief survey of recent developments

The SM of the electroweak interactions, including the EWSB mechanism for generating particle masses, had been proposed in the mid–sixties; however, it was only in the mid–seventies, most probably after the proof by 't Hooft and Veltman that it is indeed a renormalizable theory [5] and the discovery of the weak neutral current in the Gargamelle experiment [11], that all its facets began to be investigated thoroughly. After the discovery of the $W^{\pm}$ and Z bosons at CERN [12], probing the electroweak symmetry breaking mechanism became a dominant theme of elementary particle physics. The relic of this mechanism, the Higgs particle, became the Holy Grail of high–energy collider physics and *l'objet de tous nos désirs*. Finding this particle and studying its fundamental properties will be the major goal of the next generation of high–energy machines [and of the upgraded Tevatron, if enough luminosity is collected]: the CERN Large Hadron Collider (LHC), which will start operation in a few years, and the next high–energy and high–luminosity electron–positron linear collider, which hopefully will allow very detailed studies of the EWSB mechanism in a decade.

In the seventies and eighties, an impressive amount of theoretical knowledge was amassed on EWSB and on the expected properties of the Higgs boson(s), both within the framework of the SM and of its [supersymmetric and non supersymmetric] extensions. At the end of the eighties, the basic properties of the Higgs particles had been discussed and their principal decay modes and main production mechanisms at hadron and lepton colliders explored. This monumental endeavor was nicely and extensively reviewed in a celebrated book, *The Higgs Hunter's Guide* [13] by Gunion, Haber, Kane and Dawson. The constraints from the experimental data available at that time and the prospects for discovering the Higgs particle(s) at the upcoming high–energy experiments, the LEP, the SLC, the late SSC and the LHC, as well as possible higher energy e^+e^- colliders, were analyzed and summarized. The review indeed guided theoretical and phenomenological studies as well as experimental searches performed over the last fifteen years.

Meanwhile, several major developments took place. The LEP experiment, for which the search for the Higgs boson was a central objective, was completed with mixed results. On the one hand, LEP played a key role in establishing the SM as the effective theory of the strong and electroweak forces at presently accessible energies. On the other hand, it unfortunately failed to find the Higgs particle or any other new particle which could play a similar role. Nevertheless, this negative search led to a very strong limit on the mass of a SM–like Higgs boson, $M_H \gtrsim 114.4$ GeV [10]. This unambiguously ruled out a broad low Higgs mass region, and in particular the range $M_H \lesssim 5$ GeV, which was rather difficult to explore[1] before the advent of LEP1 and its very clean experimental environment. The mass range $M_H \lesssim 100$

[1]This is mainly due to the hadronic uncertainties which occur for such a small Higgs mass. Almost an entire chapter of Ref. [13] was devoted to this mass range; see pp. 32–56 and 94–129.

GeV would have been extremely difficult to probe at very high–energy hadron colliders such as the LHC. At approximately the same period, the top quark was at last discovered at the Tevatron [14]. The determination of its mass entailed that all the parameters of the Standard Model, except the Higgs boson mass, were then known[2], implying that the profile of the Higgs boson will be uniquely determined once its mass is fixed.

Other major developments occurred in the planning and design of the high–energy colliders. The project of the Superconducting Super Collider has been unfortunately terminated and the energy and luminosity parameters of the LHC became firmly established[3]. Furthermore, the option of upgrading the Tevatron by raising the c.m. energy and, more importantly, the luminosity to a value which allows for Higgs searches in the mass range $M_H \lesssim 2M_Z$ was not yet considered. In addition, the path toward future high–energy electron–positron colliders became more precise. The feasibility of the next generation machines, that is, e^+e^- linear colliders operating in the energy range from M_Z up to 1 TeV with very high luminosities has been demonstrated [as in the case of the TESLA machine] and a consensus on the technology of the future International Linear Collider (ILC) has recently emerged. The designs for the next generation machines running at energies in the multi–TeV range [such as the CLIC machine at CERN] also made rapid developments. Added to this, the option of turning future linear colliders into high–energy and high–luminosity $\gamma\gamma$ colliders by using Compton back–scattering of laser light off the high–energy electron beams and the possibility of high–energy muon colliders have been seriously discussed only in the last decade.

In parallel to these experimental and technological developments, a huge amount of effort has been devoted to the detailed study of the decay and production properties of the Higgs particle at these colliders. On the theoretical side, advances in computer technology allowed one to perform almost automatically very complicated calculations for loop diagrams and multi–particle processes and enabled extremely precise predictions. In particular, the next–to–leading order radiative corrections to Higgs production in all the important processes at hadron and e^+e^- colliders were calculated[4]. The radiative corrections to the cross sections

[2]Another important outcome is due to the heaviness of the top quark [15]: the search of the Higgs boson would have been extremely more difficult at hadron colliders if the top quark mass were smaller than M_W, a possibility for which many analyses were devoted in the past and which is now ruled out. As a by–product of the large m_t value, the cross sections for some Higgs production channels at both hadron and e^+e^- machines became rather large, thus increasing the chances for the discovery and/or study of the particle.

[3]The SSC was a project for a hadron machine with a center of mass energy of $\sqrt{s} = 40$ TeV and a yearly integrated luminosity of 10 fb^{-1} on which most of the emphasis for Higgs searches at hadron colliders was put in Ref. [13]. Of course these studies can be and actually have been adapted to the case of the LHC. Note that in the late eighties, the c.m. energy and the luminosity of the LHC were expected to be $\sqrt{s} = 17$ TeV and $\mathcal{L} = 10^{33}$ cm^{-2}s^{-1}, respectively, and the discovery range for the SM Higgs boson was considered to be rather limited, $2M_W \lesssim M_H \lesssim 300$ GeV [13].

[4]This started in the very late eighties and early nineties, when the one–loop QCD corrections to associated Higgs production with W/Z bosons and the WW/ZZ and gluon–gluon fusion mechanisms at hadron colliders and the electroweak corrections to the Higgs–strahlung production mechanism at e^+e^- colliders have been

for some production processes, such as Higgs–strahlung and gluon–gluon fusion at hadron colliders, have been calculated up to next–to–next–to–leading order accuracy for the strong interaction part and at next–to–leading order for the electroweak part, a development which occurred only over the last few years. A vast literature on the higher order effects in Higgs boson decays has also appeared in the last fifteen years and some decay modes have been also investigated to next–to–next–to–leading order accuracy and, in some cases, even beyond. Moreover, thorough theoretical studies of the various distributions in Higgs production and decays and new techniques for the determination of the fundamental properties of the Higgs particle [a vast subject which was only very briefly touched upon in Ref. [13] for instance] have been recently carried out.

Finally, a plethora of analyses of the various Higgs signals and backgrounds, many detailed parton–level analyses and Monte–Carlo simulations taking into account the experimental environment [which is now more or less established, at least for the Tevatron and the LHC and possibly for the first stage of the e^+e^- linear collider, the ILC] have been performed to assess to what extent the Higgs particle can be observed and its properties studied in given processes at the various machines.

Objectives and limitations of the review

On the experimental front, with the LEP experiment completed, we await the accumulation of sufficient data from the upgraded Tevatron and the launch of the LHC which will start operation in 2007. At this point, we believe that it is useful to collect and summarize the large amount of work carried out over the last fifteen years in preparation for the challenges ahead. This review is an attempt to respond to this need. The review is structured in three parts. In this first part, we will concentrate on the Higgs boson of the Standard Model, summarize the present experimental and theoretical information on the Higgs sector, analyze the decay modes of the Higgs bosons including all the relevant and important higher order effects, and discuss the production properties of the Higgs boson and its detection strategies at the various hadron and lepton machines presently under discussion. We will try to be as extensive and comprehensive as possible.

However, because the subject is vast and the number of studies related to it is huge[5], it is almost an impossible task to review all its aspects. In addition, one needs to cover

derived, and continued until very recently when the QCD corrections to associated Higgs production with heavy quarks at hadron colliders and the electroweak corrections to all the remaining important Higgs production processes at lepton colliders have been completed.

[5]Simply by typing "find title Higgs" in the search field of the Spires database, one obtains more than 6.700 entries. Since this number does not include all the articles dealing with the EWSB mechanism and not explicitly mentioning the name of Prof. Higgs in the title, the total number of articles written on the EWSB mechanism in the SM and its various extensions may, thus, well exceed the level of 10.000.

many different topics and each of them could have [and, actually, often does have] its own review. Therefore, in many instances, one will have to face [sometimes Cornelian...] choices. The ones made in this review will be, of course, largely determined by the taste of the author, his specialization and his own prejudice. I therefore apologize in advance if some important aspects are overlooked and/or some injustice to possibly relevant analyses is made. Complementary material on the foundations of the SM and the Higgs mechanism, which will only be briefly sketched here, can be found in standard textbooks [16] or in general reviews [17,18] and an account of the various calculations, theoretical studies and phenomenological analyses mentioned above can be found in many specialized reviews; see Refs. [19–23] for some examples. For the physics of the Higgs particle at the various colliders, in particular for the discussion of the Higgs signals and their respective backgrounds, as well as for the detection techniques, we will simply summarize the progress so far. For this very important issue, we refer for additional and more detailed informations to specialized reviews and, above all, to the proceedings which describe the huge collective efforts at the various workshops devoted to the subject. Many of these studies and reviews will be referenced in due time.

Synopsis of the review

The first part of this review (Tome I) on the electroweak symmetry breaking mechanism is exclusively devoted to the SM Higgs particle. The discussion of the Higgs sector of the Minimal Supersymmetric extension of the SM is given in an accompanying report [24], while the EWSB mechanism in other supersymmetric and non–supersymmetric extensions of the SM will be discussed in a forthcoming report [25]. In our view, the SM incorporates an elementary Higgs boson with a mass below 1 TeV and, thus, the very heavy or the no–Higgs scenarios will not be discussed here and postponed to Ref. [25].

The first chapter is devoted to the description of the Higgs sector of the SM. After briefly recalling the basic ingredients of the model and its input parameters, including an introduction to the electroweak symmetry breaking mechanism and to the basic properties of the Higgs boson, we discuss the high–precision tests of the SM and introduce the formalism which allows a description of the radiative corrections which involve the contribution of the only unknown parameter of the theory, the Higgs boson mass M_H or, alternatively, its self–coupling. This formalism will be needed when we discuss the radiative corrections to Higgs decay and production modes. We then summarize the indirect experimental constraints on M_H from the high–precision measurements and the constraints derived from direct Higgs searches at past and present colliders. We close this chapter by discussing some interesting constraints on the Higgs mass that can be derived from theoretical considerations on the energy range in which the SM is valid before perturbation theory breaks down and new phenomena should emerge. The bounds on M_H from unitarity in scattering amplitudes,

perturbativity of the Higgs self–coupling, stability of the electroweak vacuum and fine–tuning in the radiative corrections in the Higgs sector, are analyzed.

In the second chapter, we explore the decays of the SM Higgs particle. We consider all decay modes which lead to potentially observable branching fractions: decays into quarks and leptons, decays into weak massive vector bosons and loop induced decays into gluons and photons. We discuss not only the dominant two–body decays, but also higher order decays, which can be very important in some cases. We pay particular attention to the radiative corrections and, especially, to the next–to–leading order QCD corrections to the hadronic Higgs decays which turn out to be quite large. The higher order QCD corrections [beyond NLO] and the important electroweak radiative corrections to all decay modes are briefly summarized. The expected branching ratios of the Higgs particle, including the uncertainties which affect them, are given. Whenever possible, we compare the various decay properties of the SM Higgs boson, with its distinctive spin and parity $J^{\rm PC} = 0^{++}$ quantum numbers, to those of hypothetical pseudoscalar Higgs bosons with $J^{\rm PC} = 0^{+-}$ which are predicted in many extensions of the SM Higgs sector. This will highlight the unique prediction for the properties of the SM Higgs particle [the more general case of anomalous Higgs couplings will be discussed in the third part of this review].

The third chapter is devoted to the production of the Higgs particle at hadron machines. We consider both the $p\bar{p}$ Tevatron collider with a center of mass energy of $\sqrt{s} = 1.96$ TeV and the pp Large Hadron Collider (LHC) with a center of mass energy of $\sqrt{s} = 14$ TeV. All the dominant production processes, namely the associated production with W/Z bosons, the weak vector boson fusion processes, the gluon–gluon fusion mechanism and the associated Higgs production with heavy top and bottom quarks, are discussed in detail. In particular, we analyze not only the total production cross sections, but also the differential distributions and we pay special attention to three important aspects: the QCD radiative corrections or the K–factors [and the electroweak corrections when important] which are large in many cases, their dependence on the renormalization and factorization scales which measures the reliability of the theoretical predictions, and the choice of different sets of parton distribution functions. We also discuss other production processes such as Higgs pair production, production with a single top quark, production in association with two gauge bosons or with one gauge boson and two quarks as well as diffractive Higgs production. These channels are not considered as Higgs discovery modes, but they might provide additional interesting information. We then summarize the main Higgs signals in the various detection channels at the Tevatron and the LHC and the expectations for observing them experimentally. At the end of this chapter, we briefly discuss the possible ways of determining some of the properties of the Higgs particle at the LHC: its mass and total decay width, its spin and parity quantum numbers and its couplings to fermions and gauge bosons. A brief summary of the benefits

that one can expect from raising the luminosity and energy of hadron colliders is given.

In the fourth chapter, we explore the production of the SM Higgs boson at future lepton colliders. We mostly focus on future e^+e^- colliders in the energy range $\sqrt{s} = 350$–1000 GeV as planed for the ILC but we also discuss the physics of EWSB at multi–TeV machines [such as CLIC] or by revisiting the Z boson pole [the GigaZ option], as well as at the $\gamma\gamma$ option of the linear collider and at future muon colliders. In the case of e^+e^- machines, we analyze in detail the main production mechanisms, the Higgs–strahlung and the WW boson fusion processes, as well as some "subleading" but extremely important processes for determining the profile of the Higgs boson such as associated production with top quark pairs and Higgs pair production. Since e^+e^- colliders are known to be high–precision machines, the theoretical predictions need to be rather accurate and we summarize the work done on the radiative corrections to these processes [which have been completed only recently] and to various distributions which allow to test the fundamental nature of the Higgs particle. The expectation for Higgs production at the various possible center of mass energies and the potential of these machines to probe the electroweak symmetry breaking mechanism in all its facets and to check the SM predictions for the fundamental Higgs properties such as the total width, the spin and parity quantum numbers, the couplings to the other SM particles [in particular, the important coupling to the top quark] and the Higgs self–coupling [which allows the reconstruction of the scalar potential which generates EWSB] are summarized. Higgs production at $\gamma\gamma$ and at muon colliders are discussed in the two last sections, with some emphasis on two points which are rather difficult to explore in e^+e^- collisions, namely, the determination of the Higgs spin–parity quantum numbers and the total decay width.

Since the primary goal of this review is to provide the necessary material to discuss Higgs decays and production at present and future colliders, we present the analytical expressions of the partial decay widths, the production cross sections and some important distributions, including the higher order corrections or effects, when they are simple enough to be displayed. We analyze in detail the main Higgs decay and production channels and also discuss some channels which are not yet established but which can be useful and with further effort might prove experimentally accessible. We also present summary and updated plots as well as illustrative numerical examples [which can be used as a normalization in future phenomenological and experimental studies] for the total Higgs decay width and branching ratios, as well as for the cross sections of the main production mechanisms at the Tevatron, the LHC and future e^+e^- colliders at various center of mass energies. In these updated analyses, we have endeavored to include all currently available information. For collider Higgs phenomenology, in particular for the discussion of the Higgs signals and backgrounds, we simply summarize, as previously mentioned, the main points and refer to the literature for additional details and complementary discussions.

Acknowledgments

I would like first to thank the many collaborators with whom I shared the pleasure to investigate various aspects of the theme discussed in this review. They are too numerous to be all listed here, but I would like at least to mention Peter Zerwas with whom I started to work on the subject in an intensive way.

I would also like to thank the many colleagues and friends who helped me during the writing of this review and who made important remarks on the preliminary versions of the manuscript and suggestions for improvements: Fawzi Boudjema, Albert de Roeck, Klaus Desch, Michael Dittmar, Manuel Drees, Rohini Godbole, Robert Harlander, Wolfgang Hollik, Karl Jakobs, Sasha Nikitenko, Giacomo Polesello, Francois Richard, Pietro Slavich and Michael Spira. Special thanks go to Manuel Drees and Pietro Slavich for their very careful reading of large parts of the manuscript and for their efficiency in hunting the many typos, errors and awkwardnesses contained in the preliminary versions and for their attempt at improving my poor English and fighting against my anarchic way of "distributing commas". Additional help with the English by Martin Bucher and, for the submission of this review to the archives, by Marco Picco are also acknowledged.

I also thank the Djouadi *smala*, my sisters and brothers and their children [at least one of them, Yanis, has already caught the virus of particle physics and I hope that one day he will read this review], who bore my not always joyful mood in the last two years. Their support was crucial for the completion of this review. Finally, thanks to the team of *La Bonne Franquette*, where in fact part of this work has been done, for their good couscous and the nice atmosphere, as well as to Madjid Belkacem for sharing the drinks with me.

The writing of this review started when I was at CERN as a scientific associate, continued during the six months I spent at the LPTHE of Jussieu, and ended at the LPT d'Orsay. I thank all these institutions for their kind hospitality.

1 The Higgs particle in the SM

1.1 The SM of the strong and electroweak interactions

In this section, we present a brief introduction to the Standard Model (SM) of the strong and electroweak interactions and to the mechanism of electroweak symmetry breaking. This will allow us to set the stage and to fix the notation which will be used later on. For more detailed discussions, we refer the reader to standard textbooks [16] or reviews [17].

1.1.1 The SM before electroweak symmetry breaking

As discussed in the preamble, the Glashow–Weinberg–Salam electroweak theory [1] which describes the electromagnetic and weak interactions between quarks and leptons, is a Yang–Mills theory [26] based on the symmetry group $\mathrm{SU(2)_L} \times \mathrm{U(1)_Y}$. Combined with the $\mathrm{SU(3)_C}$ based QCD gauge theory [2] which describes the strong interactions between quarks, it provides a unified framework to describe these three forces of Nature: the Standard Model. The model, before introducing the electroweak symmetry breaking mechanism to be discussed later, has two kinds of fields.

• There are first the matter fields, that is, the three generations of left–handed and right–handed chiral quarks and leptons, $f_{L,R} = \frac{1}{2}(1 \mp \gamma_5)f$. The left–handed fermions are in weak isodoublets, while the right–handed fermions are in weak isosinglets[6]

$$I_f^{3L,3R} = \pm\frac{1}{2}, 0 : \begin{array}{l} L_1 = \begin{pmatrix} \nu_e \\ e^- \end{pmatrix}_L , \; e_{R_1} = e_R^- , \; Q_1 = \begin{pmatrix} u \\ d \end{pmatrix}_L , \; u_{R_1} = u_R , \; d_{R_1} = d_R \\ L_2 = \begin{pmatrix} \nu_\mu \\ \mu^- \end{pmatrix}_L , \; e_{R_2} = \mu_R^- , \; Q_2 = \begin{pmatrix} c \\ s \end{pmatrix}_L , \; u_{R_2} = c_R , \; d_{R_2} = s_R \\ L_3 = \begin{pmatrix} \nu_\tau \\ \tau^- \end{pmatrix}_L , \; e_{R_3} = \tau_R^- , \; Q_3 = \begin{pmatrix} t \\ b \end{pmatrix}_L , \; u_{R_3} = t_R , \; d_{R_3} = b_R \end{array} \quad (1.1)$$

The fermion hypercharge, defined in terms of the third component of the weak isospin I_f^3 and the electric charge Q_f in units of the proton charge $+e$, is given by (i=1,2,3)

$$Y_f = 2Q_f - 2I_f^3 \;\; \Rightarrow \;\; Y_{L_i} = -1, \; Y_{e_{R_i}} = -2, \; Y_{Q_i} = \frac{1}{3}, \; Y_{u_{R_i}} = \frac{4}{3}, \; Y_{d_{R_i}} = -\frac{2}{3} \quad (1.2)$$

Moreover, the quarks are triplets under the $\mathrm{SU(3)_C}$ group, while leptons are color singlets. This leads to the relation

$$\sum_f Y_f = \sum_f Q_f = 0 \quad (1.3)$$

[6]Throughout this review, we will assume that the neutrinos, which do not play any role here, are massless and appear only with their left–handed components.

which ensures the cancellation of chiral anomalies [27] within each generation, thus, preserving [28] the renormalizability of the electroweak theory [5].

• Then, there are the gauge fields corresponding to the spin–one bosons that mediate the interactions. In the electroweak sector, we have the field B_μ which corresponds to the generator Y of the $\mathrm{U(1)_Y}$ group and the three fields $W_\mu^{1,2,3}$ which correspond to the generators T^a [with a=1,2,3] of the $\mathrm{SU(2)_L}$ group; these generators are in fact equivalent to half of the non–commuting 2×2 Pauli matrices

$$T^a = \frac{1}{2}\tau^a\,; \quad \tau_1 = \begin{pmatrix} 0 & 1 \\ 1 & 0 \end{pmatrix}\,,\ \tau_2 = \begin{pmatrix} 0 & -i \\ i & 0 \end{pmatrix}\,,\ \tau_3 = \begin{pmatrix} 1 & 0 \\ 0 & -1 \end{pmatrix} \tag{1.4}$$

with the commutation relations between these generators given by

$$[T^a, T^b] = i\epsilon^{abc}T_c \quad \text{and} \quad [Y, Y] = 0 \tag{1.5}$$

where ϵ^{abc} is the antisymmetric tensor. In the strong interaction sector, there is an octet of gluon fields $G_\mu^{1,\cdots,8}$ which correspond to the eight generators of the $\mathrm{SU(3)_C}$ group [equivalent to half of the eight 3×3 anti–commuting Gell–Mann matrices] and which obey the relations

$$[T^a, T^b] = if^{abc}T_c \quad \text{with} \quad \mathrm{Tr}[T^aT^b] = \frac{1}{2}\delta_{ab} \tag{1.6}$$

where the tensor f^{abc} is for the structure constants of the $\mathrm{SU(3)_C}$ group and where we have used the same notation as for the generators of SU(2) as little confusion should be possible. The field strengths are given by

$$\begin{aligned} G^a_{\mu\nu} &= \partial_\mu G^a_\nu - \partial_\nu G^a_\mu + g_s\, f^{abc}G^b_\mu G^c_\nu \\ W^a_{\mu\nu} &= \partial_\mu W^a_\nu - \partial_\nu W^a_\mu + g_2\, \epsilon^{abc}W^b_\mu W^c_\nu \\ B_{\mu\nu} &= \partial_\mu B_\nu - \partial_\nu B_\mu \end{aligned} \tag{1.7}$$

where g_s, g_2 and g_1 are, respectively, the coupling constants of $\mathrm{SU(3)_C}$, $\mathrm{SU(2)_L}$ and $\mathrm{U(1)_Y}$.

Because of the non–abelian nature of the SU(2) and SU(3) groups, there are self–interactions between their gauge fields, $V_\mu \equiv W_\mu$ or G_μ, leading to

$$\begin{aligned} \text{triple gauge boson couplings} &: ig_i\,\mathrm{Tr}(\partial_\nu V_\mu - \partial_\mu V_\nu)[V_\mu, V_\nu] \\ \text{quartic gauge boson couplings} &: \frac{1}{2}g_i^2\,\mathrm{Tr}[V_\mu, V_\nu]^2 \end{aligned} \tag{1.8}$$

The matter fields ψ are minimally coupled to the gauge fields through the covariant derivative D_μ which, in the case of quarks, is defined as

$$D_\mu\psi = \left(\partial_\mu - ig_sT_aG^a_\mu - ig_2T_aW^a_\mu - ig_1\frac{Y_q}{2}B_\mu\right)\psi \tag{1.9}$$

and which leads to unique couplings between the fermion and gauge fields V_μ of the form

$$\text{fermion gauge boson couplings} \quad : \quad -g_i \overline{\psi} V_\mu \gamma^\mu \psi \tag{1.10}$$

The SM Lagrangian, without mass terms for fermions and gauge bosons is then given by

$$\begin{aligned} \mathcal{L}_{\rm SM} \;=\; & -\frac{1}{4} G^a_{\mu\nu} G^{\mu\nu}_a - \frac{1}{4} W^a_{\mu\nu} W^{\mu\nu}_a - \frac{1}{4} B_{\mu\nu} B^{\mu\nu} \\ & + \bar{L}_i \, i D_\mu \gamma^\mu \, L_i + \bar{e}_{Ri} \, i D_\mu \gamma^\mu \, e_{R_i} \; + \bar{Q}_i \, i D_\mu \gamma^\mu \, Q_i + \bar{u}_{Ri} \, i D_\mu \gamma^\mu \, u_{R_i} \; + \bar{d}_{Ri} \, i D_\mu \gamma^\mu \, d_{R_i} \end{aligned} \tag{1.11}$$

This Lagrangian is invariant under local $\mathrm{SU(3)_C} \times \mathrm{SU(2)_L} \times \mathrm{U(1)_Y}$ gauge transformations for fermion and gauge fields. In the case of the electroweak sector, for instance, one has

$$\begin{aligned} & L(x) \to L'(x) = e^{i\alpha_a(x) T^a + i\beta(x) Y} L(x) \quad , \quad R(x) \to R'(x) = e^{i\beta(x) Y} R(x) \\ & \vec{W}_\mu(x) \to \vec{W}_\mu(x) - \frac{1}{g_2} \partial_\mu \vec{\alpha}(x) - \vec{\alpha}(x) \times \vec{W}_\mu(x) \; , \; B_\mu(x) \to B_\mu(x) - \frac{1}{g_1} \partial_\mu \beta(x) \end{aligned} \tag{1.12}$$

Up to now, the gauge fields and the fermions fields have been kept massless. In the case of strong interactions, the gluons are indeed massless particles while mass terms of the form $-m_q \overline{\psi} \psi$ can be generated for the colored quarks [and for the leptons] in an SU(3) gauge invariant way. In the case of the electroweak sector, the situation is more problematic:

– If we add mass terms, $\frac{1}{2} M_V^2 W_\mu W^\mu$, for the gauge bosons [since experimentally, they have been proved to be massive, the weak interaction being of short distance], this will violate local SU(2)×U(1) gauge invariance. This statement can be visualized by taking the example of QED where the photon is massless because of the $\mathrm{U(1)_Q}$ local symmetry

$$\frac{1}{2} M_A^2 A_\mu A^\mu \to \frac{1}{2} M_A^2 (A_\mu - \frac{1}{e} \partial_\mu \alpha)(A^\mu - \frac{1}{e} \partial^\mu \alpha) \neq \frac{1}{2} M_A^2 A_\mu A^\mu \tag{1.13}$$

– In addition, if we include explicitly a mass term $-m_f \overline{\psi}_f \psi_f$ for each SM fermion f in the Lagrangian, we would have for the electron for instance

$$-\, m_e \bar{e} e = -m_e \bar{e} \Big(\frac{1}{2}(1 - \gamma_5) + \frac{1}{2}(1 + \gamma_5) \Big) e = -m_e (\bar{e}_R e_L + \bar{e}_L e_R) \tag{1.14}$$

which is manifestly non–invariant under the isospin symmetry transformations discussed above, since e_L is a member of an $\mathrm{SU(2)_L}$ doublet while e_R is a member of a singlet.

Thus, the incorporation by brute force of mass terms for gauge bosons and for fermions leads to a manifest breakdown of the local $\mathrm{SU(2)_L} \times \mathrm{U(1)_Y}$ gauge invariance. Therefore, apparently, either we have to give up the fact that $M_Z \sim 90$ GeV and $m_e \sim 0.5$ MeV for instance, or give up the principle of exact or unbroken gauge symmetry.

The question, which has been asked already in the sixties, is therefore the following: is there a [possibly nice] way to generate the gauge boson and the fermion masses without violating SU(2)×U(1) gauge invariance? The answer is yes: the Higgs–Brout–Englert–Guralnik–Hagen–Kibble mechanism of spontaneous symmetry breaking [6] or the Higgs mechanism for short. This mechanism will be briefly sketched in the following subsection and applied to the SM case.

1.1.2 The Higgs mechanism

The Goldstone theorem

Let us start by taking a simple scalar real field ϕ with the usual Lagrangian

$$\mathcal{L} = \frac{1}{2}\partial_\mu\phi\,\partial^\mu\phi - V(\phi)\ ,\ V(\phi) = \frac{1}{2}\mu^2\phi^2 + \frac{1}{4}\lambda\phi^4 \tag{1.15}$$

This Lagrangian is invariant under the reflexion symmetry $\phi \to -\phi$ since there are no cubic terms. If the mass term μ^2 is positive, the potential $V(\phi)$ is also positive if the self–coupling λ is positive [which is needed to make the potential bounded from below], and the minimum of the potential is obtained for $\langle 0|\phi|0\rangle \equiv \phi_0 = 0$ as shown in the left–hand side of Fig. 1.1. $\mathcal{L}$ is then simply the Lagrangian of a spin–zero particle of mass μ.

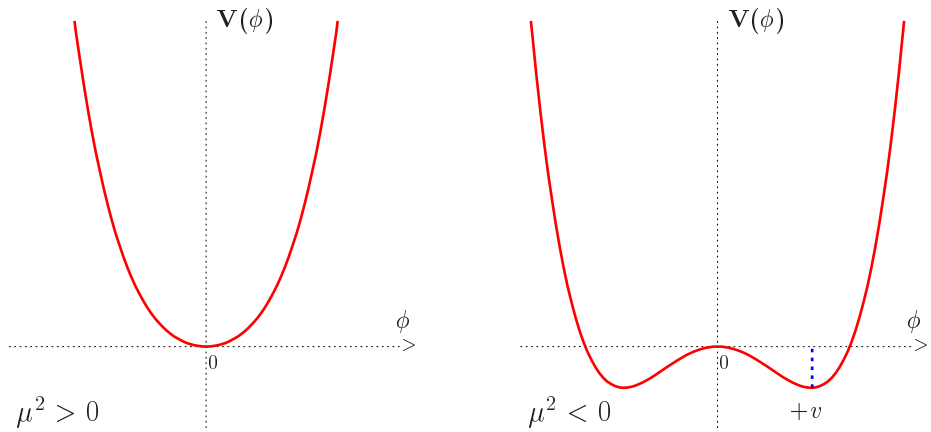

Figure 1.1: The potential V of the scalar field ϕ in the case $\mu^2 > 0$ (left) and $\mu^2 < 0$ (right).

In turn, if $\mu^2 < 0$, the potential $V(\phi)$ has a minimum when $\partial V/\partial\phi = \mu^2\phi + \lambda\phi^3 = 0$, i.e. when

$$\langle 0|\phi^2|0\rangle \equiv \phi_0^2 = -\frac{\mu^2}{\lambda} \equiv v^2 \tag{1.16}$$

and not at $\phi_0^2 = 0$, as shown in the right–hand side of Fig. 1.1. The quantity $\pm v \equiv \langle\, 0|\phi|0\,\rangle$ is called the vacuum expectation value (vev) of the scalar field ϕ. In this case, $\mathcal{L}$ is no more the Lagrangian of a particle with mass μ and to interpret correctly the theory, we must expand around one of the minima v by defining the field σ as $\phi = v + \sigma$. In terms of the new field, the Lagrangian becomes

$$\mathcal{L} = \frac{1}{2}\partial_\mu\sigma\,\partial^\mu\sigma - (-\mu^2)\,\sigma^2 - \sqrt{-\mu^2\lambda}\,\sigma^3 - \frac{\lambda}{4}\,\sigma^4 + \text{const.} \tag{1.17}$$

This is the theory of a scalar field of mass $m^2 = -2\mu^2$, with σ^3 and σ^4 being the self–interactions. Since there are now cubic terms, the reflexion symmetry is broken: it is not anymore apparent in $\mathcal{L}$. This is the simplest example of a spontaneously broken symmetry.

Let us make things slightly more complicated and consider four scalar fields ϕ_i with $i = 0, 1, 2, 3$, with a Lagrangian [the summation over the index i is understood]

$$\mathcal{L} = \frac{1}{2}\partial_\mu \phi_i \, \partial^\mu \phi_i - \frac{1}{2}\mu^2 \, (\phi_i \phi_i) - \frac{1}{4}\lambda (\phi_i \phi_i)^2 \tag{1.18}$$

which is invariant under the rotation group in four dimensions O(4), $\phi_i(x) = R_{ij}\phi_j(x)$ for any orthogonal matrix R.

Again, for $\mu^2 < 0$, the potential has a minimum at $\phi_i^2 = -\mu^2/\lambda \equiv v^2$ where v is the vev. As previously, we expand around one of the minima, $\phi_0 = v + \sigma$, and rewrite the fields $\phi_i = \pi_i$ with $i = 1, 2, 3$ [in analogy with pion physics]. The Lagrangian in terms of the new fields σ and π_i becomes then

$$\begin{aligned} \mathcal{L} &= \frac{1}{2}\partial_\mu \sigma \, \partial^\mu \sigma - \frac{1}{2}(-2\mu^2)\sigma^2 - \lambda v \, \sigma^3 - \frac{\lambda}{4}\sigma^4 \\ &+ \frac{1}{2}\partial_\mu \pi_i \, \partial^\mu \pi_i - \frac{\lambda}{4}(\pi_i \pi_i)^2 - \lambda v \pi_i \pi_i \sigma - \frac{\lambda}{2}\pi_i \pi_i \sigma^2 \end{aligned} \tag{1.19}$$

As expected, we still have a massive σ boson with $m^2 = -2\mu^2$, but also, we have three massless pions since now, all the bilinear $\pi_i \pi_i$ terms in the Lagrangian have vanished. Note that there is still an O(3) symmetry among the π_i fields.

This brings us to state the Goldstone theorem [29]: For every spontaneously broken continuous symmetry, the theory contains massless scalar (spin–0) particles called Goldstone bosons. The number of Goldstone bosons is equal to the number of broken generators. For an O(N) continuous symmetry, there are $\frac{1}{2}N(N-1)$ generators; the residual unbroken symmetry O($N-1$) has $\frac{1}{2}(N-1)(N-2)$ generators and therefore, there are $N-1$ massless Goldstone bosons, i.e. 3 for the O(4) group.

Note that exactly the same exercise can be made for a complex doublet of scalar fields

$$\phi = \begin{pmatrix} \phi^+ \\ \phi^0 \end{pmatrix} = \frac{1}{\sqrt{2}} \begin{pmatrix} \phi_1 - i\phi_2 \\ \phi_3 - i\phi_4 \end{pmatrix} \tag{1.20}$$

with the invariant product being $\phi^\dagger \phi = \frac{1}{2}(\phi_1^2 + \phi_2^2 + \phi_3^2 + \phi_4^2) = \frac{1}{2}\phi_i \phi^i$.

The Higgs mechanism in an abelian theory

Let us now move to the case of a local symmetry and consider first the rather simple abelian U(1) case: a complex scalar field coupled to itself and to an electromagnetic field A_μ

$$\mathcal{L} = -\frac{1}{4}F_{\mu\nu}F^{\mu\nu} + D_\mu \phi^* D^\mu \phi - V(\phi) \tag{1.21}$$

with D_μ the covariant derivative $D_\mu = \partial_\mu - ieA_\mu$ and with the scalar potential

$$V(\phi) = \mu^2 \phi^* \phi + \lambda \, (\phi^* \phi)^2 \tag{1.22}$$

The Lagrangian is invariant under the usual local U(1) transformation

$$\phi(x) \to e^{i\alpha(x)}\phi(x) \qquad A_\mu(x) \to A_\mu(x) - \frac{1}{e}\partial_\mu\alpha(x) \tag{1.23}$$

For $\mu^2 > 0$, $\mathcal{L}$ is simply the QED Lagrangian for a charged scalar particle of mass μ and with ϕ^4 self–interactions. For $\mu^2 < 0$, the field $\phi(x)$ will acquire a vacuum expectation value and the minimum of the potential V will be at

$$\langle\, \phi \,\rangle_0 \equiv \langle\, 0 |\, \phi \,|\, 0 \,\rangle = \left(-\frac{\mu^2}{2\lambda}\right)^{1/2} \equiv \frac{v}{\sqrt{2}} \tag{1.24}$$

As before, we expand the Lagrangian around the vacuum state $\langle\phi\rangle$

$$\phi(x) = \frac{1}{\sqrt{2}}[v + \phi_1(x) + i\phi_2(x)] \tag{1.25}$$

The Lagrangian becomes then, up to some interaction terms that we omit for simplicity,

$$\begin{aligned} \mathcal{L} &= -\frac{1}{4}F_{\mu\nu}F^{\mu\nu} + (\partial^\mu + ieA^\mu)\phi^*(\partial_\mu - ieA_\mu)\phi - \mu^2\phi^*\phi - \lambda(\phi^*\phi)^2 \\ &= -\frac{1}{4}F_{\mu\nu}F^{\mu\nu} + \frac{1}{2}(\partial_\mu\phi_1)^2 + \frac{1}{2}(\partial_\mu\phi_2)^2 - v^2\lambda\phi_1^2 + \frac{1}{2}e^2v^2A_\mu A^\mu - evA_\mu\partial^\mu\phi_2 \end{aligned} \tag{1.26}$$

Three remarks can then be made at this stage:

– There is a photon mass term in the Lagrangian: $\frac{1}{2}M_A^2A_\mu A^\mu$ with $M_A = ev = -e\mu^2/\lambda$.
– We still have a scalar particle ϕ_1 with a mass $M_{\phi_1}^2 = -2\mu^2$.
– Apparently, we have a massless particle ϕ_2, a would–be Goldstone boson.

However, there is still a problem to be addressed. In the beginning, we had four degrees of freedom in the theory, two for the complex scalar field ϕ and two for the massless electromagnetic field A_μ, and now we have apparently five degrees of freedom, one for ϕ_1, one for ϕ_2 and three for the massive photon A_μ. Therefore, there must be a field which is not physical at the end and indeed, in $\mathcal{L}$ there is a bilinear term $evA^\mu\partial_\mu\phi_2$ which has to be eliminated. To do so, we notice that at first order, we have for the original field ϕ

$$\phi = \frac{1}{\sqrt{2}}(v + \phi_1 + i\phi_2) \equiv \frac{1}{\sqrt{2}}[v + \eta(x)]e^{i\zeta(x)/v} \tag{1.27}$$

By using the freedom of gauge transformations and by performing also the substitution

$$A_\mu \to A_\mu - \frac{1}{ev}\partial_\mu\zeta(x) \tag{1.28}$$

the $A_\mu\partial^\mu\zeta$ term, and in fact all ζ terms, disappear from the Lagrangian. This choice of gauge, for which only the physical particles are left in the Lagrangian, is called the unitary gauge. Thus, the photon (with two degrees of freedom) has absorbed the would–be Goldstone boson (with one degree of freedom) and became massive (i.e. with three degrees of freedom): the longitudinal polarization is the Goldstone boson. The U(1) gauge symmetry is no more apparent and we say that it is spontaneously broken. This is the Higgs mechanism [6] which allows to generate masses for the gauge bosons.

The Higgs mechanism in the SM

In the slightly more complicated non–abelian case of the SM, we need to generate masses for the three gauge bosons $W^\pm$ and Z but the photon should remain massless and QED must stay an exact symmetry. Therefore, we need at least 3 degrees of freedom for the scalar fields. The simplest choice is a complex SU(2) doublet of scalar fields ϕ

$$\Phi = \begin{pmatrix} \phi^+ \\ \phi^0 \end{pmatrix} , \quad Y_\phi = +1 \tag{1.29}$$

To the SM Lagrangian discussed in the previous subsection, but where we ignore the strong interaction part

$$\mathcal{L}_{\rm SM} = -\frac{1}{4} W^a_{\mu\nu} W^{\mu\nu}_a - \frac{1}{4} B_{\mu\nu} B^{\mu\nu} + \overline{L}\, i D_\mu \gamma^\mu\, L + \overline{e}_R\, i D_\mu \gamma^\mu\, e_R \ \cdots \tag{1.30}$$

we need to add the invariant terms of the scalar field part

$$\mathcal{L}_S = (D^\mu \Phi)^\dagger (D_\mu \Phi) - \mu^2 \Phi^\dagger \Phi - \lambda (\Phi^\dagger \Phi)^2 \tag{1.31}$$

For $\mu^2 < 0$, the neutral component of the doublet field Φ will develop a vacuum expectation value [the vev should not be in the charged direction to preserve $\mathrm{U}(1)_{\rm QED}$]

$$\langle\, \Phi \,\rangle_0 \equiv \langle\, 0 \,|\, \Phi \,|\, 0 \,\rangle = \begin{pmatrix} 0 \\ \frac{v}{\sqrt{2}} \end{pmatrix} \quad \text{with} \quad v = \left(-\frac{\mu^2}{\lambda} \right)^{1/2} \tag{1.32}$$

We can then make the same exercise as previously:

– write the field Φ in terms of four fields $\theta_{1,2,3}(x)$ and $H(x)$ at first order:

$$\Phi(x) = \begin{pmatrix} \theta_2 + i\theta_1 \\ \frac{1}{\sqrt{2}}(v+H) - i\theta_3 \end{pmatrix} = e^{i\theta_a(x)\tau^a(x)/v} \begin{pmatrix} 0 \\ \frac{1}{\sqrt{2}}(v + H(x)\,) \end{pmatrix} \tag{1.33}$$

– make a gauge transformation on this field to move to the unitary gauge:

$$\Phi(x) \to e^{-i\theta_a(x)\tau^a(x)}\, \Phi(x) = \frac{1}{\sqrt{2}} \begin{pmatrix} 0 \\ v + H(x) \end{pmatrix} \tag{1.34}$$

– then fully expand the term $|D_\mu \Phi)|^2$ of the Lagrangian $\mathcal{L}_S$:

$$\begin{aligned} |D_\mu \Phi)|^2 &= \left| \left(\partial_\mu - i g_2 \frac{\tau_a}{2} W^a_\mu - i g_1 \frac{1}{2} B_\mu \right) \Phi \right|^2 \\ &= \frac{1}{2} \left| \begin{pmatrix} \partial_\mu - \frac{i}{2}(g_2 W^3_\mu + g_1 B_\mu) & -\frac{ig_2}{2}(W^1_\mu - iW^2_\mu) \\ -\frac{ig_2}{2}(W^1_\mu + iW^2_\mu) & \partial_\mu + \frac{i}{2}(g_2 W^3_\mu - g_1 B_\mu) \end{pmatrix} \begin{pmatrix} 0 \\ v + H \end{pmatrix} \right|^2 \\ &= \frac{1}{2}(\partial_\mu H)^2 + \frac{1}{8} g_2^2 (v+H)^2 |W^1_\mu + iW^2_\mu|^2 + \frac{1}{8}(v+H)^2 |g_2 W^3_\mu - g_1 B_\mu|^2 \end{aligned}$$

– define the new fields $W_\mu^\pm$ and Z_μ [A_μ is the field orthogonal to Z_μ]:

$$W^\pm = \frac{1}{\sqrt{2}}(W_\mu^1 \mp iW_\mu^2) \ , \ Z_\mu = \frac{g_2 W_\mu^3 - g_1 B_\mu}{\sqrt{g_2^2+g_1^2}} \ , \ A_\mu = \frac{g_2 W_\mu^3 + g_1 B_\mu}{\sqrt{g_2^2+g_1^2}} \tag{1.35}$$

– and pick up the terms which are bilinear in the fields $W^\pm, Z, A$:

$$M_W^2 W_\mu^+ W^{-\mu} + \frac{1}{2} M_Z^2 Z_\mu Z^\mu + \frac{1}{2} M_A^2 A_\mu A^\mu \tag{1.36}$$

The W and Z bosons have acquired masses, while the photon is still massless

$$M_W = \frac{1}{2} v g_2 \ , \ M_Z = \frac{1}{2} v \sqrt{g_2^2+g_1^2} \ , \ M_A = 0 \tag{1.37}$$

Thus, we have achieved (half of) our goal: by spontaneously breaking the symmetry $\mathrm{SU(2)_L} \times \mathrm{U(1)_Y} \to \mathrm{U(1)_Q}$, three Goldstone bosons have been absorbed by the $W^\pm$ and Z bosons to form their longitudinal components and to get their masses. Since the $\mathrm{U(1)_Q}$ symmetry is still unbroken, the photon which is its generator, remains massless as it should be.

Up to now, we have discussed only the generation of gauge boson masses; but what about the fermion masses? In fact, we can also generate the fermion masses using the same scalar field Φ, with hypercharge Y=1, and the isodoublet $\tilde{\Phi} = i\tau_2 \Phi^*$, which has hypercharge Y=–1. For any fermion generation, we introduce the $\mathrm{SU(2)_L} \times \mathrm{U(1)_Y}$ invariant Yukawa Lagrangian

$$\mathcal{L}_F = -\lambda_e \, \bar{L} \, \Phi \, e_R - \lambda_d \, \bar{Q} \, \Phi \, d_R - \lambda_u \, \bar{Q} \, \tilde{\Phi} \, u_R \ + \ h.c. \tag{1.38}$$

and repeat the same exercise as above. Taking for instance the case of the electron, one obtains

$$\begin{aligned} \mathcal{L}_F &= -\frac{1}{\sqrt{2}} \lambda_e \, (\bar{\nu}_e, \bar{e}_L) \begin{pmatrix} 0 \\ v+H \end{pmatrix} e_R \ + \cdots \\ &= -\frac{1}{\sqrt{2}} \, \lambda_e \, (v+H) \, \bar{e}_L e_R \ + \cdots \end{aligned} \tag{1.39}$$

The constant term in front of $\bar{f}_L f_R$ (and h.c.) is identified with the fermion mass

$$m_e = \frac{\lambda_e \, v}{\sqrt{2}} \ , \ m_u = \frac{\lambda_u \, v}{\sqrt{2}} \ , \ m_d = \frac{\lambda_d \, v}{\sqrt{2}} \tag{1.40}$$

Thus, with the same isodoublet Φ of scalar fields, we have generated the masses of both the weak vector bosons $W^\pm, Z$ and the fermions, while preserving the SU(2)×U(1) gauge symmetry, which is now spontaneously broken or hidden. The electromagnetic $\mathrm{U(1)_Q}$ symmetry, as well as the SU(3) color symmetry, stay unbroken. The Standard Model refers, in fact, to SU(3)×SU(2)×U(1) gauge invariance when combined with the electroweak symmetry breaking mechanism. Very often, the electroweak sector of the theory is also referred to as the SM; in this review we will use this name for both options.

1.1.3 The SM Higgs particle and the Goldstone bosons

The Higgs particle in the SM

Let us finally come to the Higgs boson itself. The kinetic part of the Higgs field, $\frac{1}{2}(\partial_\mu H)^2$, comes from the term involving the covariant derivative $|D_\mu \Phi|^2$, while the mass and self–interaction parts, come from the scalar potential $V(\Phi) = \mu^2 \Phi^\dagger \Phi + \lambda (\Phi^\dagger \Phi)^2$

$$V = \frac{\mu^2}{2}(0, v+H)\begin{pmatrix} 0 \\ v+H \end{pmatrix} + \frac{\lambda}{4}\left|(0, v+H)\begin{pmatrix} 0 \\ v+H \end{pmatrix}\right|^2 \tag{1.41}$$

Using the relation $v^2 = -\mu^2/\lambda$, one obtains

$$V = -\frac{1}{2}\lambda v^2 (v+H)^2 + \frac{1}{4}\lambda (v+H)^4 \tag{1.42}$$

and finds that the Lagrangian containing the Higgs field H is given by

$$\begin{aligned} \mathcal{L}_H &= \frac{1}{2}(\partial_\mu H)(\partial^\mu H) - V \\ &= \frac{1}{2}(\partial^\mu H)^2 - \lambda v^2 H^2 - \lambda v H^3 - \frac{\lambda}{4} H^4 \end{aligned} \tag{1.43}$$

From this Lagrangian, one can see that the Higgs boson mass simply reads

$$M_H^2 = 2\lambda v^2 = -2\mu^2 \tag{1.44}$$

and the Feynman rules[7] for the Higgs self–interaction vertices are given by

$$g_{H^3} = (3!) i\lambda v = 3i\,\frac{M_H^2}{v}\ ,\ g_{H^4} = (4!) i\frac{\lambda}{4} = 3i\frac{M_H^2}{v^2} \tag{1.45}$$

As for the Higgs boson couplings to gauge bosons and fermions, they were almost derived previously, when the masses of these particles were calculated. Indeed, from the Lagrangian describing the gauge boson and fermion masses

$$\mathcal{L}_{M_V} \sim M_V^2 \left(1 + \frac{H}{v}\right)^2\ ,\ \mathcal{L}_{m_f} \sim -m_f \left(1 + \frac{H}{v}\right) \tag{1.46}$$

one obtains also the Higgs boson couplings to gauge bosons and fermions

$$g_{Hff} = i\frac{m_f}{v}\ ,\ g_{HVV} = -2i\frac{M_V^2}{v}\ ,\ g_{HHVV} = -2i\frac{M_V^2}{v^2} \tag{1.47}$$

This form of the Higgs couplings ensures the unitarity of the theory [7] as will be seen later. The vacuum expectation value v is fixed in terms of the W boson mass M_W or the Fermi constant G_μ determined from muon decay [see next section]

$$M_W = \frac{1}{2} g_2 v = \left(\frac{\sqrt{2} g^2}{8 G_\mu}\right)^{1/2} \Rightarrow v = \frac{1}{(\sqrt{2} G_\mu)^{1/2}} \simeq 246 \text{ GeV} \tag{1.48}$$

[7] The Feynman rule for these vertices are obtained by multiplying the term involving the interaction by a factor $-i$. One includes also a factor $n!$ where n is the number of identical particles in the vertex.

We will see in the course of this review that it will be appropriate to use the Fermi coupling constant G_μ to describe the couplings of the Higgs boson, as some higher–order effects are effectively absorbed in this way. The Higgs couplings to fermions, massive gauge bosons as well as the self–couplings, are given in Fig. 1.2 using both v and G_μ. This general form of the couplings will be useful when discussing the Higgs properties in extensions of the SM.

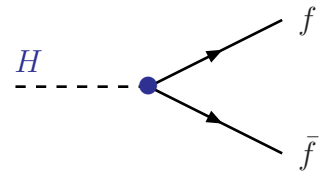

$$g_{Hff} \;=\; m_f/v \;=\; (\sqrt{2}G_\mu)^{1/2}\, m_f \qquad \times\,(i)$$

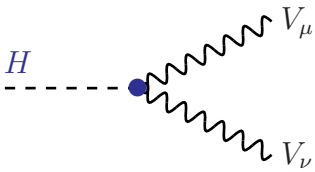

$$g_{HVV} \;=\; 2M_V^2/v \;=\; 2(\sqrt{2}G_\mu)^{1/2}\, M_V^2 \qquad \times\,(-ig_{\mu\nu})$$

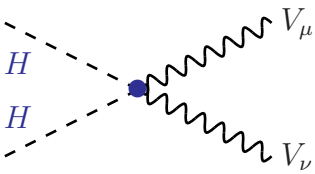

$$g_{HHVV} \;=\; 2M_V^2/v^2 \;=\; 2\sqrt{2}G_\mu\, M_V^2 \qquad \times\,(-ig_{\mu\nu})$$

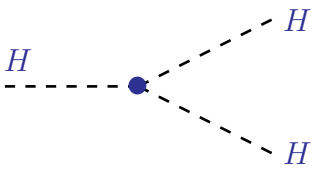

$$g_{HHH} \;=\; 3M_H^2/v \;=\; 3(\sqrt{2}G_\mu)^{1/2}\, M_H^2 \qquad \times\,(i)$$

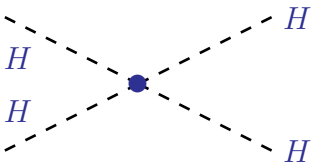

$$g_{HHHH} \;=\; 3M_H^2/v^2 \;=\; 3\sqrt{2}G_\mu\, M_H^2 \qquad \times\,(i)$$

Figure 1.2: The Higgs boson couplings to fermions and gauge bosons and the Higgs self–couplings in the SM. The normalization factors of the Feynman rules are also displayed.

Note that the propagator of the Higgs boson is simply given, in momentum space, by

$$\Delta_{HH}(q^2) = \frac{i}{q^2 - M_H^2 + i\epsilon} \tag{1.49}$$

The Goldstone bosons

In the unitary gauge, the physical spectrum of the SM is clear: besides the fermions and the massless photon [and gluons], we have the massive $V = W^\pm$ and Z bosons and the Goldstones do not appear. The propagators of the vector bosons in this gauge are given by

$$\Delta^{\mu\nu}_{VV}(q) = \frac{-i}{q^2 - M_V^2 + i\epsilon}\left[g^{\mu\nu} - \frac{q^\mu q^\nu}{M_V^2}\right] \tag{1.50}$$

The first term, $\propto g^{\mu\nu}$, corresponds to the propagation of the transverse component of the V boson [the propagator of the photon is simply $-ig^{\mu\nu}/q^2$], while the second term, $\propto q_\mu q_\nu$, corresponds to the propagation of the longitudinal component which, as can be seen, does not vanish $\propto 1/q^2$ at high energies. This terms lead to very complicated cancellations in the invariant amplitudes involving the exchange of V bosons at high energies and, even worse, make the renormalization program very difficult to carry out, as the latter usually makes use of four–momentum power counting analyses of the loop diagrams. It is more convenient to work in R_ξ gauges where gauge fixing terms are added to the SM Lagrangian [30]

$$\mathcal{L}_{\rm GF} = \frac{-1}{2\xi}\left[2(\partial^\mu W^+_\mu - i\xi M_W w^+)(\partial^\mu W^-_\mu - i\xi M_W w^-) + (\partial^\mu Z_\mu - i\xi M_Z w^0)^2 + (\partial^\mu A_\mu)^2\right] \tag{1.51}$$

$w^0 \equiv G^0$ and $w^\pm \equiv G^\pm$ being the neutral and charged Goldstone bosons and where different choices of ξ correspond to different renormalizable gauges. In this case, the propagators of the massive gauge bosons are given by

$$\Delta^{\mu\nu}_{VV}(q) = \frac{-i}{q^2 - M_V^2 + i\epsilon}\left[g^{\mu\nu} + (\xi - 1)\frac{q^\mu q^\nu}{q^2 - \xi M_V^2}\right] \tag{1.52}$$

which in the unitary gauge, $\xi = \infty$, reduces to the expression eq. (1.50). Usually, one uses the 't Hooft–Feynman gauge $\xi = 1$, where the $q^\mu q^\nu$ term is absent, to simplify the calculations; another popular choice is the Landau gauge, $\xi = 0$. In renormalizable R_ξ gauges, the propagators of the Goldstone bosons are given by

$$\begin{aligned} \Delta_{w^0 w^0}(q^2) &= \frac{i}{q^2 - \xi M_Z^2 + i\epsilon} \\ \Delta_{w^\pm w^\pm}(q^2) &= \frac{i}{q^2 - \xi M_W^2 + i\epsilon} \end{aligned} \tag{1.53}$$

and as can be seen, in the unitary gauge $\xi = \infty$, the Goldstone bosons do not propagate and decouple from the theory as they should, while in the Landau gauge they are massless and do not interact with the Higgs particle. In the 't Hooft–Feynman gauge, the Goldstone bosons are part of the spectrum and have "masses" $\propto M_V$. Any dependence on ξ should however be absent from physical matrix elements squared, as the theory must be gauge invariant.

Note that the couplings of the Goldstone bosons to fermions are, as in the case of the Higgs boson, proportional to the fermion masses

$$\begin{aligned} g_{G^0 ff} &= -2I_f^3 \frac{m_f}{v} \\ g_{G^- ud} &= \frac{-i}{\sqrt{2}v} V_{ud}[m_d(1-\gamma_5) - m_u(1+\gamma_5)] \end{aligned} \tag{1.54}$$

where V_{ud} is the CKM matrix element for quarks [see later] and which, in the case of leptons [where one has to set $m_d = m_\ell$ and $m_u = 0$ in the equation above], is equal to unity. The couplings of the Goldstones to gauge bosons are simply those of scalar spin–zero particles.

The longitudinal components of the W and Z bosons give rise to interesting features which occur at high energies and that we shortly describe below. In the gauge boson rest frame, one can define the transverse and longitudinal polarization four–vectors as

$$\epsilon^\mu_{T_1} = (0,1,0,0)\,, \quad \epsilon^\mu_{T_2} = (0,0,1,0)\,, \quad \epsilon^\mu_L = (0,0,0,1) \tag{1.55}$$

For a four–momentum $p^\mu = (E,0,0,|\vec{p}|)$, after a boost along the z direction, the transverse polarizations remain the same while the longitudinal polarization becomes

$$\epsilon^\mu_L = \left(\frac{|\vec{p}|}{M_V}, 0, 0, \frac{E}{M_V}\right) \stackrel{E \gg M_V}{\longrightarrow} \frac{p_\mu}{M_V} \tag{1.56}$$

Since this polarization is proportional to the gauge boson momentum, at very high energies, the longitudinal amplitudes will dominate in the scattering of gauge bosons.

In fact, there is a theorem, called the Electroweak Equivalence Theorem [31–33], which states that at very high energies, the longitudinal massive vector bosons can be replaced by the Goldstone bosons. In addition, in many processes such as vector boson scattering, the vector bosons themselves can by replaced by their longitudinal components. The amplitude for the scattering of n gauge bosons in the initial state to n' gauge bosons in the final state is simply the amplitude for the scattering of the corresponding Goldstone bosons

$$\begin{aligned} A(V^1 \cdots V^n \to V^1 \cdots V^{n'}) &\sim A(V_L^1 \cdots V_L^n \to V_L^1 \cdots V_L^{n'}) \\ &\sim A(w^1 \cdots w^n \to w^1 \cdots w^{n'}) \end{aligned} \tag{1.57}$$

Thus, in this limit, one can simply replace in the SM scalar potential, the W and Z bosons by their corresponding Goldstone bosons $w^\pm, w_0$, leading to

$$V = \frac{M_H^2}{2v}(H^2 + w_0^2 + 2w^+w^-)H + \frac{M_H^2}{8v^2}(H^2 + w_0^2 + 2w^+w^-)^2 \tag{1.58}$$

and use this potential to calculate the amplitudes for the processes involving weak vector bosons. The calculations are then extremely simple, since one has to deal only with interactions among scalar particles.

1.1.4 The SM interactions and parameters

In this subsection, we summarize the interactions of the fermions and gauge bosons in the electroweak SM [for the strong interactions of quarks and gluons, the discussion held in §1.1.1 is sufficient for our purpose] and discuss the basic parameters of the SM and their experimental determination.

The equations for the field rotation which lead to the physical gauge bosons, eq. (1.35), define the electroweak mixing angle $\sin\theta_W$

$$\sin\theta_W = \frac{g_1}{\sqrt{g_1^2+g_2^2}} = \frac{e}{g_2} \tag{1.59}$$

which can be written in terms of the W and Z boson masses as

$$\sin^2\theta_W \equiv s_W^2 = 1 - c_W^2 = 1 - \frac{M_W^2}{M_Z^2} \tag{1.60}$$

Using the fermionic part of the SM Lagrangian, eq. (1.11), written in terms of the new fields and writing explicitly the covariant derivative, one obtains

$$\begin{aligned} \mathcal{L}_{\rm NC} &= eJ_\mu^{\rm A}A^\mu + \frac{g_2}{\cos\theta_W}J_\mu^Z Z^\mu \\ \mathcal{L}_{\rm CC} &= \frac{g_2}{\sqrt{2}}(J_\mu^+ W^{+\mu} + J_\mu^- W^{-\mu}) \end{aligned} \tag{1.61}$$

for the neutral and charged current parts, respectively. The currents J_μ are then given by

$$\begin{aligned} J_\mu^A &= Q_f \bar{f}\gamma_\mu f \\ J_\mu^Z &= \frac{1}{4}\bar{f}\gamma_\mu[(2I_f^3 - 4Q_f\sin^2\theta_W) - \gamma_5(2I_f^3)]f \\ J_\mu^+ &= \frac{1}{2}\bar{f}_u\gamma_\mu(1-\gamma_5)f_d \end{aligned} \tag{1.62}$$

where $f_u(f_d)$ is the up–type (down–type) fermion of isospin $+(-)\frac{1}{2}$.

In terms of the electric charge Q_f of the fermion f and with $I_f^3 = \pm\frac{1}{2}$ the left–handed weak isospin of the fermion and the weak mixing angle $s_W^2 = 1 - c_W^2 \equiv \sin^2\theta_W$, one can write the vector and axial vector couplings of the fermion f to the Z boson

$$v_f = \frac{\hat{v}_f}{4s_W c_W} = \frac{2I_f^3 - 4Q_f s_W^2}{4s_W c_W} \quad , \quad a_f = \frac{\hat{a}_f}{4s_W c_W} = \frac{2I_f^3}{4s_W c_W} \tag{1.63}$$

where we also defined the reduced $Zf\bar{f}$ couplings $\hat{v}_f, \hat{a}_f$. In the case of the W boson, its vector and axial–vector couplings couplings to fermions are simply

$$v_f = a_f = \frac{1}{2\sqrt{2}s_W} = \frac{\hat{a}_f}{4s_W} = \frac{\hat{v}_f}{4s_W} \tag{1.64}$$

These results are only valid in the one–family approximation. While the extension to three families is straightforward for the neutral currents, there is a complication in the case of the charged currents: the current eigenstates for quarks q' are not identical to the mass eigenstates q. If we start by u–type quarks being mass eigenstates, in the down–type quark sector, the two sets are connected by a unitary transformation [34]

$$(d', s', b') = V(d, s, b) \tag{1.65}$$

where V is the 3×3 Cabibbo–Kobayashi–Maskawa matrix. The unitarity of V insures that the neutral currents are diagonal in both bases: this is the GIM mechanism [35] which ensures a natural absence of flavor changing neutral currents (FCNC) at the tree–level in the SM. For leptons, the mass and current eigenstates coincide since in the SM, the neutrinos are assumed to be massless, which is an excellent approximation in most purposes.

Note that the relative strength of the charged and neutral currents, $J_Z^\mu J_{\mu Z}/J^{\mu+}J_\mu^-$ can be measured by the parameter ρ [36] which, using previous formulae, is given by

$$\rho = \frac{M_W^2}{c_W^2 M_Z^2} \tag{1.66}$$

and is equal to unity in the SM, eq. (1.60). This is a direct consequence of the choice of the representation of the Higgs field responsible of the breaking of the electroweak symmetry. In a model which makes use of an arbitrary number of Higgs multiplets Φ_i with isospin I_i, third component I_i^3 and vacuum expectation values v_i, one obtains for this parameter

$$\rho = \frac{\sum_i \left[I_i(I_i+1) - (I_i^3)^2\right] v_i^2}{2\sum_i (I_i^3)^2 v_i^2} \tag{1.67}$$

which is also unity for an arbitrary number of doublet [as well as singlet] fields. This is due to the fact that in this case, the model has a custodial SU(2) global symmetry. In the SM, this symmetry is broken at the loop level when fermions of the same doublets have different masses and by the hypercharge group. The radiative corrections to this parameter will be discussed in some detail in the next section.

Finally, self–couplings among the gauge bosons are present in the SM as a consequence of the non abelian nature of the $\mathrm{SU(2)_L} \times \mathrm{U(1)_Y}$ symmetry. These couplings are dictated by the structure of the symmetry group as discussed in §1.1.1 and, for instance, the triple self–couplings among the W and the $V = \gamma, Z$ bosons are given by

$$\mathcal{L}_{WWV} = i g_{WWV} \left[W^\dagger_{\mu\nu} W^\mu V^\nu - W^\dagger_\mu V_\nu W^{\mu\nu} + W^\dagger_\mu W_\nu V^{\mu\nu}\right] \tag{1.68}$$

with $g_{WW\gamma} = e$ and $g_{WWZ} = e c_W/s_W$.

This concludes our description of the gauge interactions in the SM. We turn now to the list of the model parameters that we will need in our subsequent discussions.

The fine structure constant

The QED fine structure constant defined in the classical Thomson limit $q^2 \sim 0$ of Compton scattering, is one of the best measured quantities in Nature

$$\alpha(0) \equiv e^2/(4\pi) = 1/137.03599976\,(50) \tag{1.69}$$

However, the physics which is studied at present colliders is at scales of the order of 100 GeV and the running between $q^2 \sim 0$ and this scale must be taken into account. This running is defined as the difference between the [transverse components of the] vacuum polarization function of the photon at the two scales and, for $q^2 = M_Z^2$ for instance, one has

$$\alpha(M_Z^2) = \frac{\alpha(0)}{1-\Delta\alpha} \quad , \quad \Delta\alpha(M_Z^2) = \Pi_{\gamma\gamma}(0) - \Pi_{\gamma\gamma}(M_Z^2) \tag{1.70}$$

Since QED is a vectorial theory, all heavy particles decouple from the photon two–point function by virtue of the Appelquist–Carazzone theorem [37] and only the light particles, i.e. the SM light fermions, have to be taken into account in the running. [For instance, the top quark contribution is $\Delta^{\rm top}\alpha \sim -7 \cdot 10^{-5}$, while the small W boson contribution is not gauge invariant by itself and has to be combined with direct vertex and box corrections.]

The contribution of the e, μ and τ leptons to $\Delta\alpha$ simply reads [38]

$$\Delta\alpha^{\rm lept}(M_Z^2) = \sum_{\ell=e,\mu,\tau} \frac{\alpha}{3\pi}\left[\log\frac{M_Z^2}{m_\ell^2} - \frac{5}{3}\right] + \mathcal{O}\left(\frac{m_\ell^2}{M_Z^2}\right) + \mathcal{O}(\alpha^2) + \mathcal{O}(\alpha^3) \simeq 0.0315 \tag{1.71}$$

For the contribution of light quarks, one has to evaluate $\Pi_{\gamma\gamma}$ at very low energies where perturbation theory fails for the strong interaction. In fact, even if it were not the case, the light quark masses are not known sufficiently precisely to be used as inputs. Fortunately, it is possible to circumvent these complications and to derive the hadronic contribution in an indirect way, taking all orders of the strong interaction into account. Indeed, one can use the optical theorem to relate the imaginary part of the photon two–point function to the $\gamma f \bar{f}$ vertex amplitude and make use of the dispersion relation

$$\Delta\alpha^{\rm had}(M_Z^2) = -\frac{\alpha M_Z^2}{3\pi}{\rm Re}\left(\int_{4m_\pi^2}^{\infty} {\rm d}s' \frac{R_{\gamma\gamma}(s')}{s'(s'-M_Z^2)}\right), \; R_{\gamma\gamma}(s) = \frac{\sigma(e^+e^- \to \gamma^* \to {\rm had.})}{\sigma(e^+e^- \to \gamma^* \to \mu^+\mu^-)} \tag{1.72}$$

with the quantity $R_{\gamma\gamma}(s)$ measured in the problematic range using experimental data, and using perturbative QCD for the high energy range [39, 40]. Taking into account all available information from various experiments, one obtains for the hadronic contribution [40]

$$\Delta\alpha^{\rm had}(M_Z^2) = 0.02761 \pm 0.00036 \tag{1.73}$$

This result is slightly improved if one uses additional information from τ decays $\tau^- \to \nu_\tau W^* \to \nu_\tau +$ hadrons, modulo some reasonable theoretical assumptions. The latest world average value for the running electromagnetic coupling constant α at the scale M_Z is therefore

$$\alpha^{-1}(M_Z^2) = 128.951 \pm 0.027 \tag{1.74}$$

The Fermi coupling constant

Another quantity in particle physics which is very precisely measured is the muon decay lifetime, which is directly related to the Fermi coupling constant in the effective four–point Fermi interaction but including QED corrections [41]

$$\frac{1}{\tau_\mu} = \frac{G_\mu^2 m_\mu^5}{192\pi^3}\left(1-\frac{8m_e^2}{m_\mu^2}\right)\left[1+1.810\frac{\alpha}{\pi}+(6.701\pm 0.002)\left(\frac{\alpha}{\pi}\right)^2\right] \tag{1.75}$$

which leads to the precise value

$$G_\mu = (1.16637 \pm 0.00001)\cdot 10^{-5}\ \text{GeV}^{-2} \tag{1.76}$$

In the SM, the decay occurs through gauge interactions mediated by W boson exchange and therefore, one obtains a relation between the W, Z masses, the QED constant α and G_μ

$$\frac{G_\mu}{\sqrt{2}} = \frac{g_2}{2\sqrt{2}}\cdot\frac{1}{M_W^2}\cdot\frac{g_2}{2\sqrt{2}} = \frac{\pi\alpha}{2M_W^2 s_W^2} = \frac{\pi\alpha}{2M_W^2(1-M_W^2/M_Z^2)} \tag{1.77}$$

The strong coupling constant

The strong coupling constant has been precisely determined in various experiments in e^+e^- collisions[8] and in deep inelastic scattering; for a review, see Refs. [9, 42]. The most reliable results have been obtained at LEP where several methods can be used: inclusive hadronic rates in Z decays [$R_\ell, \sigma^0_{\rm had}$ and Γ_Z, see 1.2.1 later], inclusive rates in hadronic τ decays, event shapes and jet rates in multi–jet production. The world average value is given by [9]

$$\alpha_s = 0.1172 \pm 0.002 \tag{1.78}$$

which corresponds to a QCD scale for 5 light flavors $\Lambda^5_{\rm QCD} = 216^{+25}_{-24}$ MeV. Using this value of Λ, one can determine α_s at any energy scale μ up to three–loop order in QCD [43]

$$\alpha_s(\mu) = \frac{4\pi}{\beta_0\ell_\mu}\left[1-\frac{2\beta_1}{\beta_0^2}\frac{\log\ell_\mu}{\ell_\mu}+\frac{4\beta_1^2}{\beta_0^4\ell_\mu^2}\left(\left(\log\ell_\mu-\frac{1}{2}\right)^2+\frac{\beta_2\beta_0}{8\beta_1^2}-\frac{5}{4}\right)\right] \tag{1.79}$$

with $\ell_\mu \equiv \log(\mu^2/\Lambda^2)$ and the β_i coefficients given by

$$\beta_0 = 11-\frac{2}{3}N_f\ ,\ \beta_1 = 51-\frac{19}{3}N_f\ ,\ \beta_2 = 2857-\frac{5033}{9}N_f+\frac{325}{27}N_f^2 \tag{1.80}$$

with N_f being the number of quarks with a mass smaller than the energy scale μ.

[8]Note that measurements of α_s have been performed at various energies, from $\sqrt{s}\sim 1.8$ GeV in τ–lepton decays at LEP1 to $\sqrt{s}\sim 210$ GeV at LEP2, *en passant par* $\sqrt{s}\sim 20$ GeV at JADE, confirming in an unambiguous way the QCD prediction of asymptotic freedom. The non–abelian structure of QCD and the three–gluon vertex has also been tested at LEP in four jet events.

The fermion masses

The top quark has been produced at the Tevatron in the reaction $p\bar{p} \to q\bar{q}/gg \to t\bar{t}$ and in the SM, it decays almost 100% of the time into a b quark and a W boson, $t \to bW^+$. The top quark mass is extracted mainly in the lepton plus jets and dilepton channels of the decaying W bosons, and combining CDF and DØ results, one obtains the average mass value [15]

$$m_t = 178.0 \pm 4.3 \text{ GeV} \tag{1.81}$$

The branching ratio of the decay $t \to Wb$ [compared to decays $t \to Wq$] has been measured to be $\text{BR}(t \to Wb) = 0.94^{+0.31}_{-0.24}$ [9], allowing to extract the value of the V_{tb} CKM matrix element, $|V_{tb}| = 0.97^{+0.16}_{-0.12}$. The top quark decay width in the SM is predicted to be [44–46]

$$\Gamma_t \simeq \Gamma(t \to bW^+) = \frac{G_\mu m_t^3}{8\sqrt{2}\pi}|V_{tb}|^2 \left(1 - \frac{M_W^2}{m_t^2}\right)^2 \left(1 + 2\frac{M_W^2}{m_t^2}\right)\left(1 - 2.72\frac{\alpha_s}{\pi}\right) + \mathcal{O}(\alpha_s^2, \alpha) \tag{1.82}$$

and is of the order of $\Gamma_t \simeq 1.8$ GeV for $m_t \simeq 180$ GeV.

Besides the top quark mass, the masses of the bottom and charm quarks [and to a lesser extent the mass of the strange quark] are essential ingredients in Higgs physics. From many measurements, one obtains the following values for the pole or physical masses m_Q [47]

$$m_b = 4.88 \pm 0.07 \text{ GeV} \ , \ m_c = 1.64 \pm 0.07 \text{ GeV} \tag{1.83}$$

However, the masses which are needed in this context are in general not the pole quark masses but the running quark masses at a high scale corresponding to the Higgs boson mass. In the modified minimal subtraction or $\overline{\text{MS}}$ scheme, the relation between the pole masses and the running masses at the scale of the pole mass, $\overline{m}_Q(m_Q)$, can be expressed as [48]

$$\begin{aligned} \overline{m}_Q(m_Q) = m_Q \Big[1 - \frac{4}{3}\frac{\alpha_s(m_Q)}{\pi} + (1.0414 N_f - 14.3323)\frac{\alpha_s^2(m_Q)}{\pi^2}\Big] \\ +(-0.65269 N_f^2 + 26.9239 N_f - 198.7068)\frac{\alpha_s^3(m_Q)}{\pi^2}\Big] \end{aligned} \tag{1.84}$$

where α_s is the $\overline{\text{MS}}$ strong coupling constant evaluated at the scale of the pole mass $\mu = m_Q$. The evolution of $\overline{m}_Q$ from m_Q upward to a renormalization scale μ is

$$\overline{m}_Q(\mu) = \overline{m}_Q(m_Q)\frac{c[\alpha_s(\mu)/\pi]}{c[\alpha_s(m_Q)/\pi]} \tag{1.85}$$

with the function c, up to three–loop order, given by [49, 50]

$$\begin{aligned} c(x) &= (25x/6)^{12/25}\,[1 + 1.014x + 1.389\,x^2 + 1.091\,x^3] && \text{for } m_c < \mu < m_b \\ c(x) &= (23x/6)^{12/23}\,[1 + 1.175x + 1.501\,x^2 + 0.1725\,x^3] && \text{for } m_b < \mu < m_t \\ c(x) &= (7x/2)^{4/7}\,[1 + 1.398x + 1.793\,x^2 - 0.6834\,x^3] && \text{for } m_t < \mu \end{aligned} \tag{1.86}$$

For the charm quark mass for instance, the evolution is determined by the equation for $m_c < \mu < m_b$ up to the scale $\mu = m_b$, while for scales above the bottom mass the evolution must be restarted at $\mu = m_b$. Using as starting points the values of the t, b, c quark pole masses given previously and for $\alpha_s(M_Z) = 0.1172$ and $\mu = 100$ GeV, the $\overline{\rm MS}$ running t, b, c quark masses are displayed in Table 1.1. As can be seen, the values of the running b, c masses at the scale $\mu \sim 100$ GeV are, respectively, ~ 1.5 and ~ 2 times smaller than the pole masses, while the top quark mass is only slightly different.

For the strange quark, this approach fails badly below scales of $\mathcal{O}(1$ GeV) because of the the too strong QCD coupling. Fortunately, m_s will play only a minor role in Higgs physics and whenever it appears, we will use the value $\overline{m}_s(1\,\text{GeV}) = 0.2$ GeV.

Q	m_Q	$\overline{m}_Q(m_Q)$	$\overline{m}_Q(100$ GeV)
c	1.64 GeV	1.23 GeV	0.63 GeV
b	4.88 GeV	4.25 GeV	2.95 GeV
t	178 GeV	170.3 GeV	178.3 GeV

Table 1.1: The pole quark masses and the mass values in the $\overline{MS}$ scheme for the running masses at the scale m_Q and at a scale $\mu = 100$ GeV; $\alpha_s(M_Z) = 0.1172$.

The masses of the charged leptons are given by

$$m_\tau = 1.777 \text{ GeV}\,,\ m_\mu = 0.1056 \text{ GeV}\,,\ m_e = 0.511 \text{ MeV} \tag{1.87}$$

with the electron being too light to play any role in Higgs physics. The approximation of massless neutrinos will also have no impact on our discussion.

The gauge boson masses and total widths

Finally, an enormous number of Z bosons has been produced at LEP1 and SLC at c.m. energies close to the Z resonance, $\sqrt{s} \simeq M_Z$, and of W bosons at LEP2 and at the Tevatron. This allowed to make very precise measurements of the properties of these particles which provided stringent tests of the SM. This subject will be postponed to the next section. Here, we simply write the obtained masses and total decay widths of the two particles [8]

$$M_Z = 91.1875 \pm 0.0021 \text{ GeV} \tag{1.88}$$

$$\Gamma_Z = 2.4952 \pm 0.0023 \text{ GeV} \tag{1.89}$$

and, averaging the LEP2 [51] and Tevatron [52] measurements,

$$M_W = 80.425 \pm 0.034 \text{ GeV} \tag{1.90}$$

$$\Gamma_W = 2.133 \pm 0.069 \text{ GeV} \tag{1.91}$$

which completes the list of SM parameters that we will use throughout this review.

1.2 High–precision tests of the SM

Except for the Higgs mass, all the parameters of the SM, the three gauge coupling constants, the masses of the weak vector bosons and fermions as well as the quark mixing angles, have been determined experimentally as seen in the previous section. Using these parameters, one can in principle calculate any physical observable and compare the result with experiment. Because the electroweak constants and the strong coupling constant at high energies are small enough, the first order of the perturbative expansion, the tree–level or Born term, is in general sufficient to give relatively good results for most of these observables. However, to have a more accurate description, one has to calculate the complicated higher–order terms of the perturbative series, the so–called radiative corrections. The renormalizability of the theory insures that these higher–order terms are finite once various formally divergent counterterms are added by fixing a finite set of renormalization conditions. The theory allows, thus, the prediction of any measurable with a high degree of accuracy.

Very precise experiments, which allow a sensitivity to these quantum corrections, have been made in the last fifteen years. The e^+e^- colliders LEP and SLC, which started operation in the late 80's, have collected an enormous amount of electroweak precision data. Measurements at the Z–pole [where the production cross section is extremely large, allowing to collect more than ten million events at LEP1] of the Z boson partial and total decay widths, polarization and forward–backward asymmetries where made at the amazing accuracy of one percent to one per mille [8]. The W boson properties have been also determined at the $p\bar{p}$ collider Tevatron with a c.m. energy of $\sqrt{s} = 1.8$ TeV [52] and at LEP2 with a c.m. energy up to $\sqrt{s} = 209$ GeV [51] with a constant increase in accuracy. Many other high–precision measurements have been performed at much lower energies.

At the same time, a large theoretical effort has been devoted to the calculation of the radiative corrections to the electroweak observables, to match the accuracies which have been or which could be reached experimentally [53–56]. The availability of both highly accurate measurements and theoretical predictions, at the level of 0.1% precision and better, provides stringent tests of the SM. These high-precision electroweak data are a unique tool in the search for indirect effects, through possible small deviations of the experimental results from the theoretical predictions of the minimal SM, and constitute an excellent probe of its still untested scalar sector, as well as a probe of New Physics beyond the SM.

In this section, after summarizing the high–precision observables in the SM, we will describe the formalism needed to incorporate the radiative corrections and how the dominant part of the latter can be approximated. This will allow to set the notation which will be used later and the framework which will be necessary to discuss the searches for the virtual effects of the Higgs bosons in electroweak observables, and to incorporate the important higher–order corrections in Higgs boson decay and production.

1.2.1 Observables in Z boson decays

A large variety of precision tests can be performed in e^+e^- experiments with center–of–mass energies near the Z–resonance in the process $e^+e^- \to f\bar{f}$ which is mediated by the exchange of a photon and a Z boson [57]. The differential cross section is a binomial in $\cos\theta$, where θ is the angle between the electron and the final fermion f. At tree–level, for unpolarized initial beams and for massless final state fermions $f \neq e$, it is given by

$$\frac{\mathrm{d}\sigma}{\mathrm{d}\cos\theta} = \frac{4\pi\alpha^2}{3s} N_c \left[\frac{3}{8}(1+\cos^2\theta)\sigma_U + \frac{3}{4}\cos\theta\sigma_F \right] \tag{1.92}$$

where σ_U and σ_F are given by [Γ_Z is the total decay width of the Z boson]

$$\begin{aligned} \sigma_U &= Q_e^2 Q_f^2 + 2Q_e Q_f v_e v_f \frac{s(s-M_Z^2)}{(s-M_Z^2)^2+\Gamma_Z^2 M_Z^2} + (a_e^2+v_e^2)(v_f^2+a_f^2)\frac{s^2}{(s-M_Z^2)^2+\Gamma_Z^2 M_Z^2} \\ \sigma_F &= 2Q_e Q_f a_e a_f \frac{s(s-M_Z^2)}{(s-M_Z^2)^2+\Gamma_Z^2 M_Z^2} + a_e v_e v_f a_f \frac{s^2}{(s-M_Z^2)^2+\Gamma_Z^2 M_Z^2} \end{aligned} \tag{1.93}$$

where the vector and axial vector couplings of the fermion f to the Z boson v_f and a_f [and the reduced couplings $\hat{v}_f$ and $\hat{a}_f$ to be used later on] have been given in eq. (1.63).

For center of mass energies near the Z resonance, $\sqrt{s} \simeq M_Z$, the Z boson exchange largely dominates. Integrating eq. (1.92) over the entire range of the angle θ, one obtains the total peak cross section

$$\sigma_0(e^+e^- \to Z \to f\bar{f}) \equiv \int_{-1}^{+1} \frac{\mathrm{d}\sigma}{\mathrm{d}\cos\theta} = \frac{12\pi}{M_Z^2} \times \frac{\Gamma_e \Gamma_f}{\Gamma_Z^2} \tag{1.94}$$

with the partial Z boson decay widths into massless fermion pairs given by

$$\Gamma_f \equiv \Gamma(Z \to f\bar{f}) = \frac{2\alpha}{3} N_c M_Z (v_f^2 + a_f^2) \tag{1.95}$$

Convenient measurable quantities which have been considered at LEP1 and SLC are, in this context, the ratio of Z boson partial widths

$$R_f = \frac{\Gamma(Z \to f\bar{f})}{\Gamma(Z \to \text{hadrons})} \tag{1.96}$$

If one integrates asymmetrically eq. (1.92) and normalizes to the total cross section, one obtains the forward–backward asymmetry for the decay of a Z boson into a fermion pair

$$A_{FB}^f \equiv \left[\int_0^{+1} \frac{\mathrm{d}\sigma}{\mathrm{d}\cos\theta} - \int_{-1}^{0} \frac{\mathrm{d}\sigma}{\mathrm{d}\cos\theta} \right] \times \sigma_0^{-1} \overset{\sqrt{s}=M_Z}{=} \frac{3}{4} A_e A_f \tag{1.97}$$

where the combinations A_f are given, in terms of the vector and axial vector couplings of the fermion f to the Z boson, by

$$A_f = \frac{2a_f v_f}{v_f^2 + a_f^2} \equiv \frac{2\hat{a}_f \hat{v}_f}{\hat{v}_f^2 + \hat{a}_f^2} \tag{1.98}$$

Note that if the initial e^- beams are longitudinally polarized [as it was the case at the SLC], one can construct left–right asymmetries and left–right forward–backward asymmetries; in addition one can measure the longitudinal polarization in τ decays and also define a polarization asymmetry. In terms of the combination of couplings A_f defined above, these observables can be written as

$$A^f_{LR} = A_e \quad , \quad A^f_{LR,FB} = \frac{3}{4} A_f \quad , \quad A^\tau_{\rm pol} = A_\tau \tag{1.99}$$

In particular A^f_{LR} [which is the same for all $f \neq e$] and $A^\tau_{\rm pol}$ are very sensitive to the precise value of $\sin^2\theta_W$, being proportional to the factor $\hat{v}_e \equiv 1 - 4s^2_W \sim 0$ for $s^2_W \sim 1/4$.

The tree–level expressions discussed above give results at the one percent level and hold in most cases, except in the case of b–quark final states where mass effects, $\mathcal{O}(4m_b^2/M_Z^2) \sim 0.01$, have to be taken into account, and in the production of e^+e^- final states where the complicated t–channel gauge boson exchange contributions have to be included [this process is particularly important since it allows to determine the absolute luminosity at e^+e^- colliders]. However, for a very precise description of the Z properties, one needs to include the one–loop radiative corrections and possibly some important higher–order effects. These radiative corrections fall into three categories [see Fig. 1.3]:

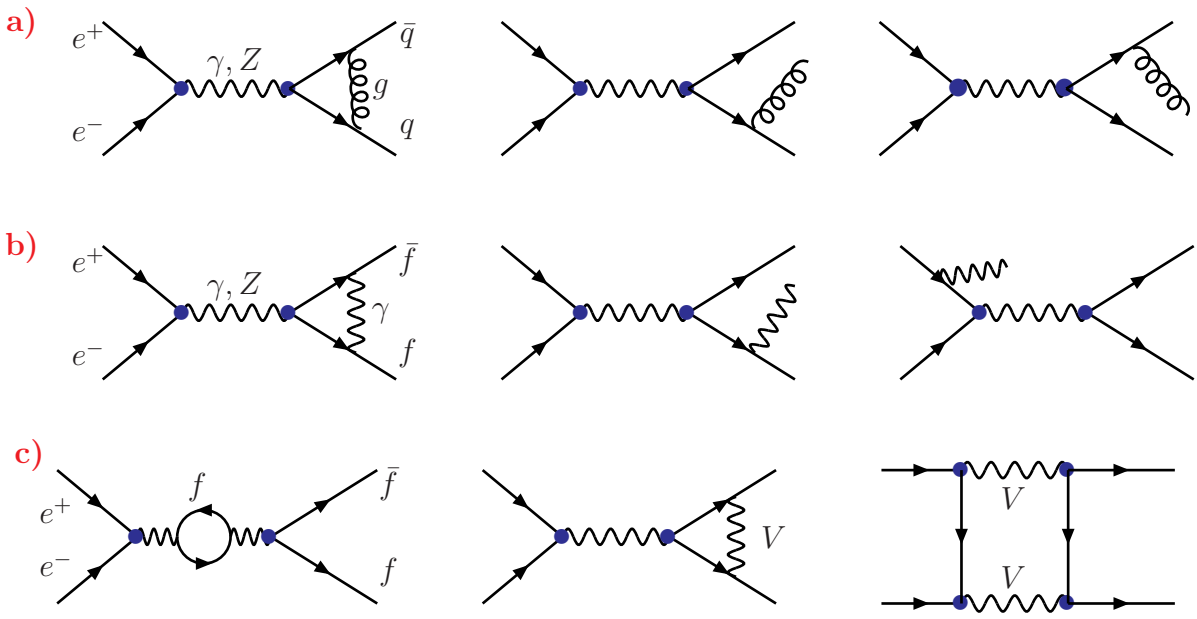

Figure 1.3: Examples of Feynman diagrams for the radiative corrections to the process $e^+e^- \to f\bar{f}$: a) virtual and real QCD corrections for quark final states, b) virtual QED corrections and initial and final state photon radiation and c) genuine electroweak corrections including self–energy, vertex and box corrections.

a) QCD corrections to final states quarks, where gluons are exchanged or emitted in the final state. For massless quarks the correction factors are

$$K^{\rm QCD}_{Z\to q\bar{q}} = 1 + \frac{\alpha_s}{\pi} + 1.41 \left(\frac{\alpha_s}{\pi}\right)^2 \tag{1.100}$$

for the partial decay widths $Z \to q\bar{q}$ or total cross section $\Gamma_q \propto \sigma(e^+e^- \to q\bar{q})$, and

$$K^{\rm QCD}_{A^q_{\rm FB}} = 1 - \frac{\alpha_s}{\pi} \tag{1.101}$$

for the forward–backward quark asymmetries. In fact these QCD factors are known to $\mathcal{O}(\alpha_s^3)$ for Γ_q and to $\mathcal{O}(\alpha_s^2)$ for A^q_{FB}; in the case of b–quarks one can include the mass effects at $\mathcal{O}(\alpha_s)$ which are also known [for a detailed discussion of all these corrections, see Ref. [58] e.g.]. Note that Γ_q allows for one of the cleanest and most precise determinations of α_s [42].

b) Pure electromagnetic corrections. These consist of initial and final state corrections where photons are exchanged in the $Zf\bar{f}$ vertices or emitted in the initial or final states. For final state corrections, it is sufficient to include the small

$$K^{\rm EM}_{Z\to f\bar{f}} = 1 + \frac{3}{4}Q_f^2\frac{\alpha}{\pi}\ ,\ K^{\rm EM}_{A^f_{FB}} = 1 - \frac{3}{4}Q_f^2\frac{\alpha}{\pi} \tag{1.102}$$

correction factors, while for initial state corrections, in particular the photon radiation (ISR), one can use the standard approach of structure function where the corrections can be exponentiated. This is performed by convoluting the Born cross section eq. (1.92) with a radiator function $G(s')$ for the full accessible c.m. energies $s' = xs$ after photon radiation

$$\sigma^{\rm ISR}(s) = \int_{x_0}^1 {\rm d}x\, G(xs)\sigma_{\rm Born}(xs)\ ,\ G(xs) = \beta(1-x)^{\beta-1}\delta_{V+S}(x) + \delta_H(x) \tag{1.103}$$

where x_0 is the minimum energy of the final state, $x_0 = 4m_f^2/s$ for $e^+e^- \to f\bar{f}$, and $G(x)$ is the radiator function, which is written in an exponentiated form to resum the infrared sensitive and large corrections. In the previous equation, $\beta = \alpha/\pi \times [\log s/m_e^2 - 1]$ and δ_{V+S}, δ_H contain, respectively, the virtual plus soft–photon contributions, and the hard–photon contributions, which are polynomials in $\log(s/m_e^2)$. Their expressions, as well as many details on ISR, FSR and their interference can be found in the reviews of Refs. [57, 59]. Note that all these corrections do not involve any other physics than well known QED.

c) Electroweak corrections. They involve non–photonic "direct" vertex and box corrections which are in general rather small [except in a few cases to be discussed later] as well as the "oblique" γ, W and Z boson self–energy corrections and the γ–Z mixing, which give the bulk of the contributions [56, 60]. In particular, the top quark [which was not yet discovered at the time LEP1 and SLC started] and the Higgs boson will enter the electroweak observables through their contributions to the W and Z boson self–energies. These electroweak corrections are discussed in some detail in the next subsection.

1.2.2 The electroweak radiative corrections

The electroweak radiative corrections can be cast into three main categories; Fig. 1.4:

a) The fermionic corrections to the gauge boson self–energies. They can be divided themselves into the light fermion $f \neq t$ contributions and the contribution of the heavy top quark $f = t$. For the contributions of quarks, one has to include the important corrections stemming from strong interactions.

b) The contributions of the Higgs particle to the W and Z boson self–energies both at the one–loop level and at the two–level when e.g. the heavy top quark is involved.

c) Vertex corrections to the Z decays into fermions, in particular into $b\bar{b}$ pairs, and vertex plus box contributions to muon decay [in which the bosonic contribution is not gauge invariant by itself and should be combined with the self–energy corrections]. There are also direct box corrections, but their contribution at the Z–peak is negligible.

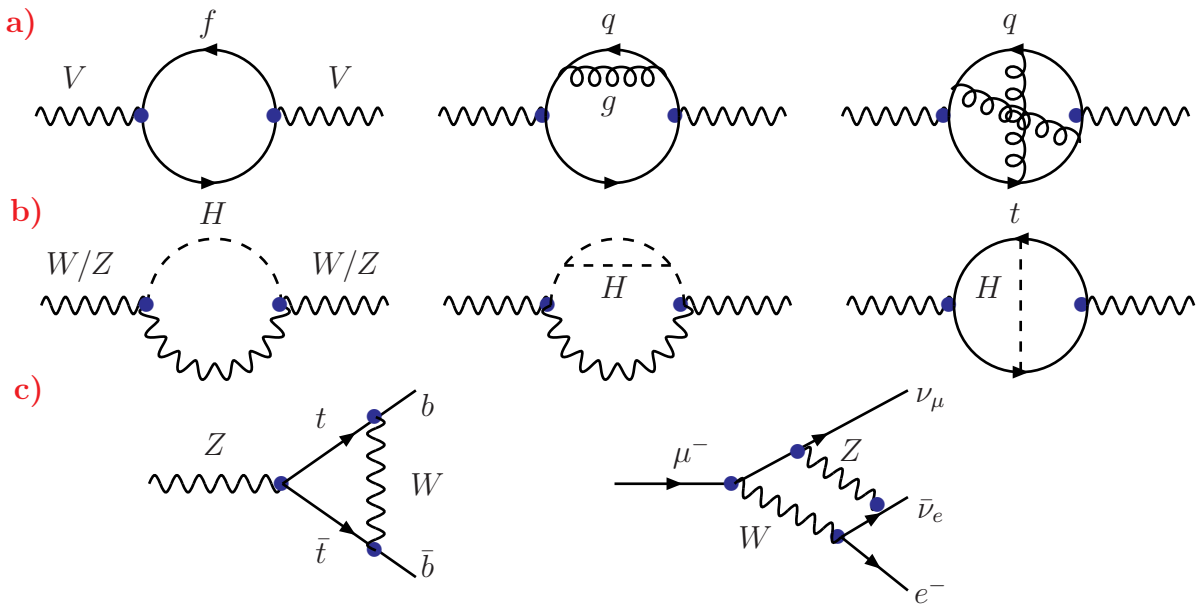

Figure 1.4: Generic Feynman diagrams for the main electroweak radiative corrections: a) fermionic contributions to the two–point functions of the $V = W/Z$ bosons, b) Higgs boson contributions to the two–point functions and c) vertex and box corrections.

The contribution of the light fermions to the vector boson self–energies can be essentially mapped into the running of the QED coupling constant which, as discussed in the previous section, is defined as the difference between the vacuum polarization function of the photon evaluated at low energies and at the scale M_Z, $\Delta\alpha(M_Z^2) = \Pi_{\gamma\gamma}(0) - \Pi_{\gamma\gamma}(M_Z^2) = 0.0590 \pm 0.00036$. Therefore, the only remaining fermionic contribution to the two–point functions is the one due to the top quark on which, besides the effects of the Higgs boson, we will mainly concentrate by studying three important quantities, $\Delta\rho$, Δr and the $Zb\bar{b}$ vertex.

The effective mixing angle and the ρ parameter

The effective weak mixing angle can be defined in the Born approximation in terms of the W and Z boson masses[9], eq. (1.60). To include higher orders, one has to renormalize the V boson masses $M_V^2 \to M_V^2 - \Pi_{VV}(M_V^2)$ where Π_{VV} is the real part of the transverse component of the self–energy of V at the scale M_V. One obtains an effective mixing angle [56, 60]

$$\bar{s}_W^2 = 1 - \frac{M_W^2}{M_Z^2} + c_W^2 \left(\frac{\Pi_{WW}(M_W^2)}{M_W^2} - \frac{\Pi_{ZZ}(M_Z^2)}{M_Z^2} \right) \sim 1 - \frac{M_W^2}{M_Z^2} + c_W^2 \Delta\rho \tag{1.104}$$

This is in fact the correction to the ρ parameter [36] which historically was used to measure the strength of the ratio of the neutral current to the charged current at zero–momentum transfer in deep–inelastic neutrino–nucleon scattering, eq. (1.66). In the SM, as already mentioned, because of a global or custodial $\mathrm{SU(2)_R}$ symmetry of the Higgs Lagrangian [which survives the spontaneous breaking of the EW symmetry], this parameter is equal to unity. However, it receives higher–order corrections usually parameterized by

$$\rho = \frac{1}{1 - \Delta\rho} \quad , \quad \Delta\rho = \frac{\Pi_{WW}(0)}{M_W^2} - \frac{\Pi_{ZZ}(0)}{M_Z^2} \tag{1.105}$$

The main contribution to this parameter is due to the (t, b) weak isodoublet. Indeed, the large mass splitting between the top and bottom quark masses breaks the custodial $\mathrm{SU(2)_R}$ symmetry and generates a contribution which grows as the top mass squared[10] [61]. Including the dominant higher–order QCD and electroweak corrections, one finds

$$\Delta\rho = 3x_t \left[1 + (\Delta\rho)^{\mathrm{QCD}} + (\Delta\rho)^{\mathrm{EW}} \right] \tag{1.106}$$

$$x_t = \frac{g_{Htt}^2}{(4\pi)^2} = \frac{G_\mu m_t^2}{8\sqrt{2}\pi^2} \sim 0.3\% \tag{1.107}$$

The higher–order QCD corrections are known at two–loop [62] and three–loop [63] orders; with α_s defined at the scale $\mu = m_t$ with 6 flavors, they are given by

$$(\Delta\rho)^{\mathrm{QCD}} = -\frac{2}{3}\frac{\alpha_s}{\pi}\left(\frac{\pi^2}{3} + 1\right) - 14.59\left(\frac{\alpha_s}{\pi}\right)^2 \tag{1.108}$$

There are also two–loop electroweak corrections stemming from fermion loops. In particular, there is a correction where a Higgs or a Goldstone boson is exchanged in loops containing top quarks and which grows as $G_\mu^2 m_t^4$ and $G_\mu^2 m_t^2 M_Z^2$. In the limit where the Higgs boson mass is much smaller than m_t, the leading piece gives a tiny correction [64]

$$(\Delta\rho)^{\mathrm{EW}} \simeq (19 - 2\pi^2)x_t \sim -x_t \tag{1.109}$$

[9] When higher–order corrections are included, different definitions of s_W^2 lead to different values. For instance, s_W^2 as defined above is different from the effective leptonic $s_W^2|_{\mathrm{eff}}^{\mathrm{lept}}$ defined in terms of a_e and v_e.

[10] Because m_t is large, the contributions are approximately the same at the scale $q^2 \sim 0$ or $q^2 \sim M_V^2$; in addition the light fermion contributions to Π_{WW} and Π_{ZZ} almost cancel in the difference, $\sim \log M_W/M_Z$. This is the reason why one can approximate the correction to s_W^2 in eq. (1.104) by the one in eq. (1.105).

However, for the more realistic case of a finite Higgs mass, the correction can be much larger [65]; in addition, the subleading $\mathcal{O}(G_\mu^2 m_t^2 M_Z^2)$ are also significant [66, 67]. Recently, the full fermionic contributions to $\Delta\rho$ and to $\sin^2\theta_W$ have been derived at the two–loop level [68]. Other higher–order corrections, such as the mixed QED–QCD contributions and the three–loop QCD corrections, are also available [69].

At the one–loop level the Higgs boson will also contribute to the ρ parameter [70]

$$(\Delta\rho)^{1-\text{Higgs}} = -\frac{3G_\mu M_W^2}{8\sqrt{2}\pi^2} f\Big(\frac{M_H^2}{M_Z^2}\Big) \ , \quad f(x) = x\left[\frac{\ln c_W^2 - \ln x}{c_W^2 - x} + \frac{\ln x}{c_W^2(1-x)}\right] \tag{1.110}$$

This contribution vanishes in the limit $s_W^2 \to 0$ or $M_W \to M_Z$, i.e. when the hypercharge group is switched off. For a very light Higgs boson the correction also vanishes

$$(\Delta\rho)^{1-\text{Higgs}} \to 0 \quad \text{for } M_H \ll M_W \tag{1.111}$$

while for a heavy Higgs boson, the contribution is approximately given by

$$(\Delta\rho)^{1-\text{Higgs}} \sim -\frac{3G_\mu M_W^2}{8\sqrt{2}\pi^2}\ \frac{s_W^2}{c_W^2} \log\frac{M_H^2}{M_W^2} \quad \text{for } M_H \gg M_W \tag{1.112}$$

This contribution has only a logarithmic dependence in the Higgs boson mass. This has to be contrasted with the general case, where the contribution of two particles with a large mass splitting grows with the mass of the heaviest particle [as is the case of the top/bottom weak isodoublet] and thus, can be very large. This logarithmic dependence is due to what is called the "Veltman screening theorem" [70, 71] which tells us that the quadratic corrections $\propto M_H^2$ appear only at the two–loop level, and are therefore screened or damped by an extra power of the electroweak coupling squared.

The two–loop Higgs corrections to the ρ parameter stemming from the exchange of the Higgs particles [and the Goldstone bosons] is known in the large Higgs mass limit since quite some time [72], but recently the three–loop contribution has been also calculated [73]. The sum of the two contributions reads for $M_H \gg M_W$

$$(\Delta\rho)^{2+3-\text{Higgs}} \sim 0.15\left(\frac{G_\mu M_W^2}{2\sqrt{2}\pi^2}\right)^2 \frac{s_W^2}{c_W^2}\frac{M_H^2}{M_W^2} - 1.73\left(\frac{G_\mu M_W^2}{2\sqrt{2}\pi^2}\right)^4 \frac{s_W^2}{c_W^2}\frac{M_H^4}{M_W^4} \tag{1.113}$$

Both the two– and three–loop corrections are extremely small for reasonable values of M_H. However, for $M_H \sim 400$ GeV, the two corrections become of the same size, $\mathcal{O}(10^{-5})$, but with opposite sign and cancel each other. For $M_H \sim 1.2$ TeV, the three–loop correction is comparable with the one–loop contribution and has the same sign.

Nevertheless, for a relatively light Higgs boson and except when it comes to very high–precision tests, one can neglect these Higgs boson corrections to the ρ parameter, and keep only the QCD and leading electroweak corrected top quark contribution. This $\Delta\rho$ correction will be the largest contribution to the electroweak corrections after $\Delta\alpha(M_Z^2)$ since, for $m_t \sim$ 180 GeV, it is at the level of $\sim 1\%$.

The Zb$\bar{\text{b}}$ vertex

In the context of precision tests, the Z boson decays into bottom quarks has a special status. First of all, because of its large mass and relatively large lifetime, the b quark can be tagged and experimentally separated from light quark and gluon jets allowing an independent measurement of the $Z \to b\bar{b}$ partial decay width and the forward backward asymmetry A^b_{FB}. Since m_b is sizable, mass effects of $\mathcal{O}(4m_b^2/M_Z^2) \sim 1\%$ have to be incorporated in these observables at both the tree–level and in the QCD corrections [74]. In addition, large radiative corrections involving the top quark and not contained in $\Delta\rho$ appear. Indeed, the latter can be exchanged together with a W boson in the $Zb\bar{b}$ vertex and the longitudinal components of the W boson [or the charged Goldstone whose coupling is proportional to the fermion mass] leads to contributions that are quadratic in the top quark mass. These corrections can be accounted for simply by shifting the reduced vector and axial–vector $Zb\bar{b}$ couplings by the amount

$$\hat{a}_b \to 2I_b^3(1+\Delta_b) \quad , \quad \hat{v}_b \to 2I_b^3(1+\Delta_b) - 4Q_b s_W^2 \tag{1.114}$$

where the rather involved expression of the vertex correction Δ_b is given in Ref. [75]. In the limit of a heavy top quark, the correction can be cast into a rather simple form

$$\Delta_b = -\frac{G_\mu m_t^2}{4\sqrt{2}\pi^2} - \frac{G_\mu M_Z^2}{12\sqrt{2}\pi^2}(1+c_W^2)\log\frac{m_t^2}{M_W^2} + \cdots \tag{1.115}$$

This correction is large [note that the logarithmic piece is also important] being approximately of the same size as the $\Delta\rho$ correction. The $Zb\bar{b}$ vertex allows thus an independent probe of the top quark; see for instance the discussions in Ref. [76].

The Higgs boson will contribute to the $Zb\bar{b}$ vertex in two ways. First, at the one–loop level, it can be exchanged between the two bottom quarks, leading to a contribution that is proportional to [75]

$$\Delta_b^{1-\text{Higgs}} \propto \frac{G_\mu m_b^2}{4\sqrt{2}\pi^2} \tag{1.116}$$

Because the b–quark mass is very small compared to the W boson mass, $m_b^2/M_W^2 \sim 1/250$, this contribution is negligible in the SM. Another contribution, similarly to what occurs in the $\Delta\rho$ case, is simply due to the two–loop corrections of $\mathcal{O}(G_\mu^2 m_t^4)$ to Δ_b, which in the limit of small Higgs boson masses is given by [65, 77]

$$\Delta_b^{2-\text{EW}} \propto -2x_t^2\left(9 - \frac{\pi^2}{3}\right) \tag{1.117}$$

which is again very small and can be safely neglected. Thus, only the Higgs boson contributions to the two–point functions have to be taken into account.

1.2.3 Observables in W boson production and decay

W pair production in e^+e^- collisions

The pair production of W bosons in e^+e^- collisions, $e^+e^- \to W^+W^-$, is the best suited process to test directly the gauge symmetry of the SM [55]. Indeed, the process is mediated by t–channel neutrino exchange and by s–channel photon and Z boson exchanges, Fig. 1.5, which involve the triple γWW and ZWW couplings that are dictated by the $\mathrm{SU(2)_L} \times \mathrm{U(1)_Y}$ gauge symmetry, eq. (1.68). There is an additional contribution from s–channel Higgs boson exchange but it is negligibly small, being proportional to the square of the electron mass[11].

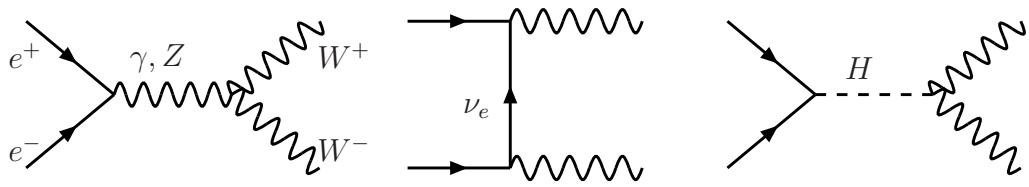

Figure 1.5: Feynman diagrams for the pair production of W bosons in e^+e^- collisions.

The total production cross section for the process $e^+e^- \to W^+W^-$ is given by [78]

$$\begin{aligned}
\sigma &= \frac{\pi\alpha^2}{2s_W^4}\frac{\beta}{s}\left\{\left[1+\frac{2M_W^2}{s}+\frac{2M_W^4}{s^2}\right]\frac{1}{\beta}\log\frac{1+\beta}{1-\beta}-\frac{5}{4}\right. \\
&+ \frac{M_Z^2(1-2s_W^2)}{s-M_Z^2}\left[2\left(\frac{M_W^4}{s^2}+\frac{2M_W^2}{s}\right)\frac{1}{\beta}\log\frac{1+\beta}{1-\beta}-\frac{s}{12M_W^2}-\frac{5}{3}-\frac{M_W^2}{s}\right] \\
&+ \left.\frac{M_Z^4(8s_W^4-4s_W^2+1)\beta^2}{48(s-M_Z^2)^2}\left[\frac{s^2}{M_W^4}+\frac{20s}{M_W^2}+12\right]\right\} \qquad (1.118)
\end{aligned}$$

with $\beta = (1-4M_W^2/s)^{1/2}$ being the velocity of the W bosons. The W bosons will decay into almost massless fermion pairs with partial decay widths given by

$$\Gamma(W \to f_i\bar{f}_j) = \frac{2}{3}N_c\,\alpha|V_{ij}|^2\,M_W\,(v_f^2+a_f^2) \qquad (1.119)$$

where V_{ij} are the Cabibbo–Kobayashi–Maskawa matrix elements and v_f and a_f the vector and axial–vector couplings of the W boson to fermions given in eq. (1.64). The same type of radiative corrections which affect the $Z \to f\bar{f}$ partial width appear also in this case.

Of course, to have an accurate description of the process, one has to consider many differential distributions, the possibility of off–shell W bosons etc.., and higher–order effects including radiative corrections, have to be implemented. A large theoretical effort has been devoted to this topic in the last two decades; see e.g. Ref. [55] for a review. Let us simply

[11] Note, however, that at extremely high energies, this suppression is compensated by terms proportional to the c.m. energies. In fact, the cross section with only the two other channels included, violates unitarity at $\sqrt{s} \gg M_W^2$, and unitarity is restored only if the Higgs boson channel is included with the couplings of the Higgs particle to electrons and W bosons exactly as predicted in the SM [7].

note here that the contribution of the Higgs particle to the radiative corrections in this reaction [79, 80] are too small to be measurable.

This process also allows to make a very precise measurement of the W boson mass. This can be performed not only via a scan in the threshold region where the cross section rises steeply, $\sigma \sim \beta$, but also in the reconstruction of the W bosons in mixed lepton/jet final states for instance. The W boson width can also be measured by scanning around the threshold.

W production in hadronic collisions

W bosons can also be produced in hadronic collisions in the Drell–Yan process, $q\bar{q}' \to W$, and detected in their leptonic decay channel $W \to \ell\nu$ for instance [81, 82]. The differential cross section for the subprocess $u\bar{d} \to W^+ \to \ell^+\nu$ is given by [83]

$$\frac{\mathrm{d}\hat{\sigma}}{\mathrm{d}\hat{\Omega}} = \frac{\alpha^2 |V_{ud}|^2}{192 s_W^2} \frac{1}{\hat{s}} \frac{\hat{u}^2}{(\hat{s} - M_W^2)^2 + \Gamma_W^2 M_W^2} \tag{1.120}$$

where $\hat{s}$ is the center–of–mass energy of the subprocess, $\hat{u}$ the square momentum difference between the up–type quark and the lepton and $\hat{\Omega}$ is the solid angle of the lepton ℓ in the parton c.m. frame. The hadronic cross section can be obtained by convoluting the previous equation with the corresponding (anti)quark densities of the protons. Defining $\tau_0 = M_W^2/s$ with s being the total hadronic c.m. energy squared, one would then have

$$\sigma(pp \to W) = \int_{\tau_0}^{1} d\tau \sum_q \frac{\mathrm{d}\mathcal{L}^{q\bar{q}}}{\mathrm{d}\tau} \hat{\sigma}(\hat{s} = \tau s) \tag{1.121}$$

Here again, radiative corrections, in particular those due to the strong interaction [84, 85] to be discussed later, have to be implemented in order to describe accurately the process.

The W boson mass can be determined [81,82] in the leptonic decay channels by measuring the transverse mass $m_T^W = \sqrt{2 p_T^\ell p_T^\nu (1 - \cos\phi)}$ where ϕ is the angle between the charged lepton and the neutrino in the transverse plane. While the lepton transverse momentum p_T^ℓ is directly measured, p_T^ν is obtained from the momentum of the system recoiling against the W in the transverse plane. The edge of the m_T^W distribution is very sensitive to the W boson mass. By fitting the experimental m_T^W distribution with Monte–Carlo events generated with different values of M_W, one can determine the M_W value which gives the best result fit. The W boson width can also be measured with a reasonable accuracy since it enters the process.

However, besides the background problems, there are many uncertainties which are involved in this measurement: the not very precise knowledge of the parton distributions, the effect of the W boson total width, the radiative decays and the approximate knowledge of the p_T spectrum and distribution of the W boson. But most of these uncertainties can be strongly constrained by using the much cleaner process $pp \to Z \to \ell^+\ell^-$, with the Z boson mass accurately determined at LEP1/SLC.

Muon decay and the radiative corrections to the W boson mass

As discussed in §1.1.4, the W boson mass is related to α, G_μ and M_Z, eq. (1.77). Including the radiative corrections, one obtains the celebrated relation [86]

$$M_W^2\left(1-\frac{M_W^2}{M_Z^2}\right)=\frac{\pi\alpha}{\sqrt{2}G_\mu}(1+\Delta r) \tag{1.122}$$

The Δr correction can be decomposed into three main components and can be written as [60]

$$1+\Delta r=\frac{1}{(1-\Delta\alpha)(1+\frac{c_W^2}{s_W^2}\Delta\rho)-(\Delta r)_{\rm rem}} \tag{1.123}$$

where the $\Delta\alpha$ and $\Delta\rho$ contributions have been discussed previously and $(\Delta r)_{\rm rem}$ collects the remaining non–leading contributions. Among these are some non–quadratic but still sizable corrections due to the top quark, additional light fermions contributions, as well as some vertex and box corrections involved in muon decay [60]

$$\begin{aligned}(\Delta r)_{\rm rem}^{\rm box+vertex} &= \frac{\alpha}{4\pi s_W^2}\left(6+\frac{7-4s_W^2}{2s_W^2}\log c_W^2\right)\\ (\Delta r)_{\rm rem}^{\rm light-fermions} &= \frac{\alpha}{4\pi s_W^2}\frac{N_f}{6}\left(1-\frac{c_W^2}{s_W^2}\right)\log c_W^2\\ (\Delta r)_{\rm rem}^{\rm log-top} &= \frac{G_\mu M_W^2}{4\sqrt{2}\pi^2}\left(\frac{c_W^2}{s_W^2}-\frac{1}{3}\right)\log\frac{m_t^2}{M_W^2}\end{aligned} \tag{1.124}$$

Note that the factorization of the light and heavy fermion contribution and the presence of the three terms in the denominators of eq. (1.123) effectively sums many important higher–order terms [56, 60], such as those of the form $(\Delta\rho)^2, (\Delta\rho\Delta\alpha), (\Delta\alpha\Delta r_{\rm rem})$ at the two–loop level and the light fermion contribution $(\Delta\alpha)^n$ to all orders.

At one–loop, the Higgs boson has a contribution to (Δr) that is also only logarithmically dependent on M_H, as in the case of $\Delta\rho$. For a heavy Higgs, $M_H \gg M_W$, it reads [86, 87]

$$(\Delta r)_{\rm rem}^{\rm 1-Higgs}\simeq\frac{G_\mu M_W^2}{8\sqrt{2}\pi^2}\frac{11}{3}\left(\log\frac{M_H^2}{M_W^2}-\frac{5}{6}\right) \tag{1.125}$$

Again, the quadratic correction $\propto M_H^2$ appears only at the two–loop level.

The complete two–loop bosonic corrections to Δr have been calculated recently [88] including the full M_H dependence and were found to be very small: a few times $\times 10^{-5}$ for M_H values in the range between 100 GeV and 1 TeV. There are also two–loop electroweak corrections stemming from fermions; the main contribution is in fact contained in $\Delta\rho$ but there is an extra piece contributing to $(\Delta r)_{\rm rem}$ which, however, is small [66, 67]. Hence, the theoretical knowledge of the W mass is rather precise, being approximately the same as for the electroweak mixing angle.

The trilinear gauge boson couplings

As mentioned previously, the gauge structure of the $SU(2)_L \times U(1)_Y$ theory is best tested by the measurement of the triple gauge boson vertices at LEP2 and eventually at the Tevatron [although possible, the test of the quartic couplings is very limited in these experiments]. This can be achieved by comparing the data with a general WWV vertex with $V = \gamma, Z$, which includes the possibility of anomalous gauge boson couplings that can be induced, for instance, by radiative corrections in the SM or by New Physics effects. We briefly discuss this aspect below, as it will be needed in another part of this report.

The most general Lorentz invariant WWV vertex that is possible in processes where the weak bosons couple to massless fermions, as is the case in the reaction $e^+e^- \to W^+W^-$ for instance, can be written as[12] [89, 90]

$$\begin{aligned}\mathcal{L}_{\rm eff}^{WWV} &= ig_{WWV}\Big[g_1^V V^\mu \left(W^-_{\mu\nu}W^{+\nu} - W^+_{\mu\nu}W^{-\nu}\right) + \kappa_V\, W^+_\mu W^-_\nu V^{\mu\nu} \\ &+ \frac{\lambda_V}{M_W^2}\, V^{\mu\nu}W^{+\rho}_\nu W^-_{\rho\mu} + ig_5^V \varepsilon_{\mu\nu\rho\sigma}\left((\partial^\rho W^{-\mu})W^{+\nu} - W^{-\mu}(\partial^\rho W^{+\nu})\right) V^\sigma \\ &+ ig_4^V W^-_\mu W^+_\nu(\partial^\mu V^\nu + \partial^\nu V^\mu) - \frac{\tilde\kappa_V}{2} W^-_\mu W^+_\nu \varepsilon^{\mu\nu\rho\sigma}V_{\rho\sigma} - \frac{\tilde\lambda_V}{2m_W^2}\, W^-_{\rho\mu}W^{+\mu}{}_\nu \varepsilon^{\nu\rho\alpha\beta}V_{\alpha\beta}\Big]\end{aligned} \tag{1.126}$$

with the overall couplings defined by $g_{WW\gamma} = e$ and $g_{WWZ} = e\cot\theta_W$ and where the reduced field strengths $W_{\mu\nu} = \partial_\mu W_\nu - \partial_\nu W_\mu$ and $V_{\mu\nu} = \partial_\mu V_\nu - \partial_\nu V_\mu$ are used. For on–shell photons, i.e. with $q^2 = 0$, the couplings $g_1^\gamma = 1$ and $g_5^\gamma = 0$ are fixed by $U(1)_Q$ gauge invariance. In the Lagrangian eq. (1.126), the couplings g_1^V, κ_V and λ_V separately conserve C and P symmetries, while g_5^V violates them but conserves CP symmetry. The couplings g_4^V, $\tilde\kappa_V$ and $\tilde\lambda_V$ parameterize a possible CP violation in the bosonic sector.

Note that the C and P conserving terms in $\mathcal{L}_{\rm eff}^{WW\gamma}$ correspond to the lowest order terms in a multipole expansion of the W boson–photon interactions, the charge Q_W, the magnetic dipole moment μ_W and the electric quadrupole moment q_W of the W^+ boson [90]

$$Q_W = eg_1^\gamma\ ,\quad \mu_W = \frac{e}{2M_W}\left(g_1^\gamma + \kappa_\gamma + \lambda_\gamma\right)\ ,\quad q_W = -\frac{e}{M_W^2}\left(\kappa_\gamma - \lambda_\gamma\right) \tag{1.127}$$

In the SM, the Lagrangian eq. (1.126) reduces to the one given in eq. (1.68) and, thus, at the tree–level, the trilinear couplings are simply given by $g_1^Z = g_1^\gamma = \kappa_Z = \kappa_\gamma = 1$, while all the other couplings in eq. (1.126) are zero. It became common practice to introduce deviations of the former set of couplings from their tree–level SM values

$$\Delta g_1^Z \equiv (g_1^Z - 1)\ ,\quad \Delta\kappa_\gamma \equiv (\kappa_\gamma - 1)\ ,\quad \Delta\kappa_Z \equiv (\kappa_Z - 1) \tag{1.128}$$

The rather precise measurement of these quantities is one of the big achievements of LEP.

[12] Additional terms with higher derivatives may be present, but they are equivalent to a dependence of the couplings on the vector boson momenta and thus, only lead to a form factor behavior of these couplings.

1.2.4 Approximating the radiative corrections

The evaluation of the complete set of the previously discussed radiative corrections is a very complicated task, in particular when initial and final state photonic corrections or processes which need some special treatment, such as Bhabha $e^+e^- \to e^+e^-$ scattering, are involved. This can be performed only with the help of very sophisticated programs which fortunately exist [54]. However, in most practical purposes, in particular when effects of New Physics are analyzed, it is sufficient to probe some quantities where the most important radiative correctives are expected to occur. This is the case, for instance, of the Δr and $\bar{s}_W^2$ observables. Here, we will shortly describe such approximations which will have some application later.

The improved Born approximation

One can express electroweak observables in the Born approximation in terms of the QED constant α, but to be accurate, one should use the running α defined at the scale where the considered process takes place, M_Z or higher energies. Since the running of α between the two latter scales is rather small, one can make the substitution $\alpha(0) \to \alpha(M_Z^2) = \alpha(0)/(1-\Delta\alpha)$ for scales larger than M_Z. The $\Delta\alpha$ corrections should in principle cancel the light fermion contributions in the two–point functions when the radiative corrections to the observables are calculated. This is in fact effectively done by using the Fermi decay constant in the tree level expressions of the observables, $\alpha(0) \to \alpha(M_Z^2) = (\sqrt{2}G_\mu/\pi)M_W^2 s_W^2$, which implicitly includes the $\Delta\alpha$ contribution. Since $\Delta\alpha$ is rather large being at the level of 6% [and which for $2 \to 2\,(3)$ processes that are proportional to $\alpha^2(\alpha^3)$, lead to contributions of the order of 12% (18%)], this gives a more accurate description of the observable, already at the tree–level. This procedure is called the naive improved Born approximation (naive IBA) [91].

The IBA is said to be naive because there are still residual contributions from $\Delta\rho$ and $(\Delta r)_{\rm rem}$ and additional contributions to $\bar{s}_W^2$ which, despite of the fact that they are smaller than $\Delta\alpha$, should be taken into account. The dominant top quark contribution which is contained in the $\Delta\rho$ piece given in eq. (1.106) can be simply included by performing the shift

$$\alpha \to \frac{\sqrt{2}G_\mu}{\pi} M_W^2 \left(1 - \frac{M_W^2}{M_Z^2}\right)(1+\Delta r)^{-1}\ ,\ \Delta r \simeq \Delta\alpha(M_Z^2) - 3\Delta\rho \tag{1.129}$$

In the context of Z physics, the IBA may be be sufficient in many purposes and can be implemented in the electroweak observables by simply performing the following substitutions:

(i) replace the electromagnetic couplings of fermions by

$$Q_f e \to Q_f \sqrt{4\pi\alpha/[1-\Delta\alpha(M_Z^2)]^{-1}} \tag{1.130}$$

(*ii*) replace the Born couplings of the fermion to the Z boson by

$$v_f \to (\sqrt{2}G_\mu M_Z^2 \rho)^{1/2}\, \hat{v}_f \quad , \quad a_f \to (\sqrt{2}G_\mu M_Z^2 \rho)^{1/2}\, \hat{a}_f \tag{1.131}$$

(*iii*) replace everywhere s_W^2, in particular in the vector couplings $\hat{v}_f = 2I_3^f - 4Q_f s_W^2$, by the effective electroweak mixing angle for leptons

$$s_W^2 \to \overline{s}_W^2 \equiv \sin^2\theta_{\rm eff}^{\rm lept} = \frac{1}{2}\left[1 - \sqrt{1 - \frac{4\pi\alpha(0)}{\sqrt{2}M_Z^2 G_\mu}\frac{1}{\rho(1-\Delta\alpha)}}\right] \tag{1.132}$$

(*iv*) and for b quark final states, perform in addition the substitution of eq. (1.114) to include the large top quark mass corrections in the $Zb\bar{b}$ vertex.

The remaining non–universal electroweak corrections are small and can be safely neglected in most cases, but obviously not when probing the small Higgs boson effects. Of course, this IBA needs to be supplemented by the important QCD corrections to hadronic processes and QED corrections, in particular ISR corrections, whenever needed.

Model independent analyses and the STU and ϵ approaches

In a more general context than the SM, it is often convenient to parametrize the radiative corrections to electroweak observables in such a way that the contributions due to many kinds of New Physics beyond the SM are easily implemented and confronted with the experimental data. If one assumes that the symmetry group of New Physics is still the $\mathrm{SU(3)_C \times SU(2)_L \times U(1)_Y}$ and, thus, there are no extra gauge bosons, and that it couples only weakly to light fermions so that one can neglect all the "direct" vertex and box corrections, one needs to consider only the oblique corrections, that is, the ones affecting the γ, Z, W two–point functions and the $Z\gamma$ mixing. If in addition the scale of the New Physics is much higher than M_Z, one can expand the complicated functions of the momentum transfer Q^2 around zero, and keep only the constant and the linear $Q^2/M_{\rm NP}^2$ terms of the series, which have very simple expressions in general. The New Physics contributions can be then expressed in terms of six functions: $\Pi'_{\gamma\gamma}(0), \Pi'_{Z\gamma}(0), \Pi_{ZZ}^{(')}$ and $\Pi_{WW}^{(')}$ ($\Pi_{\gamma\gamma}(0) = \Pi_{Z\gamma}(0) = 0$ because of the QED Ward Identity). Three of these functions will be absorbed in the renormalization of the three input parameters α, G_μ and M_Z. This leaves three variables which one can choose as being ultraviolet finite and more or less related to physical observables.

A popular choice of the three independent variables is the STU linear combinations of self–energies introduced by Peskin and Takeuchi [92]

$$\begin{aligned}
\alpha S &= 4s_W^2 c_W^2 \left[\Pi_{ZZ}(0) - (c_W^2 - s_W^2)/(s_W c_W)\cdot \Pi'_{Z\gamma}(0) - \Pi'_{\gamma\gamma}(0)\right] \\
\alpha T &= \Pi_{WW}(0)/M_W^2 - \Pi_{ZZ}(0)/M_Z^2 \\
\alpha U &= 4s_W^2 \left[\Pi'_{WW}(0) - c_W^2 \Pi'_{ZZ}(0) - 2s_W c_W \Pi'_{Z\gamma}(0) - s_W^2 \Pi'_{\gamma\gamma}(0)\right]
\end{aligned} \tag{1.133}$$

These variables measure deviations with respect to the SM predictions and, for instance, S and T are zero when the New Physics does not break the custodial isospin symmetry. The variable αT is simply the shift of the ρ parameter due to the New Physics, $\alpha T = 1-\rho-\Delta\rho|_{\rm SM}$.

Another parametrization of the radiative corrections, the ϵ approach of Altarelli and Barbieri [93], is closer to the IBA approximation discussed previously and thus, more directly related to the precision electroweak observables. The three variables which parametrize the oblique corrections are defined in such a way that they are zero in the approximation where only SM effects at the tree–level, as well as the pure QED and QCD corrections, are taken into account. Contrary to the STU approach, they are independent of the values of m_t and M_H, the contributions of which are included. In addition, a fourth variable is introduced to account for the quadratic top quark mass contribution to the $Zb\bar{b}$ vertex.

In terms the two quantities Δr_W and Δk related to, respectively, the gauge boson masses and $\sin^2\theta_{\rm eff}^{\rm lep}$ as measured from leptonic observables assuming universality,

$$M_W^2/M_Z^2\left(1-M_W^2/M_Z^2\right) = s_0^2c_0^2(1-\Delta r_W)\ ,\ v_e/a_e = 1-4\sin^2\theta_{\rm eff}^{\rm lep} = 1-4(1+\Delta k)s_0^2$$

with $s_0^2c_0^2 = \pi\alpha(M_Z)/(\sqrt{2}G_\mu M_Z^2)$, the four variables $\epsilon_{1,2,3,4}$ are defined as

$$\epsilon_1 = \Delta\rho\ ,\ \epsilon_2 = c_0^2\Delta\rho + \frac{s_0^2}{c_0^2-s_0^2}\Delta r_W - 2s_0^2\Delta k\ ,\epsilon_3 = c_0^2\Delta\rho + (c_0^2-s_0^2)\Delta k\ ,\epsilon_4 = \Delta_b \quad (1.134)$$

The variables ϵ_2 and ϵ_3 are only logarithmic in m_t and the m_t^2 terms appear only in ϵ_1 and ϵ_b; the leading terms involving the Higgs boson mass are contained in ϵ_1 and ϵ_3. The relations between the ϵs and the electroweak observables, lead to very simple formulae.

Interpolation of the radiative corrections

Once the full set of radiative corrections has been made available, one can attempt to derive simple interpolation formulae to summarize the full result, which is analytically complicated and numerically involved to handle. This is possible since the only unknown parameter in the SM is the Higgs boson mass. However, one has to include the experimental errors on some important SM input parameters. For the values of M_W and of the EW mixing angle $\sin^2\theta_{\rm eff}^{\rm lep}$ as measured from lepton asymmetries which do not involve final state QCD corrections, the interpolating formulae are indeed rather simple. Using G_μ and M_Z as inputs and taking into account the possible variations of the measurements of $\Delta\alpha^{\rm had}(M_Z), \alpha_s(M_Z)$ and m_t from their central values, one obtains for a given observable X [67]

$$X \;=\; X^0 + a_1^X a_h + a_2^X a_e + a_3^X a_t + a_4^X a_s + a_5^X a_h^2 \quad (1.135)$$

with $X^0 = (s_W^2)^0$ and M_W^0 being the [scheme dependent] theoretical results at the reference point $M_H = 100$ GeV, $m_t = 175$ GeV and the other parameters set at their experimentally

measured central values, and the reduced quantities

$$a_h = \log\left(\frac{M_H}{100\ \text{GeV}}\right),\ a_e = \frac{\Delta\alpha^{\text{had}}}{0.028} - 1,\ a_t = \left(\frac{m_t}{175\ \text{GeV}}\right)^2 - 1,\ a_s = \frac{\alpha_s(M_Z)}{0.118} - 1 \quad (1.136)$$

In the on–shell scheme, the central values X^0 and the coefficients a_i^X are displayed in Table 1.2 for the two observables $\sin^2\theta_{\text{eff}}^{\text{lep}}$ and M_W. For a Higgs boson with a mass in the range 75 GeV $\lesssim M_H \lesssim$ 375 GeV and for the SM input parameters varying within their 1σ allowed range, the previous formula reproduces the complete result with errors $\Delta\sin^2\theta_{\text{eff}}^{\text{lep}} \lesssim 1\times 10^{-5}$ and $\Delta M_W \lesssim 1$ MeV, which are well below the experimental accuracies on these observables as will be seen later.

Quantity	X^0	$10^2 a_1^X$	$10 a_2^X$	$10 a_3^X$	$10^2 a_4^X$	$10 a_5^X$
$\sin^2\theta_{\text{eff}}^{\text{lep}}$	0.231527	0.0519	0.986	– 0.277	0.045	0
M_W	80.3809	–5.73	–5.18	5.41	–8.5	–0.80

Table 1.2: The central values and the deviation coefficients a_i for $\sin^2\theta_{\text{eff}}^{\text{lep}}$ and M_W.

1.2.5 The electroweak precision data

Besides $\alpha(M_Z), G_\mu$ and M_Z which are used as the basic input parameters, there is an impressive list of electroweak observables which have been measured with a very good accuracy and which can be predicted in the SM with an equally good precision. These are:

• Observables from the Z lineshape at LEP1: the Z boson total width Γ_Z, the peak hadronic cross section σ^0_{had}, the partial decay widths of the Z boson into leptons and c, b quarks normalized to the hadronic Z decay width, $R_{\ell,c,b}$, the forward–backward asymmetries A^f_{FB} for leptons and heavy c, b quarks, as well as the τ polarization asymmetry A^τ_{pol}; the asymmetries provide a determination of $\sin^2\theta_W$ as measured from leptons and hadrons.

• The longitudinal polarization asymmetry A^f_{LR} which has been measured at the SLC and which gives the best individual measurement of $\sin^2\theta_W$, as well as the left–right forward–backward asymmetries for the heavy b, c quarks, $A^{b,c}_{LR,FB}$.

• The mass of the W boson M_W which is precisely measured at LEP2 and at the Tevatron as well as the total decay width Γ_W, eqs. (1.90–1.91).

• In addition there are high–precision measurements at low energies: (i) the ν_μ– and $\bar\nu_\mu$–nucleon deep–inelastic scattering cross sections, the ratios of which measure the left– and right–handed couplings of fermions to the Z boson which can be turned into a determination of s^2_W, and (ii) the parity violation in the Cesium and Thallium atoms which provide the weak charge Q_W that quantifies the coupling of the nucleus to the Z boson and which can also be turned into a determination of the electroweak mixing angle via $s^2_W = 1 - M^2_W/M^2_Z$.

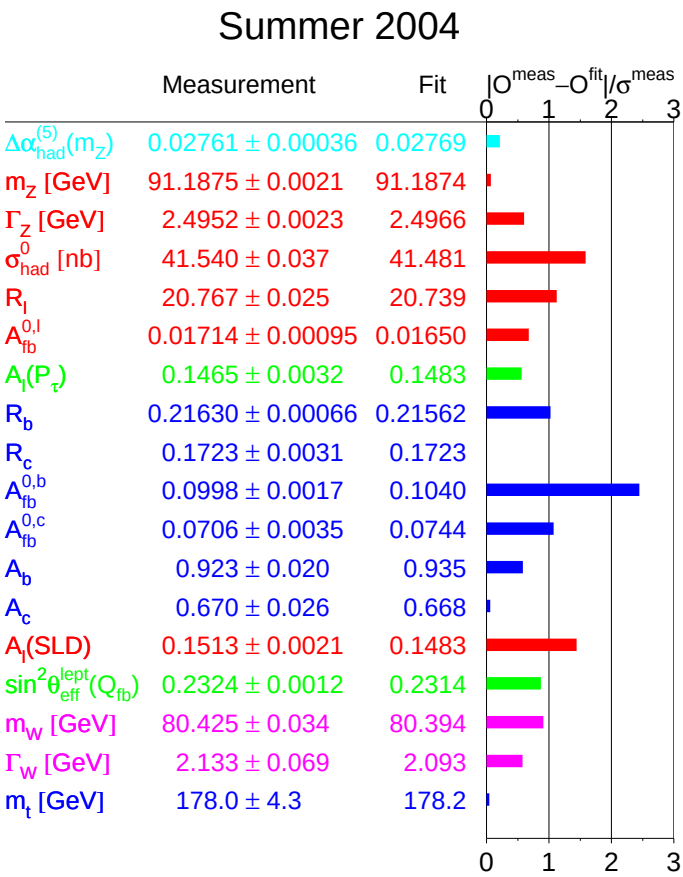

Table 1.3: Summary of electroweak precision measurements at LEP1, LEP2, SLC and the Tevatron; from Ref. [8]. The SM fit results, which have been derived including all radiative corrections, and the standard deviations are also shown.

One has in addition to include as inputs, the measurement of the top quark mass at the Tevatron, the strong coupling constant at LEP and elsewhere, as well as the value of $\Delta\alpha^{\rm had}(M_Z^2)$ as measured in e^+e^- collisions at low energies and in τ–lepton decays at LEP1. The experimental values of some of the electroweak observables mentioned above [as they were in summer 2004] are displayed in Table 1.3 together with the associated errors. Also shown are the theoretical predictions of the SM [for the best fit of M_H to be discussed later] that have been obtained by including all known radiative corrections with the central values of $\Delta\alpha^{\rm had}(M_Z^2), m_t, \alpha_s,$ *etc.*.

As can be seen from Tab. 1.3, the theoretical predictions are in remarkable agreement with the experimental data, the pulls being smaller than 2 standard deviations in all cases, except for A_{FB}^b where the deviation is at the 2.5 σ level. A few remarks are in order here:

i) From the Z lineshape and partial width measurements, one obtains a determination of the number of light neutrino flavors contributing to the invisible Z decay width

$$N_\nu = 2.9841 \pm 0.0083 \tag{1.137}$$

which agrees with the SM expectation $N_\nu = 3$ at the 2σ level.

ii) Using all these results, one derives the world average value for the effective weak mixing angle as measured from lepton asymmetries and partial widths and from hadronic asymmetries. The status for the latter parameter, again as it was in summer 2004, is as follows [8]

$$\sin^2\theta_{\rm eff}^{\rm lep} \;=\; 0.23150 \pm 0.00016 \tag{1.138}$$

iii) The values of $\sin^2\theta_{\rm eff}^{\rm lep}$ as measured from the leptonic FB and τ polarization asymmetries at LEP1 and from the longitudinal asymmetries at SLC are in a very good agreement. From these measurements, and from the measurement of the leptonic partial widths, the lepton universality of the neutral weak current has been established with a high accuracy.

iv) The forward–backward asymmetry A_{FB}^b for b quarks measured at LEP1 provides, together with the longitudinal asymmetry A_{LR}^f measured at the SLC, the most precise individual measurement of $\sin^2\theta_{\rm eff}^{\rm lep}$, but the result is 2.5 standard deviations away from the predicted value and the two individual values differ by almost three standard deviations. This has led to speculations about a signal of New Physics in the $Zb\bar{b}$ vertex. However, it turns out that this discrepancy cannot be easily explained without affecting the $Z \to b\bar{b}$ partial width R_b which is precisely measured and is compatible with the SM expectation, and the hadronic asymmetries measured at the SLC, although their errors are larger. It is likely that this anomaly is a result of a large statistical fluctuation or some experimental problem.

v) While the value of weak charge as measured in the parity violation in Cs atoms, $Q_W(Cs) = -72.74 \pm 0.46$ [94], is in accord with the SM prediction $Q = -72.93$, the measurement of $\sin^2\theta_W$ from neutrino and antineutrino deep–inelastic scattering made by the NuTeV experiment gives $\sin^2\theta_W(\nu N) = 0.2277 \pm 0.0016$ [95], which is 3 standard deviations away from the predicted value in the SM, $\sin^2\theta_W = 0.2227$. It becomes now apparent that the theoretical uncertainties in the higher–order analyses needed to extract the NuTeV value of $\sin^2\theta_W$ have been underestimated by the collaboration [96, 97].

In addition, the cross sections for the pair production of gauge bosons have been rather accurately measured at LEP2 [and, to a lesser extent, at the Tevatron]. In the case of the $e^+e^- \to W^+W^-$ process, the cross section which depends on the triple self–coupling among the W and the $V = \gamma, Z$ bosons, eq. (1.68), and on the $We\nu$–coupling given in eq. (1.64), is shown in the left–hand side of Fig. 1.6 and it agrees perfectly with the predicted value in the SM, with the s–channel exchange of γ, Z and the t–channel neutrino exchange contributions.

This agreement can be turned into a strong constraint on the anomalous C,P conserving couplings of the effective Lagrangian of eq. (1.126) which are measured to be [51]

$$\kappa_\gamma = 0.943 \pm 0.055\,,\;\; \lambda_\gamma = -0.020 \pm 0.024\,,\;\; g_1^Z = 0.998 \pm 0.025 \tag{1.139}$$

providing a stringent test of the $SU(2)_L \times U(1)_Y$ gauge structure of the theory. The contours of the two parameter fits of these three C and P conserving W boson couplings are shown in the right–hand side of Fig. 1.6.

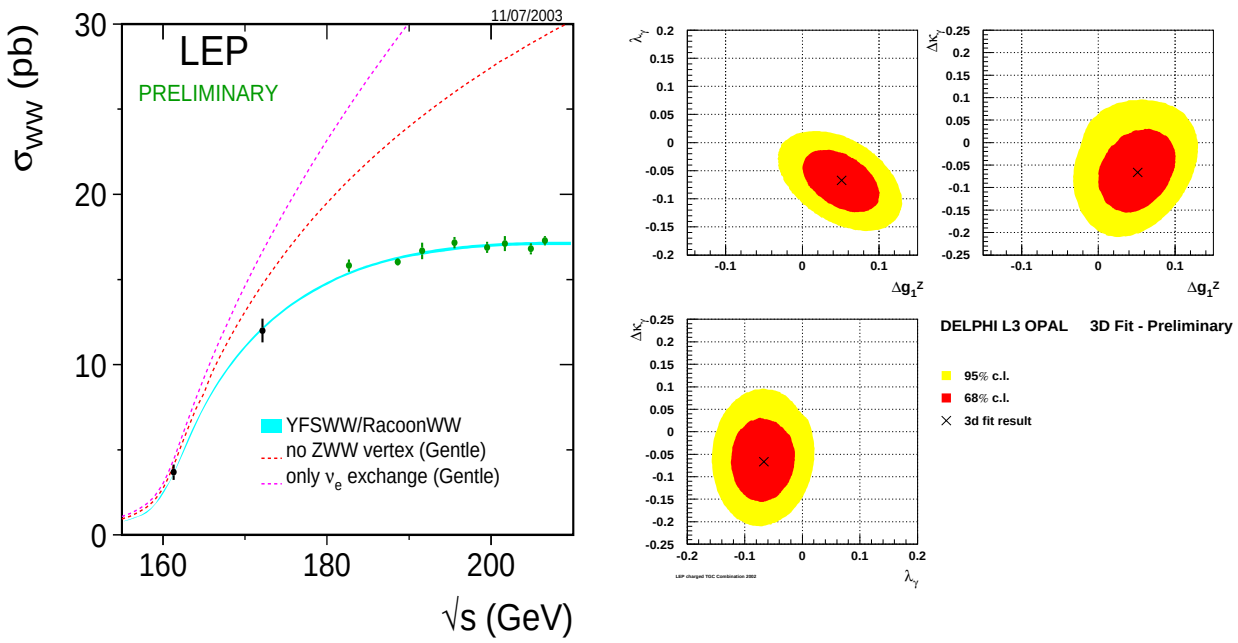

Figure 1.6: Left: the measured value of the $e^+e^- \to W^+W^-$ cross section at LEP2 and the prediction in the SM (full line) and when the s–channel Z boson or both γ and Z boson exchange diagrams are not contributing. Right: the 68% and 95% confidence level contours of the three two parameter fits to the W boson C and P conserving trilinear couplings, g_1^Z–λ_γ, g_1^Z–κ_γ and λ_γ–κ_γ, as measured at LEP2 with a c.m. energy up to $\sqrt{s} = 209$ GeV and including systematical uncertainties; the fitted values are indicated with a cross and the SM value for each fit is in the center of the grid. From Ref. [51].

In summary, the electroweak precision data have provided a decisive test of the SM. These tests have been performed at the per mille level and have probed the quantum corrections of the $SU(2)_L \times U(1)_Y$ theory. The couplings of quarks and leptons to the electroweak gauge bosons have been measured precisely and found to be those predicted by the gauge symmetry. The trilinear couplings among electroweak gauge bosons have been also measured and found to be those dictated by the gauge symmetry. If, in addition, one recalls that the $SU(3)_C$ gauge symmetry description of the strong interactions has been thoroughly tested at LEP1 and elsewhere, one concludes that the SM based on the $SU(3)_C \times SU(2)_L \times U(1)_Y$ gauge symmetry has been firmly established as the theory of the strong and electroweak interactions at present energies. The only missing ingredient of the model is the Higgs particle, which has not yet been observed directly. However, indirect constraints on this particle can be obtained from the high precision data as we will discuss now.

1.3 Experimental constraints on the Higgs boson mass

Since the Higgs particle contributes to the radiative corrections to the high–precision electroweak observables discussed previously, there are constraints on its mass which, as discussed in §1.1, is the only yet unknown free parameter in the SM. There are also constraints from direct searches of the Higgs boson at colliders and in particular at LEP. These indirect and direct constraints on M_H will be summarized in this section.

1.3.1 Constraints from high precision data

The electroweak precision measurements allow rather stringent constraints on the Higgs boson mass in the SM. Using for instance the LEP2 values of the W boson mass and the effective weak mixing angle as measured in forward–backward and polarization asymmetries, and the combined fit to the measurements giving these parameters when the complete set of radiative corrections has been included, one obtains the range where the Higgs boson mass should lie at the 1σ level that is shown in Fig. 1.7.

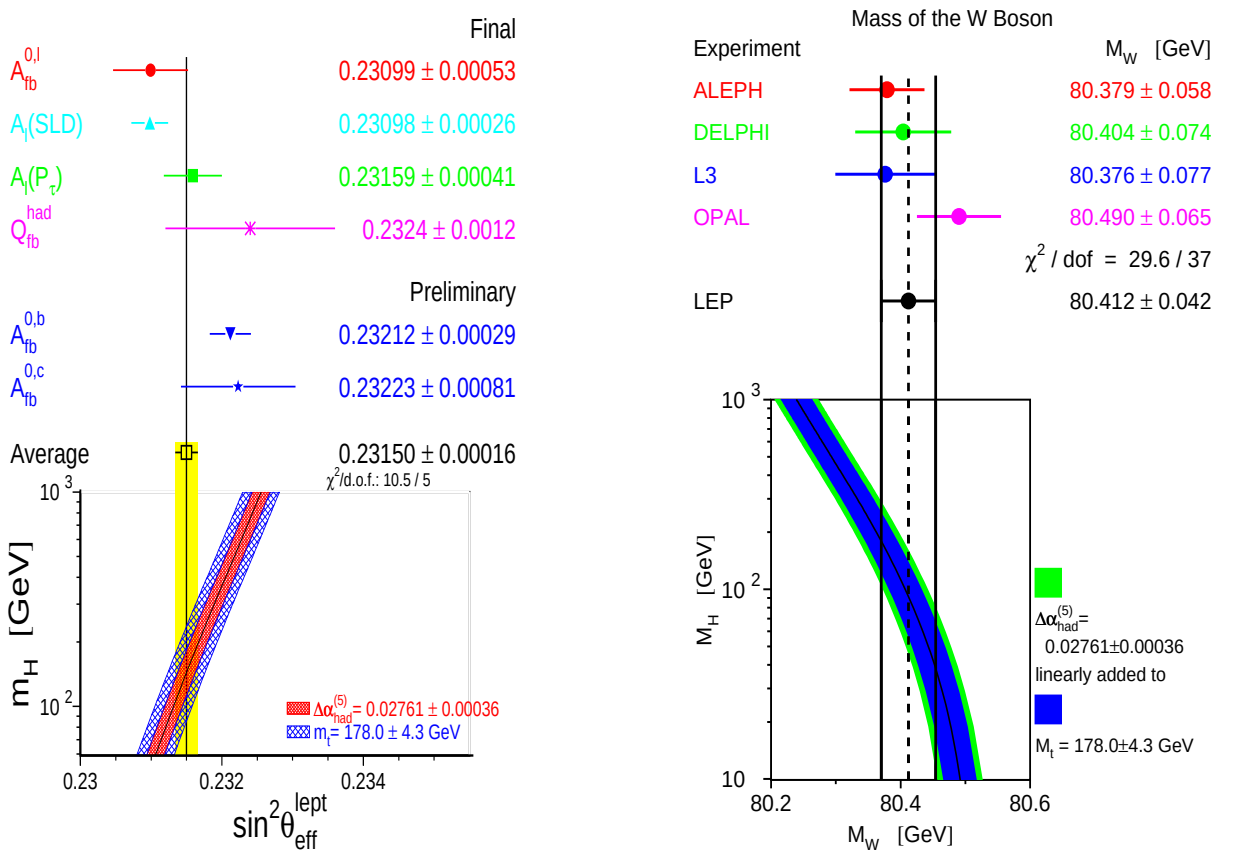

Figure 1.7: The measurement [vertical band] and the theoretical prediction [the hatched bands] for $\sin^2\theta_{\rm eff}^{\rm lept}$ and M_W as a function of the Higgs boson mass; from Ref. [8].

The vertical bands are due to the measurements and their errors, while the colored bands are for the theoretical prediction with the uncertainties due to the SM input parameters, namely, $\Delta^{\rm had}\alpha(M_Z) = 0.02761 \pm 0.00036, \alpha_s(M_Z) = 0.118 \pm 0.002$ and $m_t = 178.0 \pm 4.3$ GeV. The total width of the band is the linear sum of all these effects. As can be seen, the values of $\sin^2\theta_{\rm eff}^{\rm lept}$ and M_W agree with the SM prediction only if the Higgs particle is rather light, a value of about $M_H \sim 100$ GeV being preferred by the experimental data.

Taking into account all the precision electroweak data of Table 1.3 in a combined fit, one can determine the constraint summarized in Fig. 1.8 which shows the $\Delta\chi^2$ of the fit to all measurements as a function of M_H, with the uncertainties on $\Delta^{\rm had}, \alpha(M_Z), \alpha_s(M_Z), m_t$ as well as on M_Z included [8]. One then obtains the value of the SM Higgs boson mass

$$M_H = 114^{+69}_{-45}\ \text{GeV} \tag{1.140}$$

leading to a 95% Confidence Level (CL) upper limit in the SM

$$M_H < 260\ \text{GeV} \tag{1.141}$$

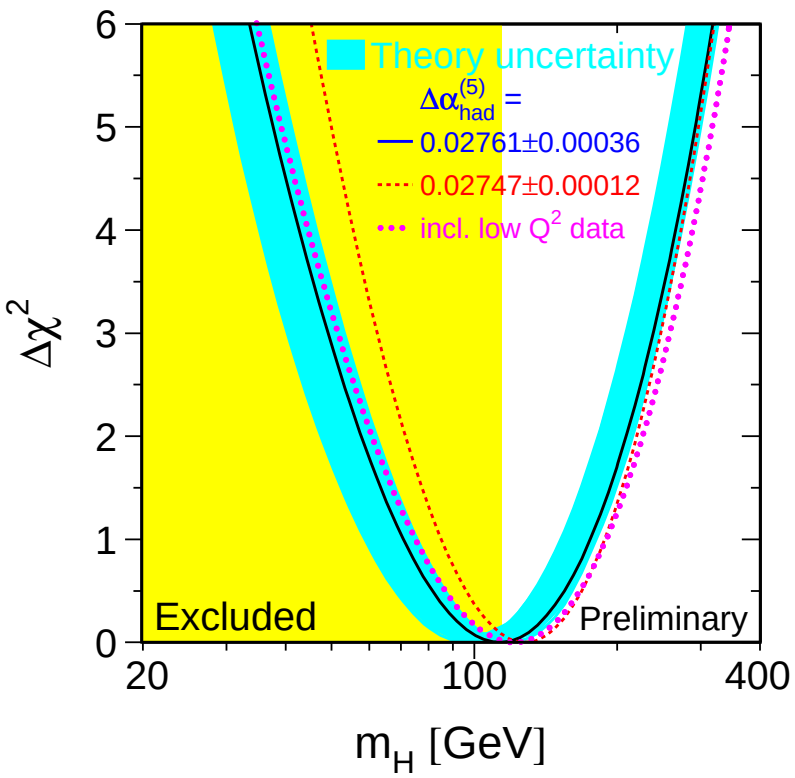

Figure 1.8: The $\Delta\chi^2$ of the fit to the electroweak precision data as a function of M_H. The solid line results when all data are included and the blue/shaded band is the estimated theoretical error from unknown higher–order corrections. The effect of including the low Q^2 data and the use of a different value for $\Delta\alpha_{\rm had}$ are also shown; from Ref. [8].

These values are relatively stable when the controversial NuTeV result is included in the fit, or when a slightly different value for $\Delta\alpha^5_{\rm had}$ is used. The area to the left to the vertical band which is very close to the minimum of the fit, shows the exclusion limit $M_H > 114.4$ GeV from direct searches at LEP2 to which we will turn our attention shortly.

It thus appears that the high–precision data, when confronted with the predictions of the SM after the radiative corrections have been incorporated, lead to stringent constraints on the Higgs sector of the SM. The data strongly disfavor a heavy Higgs boson with a mass $M_H \gtrsim 700$ GeV for which perturbation theory breaks down anyway, as will be seen in the next section. They clearly favor a light Higgs boson, $M_H \lesssim 260$ GeV, with a central value that is very close to the present lower bound from direct searches, $M_H \geq 114.4$ GeV. This is very encouraging for the next generation of high–energy experiments.

However, there are two caveats to this statement, a theoretical and an experimental one that we will discuss first. The most constraining observables, besides the W boson mass, are the LEP and SLC measurements of the leptonic asymmetries, led by the longitudinal asymmetry A_{LR}, on the one hand, and of the hadronic asymmetries, led by the forward–backward asymmetry for b–quarks A^b_{FB}, on the other hand. As can be seen from Fig. 1.7, while the former set favors a light Higgs boson, as is also the case for the measurement of M_W, the hadronic asymmetries favor a heavier Higgs particle. Because of the 3σ difference of the value of $\sin^2\theta_W$ as measured in the two sets of observables, it is only if one averages all the measurements that one obtains the central value $M_H \simeq 114$ GeV.

Because of the 2.5 standard deviation of A^b_{FB} from the theoretical prediction and the smaller deviation of A_{LR} but in the other direction, the SM fit is in fact rather poor [98]: the weighted average leading to the value $\sin^2\theta^{\rm lept}_{\rm eff}$ given in eq. (1.138), corresponds only to a 6% probability. The fit can be improved if one assumes New Physics effects which appear only in the $Zb\bar{b}$ vertex. However, as already mentioned, it is very difficult to induce new effects in A^b_{FB} without spoiling the agreement of R_b and $A^b_{LR,FB}$ with the data[13]. On the other hand, if one assumes that the discrepancy in A^b_{FB} is due to some systematical errors which have been underestimated by the experiments and remove this quantity from the global fit, one obtains a central value of M_H which is lower than the mass bound obtained from the direct Higgs boson searches at LEP2[14].

[13]Indeed, since $A^b_{FB} \propto A_e A_b$ and since $A_e \sim \hat{v}_e$ is small, one needs to alter significantly the $Zb\bar{b}$ couplings to account for the discrepancy of the asymmetry with the data: a 30% change of the right–handed $Zb\bar{b}$ coupling, $g_{bR} \sim \hat{a}_b - \hat{v}_b$, is required, an effect that is too large not to disturb the precise measurement of $R_b \sim g^2_{bR} + g^2_{bL}$ or $A^b_{LR,FB} \sim g^2_{bL} - g^2_{bR}$. This 30% change is anyway too large for a loop effect.

[14]In the past, when the top quark mass was measured to be $m_t \simeq 175 \pm 5$ GeV, the situation was even worse since the exclusion of A^b_{FB} from the fit led to a rather low M_H value, $M_H \sim 45$ GeV, with only a 5% probability that $M_H \geq 114$ GeV. This has led to some justified speculations about the validity of the SM [98]. The tension between the central value of the fit and the direct bound, has been relaxed with the recent value of $m_t \simeq 178 \pm 4.3$ GeV, which increased M_H by several tens of GeV.

The bound on the Higgs mass, eq. (1.141), is quite strong and there have been many speculations on how it can be relaxed or evaded. To do so, one has to introduce New Physics contributions which are of the same order as the one due to a heavy Higgs boson, and which conspire with the latter as to mimic the effect of a light SM Higgs particle. This has to be done without spoiling the rest of the agreement of the SM with the high–precision data.

A way to look at these new contributions is to parametrize the Higgs sector by an effective Lagrangian in which higher dimensional operators are added [99, 100]. These operators should respect the $\mathrm{SU(2)_L} \times \mathrm{U(1)_Y}$ gauge symmetry, as well as some other constraints. In this approach, one or a few higher dimensional operators which are damped by powers of the new scale Λ, produce corrections that counteract the one of a heavy Higgs boson, in such a way that the net result is compatible with the SM for $M_H \sim 100$ GeV. To produce such a conspiracy, the scale Λ should range between 2 to 10 TeV, depending on the nature of the operator or the combination of operators which generate the effect [101].

However, this approach does not tell anything about the New Physics which is behind the effective Lagrangian, and it is not actually clear whether it is possible to produce such a set of conspiring operators in a well motivated and consistent theoretical model. One therefore prefers to consider specific, and preferably well motivated, models.

In general, because of decoupling, models which contain an elementary Higgs particle generate only small radiative corrections even if they involve a large number of new particles. This is typically the case of supersymmetric extensions of the SM. In contrast, models where the Higgs boson is composite or strongly interacting can generate large effects. However, in most cases the new contributions add to the effect of a heavy Higgs boson, leading to a stronger disagreement with the precision data. This is, for instance, the case of early versions of Technicolor models which have been ruled out in the beginning of the nineties [92].

Nevertheless, there are still models of New Physics that are weakly interacting and which induce corrections that are large enough, and with the adequate sign, to accommodate a heavy Higgs boson. In Ref. [102], large classes of models have been considered and their effects on the radiative corrections have been analyzed. The conclusion of the study is that indeed, models with a heavy Higgs boson exist, but they always need some conspiracy to produce the required effect and more importantly, in most cases they predict new degrees of freedom which should be sufficiently light to be observed at the next generation of colliders[15].

[15] An example of such models are gauge extensions of the SM [for instance based on the SO(10) group or on the Superstrings–inspired E_6 symmetry] in which a heavy vector boson Z' is added. This particle will mix with the $\mathrm{SU(2)_L} \times \mathrm{U(1)_Y}$ Z boson to produce the observed Z particle; the mixing angle is inversely proportional to the Z' mass, $\theta_{\rm mix} \propto M_Z^2/M_{Z'}^2$. It has been shown in Ref. [102] that such a Z' can indeed generate any contribution to the S and T Peskin–Takeuchi parameters discussed in §1.2.4. However, to mimic the effect of a heavy Higgs boson, the Z' boson should have a rather low mass, $M_{Z'} \lesssim 1.5$ TeV, making this particle accessible at future colliders; see e.g. [103].

1.3.2 Constraints from direct searches

Searches at LEP1

The Higgs boson has been searched for at the LEP experiment, first at energies near the Z boson resonance, $\sqrt{s} \simeq M_Z$. In this case, two channels allow to probe the Higgs boson [104]. The dominant production mode is the Bjorken process [105], where the Z boson decays into a real Higgs boson and an off–shell Z boson which goes into two light fermions, $Z \to HZ^* \to Hf\bar{f}$; the Feynman diagram is shown in Fig. 1.9.

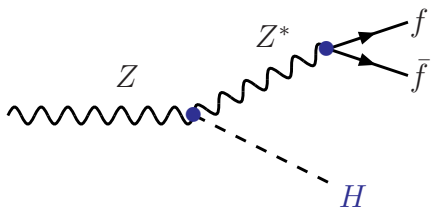

Figure 1.9: The main production mechanism for Higgs bosons in Z decays at LEP1.

The partial decay width $\Gamma(Z \to Hf\bar{f})$, when normalized to the $Z \to f\bar{f}$ decay width where the fermion $f \neq t$ is considered as massless, is given by [106]

$$\mathrm{BR}(Z \to Hf\bar{f}) \equiv \frac{\Gamma(Z \to Hf\bar{f})}{\Gamma(Z \to f\bar{f})} = \frac{G_\mu M_Z^2}{2\sqrt{2}\pi^2} \int_{2a}^{1+a^2} \mathrm{d}x\, \Gamma_0(x) \tag{1.142}$$

with the variable appearing in the integration bounds being $a = M_H/M_Z$ and x is the reduced energy of the Higgs boson $x = 2E_H/M_Z$. The function in the integrand reads

$$\Gamma_0(x) = \frac{\sqrt{x^2 - 4a^2}}{(x - a^2)^2 + \gamma^2} \left(1 - x + \frac{x^2}{12} + \frac{2a^2}{3}\right) \tag{1.143}$$

where $\gamma = \Gamma_Z/M_Z$ is the reduced total decay width of the Z boson. Neglecting the Z width in Γ_0, the integration over the variable x leads to a relatively simple analytical result [13]

$$\begin{aligned} \mathrm{BR}(Z \to Hf\bar{f}) \;=\; & \frac{G_\mu M_Z^2}{2\sqrt{2}\pi^2} \left[\frac{3a(a^4 - 8a^2 + 20)}{\sqrt{4 - a^2}} \mathrm{arcos}\left(\frac{1}{2}a(3 - a^2)\right) \right. \\ & \left. -3(a^4 - 6a^2 + 4)\ln a - \frac{1}{2}(1 - a^2)(2a^4 - 13a^2 + 47) \right] \end{aligned} \tag{1.144}$$

This branching ratio follows that of the Z decay into a given fermionic final state. For instance, $\mathrm{BR}(Z \to H\mu^+\mu^-)$ for muons and $\mathrm{BR}(Z \to H\nu\bar{\nu})$ when summing over the three neutrino species are, respectively, 3% and 18% of the total Higgs sample.

The Higgs boson can also be produced in the decay $Z \to H\gamma$ [107, 108] which occurs through triangular loops built–up by heavy fermions and the W boson; Fig. 1.10. The partial decay width, including only the dominant top quark and W contributions, reads

$$\Gamma(Z \to H\gamma) = \frac{\alpha G_\mu^2 M_W^2}{48\pi^4} M_Z^3 \left(1 - \frac{M_H^2}{M_Z^2}\right)^3 |A_t + A_W|^2 \tag{1.145}$$

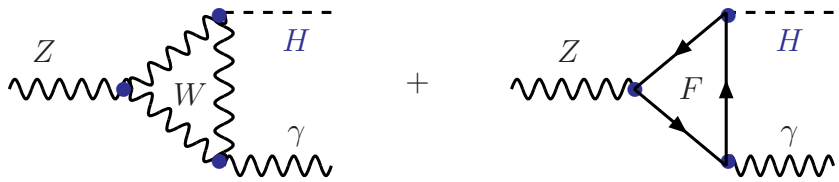

Figure 1.10: Feynman diagrams for the one–loop induced decay mode $Z \to H\gamma$ in the SM.

The complete expressions of the form factors A_t and A_W will be given later, when the reverse decay $H \to Z\gamma$ will be discussed in detail. In the case of interest here, i.e. for $M_H \lesssim M_W$, one can approximate the top quark form factors by its value in the vanishing M_H limit, $A_t = N_c Q_t \hat{v}_t/(3c_W) \sim 0.3$, but for the W form factor, a good approximation in the Higgs boson mass range relevant at LEP1, is given by [108]

$$A_W \simeq -4.6 + 0.3 M_H^2/M_W^2 \tag{1.146}$$

The two contributions interfere destructively, but the W contribution is largely dominating. We show in Table 1.4, the number of Higgs particles produced per 10^7 Z bosons, in both the loop induced process $Z \to H\gamma$ and in the Bjorken process $Z \to H\mu^+\mu^-$ [to obtain the rates for any final state f one has to multiply by a factor $\Gamma_Z/\Gamma_\mu \sim 33$]. As can be seen, the number of produced H bosons is much larger in the Bjorken process for small Higgs masses but the loop decay process becomes more important for masses around $M_H \sim 60$ GeV. However, in this case, only a handful of events can be observed.

M_H (GeV)	10	20	30	40	50	60	70
$Z \to H\mu^+\mu^-$	750	290	120	46	15.6	3.7	0.6
$Z \to H\gamma$	20.4	18.4	15.3	11.6	7.8	4.4	1.8

Table 1.4: The number of events for Higgs production at LEP1 per 10^7 Z bosons.

As will be discussed in great detail in the next chapter, the Higgs boson in the mass range relevant at LEP1 [and also LEP2], decays dominantly into hadrons [mostly $b\bar{b}$ final states for $M_H \gtrsim 10$ GeV], and less than $\sim 8\%$ of the time into τ–lepton pairs. Thus, not to be swamped by the large $e^+e^- \to$ hadron background, the Higgs boson has been searched for at LEP1 in the two topologies $Z \to (H \to \text{hadrons})(Z^* \to \nu\bar{\nu})$ leading to a final state consisting of two acoplanar jets and missing energy and $Z \to (H \to \text{hadrons})(Z^* \to e^+e^-, \mu^+\mu^-)$ with two energetic leptons isolated from the hadronic system. The absence of any Higgs boson signal by the four collaborations at LEP1 [109], allowed to set the 95% Confidence Level limit of $M_H \gtrsim 65.2$ GeV on the SM Higgs boson mass [110].

Before the advent of LEP1, the low Higgs mass range, $M_H \lesssim 5$ GeV, was very difficult to explore. Indeed, the main probes were, for Higgs masses below 20 MeV, Nuclear Physics experiments which are very sensitive to the theoretically uncertain Higgs–nucleon couplings and for larger masses, rare meson [from pions to heavy B mesons] decays which were plagued by various theoretical and experimental uncertainties[16]. On the Z resonance, this low mass range can be easily probed by considering the clean final state $Z \to Z^* H \to \mu^+\mu^- H$: since the invariant mass of the system recoiling against the lepton pair is simply the Higgs boson mass, the precise knowledge of the c.m. energy and the accurate measurement of the invariant mass and energy of the leptons allows an excellent resolution on M_H. This process therefore definitely rules out any Higgs boson with a mass below ~ 60 GeV, independently of its decay modes, provided that its coupling to the Z boson is as predicted in the SM.

Searches at LEP2

The search for Higgs bosons has been extended at LEP2 with c.m. energies up to $\sqrt{s} = 209$ GeV. In this energy regime, the dominant production process is Higgs–strahlung [32, 106, 111–113] where the e^+e^- pair goes into an off–shell Z boson which then splits into a Higgs particle and a real Z boson, $e^+e^- \to Z^* \to HZ$; see the digram of Fig. 1.11. [The cross section for the WW fusion process, to be discussed later, is very small at these energies [114].]

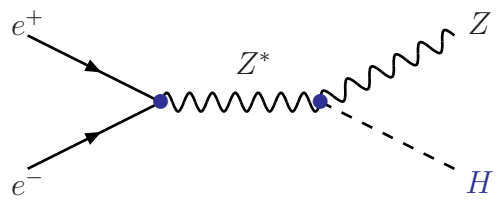

Figure 1.11: The production mechanism for SM Higgs bosons in e^+e^- collisions at LEP2.

The production cross section for this Higgs–strahlung process [which will be discussed in more details later] is given by

$$\sigma(e^+e^- \to ZH) = \frac{G_\mu^2 M_Z^4}{96\pi s}[1 + (1 - 4s_W^2)^2]\lambda^{1/2}\frac{\lambda + 12M_Z^2/s}{(1 - M_Z^2/s)^2} \tag{1.147}$$

It scales like $1/s$ and, therefore, is larger at low energies for light Higgs bosons and is suppressed by the usual two–particle phase space function $\lambda^{1/2} = [(1 - M_H^2/s - M_Z^2/s)^2 - 4M_H^2 M_Z^2/s^2]^{1/2}$. At LEP2 and for the maximal c.m. energy that has been reached, $\sqrt{s}_{\rm max} \sim 209$ GeV, it is shown in Fig. 1.12 as a function of M_H. At $M_H \sim 115$ GeV, the cross section is of the order of 100 fb which, for the integrated luminosity that has been collected, $\int \mathcal{L} \sim 0.1$ fb^{-1}, correspond to ten produced events. For a mass $M_H^{\rm max} \sim \sqrt{s} - M_Z \sim 117$ GeV, the $2 \to 2$ cross section vanishes, being suppressed by the phase–space factor $\lambda^{1/2}$.

[16]For a very detailed discussion of the SM Higgs boson searches in this low mass range, see Chapter 3.1 of *The Higgs Hunter's Guide* [13], pages 91-130.

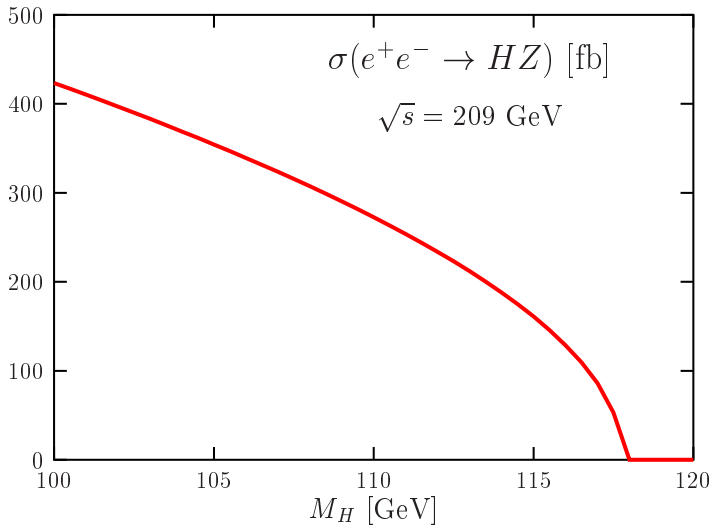

Figure 1.12: Production cross section for the SM Higgs boson at LEP2 [in femtobarns] for a center of mass energy $\sqrt{s} = 209$ GeV as a function of the Higgs boson mass.

The searches by the LEP collaborations have been made in several topologies [recall that the Higgs boson decays mainly into $b\bar{b}$ final states and the branching ratio for the decays into τ–lepton is a few percent]: $e^+e^- \to (H \to b\bar{b})(Z^* \to \nu\bar{\nu})$ and $e^+e^- \to (H \to b\bar{b})(Z^* \to \ell^+\ell^-)$ as at LEP1, as well as $e^+e^- \to (H \to \tau^+\tau^-)(Z^* \to b\bar{b})$ and $e^+e^- \to (H \to b\bar{b})(Z^* \to \tau^+\tau^-)$. Combining the results of the four LEP collaborations, no significant excess above the expected SM background has been seen, and the exclusion limit [10]

$$M_H > 114.4 \text{ GeV} \tag{1.148}$$

has been established at the 95% CL from the non–observation of a signal, as shown in Fig. 1.13. This upper limit, in the absence of additional events with respect to SM predictions, was expected to be $M_H > 115.3$ GeV. The reason for the discrepancy is that there is a 1.7σ excess [compared to the value 2.9σ reported at the end of 2000] of events for a Higgs boson mass in the vicinity of $M_H = 116$ GeV [10]. But this excess is not significant enough, since we need a 5σ signal to be sure that we have indeed discovered the Higgs boson.

Higgs bosons with SM couplings to the Z boson have been searched for in various decay modes, such as invisible decays [115] and flavor blind hadronic decays [116] by considering the recoil of the Z boson in the process $e^+e^- \to H(Z^* \to \ell^+\ell^-)$ for instance; Higgs boson masses close to the $M_H \sim 114$ GeV bound have been ruled out. The bound $M_H \gtrsim 114.4$ GeV can be evaded only if the Higgs boson has non standard couplings to the Z boson. Indeed a smaller value of the g_{HZZ} coupling compared to the SM prediction would suppress the $e^+e^- \to HZ$ cross section which is directly proportional to g^2_{HZZ}. The 95% CL bound on the Higgs boson mass as a function of its coupling relative to the SM value, $\zeta = g_{HZZ}/g^{\rm SM}_{HZZ}$ is shown in Fig. 1.14. For masses below $M_H \lesssim 80$ GeV, Higgs bosons with couplings to the Z boson an order of magnitude smaller than in the SM have thus also been ruled out [10].

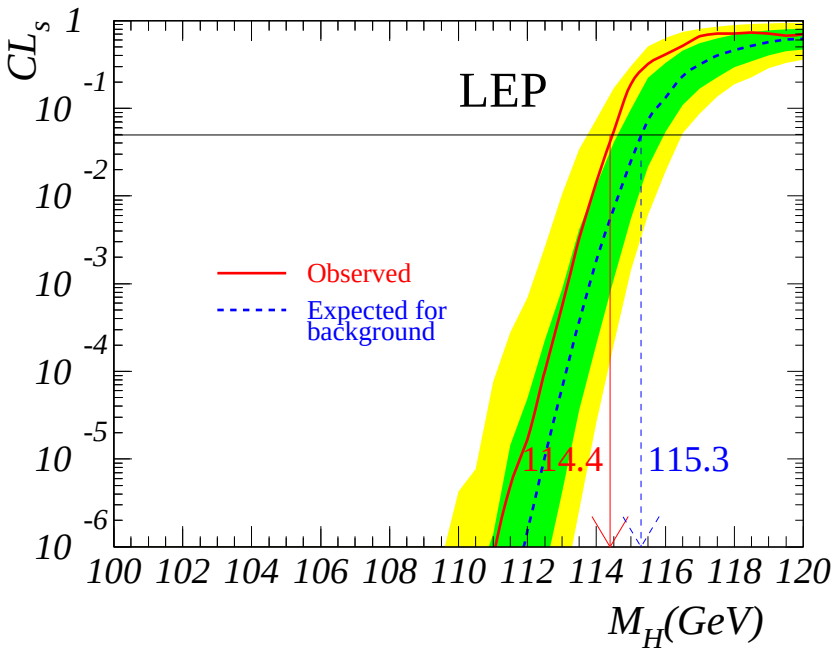

Figure 1.13: Confidence Level CL_s for the signal+background hypothesis in Higgs production at LEP2. The solid/red line is for the observation, the dashed line is the median background expectation, the dark–grey/green and light–grey/yellow shaded bands around the median expected line correspond to the 68% and 95% simulated probability bands. The intersection of the horizontal line at $CL_s = 0.05$ with the observed curve defines the 95% CL lower bound for M_H; from Ref. [10].

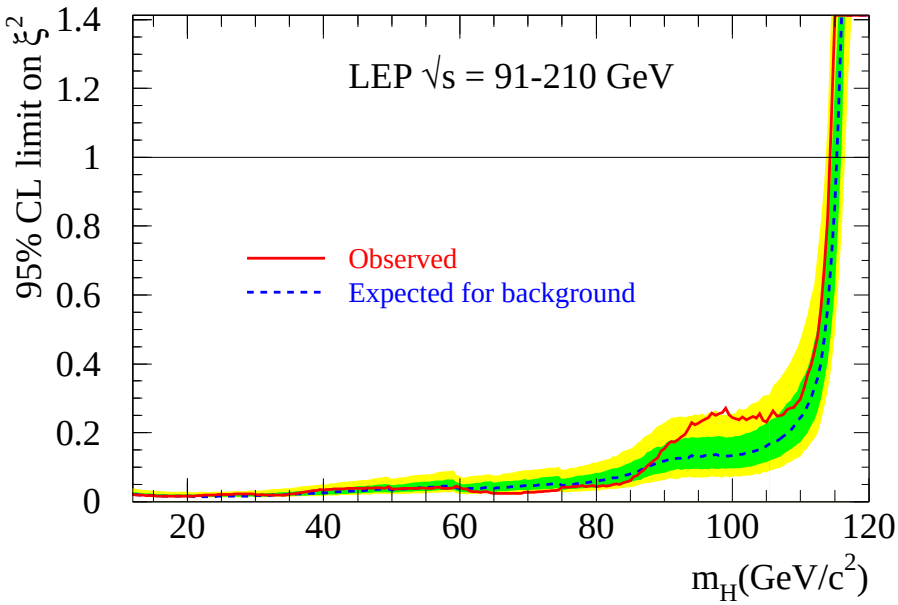

Figure 1.14: The upper bound on the coupling $\zeta^2 = (g_{HZZ}/g_{HZZ}^{\rm SM})^2$ as a function of the Higgs mass. The solid line represents the observed limit while the dark (light) shaded band is for the 68% (95%) probability band; from Ref. [10].

1.4 Theoretical constraints on the Higgs boson mass

In addition to the experimental constraints on the Higgs boson mass discussed previously, there are interesting theoretical constraints which can be derived from assumptions on the energy range in which the SM is valid before perturbation theory breaks down and new phenomena should emerge. These include constraints from unitarity in scattering amplitudes, perturbativity of the Higgs self–coupling, stability of the electroweak vacuum and fine–tuning. These constraints are summarized in this section.

1.4.1 Constraints from perturbativity and unitarity

Perturbative unitarity

One of the main arguments to abandon the old Fermi theory for the weak interaction was that it violates unitarity at energies close to the Fermi scale. Indeed, taking for instance the reaction $\nu_\mu e \to \nu_e \mu$ [which, in principle, proceeds through the t–channel exchange of a W boson and has only the J=1 partial wave], the cross section at a high energy $\sqrt{s}$ behaves like $\sigma \sim G_\mu^{-1/2} s$. However, unitarity requires that the cross section should be bounded by s^{-1} and for energies above $\sqrt{s} \sim G_\mu^{-1/2} \sim 300$ GeV, the cross section will violate unitarity. This particular problem was cured in the intermediate massive vector boson theory [i.e. including simply by hand the W boson mass and, hence, its longitudinal degree of freedom in the Lagrangian] but in other processes, such as $\nu\bar{\nu} \to W^+W^-$ through t–channel e exchange, the amplitude had also a bad high energy behavior which called for the introduction of the neutral Z boson to be exchanged in the s–channel to cancel it. In fact, if one demands that there is no such process which violates unitarity, one would end up with just the renormalizable Lagrangian of the SM discussed in §1.1; see Ref. [7].

However, there is still a potential problem in the SM, but at much higher energies than the Fermi scale. As discussed in §1.1.3, the interactions of the longitudinal components of the massive gauge bosons grow with their momenta. In processes involving the W_L and Z_L bosons, this would eventually lead to cross sections which increase with the energy which would then violate unitarity at some stage. We will briefly discuss this aspect in the following, taking as an example the scattering process $W^+W^- \to W^+W^-$ at high energies [31,70,117]; for a detailed discussion, see Ref. [118] for instance. Some contributing Feynman diagrams to this process are displayed in Fig. 1.15; there are also additional diagrams involving the s– and t–channel exchanges of γ and Z bosons.

The amplitude for the scattering of charged W bosons, in the high–energy limit $s \gg M_W^2$ and for heavy Higgs bosons, is given by

$$A(W^+W^- \to W^+W^-) \stackrel{s \gg M_W^2}{\longrightarrow} \frac{1}{v^2}\left[s + t - \frac{s^2}{s - M_H^2} - \frac{t^2}{t - M_H^2}\right] \tag{1.149}$$

where s, t are the Mandelstam variables [the c.m. energy s is the square of the sum of the momenta of the initial or final states, while t is the square of the difference between the momenta of one initial and one final state]. In fact, this contribution is coming from longitudinal W bosons which, at high energy, are equivalent to the would–be Goldstone bosons as discussed in §1.1.3. One can then use the potential of eq. (1.58) which gives the interactions of the Goldstone bosons and write in a very simple way the three individual amplitudes for the scattering of longitudinal W bosons

$$A(w^+w^- \to w^+w^-) = -\left[2\frac{M_H^2}{v^2} + \left(\frac{M_H^2}{v}\right)^2 \frac{1}{s-M_H^2} + \left(\frac{M_H^2}{v}\right)^2 \frac{1}{t-M_H^2}\right] \tag{1.150}$$

which after some manipulations, can be cast into the result of eq. (1.149) given previously.

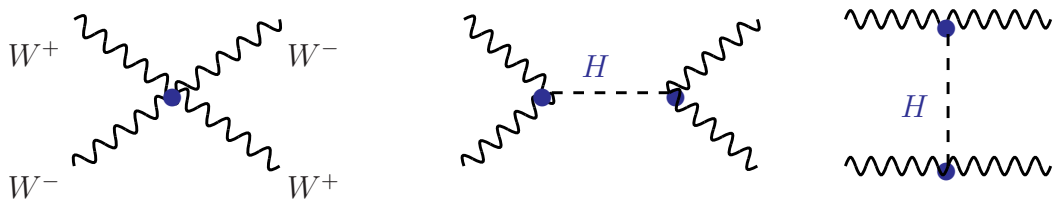

Figure 1.15: Some Feynman diagrams for the scattering of W bosons at high energy.

These amplitudes will lead to cross sections $\sigma(W^+W^- \to W^+W^-) \simeq \sigma(w^+w^- \to w^+w^-)$ which could violate their unitarity bounds. To see this explicitly, we first decompose the scattering amplitude A into partial waves a_ℓ of orbital angular momentum ℓ

$$A = 16\pi \sum_{\ell=0}^{\infty} (2\ell+1) P_\ell(\cos\theta)\, a_\ell \tag{1.151}$$

where P_ℓ are the Legendre polynomials and θ the scattering angle. Since for a $2 \to 2$ process, the cross section is given by $\mathrm{d}\sigma/\mathrm{d}\Omega = |A|^2/(64\pi^2 s)$ with $\mathrm{d}\Omega = 2\pi \mathrm{d}\cos\theta$, one obtains

$$\begin{aligned} \sigma &= \frac{8\pi}{s} \sum_{\ell=0}^{\infty}\sum_{\ell'=0}^{\infty} (2\ell+1)(2\ell'+1) a_\ell a_{\ell'} \int_{-1}^{1} \mathrm{d}\cos\theta P_\ell(\cos\theta) P_{\ell'}(\cos\theta) \\ &= \frac{16\pi}{s} \sum_{\ell=0}^{\infty} (2\ell+1)|a_\ell|^2 \end{aligned} \tag{1.152}$$

where the orthogonality property of the Legendre polynomials, $\int \mathrm{d}\cos\theta P_\ell P_{\ell'} = \delta_{\ell\ell'}$, has been used. The optical theorem tells us also that the cross section is proportional to the imaginary part of the amplitude in the forward direction, and one has the identity

$$\sigma = \frac{1}{s}\,\mathrm{Im}\,[\,A(\theta=0)\,] = \frac{16\pi}{s} \sum_{\ell=0}^{\infty} (2\ell+1)|a_\ell|^2 \tag{1.153}$$

This leads to the unitary conditions [119]

$$\begin{aligned} |a_\ell|^2 = \mathrm{Im}(a_\ell) \quad &\Rightarrow \quad [\mathrm{Re}(a_\ell)]^2 + [\mathrm{Im}(a_\ell)]^2 = \mathrm{Im}(a_\ell) \\ &\Rightarrow \quad [\mathrm{Re}(a_\ell)]^2 + [\mathrm{Im}(a_\ell) - \frac{1}{2}]^2 = \frac{1}{4} \end{aligned} \tag{1.154}$$

This is nothing else than the equation of a circle of radius $\frac{1}{2}$ and center $(0, \frac{1}{2})$ in the plane $[\mathrm{Re}(a_\ell), \mathrm{Im}(a_\ell)]$. The real part lies between $-\frac{1}{2}$ and $\frac{1}{2}$,

$$|\mathrm{Re}(a_\ell)| < \frac{1}{2} \tag{1.155}$$

If one takes the $J = 0$ partial wave for the amplitude $A(w^+w^- \to w^+w^-)$

$$a_0 = \frac{1}{16\pi s} \int_s^0 \mathrm{d}t |A| = -\frac{M_H^2}{16\pi v^2} \left[2 + \frac{M_H^2}{s - M_H^2} - \frac{M_H^2}{s} \log\left(1 + \frac{s}{M_H^2}\right) \right] \tag{1.156}$$

and assumes the Higgs boson mass to be much smaller than $\sqrt{s}$, which leads to

$$a_0 \overset{s \gg M_H^2}{\longrightarrow} -\frac{M_H^2}{8\pi v^2} \tag{1.157}$$

From the requirement of the unitarity condition, eq. (1.155), one obtains the upper bound [32]

$$M_H \lesssim 870 \text{ GeV} \tag{1.158}$$

In fact the scattering channel $W_L^+ W_L^-$ considered above can be coupled with other channels: $Z_L Z_L$, HH and $Z_L H$ [for a recent discussion, see Ref. [120] e.g.]. In addition to the four neutral particle initial states, one can also consider the two charged channels $W_L^+ H$ and $W_L^+ Z_L$ which, because of charge conservation, are not coupled to the neutral ones. The scattering amplitude is then given by a 6×6 matrix which is diagonal by block: a 4×4 block for the neutral channels and a 2×2 block for the charged channels. At high energies, the matrix elements are dominated by the quartic couplings and the full matrix in the basis

$$\left(W_L^+ W_L^- \,,\ \frac{1}{\sqrt{2}} Z_L Z_L \,,\ \frac{1}{\sqrt{2}} HH \,,\ Z_L H \,,\ W_L^+ H \,,\ W_L^+ Z_L \right) \tag{1.159}$$

with the factors $\frac{1}{\sqrt{2}}$ accounting for identical particle statistics, takes the form

$$a_0 \propto \frac{M_H^2}{v^2} \begin{pmatrix} 1 & \frac{\sqrt{2}}{4} & \frac{\sqrt{2}}{4} & 0 & 0 & 0 \\ \frac{\sqrt{2}}{4} & \frac{3}{4} & \frac{1}{4} & 0 & 0 & 0 \\ \frac{\sqrt{2}}{4} & \frac{1}{4} & \frac{3}{4} & 0 & 0 & 0 \\ 0 & 0 & 0 & \frac{1}{2} & 0 & 0 \\ 0 & 0 & 0 & 0 & \frac{1}{2} & 0 \\ 0 & 0 & 0 & 0 & 0 & \frac{1}{2} \end{pmatrix} \tag{1.160}$$

The requirement that the largest eigenvalues of a_0, respects the unitarity constraint yields [121]

$$M_H \lesssim 710 \text{ GeV} \tag{1.161}$$

Thus, in the SM, if the Higgs boson mass exceeds values of $\mathcal{O}(700 \text{ GeV})$, unitarity will be violated unless new phenomena appear and restore it. There is, however, a caveat to this conclusion. The analysis above has been performed only at tree–level and since the Higgs boson self–coupling becomes strong for large masses, $\lambda = M_H^2/(2v^2)$, the radiative corrections can be very large and, eventually, render the theory non perturbative; this tree–level result would be then lost. Thus, to apply the previous argument to set a bound on the Higgs boson mass, one has to assume that the SM remains perturbative and that higher–order corrections are not large. The unitarity argument should therefore more properly be called, the tree–level unitarity or perturbative unitarity argument.

In fact, one can use the unitarity argument in a different limit [31]: if one assumes that the Higgs boson mass is much larger than $\sqrt{s}$ [which in turn, is much larger than M_W], the unitarity constraint writes, if one takes into account only the $W_L^+W_L^- \to W_L^+W_L^-$ channel,

$$a_0 \stackrel{s \ll M_H^2}{\longrightarrow} -\frac{s}{32\pi v^2} \tag{1.162}$$

and with the condition $|\text{Re}(a_0)| < \frac{1}{2}$, one obtains

$$\sqrt{s} \lesssim 1.7 \text{ TeV} \tag{1.163}$$

Again, a more stringent bound is obtained by considering all the coupled channels above

$$\sqrt{s} \lesssim 1.2 \text{ TeV} \tag{1.164}$$

This means that if the Higgs boson is too heavy [or, equivalently, not existing at all], some New Physics beyond the SM should manifest itself at energies in the TeV range to restore unitary in the scattering amplitudes of longitudinal gauge bosons.

Therefore, from the requirement that the tree–level contributions to the partial waves of scattering processes involving gauge and Higgs bosons should not exceed the unitarity bound, one concludes that either: (i) some New Physics, which plays a role similar to that of the Higgs particle should appear in the TeV range to cancel this breakdown, or (ii) the unitarity breakdown is canceled by high–order terms which signal the failure of perturbation theory and the loss of the predictive power of the SM.

Perturbativity in processes involving the Higgs boson

In fact, it is known from a different context that for large values of the Higgs boson mass, perturbation theory is jeopardized in the SM. This occurs for instance in the decays of the

Higgs boson into massive gauge bosons, which will be discussed later in detail. Using the equivalence theorem and the Lagrangian eq. (1.58), one can write immediately the partial decay width of the Higgs boson into two longitudinal Z bosons [or W bosons]

$$\Gamma(H \to ZZ) \sim \Gamma(H \to w_0 w_0) = \left(\frac{1}{2M_H}\right) \left(\frac{2!\, M_H^2}{2v}\right)^2 \frac{1}{2} \left(\frac{1}{8\pi}\right) \to \frac{M_H^3}{32\pi v^2} \tag{1.165}$$

where the first parenthesis is for the flux factor, the second for the amplitude squared, the factor $\frac{1}{2}$ is for the two identical final particles, and the last parenthesis is for the phase space factor. For the decay $H \to WW$, one simply needs to remove the statistical factor to account for both $W^\pm$ states

$$\Gamma(H \to W^+W^-) \simeq 2\Gamma(H \to ZZ) \tag{1.166}$$

The behavior, $\Gamma_H \propto M_H^3$, compared to $\Gamma_H \propto M_H$ for decays into fermions for instance, is due to the longitudinal components that grow with the energy [which is M_H in this context].

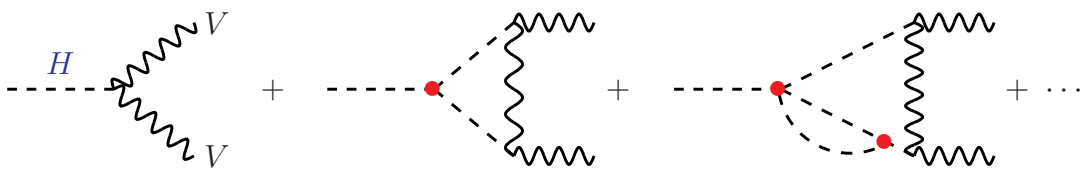

Figure 1.16: Generic diagrams for the one– and two–loop corrections to Higgs boson decays.

Let us have a brief look at these decays when higher–order radiative corrections, involving the Higgs boson and therefore the quartic coupling λ, are taken into account. Including the one–loop and two–loop radiative corrections, with some generic Feynman diagrams shown in Fig. 1.16, the partial Higgs decay width into gauge bosons is given by [121, 122]

$$\Gamma_{\text{tot}} \simeq \Gamma_{\text{Born}} \left[1 + 3\hat{\lambda} + 62\hat{\lambda}^2 + \mathcal{O}(\hat{\lambda}^3)\right] \tag{1.167}$$

with $\hat{\lambda} = \lambda/(16\pi^2)$. If the Higgs boson mass is very large, $M_H \sim \mathcal{O}(10 \text{ TeV})$, the one loop term becomes close to the Born term, $3\hat{\lambda} \sim 1$, and the perturbative series is therefore not convergent. Even worse, already for a Higgs boson mass in the TeV range, $M_H \sim \mathcal{O}(1 \text{ TeV})$, the two–loop contribution becomes as important as the one–loop contribution, $3\hat{\lambda} \sim 62\hat{\lambda}^2$. Hence, for perturbation theory to hold, M_H should be smaller than about 1 TeV.

In addition, the partial decay widths become extremely large for a very heavy Higgs particle. Indeed, taking into account only W and Z decay modes, the total width is

$$\Gamma(H \to WW + ZZ) \sim 500 \text{ GeV } (M_H/1 \text{ TeV})^3 \tag{1.168}$$

and for a mass $M_H \sim 1.3$ TeV, the total decay width becomes comparable to the mass: the Higgs boson is then "obese" and cannot be considered as a "true" resonance anymore.

The same exercise can be made in the case of the Higgs decays into fermions. Including the one– and two–loop corrections involving the quartic interaction, one obtains [70, 123]

$$\Gamma_{\rm tot} \simeq \Gamma_{\rm Born} \left[1 + 2\hat{\lambda} - 32\hat{\lambda}^2 + \mathcal{O}(\hat{\lambda}^3) \right] \tag{1.169}$$

Qualitatively, the situation is the same as for the decays into gauge bosons, although the breakdown of perturbation theory is delayed because of the smaller coefficients of the one– and two–loop corrections. These features will be discussed in the chapter on Higgs decays.

The jeopardy of perturbation theory at large Higgs masses can also be seen in the scattering of longitudinal gauge bosons from which we have previously derived the upper bound on M_H from perturbative unitarity. In the case of the $W_L^+W_L^- \to W_L^+W_L^-$ scattering, the radiative corrections have been calculated at one and two loops in Refs. [124, 125] where it has been found that at high energy, the amplitude depends on the considered energy, contrary to what was occurring in the tree level case discussed previously. However, applying Renormalization Group methods, one can absorb the logarithmic energy dependence by defining a running self–coupling λ at the energy scale $\sqrt{s}$ [see next subsection]. At two–loop order, one then finds for the $W_L^+W_L^- \to W_L^+W_L^-$ scattering cross section at very high energies [125]

$$\sigma(W_L^+W_L^- \to W_L^+W_L^-) \sim \frac{1}{s}\hat{\lambda}(s) \left(1 - 48.64\hat{\lambda} + 333.21\hat{\lambda}^2 \right) \tag{1.170}$$

Here, the coefficients of the corrections are much larger than in Higgs decays and in fact, the one–loop correction become of order unity already for $\lambda(s)$ values close to 3.

Using various criteria, such as the scheme and scale dependence of the amplitudes, to estimate at which stage the breakdown of perturbation theory occurs [126] and a comparison with non–perturbative calculations on the lattice [119], one arrives at the conclusion that perturbation theory is lost for Higgs boson masses above $M_H \sim 700$ GeV. This result is remarkably close to what has been obtained by simply using the [somewhat naive] perturbative unitarity argument.

1.4.2 Triviality and stability bounds

As seen in previous discussions, because of quantum corrections, the couplings as well as the masses which appear in the SM Lagrangian, depend on the considered energy. This is also the case for the quartic Higgs coupling which will be monotonically increasing with the energy scale $|Q|$. This leads to non–trivial constraints on this coupling and, hence, on the Higgs boson mass, that we summarize in this subsection.

The triviality bound

Let us have a look at the one–loop radiative corrections to the Higgs boson quartic coupling, taking into account for the present moment only the contributions of the Higgs boson itself. The Feynman diagrams for the tree–level and the one–loop corrections to the Higgs boson self–coupling are depicted in Fig. 1.17.

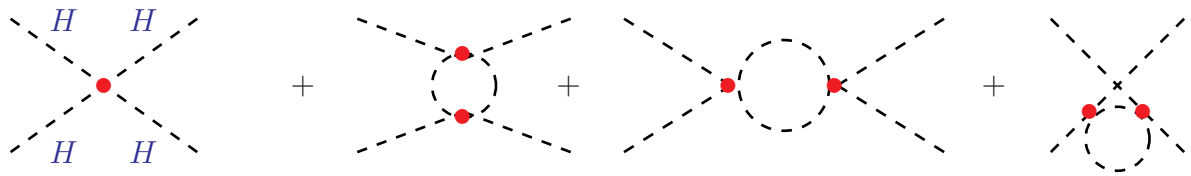

Figure 1.17: Typical Feynman diagrams for the tree–level and one–loop Higgs self–coupling.

The variation of the quartic Higgs coupling with the energy scale Q is described by the Renormalization Group Equation (RGE) [127]

$$\frac{\mathrm{d}}{\mathrm{d}Q^2}\,\lambda(Q^2) = \frac{3}{4\pi^2}\,\lambda^2(Q^2) \;\; + \text{higher orders} \tag{1.171}$$

The solution of this equation, choosing the natural reference energy point to be the electroweak symmetry breaking scale, $Q_0 = v$, reads at one–loop

$$\lambda(Q^2) = \lambda(v^2)\left[1 - \frac{3}{4\pi^2}\,\lambda(v^2)\log\frac{Q^2}{v^2}\right]^{-1} \tag{1.172}$$

The quartic couplings varies logarithmically with the squared energy Q^2. If the energy is much smaller than the electroweak breaking scale, $Q^2 \ll v^2$, the quartic coupling becomes extremely small and eventually vanishes, $\lambda(Q^2) \sim \lambda(v^2)/\log(\infty) \to 0_+$. It is said that the theory is trivial, i.e. non interacting since the coupling is zero [128].

In the opposite limit, when the energy is much higher that weak scale, $Q^2 \gg v^2$, the quartic coupling grows and eventually becomes infinite, $\lambda(Q^2) \sim \lambda(v^2)/(1-1) \gg 1$. The point, called Landau pole, where the coupling becomes infinite is at the energy

$$\Lambda_C = v\,\exp\left(\frac{4\pi^2}{3\lambda}\right) = v\,\exp\left(\frac{4\pi^2 v^2}{M_H^2}\right) \tag{1.173}$$

The general triviality argument [119, 129] states that the scalar sector of the SM is a ϕ^4–theory, and for these theories to remain perturbative at all scales one needs to have a coupling $\lambda = 0$ [which in the SM, means that the Higgs boson is massless], thus rendering the theory trivial, i.e. non–interacting. However, one can view this argument in a different way: one can use the RGE for the quartic Higgs self–coupling to establish the energy domain in which

the SM is valid, i.e. the energy cut–off Λ_C below which the self–coupling λ remains finite. In this case, and as can be seen from the previous equation, if Λ_C is large, the Higgs mass should be small to avoid the Landau pole; for instance for the value $\Lambda_C \sim 10^{16}$ GeV, one needs a rather light Higgs boson, $M_H \lesssim 200$ GeV. In turn, if the cut–off Λ_C is small, the Higgs boson mass can be rather large and for $\Lambda_C \sim 10^3$ GeV for instance, the Higgs mass is allowed to be of the order of 1 TeV.

In particular, if the cut–off is set at the Higgs boson mass itself, $\Lambda_C = M_H$, the requirement that the quartic coupling remains finite implies that $M_H \lesssim 700$ GeV. But again, there is a caveat in this argument: when λ is too large, one cannot use perturbation theory anymore and this constraint is lost. However, from simulations of gauge theories on the lattice, where the non–perturbative effects are properly taken into account, it turns out that one obtains the rigorous bound $M_H < 640$ GeV [130], which is in a remarkable agreement with the bound obtained by naively using perturbation theory.

The stability bound

In the preceding discussion, only the contribution of the Higgs boson itself has been included in the running of the quartic coupling λ. This is justified in the regime where λ is rather large. However, to be complete, one needs to also include the contributions from fermions and gauge bosons in the running. Since the Higgs boson couplings are proportional to the particle masses, only the contribution of top quarks and massive gauge bosons need to be considered. Some generic Feynman diagrams for these additional contributions are depicted in Fig. 1.18.

The one–loop RGE for the quartic coupling, including the fermion and gauge boson contributions, becomes [127]

$$\frac{\mathrm{d}\lambda}{\mathrm{dlog}Q^2} \simeq \frac{1}{16\pi^2}\left[12\lambda^2 + 6\lambda\lambda_t^2 - 3\lambda_t^4 - \frac{3}{2}\lambda(3g_2^2 + g_1^2) + \frac{3}{16}\left(2g_2^4 + (g_2^2 + g_1^2)^2\right)\right] \quad (1.174)$$

where the top quark Yukawa coupling is given by $\lambda_t = \sqrt{2}m_t/v$. The first effect of this extension is that for not too large λ values, the additional contributions will slightly alter the triviality bounds. In particular, the scale at which the New Physics should appear will depend on the precise value of the top quark mass.

Figure 1.18: Diagrams for the one–loop contributions of fermions and gauge bosons to λ.

However, it is for small values of the quartic couplings that the additional contributions can have a large impact and give some new information. Indeed, for $\lambda \ll \lambda_t, g_1, g_2$, the RGE can be approximated by

$$\frac{\mathrm{d}\lambda}{\mathrm{dlog}Q^2} \simeq \frac{1}{16\pi^2}\left[12\lambda^2 - 12\frac{m_t^4}{v^4} + \frac{3}{16}\left(2g_2^4 + (g_2^2+g_1^2)^2\right)\right] \tag{1.175}$$

and its solution, taking again the weak scale as the reference point, is

$$\lambda(Q^2) = \lambda(v^2) + \frac{1}{16\pi^2}\left[-12\frac{m_t^4}{v^4} + \frac{3}{16}\left(2g_2^4 + (g_2^2+g_1^2)^2\right)\right]\log\frac{Q^2}{v^2} \tag{1.176}$$

If the coupling λ is too small, the top quark contribution can be dominant and could drive it to a negative value $\lambda(Q^2) < 0$, leading to a scalar potential $V(Q^2) < V(v)$. The vacuum is not stable anymore since it has no minimum. The stability argument [131–133] tells us that to have a scalar potential which is bounded from below and, therefore, to keep $\lambda(Q^2) > 0$, the Higgs boson mass should be larger than the value

$$M_H^2 > \frac{v^2}{8\pi^2}\left[-12\frac{m_t^4}{v^4} + \frac{3}{16}\left(2g_2^4 + (g_2^2+g_1^2)^2\right)\right]\log\frac{Q^2}{v^2} \tag{1.177}$$

This puts a strong constraint on the Higgs boson mass, which depends on the value of the cut–off Λ_C. For relatively low and very high values for this cut–off, one obtains

$$\begin{aligned} \Lambda_C \sim 10^3 \text{ GeV} \quad &\Rightarrow \quad M_H \gtrsim 70 \text{ GeV} \\ \Lambda_C \sim 10^{16} \text{ GeV} \quad &\Rightarrow \quad M_H \gtrsim 130 \text{ GeV} \end{aligned} \tag{1.178}$$

Note, however, that the stability bound on the New Physics scale can be relaxed if the vacuum is metastable as discussed in Ref. [134]. Indeed, the SM effective potential can have a minimum which is deeper than the standard electroweak minimum if the decay of the latter into the former, via thermal fluctuations in the hot universe or quantum fluctuations at zero temperature, is suppressed. In this case, a lower bound on the Higgs mass follows from the requirement that no transition between the two vacua occurs and we always remain in the electroweak minimum. The obtained bound on M_H is in general much weaker than in the case of absolute stability of the vacuum and even disappears if the cut–off of the theory is at the TeV scale[17].

[17]Note that the first argument, i.e. thermal fluctuations, relies on several cosmological assumptions such as that the universe went through a phase of very high temperature, which has been indirectly tested so far only for temperatures of the order of a few MeV. The second argument, quantum tunneling, where the only cosmological input is the knowledge of the age of the universe which should be larger than the lifetime of the instability of the vacuum, gives less severe bounds; see Ref. [133] for instance.

Higher order effects and combined triviality and stability bounds

Thus, the positivity and the finiteness of the self–coupling λ impose, respectively, a lower bound $M_H \gtrsim 70$ GeV and an upper bound $M_H \lesssim 1$ TeV, on the SM Higgs boson mass if the cut–off is set to $\mathcal{O}(1\text{ TeV})$. These bounds are only approximative and to have more precise ones, some refinements must, however, be included [132, 135, 136].

Since the β functions of all SM couplings have been calculated up to two loops, they can be included in the analysis. For the scalar sector for instance, one has at this order

$$\frac{\mathrm{d}\lambda}{\mathrm{dlog}Q^2} \equiv \beta_\lambda = 24\frac{\lambda^2}{(16\pi^2)} - 312\frac{\lambda^3}{(16\pi^2)^2} \tag{1.179}$$

While, at one–loop, the $\lambda(\mu)$ coupling monotonically increases with the scale μ until it becomes infinite when reaching the Landau pole at the scale Λ_C, at the two–loop–level, it approaches an ultraviolet fixed–point corresponding to $\beta_\lambda = 0$. From the previous equation at two–loop, the resulting fixed–point value is $\lambda_{\rm FP} = 16\pi^2 \times 24/312 \simeq 12.1$ [however, top contributions cannot be neglected and they modify the behavior of this fixed-point.]

To obtain the upper bound on M_H, we need to choose the cut–off value for λ. Since $\lambda_{\rm FP}$ is large and perturbation theory is lost even before reaching this value, one can choose a value smaller than $\lambda_{\rm FP}$ as being this cut–off. An estimate of the stability of the bound can be made by varying the cut–off value for instance between $\lambda_{\rm FP}/4$ and $\lambda_{\rm FP}/2$, which lead to two–loop corrections which are about, respectively, 25% and 50%, of the one–loop result. Therefore, one can consider the first value as leading to a well behaved perturbative series and the second value as being at the limit where perturbation theory is valid.

For the stability bound, one simply requires that the coupling λ remains positive at the cut–off scale, $\lambda(\Lambda_C) > 0$. For an accurate determination of the bound, this requirement has to be made at the two–loop level, including matching conditions, i.e. the precise relation between the physical masses of the gauge bosons and the top quark and their corresponding couplings. The most important inputs are the Higgs and top quark masses

$$\lambda(\mu) = M_H^2/(2v^2) \times [1 + \delta_H(\mu)]\ ,\ \lambda_t(\mu) = \sqrt{2}m_t/v \times [1 + \delta_t(\mu)] \tag{1.180}$$

Including the theoretical uncertainties by a variation of the cut–off Λ_C from $\lambda_{\rm FP}/2$ to $\lambda_{\rm FP}/4$ using the matching conditions for the top quark and Higgs boson masses, and the experimental errors mainly on $\alpha_s = 0.118 \pm 0.002$ and $m_t = 175 \pm 6$ GeV, one obtains [136] the modern version of the Roman plot shown in Fig. 1.19 for the stability [lower band] and triviality [upper band] constraints, which give the allowed range of M_H as a function of the scale of New Physics Λ_C [between the bands]. The width of the bands corresponds to the various experimental and theoretical errors. As can be seen, if the New Physics scale Λ_C is

at the TeV scale, the Higgs boson mass is allowed to be in the range

$$50 \text{ GeV} \lesssim M_H \lesssim 800 \text{ GeV} \tag{1.181}$$

while, requiring the SM to be valid up to the Grand Unification scale, $\Lambda_{\rm GUT} \sim 10^{16}$ GeV, the Higgs boson mass should lie in the range

$$130 \text{ GeV} \lesssim M_H \lesssim 180 \text{ GeV} \tag{1.182}$$

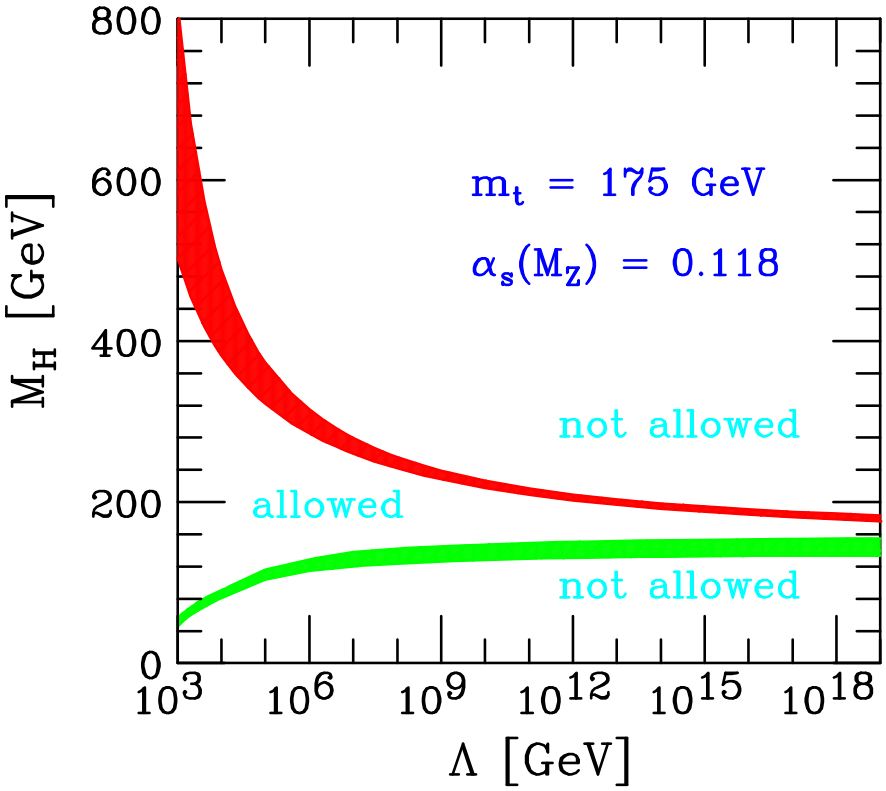

Figure 1.19: The triviality (upper) bound and the vacuum stability (lower) bound on the Higgs boson mass as a function of the New Physics or cut–off scale Λ for a top quark mass $m_t = 175 \pm 6$ GeV and $\alpha_s(M_Z) = 0.118 \pm 0.002$; the allowed region lies between the bands and the colored/shaded bands illustrate the impact of various uncertainties. From Ref. [136].

1.4.3 The fine–tuning constraint

Finally, a last theoretical constraint comes from the fine–tuning problem originating from the radiative corrections to the Higgs boson mass. The Feynman diagrams contributing to the one–loop radiative corrections are depicted in Fig. 1.20 and involve Higgs boson, massive gauge boson and fermion loops.

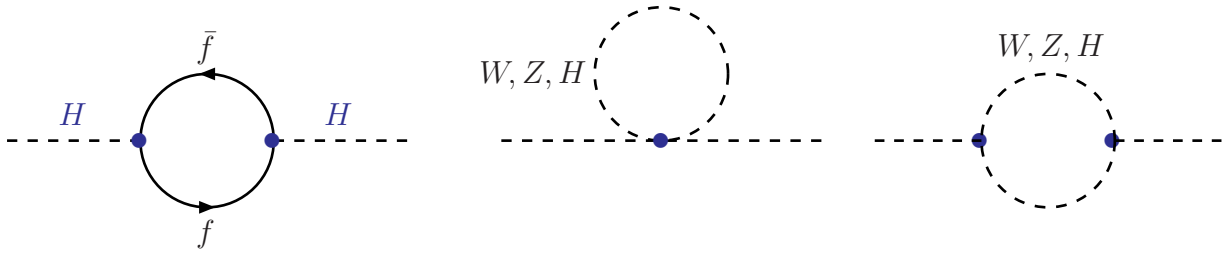

Figure 1.20: Feynman diagrams for the one–loop corrections to the SM Higgs boson mass.

Cutting off the loop integral momenta at a scale Λ, and keeping only the dominant contribution in this scale, one obtains

$$M_H^2 = (M_H^0)^2 + \frac{3\Lambda^2}{8\pi^2 v^2}\left[M_H^2 + 2M_W^2 + M_Z^2 - 4m_t^2\right] \tag{1.183}$$

where M_H^0 is the bare mass contained in the unrenormalized Lagrangian and where we retained only the contribution of the top heavy quark for the fermion loops. This is a completely new situation in the SM: we have a quadratic divergence rather than the usual logarithmic ones. If the cut–off Λ is very large, for instance of the order of the Grand Unification scale $\sim 10^{16}$ GeV, one needs a very fine arrangement of 16 digits between the bare Higgs mass and the radiative corrections to have a physical Higgs boson mass in the range of the electroweak symmetry breaking scale, $M_H \sim 100$ GeV to 1 TeV, as is required for the consistency of the SM. This is the naturalness of fine–tuning problem[18].

However, following Veltman [137], one can note that by choosing the Higgs mass to be

$$M_H^2 = 4m_t^2 - 2M_W^2 - M_Z^2 \sim (320 \text{ GeV})^2 \tag{1.184}$$

the quadratic divergences can be canceled and this would be even a prediction for the Higgs boson mass. But the condition above was given only at the one–loop level and at higher orders, the general form of the correction to the Higgs mass squared reads [138, 139]

$$\Lambda^2 \sum_{n=0}^{\infty} c_n(\lambda_i) \log^n(\Lambda/Q) \tag{1.185}$$

where $(16\pi^2)c_0 = (3/2v^2)(M_H^2 + 2M_W^2 + M_Z^2 - 4m_t^2)^2$ and the remaining coefficients c_n can be calculated recursively from the requirement that M_H^2 should not depend on the renormalization scale Q. For instance, for the two–loop coefficient, one finds [138]

$$\begin{aligned}(16\pi^2)^2 c_1 &= \lambda(114\lambda - 54g_2^2 - 18g_1^2 + 72\lambda_t)^2 + \lambda_t^2(27g_2^2 + 17g_1^2 + 96g_s^2 - 90\lambda_t^2) \\ &\quad -\frac{15}{2}g_2^4 + \frac{25}{2}g_1^4 + \frac{9}{2}g_1^2 g_2^2\end{aligned} \tag{1.186}$$

[18]Note, however that the SM is a renormalizable theory and this cancellation can occur in a mathematically consistent way by choosing a similarly divergent counterterm. Nevertheless, one would like to give a physical meaning to this scale Λ and view it as the scale up to which the SM is valid.

The higher–order coefficients have more powers of $1/(16\pi^2)$ and should therefore be more and more suppressed. The Veltman condition requires that the fine cancellation occurs to all perturbative orders, i.e. for any value of n. Given the fact that the various c_n terms of the perturbative series are independent, there is obviously no solution for M_H.

A priori, one can then conclude that the Veltman condition is not useful and cannot solve the fine–tuning problem. However, as it has been discussed in Refs. [140, 141], this is only true if the scale of New Physics is extremely large. For scales not much larger that the electroweak scale, one does not need very large cancellations. For instance, at the one–loop level, the fine–tuning problem appears only if $\Lambda \gtrsim 4\pi v \sim 2$ TeV. If the Veltman solution is by chance satisfied, then the scale Λ can be pushed at the two loop level to a much higher value, $\Lambda^2 \log \Lambda \gtrsim (16\pi^2)^2 v^2$, that is, for $\Lambda \sim 15$ TeV. If again the Veltman conjecture is satisfied, then the three–loop quadratic divergences start to be problematic only at a scale $\Lambda \gtrsim 50$ TeV. One can thus have almost no, or only a small amount of fine–tuning, up to rather high scales.

For such a scale, one simply needs to manage such that $\sum_{n=0}^{1} c_n(\lambda_i) \log^n(\Lambda/M_H) = 0$ at two–loop. It appears that first, such a solution exists and second, that the predicted M_H value becomes cut–off dependent. As mentioned previously, this prediction assumes exact cancellation and this is not required for rather low scales Λ. Following again Ref. [140], a more adequate condition would be

$$\sum_{n=0}^{1} c_n(\lambda_i) \log^n(\Lambda/M_H) \lesssim v^2/\Lambda^2 \tag{1.187}$$

and if it is satisfied, the fine–tuning might be acceptable. But, as is well known, there is a problem with the definition of the amount of fine–tuning, that is largely a subjective matter. Following again Ref. [140], one can define it as the sensitivity of the electroweak scale to the cut–off Λ, $\Delta M_W^2(\Lambda)/M_W^2$. This leads then to the measure

$$\Delta_{\rm FT} = \left| \frac{\Delta M_W^2}{M_W^2} \right| = \left| \frac{\Delta M_H^2}{M_H^2} \right| = \frac{2\Lambda^2}{M_H^2} \left| \sum_n c_n \log^n(\Lambda/M_H) \right| \tag{1.188}$$

For a given value of $\Delta_{\rm FT}$, the weak scale is fine–tuned to one part in $\Delta_{\rm FT}$: the larger than unity is the value of $\Delta_{\rm FT}$, the more fine–tuning we have and there is no fine–tuning if $\Delta_{\rm FT} \leq 1$. One can see from the previous equation that the fine–tuning is large not only when Λ increases but also when the Higgs boson is light.

The Higgs boson mass is shown in Fig. 1.21 as a function of the maximal value of the cut–off scale Λ. Also shown, are the regions not allowed by the triviality and stability bounds on M_H, as well as the ("electroweak") area ruled out by high–precision measurements[19]. The

[19]More details on how these constraints have been obtained can be found in Ref. [140].

regions of fine–tuning less than 10 and 100 are given, respectively, by the light and dark hatched regions. The white region corresponds to the one where all constraints are fulfilled and where the Veltman condition is approximately satisfied.

For low values of the scale, $\Lambda \lesssim 1$ TeV, there is no fine–tuning problem for any reasonable Higgs boson mass value. But as Λ increases, the range of Higgs masses where the fine–tuning is smaller than 10% or 1% becomes narrow. For instance, with $\Lambda \sim 3$ TeV, the Higgs boson mass must be above ~ 150 GeV while with $\Lambda \sim 10$ TeV, only a narrow range around $M_H \sim 200$ GeV for $\Delta_{\rm FT} = 10$, sometimes called the Veltman throat, is allowed. For even higher scales, only the line with $M_H \sim 200$ GeV, where the Veltman condition is approximately satisfied, survives.

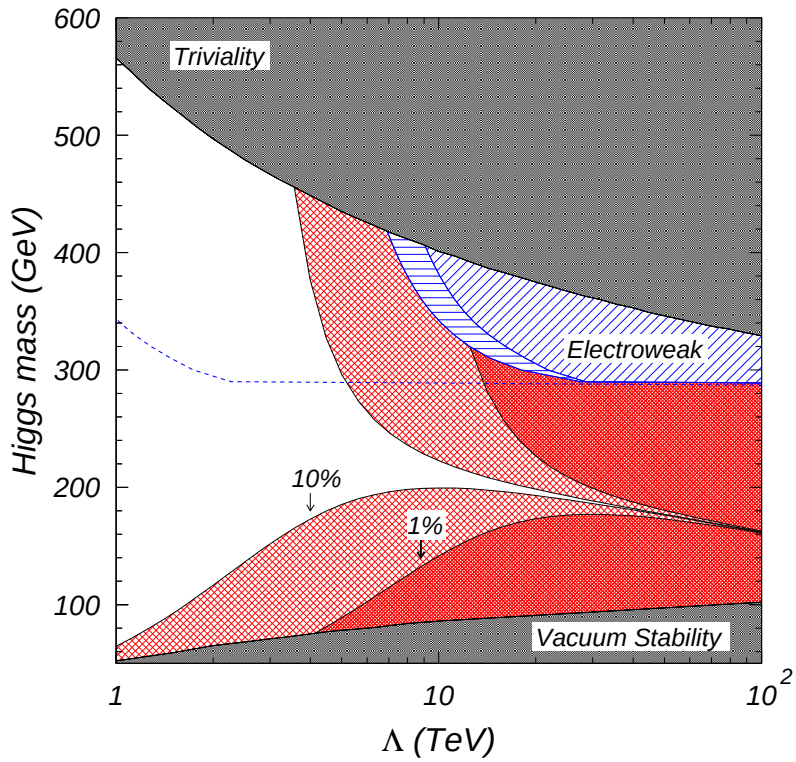

Figure 1.21: The contours for the fine–tuning parameter $\Delta_{\rm FT}$ in the plane (M_H, Λ). The dark (light) hatched region marked "1%" ("10%") represents fine–tunings of greater than 1 part in 100 (10). The constraints from triviality, stability and electroweak precision data are also shown. The empty region is consistent with all constraints and has $\Delta_{\rm FT}$ less than 10%. From Ref. [140].

Thus, one can obtain a very useful information by considering the fine–tuning problem in the SM at scales of a few tens of TeV. In the vicinity of these scales, a Higgs boson with a mass $M_H \sim 200$ GeV can still allow for an acceptable amount of fine–tuning.

2 Decays of the SM Higgs boson

In the Standard Model, once the Higgs mass is fixed, the profile of the Higgs particle is uniquely determined. The Higgs couplings to gauge bosons and fermions are directly proportional to the masses of the particles and the Higgs boson will have the tendency to decay into the heaviest ones allowed by phase space. Since the pole masses of the gauge bosons and fermions are known [the electron and light quark masses are too small to be relevant]

$$M_Z = 91.187 \text{ GeV} \ , \ M_W = 80.425 \text{ GeV} \ , \ m_\tau = 1.777 \text{ GeV} \ , \ m_\mu = 0.106 \text{ GeV} \ ,$$
$$m_t = 178 \pm 4.3 \text{ GeV} \ , \ m_b = 4.88 \pm 0.07 \text{ GeV} \ , \ m_c = 1.64 \pm 0.07 \text{ GeV} \tag{2.1}$$

all the partial widths for the Higgs decays into these particles can be predicted.

The decay widths into massive gauge bosons $V = W, Z$ are directly proportional to the HVV couplings, which in the SM are given in terms of the fields by

$$\mathcal{L}(HVV) \ = \ \left(\sqrt{2}G_\mu\right)^{1/2} M_V^2 H V^\mu V_\mu \tag{2.2}$$

These are S–wave couplings and even under parity and charge conjugation, corresponding to the $J^{\rm PC} = 0^{++}$ assignment of the Higgs spin and parity quantum numbers. The decay widths into fermions are proportional to the $Hf\bar{f}$ couplings which are of the scalar type

$$g_{H\bar{f}f} \propto \frac{m_f}{v} = (\sqrt{2}G_\mu)^{1/2} m_f \tag{2.3}$$

In this section, we will discuss all the decay modes of the SM Higgs boson: decays into quarks and leptons, into real or virtual gauge bosons and loop induced decays into photons [including $Z\gamma$ final states] and gluons, and summarize the important QCD and electroweak radiative corrections to these processes.

The $J^{\rm PC} = 0^{++}$ quantum numbers of the SM Higgs particle lead also to unique predictions for the angular and energy distributions of the partial decay widths. Whenever possible, we will confront these properties with those of an hypothetical CP–odd Higgs particle[20], that we will denote by A, and which is predicted in many extensions of the SM. In this case, the Higgs coupling to vector gauge bosons is a P–wave coupling corresponding to the $J^{\rm PC} = 0^{+-}$ assignment and, if CP symmetry is conserved, does not occur at the tree–level and is only induced by higher loop effects. With η being a dimensionless factor, the effective point–like coupling can be written as

$$\mathcal{L}(AVV) = \frac{1}{4}\eta \left(\sqrt{2}G_\mu\right)^{1/2} M_V^2 A V^{\mu\nu} \widetilde{V}_{\mu\nu} \ , \qquad \widetilde{V}^{\mu\nu} = \epsilon^{\mu\nu\rho\sigma} V_{\rho\sigma} \tag{2.4}$$

In the presence of fermions, the couplings of the A boson are of the pseudoscalar type

$$g_{A\bar{f}f} \propto \frac{m_f}{v}\gamma_5 = (\sqrt{2}G_\mu)^{1/2} m_f \gamma_5 \tag{2.5}$$

[20]The decays of the Higgs bosons [142–144] in the general case of anomalous Higgs couplings [99,100] will be discussed in another part of this review.

2.1 Decays to quarks and leptons

2.1.1 The Born approximation

In the Born approximation, the partial width of the Higgs boson decay into fermion pairs, Fig. 2.1, is given by [111, 145]

$$\Gamma_{\rm Born}(H \to f\bar{f}) = \frac{G_\mu N_c}{4\sqrt{2}\pi} M_H\, m_f^2\, \beta_f^3 \tag{2.6}$$

with $\beta = (1 - 4m_f^2/M_H^2)^{1/2}$ being the velocity of the fermions in the final state and N_c the color factor $N_c = 3\,(1)$ for quarks (leptons). In the lepton case, only decays into $\tau^+\tau^-$ pairs and, to a much lesser extent, decays into muon pairs are relevant.

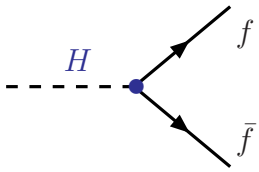

Figure 2.1: The Feynman diagram for the Higgs boson decays into fermions.

The partial decay widths exhibit a strong suppression near threshold, $\Gamma(H \to f\bar{f}) \sim \beta_f^3 \to 0$ for $M_H \simeq 2m_f$. This is typical for the decay of a Higgs particle with a scalar coupling eq. (2.3). If the Higgs boson were a pseudoscalar A boson with couplings given in eq. (2.5), the partial decay width would have been suppressed only by a factor β_f [146]

$$\Gamma_{\rm Born}(A \to f\bar{f}) = \frac{G_\mu N_c}{4\sqrt{2}\pi} M_H\, m_f^2\, \beta_f \tag{2.7}$$

More generally, and to anticipate the discussions that we will have on the Higgs CP–properties, for a Φ boson with mixed CP–even and CP–odd couplings $g_{\Phi\bar{f}f} \propto a + ib\gamma_5$, the differential rate for the fermionic decay $\Phi(p_+) \to f(p,s)\bar{f}(\bar{p},\bar{s})$ where s and $\bar{s}$ denote the polarization vectors of the fermions and the four–momenta are such that $p_\pm = p \pm \bar{p}$, is given by [see Ref. [147] for instance]

$$\begin{aligned}\frac{{\rm d}\Gamma}{{\rm d}\Omega}(s,\bar{s}) \;=\; & \frac{\beta_f}{64\pi^2 M_\Phi}\Big[(|a|^2+|b|^2)\Big(\frac{1}{2}M_\Phi^2 - m_f^2 + m_f^2 s\cdot\bar{s}\Big) \\ & +(|a|^2-|b|^2)\Big(p_+\cdot s\, p_+\cdot\bar{s} - \frac{1}{2}M_\Phi^2 s\cdot\bar{s} + m_f^2 s\cdot\bar{s} - m_f^2\Big) \\ & -{\rm Re}(ab^*)\epsilon_{\mu\nu\rho\sigma}p_+^\mu p_-^\nu s^\rho \bar{s}^\sigma - 2{\rm Im}(ab^*)m_f p_+\cdot(s+\bar{s})\Big]\end{aligned} \tag{2.8}$$

The terms proportional to ${\rm Re}(ab^*)$ and ${\rm Im}(ab^*)$ represent the CP–violating part of the couplings. Averaging over the polarizations of the two fermions, these two terms disappear and we are left with the two contributions $\propto \frac{1}{2}|a|^2(M_\Phi^2 - 2m_f^2 - 2m_f^2)$ and $\propto \frac{1}{2}|b|^2(M_\Phi^2 - 2m_f^2 + 2m_f^2)$ which reproduce the β_f^3 and β_f threshold behaviors of the pure CP–even ($b = 0$) and CP–odd ($a = 0$) states noted above.

2.1.2 Decays into light quarks and QCD corrections

In the case of the hadronic decays of the Higgs boson, the QCD corrections turn out to be quite large and, therefore, must be included. At the one–loop level, the Feynman diagrams for the corrections are shown in Fig. 2.2: one has to include gluon–exchange [which multiplies the Born term] and the emission of a gluon in the final state [which has to be squared and added to the former]. In the limit where M_H is much larger than the quark masses, $M_H \gg 2m_f$, one obtains for the next–to–leading order (NLO) decay width [the quark mass is kept only in the Yukawa coupling and in the leading logarithmic term] [148, 149]

$$\Gamma_{\rm NLO}(H \to q\bar{q}) \simeq \frac{3G_\mu}{4\sqrt{2}\pi} M_H\, m_q^2 \left[1 + \frac{4}{3}\frac{\alpha_s}{\pi}\left(\frac{9}{4} + \frac{3}{2}\log\frac{m_q^2}{M_H^2}\right)\right] \tag{2.9}$$

As can be seen, there is a large logarithmic $\log(m_q/M_H)$ contribution which, for very light quarks, might render the partial decay width very small and even drive it to negative values [a definitely not physical situation]. However, these large logarithms can be absorbed in the redefinition of the quark masses: by using the running quark masses in the $\overline{\rm MS}$ scheme at the scale of the Higgs mass, as discussed in §1.1.4, these logarithms are summed to all orders in the strong interaction coupling constant [148].

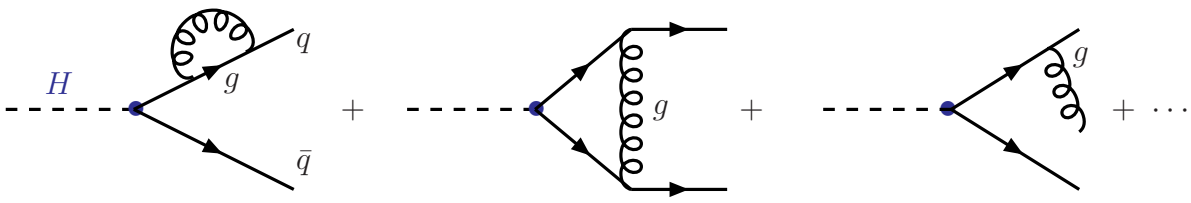

Figure 2.2: Generic diagrams for the one–loop QCD corrections to Higgs decays into quarks.

Including the $\mathcal{O}(\alpha_s^2)$ [49] and $\mathcal{O}(\alpha_s^3)$ [150] QCD radiative corrections, the partial Higgs decay widths into light quarks can be then written as

$$\Gamma(H \to q\bar{q}) \;=\; \frac{3G_\mu}{4\sqrt{2}\pi} M_H\, \overline{m}_q^2(M_H)\left[1 + \Delta_{qq} + \Delta_H^2\right] \tag{2.10}$$

with the running quark mass $\overline{m}_q(M_H^2)$ and the strong coupling constant $\bar{\alpha}_s \equiv \alpha_s(M_H^2)$ both defined at the scale M_H. In the $\overline{\rm MS}$ renormalization scheme, with N_f the number of light quark flavors, one has for the QCD correction factor Δ_{qq}

$$\Delta_{qq} = 5.67\frac{\bar{\alpha}_s}{\pi} + (35.94 - 1.36N_f)\frac{\bar{\alpha}_s^2}{\pi^2} + (164.14 - 25.77N_f + 0.26N_f^2)\frac{\bar{\alpha}_s^3}{\pi^3} \tag{2.11}$$

Since the values of the running b and c quark masses at the scale $\mu \sim M_H = 100$ GeV are typically, respectively, a factor ~ 1.5 and a factor of ~ 2 smaller than the pole masses, the partial decay widths are suppressed by large factors compared to the case where the pole

masses are used. This is shown in Fig 2.3 where $\Gamma(H \to b\bar{b})$ and $\Gamma(H \to c\bar{c})$ are displayed as functions of the Higgs mass M_H in the Born approximation, using only the running quark masses and with the full set of QCD corrections implemented. Note that the latter increase the partial widths by approximately 20%.

The additional correction at $\mathcal{O}(\alpha_s^2)$ involves logarithms of the masses of the light quarks and the heavy top quark and is given by [151]

$$\Delta_H^2 \;=\; \frac{\bar{\alpha}_s^2}{\pi^2}\left(1.57 - \frac{2}{3}\log\frac{M_H^2}{m_t^2} + \frac{1}{9}\log^2\frac{\overline{m}_q^2}{M_H^2}\right) \tag{2.12}$$

Because of chiral symmetry, all this discussion holds true if the Higgs particle were a pseudoscalar boson; the only exception is that the correction Δ_H^2 would be different, since it involves the quark masses which break the symmetry.

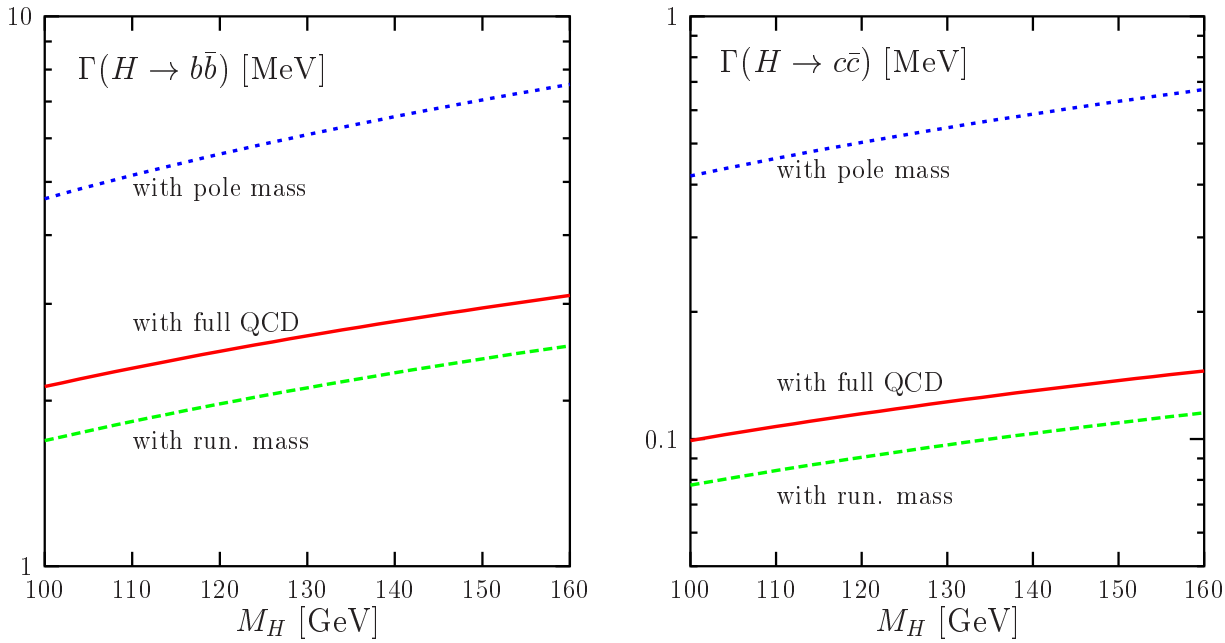

Figure 2.3: The partial widths for the decays $H \to b\bar{b}$ (left) and $H \to c\bar{c}$ (right) as a function of M_H. They are shown in the Born approximation (dotted lines), including only the running quark masses (dashed lines) and with the full set of QCD corrections (solid lines). The input pole masses are $m_b = 4.88$ GeV and $m_c = 1.64$ GeV and the running strong coupling constant is taken at the scale of the Higgs mass and is normalized to $\alpha_s(M_Z) = 0.1172$.

2.1.3 The case of the top quark

For Higgs bosons decaying into top quarks, the QCD corrections do not lead to large logarithms since m_t is comparable to M_H. However, these corrections can be sizable, in particular near the threshold $M_H \sim 2m_t$. At next–to–leading–order, they are given by

$$\Gamma(H \to t\bar{t}\,) = \frac{3G_\mu}{4\sqrt{2}\pi}\; M_H\, m_t^2\, \beta_t^3 \left[1 + \frac{4}{3}\frac{\alpha_s}{\pi}\Delta_H^t(\beta_t)\right] \tag{2.13}$$

Using the Spence function defined by $\mathrm{Li}_2(x) = -\int_0^x dy y^{-1} \log(1-y)$, the QCD correction factor in the massive case reads [148, 149, 152]

$$\Delta_H^t(\beta) = \frac{1}{\beta} A(\beta) + \frac{1}{16\beta^3}(3 + 34\beta^2 - 13\beta^4) \log \frac{1+\beta}{1-\beta} + \frac{3}{8\beta^2}(7\beta^2 - 1) \tag{2.14}$$

with

$$\begin{aligned} A(\beta) &= (1+\beta^2) \left[4\mathrm{Li}_2 \left(\frac{1-\beta}{1+\beta} \right) + 2\mathrm{Li}_2 \left(-\frac{1-\beta}{1+\beta} \right) - 3 \log \frac{1+\beta}{1-\beta} \log \frac{2}{1+\beta} \right. \\ &\quad \left. -2 \log \frac{1+\beta}{1-\beta} \log \beta \right] - 3\beta \log \frac{4}{1-\beta^2} - 4\beta \log \beta \end{aligned} \tag{2.15}$$

Part of the full massive two–loop corrections, i.e. corrections of $\mathcal{O}(N_f \alpha_s^2)$ which are expected to provide the largest contribution, have been computed some time ago [153] and the full two–loop corrections have been derived slightly after [154].

The left–hand side of Fig. 2.4 shows the partial $H \to t\bar{t}$ decay width in the Born approximation, with the running top quark mass and including the full set of one–loop QCD corrections. As can be seen, and contrary to the $b\bar{b}$ and $c\bar{c}$ cases, the corrections are rather moderate in this case.

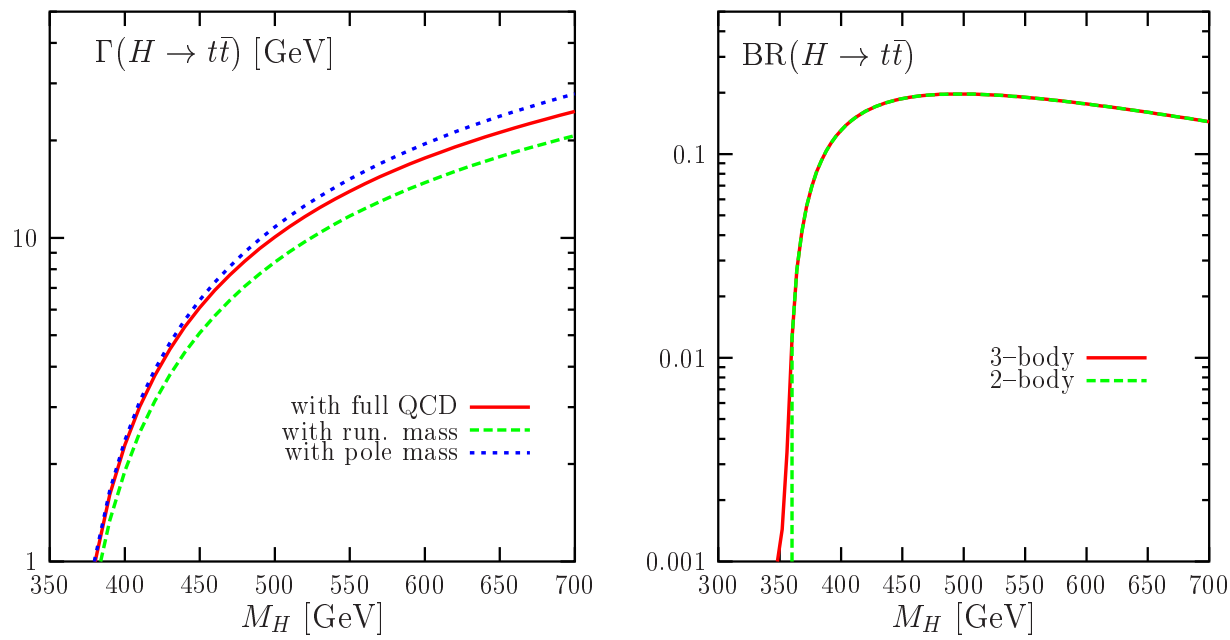

Figure 2.4: The partial width for the decay $H \to t\bar{t}$ as a function of M_H. In the left figure, it is shown in the Born approximation (dotted line), with the running top mass (dashed lines) and with the full set of QCD corrections (solid lines). In the right figure the partial width is shown with (solid line) and without (dashed line) the inclusion of the three–body decay. The inputs are $m_t = 178$ GeV and $\alpha_s(M_Z) = 0.1172$.

Another special feature in the case of top quarks is that the three–body decays $H \to t\bar{t}^* \to t\bar{b}W^-$ into on–shell and off–shell top states are possible [155–157], see Fig. 2.5. These three–body decays reach the percent level slightly below the $2m_t$ threshold, when compared to the two–body decay as shown in the right–hand side of Fig. 2.4. A smooth transition from below to above threshold occurs when the top quark width is included.

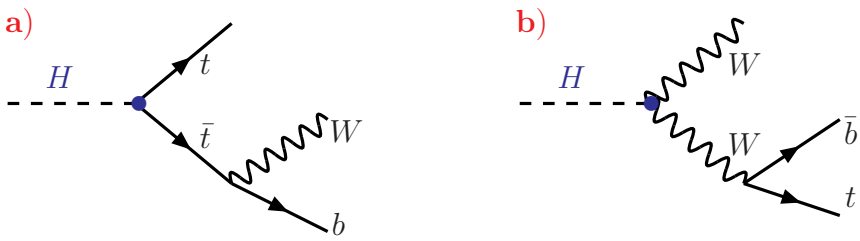

Figure 2.5: Diagrams for the three–body decays of the Higgs boson into tbW final states.

Taking into account only the diagram of Fig. 2.5a where the top quark is off–shell and which provides the dominant contribution [the virtuality of the W boson in the other diagram is too large, thus strongly suppressing the contribution], the differential partial width or Dalitz density for this decay can be written as

$$\frac{\mathrm{d}\Gamma}{\mathrm{d}x_1\mathrm{d}x_2}(H \to t\bar{t}^* \to t\bar{b}W^-) = \frac{3G_\mu^2}{32\pi^3}\, M_H^3\, m_t^2\, \frac{\Gamma_H^t}{y_1^2 + \gamma_t\kappa_t} \tag{2.16}$$

with the reduced energies $x_{1,2} = 2E_{t,b}/M_H$, the scaling variables $y_{1,2} = 1 - x_{1,2}$, $\kappa_i = M_i^2/M_H^2$ and the reduced decay width of the virtual top quark $\gamma_t = \Gamma_t^2/M_H^2$. The squared amplitude is given by [156]

$$\begin{aligned}\Gamma_H^t \;=\;& y_1^2(1 - y_1 - y_2 + \kappa_W - 5\kappa_t) + 2\kappa_W(y_1y_2 - \kappa_W - 2\kappa_t y_1 + 4\kappa_t\kappa_W) \\ & -\kappa_t y_1 y_2 + \kappa_t(1 - 4\kappa_t)(2y_1 + \kappa_W + \kappa_t)\end{aligned} \tag{2.17}$$

The differential decay width has to be integrated over the allowed range of the x_1, x_2 variables. The boundary condition is

$$\left| \frac{2(1 - x_1 - x_2 + \kappa_t + \kappa_b - \kappa_W) + x_1x_2}{\sqrt{x_1^2 - 4\kappa_t}\sqrt{x_2^2 - 4\kappa_b}} \right| \leq 1 \tag{2.18}$$

The additional diagram leading to the same final state, with the Higgs boson decaying into two W bosons with one of them being off–shell and decays into $t\bar{b}$ final states, $H \to WW^* \to t\bar{b}W$, gives very small contributions and can be safely neglected.

2.1.4 Distinction between scalar and pseudoscalar Higgs bosons

The distinction between a scalar and a pseudoscalar Higgs particle can be made by investigating the angular correlations in the decays into heavy fermions [158–163]. In the processes $H/A \to t\bar{t} \to (W^+b)(W^-\bar{b})$, denoting the spin vector of the t and $\bar{t}$ states in their respective rest frames by s and $\bar{s}$, and orienting the z axis along the t flight direction, the spin dependence is different in the two cases; from eq. (2.8) one obtains [159]

$$\Gamma(H/A \to t\bar{t}) \propto 1 - s_z\bar{s}_z \pm s_\perp\bar{s}_\perp \tag{2.19}$$

Denoting by $\theta^*_\pm$ the polar angle between the $W^\pm$ bosons and the t–quark in the $W^\pm$ rest frames and by ϕ^* the relative azimuthal angle between the decay planes of the two W bosons, Fig. 2.6, and using the abbreviations $c_{\theta^*_+} = \cos\theta^*_+$ *etc*, the angular distributions of the $W^\pm$ bosons in the decays of scalar and pseudoscalar Higgs particles are given by [160, 164]

$$\frac{\mathrm{d}\Gamma(H/A \to W^+W^-b\bar{b})}{\Gamma_{H/A}\mathrm{d}c_{\theta^*_+}\mathrm{d}c_{\theta^*_-}\mathrm{d}\phi^*} = \frac{1}{8\pi}\left[1 + \left(\frac{m_t^2 - 2M_W^2}{m_t^2 + 2M_W^2}\right)^2 \left(c_{\theta^*_+}c_{\theta^*_-} \mp s_{\theta^*_+}s_{\theta^*_-}c_{\phi^*}\right)\right] \tag{2.20}$$

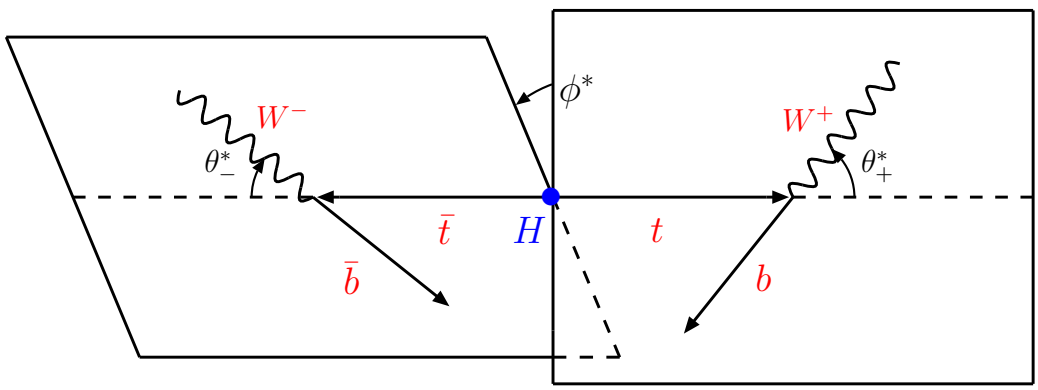

Figure 2.6: The definition of the polar angles $\theta^*_\pm$ and the azimuthal angle ϕ^* for the sequential decay $H \to t\bar{t} \to (bW^+)(\bar{b}W^-)$. The polar angles are defined in the $t, \bar{t}$ rest frames, with respect to the t flight direction. The angle ϕ^* stays the same after boost along the $t\bar{t}$ directions.

[The QCD corrections to the angular distributions can be found in Ref. [165] for instance]. If the Higgs boson mass is precisely known, the Higgs rest frame can be reconstructed. Because the boost of the Higgs boson to quarks is not too large and the mass ratio between daughter–to–parent parent particles in the decay is significant, the kinematical reconstruction of the full event should not be very difficult.

If the integral over the polar angles is performed, one obtains a simple asymmetry in the azimuthal angle which projects out the parity of the Higgs boson [159, 160]

$$\frac{1}{\Gamma_{H/A}}\frac{\mathrm{d}\Gamma(H/A \to W^+W^-b\bar{b})}{\mathrm{d}\phi^*} = \frac{1}{2\pi}\left[1 \mp \frac{\pi^2}{16}\left(\frac{m_t^2 - 2M_W^2}{m_t^2 + 2M_W^2}\right)^2 c_{\phi^*}\right] \tag{2.21}$$

allowing to determine the azimuthal angle up to a two–fold ambiguity. The distribution of the decays $H/A \to t\bar{t} \to b\bar{b}W^+W^-$ as a function of the azimuthal angle is shown in Fig. 2.7. One sees that the separation between the scalar and pseudoscalar cases can clearly be made.

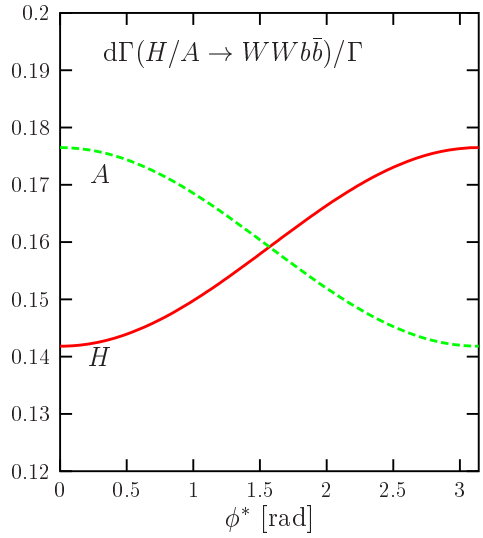

Figure 2.7: Distribution of the decays $H/A \to t\bar{t} \to b\bar{b}W^+W^-$ in the azimuthal angle ϕ^*.

One can perform the same study when integrating over the b–quark directions and consider the W bosons decaying into leptons $W^\pm \to \ell^\pm \nu_e$. The angular distribution is still given by eq. (2.20) but with $\theta^*_\pm$ denoting this time the polar angles between the charged leptons and the top quarks in the rest frame of the latter, and with the mass factor $(m_t^2 - 2M_W^2)^2/(m_t^2 + 2M_W^2)^2$ omitted.

CP quantum number studies of the Higgs particles can also be performed for smaller Higgs masses, in the decays into light fermions. In the case of $b\bar{b}$ final state decays [which are dominant for relatively light Higgs bosons], it is unfortunately very difficult, because of depolarization effects, to extract the spin information of the bottom quark. A much cleaner channel is provided by the Higgs decays into $\tau^+\tau^-$ pairs [160, 166, 167], although the rates are suppressed by an order of magnitude compared to the $b\bar{b}$ case. A possible channel would be the decays $H/A \to \tau^+\tau^- \to \pi^+\bar{\nu}\pi^-\nu$.

Defining again the polar angles $\theta^*_\pm$ as those giving the $\pi^\pm$ and τ^- directions and the azimuthal angle ϕ^* as the angle between the decays planes of $\tau^\pm$, the angular distribution will be as in the case of $H/A \to t\bar{t} \to WWb\bar{b}$ with $W^\pm \to \ell^\pm\nu_e$ [160]

$$\frac{1}{\Gamma_{H/A}} \frac{d\Gamma(H/A \to \pi^+\bar{\nu}_\tau\pi^-\nu_\tau)}{dc_{\theta^*_+} dc_{\theta^*_-} d\phi^*} = \frac{1}{8\pi}\left[1 + c_{\theta^*_+} c_{\theta^*_-} \mp s_{\theta^*_+} s_{\theta^*_-} c_{\phi^*}\right] \tag{2.22}$$

leading, once the polar angles are integrated out, to an asymmetry in the azimuthal angle

$$\frac{d\Gamma_{H/A}}{\Gamma_{H/A} d\phi^*} = \frac{1}{2\pi}\left[1 \mp \frac{\pi^2}{16}\, c_{\phi^*}\right] \tag{2.23}$$

The asymmetry is shown in Fig. 2.8 and the distinction between the scalar and pseudoscalar cases is even easier than in the case of top quarks in Fig. 2.7, since the suppression factor $(m_t^2 - 2M_W^2)^2/(m_t^2 + 2M_W^2)^2$ is absent.

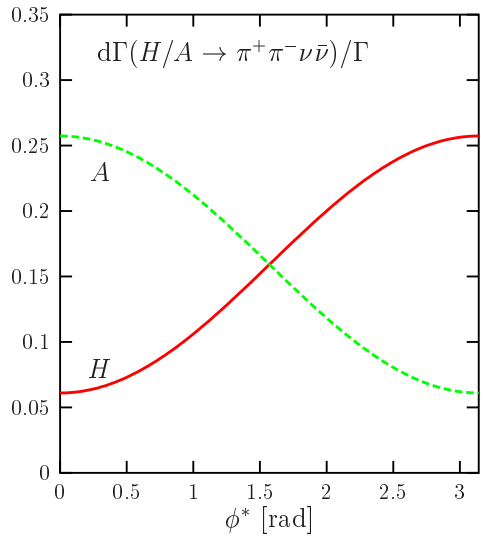

Figure 2.8: Distribution of the decays $H/A \to \tau^+\tau^- \to \pi^+\bar{\nu}_\tau\pi^-\nu_\tau$ in the azimuthal angle ϕ^*.

An observable which is sensitive to the Higgs parity is the angle δ between the pions in the rest frame of the Higgs boson [160, 164, 166, 167]

$$16\vec{\pi}^+ \cdot \vec{\pi}^- = M_H^2 \left[(1 + \beta_\tau\beta_\pi c_{\theta^*_-})^2 - 16\frac{m_\pi^2}{M_H^2}\right]^{\frac{1}{2}} \left[(1 - \beta_\tau\beta_\pi c_{\theta^*_+})^2 - 16\frac{m_\pi^2}{M_H^2}\right]^{\frac{1}{2}} \cos\delta \qquad (2.24)$$

where $\beta_\tau = (1 - 4m_\tau^2/M_H^2)^{1/2}$ and $\beta_\pi = (m_\tau^2 - m_\pi^2)/(m_\tau^2 + m_\pi^2)$ are the rest frame boosts of, respectively, the Higgs to the τ–lepton and the τ–lepton to the pions. The azimuthal angle ϕ^* can be then written in terms of the angles $\theta^*_\pm$ and δ and, integrating over the polar angles, one obtains for the distributions a rather complicated function of δ. However, for $\delta = \pi$, the distributions are rather simple and very different for 0^{++} and 0^{+-} states. For a scalar Higgs boson decay, it reaches its maximum for $\delta = \pi$

$$\frac{1}{\Gamma_H}\frac{\mathrm{d}\Gamma(H)}{\mathrm{d}\cos\delta} \simeq \frac{2}{15}\frac{5 + \beta_\tau^2}{1 - \beta_\tau^2} \qquad (2.25)$$

while for a pseudoscalar Higgs boson, it peaks at a small value of $\pi - \delta$ for $m_\pi \sim 0$

$$\frac{1}{\Gamma_A}\frac{\mathrm{d}\Gamma(A)}{\mathrm{d}\cos\delta} \simeq (1 + \cos\delta)\frac{1}{20}\frac{5 + 10\beta_\tau^2 + \beta_\tau^4}{(1 - \beta_\tau^2)^2} \qquad (2.26)$$

The analysis for Higgs decays into multi–pion final states, such as $H/A \to \tau^+\tau^- \to \rho^+\bar{\nu}_\tau\rho^-\nu_\tau \to \pi^+\pi^0\bar{\nu}_\tau\pi^-\pi^0\nu_\tau$ follows the same line if the hadron system is treated as a single particle; see Refs. [160, 167] for more details.

2.2 Decays into electroweak gauge bosons

2.2.1 Two body decays

Above the WW and ZZ kinematical thresholds, the Higgs boson will decay mainly into pairs of massive gauge bosons; Fig. 2.9a. The decay widths are directly proportional to the HVV couplings given in eq. (2.2) which, as discussed in the beginning of this chapter, correspond to the $J^{\rm PC} = 0^{++}$ assignment of the SM Higgs boson spin and parity quantum numbers. These are S–wave couplings, $\sim \vec{\epsilon}_1 \cdot \vec{\epsilon}_2$ in the laboratory frame, and linear in $\sin\theta$, with θ being the angle between the Higgs and one of the vector bosons.

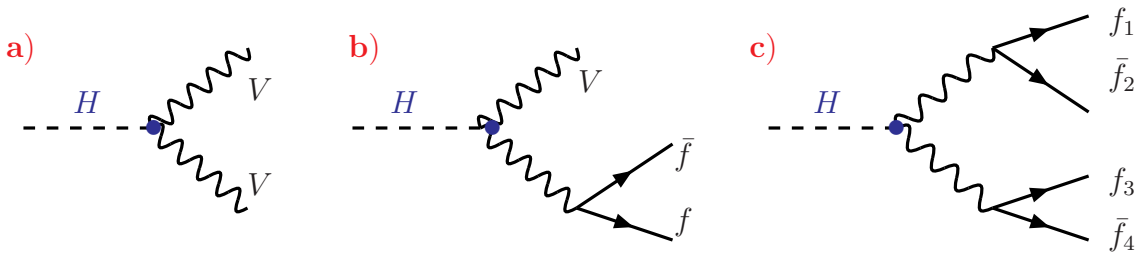

Figure 2.9: Diagrams for the Higgs boson decays into real and/or virtual gauge bosons.

The partial width for a Higgs boson decaying into two real gauge bosons, $H \to VV$ with $V = W$ or Z, are given by [32, 145]

$$\Gamma(H \to VV) = \frac{G_\mu M_H^3}{16\sqrt{2}\pi}\, \delta_V \sqrt{1-4x}\,(1-4x+12x^2)\ , \quad x = \frac{M_V^2}{M_H^2} \tag{2.27}$$

with $\delta_W = 2$ and $\delta_Z = 1$. For large enough Higgs boson masses, when the phase space factors can be ignored, the decay width into WW bosons is two times larger than the decay width into ZZ bosons and the branching ratios for the decays would be, respectively, 2/3 and 1/3 if no other decay channel is kinematically open.

For large Higgs masses, the vector bosons are longitudinally polarized [159]

$$\frac{\Gamma_L}{\Gamma_L + \Gamma_T} = \frac{1-4x+4x^2}{1-4x+12x^2} \overset{M_H \gg M_V}{\longrightarrow} 1 \tag{2.28}$$

while the L, T polarization states are democratically populated near the threshold, at $x = 1/4$. Since the longitudinal wave functions are linear in the energy, the width grows as the third power of the Higgs mass, $\Gamma(H \to VV) \propto M_H^3$. As discussed in §1.4.1, a heavy Higgs boson would be obese since its total decay width becomes comparable to its mass

$$\Gamma(H \to WW + ZZ) \sim 0.5 \text{ TeV}\, [M_H/1 \text{ TeV}]^3 \tag{2.29}$$

and behaves hardly as a resonance.

2.2.2 Three body decays

Below the WW/ZZ kinematical thresholds, the Higgs boson decay modes into gauge bosons, with one of them being off–shell, Fig. 2.9b, are also important. For instance, from $M_H \gtrsim 130$ GeV, the Higgs boson decay into WW pairs with one off–shell W boson, starts to dominate over the $H \to b\bar{b}$ mode. This is due to the fact that in these three–body decays, although suppressed by an additional power of the electroweak coupling squared compared to the dominant $H \to b\bar{b}$ case and by the virtuality of the intermediate vector boson state, there is a compensation since the Higgs couplings to W bosons are much larger than the Higgs Yukawa coupling to b quarks.

The partial width for the decay $H \to VV^* \to Vf\bar{f}$, the charges of the vector bosons V summed over and assuming massless fermions, is given by [168]

$$\Gamma(H \to VV^*) = \frac{3G_\mu^2 M_V^4}{16\pi^3} M_H \delta'_V R_T(x) \tag{2.30}$$

with $\delta'_W = 1$, $\delta'_Z = \frac{7}{12} - \frac{10}{9}\sin^2\theta_W + \frac{40}{9}\sin^4\theta_W$ and

$$\begin{aligned} R_T(x) &= \frac{3(1-8x+20x^2)}{(4x-1)^{1/2}} \arccos\left(\frac{3x-1}{2x^{3/2}}\right) - \frac{1-x}{2x}(2-13x+47x^2) \\ &\quad -\frac{3}{2}(1-6x+4x^2)\log x \end{aligned} \tag{2.31}$$

The invariant mass (M_*) spectrum of the off–shell vector boson peaks close to the kinematical maximum corresponding to zero–momentum of the on–shell and off–shell final state bosons

$$\frac{\mathrm{d}\Gamma(H \to VV^*)}{\mathrm{d}M_*^2} = \frac{3G_\mu^2 M_V^4}{16\pi^3 M_H} \delta'_V \frac{\beta_V (M_H^4 \beta_V^2 + 12 M_V^2 M_*^2)}{(M_*^2 - M_V^2)^2 + M_V^2 \Gamma_V^2} \tag{2.32}$$

with $\beta_V^2 = [1-(M_V+M_*)^2/M_H^2][1-(M_V-M_*)^2/M_H^2]$. Since both V and V^* preferentially have small momenta, the transverse and longitudinal polarization states are populated with almost equal probabilities. Neglecting the widths of the vector bosons, Γ_V, one finds after summing over all M_* values

$$\frac{\Gamma_L}{\Gamma_L + \Gamma_T} = \frac{R_L(M_V^2/M_H^2)}{R_T(M_V^2/M_H^2)} \tag{2.33}$$

where R_T is given in eq. (2.31) and R_L reads [159]

$$\begin{aligned} R_L(x) &= \frac{3-16x+20x^2}{(4x-1)^{1/2}} \arccos\left(\frac{3x-1}{2x^{3/2}}\right) - \frac{1-x}{2x}(2-13x+15x^2) \\ &\quad -\frac{1}{2}(3-10x+4x^2)\log x \end{aligned} \tag{2.34}$$

[Note that for heavy Higgs bosons, the three–body modes $H \to W^+W^-Z$ and $H \to t\bar{t}Z$ have been considered [155, 169]; they lead to marginal branching ratios.]

2.2.3 Four body decays

In fact, even Higgs decays into two off–shell gauge bosons, Fig. 2.9c, can be relevant [170,171]; see also Ref. [144]. The branching ratios for the latter reach the percent level for Higgs masses above about 100 (110) GeV for both W (Z) boson pairs off–shell. For higher masses, it is sufficient to allow for one off–shell gauge boson only. The decay width can be cast into the compact form [170]

$$\Gamma(H \to V^* V^*) = \frac{1}{\pi^2} \int_0^{M_H^2} \frac{\mathrm{d}q_1^2 M_V \Gamma_V}{(q_1^2 - M_V^2)^2 + M_V^2 \Gamma_V^2} \int_0^{(M_H - q_1)^2} \frac{\mathrm{d}q_2^2 M_V \Gamma_V}{(q_2^2 - M_V^2)^2 + M_V^2 \Gamma_V^2} \Gamma_0 \tag{2.35}$$

with q_1^2, q_2^2 being the squared invariant masses of the virtual gauge bosons, M_V and Γ_V their masses and total decay widths, and in terms of $\lambda(x, y; z) = (1 - x/z - y/z)^2 - 4xy/z^2$ with $\delta_V = 2(1)$ for $V = W(Z)$, the matrix element squared Γ_0 is

$$\Gamma_0 = \frac{G_\mu M_H^3}{16\sqrt{2}\pi} \delta_V \sqrt{\lambda(q_1^2, q_2^2; M_H^2)} \left[\lambda(q_1^2, q_2^2; M_H^2) + \frac{12 q_1^2 q_2^2}{M_H^4} \right] \tag{2.36}$$

Taking into account the total decay width of the vector bosons in the denominators of eq. (2.35), this expression for the four–body decay mode can be in fact used to reproduce the partial widths of the two–body and three–body decay modes, once the thresholds are crossed. Fig. 2.10 shows the branching ratios for the decays $H \to WW$ and $H \to ZZ$ in the three cases of two–body, three–body and four–body modes.

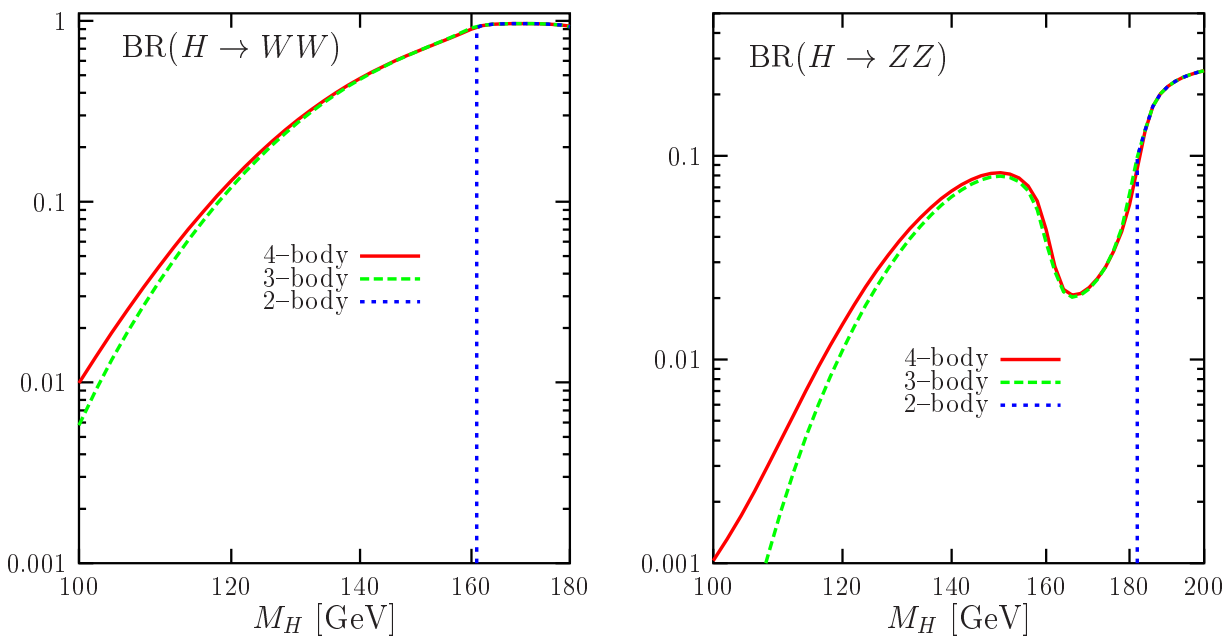

Figure 2.10: The branching ratios for the decays $H \to W^+W^-$ (left) and ZZ (right) as a function of M_H at the two– (dotted), three– (dashed) and four–body (solid) levels.

2.2.4 CP properties and comparison with the CP–odd case

Let us now confront the angular distributions of the final state fermions in the decay processes $H/A \to V\ V^* \to (f_1\bar{f}_2)(f_3\bar{f}_4)$, which are different for a CP–even and a CP–odd Higgs particle [159,172–174]. Denoting the polar and azimuthal angles of the fermions f_1, f_3 in the rest frames of the vector bosons by $(\theta_1, 0)$ and (θ_3, ϕ_3) [see Fig. 2.11 for the conventions and definitions], the angular distribution is given by [159]

$$\begin{aligned}\frac{\mathrm{d}\Gamma(H\to VV)}{\mathrm{d}c_{\theta_1}\mathrm{d}c_{\theta_3}\mathrm{d}\phi_3} \sim\ & s^2_{\theta_1}s^2_{\theta_3} + \frac{1}{2\gamma_1\gamma_3(1+\beta_1\beta_3)}s_{2\theta_1}s_{2\theta_3}c_{\phi_3} \\ & + \frac{1}{2\gamma_1^2\gamma_3^2(1+\beta_1\beta_3)^2}\left[\left(1+c^2_{\theta_1}\right)\left(1+c^2_{\theta_3}\right) + s^2_{\theta_1}s^2_{\theta_3}c_{2\phi_3}\right] \\ & - \frac{4A_{f_1}A_{f_3}}{\gamma_1\gamma_3(1+\beta_1\beta_3)}\left[s_{\theta_1}s_{\theta_3}c_{\phi_3} + \frac{1}{\gamma_1\gamma_3(1+\beta_1\beta_3)}c_{\theta_1}c_{\theta_3}\right]\end{aligned} \tag{2.37}$$

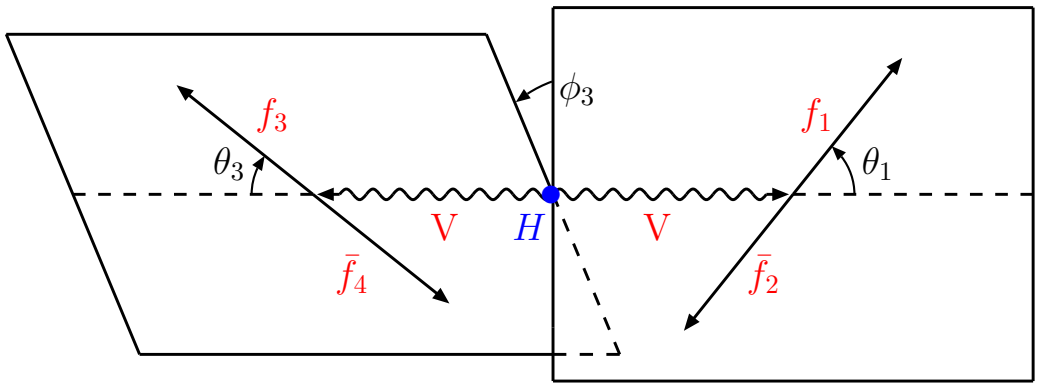

Figure 2.11: The definition of the polar angles $\theta_{1,3}$ and the azimuthal angle ϕ_3 for the sequential decay $H \to VV \to (f_1\bar{f}_2)(f_3\bar{f}_4)$ in the rest frame of the Higgs particle.

where the combination of $Vf\bar{f}$ couplings is $A_f = 2\hat{v}_f\hat{a}_f/(\hat{v}_f^2 + \hat{a}_f^2)$; for $V = W$, the weak charges are as usual $\hat{v}_f = \hat{a}_f = \sqrt{2}$ while for $V = Z$, $\hat{v}_f = 2I_f^3 - 4Q_f \sin^2\theta_W$ and $\hat{a}_f = 2I_f^3$. $\beta_i, \gamma_i = (1-\beta_i^2)^{-1/2}$ are the velocities and γ factors of the [on/off–shell] vector bosons and $s_\theta \equiv \sin\theta$, *etc.* The dependence on the azimuthal angle between the decay planes disappears for large Higgs masses, $\sim 1/\gamma$, a consequence of the asymptotic longitudinal V polarization. After integrating out the polar angles, we are left with [159]

$$\begin{aligned}\frac{\mathrm{d}\Gamma(H\to VV)}{\mathrm{d}\phi_3} &\sim 1 + a_1 c_{\phi_3} + a_2 c_{2\phi_3} \\ a_1 = -\frac{9\pi^2}{32}\frac{\gamma_1\gamma_3(1+\beta_1\beta_3)}{\gamma_1^2\gamma_3^2(1+\beta_1\beta_3)^2+2}A_{f_1}A_{f_3}\ ,\ & a_2 = \frac{1}{2}\frac{1}{\gamma_1^2\gamma_3^2(1+\beta_1\beta_3)^2+2}\end{aligned} \tag{2.38}$$

where the coefficient a_1 measures the P–odd amplitude.

These are unique predictions for the SM Higgs boson with $J^{\rm PC} = 0^{++}$ quantum numbers. One can again confront these predictions with what is expected in the case of a $J^{\rm PC} = 0^{+-}$ CP–odd Higgs boson[21]. The AVV coupling has been defined in eq. (2.4), and reduces to $(\vec{\epsilon}_1 \times \vec{\epsilon}_2) \cdot (\vec{p}_1 - \vec{p}_2)$ in the laboratory frame. The CP–odd angular distributions in the decays $A \to VV \to (f_1 \bar{f}_2)\,(f_3 \bar{f}_4)$ are given by [159]

$$\frac{{\rm d}\Gamma(A \to VV)}{{\rm d}c_{\theta_1}{\rm d}c_{\theta_3}{\rm d}\phi_3} \sim 1 + c^2_{\theta_1} c^2_{\theta_3} - \frac{1}{2} s^2_{\theta_1} s^2_{\theta_3} - \frac{1}{2} s^2_{\theta_1} s^2_{\theta_3} c_{2\phi_3} - 2 A_{f_1} A_{f_3} c_{\theta_1} c_{\theta_3} \tag{2.39}$$

and simply reduces, after integrating over the polar angles, to

$$\frac{{\rm d}\Gamma(A \to VV)}{{\rm d}\phi_3} \sim 1 - \frac{1}{4} c_{2\phi_3} \tag{2.40}$$

The normalization follows from the total and differential decay widths. Since the A boson does not decay into longitudinal gauge bosons, the partial width for the two–body decay is

$$\Gamma(A \to VV) = \frac{G_\mu M_H^3}{16\pi^3 M_A}\, \delta_V\, \eta^2\, (8x^2)\, \sqrt{1-4x} \tag{2.41}$$

while for the three–body decay, one has

$$\Gamma(A \to VV^*) = \frac{3 G_\mu^2 M_V^6}{8\pi^3 M_A} \delta'_V \eta^2 R_A \left(\frac{M_V^2}{M_A^2}\right) \tag{2.42}$$

with

$$\begin{aligned} R_A(x) &= (1-7x)(4x-1)^{1/2} \arccos\left(\frac{3x-1}{2x^{3/2}}\right) - \frac{1-x}{6}(17-64x-x^2) \\ &\quad + \frac{1}{2}(1-9x+6x^2)\log x \end{aligned} \tag{2.43}$$

The invariant mass spectrum of the off–shell vector bosons reads

$$\frac{{\rm d}\Gamma(A \to VV^*)}{{\rm d}M_*^2} = \frac{3 G_\mu^2 M_V^6}{8\pi^3 M_A} \delta'_V \eta^2 \frac{M_*^2 \beta_V^3}{(M_*^2 - M_V^2)^2 + M_V^2 \Gamma_V^2} \tag{2.44}$$

The fraction of the decay of the Higgs bosons into longitudinal vector bosons [which is zero in the CP–odd Higgs case] and the distributions with respect to the invariant mass of the off–shell gauge boson in the decays $H/A \to Z^* Z$ for $M_{H/A} = 150$ GeV are shown in Fig. 2.12. The mass and momentum distributions of the decay width are determined by the P–wave decay characteristics and the transverse polarization of the gauge bosons. The dependence on the azimuthal angle is shown in Fig. 2.13 for the decays $H/A \to ZZ \to 4\mu$ and $H/A \to WW \to 4f$ with $M_{H/A} = 300$ GeV. Again, the difference between the CP–even and CP–odd cases is noticeable. In the case of $H \to ZZ$ decays, the variation with the azimuthal angle is small since the factor in front of $\cos\phi_3$ is tiny, $a_1 \propto v_e^2 \ll 1$ [while $v_f = \sqrt{2}$ for W bosons]; the coefficient of $\cos 2\phi_3$ drops like $1/\gamma^4$ in the scalar case.

[21] The more general case where both CP–even and CP–odd couplings are present can be found in Ref. [175].

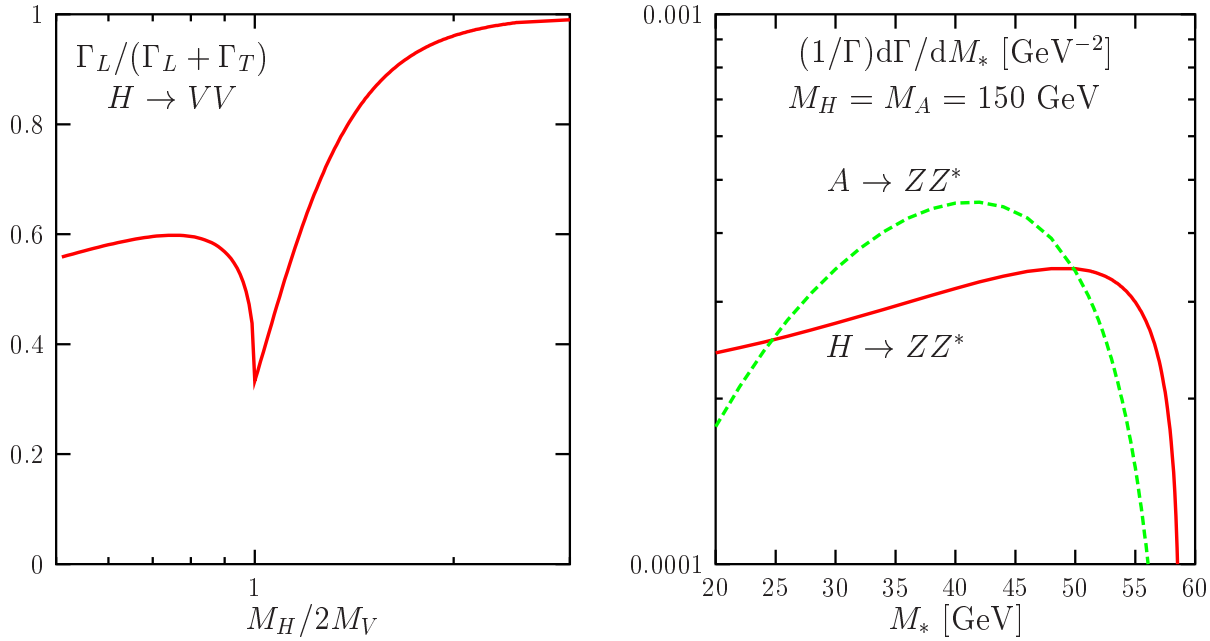

Figure 2.12: The decay width of the Higgs boson into longitudinal gauge bosons as a function of the ratio $M_H/2M_V$ (left) and the distribution with respect to the invariant mass of the off–shell gauge boson in the decays $H/A \to ZZ^*$ for $M_H = M_A = 150$ GeV (right).

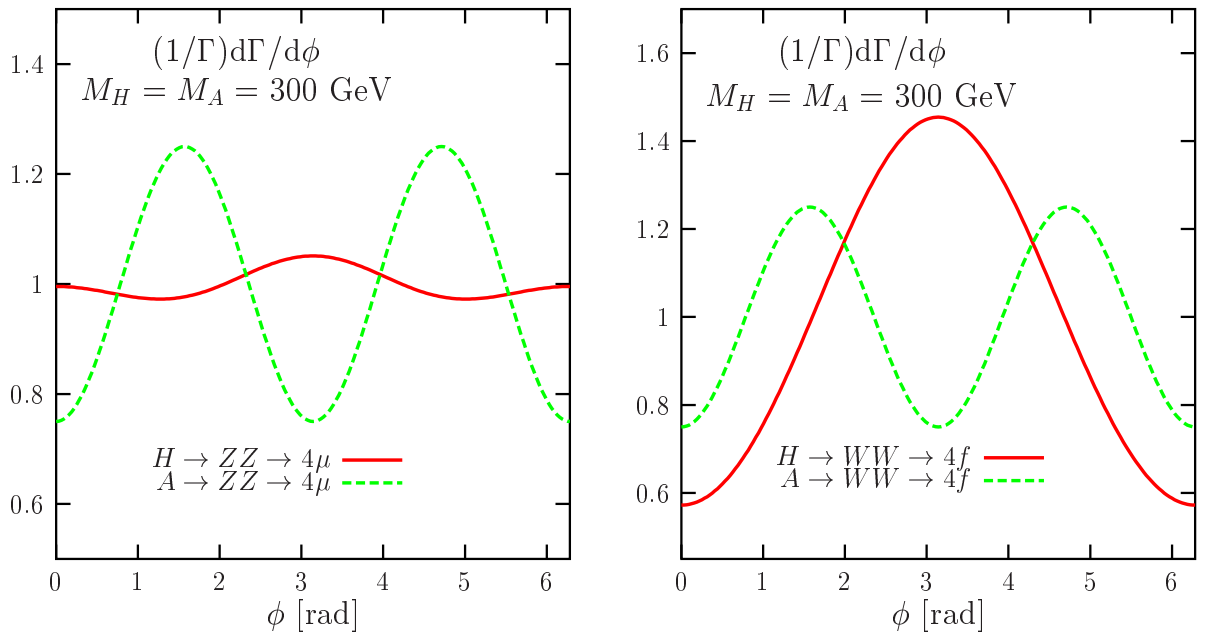

Figure 2.13: The azimuthal dependence in the decays $H/A \to ZZ \to 4\mu^\pm$ (left) and $H/A \to WW \to 4f$ for CP–even and CP–odd Higgs bosons with masses $M_H = M_A = 300$ GeV.

2.3 Loop induced decays into $\gamma\gamma, \gamma Z$ and gg

Since gluons and photons are massless particles, they do not couple to the Higgs boson directly. Nevertheless, the Hgg and $H\gamma\gamma$ vertices, as well as the $HZ\gamma$ coupling, can be generated at the quantum level with loops involving massive [and colored or charged] particles which couple to the Higgs boson. The $H\gamma\gamma$ and $HZ\gamma$ couplings are mediated by W boson and charged fermions loops, while the Hgg coupling is mediated only by quark loops; Fig. 2.14. For fermions, only the heavy top quark and, to a lesser extent, the bottom quark contribute substantially for Higgs boson masses $M_H \gtrsim 100$ GeV.

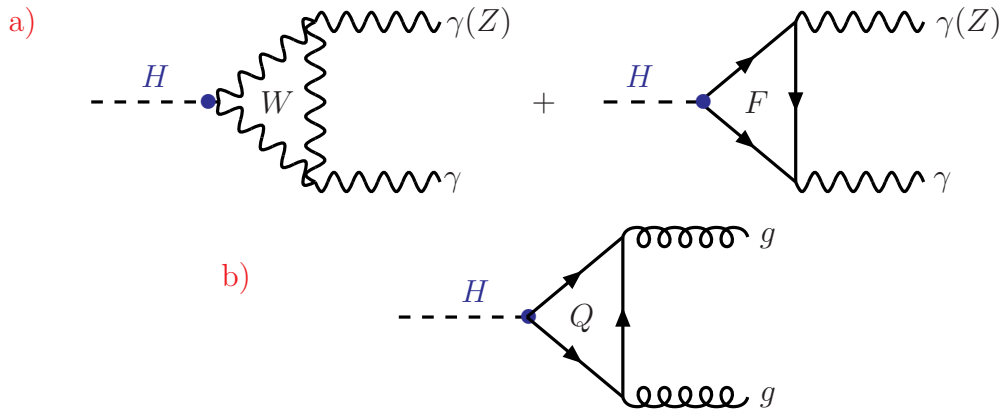

Figure 2.14: Loop induced Higgs boson decays into a) two photons ($Z\gamma$) and b) two gluons.

For masses much larger than the Higgs boson mass, these virtual particles do not decouple since their couplings to the Higgs boson grow with the masses, thus compensating the loop mass suppression. These decays are thus extremely interesting since their strength is sensitive to scales far beyond the Higgs boson mass and can be used as a possible probe for new charged and/or colored particles whose masses are generated by the Higgs mechanism and which are too heavy to be produced directly.

Unfortunately, because of the suppression by the additional electroweak or strong coupling constants, these loop decays are important only for Higgs masses below ~ 130 GeV when the total Higgs decay width is rather small. However, these partial widths will be very important when we will discuss the Higgs production at hadron and photon colliders, where the cross sections will be directly proportional to, respectively, the gluonic and photonic partial decay widths. Since the entire Higgs boson mass range can be probed in these production processes, we will also discuss the amplitudes for heavy Higgs bosons.

In this section, we first analyze the decays widths both at leading order (LO) and then including the next–to–leading order (NLO) QCD corrections. The discussion of the LO electroweak corrections and the higher–order QCD corrections will be postponed to the next section.

2.3.1 Decays into two photons

The partial width at leading order

The decay of the SM Higgs boson into two photons is mediated by W boson and heavy charged fermion loops. The partial decay width can be cast into the form [111, 176–178]

$$\Gamma\left(H \to \gamma\gamma\right) = \frac{G_\mu\, \alpha^2\, M_H^3}{128\sqrt{2}\,\pi^3} \left| \sum_f N_c Q_f^2 A_{1/2}^H(\tau_f) + A_1^H(\tau_W) \right|^2 \tag{2.45}$$

with the form factors for spin–$\frac{1}{2}$ and spin–1 particles given by

$$\begin{aligned} A_{1/2}^H(\tau) &= 2[\tau + (\tau-1) f(\tau)]\,\tau^{-2} \\ A_1^H(\tau) &= -[2\tau^2 + 3\tau + 3(2\tau-1) f(\tau)]\,\tau^{-2} \end{aligned} \tag{2.46}$$

and the function $f(\tau)$ defined as

$$f(\tau) = \begin{cases} \arcsin^2\sqrt{\tau} & \tau \leq 1 \\ -\dfrac{1}{4}\left[\log\dfrac{1+\sqrt{1-\tau^{-1}}}{1-\sqrt{1-\tau^{-1}}} - i\pi\right]^2 & \tau > 1 \end{cases} \tag{2.47}$$

The parameters $\tau_i = M_H^2/4M_i^2$ with $i = f, W$ are defined by the corresponding masses of the heavy loop particles. The electromagnetic constant in the coupling should be taken at the scale $q^2 = 0$ since the final state photons are real.

Since the $Hf\bar{f}$ coupling is proportional to m_f, the contribution of light fermions is negligible so that in the SM with three families, only the top quark and the W boson effectively contribute to the $\gamma\gamma$ width. If the Higgs boson mass is smaller than the WW and $f\bar{f}$ pair thresholds, the amplitudes are real and above the thresholds they are complex; Fig. 2.15. Below thresholds, the W amplitude is always dominant, falling from $A_1^H = -7$ for very small Higgs masses to $A_1^H = -5 - 3\pi^2/4$ at the WW threshold; for large Higgs masses the W amplitude approaches $A_1^H \to -2$. The fermionic contributions increase from $A_{1/2}^H = 4/3$ for small τ_f values to $A_{1/2}^H \sim 2$ at the $2m_f$ threshold; far above the fermion threshold, the amplitude vanishes linearly in τ_f modulo logarithmic coefficients,

$$\begin{aligned} M_H^2 \gg 4m_f^2 \quad &: \quad A_{1/2}^H(\tau_f) \to -[\log(4\tau_f) - i\pi]^2/(2\tau_f) \\ M_H^2 \ll 4m_f^2 \quad &: \quad A_{1/2}^H(\tau_f) \to 4/3 \end{aligned} \tag{2.48}$$

In Fig. 2.16, we display the partial decay width $\Gamma(H \to \gamma\gamma)$. The width varies rapidly from a few KeV for $M_H \sim 100$ GeV to ~ 100 KeV for $M_H \sim 300$ GeV as a consequence of the growth $\propto M_H^3$. The contribution of the W boson loop interferes destructively with the quark loop and for Higgs masses of about 650 GeV, the two contributions nearly cancel each other. The contribution of the b–loop is negligible, while the t quark contribution with $m_t \to \infty$ is a good approximation for Higgs masses below the $2m_t$ threshold.

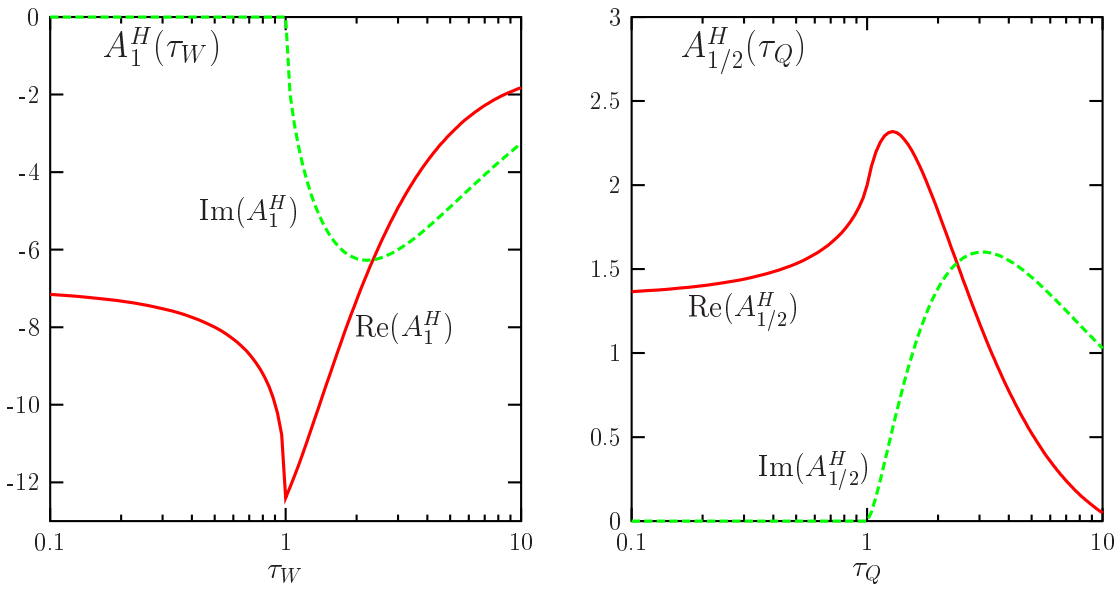

Figure 2.15: Real and imaginary parts of the W boson (left) and heavy fermion (right) amplitudes in the decay $H \to \gamma\gamma$ as a function of the mass ratios $\tau_i = M_H^2/4M_i^2$.

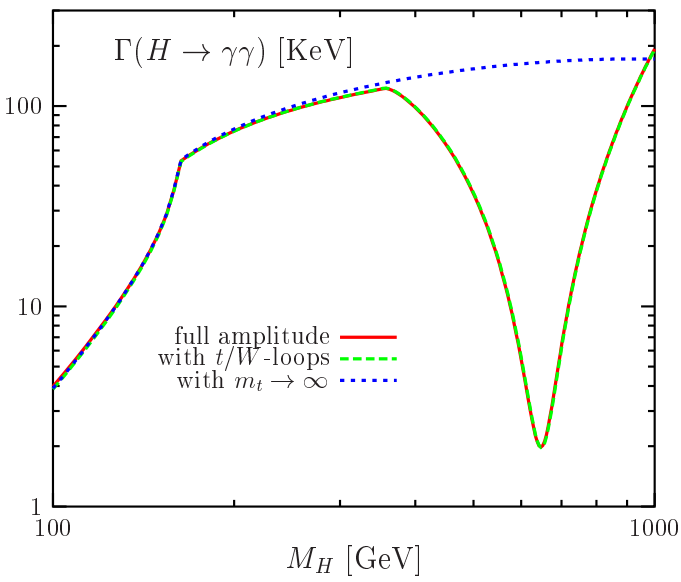

Figure 2.16: The partial width for the decay $H \to \gamma\gamma$ as a function of M_H with the W and all third generation fermion contributions (solid) and with W and only the top quark contribution (dashed) and with the W and t quark contributions for $m_t \to \infty$ (dotted lines).

The NLO QCD corrections

The QCD corrections to the quark amplitude in the decay $H \to \gamma\gamma$ consist only of two–loop virtual corrections and the corresponding counterterms; some generic diagrams are shown in Fig. 2.17. There are no real corrections since the decay $H \to \gamma\gamma + g$ does not occur due to color conservation. The calculation can be done in the on–shell scheme, in which the quark

mass m_Q is defined as the pole of the propagator and the quark wave function is renormalized with a renormalization constant $Z_2^{1/2}$ such that the residue at the pole is equal to unity. The photon–quark vertex is renormalized at zero–momentum transfer and the standard QED Ward identity renders the corresponding renormalization factor equal to the one of the wave function. Since in the SM the fermion masses are generated by the interaction with the Higgs field, the renormalization factor Z_{HQQ} associated with the Higgs–quark vertex is fixed unambiguously by the renormalization factors Z_m for the mass and Z_2 for the wave function. From the bare Lagrangian [the subscript 0 stands for bare quantities]

$$\mathcal{L}_0 \;=\; -m_0\bar{Q}_0Q_0\frac{H}{v} = -m_Q\bar{Q}Q\frac{H}{v} + Z_{HQQ}m_Q\bar{Q}Q\frac{H}{v} \tag{2.49}$$

one finds $Z_{HQQ} = 1 - Z_2Z_m$ [148, 149]. Thus, in contrast to the photon–fermion vertex, the scalar HQQ vertex is renormalized at zero momentum transfer by a finite amount γ_m after subtracting Z_{HQQ} due to the lack of a corresponding Ward identity.

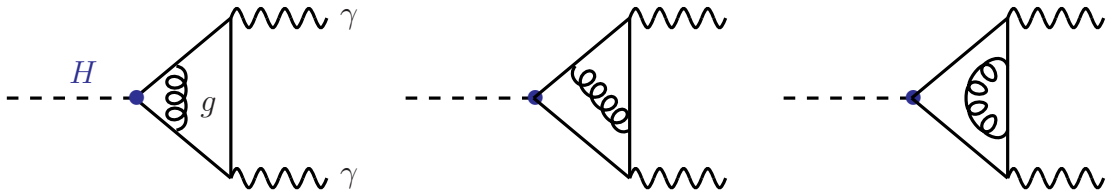

Figure 2.17: QCD corrections to the quark amplitude for the $H \to \gamma\gamma$ decay.

The two–loop amplitudes for the $H \to \gamma\gamma$ decay have been calculated in Refs. [179–181]. In the general massive case, the five–dimensional Feynman parameter integrals have been reduced analytically down to one–dimensional integrals over polylogarithms which were evaluated numerically [180]. Very recently [181], these integrals have been derived analytically. The QCD corrections of the quark contribution to the two–photon Higgs decay amplitude can be parameterized as

$$A^H_{1/2}(\tau_Q) = A^H_{1/2}(\tau_Q)|_{\rm LO}\left[1 + \frac{\alpha_s}{\pi}\,C_H(\tau_Q)\right] \tag{2.50}$$

In principle, the scale in α_s is arbitrary to this order although, in practice, it should be chosen to be, typically, of order M_H. However, the renormalization scale should be defined at $\mu_Q = \frac{1}{2}M_H$ for two reasons: (i) the $Q\overline{Q}$ decay threshold is defined at the correct position $2m_Q(m_Q) = 2m_Q$ and (ii) it turns out a posteriori that all relevant large logarithms are effectively absorbed into the running mass for the entire range of the variable τ. Note that near the threshold [182], within a margin of a few GeV, the perturbative analysis is in principle not valid since the formation of a P–wave 0^{++} resonance, interrupted by the rapid quark decay modifies the amplitude in this range. Since $Q\overline{Q}$ pairs cannot form 0^{++} states at the threshold, ImC_H vanishes there and ReC_H develops a maximum very close to this threshold.

The real and imaginary parts of the correction factor C_H are shown in Fig. 2.18 as a function of τ_Q with the scale set to $\mu_Q = \frac{1}{2}M_H$ (left) and $\mu_Q = m_Q$ (right). In the limit $m_Q \to \infty$, the correction factor can be evaluated analytically and one finds [179]

$$M_H^2/4m_Q^2 \to 0 : \quad 1 + C_H \frac{\alpha_s}{\pi} \to 1 - \frac{\alpha_s}{\pi} \tag{2.51}$$

In the opposite limit $m_Q(\mu_Q^2) \to 0$ the leading and subleading logarithms of the correction factor can also be evaluated analytically

$$m_Q(\mu_Q^2) \to 0 : \quad \begin{cases} \mathrm{Re}C_H \to -\frac{1}{18}[\log^2(4\tau) - \pi^2] - \frac{2}{3}\log(4\tau) + 2\log\frac{\mu_Q^2}{m_Q^2} \\ \mathrm{Im}C_H \to \frac{\pi}{3}\left[\frac{1}{3}\log(4\tau) + 2\right] \end{cases} \tag{2.52}$$

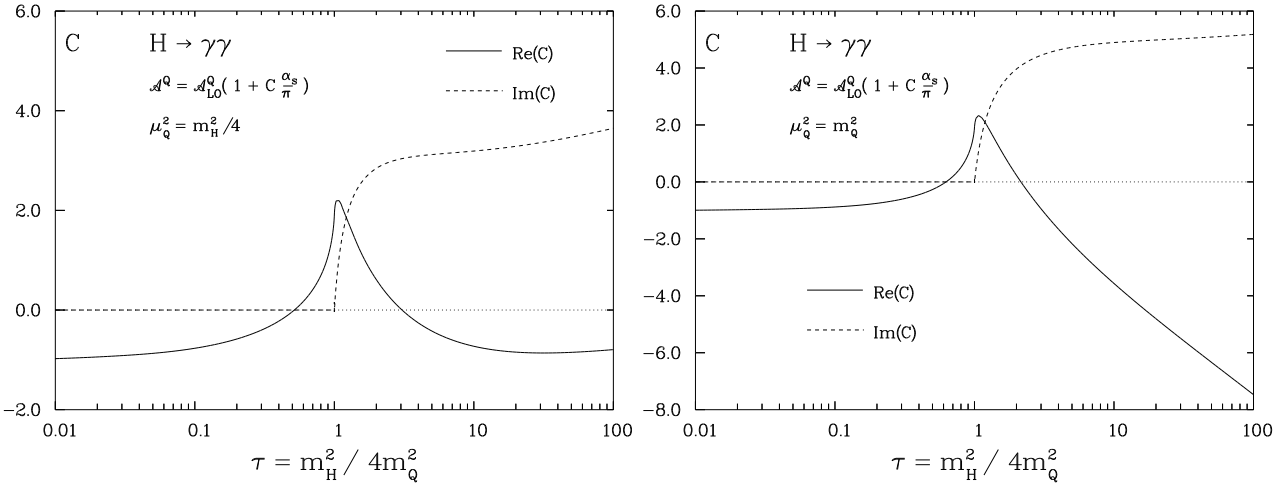

Figure 2.18: The QCD correction factor to the real and imaginary parts of the quark amplitude $A_{1/2}^H$ in the $H \to \gamma\gamma$ decay as a function of $\tau_Q = M_H^2/4m_Q^2$. The scale at which the correction is evaluated is $\mu_Q = \frac{1}{2}M_H$ (left) and $\mu_Q = m_Q$ (right).

The QCD correction factor to the partial decay width relative to the lowest order result, $\Gamma = \Gamma_{\rm LO}(1+\delta)$ is shown in Fig. 2.19 as a function of the Higgs boson mass. The correction is very large slighly above the $t\bar{t}$ threshold and in the area $M_H \sim 650$ GeV where the destructive $W-$ and $t-$loop interference makes the decay amplitude nearly vanish.

2.3.2 Decays into a photon and a Z boson

Similarly to the $\gamma\gamma$ case, the $H \to Z\gamma$ coupling is built up by the heavy top quark and W boson loops. The partial decay width is given by [107, 108]

$$\Gamma(H \to Z\gamma) = \frac{G_\mu^2 M_W^2\, \alpha\, M_H^3}{64\,\pi^4}\left(1 - \frac{M_Z^2}{M_H^2}\right)^3 \left|\sum_f N_f \frac{Q_f \hat{v}_f}{c_W} A_{1/2}^H(\tau_f, \lambda_f) + A_1^H(\tau_W, \lambda_W)\right|^2 \tag{2.53}$$

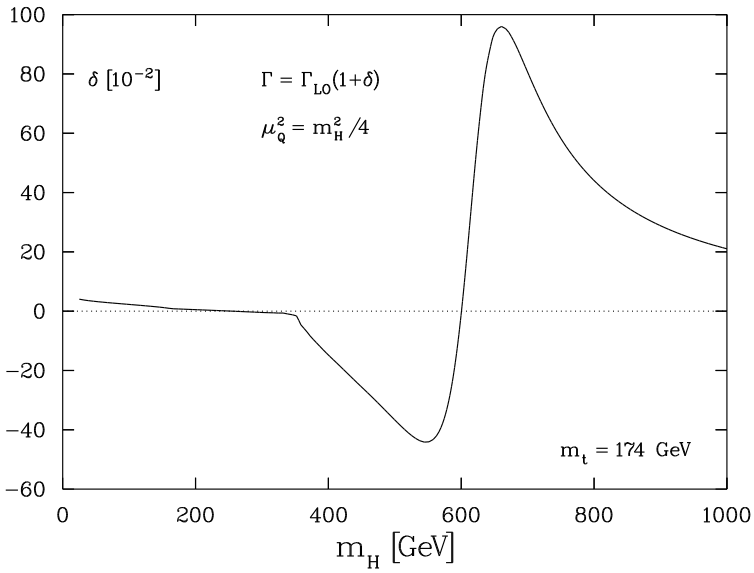

Figure 2.19: The QCD correction factor for the partial width $\Gamma(H \to \gamma\gamma)$ as a function of M_H. The pole quarks masses are $m_t = 174$ GeV and $m_b = 5$ GeV and the QCD couplings is normalized at $\alpha_s(M_Z) = 0.118$. The renormalization scale is set to $\mu_Q = \frac{1}{2}M_H$.

with now $\tau_i = 4M_i^2/M_H^2$, $\lambda_i = 4M_i^2/M_Z^2$ and the form factors

$$\begin{aligned} A^H_{1/2}(\tau,\lambda) &= [I_1(\tau,\lambda) - I_2(\tau,\lambda)] \\ A^H_1(\tau,\lambda) &= c_W \left\{ 4\left(3 - \frac{s_W^2}{c_W^2}\right) I_2(\tau,\lambda) + \left[\left(1+\frac{2}{\tau}\right)\frac{s_W^2}{c_W^2} - \left(5+\frac{2}{\tau}\right)\right] I_1(\tau,\lambda) \right\} \end{aligned} \tag{2.54}$$

with $\hat{v}_f = 2I_f^3 - 4Q_f s_W^2$ as usual. The functions I_1 and I_2 are given by

$$\begin{aligned} I_1(\tau,\lambda) &= \frac{\tau\lambda}{2(\tau-\lambda)} + \frac{\tau^2\lambda^2}{2(\tau-\lambda)^2}\left[f(\tau^{-1}) - f(\lambda^{-1})\right] + \frac{\tau^2\lambda}{(\tau-\lambda)^2}\left[g(\tau^{-1}) - g(\lambda^{-1})\right] \\ I_2(\tau,\lambda) &= -\frac{\tau\lambda}{2(\tau-\lambda)}\left[f(\tau^{-1}) - f(\lambda^{-1})\right] \end{aligned} \tag{2.55}$$

where the function $f(\tau)$ is defined in eq. (2.47) while the function $g(\tau)$ can be expressed as

$$g(\tau) = \begin{cases} \sqrt{\tau^{-1}-1}\arcsin\sqrt{\tau} & \tau \geq 1 \\ \dfrac{\sqrt{1-\tau^{-1}}}{2}\left[\log\dfrac{1+\sqrt{1-\tau^{-1}}}{1-\sqrt{1-\tau^{-1}}} - i\pi\right] & \tau < 1 \end{cases} \tag{2.56}$$

Due to charge conjugation invariance, only the vectorial Z coupling contributes to the fermion loop so that in the limit $M_H \gg M_Z$, the $HZ\gamma$ amplitude reduces to the $H\gamma\gamma$ amplitude modulo the different Z and γ couplings to fermions and W bosons.

The partial width for this decay is shown in Fig. 2.20 as a function of M_H. As mentioned in §1.3.2 where the reverse decay $Z \to H\gamma$ was discussed, the W loop contribution is by far dominating. Below the WW threshold, where this decay might have a visible branching

ratio, it can be approximated by $A_1^H \simeq -4.6 + 0.3 M_H^2/M_W^2$. The top quark contribution interferes destructively with the W loop but is very small; for low Higgs boson masses it can be approximated by $A_{1/2}^H = N_c Q_t \hat{v}_t/(3c_W) \sim 0.3$. The partial decay width, varies from a few KeV for $M_H \sim 120$ GeV to ~ 100 KeV for $M_H \sim 2M_W$.

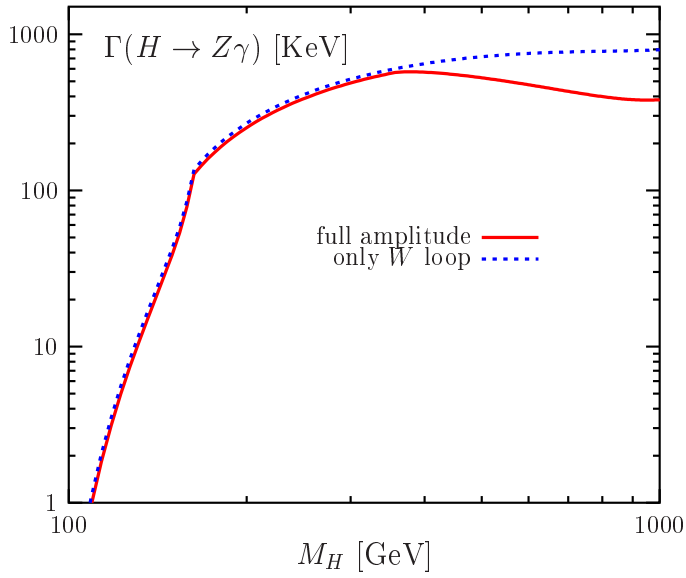

Figure 2.20: The partial width for the decay $H \to Z\gamma$ as a function of M_H with the full W boson and top quark contributions (solid line) and with the W and top quark contribution but with $m_t \to \infty$ (dotted line).

The QCD corrections to the quark loop, calculated in Ref. [183], are rather small in the interesting mass range, $M_H \lesssim 2M_W$. In the heavy top quark limit, which can be used here, the correction factor for the top quark amplitude is exactly as in the $H \to \gamma\gamma$ case

$$A_{1/2}^H(\tau_t, \lambda_t) \to A_{1/2}^H(\tau_t, \lambda_t) \times \left[1 - \frac{\alpha_s}{\pi}\right] \qquad \text{for } M_H^2 \ll 4m_t^2 \tag{2.57}$$

2.3.3 Decays into gluons

The partial width at leading order

The decay of the Higgs boson into two gluons is mediated by loops involving heavy quarks, with the main contribution coming from top quarks and a small contribution from bottom quarks. At the one–loop (leading) order, the partial decay width reads [184, 185]

$$\Gamma\left(H \to gg\right) = \frac{G_\mu\, \alpha_s^2\, M_H^3}{36\sqrt{2}\,\pi^3} \left| \frac{3}{4} \sum_Q A_{1/2}^H(\tau_Q) \right|^2 \tag{2.58}$$

The parameter $\tau_Q = M_H^2/4m_Q^2$ is defined by the pole mass m_Q of the heavy quark. The form factor $A_{1/2}^H(\tau_Q)$, similarly to the $H \to \gamma\gamma$ case, is given in eq. (2.46) and is again normalized

such that for $m_Q \gg M_H$, it reaches $\frac{4}{3}$, while it approaches zero in the chiral limit $m_Q \to 0$. When crossing the quark threshold, $M_H = 2m_Q$, the amplitude develops an imaginary part.

The gluonic decay width is shown as a function of the Higgs mass in Fig. 2.21 in the exact case where top and bottom quark loops, with $m_t = 178$ GeV and $m_b = 5$ GeV, are included (solid line), when only the top quark contribution is included (dashed line) and when the top quark mass is sent to infinity (dotted line). As can be seen, keeping only the top quark contribution is a good approximation, better than 10% even for $M_H \sim 100$ GeV, and below the $M_H = 2m_t$ threshold, the heavy top–quark approximation is quite reliable.

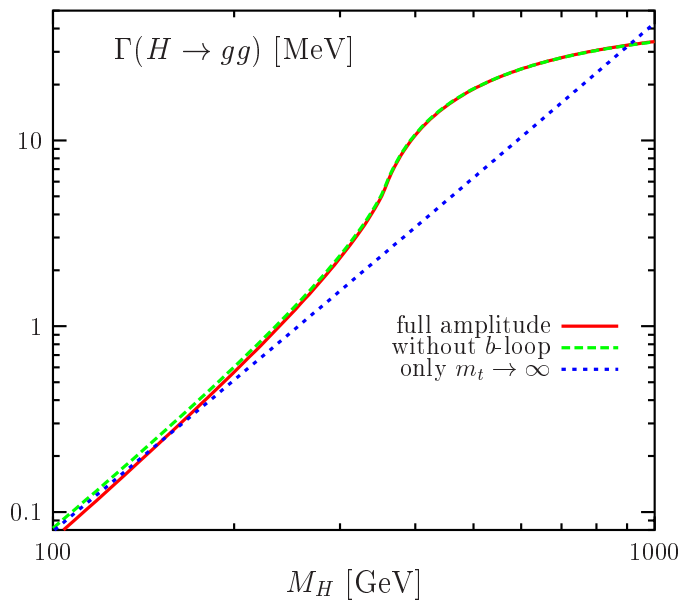

Figure 2.21: The partial width for the decay $H \to gg$ as a function of the Higgs boson mass with the top and bottom quark contributions included (solid line), with only the top quark contribution included (dashed line) and in the limit of infinite top quark mass (dotted line).

The QCD corrections at NLO

To incorporate the QCD corrections to the gluonic Higgs boson decay width, one needs to consider virtual corrections where the gluons are attached to the quark lines, as in the case of the $H \to \gamma\gamma$ decay at NLO, but also corrections involving the triple and quartic gluon vertices; Fig. 2.22a. These corrections are finite in the ultraviolet [since the complementary virtual corrections involved in the $H \to \gamma\gamma$ amplitude are also finite] once the proper counterterms associated with the renormalization of the QCD coupling $[Z_g - 1 = (Z_1 - 1) - \frac{3}{2}(Z_3 - 1)]$ have been added; α_s can be defined in the $\overline{\text{MS}}$ scheme with five active quark flavors and the heavy top quark decoupled. However, there are left–over infrared and collinear singularities which are canceled only if the real corrections with three gluon and a gluon plus a quark–antiquark pair final states $H \to gg + g$ and $g + q\bar{q}$ are added, Fig. 2.22b. The $q\bar{q}$ final

states will be assumed to be massless and, as a consequence of chiral symmetry, there is no interference of the amplitude for $H \to g + q\bar{q}$ and the one $H \to q\bar{q}^* \to q\bar{q}g$ in which the Higgs boson couples directly to quarks [this interference will be discussed in more detail later].

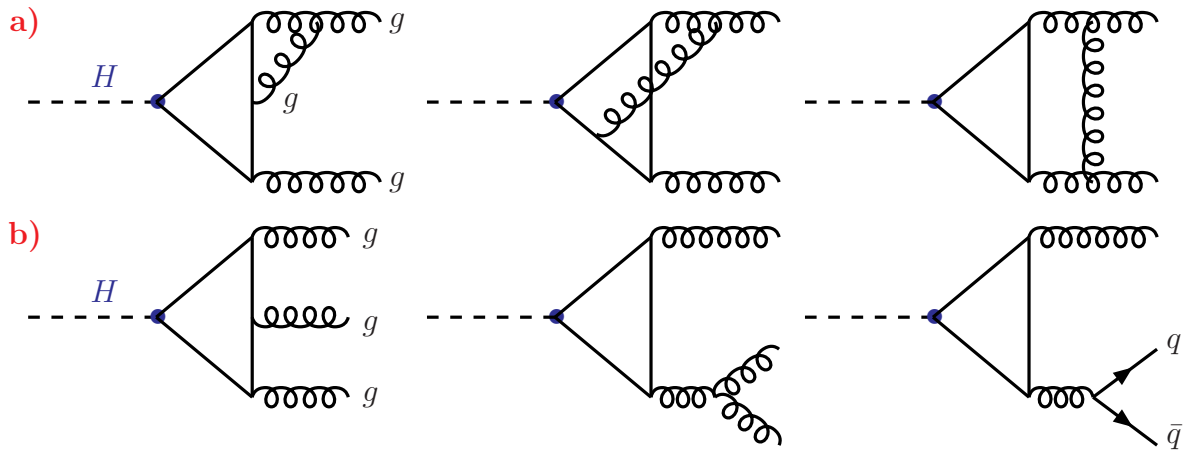

Figure 2.22: Typical Feynman diagrams for the QCD corrections to the process $H \to gg$ at NLO: a) virtual corrections not present in the decay $H \to \gamma\gamma$ and b) real corrections.

The calculation of the NLO QCD correction in the full massive case has been performed in Ref. [180] where the rather complicated analytical expressions can be found. The total correction can be cast into the form

$$\Gamma(H \to gg(g),\ gq\bar{q}) = \Gamma_{\rm LO}(H \to gg)\left[1 + E_H(\tau_Q)\frac{\alpha_s}{\pi}\right] \tag{2.59}$$

and one obtains for the correction factor

$$E_H(\tau_Q) = \frac{95}{4} - \frac{7}{6}N_f + \frac{33 - 2N_f}{6}\ \log\frac{\mu^2}{M_H^2} + \Delta E_H(\tau_Q) \tag{2.60}$$

where μ is the renormalization point and defines the scale of α_s. The first three terms survive in the limit of large loop masses while ΔE_H vanishes in this limit [186–189].

The QCD radiative corrections turn out to be quite important, nearly doubling the gluonic partial decay width; Fig. 2.23. In the mass range $M_H \lesssim 2M_W$, assuming $N_f = 5$ light quarks and a scale $\mu = M_H$, the leading order term is corrected by a factor

$$K = 1 + \frac{215}{12}\frac{\alpha_s^{N_f=5}(M_H)}{\pi} \tag{2.61}$$

leading to an increase of the partial width by $\sim 70\%$. Near the $t\bar{t}$ threshold, when the Hgg form factor develops an imaginary part, the correction is also at the level of 70%. It decreases slowly with the Higgs mass to reach 40% at $M_H \sim 1$ TeV. Also shown in Fig. 2.23 are the QCD corrections in the heavy top quark limit, but where the LO amplitude includes the full

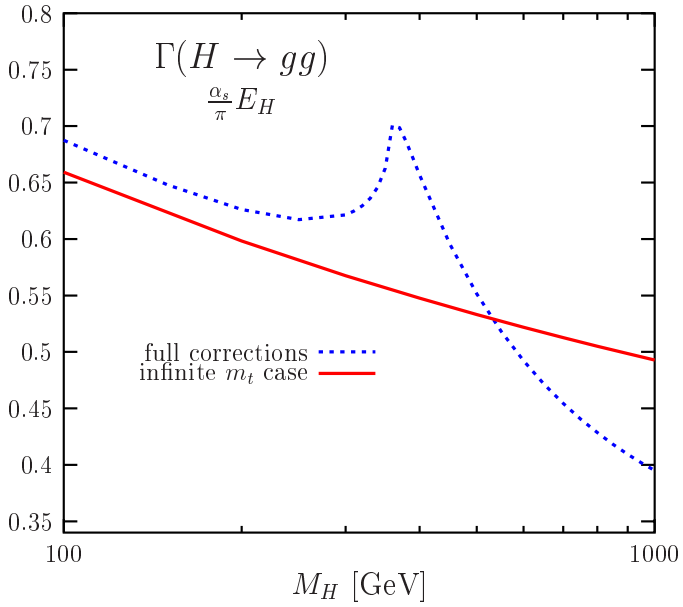

Figure 2.23: The QCD correction factor for the partial width $\Gamma(H \to gg)$ as a function of the Higgs boson mass in the full massive case with $m_t = 178$ GeV (dotted line) and in the heavy top quark limit (solid line). The strong coupling constant is $\alpha_s(M_Z) = 0.118$.

m_t dependence. As can be seen, this procedure approximates quite well the full result in the mass range $M_H \lesssim 300$ GeV, the difference being less than a ten percent.

Since b quarks, and eventually c quarks, can in principle be tagged experimentally, it is physically meaningful to include gluon splitting $g^* \to b\bar{b}\,(c\bar{c})$ in $H \to gg^* \to gb\bar{b}\,(c\bar{c})$ decays to the inclusive decay probabilities $\Gamma(H \to b\bar{b} + \ldots)$ *etc.* [180, 190]. The contribution of the b, c quark final states in $H \to g + q\bar{q}$ reads

$$-\frac{7}{3} + \frac{1}{3}\left[\log\frac{M_H^2}{m_b^2} + \log\frac{M_H^2}{m_c^2}\right] \tag{2.62}$$

Separating this contribution generates large logarithms, which can be effectively absorbed by redefining the number of active flavors in the gluonic decay mode, i.e. by evaluating α_s with $N_f = 3$ when both the charm and bottom quark contributions are subtracted. The contributions of the subtracted flavors have then to be added to the corresponding heavy quark decay modes discussed in §2.1 [some details will be given in the next section].

2.4 The electroweak corrections and QCD improvements

In this section, we discuss the electroweak radiative corrections and the higher–order QCD corrections to the Higgs decay modes. Some of these corrections have been reviewed in Refs. [19] and [21, 22] for, respectively, the electroweak and higher–order QCD parts.

The electroweak radiative corrections to the decays of Higgs bosons into fermions and gauge bosons can be classified in three categories:

(*i*) The fermionic corrections, which can be separated into the loop contributions of the light fermions and those due to the heavy top quark. Most of the former corrections are involved in the running of α and can be readily taken into account by using the improved Born approximation discussed in §1.2.4. For the top quark correction, a universal part is due to the renormalization of the Higgs wave function and vev and appears for all fermion species and for gauge bosons. These corrections are in general the dominant electroweak corrections for a SM Higgs boson with a mass $M_H \lesssim 2m_t$.

(*ii*) Corrections due to the Higgs boson itself that are proportional to the Higgs self–coupling λ. These corrections are important only when $M_H \gg M_W$, when the coupling λ becomes sizable. We have seen in §1.4.1 that for $M_H \sim \mathcal{O}(1\text{ TeV})$, they can be so large that perturbation theory breaks down.

(*iii*) The electromagnetic and the remaining weak corrections which do not depend on λ and which are not quadratic in the top–quark mass. These corrections are process dependent and, in general, they lead to small contributions, except in very special cases such as the $H \to t\bar{t}$ decay where the heavy top quark limit cannot be applied.

Collecting all these electroweak contributions, the correction factor for a given Higgs decay channel $H \to XX$ [also including the decay $H \to Z\gamma$], can be then written as

$$K^{\rm EW}_{H\to XX} = 1 + \delta^t_{HXX} + \delta^\lambda_{HXX} + \delta^e_{HXX} + \delta^w_{HXX} \tag{2.63}$$

The present knowledge of the electroweak radiative corrections to the SM Higgs decays is as follows. The complete one–loop calculations of the $H \to f\bar{f}$ and $H \to VV$ decays have been carried out in the massive cases in Refs. [191, 192] and [191, 193], respectively. The knowledge of the partial widths for these decays has been improved by considering higher–order corrections either in α_s or in the dominant electroweak coupling $G_\mu m_t^2$. The two–loop $\mathcal{O}(\alpha_s G_\mu m_t^2)$ heavy–top corrections to the light–fermion and bottom Yukawa couplings have been calculated in Refs. [194, 195] and [196], respectively, and those to the HVV couplings in Ref. [197]. The three–loop $\mathcal{O}(\alpha_s^2 G_\mu m_t^2)$ corrections may be found in Ref. [198] for the the $H \to \ell^+\ell^-$ and $H \to VV$ decays and in Ref. [199] for the decay $H \to q\bar{q}$, including the $b\bar{b}$ case. The two–loop $\mathcal{O}(G_\mu^2 m_t^4)$ pure electroweak corrections for the $H \to f\bar{f}$ and $H \to VV$ decays have been derived in Ref. [200]. The radiative corrections due to the Higgs self–couplings have been calculated at one and two loops in Refs. [121, 122] for decays into massive gauge bosons and in Refs. [121, 123] for decays into fermions.

As for the loop induced Higgs boson vertices, the leading two–loop electroweak corrections, which are of $\mathcal{O}(G_\mu m_t^2)$ relative to the one–loop results, have been calculated in Refs. [201] for the Hgg coupling and in Refs. [200, 202] for the $H\gamma\gamma$ and $HZ\gamma$ couplings.

Recently, the two–loop electroweak corrections induced by light fermion loops have been calculated for the $H \to \gamma\gamma$ and $H \to gg$ decays [203, 204]. Furthermore, still in the heavy top quark limit, the NNLO QCD corrections to the decays $H \to \gamma\gamma$ [205] and $H \to gg$ [206] have been evaluated. Other corrections [207–209] are also available and will be discussed.

The dominant heavy top–quark corrections, including the two–loop order in $G_\mu m_t^2$ and in α_s, as well as the NNLO QCD corrections to the loop induced decays, can be derived using a low energy theorem in which the top quark has been integrated out by sending its mass to infinity. The results can nevertheless be extrapolated to Higgs boson masses up to the $M_H \sim 2m_t$ threshold in principle. In the following, we first discuss this low energy theorem and its applications for SM Higgs boson decays.

2.4.1 The low energy theorem

In the case of the top quark loop contributions to the interactions of a light Higgs boson with $M_H \ll 2m_t$, a rather simple and efficient way of deriving the corrections is to construct an effective Lagrangian where the top quark is integrated out. This can be done by considering the limit of a massless Higgs boson or, equivalently, of a very heavy top quark and using a low energy theorem proposed in Refs. [111, 176, 210] and extended to higher orders in Refs. [180, 211]. The low–energy theorem relates the amplitudes of two processes which differ only by the emission of a Higgs boson with vanishing momentum. Indeed, if one recalls the discussion in §1.1.3, the coupling of a Higgs boson to a fermion with a mass m_i is generated by simply performing the substitution

$$m_i^0 \to m_i^0(1 + H^0/v^0) \tag{2.64}$$

in the bare Lagrangian [the index 0 stands for bare quantities], where the Higgs boson is a constant field. This implies the following relation between two matrix elements with and without the attachment of a Higgs field with zero–momentum p_H

$$\lim_{p_H \to 0} \mathcal{M}(X \to Y + H) = \frac{1}{v_0} m_i^0 \frac{\partial}{\partial m_i^0} \mathcal{M}(X \to Y) \tag{2.65}$$

However, in higher orders, there is a subtlety in the use of this relation: when renormalizing the $Hf\bar{f}$ interaction, the counterterm for the Higgs–fermion Yukawa coupling is not the $Hf\bar{f}$ vertex with a subtraction at zero momentum transfer, $\Gamma_{Hf\bar{f}}(q^2 = 0)$ [which is implicitly used in the low–energy theorem] but, rather, is determined by the counterterms for the fermion mass Z_m and wave–function Z_2 as discussed previously. This has to be corrected for and, in fact, this can be done by replacing the differentiation with respect to the bare mass with a differentiation with respect to the renormalized mass, which gives rise to a finite contribution which is simply the anomalous mass dimension of the fermion

$$m_0 \frac{\partial}{\partial m_0} = \frac{m}{1 + \gamma_m} \frac{\partial}{\partial m} \tag{2.66}$$

which relates the bare mass m_0 and the renormalized mass m, $\mathrm{dlog}\, m_0 = (1+\gamma_m)\mathrm{d}\log m$.

It is well known that this low energy theorem can be exploited to derive the $H\gamma\gamma$ coupling in lowest order [176, 210], but the theorem is also valid if radiative QCD corrections are included [180, 211]. The contribution of a heavy quark to the vacuum polarization of the photon at zero–momentum transfer is given in dimensional regularization, with $n = 4-\epsilon$ being the number of space dimensions, by

$$\Pi = -Q_Q^2 \frac{\alpha}{\pi}\Gamma(\epsilon)\left(\frac{4\pi\mu^2}{m_Q^2}\right)^{\epsilon}\left[1+\frac{\alpha_s}{2\pi}\Gamma(1+\epsilon)\left(\frac{4\pi\mu^2}{m_Q^2}\right)^{\epsilon}+\mathcal{O}(\epsilon)\right] \tag{2.67}$$

so that $m_Q(\partial\Pi/\partial m_Q) = 2Q_Q^2\frac{\alpha}{\pi}\left(1+\frac{\alpha_s}{\pi}\right)$. From the anomalous quark mass dimension to lowest order, $\gamma_m = 2\alpha_s/\pi$, one immediately obtains the correction C_H of the $H\gamma\gamma$ coupling in agreement with what has been discussed in the previous section, §2.3.1,

$$M_H^2/4m_Q^2 \to 0 : \quad 1 + C_H\frac{\alpha_s}{\pi} \to \frac{1+\alpha_s/\pi}{1+2\alpha_s/\pi} = 1-\frac{\alpha_s}{\pi} \tag{2.68}$$

The same result can also be derived by exploiting well–known results on the anomaly in the trace of the energy–momentum tensor [212]

$$\Theta_{\mu\mu} = (1+\gamma_m)m_0\overline{Q}_0Q_0 + \frac{1}{4}\frac{\beta_\alpha}{\alpha}F_{\mu\nu}F_{\mu\nu} \tag{2.69}$$

with β_α denoting the mixed QED/QCD β function defined by $\partial\alpha(\mu^2)/\partial\log\mu{=}\beta_\alpha$. Since the matrix element $\langle\gamma\gamma|\Theta_{\mu\mu}|0\rangle$ vanishes at zero–momentum transfer, the coupling of the two–photon state to the Higgs source $(m_0/v)\overline{Q}_0Q_0$ is simply given by the effective Lagrangian

$$\mathcal{L}(H\gamma\gamma) = \frac{H}{v}F^{\mu\nu}F_{\mu\nu}\frac{1}{4}\frac{\beta_\alpha^Q}{\alpha}\frac{1}{1+\gamma_m} \tag{2.70}$$

including only the heavy quark contribution to the QED/QCD β function. With $\beta_\alpha^Q = 2Q_Q^2\alpha^2/\pi(1+\alpha_s/\pi)$ and $\gamma_m = 2\alpha_s/\pi$, one recovers again the previous result for the QCD correction to the $H\gamma\gamma$ coupling.

2.4.2 EW corrections to decays into fermions and massive gauge bosons

Heavy top quark corrections

If one only wishes to extract the leading correction to the Higgs couplings due to a heavy top quark, one may work in the framework of a Yukawa Lagrangian where it couples only to the Higgs boson and to the longitudinal components of the gauge bosons, a situation which corresponds to the gaugeless limit of the SM; of course, the interactions due to light quarks and gluons have to be kept when considering the QCD corrections.

The bare Lagrangian describing the interactions of the Higgs boson with fermions and vector bosons

$$\mathcal{L} = \frac{H_0}{v_0}\left(-\sum_f m_{f0}\bar{f}_0 f_0 + 2M_{W0}^2 W_{0\mu}^\dagger W_0^\mu + M_{Z0}^2 Z_{0\mu}^\dagger Z_0^\mu\right) \tag{2.71}$$

contains the overall factor H_0/v_0, which undergoes a finite renormalization. Working in the on–shell scheme, where G_μ and the physical W boson mass are used as inputs, and performing the renormalization of all the fields and couplings that are involved, one obtains a universal electroweak correction which appears in the Higgs boson couplings to all particles

$$\begin{aligned}\frac{H_0}{v_0} &\to (\sqrt{2}G_\mu)^{1/2} H \left(1 - \frac{\Delta M_W^2}{M_W^2}\right)^{-1/2} [1 + \mathrm{Re}\Pi'_{HH}(M_H^2)]^{-1/2} \\ &\to (\sqrt{2}G_\mu)^{1/2} H\,(1+\delta_u)\end{aligned} \tag{2.72}$$

In the heavy top quark limit, one sets the momentum transfer to zero in the boson propagators, since $m_t \gg M_W$ and M_H, and extracts the leading components which grow as m_t^2. Including the QCD corrections up to $\mathcal{O}(\alpha_s^2)$ and electroweak corrections to $\mathcal{O}(G_\mu m_t^2)$ to this terms, one obtains results similar to what has been obtained for $\Delta\rho$ at this order, eq. (1.106), with the Higgs boson mass set to zero in the corrections $(\Delta\rho)^{\mathrm{EW}}$. Using the abbreviations $x_t = G_\mu m_t^2/(8\sqrt{2}\pi^2)$ and $a_s = \alpha_s^{N_f=6}(m_t)/\pi$, the end result for the contribution δ_u will be then [194, 195]

$$\delta_u = x_t\left[\frac{7}{2} + 3\left(\frac{149}{8} - \pi^2\right)x_t - \left(3 + \frac{\pi^2}{3}\right)a_s - 56.7a_s^2\right] \tag{2.73}$$

For the Higgs boson couplings to leptons, this is in fact the only heavy top quark correction which is involved, unless one moves to higher orders in the electroweak coupling. For the couplings to light quarks $q \neq b, t$ the same correction δ_u appears, except from the small $\mathcal{O}(x_t a_s^2)$ term which is different. However, in the case of the bottom quarks as well as for the massive gauge bosons, there are extra contributions due to the exchange of the top quark in the vertices. As previously mentioned, to derive these additional terms, one can use again the low–energy theorem with the additional information provided by the knowledge of the particle self–energies. In the case of b quarks, one obtains the non–universal correction from the Lagrangian

$$\mathcal{L}(Hb\bar{b}) = -m_b\,\bar{b}b\,\frac{H^0}{v_0}\left(1 + \delta_{Hbb}^{\mathrm{non-univ}}\right) = -m_b\bar{b}b\frac{H^0}{v^0}\left(1 - \frac{m_{t0}\partial\Sigma_{bb}}{\partial m_{t0}}\right) \tag{2.74}$$

where Σ_b is the two–point function of the b quark, which receives contributions from the top quark when exchanged together with a W boson in the propagator loop. The non universal corrections in this case is obtained to be [196]

$$\delta_{Hbb}^{\mathrm{non-univ}} = -3x_t\left(1 - \frac{1}{3}a_s - 11.2a_s^2\right) \tag{2.75}$$

Combined to the universal corrections, $\delta_u \sim \frac{7}{2}x_t$, this leads to a large cancellation which gives a rather small total correction, $\delta_b = \frac{1}{2}x_t$, at the one–loop level.

In the case of the massive gauge bosons, besides the correction δ_u, one has also to include a non–universal vertex correction, which is different for W and Z bosons at higher orders. Again, using the knowledge on the W and Z boson two–point functions and setting their momentum transfer to zero, the non–universal correction is obtained from the differentiation with respect to the top mass of the bare $M_V^2 V_\mu V^\mu$ interaction

$$\delta_{HVV} = (1+\delta_u)\left(1 - \frac{m_t^2 \partial}{\partial m_t^2}\right)\frac{\Pi_{VV}(0)}{M_V^2} \tag{2.76}$$

One then obtains for the total heavy top quark correction at the same order as for the correction δ_u [197]

$$\begin{aligned} \delta_w &= x_t\left[-\frac{5}{2} + \left(\frac{39}{8} - 3\pi^2\right)x_t + \left(9 - \frac{\pi^2}{3}\right)a_s + 27.0a_s^2\right] \\ \delta_z &= x_t\left[-\frac{5}{2} + \left(\frac{177}{8} + 3\pi^2\right)x_t + \left(15 - \frac{\pi^2}{3}\right)a_s + 17.1a_s^2\right] \end{aligned} \tag{2.77}$$

Adding up all the previous results, one finds for the heavy top correction factor δ^t_{HXX} in eq. (2.63), for the fermionic and bosonic decay widths of the Higgs boson [in which the HXX coupling appears squared]

$$\delta^t_{HXX} = (1+\delta_x)^2 - 1 \tag{2.78}$$

The remaining electroweak corrections

In the case of light fermions, the electromagnetic corrections are simply given by [192]

$$\delta^e_{Hff} = \frac{3}{2}\frac{\alpha}{\pi}Q_f^2\left(\frac{3}{2} - \log\frac{M_H^2}{m_f^2}\right) \tag{2.79}$$

For quark final states, the large logarithms $\log M_H^2/m_q^2$ can be absorbed in the running quark masses analogously to the QCD corrections. In this case, the electromagnetic correction, supplemented by the NLO QCD correction, reads [207]

$$\delta^e_{Hqq} = 4.2\, Q_q^2\,\frac{\overline{\alpha}(M_H)}{\pi}\left[1 + 5.2\frac{\alpha_s}{\pi}\right] \tag{2.80}$$

The remaining weak corrections can be approximated by [the reduced vector and axial couplings $\hat{v}_f$ and $\hat{a}_f$ have been defined previously] [19]

$$\delta^w_{Hff} = \frac{G_\mu M_Z^2}{8\sqrt{2}\pi^2}\left[c_W^2\left(-5 + \frac{3}{s_W^2}\log c_W^2\right) - \frac{6\hat{v}_f^2 - \hat{a}_f^2}{2}\right] \tag{2.81}$$

In the case of Higgs decays into massive gauge bosons, the electromagnetic corrections for $H \to ZZ$ are absent, while the vertex corrections and the photon real emission in the decay $H \to W^+W^-$ do not form a gauge invariant and meaningful set, and must be combined with the photonic contributions to the self–energies [193]. The remaining electroweak corrections [except for the ones involving the self–coupling λ] are in general small.

For Higgs boson decay into top quarks, since m_t cannot be set to zero or infinity anymore, the situation is more complicated. The electromagnetic corrections with virtual photon exchange and real photon emission [the running of α is again taken care of by using the IBA with G_μ as input] are the same as the QCD corrections discussed in §2.1.3 if the strong coupling α_s is replaced by the proper electromagnetic factor

$$\delta^e_{Htt} = \frac{3}{4} Q_t^2 \frac{\alpha}{\pi} \Delta^t_H(\beta_t) \tag{2.82}$$

Because of the Coulomb singularity, these corrections are large near threshold, $M_H \sim 2m_t$, but are small far above threshold leading to a correction less than 1%.

For the electroweak corrections, which are interesting since they involve the Higgs contributions [and if $M_H \sim 2m_t$, mixing between the Higgs boson and the spin zero $t\bar{t}$ bound state would occur], the expression is rather complicated since $m_t \neq 0$ [192]. However a simple interpolating formula can be obtained, which approximates the full result to the level of 1% even in the threshold region. In terms of $h_t = M_H^2/4m_t^2$ and $\ell_t = \log M_H/m_t$, one has [19]

$$\delta^w_{Htt} = \frac{G_\mu m_t^2}{2\sqrt{2}\pi^2} \left(1 + \frac{5}{2h_t}\right) \ell_t \left(\ell_t - 2\right) + 1.059 h_t + 3.477 + \frac{0.272}{h_t} - \frac{1.296}{h_t^2} - \frac{0.182}{h_t^3} \tag{2.83}$$

Numerically, this correction is extremely small near the threshold and increases monotonically to reach the level of $\sim 15\%$ for $M_H \sim 1$ TeV.

Higgs self–coupling corrections

Finally, one has to include the corrections due to the triple and quartic Higgs boson couplings. In the regime where the Higgs boson mass is large, one obtains at two–loop order in the on–shell scheme [122, 123]

$$\begin{aligned} \delta^\lambda_{Hff} &= (13 - 2\sqrt{3}\pi) \left(\frac{\lambda}{16\pi^2}\right) - 32.66 \left(\frac{\lambda}{16\pi^2}\right)^2 \\ \delta^\lambda_{HVV} &= \left(19 - 6\sqrt{3}\pi - \frac{5\pi^2}{3}\right) \left(\frac{\lambda}{16\pi^2}\right) + 62.0 \left(\frac{\lambda}{16\pi^2}\right)^2 \end{aligned} \tag{2.84}$$

Numerically, the result as a function of the Higgs boson mass is

$$\begin{aligned} \delta^\lambda_{Hff} &= 0.11 \left(M_H/1 \text{ TeV}\right)^2 - 0.09 \left(M_H/1 \text{ TeV}\right)^2 \\ \delta^\lambda_{HVV} &= 0.15 \left(M_H/1 \text{ TeV}\right)^2 + 0.17 \left(M_H/1 \text{ TeV}\right)^2 \end{aligned} \tag{2.85}$$

As discussed in §1.4.1, if the Higgs boson mass is very large, $M_H \sim \mathcal{O}(10 \text{ TeV})$, the one loop terms of these expansions become close to the Born terms and the perturbative series does not converge. In fact, already for a Higgs boson mass close to $M_H \sim 1$ TeV, the two–loop contributions become as important as the one–loop contributions. Hence, for perturbation theory to hold, M_H should be smaller than about one TeV. In this mass regime, however, the total correction δ^{λ}_{HVV} is moderate, being at the level of $\delta^{\lambda}_{HVV} \sim 20\%$ for $M_H \sim 1$ TeV. In the case of fermionic decays, the total correction is even smaller, $\delta^{\lambda}_{Hff} \simeq 2\%$ for $M_H \simeq 1$ TeV, because of the accidental cancellation of the one–loop and two–loop contributions.

2.4.3 NNLO QCD and EW corrections to the loop induced decays

The NNLO QCD corrections

One can use the low energy theorem discussed in §2.4.1 to derive the higher–order QCD corrections to the $H\gamma\gamma$ and Hgg couplings in the heavy top quark limit. In the case of the $H\gamma\gamma$ operator, the QED/QCD β function and the anomalous mass dimension γ_m are known to four loops. The contribution of the top quark to the $H\gamma\gamma$ coupling at $\mathcal{O}(\alpha_s^2)$, with $N_f = 6$ flavors and a renormalization scale μ, is found to be [205]

$$\mathcal{L}_{\text{eff}}(H\gamma\gamma) = \frac{Q_t^2 \alpha}{2\pi} \left(\sqrt{2} G_F\right)^{1/2} \left[1 - \frac{\alpha_s}{\pi} - \left(\frac{31}{4} + \frac{7}{4} \log \frac{\mu^2}{m_t^2}\right) \left(\frac{\alpha_s}{\pi}\right)^2\right] F_{\mu\nu} F_{\mu\nu}\, H \tag{2.86}$$

In the case of the Hgg operator in the heavy top quark limit

$$\mathcal{L}_{\text{eff}}(Hgg) = \frac{H}{v} G^a_{\mu\nu} G^{a\mu\mu}\, C_g \tag{2.87}$$

the QCD correction can be again expressed in terms of the heavy quark contribution $\beta_Q(\alpha_s)$ to the QCD β function and to the anomalous quark mass dimension γ_m as

$$\mathcal{L}_{\text{eff}}(Hgg) = -\frac{\alpha_s}{4} \frac{H}{v} G^a_{\mu\nu} G^{a\mu\nu} \frac{\beta_Q(\alpha_s)}{\alpha_s^2} \frac{1}{1 + \gamma_m(\alpha_s)} \tag{2.88}$$

which is valid at two loops [at three loops, some subtelties appear and are discussed in Ref. [21] for instance]. At $\mathcal{O}(\alpha_s^2)$, the anomalous quark mass dimension is given by [213]

$$\gamma_m(\alpha_s) = 2\frac{\alpha_s}{\pi} + \left(\frac{101}{12} - \frac{5}{18}(N_f + 1)\right) \left(\frac{\alpha_s}{\pi}\right)^2 \tag{2.89}$$

while the QCD β function at NNLO in the $\overline{\text{MS}}$ scheme is given by [43]

$$\beta_Q(\alpha_s) = \frac{\alpha_s^2}{3\pi} \left[1 + \frac{19}{4}\frac{\alpha_s}{\pi} + \frac{7387 - 325 N_f}{288} \left(\frac{\alpha_s}{\pi}\right)^2\right] \tag{2.90}$$

From these expressions and taking care of the fact that the $\overline{\text{MS}}$ strong coupling α_s of the effective theory should include only the $N_f = 5$ light flavors [see again Ref. [21] for details],

one arrives, using a consistent α_s expansion at the final result for the coefficient function C_g at NNLO with a scale taken to be $\mu = m_t$, to [199]

$$C_g = -\frac{\alpha_s}{12\pi}\left[1 + \frac{11}{4}\frac{\alpha_s}{\pi} + \frac{2777 - 201N_f}{288}\left(\frac{\alpha_s}{\pi}\right)^2 + \cdots\right] \tag{2.91}$$

However, contrary to the two–photon case, $\mathcal{L}_{\rm eff}(Hgg)$ does not describe the Hgg interaction in total: it accounts only for the interactions mediated by the heavy quarks directly but it does not include the interactions of the light fields. It must be added to the light–quark and gluon part of the basic QCD Lagrangian, i.e. the effective coupling has to be inserted into the blobs of the effective diagrams shown in Fig. 2.24 for the interaction of the Higgs boson with gluons and massless quarks.

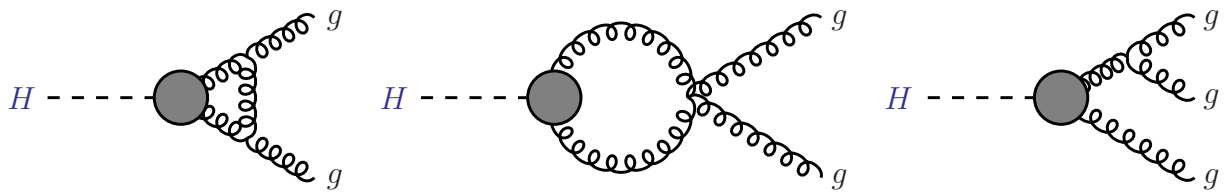

Figure 2.24: Effective diagrams contributing to the Hgg interaction in the limit where the top quark is heavy and has been integrated out. The blob represents the effective Hgg coupling.

For instance, for the Higgs decay into gluons at NLO, one adds to the contribution to the effective Hgg coupling squared $(1 + \frac{11}{4}\frac{\alpha_s}{\pi})^2$, the gluon and light quarks contributions from the pure gluonic virtual corrections and the real correction from $H \to ggg$ and $H \to gq\bar{q}$ with N_f light quarks, $\left(\frac{73}{4} - \frac{7N_f}{6}\right)$, leading to the total contribution for $\mu^2 = M_H^2$

$$\frac{11}{2}\frac{\alpha_s}{\pi} + \left(\frac{73}{4} - \frac{7N_f}{6}\right)\frac{\alpha_s}{\pi} = \left(\frac{95}{4} - \frac{7N_f}{6}\right)\frac{\alpha_s}{\pi} \tag{2.92}$$

which was given in eq. (2.60) for the gluonic Higgs partial width at NLO.

At NNLO, the calculation has also been done for the interaction of the Higgs boson with the light fields and this will be discussed later when we will address the question of Higgs production in the $gg \to H$ fusion mechanism. Here, we simply give the final result for the correction factor for the partial $H \to gg$ decay width at NNLO, for a number of light flavors $N_f = 5$ and with a scale $\mu = M_H$, which reads [206]

$$K^{\rm QCD}_{H\to gg} = 1 + \frac{215}{12}\frac{\alpha_s(M_H)}{\pi} + \frac{\alpha_s^2(M_H)}{\pi^2}\left(156.8 - 5.7\log\frac{m_t^2}{M_H^2}\right) \tag{2.93}$$

The three–loop correction amounts to $\sim 20\%$ of the [one–loop] Born term and $\sim 30\%$ of the two–loop term, therefore showing a good convergence behavior of the perturbative series.

Electroweak and self–coupling corrections

We now turn to the dominant electroweak corrections to the Higgs boson loop induced decays, those which are proportional to $G_\mu m_t^2$. Again, one can use a variant of the low energy theorem discussed previously to calculate the two–loop $\mathcal{O}(G_\mu m_t^2)$ correction to the Hgg coupling [176, 210]. The obtained effective Hgg coupling at this order is given by

$$\mathcal{L}(Hgg) = (\sqrt{2}G_\mu)^{1/2} \frac{\alpha_s}{12\pi} \, HG_{\mu\nu}G^{\mu\nu} \, (1 + \delta_1 + \delta_2 + \delta_3) \tag{2.94}$$

Here, δ_1 is the contribution of the top quark to the QCD β function at $\mathcal{O}(\alpha_s G_\mu m_t^2)$, which can be evaluated by considering the two–loop diagrams where Higgs and Goldstone bosons are exchanged in the heavy quark loop

$$\frac{\beta(\alpha_s)}{g_s} = \frac{\alpha_s}{6\pi}(1 + \delta_1) \Rightarrow \delta_1 = -12 \frac{G_\mu m_t^2}{8\sqrt{2}\pi^2} \tag{2.95}$$

The term δ_2 is simply the contribution of the anomalous quark mass dimension

$$\delta_2 = (Z_2^Q - 1) - \frac{\delta m_Q}{m_Q} + \Gamma_{HQ\bar{Q}}(q^2 = 0) = 6 \frac{G_\mu m_t^2}{8\sqrt{2}\pi^2} \tag{2.96}$$

Finally, δ_3 represents the renormalization of the Higgs wave function and vev

$$\delta_3 = -\frac{1}{2} \left[\frac{\Pi_{WW}(0)}{M_W^2} + \frac{\partial \Pi_{HH}(M_H^2 = 0)}{\partial M_H^2} \right] = 7 \frac{G_\mu m_t^2}{8\sqrt{2}\pi^2} \tag{2.97}$$

Due to the large cancellation between the three components, $\delta_1 = -12, \delta_2 = +6$ and $\delta_3 = 7$ in units of $\frac{1}{2}x_t = G_\mu m_t^2/(16\sqrt{2}\pi^2)$, the total correction factor at this order is rather small. The $\mathcal{O}(G_\mu m_t^2)$ correction to the NLO QCD term has also been also calculated [208] and the total correction factor for the gluonic decay width is then

$$\delta^t_{Hgg} = x_t \left(1 + 30.3 \frac{\alpha_s}{\pi} \right) \tag{2.98}$$

For $m_t \sim 180$ GeV, the total factor is very small being at the level of 0.5%. Recently, these top quark corrections to the $H \to gg$ decays have been calculated exactly in the mass range $M_H \lesssim 2M_W$ [204]. The numerical result turned out to be quite different from the one obtained in the infinite top mass limit, even for a low mass Higgs boson. However, the correction factor is still rather small.

The electromagnetic corrections to the Hgg amplitude can be straightforwardly adapted from those of the NLO QCD corrections to the $H\gamma\gamma$ coupling. Indeed, the only contributions which are involved are those in which a photon is exchanged in the internal quark lines. One then obtains, after the appropriate change of the QCD and electric charge factors

$$\delta^e_{Hgg} = -\frac{3}{4} Q_t^2 \frac{\alpha}{\pi} = -\frac{1}{3} \frac{\alpha}{\pi} \tag{2.99}$$

a correction which is extremely small, being at the per mille level.

In the case of the $H\gamma\gamma$ coupling, while the correction to the fermionic loop can be carried out along the same lines as in the case of the Hgg coupling, for the W boson loop several subtleties arise. First, the application of the low–energy theorem is restricted to the mass range $M_H \lesssim 160$ GeV in this case. A second complication is due to the fact that when considering the leading m_t correction, owing to QED–like Ward identities, there is no $\mathcal{O}(G_\mu^2 m_t^4)$ correction [as one notices from the Hgg case] and the largest correction scales only quadratically with the top mass. In the calculation of this $\mathcal{O}(G_\mu^2 m_t^2)$ correction, one cannot simply use the gaugeless limit of the SM since the contributions involving virtual W bosons cannot be neglected. In fact, after integrating out the heavy fermion contribution, one has two dimension four operators which produce $\mathcal{O}(G_\mu^2 m_t^2)$ corrections to the $H\gamma\gamma$ amplitude

$$\mathcal{L}(H\gamma\gamma) = (\sqrt{2}G_\mu)^{1/2} H \left(c_1 F_{\mu\nu} F^{\mu\nu} + c_2 M_W^2 W_\mu^\dagger W^\mu + \cdots \right) \tag{2.100}$$

with the dots standing for the contribution of higher–order operators. While the coefficient c_2 has been previously derived, one needs to perform an explicit two–loop calculation to derive the coefficient c_1. This can be done again by considering only diagrams involving, along with top quarks, virtual Goldstone bosons minimally coupled to photons. Once the relevant contribution to the photon self–energy has been calculated, one can use the low–energy theorem to relate it to the $H\gamma\gamma$ amplitude in the kinematical regime where $M_H \lesssim 2M_W \lesssim 2m_t$. The calculation has been performed in Ref. [202] and the obtained correction factor can be attributed to the W amplitude and written as

$$A_1^H(\tau_W) \to A_1^H(\tau_W)\,(1 - 2.9x_t) \tag{2.101}$$

The total correction decreases the $H \to \gamma\gamma$ decay width by approximately 2.5% and, thus, fully cancels the positive $\mathcal{O}(\alpha_s/\pi)$ QCD correction in the heavy top limit.

In the loop induced decays, there are also corrections due to the light fermions, $f \neq t$. At the one–loop level, these contributions are suppressed by their couplings to the Higgs boson and are thus negligible. However, at the two–loop level, one can avoid this suppression by coupling them to the W and Z bosons which are then directly attached to the Higgs boson. These corrections have been calculated only recently [203].

In the case of the $H \to gg$ decay, the light quark contributions generate a correction to the partial decay width that is positive and increases from $\sim 4.5\%$ at $M_H \sim 115$ GeV to $\sim 9\%$ at $M_H \sim 2M_W$ [the correction varies from 4.5% to 7.5% in this mass range, if the the heavy top contribution is included]. Above this value, the correction decreases sharply and stays below -2% for $M_H \lesssim 2m_t$. In the case of the $H \to \gamma\gamma$ decay, below the $2M_W$ threshold, the light fermion contribution leads to a correction of the same size as the QCD

correction, i.e. $\sim 1\%$, but with opposite sign. Above the $2M_W$ threshold, the corrections are larger and lead to a suppression of the decay width by a few percent.

Finally, one has to include the Higgs self–coupling corrections which appear only in the bosonic contribution to the $H\gamma\gamma$ amplitude at two loops. The calculation can be done using the equivalence theorem where the W boson is replaced by its corresponding Goldstone boson which can be taken as massless [but only at the end of the calculation, since it serves as an infrared cut–off in intermediate steps]. In this limit one obtains [209]

$$\delta^{\lambda}_{H\gamma\gamma} = -12.1 \frac{\lambda^2}{16\pi^2} \tag{2.102}$$

The correction is small for $M_H \lesssim 500$ GeV, but is significant for values $M_H \sim 650$ GeV where the amplitude almost vanishes because of the t and W negative interference. For $M_H \sim 1$ TeV, the correction becomes large and decreases the partial width by approximately -30%.

2.4.4 Summary of the corrections to hadronic Higgs decays

Let us finally reconsider the QCD corrections to the hadronic Higgs boson decays in the light of all the corrections that have been discussed previously. As already mentioned, at higher orders, the Higgs decays into gluons and light quarks are mixed and already at the next–to–leading order, the two decays $H \to gg^* \to g\bar{q}q$ and $H \to \bar{q}^* q \to g\bar{q}q$ lead the same final states. The two decays cannot therefore be considered separately at higher orders. The present knowledge of the higher–order QCD corrections [and the leading electroweak corrections] to the full decay $H \to$ hadrons has been discussed in detail in Ref. [22]. In this subsection, we will simply give the full result for the hadronic Higgs decay width that one obtains for $M_H \lesssim 2M_W$ by including all the corrections which are known up to $\mathcal{O}(\alpha_s^3), \mathcal{O}(\alpha\alpha_s), \mathcal{O}(G_\mu m_t^2 \alpha_s^2)$ and $\mathcal{O}(\lambda^2)$.

Writing the interaction Lagrangian of the Higgs boson with quarks and gluons as

$$\mathcal{L}_{\rm had} = \sqrt{2} G_\mu H \Big[m_q \bar{q} q C_q + G^a_{\mu\nu} G^{\mu\nu}_a C_g \Big] \tag{2.103}$$

the decay width of the Higgs boson, summing the gluonic and light–quark decays and working in the approximation of an infinitely heavy top quark, can be written as [22]

$$\begin{aligned} \Gamma(H \to \text{hadrons}) = \sum_q & A_{q\bar{q}} K^{\rm EW}_{H\to qq} \left[(1+\Delta_{qq}) (C_q)^2 + \Delta_{qg} C_g C_q + \delta^{\rm me}_q \right] \\ & + A_{gg} K^{\rm EW}_{H\to gg} \left[\Delta_{gg} (C_g)^2 + \delta^{\rm me}_g \right] \end{aligned} \tag{2.104}$$

where the tree–level $q\bar{q}$ and gg squared amplitudes are given by

$$A_{qq} = \frac{3 G_\mu M_H}{4\sqrt{2}\pi} \overline{m}_q^2 (M_H^2) \quad , \quad A_{gg} = \frac{4 G_\mu M_H^3}{\sqrt{2}\pi} \tag{2.105}$$

and the coefficients of the operators appearing in the Lagrangian, by

$$C_g = -\frac{1}{12}\frac{\alpha_s}{\pi}\left[1+\left(\frac{11}{4}-\frac{1}{6}\ell_t\right)\frac{\alpha_s}{\pi}+\left(9.35-0.7N_f+(0.33N_f-0.52\ell_t)+0.028\ell_t^2\right)\left(\frac{\alpha_s}{\pi}\right)^2\right]$$
$$C_q = 1+\left(\frac{5}{18}-\frac{1}{3}\ell_t\right)\left(\frac{\alpha_s}{\pi}\right)^2+\left(1.35+0.25N_f-2.9\ell_t+(0.056N_f-0.8)\ell_t^2\right)\left(\frac{\alpha_s}{\pi}\right)^3 \quad (2.106)$$

with $\alpha_s \equiv \alpha_s^5(M_H^2)$ defined at the scale M_H with $N_f = 5$ light quarks and $\ell_t = \log(M_H^2/m_t^2)$. The various terms appearing in equation eq. (2.104), are as follows:

• Δ_{qq} is the pure QCD corrections to the decays into quarks eq. (2.11) up to $\mathcal{O}(\alpha_s^3)$, supplemented by the contributions of order α and the mixed QCD/QED contribution at $\mathcal{O}(\alpha\alpha_s)$ eq. (2.80)

$$\begin{aligned}\Delta_{qq} &= \frac{\alpha_s}{\pi}\left[\frac{17}{3}+(35.94-1.36N_f)\frac{\alpha_s}{\pi}+(164.14-25.77N_f+0.26N_f^2)\left(\frac{\alpha_s}{\pi}\right)^2\right] \\ &\quad +\frac{\alpha(M_H)}{\pi}Q_q^2\left[4.25+11.71\frac{\alpha_s}{\pi}\right] \end{aligned} \quad (2.107)$$

• Δ_{gg} is the QCD correction to the gluonic decay mode due to the light quark and gluon fields

$$\Delta_{gg} = 1+(18.25-1.17N_f)\frac{\alpha_s}{\pi}+(243-39.4N_f+0.9N_f^2)\left(\frac{\alpha_s}{\pi}\right)^2 \quad (2.108)$$

• Δ_{qg} is the mixed contribution in quark and gluon Higgs decays

$$\Delta_{qg} = -\frac{\alpha_s}{\pi}\left[30.67+(524.85-20.65N_f)\frac{\alpha_s}{\pi}\right] \quad (2.109)$$

If one considers final states involving quarks only, one has to subtract from the previous equation the gluonic contribution as discussed previously; at $\mathcal{O}(\alpha_s)$, one has for instance

$$\Delta'_{gg} = \frac{\alpha_s}{\pi}\left[13.56-\frac{4}{3}\log^2(m_q^2/M_H^2)+\mathcal{O}\left(\frac{\alpha_s^2}{\pi^2}\right)\right] \quad (2.110)$$

• $K^{\rm EW}_{H\to qq}$ and $K^{\rm EW}_{H\to gg}$ are the sum of the electroweak corrections for the quark and gluonic decays discussed previously [but without the electromagnetic corrections for the former decay since they are included in Δ_{qq}]. Note that in this case, α_s is defined at the scale m_t.

• Finally, $\delta_q^{\rm me}$ and $\delta_g^{\rm me}$ are the remaining contributions that contain the light quark masses and non–leading terms in m_t in fermionic and gluonic Higgs decays. Since higher–order terms $\mathcal{O}(M_H^4/m_t^4)$ and $\mathcal{O}(\bar m_b^4/M_H^4)$ are very small for $M_Z \lesssim M_H \lesssim 2M_W$, one can simply retain the first terms in the M_H^2/m_t^2 and $\bar m_q^2/M_H^2$ expansions

$$\begin{aligned}\delta_q^{\rm me} &= \left(\frac{\alpha_s}{\pi}\right)^2\frac{M_H^2}{m_t^2}\left[0.241-0.07\log\frac{M_H^2}{m_t^2}\right]-6\frac{\bar m_q^2}{M_H^2}\left[1+6.67\frac{\alpha_s}{\pi}\right] \\ \delta_g^{\rm me} &= 0.1167\frac{M_H^2}{m_t^2}\left(\frac{\alpha_s}{\pi}\right)^2\left[1+\left(17.85-2\log\frac{M_H^2}{m_t^2}\right)\frac{\alpha_s}{\pi}\right] \end{aligned} \quad (2.111)$$

This completes the discussion of the main QCD and electroweak radiative corrections to the hadronic decays of an intermediate mass Higgs boson.

2.5 The total decay width and the Higgs branching ratios

The decay branching ratios and the total width of the SM Higgs boson are shown in Figs. 2.25 and 2.26, respectively, as a function of the Higgs mass. They have been obtained using the FORTRAN code HDECAY [214] with the fermion and gauge boson mass inputs of eq. (2.1) and with the strong coupling constant normalized to $\alpha_s(M_Z) = 0.1172$. Included are all decay channels that are kinematically allowed and that have branching ratios larger than 10^{-4}, *y compris* the loop mediated, the three body $\bar{t}t^*$ and VV^* decay modes and the double off–shell decays of the Higgs boson into massive gauge bosons which then decay into four massless fermions. In addition, all relevant two–loop QCD corrections to the decays into quark pairs and to the quark loop mediated decays into gluons [and photons] are incorporated; the smaller leading electroweak radiative corrections are also included. To be as complete as possible, we also present in Table 2.1 the numerical values of the branching ratios and total decay width for selected values of M_H, as it might be useful to have a normalization as close as possible to the state of the art, to be used in other theoretical or experimental studies.

To discuss the Higgs decays, it is useful to consider three distinct mass ranges:

- the "low mass" range 110 GeV $\lesssim M_H \lesssim$ 130 GeV,
- the "intermediate mass" range 130 GeV $\lesssim M_H \lesssim$ 180 GeV,
- the "high mass" range 180 GeV $\lesssim M_H \lesssim$ 1 TeV.

The main features of the branching ratios and total width can be summarized as follows.

In the "low mass" range, 100 GeV $\lesssim M_H \lesssim$ 130 GeV, the main decay mode of the Higgs boson is by far $H \to b\bar{b}$ with a branching ratio of $\sim$75–50% for $M_H =$ 115–130 GeV, followed by the decays into $\tau^+\tau^-$ and $c\bar{c}$ pairs with branching ratios of the order of $\sim$ 7–5% and $\sim$ 3–2%, respectively. Also of significance is the $H \to gg$ decay with a branching fraction of $\sim$7% for $M_H \sim$ 120 GeV. The $\gamma\gamma$ and $Z\gamma$ decays are rare, with branching ratios at the level of a few per mille, while the decays into pairs of muons and strange quarks [where $\bar{m}_s(1\text{ GeV}) = 0.2$ GeV is used as input] are at the level of a few times 10^{-4}. The $H \to WW^*$ decays, which are below the 1% level for $M_H \sim$ 100 GeV, dramatically increase with M_H to reach $\sim$ 30% at $M_H \sim$ 130 GeV; for this mass value, $H \to ZZ^*$ occurs at the percent level.

In the "intermediate mass" range, the Higgs boson decays mainly into WW and ZZ pairs, with one virtual gauge boson below the $2M_V$ kinematical thresholds. The only other decay mode which survives is the $b\bar{b}$ decay which has a branching ratio that drops from 50% at $M_H \sim$ 130 GeV to the level of a few percent for $M_H \sim 2M_W$. The WW decay starts to dominate at $M_H \sim$ 130 GeV and becomes gradually overwhelming, in particular for $2M_W \lesssim M_H \lesssim 2M_Z$ where the W boson is real [and thus the decay $H \to WW$ occurs at the two–body level] while the Z boson is still virtual, strongly suppressing the $H \to ZZ^*$ mode and leading to a WW branching ratio of almost 100%.

M_H (GeV)	BR($b\bar{b}$)	BR($\tau\tau$)	BR($\mu\mu$)	BR($s\bar{s}$)	BR($c\bar{c}$)	BR($t\bar{t}$)
115	0.736	$7.21 \cdot 10^{-2}$	$2.51 \cdot 10^{-4}$	$6.23 \cdot 10^{-4}$	$3.39 \cdot 10^{-2}$	–
120	0.683	$6.78 \cdot 10^{-2}$	$2.35 \cdot 10^{-4}$	$5.79 \cdot 10^{-4}$	$3.15 \cdot 10^{-2}$	–
130	0.533	$5.36 \cdot 10^{-2}$	$1.86 \cdot 10^{-4}$	$4.51 \cdot 10^{-4}$	$2.45 \cdot 10^{-2}$	–
140	0.349	$3.56 \cdot 10^{-2}$	$1.23 \cdot 10^{-4}$	$2.95 \cdot 10^{-4}$	$1.60 \cdot 10^{-2}$	–
150	0.179	$1.85 \cdot 10^{-2}$	–	$1.51 \cdot 10^{-4}$	$8.23 \cdot 10^{-3}$	–
160	$4.11 \cdot 10^{-2}$	$4.30 \cdot 10^{-3}$	–	–	$1.89 \cdot 10^{-3}$	–
170	$8.64 \cdot 10^{-3}$	$9.13 \cdot 10^{-4}$	–	–	$3.97 \cdot 10^{-4}$	–
180	$5.53 \cdot 10^{-3}$	$5.90 \cdot 10^{-4}$	–	–	$2.54 \cdot 10^{-4}$	–
200	$2.65 \cdot 10^{-3}$	$2.89 \cdot 10^{-4}$	–	–	$1.22 \cdot 10^{-4}$	–
300	$6.21 \cdot 10^{-4}$	–	–	–	–	–
400	$2.35 \cdot 10^{-4}$	–	–	–	–	0.131
500	$1.20 \cdot 10^{-4}$	–	–	–	–	0.197
600	–	–	–	–	–	0.176
700	–	–	–	–	–	0.144
1000	–	–	–	–	–	0.070

M_H (GeV)	BR(gg)	BR ($\gamma\gamma$)	BR($Z\gamma$)	BR(WW)	$BR(ZZ)$	Γ_H (GeV)
115	$6.74 \cdot 10^{-2}$	$2.04 \cdot 10^{-3}$	$6.75 \cdot 10^{-4}$	$7.48 \cdot 10^{-2}$	$8.04 \cdot 10^{-3}$	$3.27 \cdot 10^{-3}$
120	$6.84 \cdot 10^{-2}$	$2.16 \cdot 10^{-3}$	$1.06 \cdot 10^{-3}$	0.130	$1.49 \cdot 10^{-2}$	$3.65 \cdot 10^{-3}$
130	$6.30 \cdot 10^{-2}$	$2.21 \cdot 10^{-3}$	$1.91 \cdot 10^{-3}$	0.283	$3.80 \cdot 10^{-2}$	$5.00 \cdot 10^{-3}$
140	$4.82 \cdot 10^{-2}$	$1.93 \cdot 10^{-3}$	$2.47 \cdot 10^{-3}$	0.480	$6.71 \cdot 10^{-2}$	$8.11 \cdot 10^{-3}$
150	$2.87 \cdot 10^{-2}$	$1.39 \cdot 10^{-3}$	$2.39 \cdot 10^{-3}$	0.679	$8.27 \cdot 10^{-2}$	$1.67 \cdot 10^{-2}$
160	$7.57 \cdot 10^{-3}$	$5.54 \cdot 10^{-4}$	$1.23 \cdot 10^{-3}$	0.900	$4.36 \cdot 10^{-1}$	$0.77 \cdot 10^{-1}$
170	$1.82 \cdot 10^{-3}$	$1.50 \cdot 10^{-4}$	$3.97 \cdot 10^{-4}$	0.965	$2.25 \cdot 10^{-2}$	0.383
180	$1.32 \cdot 10^{-3}$	$1.02 \cdot 10^{-4}$	$2.98 \cdot 10^{-4}$	0.934	$5.75 \cdot 10^{-1}$	0.628
200	$8.06 \cdot 10^{-4}$	–	$1.77 \cdot 10^{-4}$	0.735	0.261	1.425
300	$5.47 \cdot 10^{-4}$	–	–	0.691	0.307	8.50
400	$7.37 \cdot 10^{-4}$	–	–	0.592	0.276	28.65
500	$5.48 \cdot 10^{-4}$	–	–	0.542	0.260	67.81
600	$3.84 \cdot 10^{-4}$	–	–	0.554	0.269	123.3
700	$2.70 \cdot 10^{-4}$	–	–	0.575	0.281	201.3
1000	–	–	–	0.622	0.308	667.2

Table 2.1: The Higgs decay branching ratios and total widths in the SM.

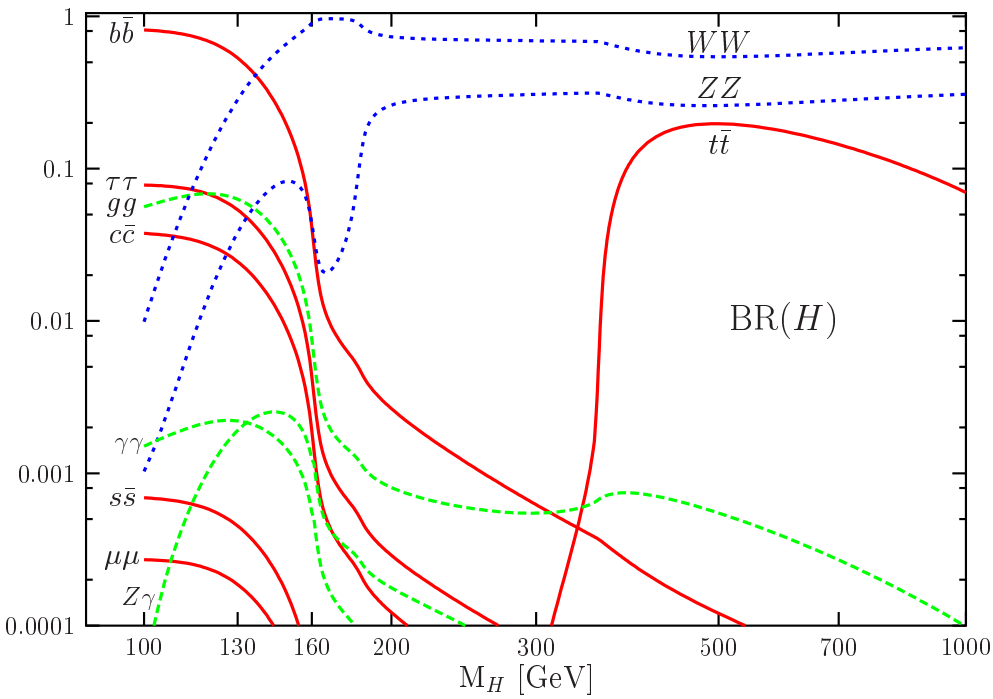

Figure 2.25: The SM Higgs boson decay branching ratios as a function of M_H.

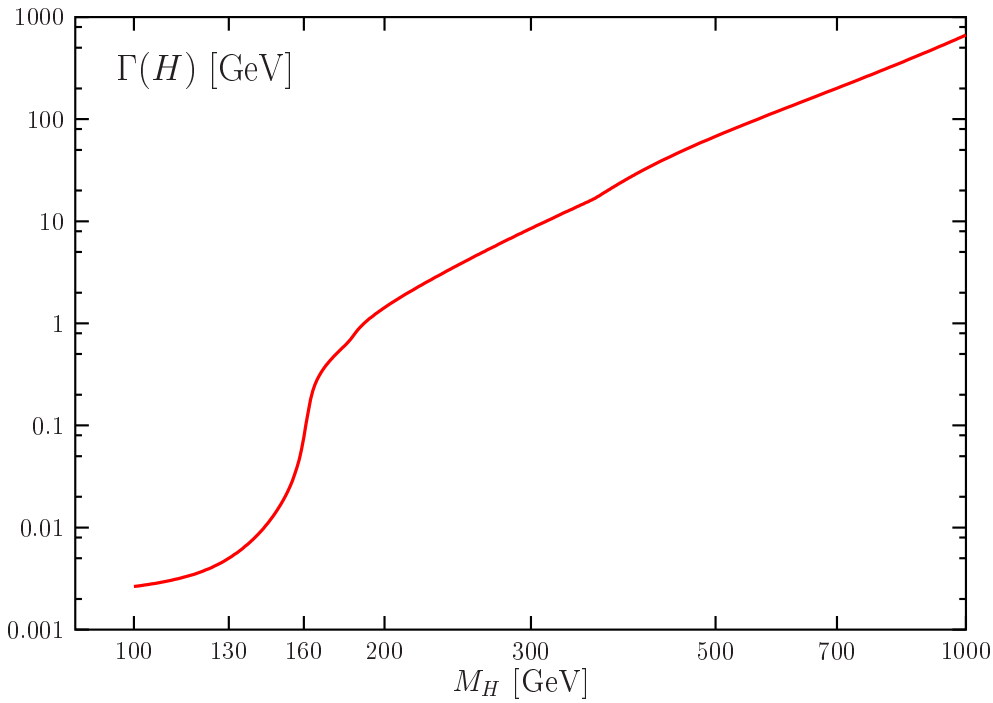

Figure 2.26: The SM Higgs boson total decay width as a function of M_H.

In the "high mass" range, $M_H \gtrsim 2M_Z$, the Higgs boson decays exclusively into the massive gauge boson channels with a branching ratio of $\sim 2/3$ for WW and $\sim 1/3$ for ZZ final states, slightly above the ZZ threshold. The opening of the $t\bar{t}$ channel for $M_H \gtrsim 350$ GeV does not alter significantly this pattern, in particular for high Higgs masses: the $H \to t\bar{t}$ branching ratio is at the level of 20% slightly above the $2m_t$ threshold and starts decreasing for $M_H \sim 500$ GeV to reach a level below 10% at $M_H \sim 800$ GeV. The reason is that while the $H \to t\bar{t}$ partial decay width grows as M_H, the partial decay width into (longitudinal) gauge bosons increases as M_H^3.

Finally, for the total decay width, the Higgs boson is very narrow in the low mass range, $\Gamma_H < 10$ MeV, but the width becomes rapidly wider for masses larger than 130 GeV, reaching ~ 1 GeV slightly above the ZZ threshold. For larger Higgs masses, $M_H \gtrsim 500$ GeV, the Higgs boson becomes obese: its decay width is comparable to its mass because of the longitudinal gauge boson contributions in the decays $H \to WW, ZZ$. For $M_H \sim 1$ TeV, one has a total decay width of $\Gamma_H \sim 700$ GeV, resulting in a very broad resonant structure. However, as previously discussed, for this large Higgs mass value, perturbation theory is jeopardized anyway.

A final word must be devoted to the uncertainties on these Higgs decay branching ratios. As discussed at length in this section, the strong coupling constant α_s and the quark masses play a prominent role in Higgs physics. However, these parameters are affected by relatively large experimental errors which then translate into sizable uncertainties in the Higgs boson decay branching ratios and in the total decay width[22]. Following Ref. [190], and using the updated values of the quark masses given in eq. (2.1) and of $\alpha_s(M_Z) = 0.1172 \pm 0.002$, we show in Fig. 2.27 the effect of varying the input parameters [but only one at a time] by one standard deviation from their central values.

In the low to intermediate mass range where the Higgs decays into light quarks and gluons are significant, these errors are rather large. In particular, the branching ratios for the charm and gluonic decays have uncertainties at the level of 20% and 10%, respectively. The main reason for these errors is the $\sim 2\%$ uncertainty in α_s, which translates into a 4% (6%) error in $\Gamma(H \to gg) \propto \alpha_s^2\,(\alpha_s^3)$ at the one– (two)–loop level, and in a very strong variation of the charm quark mass, $m_c(\mu) \sim [\alpha_s(\mu)]^{12/13}$, at the high scales. The error on m_t does not affect substantially the $H \to gg$ branching ratio since, as already noticed, the heavy top quark limit is a good approximation for these Higgs mass values. The uncertainty on the dominant $H \to b\bar{b}$ branching ratio is small since the experimental error on the b–quark mass is relatively smaller and its running is less important than in the case of charm quarks; in addition for low Higgs masses, $\Gamma(H \to b\bar{b})$ controls the total width and most of

[22]Thus, contrary to what is sometimes claimed in the literature, these as not "theoretical errors" but mostly a reflection of the poor knowledge of the quark masses and QCD coupling constant.

the uncertainty cancels in the branching ratio. The error on the $H \to \tau^+\tau^-$ branching ratio is simply due to that of $\Gamma(H \to b\bar{b})$ in the total Higgs decay width.

[Note that, in the high mass range above the $t\bar{t}$ threshold, the errors on the top quark mass and the strong coupling constant do not affect significantly the branching fraction of the $H \to t\bar{t}$ decay, the error being at the percent level for $M_H \gtrsim 500$ GeV, and *a fortiori* the branching ratios for $H \to WW, ZZ$ which dominate in this Higgs mass range.]

Thus, although the expected hierarchy of the Higgs decay modes is still visible from Fig. 2.27, a more precise measurement of α_s and the quark masses will be necessary to check completely the predictions of the SM for the Higgs decay branching ratios which, as will be discussed in the next sections, can be measured at the level of a few percent. In turn, if we are confident enough that the observed Higgs is the SM Higgs particle, one can turn the experimental measurement of the branching ratios into a determination of the light quark masses and α_s at the scale of the Higgs mass, in much the same way as the running b–quark mass has been determined in Z decays at LEP1 [47].

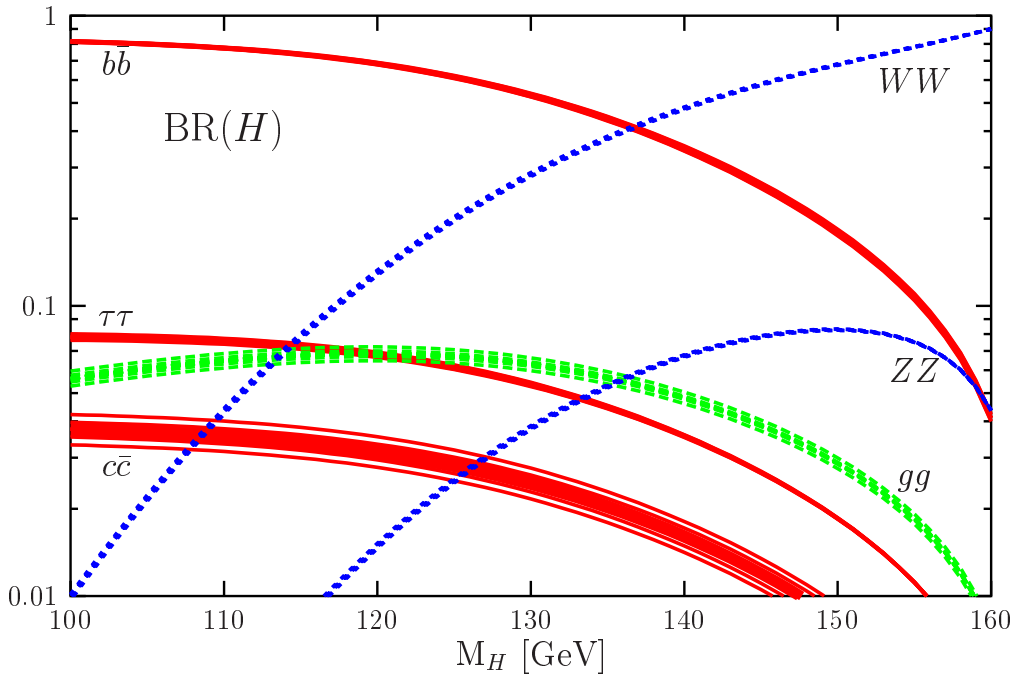

Figure 2.27: The SM Higgs boson decay branching ratios in the low and intermediate Higgs mass range including the uncertainties from the quark masses $m_t = 178 \pm 4.3$ GeV, $m_b = 4.88 \pm 0.07$ GeV and $m_c = 1.64 \pm 0.07$ GeV as well as from $\alpha_s(M_Z) = 0.1172 \pm 0.002$.

3 Higgs production at hadron colliders

3.1 Higgs bosons at hadron machines

3.1.1 Generalities about hadron colliders

The $p\bar{p}$ collider[23] Tevatron at Fermilab is the highest energy accelerator available today. In the previous Run I, the collider was operating at an energy of $\sqrt{s} = 1.8$ TeV in the $p\bar{p}$ center of mass, and the CDF and DØ experiments each have collected data corresponding to about $\int \mathcal{L} dt \sim 100$ pb^{-1} of integrated luminosity[24]. The upgrade with the Main Injector allows the machine to possibly deliver an order of magnitude more instantaneous luminosity. In Run II, it is expected that 5 fb^{-1} of data will be collected, with the possibility of increasing the sample to 10 fb^{-1} if the machine runs efficiently until the end of the decade [215]; see Ref. [216] for the luminosity delivered by the machine. In Run II, the energy of the machine has been raised from $\sqrt{s} = 1.8$ TeV to $\sqrt{s} = 1.96$ TeV which, typically, increased the cross sections for some physics processes by about 30%. The CDF and DØ detectors have also been upgraded, allowing them to make more sensitive searches than previously [217, 218].

The CERN Large Hadron Collider (LHC) under construction is a pp collider designed to run at an energy $\sqrt{s} = 14$ TeV in the pp center of mass and a luminosity of $\mathcal{L} = 10^{34}\,\text{cm}^{-2}\,\text{s}^{-1}$ (high luminosity regime). The first collisions are expected in June 2007 but only with an instantaneous luminosity of $\mathcal{L} = 10^{33}\,\text{cm}^{-2}\,\text{s}^{-1}$ (low luminosity regime); see [219, 220]. At the end of the decade, the accumulated integrated luminosity is expected to be $\mathcal{L} = 30$ fb^{-1}, to be increased to 100 fb^{-1} per year when the machine runs at the design luminosity. The hope is to collect at least 300 fb^{-1} of data per experiment during the entire LHC operation [219]. There are plans, the so-called SLHC, to operate the LHC at still the same energy $\sqrt{s} \sim 14$ TeV, i.e. retaining the present magnets and dipoles, but at the luminosity of $\mathcal{L} = 10^{35}\,\text{cm}^{-2}\,\text{s}^{-1}$ leading to 1 ab^{-1} integrated luminosity per year [221–223]. With new magnets with field strengths of approximately 16 Tesla (which do not currently exist), the energy of the collider could be raised to $\sqrt{s} = 28$ TeV. Designs for a very large hadron collider (VLHC), with a c.m. of mass energy of the order of 40 TeV to 200 TeV [a revival of the ancient Eloisatron idea, see Ref. [224] for instance], are currently studied [225, 226]. The SLHC and VLHC options will only be briefly discussed in this report.

The two general purpose experiments under construction, ATLAS [227, 228] and CMS [229, 230], have been optimized to cover a large spectrum of possible signatures in the LHC environment [231]. However, the Higgs search, together with Supersymmetry, has been the major guide to define the detector requirements and performances for the experiments, and most of the simulation studies have been performed for these two physics cases.

[23] For simplicity, we will use sometimes the notation pp for both pp and $p\bar{p}$ collisions in this review.
[24] Also for simplicity, we will denote by $\mathcal{L}$ both the instantaneous and integrated luminosities.

The total cross section at hadron colliders is extremely large. It is about 100 mb at the LHC, resulting in an interaction rate of $\approx 10^9$ Hz at the design luminosity. In this hostile environment, the detection of processes with signal to total hadronic cross section ratios of about 10^{-10}, as is the case for the production a SM Higgs boson in most channels, will be a difficult experimental challenge [232–240]. The huge QCD–jet backgrounds prevents from detecting the produced Higgs boson [and any particle in general] in fully hadronic modes. Recalling that when ignoring the light quark and gluon modes, the Higgs decays mostly into $b\bar{b}, \tau\tau, WW, ZZ$ and $\gamma\gamma, Z\gamma$ final states in the mass range below $M_H \lesssim 160$ GeV and into WW, ZZ and $t\bar{t}$ final states above this mass value, the following general requirements have to be met in order to extract a signal in the entire Higgs mass range:

– In the decay $H \to WW, ZZ$, at least one of the W/Z bosons has to be observed in its leptonic decays which have small branching ratios, BR$(W \to \ell\nu) \simeq 20\%$ with $\ell = \mu, e$ and BR$(Z \to \ell^+\ell^-) \simeq 6\%$; in the latter case the invisible neutrino decays, BR$(Z \to \nu\nu) \simeq 18\%$, can also be sometimes used to increase the statistics. A very good detection of isolated high transverse momentum muons and electrons and an accurate calorimetry with hermetic coverage to measure the transverse energy of the missing neutrinos is thus required.

– A very high resolution on the photons is necessary to isolate the narrow $\gamma\gamma$ signal peak in the decay $H \to \gamma\gamma$ from the large continuum $\gamma\gamma$ background. Since the Higgs boson width is small, a few MeV for $M_H \simeq$120–140 GeV, the measured mass peak is entirely dominated by the experimental resolution. Furthermore, the very large number of high transverse momentum π^0 decaying into two photons should be rejected efficiently.

– In the dominant Higgs decay mode in the low mass range, $H \to b\bar{b}$, excellent micro–vertex detectors are needed to identify the b–quark jets with a high efficiency and a high purity. τ–lepton identification is also important to detect the decays $H \to \tau^+\tau^-$ and the invariant mass of the final state should be reconstructed with a good resolution.

Together with good granularity and hermeticity coverage for jet resolution and missing transverse energy, these requirements are apparently met by the CDF and DØ detectors at Tevatron [218] and are expected to be met by the ATLAS and CMS detectors at LHC.

The most unambiguous signal for a Higgs boson [and for any new particle] is a peak in the invariant mass distribution of its decay products. The narrow mass peak can be discovered without any Monte–Carlo simulation for the backgrounds, since the latter can be precisely measured from the side bands. In addition, the discovery can be made even if the signal is rather low and the background large, since the significance is $\propto S/\sqrt{S+B}$. This however is not true when it comes to study some properties of the Higgs boson, such as its couplings and its spin–parity quantum numbers. In this case, Monte–Carlo simulations are needed to determine the cross sections and the various characteristics distributions of the signal and backgrounds. The most precise theoretical predictions are therefore required.

3.1.2 Higgs production at hadron machines

In the Standard Model, the main production mechanisms for Higgs particles at hadron colliders make use of the fact that the Higgs boson couples preferentially to the heavy particles, that is the massive W and Z vector bosons, the top quark and, to a lesser extent, the bottom quark. The four main production processes, the Feynman diagrams of which are displayed in Fig. 3.1, are thus: the associated production with W/Z bosons [241, 242], the weak vector boson fusion processes [112, 243–246], the gluon–gluon fusion mechanism [185] and the associated Higgs production with heavy top [247, 248] or bottom [249, 250] quarks:

$$\text{associated production with } W/Z: \quad q\bar{q} \longrightarrow V + H \tag{3.1}$$

$$\text{vector boson fusion}: \quad qq \longrightarrow V^*V^* \longrightarrow qq + H \tag{3.2}$$

$$\text{gluon} - \text{gluon fusion}: \quad gg \longrightarrow H \tag{3.3}$$

$$\text{associated production with heavy quarks}: \quad gg, q\bar{q} \longrightarrow Q\bar{Q} + H \tag{3.4}$$

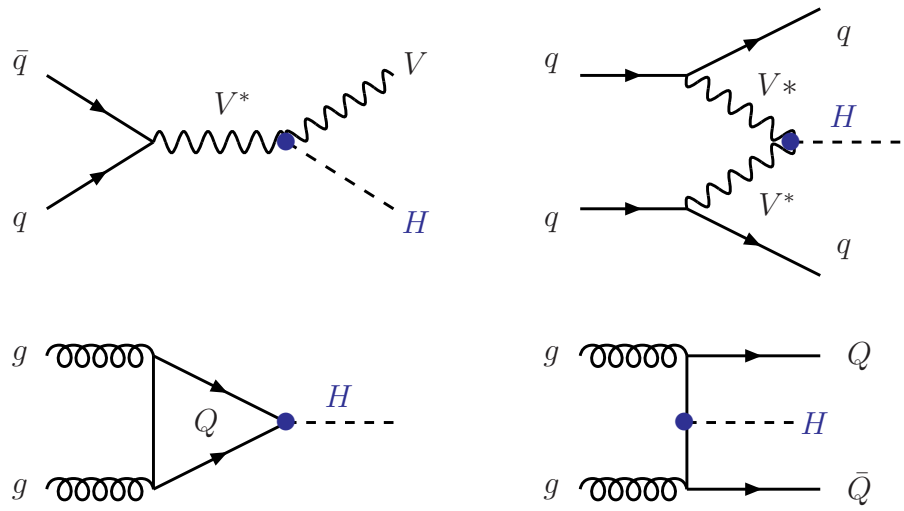

Figure 3.1: The dominant SM Higgs boson production mechanisms in hadronic collisions.

There are also several mechanisms for the pair production of the Higgs particles

$$\text{Higgs pair production}: \quad pp \longrightarrow HH + X \tag{3.5}$$

and the relevant sub–processes are the $gg \to HH$ mechanism, which proceeds through heavy top and bottom quark loops [251, 252], the associated double production with massive gauge bosons [253, 254], $q\bar{q} \to HHV$, and the vector boson fusion mechanisms $qq \to V^*V^* \to HHqq$ [255, 256]; see also Ref. [254]. However, because of the suppression by the additional electroweak couplings, they have much smaller production cross sections than the single Higgs production mechanisms listed above.

Also suppressed are processes where the Higgs is produced in association with one [258, 259], two [260, 261] or three [262] hard jets in gluon–gluon fusion, the associated Higgs production with gauge boson pairs [263, 264], the production with a vector boson and two jets [264–266]. Other production processes exist which have even smaller production cross sections [155, 267–272]. Finally, Higgs bosons can also be produced in diffractive processes [273–277]. For the interesting exclusive central diffractive processes [275–277], the mechanism is mediated by color singlet exchanges leading to the diffraction of the incoming hadrons and a centrally produced Higgs boson. A mixture of perturbative and non perturbative aspects of QCD is needed to evaluate the cross sections, leading to uncertainties in the predictions.

In this chapter, we discuss all these processes in detail, analyzing not only the total production cross sections but also the differential distributions and, in particular, the Higgs boson transverse momentum and rapidity distributions. In addition, we pay a special attention to three very important points: the QCD radiative corrections or the K–factors, the residual cross sections dependence on the renormalization and factorization scales, and the choice of different sets of parton distributions functions (PDFs) with which one has to convolute the partonic cross sections to obtain the total hadronic cross sections.

3.1.3 The higher–order corrections and the K–factors

It is well known that for processes involving strongly interacting particles, as is the case for the ones that we will consider here, the lowest order (LO) cross sections are affected by large uncertainties arising from higher–order (HO) corrections. If at least the next–to–leading order (NLO) QCD corrections to these processes are included, the total cross sections can be defined properly and in a reliable way in most cases: the renormalization scale μ_R at which one defines the strong coupling constant and the factorization scale μ_F at which one performs the matching between the perturbative calculation of the matrix elements and the non perturbative part which resides in the parton distribution functions, are fixed and the generally non–negligible radiative corrections are taken into account.

The impact of higher–order QCD corrections is usually quantified by calculating the K–factor, which is defined as the ratio of the cross section for the process [or its distribution] at HO with the value of α_s and the PDFs evaluated also at HO, over the cross section [or distribution] at LO with α_s [for those processes which are QCD processes at LO] and the PDFs consistently also evaluated at LO[25]

$$K = \frac{\sigma_{\rm HO}(pp \to H + X)}{\sigma_{\rm LO}(pp \to H + X)} \tag{3.6}$$

[25]Note that if the K–factor is defined as the ratio of NLO to LO cross sections both evaluated with α_s and PDFs at NLO, it would be in many cases larger since the value of the strong coupling constant, which appears in both the matrix element squared of the hard process and in the parton distribution functions, is smaller at NLO, $\alpha_s^{\rm NLO}(M_Z) \sim 0.12$, than at LO, $\alpha_s^{\rm LO}(M_Z) \sim 0.13$, thereby decreasing the LO cross section.

All the dominant Higgs production processes which are addressed here will be discussed at least at NLO [278]. At this order, the QCD corrections are known since more than a decade for the associated production with W/Z bosons [279–281], the vector boson fusion processes [281–284] and the gluon–gluon mechanism [180, 187, 285, 286], while the NLO corrections to the associated production with heavy quarks have been calculated only recently [287–291]. To improve further the theoretical predictions for the cross sections, one can also resum the soft and collinear gluon radiation parts which in general lead to large logarithms and include the dominant electroweak radiative corrections which however, are much smaller than the QCD corrections, in particular when the improved Born approximation of §1.2.4 is used.

The QCD corrections to the transverse momentum and rapidity distributions are also available in the case of vector boson fusion [283, 284] and gluon–gluon fusion [292–298]. In the latter case, the resummation of the large logarithms for the P_T distribution has been performed at next–to–next–to–leading–logarithm (NNLL) accuracy. The QCD corrections to the various distributions in the associated Higgs production with $t\bar{t}$ are discussed in [287].

In two cases, the associated HV production [299] and the $gg \to H$ fusion mechanism in the approximation where the top quark is very heavy [300–303], the calculation of the production cross sections at NNLO has been performed recently and will be discussed. However, these calculations are not sufficient to obtain a full NNLO prediction: the cross sections must be folded with the NNLO evolved PDFs, which are also necessary. The latter require the calculation of the Altarelli–Parisi splitting functions [304] up to three loops and until very recently the latter were not completely known at this order. Nevertheless, a large number of moments of these functions were available [305] which, when combined with additional information on the behavior at small x, allowed to obtain an approximation of the splitting functions at the required order. The NNLO MRST [306] parton distributions followed this approach and have been therefore adopted for NNLO calculations[26].

3.1.4 The scale dependence

The evaluation of the residual theoretical uncertainties in the production cross sections or distributions, due to the not yet calculated higher–order corrections, is generally based on the exploration of the cross section dependence on the renormalization scale μ_R and on the factorization scale μ_F. Starting from a median scale μ_0 which, with an educated guess, is considered as the "natural scale" of the process and is expected to absorb the large logarithmic corrections, the by now standard convention is to vary the two scales, either

[26]The calculation of the N_f part of the non–singlet structure function in DIS, from which one can extract the corresponding splitting function, is available since some time and has been compared to the approximate result of Ref. [305] and full agreement has been obtained, giving a great confidence that the approximate NNLO PDFs are rather accurate. Recently, the full calculation of the NNLO splitting function has been completed [307] and they alter the NNLO MRST PDFs only by a small amount [308].

collectively or independently [i.e. keeping one scale fixed at the reference value], within

$$\mu_0/a \leq \mu_F, \mu_R \leq a\mu_0 \tag{3.7}$$

The value of the constant a is in general chosen to be 2 or 3, the latter case being more conservative and will be adopted in most cases. In some situations in which widely different scales are involved in the processes, it is more prudent to use larger values for a, as will be seen in the case of Higgs production in bottom quark fusion for instance.

Note that the scale dependence at leading order can be studied by defining a kind of K–factor for the LO cross section, $K_{\rm LO}$, by evaluating the latter at given factorization and renormalization scales μ_F and μ_R, and normalizing to the LO cross sections evaluated at the median scale μ_0

$$K_{\rm LO} = \sigma_{\rm LO}(\mu_F, \mu_R)/\sigma_{\rm LO}(\mu_F = \mu_R = \mu_0) \tag{3.8}$$

By varying the scales μ_R and μ_F, one then obtains an uncertainty band: the narrower the band is, the smaller the higher–order corrections are expected to be. Note that the scale uncertainty should be in principle reduced when higher–order corrections are included, that is, the scale variation should be smaller at NNLO, than at NLO, than at LO. However, this is not the case all the time, and a counter–example will be discussed later.

One should nevertheless caution that the variation of the cross section with respect to the scale choice is unphysical: it is just a reflexion of the truncation of the perturbative series; if the cross sections are known to all orders, they will not exhibit this dependence. The scale variation is thus, by no means a rigorous way to estimate the theoretical uncertainty. At best, it might only give an indication of the "full" uncertainty. This can be seen in many cases, where for instance the NLO and LO uncertainty bands for some production cross sections do not overlap at all, as will be shown later.

3.1.5 The parton distribution functions

Parton distribution functions (PDFs), which describe the momentum distribution of a parton in the proton, play a central role at hadron colliders. A precise knowledge of the PDFs over a wide range of the proton momentum fraction x carried by the parton and the squared center of mass energy Q^2 at which the process takes place, is mandatory to precisely predict the production cross sections of the various signal and background processes. However, they are plagued by uncertainties, which arise either from the starting distributions obtained from a global fit to the available data from deep–inelastic scattering, Drell–Yan and hadronic data, or from the DGLAP evolution [304, 309] to the higher Q^2 relevant to the scattering processes. Together with the effects of unknown perturbative higher–order corrections, these uncertainties dominate the theoretical error on the predictions of the cross sections.

The CTEQ [310] and MRST [311] collaborations, as well as Alekhin [312] and others [313], recently introduced new schemes, which provide the possibility of estimating the intrinsic and spread uncertainties on the prediction of physical observables at hadron colliders. The CTEQ and MRST schemes are based on the Hessian matrix method which enables a characterization of a parton parametrization in the neighborhood of the global χ^2 minimum fit and gives an access to the uncertainty estimation through a set of PDFs that describes this neighborhood. The corresponding PDFs are constructed as follows: (i) a global fit of the data is performed using the free parameters $N_{\rm PDF} = 20$ for CTEQ and $N_{\rm PDF} = 15$ for MRST; this provides the nominal PDF (reference set) denoted by S_0 and corresponding to CTEQ6M and MRST2001C, respectively; (ii) the global χ^2 of the fit is increased by $\Delta\chi^2 = 100$ for CTEQ and $\Delta\chi^2 = 50$ for MRST, to obtain the error matrix; (iii) the error matrix is diagonalized to obtain $N_{\rm PDF}$ eigenvectors corresponding to $N_{\rm PDF}$ independent directions in the parameter space; (iv) for each eigenvector, up and down excursions are performed in the tolerance gap, leading to $2N_{\rm PDF}$ sets of new parameters, corresponding to 40 new sets of PDFs for CTEQ and 30 sets for MRST. They are denoted by S_i, with $i = 1, 2N_{\rm PDF}$.

To build the Alekhin PDFs [312], only light–target deep–inelastic scattering data are used. This PDF set involves 14 parameters, which are fitted simultaneously with α_s and the structure functions, leading to $2N_{\rm PDF} = 30$ sets of PDFs for the uncertainty estimation. Note that the three PDF sets use different values for α_s: at NLO, the central sets CTEQ6M, MRST2001C and A02 use, respectively, $\alpha_s^{\rm NLO}(M_Z) = 0.118$, 0.119 and 0.117.

The three sets of PDFs discussed above can be used to calculate the uncertainty on a cross section σ in the following way [314]: one first evaluates the cross section with the nominal PDF S_0 to obtain the central value σ_0. One then calculates the cross section with the S_i PDFs, giving $2N_{\rm PDF}$ values σ_i, and defines, for each σ_i value, the deviations $\sigma_i^{\pm} = \mid \sigma_i - \sigma_0 \mid$ when $\sigma_i \gtrless \sigma_0$. The uncertainties are summed quadratically to calculate $\Delta\sigma^{\pm} = \sqrt{\sum_i \sigma_i^{\pm 2}}$. The cross section, including the error, is then given by $\sigma_0|^{+\Delta\sigma^+}_{-\Delta\sigma^-}$. This procedure will be applied to estimate the uncertainties in the cross sections for SM Higgs production in the four main mechanisms. The spread in the cross section prediction will depend on the considered partons and their x regime that we will briefly summarize below.

The differences between the PDFs originate from three main sources: (i) the choice of the data used in the global fit, (ii) the theoretical assumptions made for the fit and (iii) the choice of the tolerance used to define the error in the PDFs. Thus, for example, the MRST and CTEQ differences arise from points (ii) and (iii) only, with point (iii) dominating in most cases. The differences between the two approaches [310, 311] are explained in detail in Ref. [311], and for instance the CTEQ6 high–x gluon is larger than the MRST2001 one. The differences with the Alekhin analysis, which does not use the Tevatron data, are larger.

To be more qualitative, we present in Fig. 3.2, the MRST and Alekhin densities for the

gluon and for the up and down quarks and antiquarks, normalized to the CTEQ6 ones, for a wide range of x values and for a fixed c.m. energy $Q^2 = (100\ \text{GeV})^2$. One notices the following main features: (i) the MRST gluon PDF is smaller than the CTEQ one, except for values $x \sim 0.1$; in contrast, the Alekhin gluon PDF is larger than the CTEQ one for all x values, except for $x \sim 0.01$ and for very high x. (ii) The MRST (anti)quark PDFs are practically equal in magnitude and are smaller than the CTEQ ones for low x, while they are in general slightly larger for higher x, except for values near unity; in the Alekhin case, all (anti)quark PDFs are larger than the CTEQ ones, except for the $\bar{u}$ density above $x \sim 0.05$. For values, $x \gtrsim 10^{-4}$, the differences between the Alekhin and the CTEQ6 PDFs are more pronounced than the differences between the MRST and the CTEQ ones.

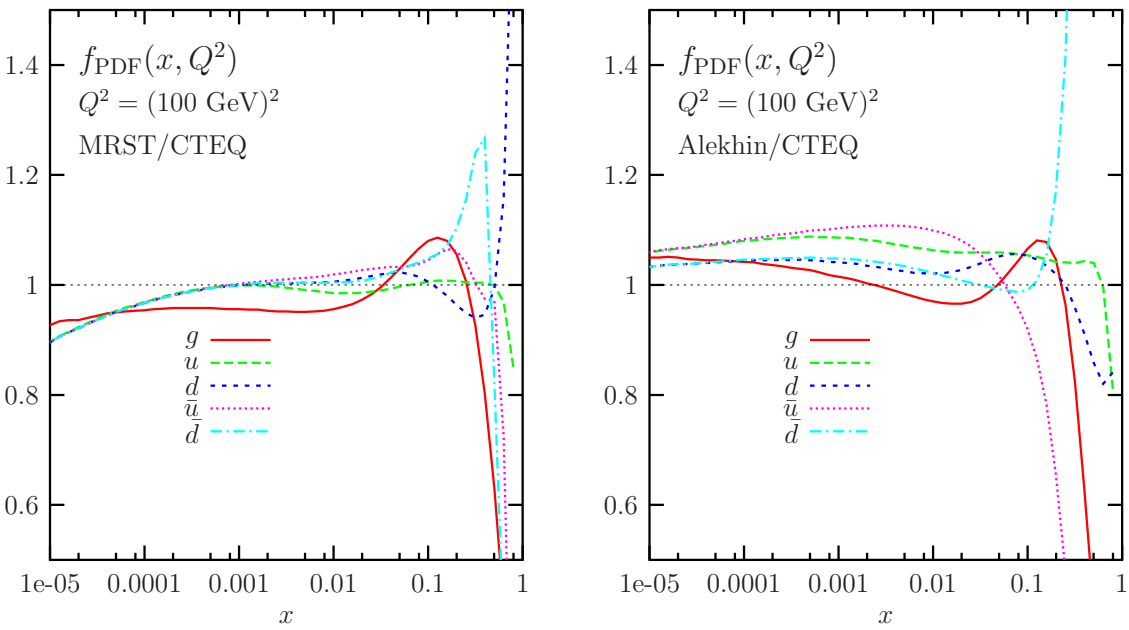

Figure 3.2: MRST and Alekhin densities for the gluon, up quark/down quark and antiquarks, normalized to the CTEQ6 ones, as a function of x and for $Q^2 = (100\ \text{GeV})^2$; from Ref. [314].

As for the CTEQ and MRST parameterizations, three different behaviors of the uncertainty bands according to three x ranges can be distinguished: decreasing uncertainties at low x, constant or slightly oscillating ones at intermediate x, and increasing ones at high x. The magnitude of these uncertainties depends on the considered parton and on the c.m. energy Q^2. In the case of quarks, the three behaviors are observed: the low-x behavior extends up to $x \sim$ few 10^{-3}, and the high–x one starts in the neighborhood of $x = 0.7$. At high Q^2, the uncertainties at high and low–x values exceed a few tens of a percent and in the intermediate regime, they are less than a few percent. In the gluon case and at high Q^2, the low–x and the intermediate–x bands are not well separated as in the case of quarks; the uncertainty band reaches also the few percent level. The high–x regime starts in the neighborhood of $x \sim 0.3$, i.e earlier than in the case of quarks.

3.2 The associated production with W/Z bosons

3.2.1 The differential and total cross sections at LO

It is useful to consider the cross section for the associated production of the Higgs particle with massive gauge bosons, which then decay into two massless fermions, in a completely differential form so that various distributions can be presented and cuts can be imposed on the final decay products. For the Higgs boson, since it is a scalar particle, the incorporation of its decays into a given final state, $H \to X$, is simply done by multiplying the matrix element squared by the branching ratio $\mathrm{BR}(H \to X)$ and generating the final state X isotropically in the rest frame of the H boson.

The general form of the matrix element squared for the process

$$q_1(p_1)\bar{q}_2(p_2) \to V^*(k = p_1 + p_2) \to V(k_1 = p_3 + p_4)H(k_2) \to f_3(p_3)\bar{f}_4(p_4)H(k_2) \tag{3.9}$$

where the momenta of the particles are explicitly written, with $\hat{s} = k^2 = (p_1 + p_2)^2$ being the c.m. energy of the partonic subprocess, can be expressed as

$$\begin{aligned} |\mathcal{M}|^2 \;=\; & 2\sqrt{2}N_c^f G_\mu^3 M_V^8 \frac{1}{(k^2 - M_V^2)^2 + \Gamma_V^2 M_V^2} \frac{1}{(k_1^2 - M_V^2)^2 + \Gamma_V^2 M_V^2} \Big[\\ & + \Big((\hat{v}_{q_1} + \hat{a}_{q_1})^2 (\hat{v}_{f_3} + \hat{a}_{f_3})^2 + (\hat{v}_{q_1} - \hat{a}_{q_1})^2 (\hat{v}_{f_3} - \hat{a}_{f_3})^2 \Big) (p_1 \cdot p_4)(p_2 \cdot p_3) \\ & + \Big((\hat{v}_{q_1} + \hat{a}_{q_1})^2 (\hat{v}_{f_3} - \hat{a}_{f_3})^2 + (\hat{v}_{q_1} - \hat{a}_{q_1})^2 (\hat{v}_{f_3} + \hat{a}_{f_3})^2 \Big) (p_1 \cdot p_3)(p_2 \cdot p_4) \Big] \end{aligned} \tag{3.10}$$

where the reduced fermion couplings to gauge bosons are as usual: $\hat{a}_f = 2I_f^3, \hat{v}_f = 2I_f^3 - 4Q_f s_W^2$ for $V = Z$ and $\hat{v}_f = \hat{a}_f = \sqrt{2}$ for $V = W$. Averaging over the quark spins and colors, dividing by the flux factor, and integrating over the three–particle phase–space, one obtains the total cross section of the subprocess. In the case where the decay products of the final vector boson are ignored, one would have a simple $2 \to 2$ subprocess, with an integrated cross section at lowest order given by [241, 242]

$$\hat{\sigma}_{\mathrm{LO}}(q\bar{q} \to VH) = \frac{G_\mu^2 M_V^4}{288\pi\hat{s}} (\hat{v}_q^2 + \hat{a}_q^2) \lambda^{1/2}(M_V^2, M_H^2; \hat{s}) \frac{\lambda(M_V^2, M_H^2; \hat{s}) + 12M_V^2/\hat{s}}{(1 - M_V^2/\hat{s})^2} \tag{3.11}$$

with λ being the usual two–body phase space function $\lambda(x, y; z) = (1 - x/z - y/z)^2 - 4xy/z^2$.

Note that the Higgs and the vector bosons have opposite transverse momenta and the differential partonic distribution with respect to the p_T is given by

$$\frac{\mathrm{d}\hat{\sigma}_{\mathrm{LO}}}{\mathrm{d}p_T^2} = \frac{G_\mu^2 M_V^4}{24\pi} \frac{v_q^2 + a_q^2}{(\hat{s} - M_Z^2)^2} \frac{2M_Z^2 + p_T^2}{2(M_Z^2 + M_H^2) - \hat{s}\sqrt{\lambda - 4p_T^2/\hat{s}}} \tag{3.12}$$

The partonic cross section can be recovered by integrating p_T in the range $0 \leq p_T \leq \frac{\sqrt{\hat{s}\lambda}}{2}$.

In fact, this process can be viewed simply as the Drell–Yan production of a virtual vector boson with $k^2 \neq M_V^2$, which then splits into a real vector boson and a Higgs particle. The energy distribution of the full subprocess can be written at leading order as

$$\hat{\sigma}(q\bar{q} \to HV) = \hat{\sigma}(q\bar{q} \to V^*) \times \frac{\mathrm{d}\Gamma}{\mathrm{d}k^2}(V^* \to HV) \tag{3.13}$$

where, in terms of $0 \leq k^2 \leq Q^2 = \hat{s}$ and the two-body phase-space function λ, one has

$$\frac{\mathrm{d}\Gamma}{\mathrm{d}k^2}(V^* \to HV) = \frac{G_\mu M_V^4}{2\sqrt{2}\pi^2} \frac{\lambda^{1/2}(M_V^2, M_H^2; k^2)}{(k^2 - M_V^2)^2} \left(1 + \frac{\lambda(M_V^2, M_H^2; k^2)}{12 M_V^2/k^2}\right) . \tag{3.14}$$

The total production cross section is then obtained by convoluting with the parton densities and summing over the contributing partons

$$\sigma_{\mathrm{LO}}(pp \to VH) = \int_{\tau_0}^{1} \mathrm{d}\tau \sum_{q,\bar{q}} \frac{\mathrm{d}\mathcal{L}^{q\bar{q}}}{\mathrm{d}\tau} \hat{\sigma}_{\mathrm{LO}}(\hat{s} = \tau s) \tag{3.15}$$

where $\tau_0 = (M_V + M_H)^2/s$, s being the total hadronic c.m. energy and the parton luminosity is defined in terms of the parton densities $q_i(x_i, \mu_F^2)$ defined at a factorization scale μ_F, by

$$\sum_{q,\bar{q}} \frac{\mathrm{d}\mathcal{L}^{q\bar{q}}}{\mathrm{d}\tau} = \sum_{q_1,\bar{q}_2} \int_{\tau}^{1} \frac{\mathrm{d}x}{x} \left[q_1(x, \mu_F^2)\, \bar{q}_2(\tau/x, \mu_F^2)\right] \tag{3.16}$$

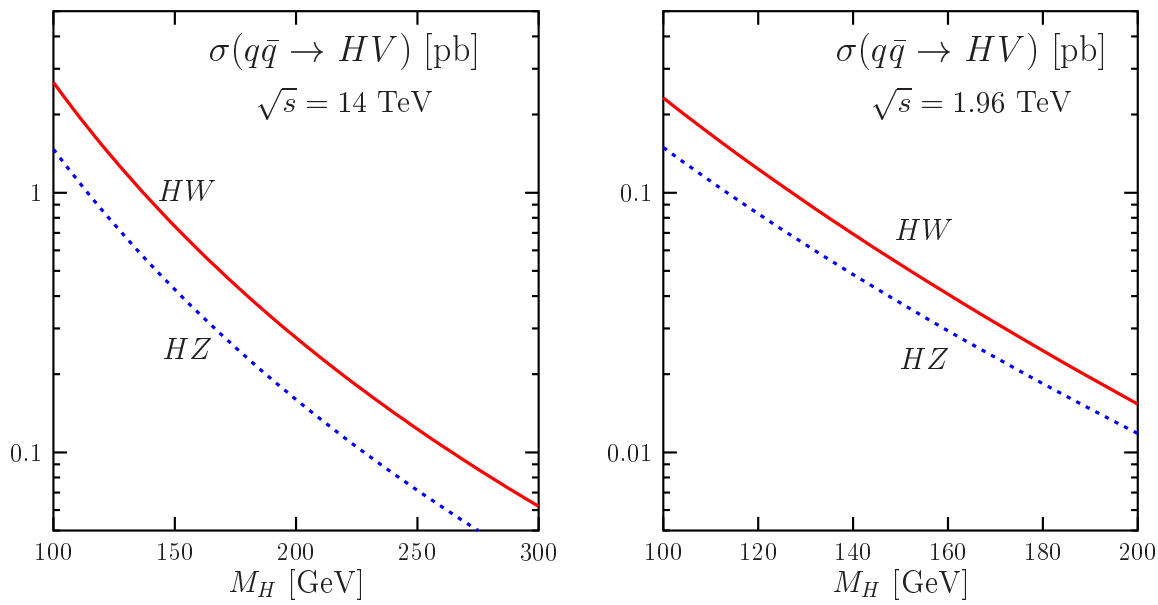

Figure 3.3: Total production cross sections of Higgs bosons in the strahlung $q\bar{q} \to H + W/Z$ processes at leading order at the LHC (left) and at the Tevatron (right). For $q\bar{q} \to HW$, the final states with both W^+ and W^- have been added. The MRST set of PDFs has been used.

The total production cross sections are shown as a function of the Higgs boson mass for the Tevatron and the LHC in both the $HW^\pm$ and HZ channels in Fig. 3.3; the MRST parton densities are used. The cross sections for $W^\pm$ final states are approximately two times larger than the ones for the HZ final state at both colliders. If, in addition, one requires the gauge bosons to decay into charged leptons $\ell = \mu + e$, the charged channel is much more interesting since $\mathrm{BR}(W^\pm \to \ell^\pm \nu) \sim 20\%$ while $\mathrm{BR}(Z \to \ell^+\ell^-) \simeq 6\%$. The various detection channels at the LHC [315–319] and at the Tevatron [320–323] and [319] will be discussed in §3.7.

3.2.2 The QCD radiative corrections

The NLO corrections

The factorization of the $pp \to HV$ cross section eq. (3.13) holds in principle at any order of perturbation theory in the strong interaction and one can thus write

$$\frac{\mathrm{d}\hat{\sigma}}{\mathrm{d}k^2}(pp \to HV + X) = \sigma(pp \to V^* + X) \times \frac{\mathrm{d}\Gamma}{\mathrm{d}k^2}(V^* \to HV) \ , \tag{3.17}$$

where $\mathrm{d}\Gamma/\mathrm{d}k^2$ is given by eq. (3.14). Therefore, the QCD corrections to the Higgs–strahlung process, derived at NLO in Refs. [279–281], are simply the corrections to the Drell–Yan process [84, 85], as pointed out in Ref. [316, 324].

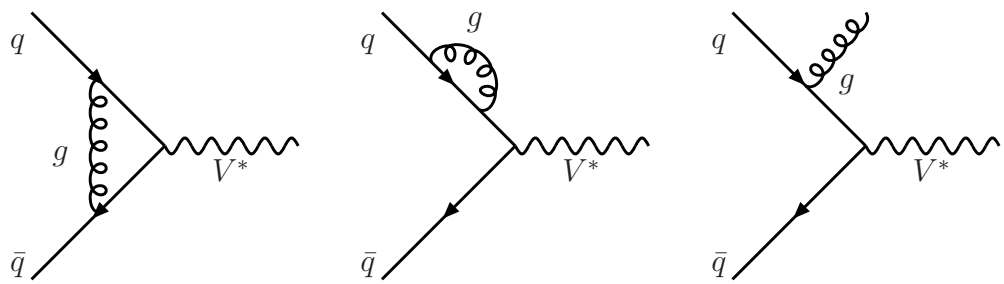

Figure 3.4: NLO QCD corrections to the vector boson–quark–antiquark vertex.

At NLO, the QCD corrections to the Drell–Yan process consist of virtual corrections with gluon exchange in the $q\bar{q}$ vertex and quark self-energy corrections, which have to be multiplied by the tree-level term, and the emission of an additional gluon, the sum of which has to be squared and added to the corrected tree–level term; see Fig. 3.4.

Including these contributions, and taking into account the virtuality of the vector boson, the LO cross section is modified in the following way

$$\sigma_{\mathrm{NLO}} \ = \ \sigma_{\mathrm{LO}} + \Delta\sigma_{q\bar{q}} + \Delta\sigma_{qg} \tag{3.18}$$

with

$$\begin{aligned} \Delta\sigma_{q\bar{q}} &= \frac{\alpha_s(\mu_R)}{\pi} \int_{\tau_0}^1 d\tau \sum_q \frac{d\mathcal{L}^{q\bar{q}}}{d\tau} \int_{\tau_0/\tau}^1 dz \ \hat{\sigma}_{\mathrm{LO}}(\tau z s) \ \omega_{q\bar{q}}(z) \\ \Delta\sigma_{qg} &= \frac{\alpha_s(\mu_R)}{\pi} \int_{\tau_0}^1 d\tau \sum_{q,\bar{q}} \frac{d\mathcal{L}^{qg}}{d\tau} \int_{\tau_0/\tau}^1 dz \ \hat{\sigma}_{\mathrm{LO}}(\tau z s) \ \omega_{qg}(z) \end{aligned} \tag{3.19}$$

with the coefficient functions [84]

$$\begin{aligned}
\omega_{q\bar{q}}(z) &= -P_{qq}(z)\log\frac{\mu_F^2}{\tau s} + \frac{4}{3}\left[\left(\frac{\pi^2}{3}-4\right)\delta(1-z) + 2(1+z^2)\left(\frac{\log(1-z)}{1-z}\right)_+\right] \\
\omega_{qg}(z) &= -\frac{1}{2}P_{qg}(z)\log\left(\frac{\mu_F^2}{(1-z)^2\tau s}\right) + \frac{1}{8}\Big[1+6z-7z^2\Big]
\end{aligned} \tag{3.20}$$

where μ_R denotes the renormalization scale and P_{qq}, P_{qg} are the well–known Altarelli–Parisi splitting functions which are given by [304, 325]

$$\begin{aligned}
P_{qq}(z) &= \frac{4}{3}\left[\frac{1+z^2}{(1-z)_+} + \frac{3}{2}\delta(1-z)\right] \\
P_{qg}(z) &= \frac{1}{2}\Big[z^2+(1-z)^2\Big]
\end{aligned} \tag{3.21}$$

The index + denotes the usual distribution $\mathcal{F}_+(z) = \mathcal{F}(z) - \delta(1-z)\int_0^1 dz'\mathcal{F}(z')$. Note that the cross section depends explicitly on $\log(\mu_F^2/Q^2)$; the scale choice $\mu_F^2 = Q^2$ therefore avoids the occurrence of these potentially large logarithms. The renormalization scale dependence enters in the argument of α_s and is rather weak. In most of our discussion, we will set the two scales at the invariant mass of the HV system $\mu_F = \mu_R = M_{HV}$. For this choice, the NLO corrections increase the LO cross section by approximately 30%.

The NNLO corrections

The NNLO corrections, i.e. the contributions at $\mathcal{O}(\alpha_s^2)$, to the Drell–Yan process $pp \to V^*$ consist of the following set of corrections besides the one–loop squared terms [see also Fig. 3.5a–c]: *a*) two-loop corrections to $q\bar{q} \to V^*$, which have to be multiplied by the Born term; *b*) one–loop corrections to the processes $qg \to qV^*$ and $q\bar{q} \to gV^*$, which have to be multiplied by the tree–level gq and $q\bar{q}$ terms initiated by the diagrams shown in Fig. 3.4; *c*) tree–level contributions from $q\bar{q}, qq, qg, gg \to V^*+$ 2 partons in all possible ways, with the sums of these diagrams for a given initial and final state to be squared and added.

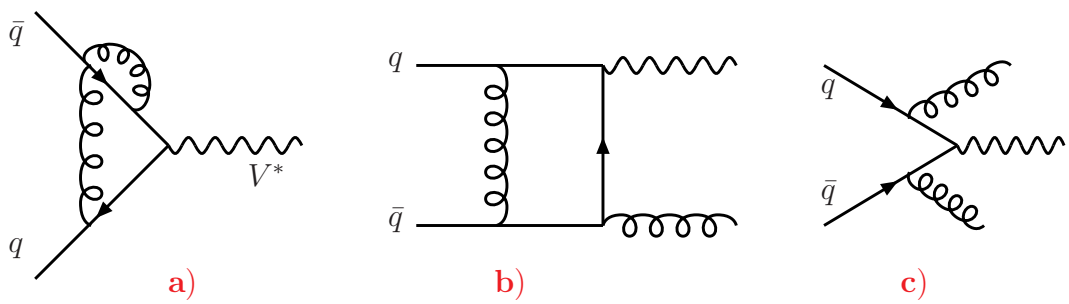

Figure 3.5: Diagrams for the NNLO QCD corrections to the process $q\bar{q} \to W^*$.

These corrections have been calculated a decade ago in Ref. [85] and recently updated [300]. However, these calculations are not sufficient to obtain a full NNLO prediction: in the

case of $pp \to HZ$ production, because the final state is electrically neutral, two additional sets of corrections need to be considered at $\mathcal{O}(\alpha_s^2)$ [299].

Indeed, contrary to charged W bosons, the neutral Z bosons can be produced via an effective Z–gluon–gluon coupling induced by quark loops. This can occur at the two–loop level in a box+triangle diagram in $q\bar{q} \to Z^*$ [to be multiplied by the Born term], or at the one–loop level where vertex diagrams appear for the $q\bar{q} \to gZ^*$ and $qg \to qZ^*$ processes [to be multiplied by the respective $\mathcal{O}(\alpha_s)$ tree–level terms]. Because gluons have only vector couplings to quarks and the effective Zgg coupling must be a color singlet, only the axial–vector part $a_q = 2I_Q^3$ of the $Zq\bar{q}$ coupling will contribute as a consequence of Furry's theorem [326]. Since a_q differs only by a sign for isospin up– and down–type quarks, their contribution vanishes in the case of quarks that are degenerate in mass. Thus, in the SM, only the top and bottom quarks will contribute to these topologies. These corrections have been evaluated in Refs. [327, 328] and have been shown to be extremely small and can be safely neglected.

Another set of diagrams that contribute at $\mathcal{O}(\alpha_s^2)$ to ZH and not to WH production [again because of charge conservation] is the gg initiated mechanism $gg \to HZ$ [329, 330]. It is mediated by quark loops [see Fig. 3.6] which enter in two ways. There is first a triangular diagram with $gg \to Z^* \to HZ$, in which only the top and bottom quark contributions are present, since because of C–invariance, the Z boson couples only axially to the internal quarks and the contribution of a mass degenerate quark weak–isodoublet vanishes. There are also box diagrams where both the H and Z bosons are emitted from the internal quark lines and where only the contribution involving heavy quarks which couple strongly to the Higgs boson [the top quark and, to a lesser extent, the bottom quark] are important. It turns out that the two contributing triangle and box amplitudes interfere destructively.

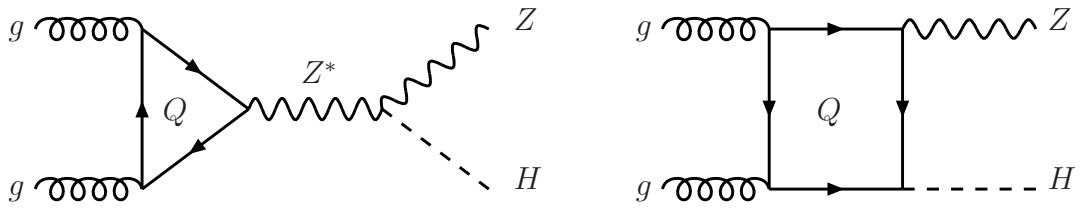

Figure 3.6: Diagrams for the $gg \to HZ$ process, which contributes to $\mathcal{O}(\alpha_s^2)$.

At the LHC, the contribution of this gluon–gluon fusion mechanism to the $pp \to HZ$ total production cross section can be substantial. This is due to the fact that the suppression of the cross section by a power $(\alpha_s/\pi)^2$ is partly compensated by the increased gluon luminosity at high energies. In addition, the tree–level cross section for $q\bar{q} \to HZ$ drops for increasing c.m. energy and/or M_H values, since it is mediated by s–channel gauge boson exchange. Note that the cross section for this process is negligible at the Tevatron because of the low gluon luminosity and the reduced phase space.

Numerical results

The K–factors, defined as the ratios of the cross sections at higher order with α_s and the PDFs evaluated also at higher order, relative to the LO order cross sections with α_s and the PDFs consistently evaluated also at LO, are shown at NLO and NNLO in Figs. 3.7 in solid black lines for the LHC (left–hand side) and the Tevatron (right–hand side) as a function of the Higgs mass for the process $pp \to HW$. The scales have been fixed to $\mu_F = \mu_R = M_{HV}$, where M_{HV} is the invariant mass of the HV system, and the MRST sets of PDFs for each perturbative order are used in a consistent manner.

The NLO K–factor is practically constant at the LHC, increasing only from $K_{\rm NLO} = 1.27$ for $M_H = 110$ GeV to $K_{\rm NLO} = 1.29$ for $M_H = 300$ GeV. The NNLO contributions increase the K–factor by a mere 1% for the low M_H value and by 3.5% for the high value. At the Tevatron, the NLO K–factor is somewhat higher than at the LHC, enhancing the cross section by $K_{\rm NLO} = 1.35$ for $M_H = 110$ GeV and $K_{\rm NLO} = 1.3$ for $M_H = 300$ GeV with a monotonic decrease. The NNLO corrections increase the K–factor uniformly by about 10%. Thus, these NNLO corrections are more important at the Tevatron than at the LHC.

Because of the slightly different phase space and scale, the K–factor for $pp \to ZH$ is not identical to the K–factor for $pp \to WH$. However, since $(M_Z^2 - M_W^2)/\hat{s}$ is small and the dependence of $d\Gamma$ in eq. (3.13) on k^2 is not very strong in the range that we are considering, the K–factors for the two processes are very similar when the contribution of the $gg \to HZ$ component to be discussed later is not included.

The bands around the K–factors in Fig. 3.7 represent the variation of the cross sections when they are evaluated at renormalization and factorization scale values that are independently varied from $\frac{1}{3}M_{HV} \leq \mu_F\,(\mu_R) \leq 3M_{HV}$, while the other is fixed to $\mu_R\,(\mu_F) = M_{HV}$; the normalization is provided by the production cross section evaluated at scales $\mu_F = \mu_R = M_{HV}$. A K–factor for the LO cross section, $K_{\rm LO}$, has also been defined by evaluating the latter at given factorization and renormalization scales and normalizing to the LO cross sections evaluated at the central scale, which, in our case, is given by $\mu_F = \mu_R = M_{HV}$. As can be seen, except from the accidental cancellation of the scale dependence of the LO cross section at the LHC for $M_H \sim 260$ GeV, the decrease of the scale variation is strong when going from LO to NLO and then to NNLO. For $M_H = 120$ GeV, the uncertainty from the scale choice at the LHC drops from 10% at LO, to 5% at NLO, and to 2% at NNLO. At the Tevatron and for the same Higgs boson mass, the scale uncertainty drops from 20% at LO, to 7% at NLO, and to 3% at NNLO.

If this variation of the cross section with the two scales is taken as an indication of the uncertainties due to the not yet calculated higher–order corrections, one concludes that once the NNLO contributions are included in the prediction, the cross section for the $pp \to HV$ process is known at the rather accurate level of a few percent.

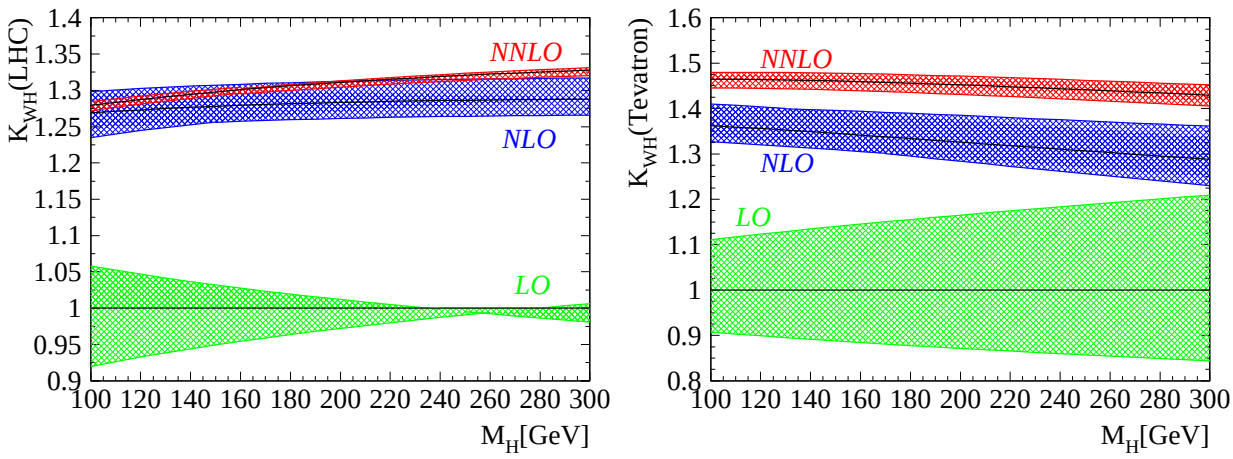

Figure 3.7: The K–factors for $pp \to HW$ at the LHC (left) and the Tevatron (right) as a function of M_H at LO, NLO and NNLO (solid black lines). The bands represent the spread of the cross section when the renormalization and factorization scales are varied in the range $\frac{1}{3}M_{HV} \leq \mu_R\,(\mu_F) \leq 3M_{HV}$, the other scale being fixed at $\mu_F(\mu_R) = M_{HV}$; from Ref. [299].

3.2.3 The electroweak radiative corrections

The associated $W/Z + H$ process is the only Higgs production mechanism for which the complete calculation of the $\mathcal{O}(\alpha)$ electroweak corrections has been performed [331]. There are a few hundred Feynman diagrams contributing at the one–loop level, and some generic ones are shown in Fig. 3.8. The radiative corrections can be cast into three categories.

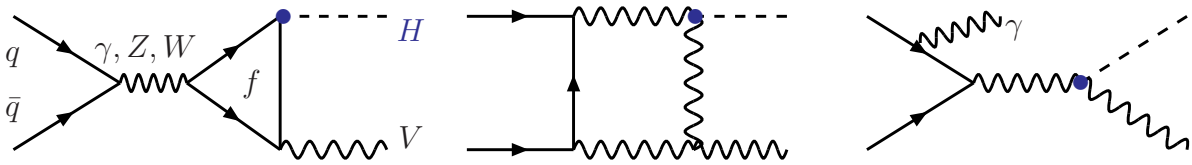

Figure 3.8: Generic diagrams for the $\mathcal{O}(\alpha)$ corrections to the $pp \to HV$ production process.

There are first QED corrections in which photons are exchanged in the initial quark–antiquark states and, in order to obtain infrared finite corrections, real–photon bremsstrahlung has to be added. Having done this, $\mathcal{O}(\alpha)$ corrections due to collinear photon emission and involving logarithms of the initial state quark masses are still present. These mass singularities are absorbed into the PDFs in exactly the same way as in QCD by $\overline{\text{MS}}$ factorization. This, however, also requires the inclusion of the corresponding $\mathcal{O}(\alpha)$ corrections into the DGLAP evolution of these distributions and into their fit to experimental data, which has not been performed yet. Nevertheless, an approximate inclusion of these corrections to the DGLAP evolution shows [332] that the impact of these corrections on the quark distributions is well below 1%, at least in the x range that is relevant at the Tevatron and the LHC. This is also supported by a recent analysis of the MRST collaboration [333] which took into account these effects into the DGLAP equations.

The bulk of the electroweak corrections can be in principle incorporated by using the improved Born approximation discussed in §1.2.4. Using the Fermi coupling constant G_μ rather than $\alpha(0)$ as input in the tree–level cross section, $\pi\alpha \to \sqrt{2}G_\mu M_W^2(1 - M_W^2/M_Z^2)$, takes into account the contribution $\Delta r \simeq \Delta\alpha(M_Z^2) - 3\Delta\rho$. In this case, the large universal corrections originating from the light fermion contributions to the running of α [$2 \times \Delta\alpha(M_Z) \sim 12\%$, since the cross section is proportional to α^2] and those which are quadratic in the top quark [$2 \times 3\Delta\rho \sim 6\%$] are automatically included. One has also to include the contributions that are quadratic in the top mass and which are contained in the HVV vertex as it was discussed in §2.4.2, i.e. $\delta_{HVV} \sim -5x_t$ with $x_t = G_\mu^2 m_t^2/(8\sqrt{2}\pi^2)$ at this order.

Finally, one has to include the bosonic one–loop corrections which involve many self–energy, vertex and box correction diagrams and which have to be calculated by brute force using standard techniques. The calculation of Ref. [331] has been performed in the on–shell renormalization scheme. It turns out that the non–universal bosonic contributions are rather large and negative and, in fact, dominate over the fermionic corrections and even over the photonic initial state corrections.

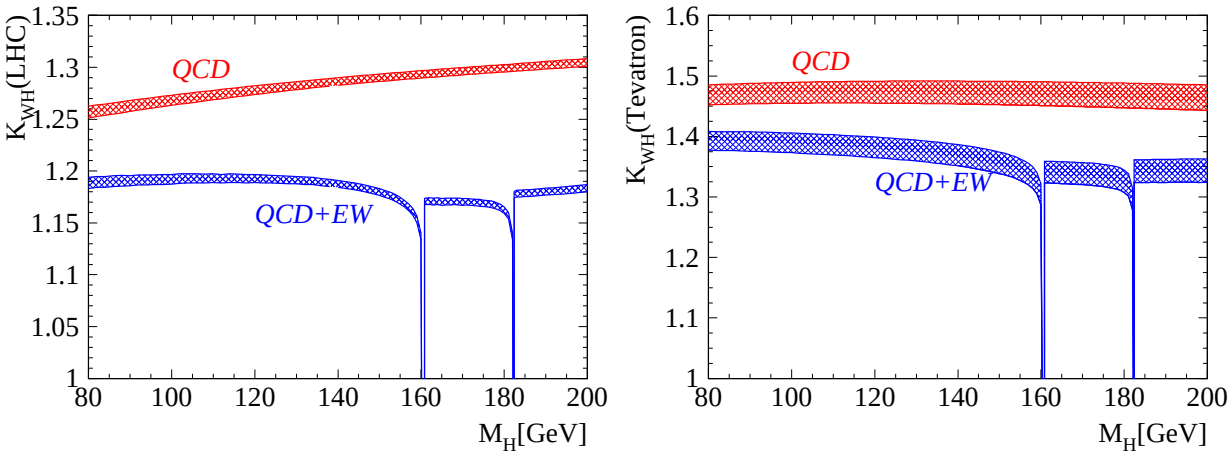

Figure 3.9: K–factors for WH and ZH production at the LHC (left figure) and the Tevatron (right figure) after including the NNLO QCD and the electroweak $\mathcal{O}(\alpha)$ corrections [334].

The fermionic contributions being positive and the bosonic ones negative, there is a partial cancellation of the two contributions and, since the bosonic corrections are more important, the net effect is that the total electroweak corrections decrease the $q\bar{q} \to HV$ production cross section at both the Tevatron and the LHC by approximately 5 to 10% for Higgs masses in the range 100–200 GeV where the production rates are large enough. This is shown in Fig. 3.9 where we display the K–factors for $pp \to HW$ at the Tevatron and LHC as functions of M_H, when only NLO+NNLO QCD corrections are included (upper bands) and when the electroweak corrections are also taken into account (lower bands). The thickness of the bands is due to the scale variation as discussed previously. The unphysical singularities

in the electroweak corrections at the $M_H = 2M_W$ and $2M_Z$ thresholds can be removed by including the finite width of the particles. Note that at the LHC, the electroweak correction is almost the same for $pp \to HW$ and $pp \to HZ$, the difference being less than 2%.

3.2.4 The total cross section and the PDF uncertainties

In Fig. 3.10, we present the total production cross sections for the processes $q\bar{q} \to HW$ and HZ at the Tevatron and the LHC as a function of M_H, when both the NNLO QCD and the electroweak corrections are added. In the case of the HZ process, the contribution of the $gg \to ZH$ subprocess to the total cross section is not included, but it is displayed separately in the LHC case. For Higgs masses in the range 100 GeV $\lesssim M_H \lesssim$ 250 GeV where $\sigma(q\bar{q} \to HZ)$ is significant, $\sigma(gg \to HZ)$ is at the level of 0.1 to 0.01 pb and represents about 10% of the total cross section for low M_H values. The $gg \to HZ$ cross section is thus much larger than the contribution of the NNLO correction and, therefore, generates a scale uncertainty that is larger than in the HW production case.

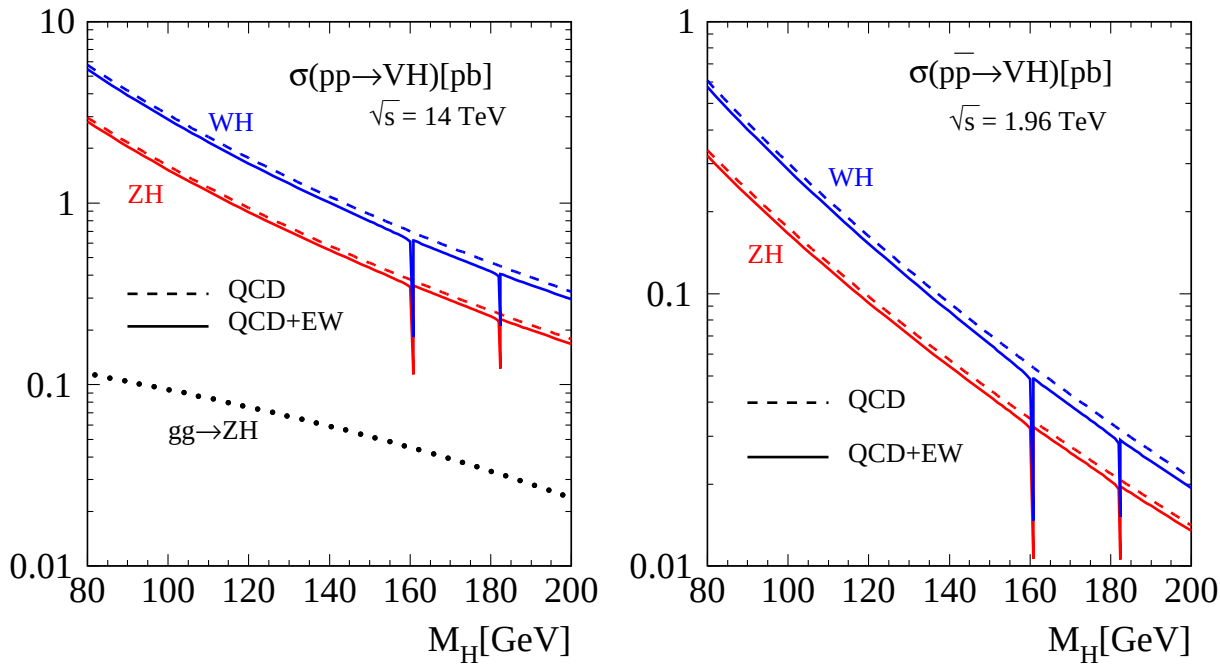

Figure 3.10: The total production cross sections for $pp \to HW$ and HZ at the LHC (left) and the Tevatron (right) as a function of M_H when the NNLO QCD and the electroweak corrections are included. The MRST parton densities have been used. The contribution of the $gg \to HZ$ process is shown separately in the case of the LHC; from Ref. [334].

Finally, let us discuss the PDF uncertainties in the $pp \to HV$ cross sections, following the lines introduced in §3.1.5. In Fig. 3.11, we show as a function of M_H and for the LHC and the Tevatron, the central values and the uncertainty band limits of the NLO QCD $q\bar{q} \to HW$ cross section for the CTEQ, MRST and Alekhin parameterizations. In the inserts to these

figures, we show the spread uncertainties in the predictions for the cross sections, when they are normalized to the prediction of the reference CTEQ6M set.

At the LHC, the uncertainty band is almost constant and for CTEQ, is of the order of 4% over the Higgs mass range between 100 and 200 GeV. At the Tevatron, the uncertainty band increases with the Higgs mass and exceeds 6% at $M_H \sim 200$ GeV. The uncertainty in the MRST parameterization is twice smaller. To produce a vector plus a Higgs boson in this mass range, the incoming quarks originate from the intermediate–x regime at the LHC, at Tevatron energies, however, some of the participating quarks originate from the high–x regime, which explains the increasing behavior of the uncertainty bands observed in this case. The different magnitude of the cross sections, $\sim 12\%$ ($\sim 8\%$) larger in the Alekhin case than for CTEQ at the LHC (Tevatron), is due to the larger quark and antiquark densities of the former parameterization. For this particular PDF set, the difference in the shifts of the central values in the LHC and Tevatron cases is due to the different initial states, pp [where $\bar{q}$ comes from the sea] versus $p\bar{p}$ [where it is valence+sea $\bar{q}$]; see Fig. 3.2.

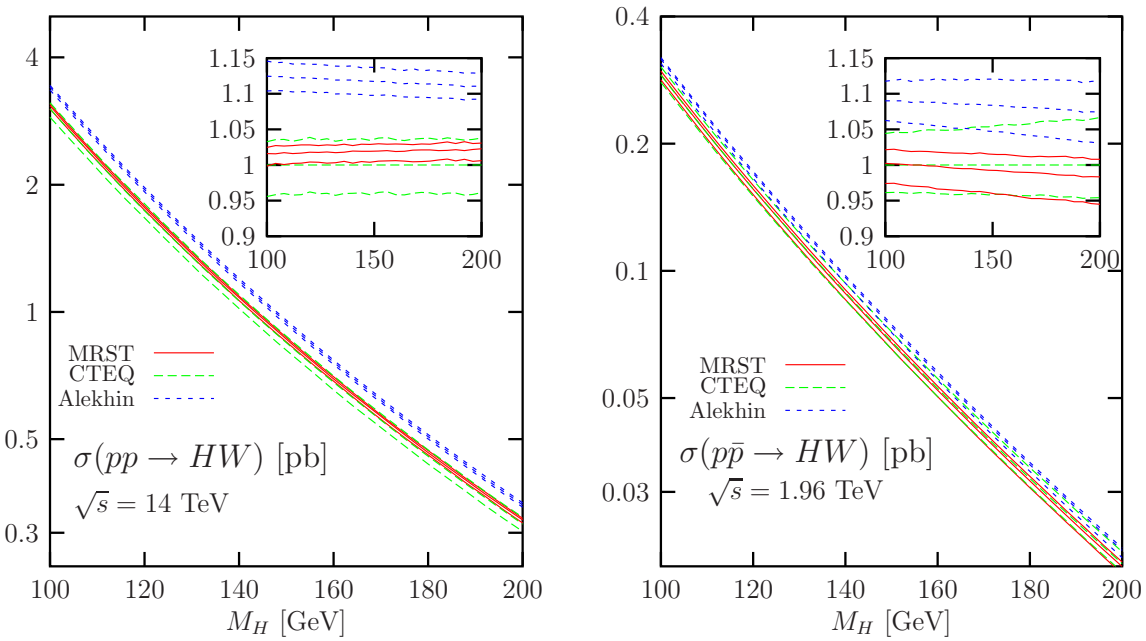

Figure 3.11: The CTEQ, MRST and Alekhin PDF uncertainty bands for the NLO cross sections for the production of the Higgs boson at the LHC (left) and at the Tevatron (right) in the $q\bar{q} \to HW$ process. The inserts show the spread in the predictions; from Ref. [314].

Note that an additional systematic error of about 5% arises from the pp luminosity. If one uses the Drell–Yan processes to measure directly the q and $\bar{q}$ luminosities at hadron colliders, the errors on the cross sections for associated HV production when normalized to this rate would lead to a total systematical uncertainty of less than 1% [335]. In this case, the dominant part the of the K–factor will also drop out in the ratio.

3.3 The vector boson fusion processes

3.3.1 The differential and total cross sections at LO

The matrix element squared for the massive vector boson fusion process [243–246], in terms of the momenta of the involved particles

$$q_1(p_1)\, q_2(p_2) \to V^*(q_1 = p_3 - p_1)\, V^*(q_2 = p_4 - p_2)\, q_3(p_3)\, q_4(p_4) \to q_3(p_3)\, q_4(p_4)\, H(k) \quad (3.22)$$

with $V = W, Z$, is given by

$$|\mathcal{M}|^2 \;=\; 4\sqrt{2} N_c^f G_\mu^3 M_V^8 \frac{C_+(p_1\cdot p_2)(p_3\cdot p_4) + C_-(p_1\cdot p_4)(p_2\cdot p_3)}{(q_1^2 - M_V^2)^2 (q_2^2 - M_V^2)^2} \quad (3.23)$$

where, in terms of the usual vector and axial-vector couplings of the gauge bosons to fermions $\hat{a}_f = 2I_f^3, \hat{v}_f = 2I_f^3 - 4Q_f s_W^2$ for $V = Z$ and $\hat{v}_f = \hat{a}_f = \sqrt{2}$ for $V = W$, $C_\pm$ read

$$C_\pm = (\hat{v}_{q_1}^2 + \hat{a}_{q_1}^2)(\hat{v}_{q_3}^2 + \hat{a}_{q_3}^2) \pm 4\hat{v}_{q_1}\hat{a}_{q_1}\hat{v}_{q_3}\hat{a}_{q_3} \quad (3.24)$$

giving rise to the differential distribution

$$\mathrm{d}\hat{\sigma}_{\rm LO} = \frac{1}{4}\frac{1}{9}\frac{1}{2\hat{s}} \times |\mathcal{M}|^2 \times \frac{1}{(2\pi)^5}\frac{\mathrm{d}^3k}{2\mathrm{d}E_H}\frac{\mathrm{d}^3p_3}{2\mathrm{d}E_3}\frac{\mathrm{d}^3p_4}{2\mathrm{d}E_4}\,\delta^4(p_1 + p_2 - p_3 - p_4 - k) \quad (3.25)$$

The integration over the variables p_3 and p_4 are conveniently performed in the rest frame of the two quarks $\vec{p}_3 + \vec{p}_4 = 0$, and one finds [245, 246]

$$\frac{\mathrm{d}\hat{\sigma}_{\rm LO}}{\mathrm{d}E_H \mathrm{d}\cos\theta} = \frac{G_\mu^3 M_V^8}{9\sqrt{2}\,\pi^3\hat{s}}\frac{p_H}{32 s_1 s_2 r}\Big[C_+\mathcal{H}_+ + C_-\mathcal{H}_-\Big] \quad (3.26)$$

with

$$\begin{aligned}
\mathcal{H}_+ \;&=\; (h_1+1)(h_2+1)\left[\frac{2}{h_1^2-1} + \frac{2}{h_2^2-1} - \frac{6s_\chi^2}{r} + \left(\frac{3t_1t_2}{r} - c_\chi\right)\frac{\ell}{\sqrt{r}}\right] \\
&\quad - \left[\frac{2t_1}{h_2-1} + \frac{2t_2}{h_1-1} + \left(t_1 + t_2 + s_\chi^2\right)\frac{\ell}{\sqrt{r}}\right] \\
\mathcal{H}_- \;&=\; 2(1-c_\chi)\left[\frac{2}{h_1^2-1} + \frac{2}{h_2^2-1} - \frac{6s_\chi^2}{r} + \left(\frac{3t_1t_2}{r} - c_\chi\right)\frac{\ell}{\sqrt{r}}\right]
\end{aligned} \quad (3.27)$$

In these equations, $p_H = \sqrt{E_H^2 - M_H^2}$ is the Higgs boson momentum, θ is the scattering angle, while $\epsilon_\nu = \sqrt{\hat{s}} - E_H$ and $s_\nu = \epsilon_\nu^2 - p_H^2$ are the energy and the invariant mass of the final state quark pair. The other abbreviations are

$$s_{1,2} = \sqrt{\hat{s}}(\epsilon_\nu \pm p_H\cos\theta)\ ,\ h_{1,2} = 1 + 2M_V^2/s_{1,2}\ ,\ t_{1,2} = h_{1,2} + c_\chi h_{2,1} \quad (3.28)$$

$$c_\chi = 1 - \frac{2\hat{s}s_\nu}{s_1 s_2} = 1 - s_\chi^2,\ r = h_1^2 + h_2^2 + 2c_\chi h_1 h_2 - s_\chi^2\ ,\ \ell = \log\frac{h_1h_2 + c_\chi + \sqrt{r}}{h_1h_2 + c_\chi - \sqrt{r}}$$

To derive the partonic total cross section, $\hat{\sigma}_{\rm LO}(qq \to qqH)$, the differential cross section must be integrated over the region

$$-1 < \cos\theta < 1 \quad \text{and} \quad M_H < E_H < \frac{\sqrt{\hat{s}}}{2}\left(1 + \frac{M_H^2}{\hat{s}}\right) \tag{3.29}$$

Summing over the contributing partons, including both the WW and ZZ fusion channels and folding with the parton luminosities, one obtains the total hadronic cross section $\sigma(pp \to V^*V^* \to qqH)$ at LO. The cross sections, using the CTEQ set of parton densities, are shown in Fig. 3.12 as a function of M_H for $p\bar{p}$ at the Tevatron and for pp at the LHC. In the latter case, the separate WW and ZZ contributions, as well as their total sum, are displayed; the interference between the WW and ZZ contributions is less than 1% and can be neglected.

While they are rather large at the LHC, in particular for Higgs bosons in the mass range 100 GeV $\lesssim M_H \lesssim$ 200 GeV where they reach the level of a few picobarns, the total cross sections are very small at the Tevatron and they barely reach the level of 0.1 pb even for $M_H = 100$ GeV. This is due to the fact that the main contribution originates from longitudinal gauge bosons [which as, discussed previously, have interactions which grow with energy], and the partonic cross sections rise logarithmically with the c.m. energy of the subprocess, $\hat{\sigma} \propto \log \hat{s}/M_V^2$, giving much larger rates at high energies. In our subsequent discussion, we will therefore consider this process only in the case of the LHC.

Note also that the main contribution to the cross section is due to the WW fusion channel, $\sigma(WW \to H) \sim 3\sigma(ZZ \to H)$ at the LHC, a consequence of the fact that the W boson couplings to fermions are larger than those of the Z boson.

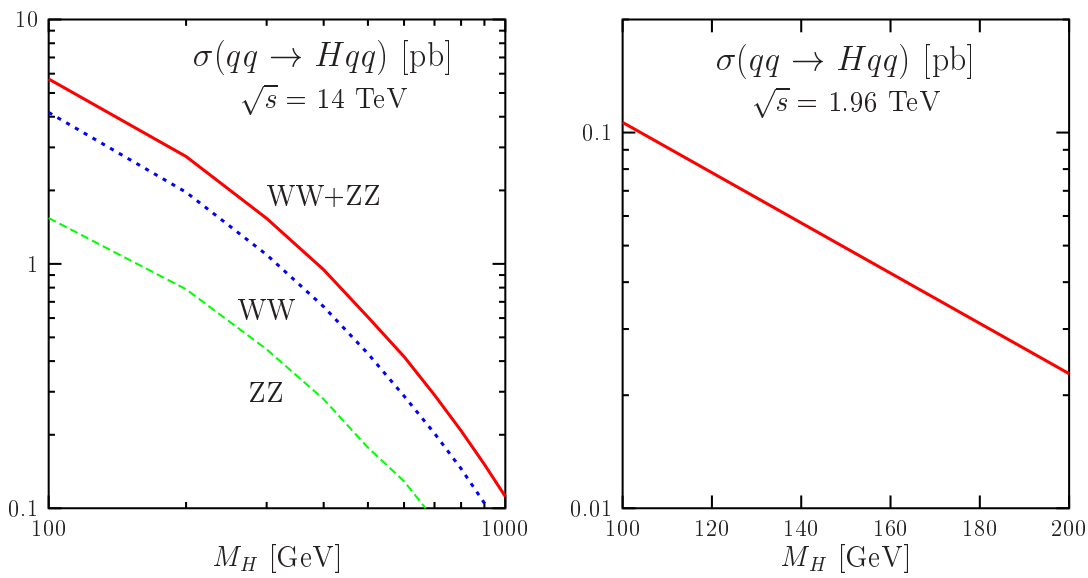

Figure 3.12: Individual and total cross sections in the vector fusion $qq \to V^*V^* \to Hqq$ processes at leading order at the LHC (left) and total cross section at the Tevatron (right).

3.3.2 The cross section at NLO

The QCD corrections to the vector boson fusion process, $qq \to qqV^*V^* \to qqH$ consist of the virtual quark self energy and vertex corrections and the additional gluon emission from the initial and final states, $qq \to Hqq + g$; the gluon initiated subprocess $gq \to Hqq + q$ has also to be taken into account. Some generic Feynman diagrams are shown in Fig. 3.13.

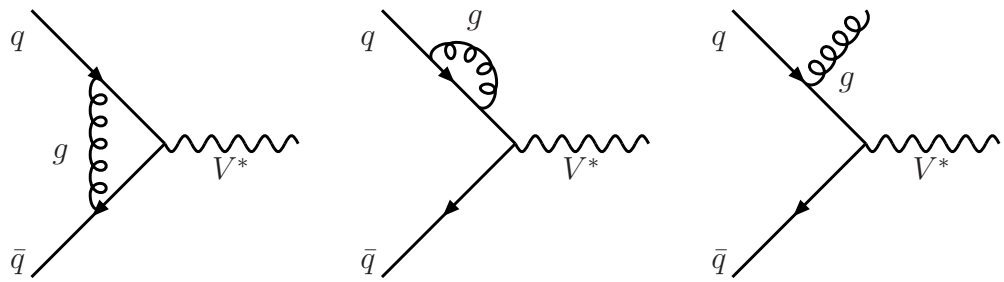

Figure 3.13: Feynman diagrams for NLO QCD corrections to the V^*qq vertex.

Since at the lowest order the incoming/outgoing quarks are in color singlets, at NLO no gluons will be exchanged between the first and the second incoming (outgoing) quark line [this will be no longer true at $\mathcal{O}(\alpha_s^2)$] and, hence, the QCD corrections only consist of the well–known corrections to the structure functions $F_i(x, M^2)$. The NLO corrections can therefore be more conveniently calculated in the structure function approach. In this case, the differential LO partonic cross section can be cast into the form [21, 281, 282]

$$\begin{aligned}
\mathrm{d}\sigma_{\mathrm{LO}} &= \frac{1}{4}\frac{\sqrt{2}G_\mu^3 M_V^8 q_1^2 q_2^2}{[q_1^2 - M_V^2]^2[q_2^2 - M_V^2]^2}\left\{F_1(x_1,\mu_F^2)F_1(x_2,\mu_F^2)\left[2 + \frac{(q_1q_2)^2}{q_1^2q_2^2}\right]\right. \\
&+ \frac{F_1(x_1,\mu_F^2)F_2(x_2,\mu_F^2)}{P_2q_2}\left[\frac{(P_2q_2)^2}{q_2^2} - m_P^2 + \frac{1}{q_1^2}\left(P_2q_1 - \frac{P_2q_2}{q_2^2}q_1q_2\right)^2\right] \\
&+ \frac{F_2(x_1,\mu_F^2)F_1(x_2,\mu_F^2)}{P_1q_1}\left[\frac{(P_1q_1)^2}{q_1^2} - m_P^2 + \frac{1}{q_2^2}\left(P_1q_2 - \frac{P_1q_1}{q_1^2}q_1q_2\right)^2\right] \\
&+ \frac{F_2(x_1,\mu_F^2)F_2(x_2,\mu_F^2)}{(P_1q_1)(P_2q_2)}\left[P_1P_2 - \frac{(P_1q_1)(P_2q_1)}{q_1^2} - \frac{(P_2q_2)(P_1q_2)}{q_2^2} + \frac{(P_1q_1)(P_2q_2)(q_1q_2)}{q_1^2q_2^2}\right]^2 \\
&+ \left.\frac{F_3(x_1,\mu_F^2)F_3(x_2,\mu_F^2)}{2(P_1q_1)(P_2q_2)}\left[(P_1P_2)(q_1q_2) - (P_1q_2)(P_2q_1)\right]\right\}\mathrm{d}x_1\mathrm{d}x_2\frac{\mathrm{dPS}_3}{\hat{s}} \qquad (3.30)
\end{aligned}$$

where dPS_3 denotes the three–particle phase space, m_P the proton mass, $P_{1,2}$ the proton momenta and $q_{1,2}$ the momenta of the virtual vector bosons V^*. The functions $F_i(x, \mu_F^2)$, with $i = 1, 2, 3$, are the usual structure functions from deep–inelastic scattering processes at the factorization scale μ_F and read

$$F_1(x,\mu_F^2) = \sum_q (\hat{v}_q^2 + \hat{a}_q^2)[q(x,\mu_F^2) + \bar{q}(x,\mu_F^2)]$$

$$
\begin{aligned}
F_2(x,\mu_F^2) &= 2x\sum_q (\hat{v}_q^2+\hat{a}_q^2)[q(x,\mu_F^2)+\bar{q}(x,\mu_F^2)] \\
F_3(x,\mu_F^2) &= 4\sum_q \hat{v}_q\hat{a}_q[-q(x,\mu_F^2)+\bar{q}(x,\mu_F^2)]
\end{aligned} \tag{3.31}
$$

The QCD corrections only consist of the well–known corrections to the structure functions $F_i(x,M^2)$ and the final result for the corrected cross section at $\mathcal{O}(\alpha_s)$ can be simply obtained from the replacements [21, 281, 282]

$$
F_i(x,\mu_F^2) \to F_i(x,\mu_F^2) + \Delta F_i(x,\mu_F^2,Q^2) \tag{3.32}
$$

$$
\begin{aligned}
\Delta F_1(x,\mu_F^2,Q^2) &= \frac{\alpha_s(\mu_R)}{\pi}\sum_q (\hat{v}_q^2+\hat{a}_q^2)\int_x^1 \frac{dy}{y}\left\{\frac{2}{3}[q(y,\mu_F^2)+\bar{q}(y,\mu_F^2)]\right. \\
&\left[-\frac{3}{4}P_{qq}(z)\log\frac{\mu_F^2 z}{Q^2}+(1+z^2)\mathcal{D}_1(z)-\frac{3}{2}\mathcal{D}_0(z)+3-\left(\frac{9}{2}+\frac{\pi^2}{3}\right)\delta(1-z)\right] \\
&\left.+\frac{1}{4}g(y,\mu_F^2)\left[-2P_{qg}(z)\log\frac{\mu_F^2 z}{Q^2(1-z)}+4z(1-z)-1\right]\right\}
\end{aligned} \tag{3.33}
$$

$$
\begin{aligned}
\Delta F_2(x,\mu_F^2,Q^2) &= 2x\frac{\alpha_s(\mu_R)}{\pi}\sum_q (\hat{v}_q^2+\hat{a}_q^2)\int_x^1 \frac{dy}{y}\left\{\frac{2}{3}[q(y,\mu_F^2)+\bar{q}(y,\mu_F^2)]\right. \\
&\left[-\frac{3}{4}P_{qq}(z)\log\frac{\mu_F^2 z}{Q^2}+(1+z^2)\mathcal{D}_1(z)-\frac{3}{2}\mathcal{D}_0(z)+3+2z-\left(\frac{9}{2}+\frac{\pi^2}{3}\right)\delta(1-z)\right] \\
&\left.+\frac{1}{4}g(y,\mu_F^2)\left[-2P_{qg}(z)\log\frac{\mu_F^2 z}{Q^2(1-z)}+8z(1-z)-1\right]\right\}
\end{aligned} \tag{3.34}
$$

$$
\begin{aligned}
\Delta F_3(x,\mu_F^2,Q^2) &= \frac{\alpha_s(\mu_R)}{\pi}\sum_q 4\hat{v}_q\hat{a}_q\int_x^1 \frac{dy}{y}\left\{\frac{2}{3}[-q(y,\mu_F^2)+\bar{q}(y,\mu_F^2)]\right. \\
&\left.\left[-\frac{3}{4}P_{qq}(z)\log\frac{\mu_F^2 z}{Q^2}+(1+z^2)\mathcal{D}_1(z)-\frac{3}{2}\mathcal{D}_0(z)+2+z-\left(\frac{9}{2}+\frac{\pi^2}{3}\right)\delta(1-z)\right]\right\}
\end{aligned} \tag{3.35}
$$

where $z=x/y$ and the Altarelli–Parisi splitting functions P_{qq}, P_{qg} are as given in eq. (3.21); the notation $\mathcal{D}_i(z) = \left[\log^i(1-z)/(1-z)\right]_+$ with $i=0,1$ has been introduced before. μ_R is the renormalization scale at which α_s is evaluated and the physical scale Q is given by $Q^2=-q_i^2$ for $x=x_i$ with $i=1,2$. These expressions have to be inserted in the LO differential cross section eq. (3.30) and the full result expanded up to NLO. The typical renormalization and factorization scales are fixed by the corresponding vector–boson momentum transfer at each leg, $\mu_R^2=\mu_F^2=-q_i^2$ for $x=x_i$.

The correcting K–factor, again defined as $K=\sigma_{\rm NLO}/\sigma_{\rm LO}$ with α_s and the PDFs consistently taken at the respective order, where the renormalization and factorization scales are set to $\mu_R=\mu_F=Q$, is practically constant at the LHC in the entire Higgs mass range $100 \lesssim M_H \lesssim 1$ TeV, and increases the LO cross section by about 5 to 10%. More details on the K–factor and the scale dependence at LO and NLO will be given later, after the discussion of the specific kinematics of the vector boson fusion process to which we turn now.

3.3.3 Kinematics of the process

Because weak vector boson fusion is a three–body production process and is mediated by t–channel gauge boson exchange, its kinematics is rather complicated. However, its characteristics distributions play an extremely important role once it comes to discriminate the signal from the many large QCD backgrounds. In particular, forward jet–tagging [336–338] and central jet–vetoing [338,339] are essential ingredients. We therefore summarize the main features of the various distributions; for more details, see the reviews of Refs. [340,341].

To study the kinematics of the $pp \to Hqq$ process, it is more convenient to write the differential partonic cross section, eq. (3.26), in terms of the transverse momentum and rapidity of the Higgs boson. The latter, in terms of p_H, E_H and $\cos\theta$, are given by

$$E_H = \sqrt{M_H^2 + p_T^2}\ \mathrm{ch}(y) \quad , \quad p_H \cos\theta = \sqrt{M_H^2 + p_T^2}\ \mathrm{sh}(y) \tag{3.36}$$

The total partonic cross section is obtained by integrating the double differential distribution [which is given in eq. (3.26) and where the above changes have been performed]

$$\hat{\sigma}_{\rm LO}(qq \to Hqq) = \int_{y_-}^{y_+} \mathrm{d}y \int_0^{p_T^{\rm max}} \mathrm{d}p_T\, (2\pi p_T)\, \frac{\mathrm{d}^2\hat{\sigma}_{\rm LO}}{\mathrm{d}y \mathrm{d}p_T} \tag{3.37}$$

the integration bounds on the rapidity and the transverse momentum being

$$y_\pm = \pm \log \frac{\sqrt{\hat{s}}}{M_H} \quad , \quad p_T^{\rm max} = \left[\left(\frac{\hat{s} + M_H^2}{2\sqrt{\hat{s}}\,\mathrm{ch}(y)} \right)^2 - M_H^2 \right]^{1/2} \tag{3.38}$$

Similarly to the emission of a Weizsäcker–Williams photon from an energetic electron or positron beam, the intermediate vector bosons in the fusion process tend to carry only a small fraction of the initial parton energies. At the same time, they must have an energy of $\mathcal{O}(\frac{1}{2}M_H)$ to produce the Higgs boson. Thus, the two quarks in the final state have very large energies, of order 1 TeV at the LHC. In contrast, they have small transverse momenta, $p_T \sim M_V$, which are set by the vector boson propagators in the amplitude squared eq. (3.23), $1/(q_{1,2}^2 - M_V^2) \lesssim 1/(p_{T3,4}^2 + M_V^2)$, and which suppress the cross section for p_T values larger than M_V. The relatively small transverse momenta and high energies of the final state quarks correspond to rather small scattering angles $\theta_{3,4}$. In terms of the pseudo–rapidity

$$\eta = \frac{1}{2} \log \frac{1+\cos\theta}{1-\cos\theta} \tag{3.39}$$

one obtains typically, $1 \lesssim \eta \lesssim 5$. This is exemplified in Fig. 3.14 where the transverse momenta and rapidity distributions of the two scattered quarks are shown at the LHC for a Higgs boson mass $M_H = 120$ GeV. One can see that the rapidity distributions tend to be central, in particular in the case of one of the jets. One also sees that the average transverse

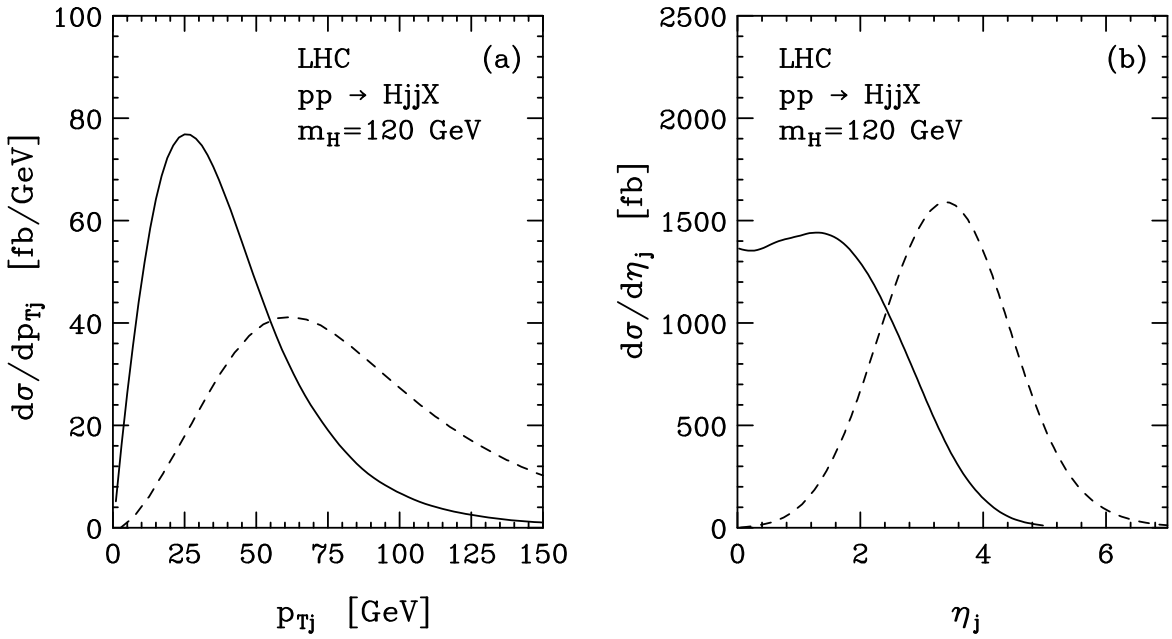

Figure 3.14: The transverse momentum (left) and pseudo–rapidity (right) distributions of the two scattered jets in the fusion process $qq \to Hqq$ at the LHC with $M_H = 120$ GeV. Shown are the p_T distributions for the lowest (solid) and highest (dashed) jets and the $|\eta|$ distribution for the most central (solid) and most forward (dashed) jets; from Ref. [340]

momentum of one of the quarks is substantially smaller, a factor of two less, than for the other quark and that small values, $p_T \sim 35$ GeV, are possible.

Therefore, requiring that the two scattered jets have a large invariant mass, a sizable p_T and rapidity distributions which are central, will substantially reduce the backgrounds

$$\text{Cut 1}: \quad m_{q_3,q_4} \gtrsim 1 \text{ TeV} \ , \ p_{T_{q_3,q_4}} \gtrsim 20 \text{ GeV} \ , \ |\eta_{q_3,q_4}| \lesssim 5 \tag{3.40}$$

Because of the scalar nature of the Higgs boson, its decay $H \to X_1 X_2$ is isotropic and can be treated separately from the production process. One can then discuss the kinematics of Higgs production in the vector boson fusion channel, independently of the detection channel. Nevertheless, the Higgs decay products should be observable, i.e. they must have a substantial p_T and they must be well separated from the jets. The decay products tend to be very central as is exemplified in Fig. 3.15 in the case of the $H \to \gamma\gamma$ decay [342], where the normalized pseudo–rapidity of the most forward photon is shown for $M_H = 120$ GeV. In contrast, the photons in the irreducible QCD background $pp \to jj\gamma\gamma$ are more forward. Thus, a second cut will reduce the background without affecting too much the signal

$$\text{Cut 2}: \quad p_{T_{X1,X2}} \gtrsim 20 \text{ GeV} \ , \ |\eta_{X_1,X_2}| \lesssim 2.5 \ , \ \Delta R_{qX} \gtrsim 0.7 \tag{3.41}$$

where $\Delta R_{qX} = \sqrt{(\eta_X - \eta_q)^2 + (\phi_X - \phi_q)^2}$ is the separation between one of the jets and one of the Higgs decay products in the rapidity–azimuthal angle.

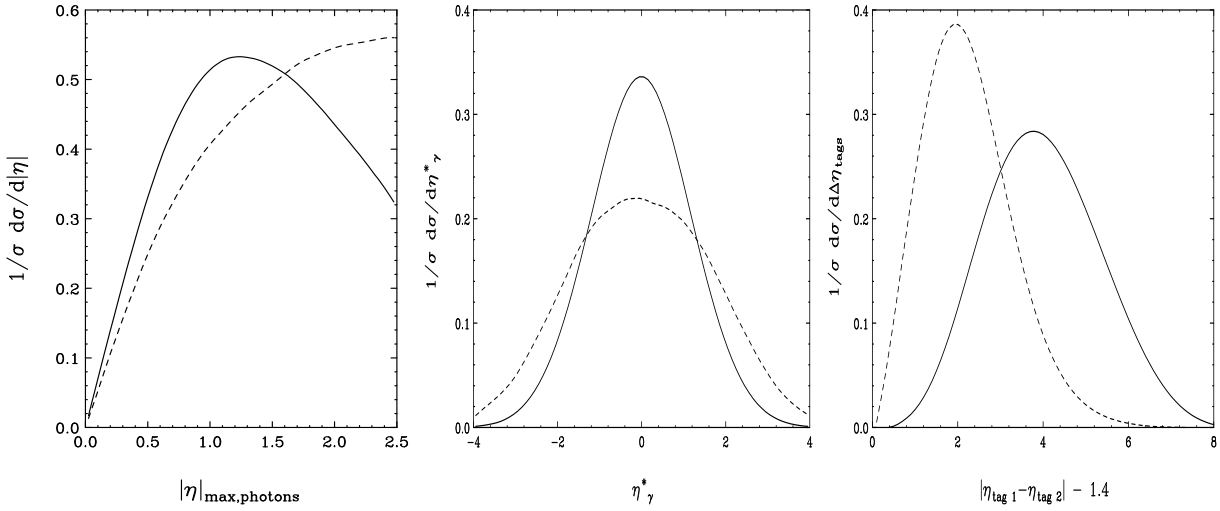

Figure 3.15: The normalized pseudo–rapidity distributions of the most forward photon (left), of both photons with respect to the center of the tagging jets (center), and of the two jet rapidity gap (right) in $jj\gamma\gamma$ events at the LHC; the solid lines are for the $H \to \gamma\gamma$ signal with $M_H = 120$ GeV and the dotted lines are for the QCD background; from Ref. [341].

In fact, Higgs production takes place in the central region and its decay products will also tend to be central. This is again in contrast to the QCD background which gives a higher rapidity for the X final states. To visualize more clearly this feature, one can define a shifted rapidity η_X^* which is the rapidity of X with respect to the center of the two jets, $\eta_X^* = \eta_X - \frac{1}{2}(\eta_{q_3} + \eta_{q_4})$. As shown in the central plot of Fig. 3.15, where the example of $H \to \gamma\gamma$ with $M_H = 120$ GeV is again used, this pseudo–rapidity is more central in the signal than in the QCD background. One can thus make the additional requirement that the decay products $X_{1,2}$ fall between the two tagged jets in rapidity, with a minimum separation in η. Typically one can demand that

$$\text{Cut 3}: \quad \eta_{q,\,\min} + 0.7 \lesssim \eta_{X_{1,2}} \lesssim \eta_{q,\,\max} - 0.7 \ , \ \eta_{q_3} \cdot \eta_{q_4} < 0 \tag{3.42}$$

where it is also required that the two jets are produced in opposite hemispheres and, thus, the product of their pseudo–rapidities is negative.

In addition, the two forward tagging jets tend to be very well separated in pseudo–rapidity. This is shown in the right–hand side of Fig. 3.15 in the case of the $jj\gamma\gamma$ events for both the $H \to \gamma\gamma$ signal with again $M_H = 120$ GeV and the QCD background. Requiring a rapidity gap between the two forward jets, the QCD backgrounds are significantly suppressed

$$\text{Cut 4}: \quad \Delta\eta_{qq} = |\eta_{q_3} - \eta_{q_4}| \gtrsim 4.4 \tag{3.43}$$

The cuts 1–4 form the basic ingredients to isolate the vector boson fusion signal at the LHC from the various QCD backgrounds. For Higgs masses in the range 100–200 GeV,

approximately 30% of the Higgs signal events from the initial sample are left over after these cuts have been imposed; for a detailed discussion see Ref. [341]. Additional and more specialized cuts can be applied for specific Higgs decays, in particular for the $H \to \tau^+\tau^-$ [343], $H \to W^+W^- \to \ell\ell\nu\nu$ [344, 345], and even $H \to \mu^+\mu^-$ [346] or $b\bar{b}$ [347] final states.

Finally, another important discriminant between the Higgs signal and the backgrounds is the amount of hadronic activity in the central region. Indeed, and as mentioned when studying the QCD corrections, the vector boson fusion process proceeds without color exchange between the scattered quarks, and gluons will be preferentially emitted at rather small angles in the forward and backward directions and not in the central region. This is opposite to the QCD background which proceeds via color exchange of the incident partons and where the gluons are very often in the central region. Therefore vetoing any jet activity in the central region will substantially reduce the backgrounds.

The forward jet–tagging and the central jet vetoing techniques have been discussed in numerous papers and have been shown to efficiently allow to isolate a Higgs production signal in the vector boson fusion process [there are, however, still some experimental issues such as the central jet veto efficiencies and to a lesser extent, the forward jet reconstruction, which need further detailed studies]. Combined with the possibility of having large production rates at the LHC for a Higgs boson in the 100 to 200 GeV mass range, this process offers therefore a very promising channel not only for the production of the SM Higgs boson but also for the study of its properties.

3.3.4 Dependence on the scale and on the PDFs at NLO

Since rather stringent cuts have to be applied to the vector boson fusion process in order to suppress the various backgrounds, one may wonder if the NLO corrections and their residual scale dependence are the same as in the case of the inclusive cross section, i.e. without applying the cuts. This question has been addressed recently [283, 284] by implementing the full one–loop QCD corrections to the $qq \to Hqq$ process into a parton–level Monte–Carlo program [348]. With cuts similar to those discussed in the previous subsection [see the original reference for the details], the output for the production cross section is shown in Fig. 3.16 for a Higgs boson in the mass range between 100 and 200 GeV.

In the left–hand side of the figure, the cross section is displayed at LO (dotted line) and at NLO for two methods of tagging the forward jets: one chooses the tagging jets as being either the two highest P_T jets (P_T method, solid line) or the two highest energy jets (E method, dashed line). One first notices that with the cuts of Ref. [283], the acceptance is less than $\sim 25\%$ of the initial cross section, *c.f.* Fig. 3.12. The corrections are modest and, in the chosen Higgs mass range, they are of the order of 3% to 5% in the P_T method and 6% to 9% in the E method, the largest variation being for low Higgs masses.

To illustrate the impact of the choice of the factorization and renormalization scales on the $qq \to Hqq$ production cross section at the LHC, we show in the right–hand side of Fig. 3.16 the LO and NLO K–factors as functions of the Higgs mass when the central value of the scales $\mu_F = \mu_R = Q_V$ is divided or multiplied by a factor of two, $\mu_F = \mu_R = \frac{1}{2}Q_V$ and $2Q_V$ [note that the variation with the renormalization scale μ_R is small since α_s enters only at NLO and the contribution of this order to the total production cross section is tiny]. Again, the K–factor at leading order is defined as $K_{\rm LO} = \sigma_{\rm LO}(\mu_F, \mu_R)/\sigma_{\rm LO}(\mu_F = \mu_R = Q_V)$. As can be seen, the uncertainty on the total cross section that is generated by the scale variation is relatively large at LO, the spread being of the order of $\Delta\sigma/\sigma \simeq \pm 3\%$ for low Higgs masses and reaching the level of 5% at high Higgs masses. At NLO, the cross section varies only slightly, with a spread smaller than $\sim 2\%$ for the displayed Higgs mass range. This implies that the vector boson fusion cross section at NLO is well under control and that the higher–order QCD corrections are presumably very small[27].

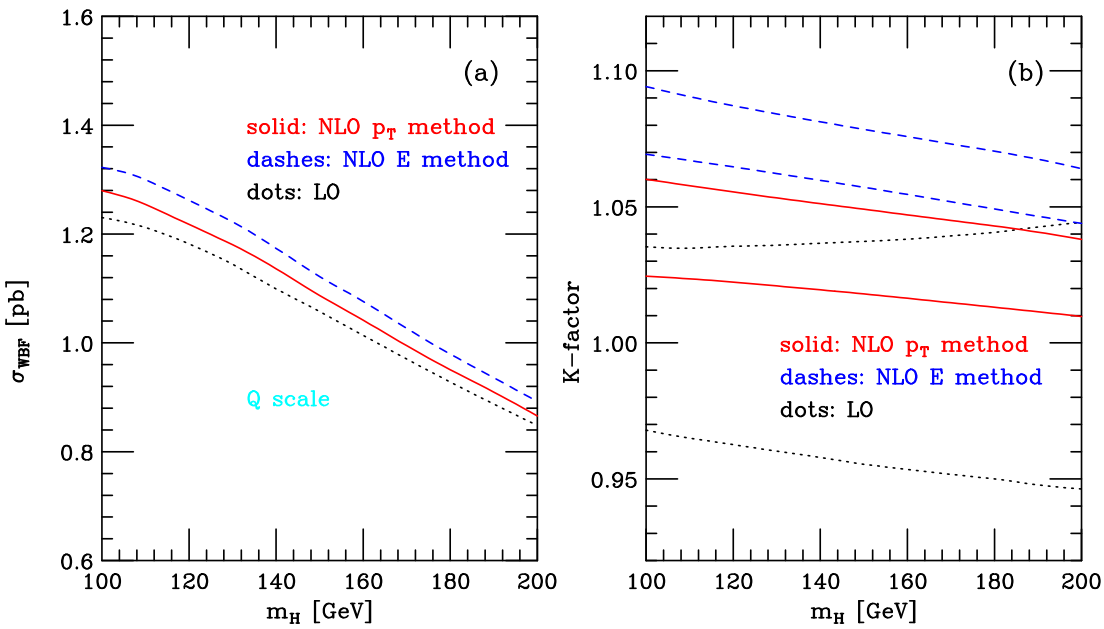

Figure 3.16: Left: the $pp \to Hqq$ cross section at the LHC after cuts as a function of M_H at LO (dotted line) and NLO with the tagging jets defined in the P_T (solid line) and E (dashed line) methods. Right: The scale variation of the LO and NLO cross sections for Higgs production in the $qq \to qqH$ fusion process as a function of M_H at the LHC [283].

Note that the NLO QCD corrections for the p_T and η distributions in $pp \to Hqq$ have also been calculated in this reference. In general, they are of the same size as the corrections to the total cross section, $\sim 10\%$, but they can reach larger values depending on the phase–space regions; see Ref. [283] for details.

[27]The electroweak corrections to this process have not been calculated yet. However, if one uses the IBA discussed in §1.2.4, the bulk of these corrections is incorporated and the remaining piece should be rather small. See the discussion in the next chapter, when this process will be considered in e^+e^- collisions.

Turning to the PDF uncertainties in the prediction for the $qq \to Hqq$ cross section at NLO, we will follow again the procedure outlined in §3.1.5. The central values and the uncertainty band limits of the NLO cross sections are shown for the CTEQ, MRST and Alekhin parameterizations in Fig. 3.17 as a function of M_H at LHC energies. We also show in the insert to this figure, the spread uncertainties in the predictions when the cross sections are normalized to the values obtained using the reference CTEQ6M set.

In the entire Higgs mass range from 100 GeV to 1 TeV, the incoming quarks involved in this process originate from the intermediate–x regime and the uncertainty band is almost constant, ranging between 3% and 4% in the CTEQ parameterization; as usual, the uncertainty is twice smaller in the MRST case. When using the Alekhin set of PDFs, the behavior is different, because the quark PDF behavior is different, as discussed in the case of the $q\bar{q} \to HV$ production channel. The decrease in the central value with higher Higgs masses [which is absent in the $q\bar{q} \to HV$ case, since we stopped the M_H variation at 200 GeV] is due to the fact that we reach here the high–x regime, where the Alekhin $\bar{u}$ PDF drops steeply; see Fig 3.2. Thus, as in the case of the $q\bar{q} \to HV$ process, the PDF uncertainties are below the 5% level if the Alekhin parametrisation is ignored and, therefore, rather small. In view of the small QCD corrections and scale dependence, weak boson fusion can thus also be considered as a rather clean Higgs production process.

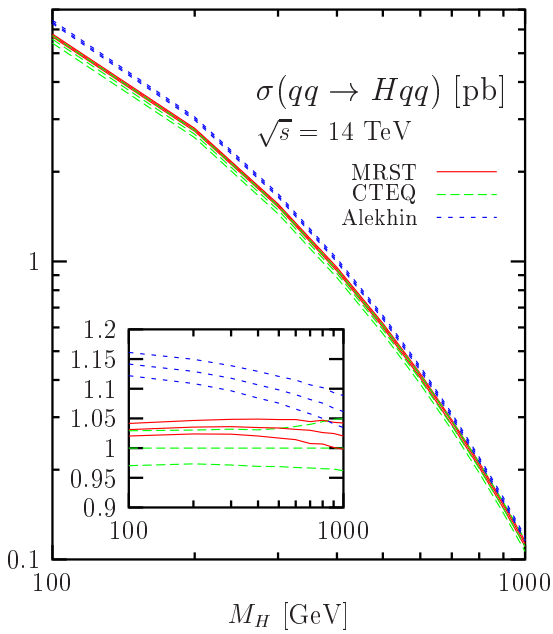

Figure 3.17: The CTEQ, MRST and Alekhin PDF uncertainty bands for the NLO cross section of the vector boson fusion process $pp \to Hqq$ at the LHC. In the insert is shown the spread uncertainty, when the cross sections are normalized to the default CTEQ PDF set; from Ref. [314].

3.3.5 The effective longitudinal vector boson approximation

Before closing this section, let us reconsider the total $pp \to Hqq$ production cross section in the light of the previous discussion. Following Ref. [245] and recalling that the transverse momenta of the scattered quarks are small, one may write the parton four–momenta as

$$p_{3/4} = \left(x_{3/4}E + p_{T3/4}^2/(2x_{3/4}E), \vec{p}_{T3/4}, \pm x_{3/4}E\right) \ , \ p_{1/2} = (E, \vec{0}, \pm E) \tag{3.44}$$

with E being half of the parton c.m. energy, and neglect terms of the order of $p_{T3,4}^2/E^2 \ll 1$ in the amplitude squared. On then immediately obtains for the invariants of eq. (3.23)

$$(p_1 \cdot p_2)(p_3 \cdot p_4) \simeq (p_1 \cdot p_4)(p_2 \cdot p_3) \simeq 4E^4 x_3 x_4 \tag{3.45}$$

leading to an amplitude squared for the process that is simply given by

$$|\mathcal{M}|^2 \ = \ \sqrt{2} N_c^f G_\mu^3 M_V^8 \frac{(C_+ + C_-)(x_3 x_4)^3 \hat{s}^2}{(p_{T3}^2 + x_3 M_V^2)^2 (p_{T4}^2 + x_4 M_V^2)^2} \tag{3.46}$$

The three–body phase space also simplifies to

$$\mathrm{dPS}_3 \simeq \frac{1}{8(2\pi)^5} \frac{\mathrm{d}x_3}{x_3} \frac{\mathrm{d}x_4}{x_4} \mathrm{d}^2\vec{p}_{T3} \mathrm{d}^2\vec{p}_{T4} \frac{2}{\hat{s}} \delta\left((1-x_3)(1-x_4) - \frac{M_H^2}{\hat{s}}\right) \tag{3.47}$$

The integrations on the transverse momenta can therefore be easily done, leading to

$$\int \frac{\mathrm{d}^2\vec{p}_{Ti}}{(p_{Ti}^2 + x_i M_V^2)^2} \simeq \pi \int_0^\infty \frac{\mathrm{d}p^2}{(p^2 + x_i M_V^2)^2} = \frac{\pi}{x_i M_V^2} \tag{3.48}$$

and, with the help of the delta function, the integrations on $x_{3,4}$ are straightforward. One finally obtains for the total partonic cross section

$$\hat{\sigma}_{\mathrm{LO}}(qq \to qqH) \simeq \frac{G_\mu^3 M_V^4 N_c}{128\sqrt{2}\pi^3} (C_+ + C_-) \left[\left(1 + \frac{M_H^2}{\hat{s}}\right) \log \frac{\hat{s}}{M_H^2} - 2 + 2\frac{M_H^2}{\hat{s}}\right] \tag{3.49}$$

This is nothing else than the cross section for Higgs boson production in the effective longitudinal vector boson approximation [31], where one calculates the cross section for the subprocess where the Higgs boson is produced in the fusion of $V_L V_L$ [which according to the equivalence theorem can be replaced by their corresponding Goldstone bosons] and then folds the result with the V_L spectra [243, 256, 349]. Since we will use this approximation in the course of our discussion, we briefly summarize its salient features.

Just as in the Weizsäcker–Williams approximation in the processes $e^+e^- \to e^\pm X$, where the final state X particle is produced at small angles through the exchange of a photon, and where the bulk of the production rate is described by the cross section $\hat{\sigma}$ for the subprocess $\gamma e^\pm \to X$ folded by the probability of the the initial e^+e^- state to radiate a photon [350]

$$\sigma(e^+e^- \to e^\pm X) = \int \mathrm{d}z P_{\gamma/e^\pm}(z) \hat{\sigma}(\hat{s} = zs) \ , \ P_{\gamma/e^\pm}(z) = \frac{\alpha}{2\pi} \frac{1 + (1-z)^2}{z} \log \frac{s}{m_e^2} \tag{3.50}$$

where $\sqrt{s}$ is the total c.m. energy and m_e the electron mass, the process $qq \to qqV^*V^* \to qqH$ at very high energies can be viewed as originating from the subprocess $VV \to H$ with the real vector bosons being radiated from the initial quarks. The only difference with the Weizsäcker–Williams approximation is that the W/Z bosons are massive and thus have a longitudinal degree of polarization. The distribution functions for the transverse and longitudinal polarizations in this case are given by

$$\begin{aligned} P_{V_\pm/q}(z) &= \frac{\alpha}{4\pi}\frac{1}{z}\left[(v_q \mp a_q)^2 + (v_q \pm a_q)^2(1-z)^2\right]\log\frac{\hat{s}}{M_V^2} \\ P_{V_L/q}(z) &= \frac{\alpha}{\pi}\frac{1-z}{z}\,(v_q^2 + a_q^2) \end{aligned} \tag{3.51}$$

One recovers the photon case in eq. (3.50) by appropriately replacing the quark weak charge by the electron electric charge, $v_q \to 1, a_q \to 0$. The VV luminosity in the process $VV \to X$

$$\left.\frac{\mathrm{d}\mathcal{L}}{\mathrm{d}\tau}\right|_{VV/qq} = \int_\tau^1 P_{V/q}(z)P_{V/q}(\tau/z)\frac{\mathrm{d}z}{z} \tag{3.52}$$

with $\tau = M_X^2/\hat{s}$ where $\hat{s}$ is the qq c.m. energy, is then given by

$$\begin{aligned} \left.\frac{\mathrm{d}\mathcal{L}}{\mathrm{d}\tau}\right|_{V_TV_T/qq} &= \frac{\alpha}{8\pi^3}(v_q^2+a_q^2)^2\frac{1}{\tau}\log\frac{\hat{s}}{M_V^2}\Big[(2+\tau)^2\log(1/\tau) - 2(1-\tau)(3+\tau)\Big] \\ \left.\frac{\mathrm{d}\mathcal{L}}{\mathrm{d}\tau}\right|_{V_LV_L/qq} &= \frac{\alpha}{4\pi^3}(v_q^2+a_q^2)^2\frac{1}{\tau}\Big[(1+\tau)\log(1/\tau) - 2(1-\tau)\Big] \end{aligned} \tag{3.53}$$

In principle, at high energies, the luminosity for transverse gauge bosons is much larger than for longitudinal ones because of the $\log^2(M_V^2/\hat{s})$ term. However, for large masses, the Higgs boson is produced in the subprocess $VV \to H$ mainly through the longitudinal components which give rates $\propto M_H^3$. The effective cross section in this case is simply given by

$$\sigma_{\text{eff}} = \frac{16\pi^2}{M_H^3}\,\Gamma(H \to V_LV_L)\,\left.\frac{\mathrm{d}\mathcal{L}}{\mathrm{d}\tau}\right|_{V_LV_L/qq} \tag{3.54}$$

which, when the expression of the luminosity is inserted reproduces the result of eq. (3.49).

In the case of the partonic process [at the hadronic level, a difference is generated by the parton densities], the contribution of the WW fusion channel is one order of magnitude larger than the one of the ZZ channel because of the larger charged current couplings. However, in practice, the effective longitudinal approximation approaches the exact result only by a factor 2 to 5, depending on the considered c.m. energy and the Higgs mass. For light Higgs bosons, it can be improved by including the transverse vector boson components, see Ref. [351]. This approximation should therefore be used only as an indication of the order of magnitude of the cross sections.

3.4 The gluon–gluon fusion mechanism

3.4.1 The production cross section at LO

Higgs production in the gluon–gluon fusion mechanism is mediated by triangular loops of heavy quarks. In the SM, only the top quark and, to a lesser extent, the bottom quark will contribute to the amplitude. The decreasing Hgg form factor with rising loop mass is counterbalanced by the linear growth of the Higgs coupling with the quark mass. In this section we discuss the analytical features of the process. The relevant phenomenological aspects at the LHC [242, 315, 352–357] and the Tevatron [358–360] will be presented in §3.7.

To lowest order, the partonic cross section can be expressed by the gluonic width of the Higgs boson discussed in §2.3.3,

$$\hat{\sigma}_{\rm LO}(gg \to H) \;=\; \sigma_0^H\, M_H^2\, \delta(\hat{s} - M_H^2) \;=\; \frac{\pi^2}{8M_H}\, \Gamma_{\rm LO}(H \to gg)\, \delta(\hat{s} - M_H^2) \tag{3.55}$$

where $\hat{s}$ is the gg invariant energy squared. Substituting in this LO approximation the Breit–Wigner form of the Higgs boson width, in place of the zero–width δ distribution

$$\delta(\hat{s} - M_H^2) \to \frac{1}{\pi}\, \frac{\hat{s}\Gamma_H/M_H}{(\hat{s} - M_H^2)^2 + (\hat{s}\Gamma_H/M_H)^2} \tag{3.56}$$

recalling the lowest–order two–gluon decay width of the Higgs boson, one finds for the cross section [185]

$$\sigma_0^H = \frac{G_\mu \alpha_s^2(\mu_R^2)}{288\sqrt{2}\pi} \left| \frac{3}{4} \sum_q A_{1/2}^H(\tau_Q) \right|^2 \tag{3.57}$$

The form factor $A_{1/2}^H(\tau_Q)$ with $\tau_Q = M_H^2/4m_Q^2$ is given in eq. (2.46) and is normalized such that for $m_Q \gg M_H$, it reaches $\frac{4}{3}$ while it approaches zero in the chiral limit $m_Q \to 0$.

The proton–proton cross section at LO in the narrow–width approximation reads

$$\sigma_{\rm LO}(pp \to H) = \sigma_0^H \tau_H \frac{d\mathcal{L}^{gg}}{d\tau_H} \quad \text{with} \quad \frac{d\mathcal{L}^{gg}}{d\tau} = \int_\tau^1 \frac{dx}{x}\, g(x, \mu_F^2) g(\tau/x, \mu_F^2) \tag{3.58}$$

where the Drell–Yan variable is defined as usual by $\tau_H = M_H^2/s$ with s being the invariant collider energy squared. The expression of the luminosity $\tau_H d\mathcal{L}^{gg}/d\tau_H$ is only mildly divergent for $\tau_H \to 0$.

The total hadronic cross sections at LO are shown in Fig. 3.18 as a function of the Higgs boson mass for the LHC and the Tevatron energies. We have chosen $m_t = 178$ GeV, $m_b = 4.88$ GeV and $\alpha_s(M_Z) = 0.13$ as inputs and used the CTEQ parametrization for the parton densities. For the Tevatron, the cross section is monotonically decreasing with the Higgs boson mass, starting slightly below 1 pb for $M_H \sim 100$ GeV and reaching $\sigma \sim 0.01$ pb for $M_H \sim 300$ GeV. At the LHC, the cross section is two orders of magnitude larger, being

at the level of $\sim$ 30 pb for $M_H \sim 100$ GeV and is still sizable, $\sigma \sim 1$ pb, for $M_H \sim 700$ GeV. There is a kink at $M_H \sim 350$ GeV, i.e. near the $t\bar{t}$ threshold where the Hgg amplitude develops an imaginary part.

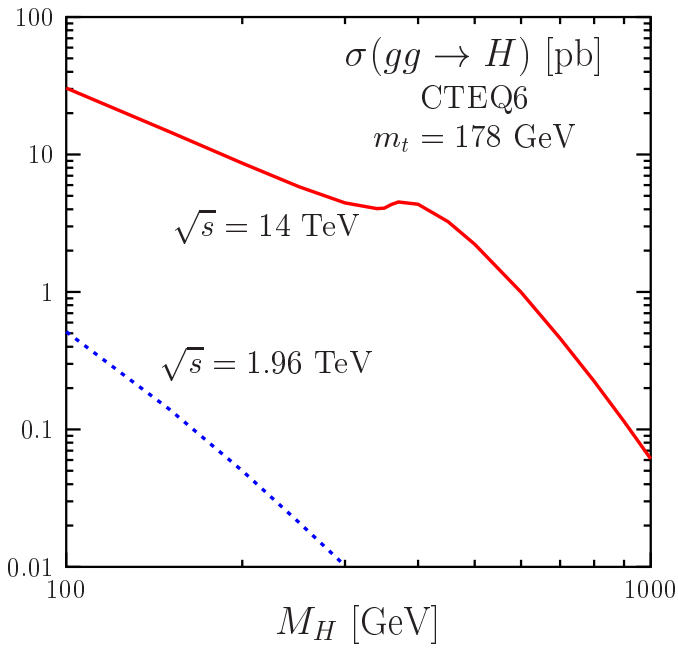

Figure 3.18: The hadronic production cross section for the gg fusion process at LO as a function of M_H at the LHC and the Tevatron. The inputs are $m_t = 178$ GeV, $m_b = 4.88$ GeV, the CTEQ set of PDFs has been used and the scales are fixed to $\mu_R = \mu_F = M_H$.

As discussed in §2.3.3, the cross section in the case where the internal quark is assumed to have an infinite mass, $m_q \to \infty$, i.e. when the form factor $\frac{3}{4}A^H_{1/2}$ is equal to unity, is a rather good approximation for Higgs masses below the $t\bar{t}$ threshold, and it reproduces the exact result at the level of 10%. For low Higgs masses, the difference is in fact due to the contribution of the bottom quark loop: although the b–quark mass is small, the form factor $A^H_{1/2}(\tau_b)$ exhibits a dependence on $m_b^2/M_H^2 \times \log^2(m_b^2/M_H^2)$ which is not that small. Together with the π^2 terms and the imaginary part, the b–quark loop generates a non–negligible contribution which interferes destructively with the contribution of the top–quark loop. Above the $t\bar{t}$ threshold, $M_H \gtrsim 350$ GeV, the approximation of an infinite loop quark mass fails since it cannot reproduce the imaginary part of the form factor.

3.4.2 The cross section at NLO

To incorporate the QCD corrections to $\sigma(pp \to H + X)$, one has to consider the processes

$$gg \to H(g) \quad \text{and} \quad gq \to Hq, \quad q\bar{q} \to Hg \tag{3.59}$$

Characteristic diagrams of the QCD radiative corrections are shown in Fig. 3.19. They involve the virtual corrections to the $gg \to H$ subprocess, which modify the LO fusion cross section by a coefficient linear in α_s, and the radiation of gluons in the final state. In addition, Higgs bosons can be produced in gluon–quark collisions and quark–antiquark annihilation which contribute to the cross section at the same order of α_s.

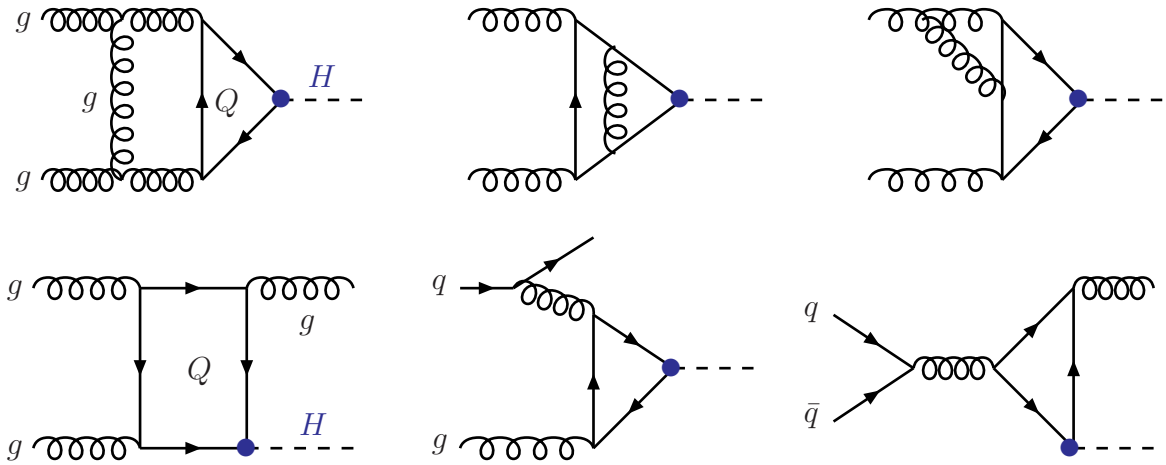

Figure 3.19: Typical diagrams for the virtual and real QCD corrections to $gg \to H$.

The cross sections for the subprocesses $ij \to H + X$, $i, j = g, q, \overline{q}$, can be written as

$$\hat{\sigma}_{ij} = \sigma_0 \left\{ \delta_{ig}\delta_{jg} \left[1 + C^H(\tau_Q)\frac{\alpha_s}{\pi} \right] \delta(1-\hat{\tau}) + D^H_{ij}(\hat{\tau}, \tau_Q)\frac{\alpha_s}{\pi}\Theta(1-\hat{\tau}) \right\} \tag{3.60}$$

where the new scaling variable $\hat{\tau}$, supplementing $\tau_H = M_H^2/s$ and $\tau_Q = M_H^2/4m_Q^2$ introduced earlier, is defined at the parton level as $\hat{\tau} = M_H^2/\hat{s}$; Θ is the step function.

The coefficients $C^H(\tau_Q)$ and $D^H_{ij}(\hat{\tau}, \tau_Q)$ have been determined in Refs. [180,286] for arbitrary Higgs boson and quark masses and the lengthy analytical expressions have been given there [see also §2.3.3 for some details on the calculation and on the renormalization scheme]. If all the corrections eq. (3.60) are added up, ultraviolet and infrared divergences cancel. However collinear singularities are left over and are absorbed into the renormalization of the parton densities [84, 325] where the $\overline{\text{MS}}$ factorization scheme can be adopted.

The final result for the hadronic cross section at NLO can be cast into the form

$$\sigma(pp \to H + X) = \sigma_0^H \left[1 + C^H \frac{\alpha_s}{\pi} \right] \tau_H \frac{d\mathcal{L}^{gg}}{d\tau_H} + \triangle\sigma^H_{gg} + \triangle\sigma^H_{gq} + \triangle\sigma^H_{q\overline{q}} \tag{3.61}$$

The coefficient C^H denotes the contributions from the virtual two–loop quark corrections regularized by the infrared singular part of the cross section for real gluon emission. It splits into the infrared term π^2, a term depending on the renormalization scale μ_R of the coupling

constant, and a piece c^H which depends on the mass ratio τ_Q.

$$C^H = \pi^2 + c^H + \frac{33-2N_f}{6}\log\frac{\mu_R^2}{M_H^2} \tag{3.62}$$

with

$$c^H = \mathrm{Re}\sum_Q A^H_{1/2}(\tau_Q)\, c^H_Q(\tau_Q) / \sum_Q A^H_{1/2}(\tau_Q) \tag{3.63}$$

The (non–singular) contributions from gluon radiation in gg scattering, from gq scattering and $q\overline{q}$ annihilation, depend on the renormalization scale μ_R and the factorization scale μ_F of the parton densities

$$\begin{aligned}
\triangle\sigma^H_{gg} &= \int_{\tau_H}^1 d\tau \frac{d\mathcal{L}^{gg}}{d\tau}\frac{\alpha_s(\mu_R)}{\pi}\sigma_0^H \left\{ -zP_{gg}(z)\log\frac{\mu_F^2}{\tau s} + d^H_{gg}(z,\tau_Q) \right. \\
&\qquad \left. +12\left[\left(\frac{\log(1-z)}{1-z}\right)_+ - z\left[2-z(1-z)\right]\log(1-z)\right]\right\} \\
\triangle\sigma^H_{gq} &= \int_{\tau_H}^1 d\tau \sum_{q,\overline{q}} \frac{d\mathcal{L}^{gq}}{d\tau}\frac{\alpha_s(\mu_R)}{\pi}\sigma_0^H \left\{ \left[-\frac{1}{2}\log\frac{\mu_F^2}{\tau s} + \log(1-z)\right] zP_{gq}(z) + d^H_{gq}(z,\tau_Q)\right\} \\
\triangle\sigma^H_{q\overline{q}} &= \int_{\tau_H}^1 d\tau \sum_{q} \frac{d\mathcal{L}^{q\overline{q}}}{d\tau}\frac{\alpha_s(\mu_R)}{\pi}\sigma_0^H d^H_{q\overline{q}}(z,\tau_Q)
\end{aligned} \tag{3.64}$$

with $z = \tau_H/\tau$ and the standard Altarelli–Parisi splitting functions given by

$$\begin{aligned}
P_{gg}(z) &= 6\left[\left(\frac{1}{1-z}\right)_+ + \frac{1}{z} - 2 + z(1-z)\right] + \frac{33-2N_f}{6}\,\delta(1-z) \\
P_{gq}(z) &= \frac{4}{3}\frac{1+(1-z)^2}{z}
\end{aligned} \tag{3.65}$$

where F_+ denotes the usual + distribution such that $F(\hat\tau)_+ = F(\hat\tau) - \delta(1-\hat\tau)\int_0^1 \mathrm{d}\hat\tau' F(\hat\tau')$.

The coefficients d^H_{gg}, d^H_{gq} and $d^H_{q\overline{q}}$, as well as c^H, have been evaluated for arbitrary quark masses [180, 188, 286]. In the limit where the Higgs mass is very large compared with the quark mass, $\tau_Q = M_H^2/4m_Q \gg 1$, as is the case of the bottom quark contribution, a compact analytic result can be derived, which is valid to leading and subleading logarithmic accuracy

$$\begin{aligned}
c^H(\tau_Q) &\to \frac{5}{36}\left[\log^2(4\tau_Q) - \pi^2\right] - \frac{4}{3}\log(4\tau_Q) \\
d^H_{gg}(\hat\tau,\tau_Q) &\to -\frac{2}{5}\log(4\tau_Q)\left[7 - 7\hat\tau + 5\hat\tau^2\right] - 6\log(1-\hat\tau)\left[1-\hat\tau+\hat\tau^2\right] \\
&\quad +2\frac{\log\hat\tau}{1-\hat\tau}\left[3 - 6\hat\tau - 2\hat\tau^2 + 5\hat\tau^3 - 6\hat\tau^4\right] \\
d^H_{gq}(\hat\tau,\tau_Q) &\to \frac{2}{3}\left[\hat\tau^2 - \left(1+(1-\hat\tau)^2\right)\left(\frac{7}{15}\log(4\tau_Q) + \log\left(\frac{1-\hat\tau}{\hat\tau}\right)\right)\right] \\
d^H_{q\overline{q}}(\hat\tau,\tau_Q) &\to 0
\end{aligned} \tag{3.66}$$

In the limit of large quark masses, $\tau_Q = M_H^2/4m_Q^2 \ll 1$, as is the case for the top quark when the Higgs mass is small, one also obtains very simple expressions for the coefficients

$$c^H(\tau_Q) \to \frac{11}{2}\,,\; d_{gg}^H \to -\frac{11}{2}(1-z)^3\,,\; d_{gq}^H \to -1+2z-\frac{1}{3}z^2\,,\; d_{q\bar{q}}^H \to \frac{32}{27}(1-z)^3 \qquad (3.67)$$

In this heavy quark case, the corrections of $\mathcal{O}(M_H^2/m_Q^2)$ in a systematic Taylor expansion have been shown to be very small [189]. In fact, the leading term provides an excellent approximation up to the quark threshold $M_H \sim 2m_Q$.

The results for the K–factors, defined as the ratios $K_{\rm tot} = \sigma_{\rm NLO}/\sigma_{\rm LO}$, with the cross section $\sigma_{\rm NLO}$ normalized to the LO cross section $\sigma_{\rm LO}$, evaluated consistently for parton densities and an α_s value at LO, are displayed in Fig. 3.20 as a function of M_H for the LHC (left) and the Tevatron (right). Again the CTEQ6 parametrization for the structure functions defined in the $\overline{\rm MS}$ scheme is used and the top and bottom quark pole masses are fixed to $m_t = 178$ GeV and $m_b = 4.88$ GeV. Both the renormalization and the factorization scales have been set to the Higgs mass $\mu_R = \mu_F = M_H$.

The K–factors have been decomposed into their various components: $K_{\rm virt}$ accounts for the virtual corrections after regularization [corresponding to the coefficient C^H], while K_{ij} with $i,j = g,q,\bar{q}$ stand for the real corrections in the three channels given in eq. (3.64). One sees that $K_{\rm virt}$ and K_{gg} are rather large, being both of the order of 50%, while $K_{q\bar{q}}$ and K_{gq} are tiny, the latter being negative. The total K–factor is large, increasing the total production cross section by about 60% and 90% for the low and high range of the Higgs mass at the LHC and by a factor 2.2 to 2.8 for $M_H = 100$–300 GeV at the Tevatron.

Apart for the small kink in the $M_H \sim 2m_t$ threshold region, $K_{\rm tot}$ is only mildly depending on the Higgs mass. In fact, if one compares the exact numerical results for the cross section at NLO with the approximation of a very heavy top quark, it turns out that multiplying the LO cross section, which includes the full m_t and m_b dependence, with the K–factor taken in the asymptotic limit $m_t \to \infty$ and where the b–quark contribution has been neglected, provides a good approximation

$$\sigma_{\rm NLO} \simeq K_{\rm tot}|_{m_t\to\infty} \times \sigma_{\rm LO}(\tau_t,\tau_b) \qquad (3.68)$$

The difference between this approximation and the exact result is less than 10% even for Higgs boson masses beyond the $M_H = 2m_t$ threshold and up to $M_H \sim 700$ GeV [361].

Finally, note that the two–loop electroweak corrections to the $gg \to H$ production cross section are the same as the ones discussed previously in §2.4.3 for the decay $H \to gg$. While the top quark correction is rather small, being less than one percent [201], the light fermion electroweak contributions [203, 204] are much larger in the $M_H \lesssim 2M_W$ range where they reach the level of 5–9%; for $M_H \gtrsim 2M_W$ these corrections become again very small.

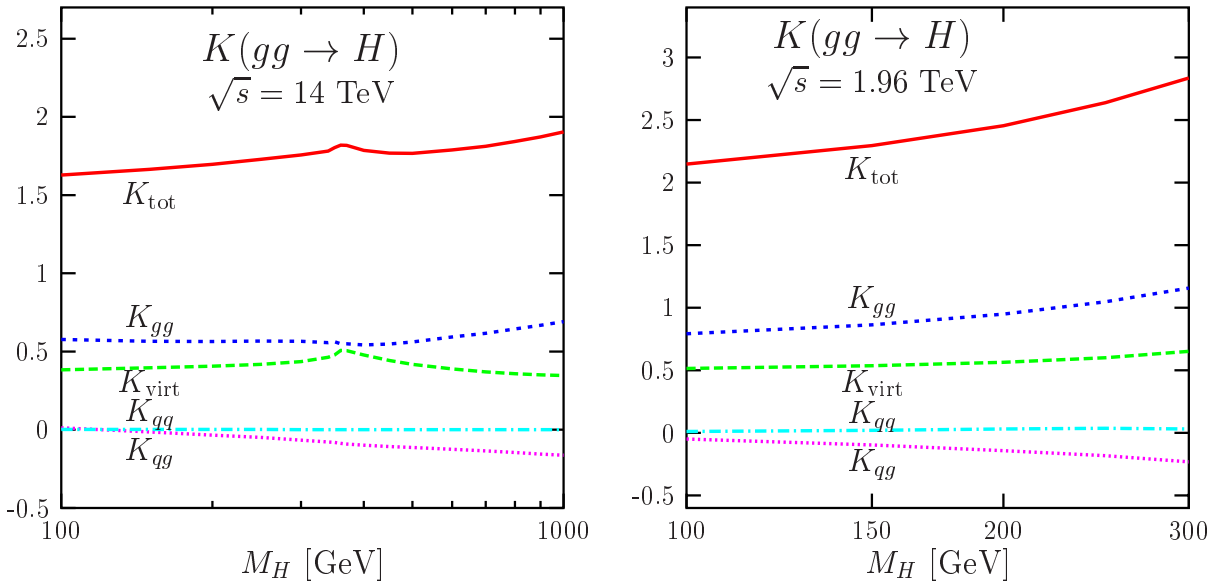

Figure 3.20: The total K factor and its various components, $K_{\rm virt}$, K_{gg} and $K_{q\bar{q}}$, for Higgs production in the gg fusion process as a function of M_H at the LHC (left) and the Tevatron (right). The CTEQ6 parton densities have been adopted and the renormalization and factorization scales are fixed to $\mu_R = \mu_F = M_H$; $m_t = 178$ GeV and $m_b = 4.88$ GeV.

Dependence on the PDFs

The central values and the uncertainty band limits of the NLO cross sections are shown for the CTEQ, MRST and Alekhin parameterizations in Fig. 3.21 for the $gg \to H$ process. As usual, in the inserts to these figures, we show the spread uncertainties in the predictions for the cross sections, when normalized to the prediction of the reference CTEQ6M set.

At the LHC, the uncertainty band for the CTEQ set of PDFs decreases from the level of about 5% at $M_H \sim 100$ GeV, down to the 3% level at $M_H \sim 300$ GeV. This is because Higgs bosons with relatively small masses are mainly produced by asymmetric low–x–high–x gluons with a low effective c.m. energy. To produce heavier Higgs bosons, a symmetric process in which the participation of intermediate–x gluons with high density is needed, resulting in a smaller uncertainty band. At higher masses, $M_H \gtrsim 300$ GeV, the participation of high–x gluons becomes more important, and the uncertainty band increases to reach the 10% level at Higgs masses of about 1 TeV. At the Tevatron, because of the smaller c.m. energy, the high–x gluon regime is already reached for low Higgs masses and the uncertainties increase from 5% to 15% for M_H varying between 100 GeV and 200 GeV. As discussed previously and shown in Fig. 3.2, the MRST gluon PDF is smaller than the CTEQ one for low x and larger for relatively high x (~ 0.1): this explains the increasing cross section obtained with MRST compared to the one obtained with CTEQ, for increasing Higgs masses at the LHC. At the Tevatron the gluons are already in the high–x regime.

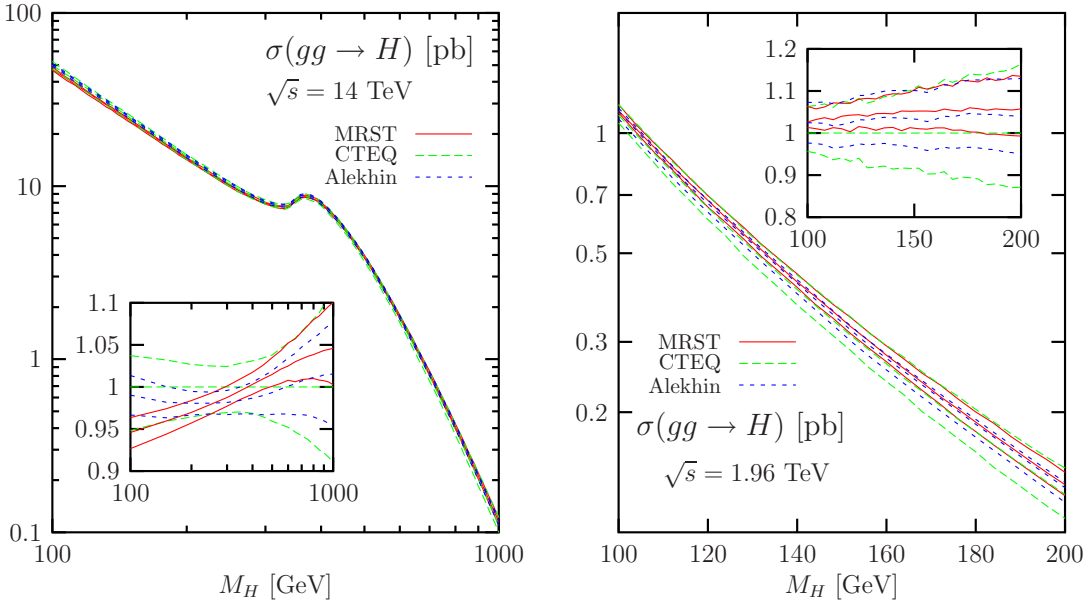

Figure 3.21: The CTEQ, MRST and Alekhin PDF uncertainty bands for the NLO $gg \to H$ cross sections at the LHC (left) and Tevatron (right). The inserts show the spread in the predictions, when the NLO cross sections are normalized to the CTEQ6 reference set [314].

The variation of the cross section with the renormalization and factorization scales will be discussed later after inclusion of the NNLO corrections to which we turn now.

3.4.3 The cross section beyond NLO in the heavy top quark limit

The calculation at NNLO

Recently, the very complicated three–loop NNLO QCD corrections to the $gg \to H$ fusion process have been calculated by three different groups [300–302] in the limit of a very heavy top quark. In this limit, the Feynman diagrams contributing to the process factorize into two pieces: a massive component where the heavy quark has been integrated out and which represents an effective coupling constant which multiplies the Hgg vertex, and a massless component involving only gluons and light quarks, which describes the short distance effects and where the finite momenta of the particles have to be taken into account. The calculation effectively reduces then to a two–loop calculation with massless particles.

However, many Feynman diagrams, some of which are displayed in Fig. 3.22, have to be evaluated at this order and they can be cast into three categories [which lead to more than one thousand square and interference terms] besides the one–loop squared contribution: *a*) two loop virtual corrections for the process $gg \to H$ which have to be multiplied by the effective Born amplitude; *b*) one loop single real emission diagrams for the $gg \to Hg$, $gq \to Hq$ and $q\bar{q} \to Hg$ processes, which have to be multiplied by the Born amplitude for the same processes; *c*) tree–level double real emission diagrams for the processes $gg \to Hgg$, $gg \to Hq\bar{q}$, $gq \to Hgq$, $qq \to Hqq$ and $q\bar{q} \to Hq\bar{q}$, which have to be squared.

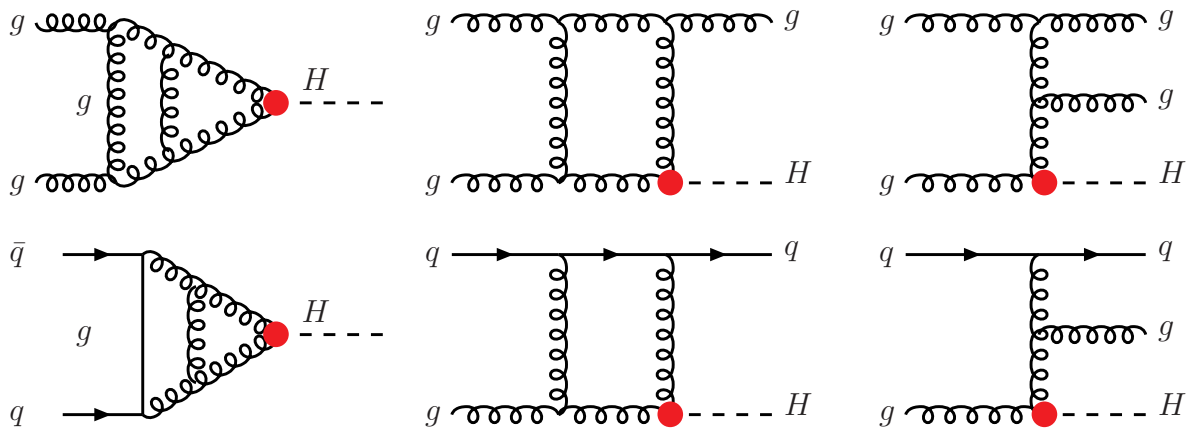

Figure 3.22: Typical diagrams for the QCD corrections to $gg \to H$ at NNLO in the heavy quark limit. ● denotes the effective Hgg vertex where the quark has been integrated out.

This *tour de force* has been made possible thanks to two simplifying features: the possibility of using the low energy theorem discussed in §2.4.1, which allows to calculate the corrections to the effective Hgg vertex, and the development of new techniques [362] to evaluate massless three–point functions at the two–loop level in complete analogy to massless three–loop propagator diagrams which are standard and can be done fully automatically.

As already discussed in §2.4.3, the NNLO QCD corrected Hgg effective operator in the heavy quark limit, $\mathcal{L}_{\rm eff}(Hgg)$, can be obtained [21,206,361] by means of the low–energy theorem, eq. (2.91). This operator does not describe the Hgg interaction in total: it accounts only for the interactions mediated by the heavy quarks directly, but it does not include the interactions of the light fields. It must be added to the light–quark and gluon part of the basic QCD Lagrangian, i.e. the effective coupling has to be inserted into the blobs of the effective two–loop diagrams shown in Fig. 3.22. The NNLO corrections to inclusive Higgs production in $gg \to H$ can be cast then into the three categories which have been already encountered when we discussed the NLO case. In terms of the variable $\hat{\tau}$ defined as $\hat{\tau} = M_H^2/\hat{s}$, one has δ function terms $\propto \delta(1-\hat{\tau})$, large logarithms of the form $\log^n(1-\hat{\tau})/(1-\hat{\tau})$, and hard scattering terms that have at most a logarithmic singularity in the limit $\hat{\tau} \to 1$

$$\hat{\sigma}_{ij}^{(2)} = a^{(2)}\delta(1-\hat{\tau}) + \sum_{k=0}^{3} b_k^{(2)} \mathcal{D}_k(\hat{\tau}) + \sum_{l=0}^{\infty}\sum_{k=0}^{3} c_{lk}^{(2)} (1-\hat{\tau})^l \ell^k \tag{3.69}$$

where $\ell_k = \log^k(1-\hat{\tau})$ and $\mathcal{D}_k(\hat{\tau})$, with now $i = 1,2,3$, are the usual + distributions defined earlier. The virtual corrections [363], which are of course UV finite when all contributions are added up, and in particular the coefficient function C_g of the Hgg effective operator contribute only to the coefficient $a^{(2)}$ in front of the delta function [363,364]. The soft corrections to the $gg \to H$ cross section, i.e. when the momenta of the final state gluons or quarks tend to zero, contribute to both the $a^{(2)}$ and $b^{(2)}$ terms; they have been evalu-

ated in Refs. [365, 366] and, when added to the virtual corrections, the infrared divergences cancel out after mass factorization. The combination of the virtual+soft with the collinear terms $\propto \ell^3$ gives the "soft+subleading" [365] or "soft+virtual+collinear corrections" [366] approximations which include also the contributions to the coefficient $c_{03}^{(2)}$ which has been evaluated in Ref. [361] using resummation techniques.

The remaining pieces which have to be evaluated at NNLO [300] are then the coefficients $c_{lk}^{(2)}$ with $k = 0, \cdots 3$ and $l \geq 0$ which receive contributions from all sub–processes. One can perform this calculation by making a systematic expansion of the partonic cross section around the soft limit $\hat{\tau} \sim 1$, leading to a series in $(1-\hat{\tau})^n$ whose coefficients depend on $\ell^n \equiv \log^n(1-\hat{\tau})$ with $n = 0, 1, 2, 3$ at NNLO. However, because the bulk of the cross section is at the threshold $\hat{\tau} \to 1$, the series converges very rapidly and it is sufficient to keep only the contributions of the terms up to order $(1-\hat{\tau})^1$. The convergence can be improved [367] by pulling out a factor $\hat{\tau}$ before expanding in $(1-\hat{\tau})$. In practice, the expansion to order $(1-\hat{\tau})^1$ reproduces the exact result, with all terms up to order $(1-\hat{\tau})^{16}$ or equivalently with the exact calculation as performed in Refs. [301, 302], with an accuracy of order 1%.

This approach leads to a rather simple analytical result. Summing the soft and hard contributions, one obtains the following partonic cross sections up to NNLO [we display the LO and NLO contributions for completeness] in the various production channels, normalized to $\sigma_0^H = G_\mu \alpha_s^2/(288\sqrt{2}\pi)$ introduced before and using $\ell_H = \log(M_H^2/m_t^2)$ [300]

$$
\begin{aligned}
\hat{\sigma}_{gg}^{(2)} &= \delta(1-\hat{\tau}) + \frac{\alpha_s}{\pi}\Big[15.37\,\delta(1-\hat{\tau}) + 6 - 24\ell - 9(1+4\ell)(1-\hat{\tau}) + 12\mathcal{D}_1(\hat{\tau})\Big] \\
&+ \left(\frac{\alpha_s}{\pi}\right)^2 \Big[87.76\,\delta(1-\hat{\tau}) + 5.71\ell_H - 531.134 + 39.92\ell + 185.5\ell^2 + 144\ell^3 \\
&\qquad +(632.06 + 632.87\ell - 559.58\ell^2 + 216\ell^3)(1-\hat{\tau}) \\
&\qquad +222.91\mathcal{D}_0(\hat{\tau}) - 31.71\mathcal{D}_1(\hat{\tau}) - 23\mathcal{D}_2(\hat{\tau}) + 72\mathcal{D}_3(\hat{\tau})\Big] \\
\hat{\sigma}_{qg}^{(2)} &= \frac{2}{3}\frac{\alpha_s}{\pi}\Big[1 + 2\ell - (1-\hat{\tau})\Big] \\
&+ \left(\frac{\alpha_s}{\pi}\right)^2 \Big[29.93 + 6.47\ell + 2.63\ell^2 + 6.79\ell^3(-40.19 + 50.33\ell - 16.5\ell^2)(1-\hat{\tau})\Big] \\
\hat{\sigma}_{qq}^{(2)} &= \left(\frac{\alpha_s}{\pi}\right)^2 \Big[-0.70 - 1.78\ell + 1.78\ell^2\Big]
\end{aligned}
\tag{3.70}
$$

where the scale dependence has been explicitly suppressed by setting the factorization and renormalization scales to $\mu_R = \mu_F = M_H$ [the dependence can be reconstructed by requiring the total cross section to be scale invariant] and the number of light quarks has been set to $N_f = 5$. The component $\hat{\sigma}_{qq}^{(2)}$ denotes the flavor singlet and non–singlet contributions in both the channels qq and $q\bar{q} \to H + X$, the contributions of which are equal at order $(1-\hat{\tau})$

$$
\hat{\sigma}_{qq,S}^{(2)} = \hat{\sigma}_{qq,NS}^{(2)} = \hat{\sigma}_{q\bar{q},S}^{(2)} = \hat{\sigma}_{q\bar{q},NS}^{(2)} \tag{3.71}
$$

The K–factors and the scale dependence up to NNLO

The cross sections $\sigma(pp \to H + X)$ at the three orders LO, NLO and NNLO, are shown in Fig. 3.23 at the LHC and the Tevatron as a function of the Higgs mass, using the MRST parton distributions which include the approximated NNLO PDFs. The factorization and renormalization scales are set to $\mu_R = \mu_F = \frac{1}{2}M_H$ (upper curves) and $\mu_R = \mu_F = 2M_H$ (lower curves). To improve the heavy quark approximation, the LO cross section contains the full top mass dependence where $m_t = 175$ GeV has been used. Considering first the relative magnitude of the cross sections at the different orders of perturbation theory, one can see that while from LO to NLO, the cross section increases at the LHC by 70% for moderate Higgs boson masses, the increase from NLO to NNLO of about 30%, is more modest. This explicitly shows the nice convergence behavior of the perturbative series. The K–factors are larger at the Tevatron, since they increase the cross section by a factor of about three at NNLO, the bulk of which is provided by the NLO correction.

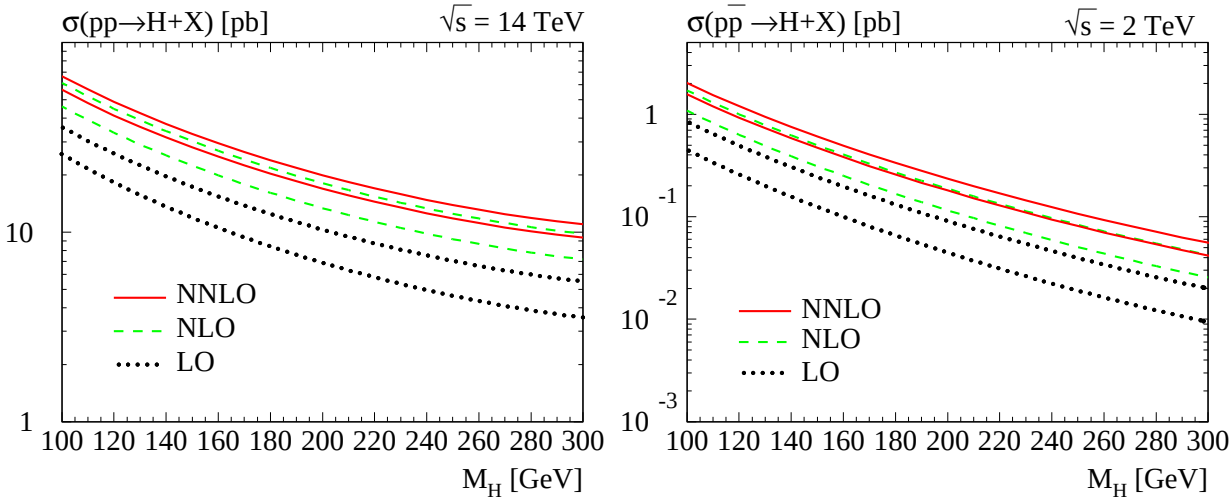

Figure 3.23: The cross sections for Higgs production in the $gg \to H + X$ fusion mechanism at the LHC (left) and Tevatron (right) at LO (dotted), NLO (dashed) and NNLO (solid) for two factorization and renormalization scales: $\mu_R = \mu_F = \frac{1}{2}M_H$ (upper curves) and $\mu_R = \mu_F = 2M_H$ (lower curves). The MRST PDFs are used; from Ref. [368].

When considering the effect of the variation of the renormalization and factorization scales on the cross section, by multiplying and dividing by a factor of two the median scale $\mu_F = \mu_R = M_H$, one first sees that globally, the scale dependence is reduced when going from LO, to NLO and then to NNLO. The residual scale dependence at NNLO is 25% at the LHC and 15% at the Tevatron, a factor two and a factor of four smaller than the dependence on the scale choice, at respectively, NLO and LO.

It has been noticed in Refs. [303, 368] that at the LHC the dependence on the renormalization and factorization scales have different signs: the cross section increases (decreases)

with increasing $\mu_F\,(\mu_R)$ values when the other scale is fixed, to $\mu_R\,(\mu_F) = M_H$ for instance [at the Tevatron the dependence on μ_R and μ_F go the same direction]; the decrease with μ_R is much stronger. It is thus more appropriate to choose smaller values for the scale than the standard choice $\mu_R = \mu_R = M_H$. This is shown in Fig. 3.24 where the scales are varied within a factor $\frac{1}{4}$ and 4 with respect to the default scale $\mu_F = \mu_R = M_H = 115$ GeV, first collectively and then by varying $\mu_F\,(\mu_R)$ while the other scale is fixed at the default value.

With the choice $\mu_R = \mu_F = \frac{1}{2}M_H$ e.g., the NLO correction increases while the NNLO correction decreases, with a total cross section which increases compared to the choice $\mu_R = \mu_F = M_H$. Therefore, since the difference between the NLO and NNLO contributions is small, the convergence of the perturbative series is improved for $\mu_R = \mu_F = \frac{1}{2}M_H$. This choice is supported by the fact that these fixed order results are in a better agreement with recent estimates of the cross section with a resummation of the dominant corrections which are due the contribution near the threshold $\hat{\tau} \to 1$ to which we turn now.

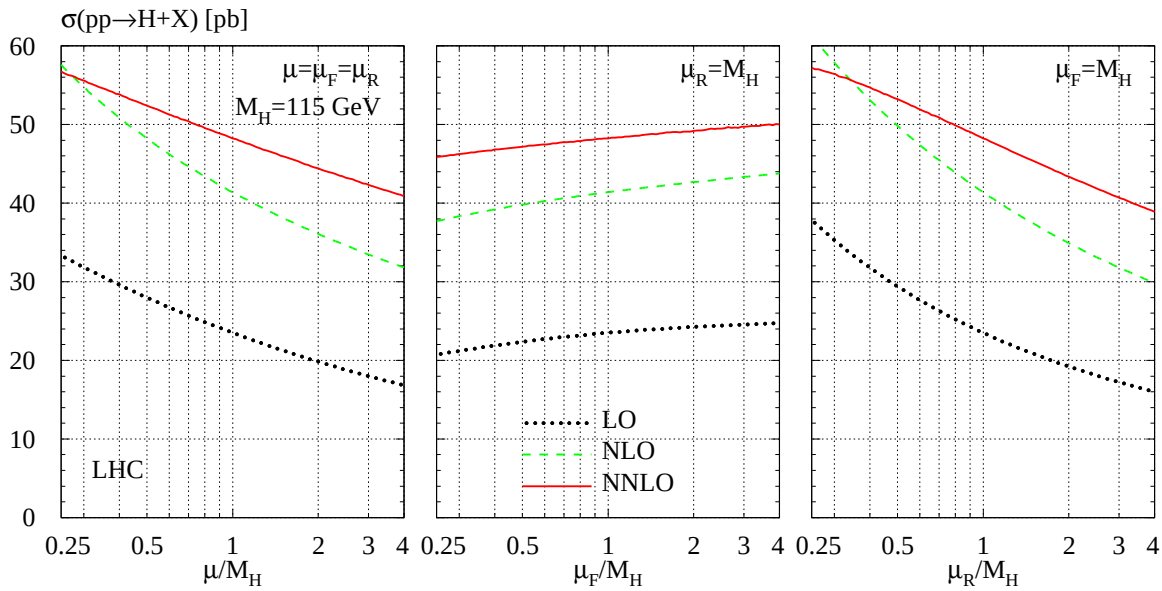

Figure 3.24: The scale dependence of $\sigma(gg \to H)$ at LHC for $M_H = 115$ GeV: variation of $\mu \equiv \mu_R = \mu_F$ (left), μ_F with $\mu_R = M_H$ (center) and μ_R with $\mu_F = M_H$ (right); from [368].

The soft–gluon resummation up to NNLL

As mentioned when we discussed the necessary ingredients to perform the $gg \to H$ calculation at NNLO, the corrections to the cross section, eq. (3.60), fall into three categories: virtual and soft corrections which generate the $\delta(1-\hat{\tau})$ terms and the $\mathcal{D}_k$ distributions, collinear logarithmic contributions that are controlled by the regular part of the Altarelli–Parisi splitting kernels and the hard scattering terms. The soft gluon corrections contribute to the most singular terms above and they involve only the gg initial state which, as already seen at NLO, is the channel where the most important part of the correction originates from.

The soft gluon contributions in the $gg \to H$ process can be resummed up to the next–to–next–to–leading logarithm (NNLL) order in the heavy top quark limit [303], that is, all large logarithmic terms $\alpha_s^n \log^m(1-\hat{\tau})$ in the + distributions with $1 \leq m \leq 2n$ in the limit $\hat{\tau} \to 1$ can be exponentiated. The resummation relies on the basic factorization theorem for partonic cross sections into soft, collinear and hard parts near the phase–space boundary [369], and can be performed in the Mellin or N–moment space [370] for instance. The formalism and the calculation's technique have been presented in detail in Refs. [303, 361].

The resummation of the logarithms in the soft gluon contributions is formally justified only near the thresholds $\hat{\tau} \to 1$. However, it can be used away from the threshold and the expectation is that the soft+virtual corrections, eventually supplemented by the collinear parton radiation (SVC), is a good approximation of the exact result for the cross section. Indeed, owing to the suppression of the gluon densities at large x, the partonic c.m. energy $\sqrt{\hat{s}}$ is much smaller than the c.m. energy of the hadron collider, $s = x_1 x_2 \hat{s}$, and the dominant value of $\hat{\tau}$ which appears in the hard scattering terms of the partonic cross section can be close to unity also when $\sqrt{s}$ is not close to M_H [366,367]. This has been verified both at NLO and NNLO: SVC approximates the exact result quite well, in particular at LHC energies.

The results for the resummed cross sections, in terms of the K–factors, are shown in Fig. 3.25 for the LHC as a function of M_H, for the LL, NLL and NNLL approximations (right) and are compared with the fixed order results at LO, NLO and NNLO (left). The bands result from a scale variation $\frac{1}{2}M_H \leq \mu_{F,R} \leq 2M_H$. One can note that the scale dependence after resummation is smaller than at fixed order and that, at NNLO, the resummation increases the central value of the cross section by $\sim 5\%$ in the low Higgs mass range.

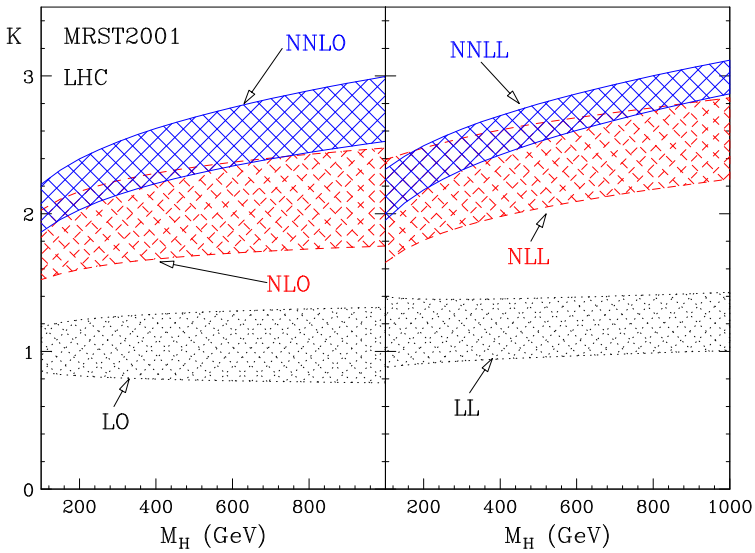

Figure 3.25: Fixed order (left) and resummed (right) K–factors for $gg \to H + X$ at the LHC as a function of M_H. The MRST2001 parton distributions have been used; from Ref. [303].

3.4.4 The distributions and Higgs + n jet production

The transverse momentum and rapidity distributions

At leading order, the Higgs boson produced in the fusion process $gg \to H$ has no transverse momentum. The p_T of the Higgs boson is generated at higher orders, when additional partons are radiated and balance the Higgs p_T [258, 259, 292–295]. The leading order for the Higgs boson transverse momentum and rapidity is therefore part of the NLO for the production cross section, when the processes responsible for them, $gg \to Hg, gq \to Hq$ and $q\bar{q} \to Hg$, take place. The p_T and y_H distributions have been calculated in the full massive case at LO [258, 259] and it was shown that the heavy top quark limit is a reasonably good approximation, provided of course that $M_H \lesssim 2m_t$, but more importantly in this case, that $p_T \lesssim m_t$, which is typically the case as will be seen shortly. We therefore restrict ourselves to the heavy quark limit and summarize the salient features of these distributions.

Defining the momenta of the initial particles involved in the process $ij \to Hk$, with $i, j, k = g, q, \bar{q}$, as $p_{i,j} = x_{i,j}\, p_{1,2}$ with $p_{1,2}$ the incoming hadron momenta, and as p_k the momentum of the final parton, the differential partonic cross section in terms of the Higgs transverse momentum p_T and rapidity y_H can be written in the heavy quark limit as

$$\frac{\mathrm{d}^2\hat{\sigma}(ij \to kH)}{\mathrm{d}p_T^2 \mathrm{d}y_H} = \frac{G_\mu \alpha_s^3}{576\sqrt{2}\pi^2}\, \mathcal{H}_{ij\to kH}(p_T, y_H)$$
$$\mathcal{H}_{gg\to Hg} = 3\frac{\hat{s}^4 + \hat{t}^4 + \hat{u}^4 + M_H^8}{\hat{s}^2\hat{t}\hat{u}}\,,\ \mathcal{H}_{gq\to Hq} = -\frac{4}{3}\frac{\hat{s}^2 + \hat{u}^2}{\hat{s}\hat{t}}\,,\ \mathcal{H}_{q\bar{q}\to Hg} = \frac{32}{9}\frac{\hat{t}^2 + \hat{u}^2}{\hat{s}^2} \tag{3.72}$$

with the Mandelstam variables $\hat{s}, \hat{t}, \hat{u}$ given in terms of y_H and the transverse mass squared $m_T^2 = M_H^2 + p_T^2$ as $\hat{s} = (p_i + p_j)^2 = (p_k + p_H)^2 = s x_i x_j$ and $\hat{t}/\hat{u} = (p_{i/j} - p_k)^2 = (p_{j/i} - p_H)^2 = M_H^2 - \sqrt{s} x_j m_T e^{\pm y_H}$, with s being the total hadronic c.m. energy. The expressions are singular for $\hat{t}, \hat{u} \to 0$ and, in particular, $\mathcal{H}_{gg\to Hg}$ is singular in both $\hat{t}$ and $\hat{u}$. The singularities can be regularized by moving to $n = 4 - 2\epsilon$ space–time dimensions.

To include the NLO corrections to the differential distribution, and similarly to part of the NNLO corrections for the total cross section, one has to calculate: (i) the virtual corrections to Higgs production with a parton, which has to be multiplied by the Born term of the same process, and (ii) the real corrections due to the production of the Higgs boson with two partons, the sum of which has to be squared. In addition, one has to add the corrections to the Altarelli–Parisi splitting functions from the parton densities at NLO.

These corrections have been calculated by several groups [293–298], using different methods and different schemes. In all cases, the heavy top quark limit has been used. We summarize below the main results at NLO, concentrating on the case of the LHC where the transverse momentum and rapidity distributions of the Higgs boson are very important ingredients. Unless otherwise stated, the Higgs mass is set to $M_H = 120$ GeV and the heavy

top limit is assumed; the renormalization and factorization scales are set equal and fixed to the transverse Higgs mass, $\mu_R = \mu_F = m_T = \sqrt{M_H^2 + p_T^2}$.

The left–hand side of Fig. 3.26 shows the p_T distribution of the Higgs boson at NLO for several fixed rapidity values. One first notices that the differential distribution decreases with increasing rapidity and with increasing p_T and that at small values of the latter, $p_T \to 0$, it diverges to $-\infty$ [while at LO it diverges to $+\infty$]. In the low p_T regime, $p_T \lesssim 30$ GeV, the spectrum is unstable due to occurrence of large logarithms; the perturbative treatment is therefore not reliable and resummation techniques, to be discussed later, are required. Note that at small and moderate p_T, the cross section is dominated by the gluonic $gg \to H + X$ contribution, while for p_T values beyond 200 GeV the contribution of the $gq \to HX$ process becomes comparable; the (anti)quark initiated processes give very small contributions.

The NLO corrections increase the p_T distribution except for small p_T. While the increase is very strong for p_T values below 30 GeV [recall that the distribution at LO was diverging in the opposite direction], it becomes moderate for p_T values in the range of applicability of perturbation theory. The K–factor, defined as $K = \mathrm{d}\sigma_{\rm NLO}/\mathrm{d}\sigma_{\rm LO}$, rises slowly from $K \sim 1.6$ at $p_T = 30$ GeV to $K \sim 1.8$ for $p_T = 200$ GeV when the total rate becomes too small.

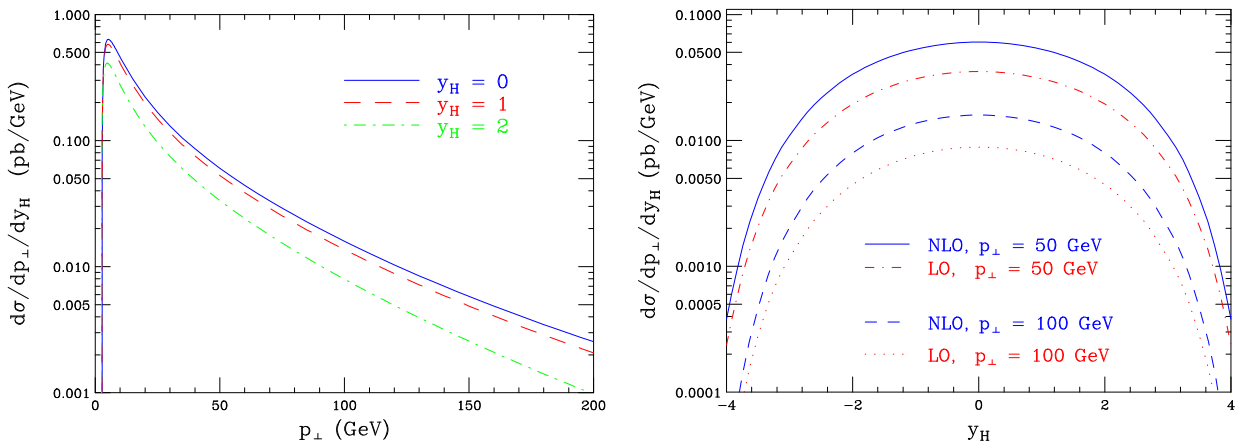

Figure 3.26: The Higgs transverse momentum dependence at NLO for three values of the rapidity $y_H = 0, 1, 2$ (left) and the rapidity dependence for two different transverse momenta $p_T = 50$ and 100 GeV at both LO and NLO (right). The CTEQ5 set of PDFs has been used while $M_H = 120$ GeV and the scales are set to $\mu_R = \mu_F = m_T$; from Ref. [294].

The right–hand side of Fig. 3.26 shows the rapidity dependence of the cross section for fixed values of the transverse momentum, $p_T = 50$ and 100 GeV, at both LO and NLO. As usual, the differential cross section is smaller for higher p_T values. It is maximal at $y_H = 0$ and falls off steeply for large rapidity values due to the restriction of the available phase, reaching zero for $|y_H| \gtrsim 4$. The NLO corrections increase the distribution: the K–factor for reasonable p_T values is at the level ~ 1.6 and is almost independent on the value of the rapidity, except at the boundary of the phase space where it drops slightly.

Thus, the NLO corrections acquire a size of about 60% to 80% over the entire perturbative range of p_T and y_H values. The variation with the renormalization and factorization scale has also been discussed and found to follow the same trend as in the production cross section at NLO: a variation from the central value $\mu_F = \mu_R = m_T$ by a factor of two generates an uncertainty of about 20%. There is also an uncertainty originating from the choice of the PDFs, which is similar to what has been observed for the total cross section and which is thus smaller than the scale uncertainty.

Let us make a final comment on the low p_T case. As already mentioned, the distribution diverges to $+\infty$ at LO and to $-\infty$ at NLO for $p_T \to 0$. This is because in the region $p_T \ll M_H$, where the cross section is in fact the largest, the expansion parameter is not α_s/π but rather, $(\alpha_s/\pi)\log^2(M_H^2/p_T^2)$ which is close to unity and invalidates perturbation theory. However, the large logarithms, as singular as $(1/p_T^2)\alpha_s^n \log^m(M_H^2/p_T^2)$, with $1 < m < 2n-1$, can be systematically resummed to all orders [371] as in the case of the total cross section, resulting in a well behaved spectrum for $p_T \to 0$; see for instance Refs. [294,295] for details.

In the case of the $gg \to H$ process, the resummation has been performed at the NNLL level of accuracy. This resummation for the low p_T region, and the fixed order calculation at NLO for the high p_T region, have been consistently matched at intermediate p_T values to provide a smooth transition. The result for the p_T distribution is shown in Fig. 3.27 at the LHC for a Higgs mass of $M_H = 125$ GeV. In the left figure, the NLO and NLO+NNLL approximations are displayed and, as can be seen, the divergent behavior of this distribution is removed by the resummation, the effects of which are relevant up to values $p_T \sim 100$ GeV. The scale variation is shown in the right figure in the NLO+NNLL case: the spread is at the level of 10% near the peak and increases to 20% for lower p_T values, $p_T \sim 100$ GeV.

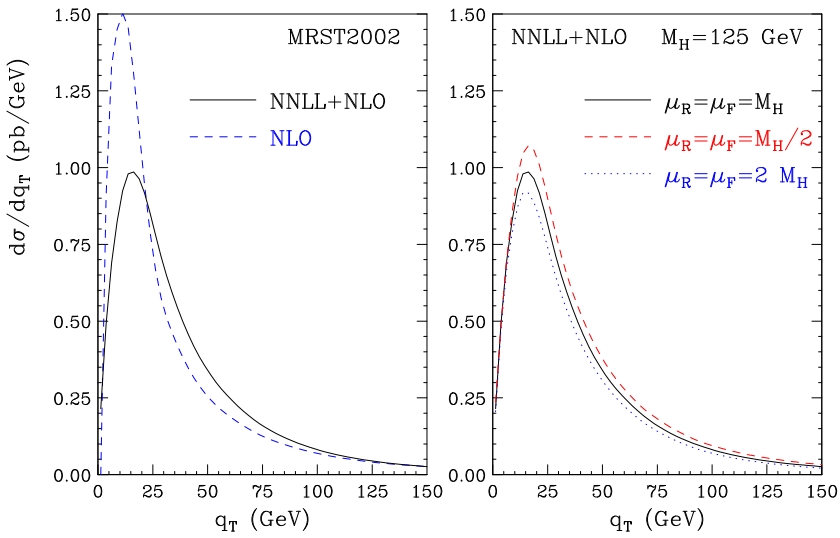

Figure 3.27: The p_T distribution in $gg \to H$ at the LHC for $M_H = 125$ GeV: at NLO and NLO+NNLL for scales $\mu_R = \mu_F = M_H$ (left) and at NLO+NNLL when the scales are collectively varied by a factor of two; from Ref. [295].

Higgs boson plus n jet production

It has been suggested that Higgs production with one high p_T jet might have a much smaller background at the LHC, in particular in the decay channel $H \to \gamma\gamma$ [372], than the $gg \to H$ channel alone. At LO, the process is just the $gg \to Hg, qg \to Hq$ and $q\bar{q} \to Hg$ processes that we have discussed previously and for which we have displayed the partonic differential cross sections in the heavy top limit, eq. (3.72). In this limit, the NLO corrections to $pp \to H + j$ are those which appear in the $\mathcal{O}(\alpha_s^2)$ real corrections to the NNLO $gg \to H$ cross section.

The Higgs plus 2 jet production process is generated by $q\bar{q}$ scattering mediated by triangles involving top quarks, gq scattering mediated by boxes and triangles and gg fusion mediated by triangles up to pentagon diagrams, and is known exactly at LO [261]. This mechanism has been discussed in connection with the vector boson fusion process, since it leads to the same final states, the gluons and the light quarks being indistinguishable, and may act as a background in the study of the former process. Characteristics which discriminate between the processes have been worked out and summarized in Fig. 3.28. The main points have been already discussed in §3.3.3: with basic (inclusive) cuts $p_{Tj} \gtrsim 20$ GeV, $|\eta_j| < 5$ and $R_{jj} > 0.6$, gluon fusion dominates, while the specific additional cuts $m_{jj} > 0.6$ TeV, $|\eta_{j1} - \eta_{j2}| > 4.2$ and $\eta_{j1} \cdot \eta_{j2} < 0$, select the vector boson fusion (WBF) process [373].

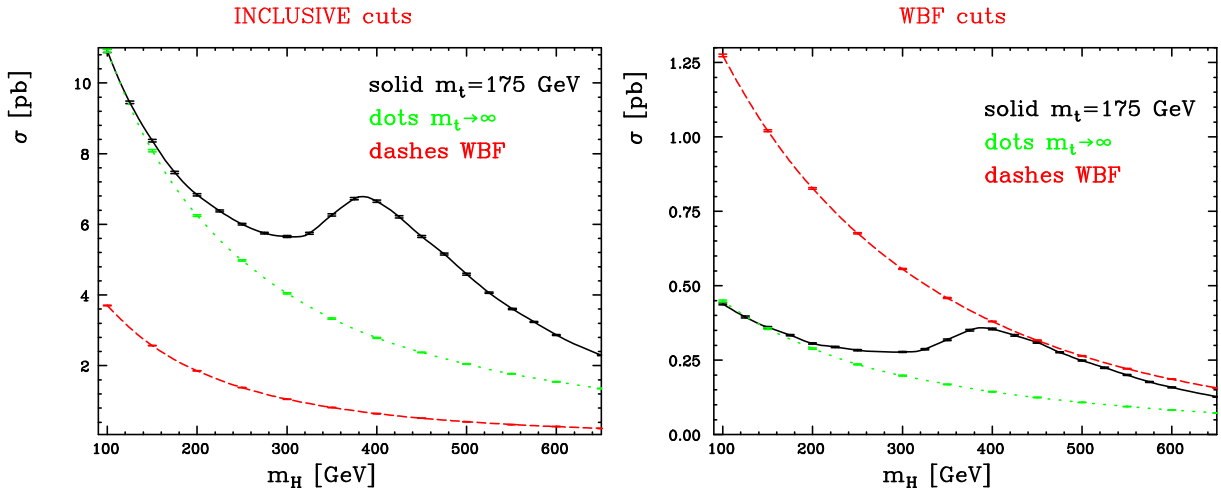

Figure 3.28: Higgs production with 2 jets at the LHC as a function of M_H, in gluon fusion with $m_t = 175$ GeV (solid line) and $m_t \to \infty$ (dotted line) and in vector boson fusion (dashed). The left (right) part shows the cross section with the inclusive (WBF) cuts [373].

Recently, associated Higgs production with 3 jets has been calculated in the $m_t \to \infty$ limit [262]. This is part of the NLO corrections to the Higgs+2 jet process, which exhibits a strong dependence on the renormalization scale μ_R since it is a LO process but of $\mathcal{O}(\alpha_s^4)$. The very complicated virtual corrections need to be derived which, when combined with the Higgs+3 jet real corrections, will hopefully stabilize the scale dependence of the $H + 2j$ rate.

3.5 Associated Higgs production with heavy quarks

3.5.1 The cross sections at the tree level

The process where the Higgs boson is produced in association with heavy quark pairs, $pp \to Q\bar{Q}H$ [247, 248], with the final state quarks being either the top quark or the bottom quark [in this case, see also Refs. [249, 250] for instance], is the most involved of all SM Higgs production mechanisms. At tree–level, it originates from $q\bar{q}$ annihilation into heavy quarks with the Higgs boson emitted from the quarks lines; this is the main source at the Tevatron. At higher energies, when the gluon luminosity becomes important, the process proceeds mainly through gluon fusion, with the Higgs boson emitted from both the external and internal quark lines. A generic set of Feynman diagrams is shown in Fig. 3.29; those which are not shown differ only in the way the Higgs line is attached to the final state quark line and the gluon symmetrization in the last diagram.

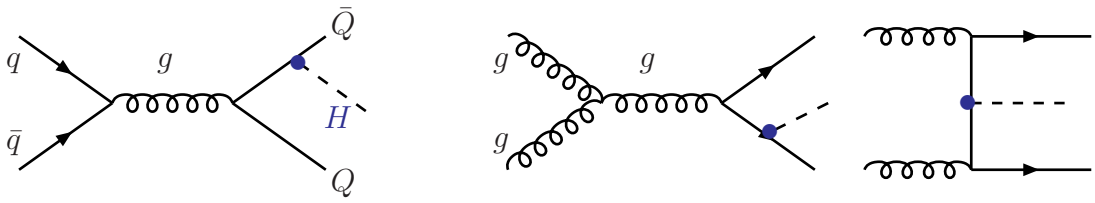

Figure 3.29: Generic Feynman diagrams for associated Higgs production with heavy quarks in hadronic collisions, $pp \to q\bar{q}, gg \to Q\bar{Q}H$, at LO.

Added to the complication that one has to calculate the amplitude of 10 Feynman diagrams and square them, one has to deal with the rather involved phase space with three massive particles in the final state. This is the reason why the complete analytical expression of the cross section is not available in the literature. If only $q\bar{q}$ annihilation is considered, which is a good approximation in the case of the Tevatron, the matrix element squared in terms of the momenta $q(\bar{q}), p(\bar{p})$ and k of respectively, the initial light and final heavy quark (antiquark) and the Higgs particle, with $Q^2 = (q+\bar{q})^2 = (p+\bar{p}+k)^2 = \hat{s}$, is given by [248]

$$\begin{aligned}
|\mathcal{M}_{q\bar{q}}|^2 \;=\; & \frac{32}{(2k.\bar{p}+M_H^2)(2k.p+M_H^2)}\Bigg\{Q^2(Q.k)^2\left[1+\frac{Q^2(4m_Q^2-M_H^2)}{(2k.\bar{p}+M_H^2)(2k.p+M_H^2)}\right] \\
& +\left(\frac{1}{2}Q^2m_Q^2-2(p.q)(p.\bar{q})\right)\left[Q^2-4m_Q^2+M_H^2+\frac{2k.Q(4m_Q^2-M_H^2)}{2k.\bar{p}+M_H^2}\right] \\
& +\left(\frac{1}{2}Q^2m_Q^2-2(\bar{p}.q)(\bar{p}.\bar{q})\right)\left[Q^2-4m_Q^2+M_H^2+\frac{2k.Q(4m_Q^2-M_H^2)}{2k.p+M_H^2}\right] \\
& -(Q^2+M_H^2-4m_Q^2)\Big[2(p.q)(\bar{p}.\bar{q})+2(p.\bar{q})(\bar{p}.q)-Q^2(p.\bar{p})\Big]\Bigg\} \qquad (3.73)
\end{aligned}$$

where the coupling factors, $g_s^4(\sqrt{2}m_Q^2G_\mu)$, with $g_s^2 = 4\pi\alpha_s$, have been removed.

For the gluon fusion diagrams, denoting by ϵ_1 and ϵ_2 the polarization four–vectors of the gluons and by g_1 and g_2 their four–momenta, the various amplitudes are given by [the generators T^a and the SU(3) structure constants f^{abc} are discussed in §1.1.1] [248]

$$\begin{aligned}
\mathcal{M}^a_{gg} &= -T^a_{ik}T^b_{kj}\,\bar{u}^j(p)\,\frac{\not{k}+\not{p}+m_Q}{2p.k+M_H^2}\not{\epsilon}_2\frac{-\not{\bar{p}}+\not{g}_1+m_Q}{-2g_1.\bar{p}}\not{\epsilon}_1\,v^i(\bar{p}) + \left[\begin{array}{c} g_1\leftrightarrow g_2,\epsilon_1\leftrightarrow\epsilon_2 \\ g_1\leftrightarrow g_2,\epsilon_1\leftrightarrow\epsilon_2,p\leftrightarrow\bar{p} \\ p\leftrightarrow\bar{p}\end{array}\right] \\
\mathcal{M}^b_{gg} &= -T^a_{ik}T^b_{kj}\,\bar{u}^j(p)\,\not{\epsilon}_2\frac{\not{p}-\not{g}_2+m_Q}{-p.g_2}\frac{-\not{\bar{p}}+\not{g}_1+m_Q}{-g_1.\bar{p}}\not{\epsilon}_1\,v^i(\bar{p}) + [g_1\leftrightarrow g_2,\epsilon_1\leftrightarrow\epsilon_2] \qquad (3.74)\\
\mathcal{M}^c_{gg} &= if^{abc}T^c_{ij}\,\bar{u}^j(p)\,\frac{\not{\epsilon}_1\not{\epsilon}_2 Q^\lambda}{\hat{s}}\Big[2g_1^\nu g_2^{\lambda\mu}+(g_2-g_1)^\lambda g^{\mu\nu}-2g_2^\mu g^{\nu\lambda}\Big]\frac{\not{\bar{p}}+\not{k}-m_Q}{2k.\bar{p}+M_H^2}\,v^i(\bar{p}) + [p\leftrightarrow\bar{p}]
\end{aligned}$$

where, again, the product of couplings $g_s^2(\sqrt{2}m_Q^2G_\mu)^{1/2}$ has been factorized out. The gluon polarization vectors obey the transversality condition $\epsilon_i.g_i=0$ and SU(3) gauge invariance can be checked by making the substitutions $\epsilon_i\to g_i$; one can also use the gauge condition $\epsilon_1.g_2=\epsilon_2.g_1$ to simplify the calculation. In the amplitude squared, summed over the final quarks color and spin and averaged over the gluon color and polarizations,

$$|\mathcal{M}_{gg}|^2 = \frac{1}{256}\sum_{\text{spin, color}}|\mathcal{M}^a_{gg}+\mathcal{M}^b_{gg}+\mathcal{M}^c_{gg}|^2 \qquad (3.75)$$

one has to perform the trace over the γ matrices and the sum over the indices of the QCD Gell–Mann matrices and the f^{abc} structures functions

$$(T^a_{ik}T^b_{kj})^2 = 24\ ,\ (f^{abc}T^c_{ij})^2 = 12\ ,\ (T^a_{ik}T^b_{kj})(f^{abc}T^c_{ij})^2 = 0 \qquad (3.76)$$

The average over the gluon polarizations, since the gluons are massless, should be performed in an axial gauge and, for instance, one can use[28]

$$\sum_{\lambda_i=1}^{2}\epsilon_i^\mu(g_i,\lambda_i)\epsilon_i^\nu(g_i,\lambda_i) = -g^{\mu\nu}+\frac{2}{\hat{s}}(g_1^\mu g_2^\nu+g_1^\nu g_2^\mu) \qquad (3.77)$$

The obtained expression for the amplitude squared is too long to be reproduced. One has then to integrate over the phase space to obtain the cross section at the partonic level for each subprocess $ij\to Q\bar{Q}H$ [with $ij=q\bar{q},gg$]

$$\hat{\sigma}^{ij}_{\rm LO} = \frac{1}{2\hat{s}}\frac{\alpha_s^2G_\mu m_Q^2}{\sqrt{2}\pi^3}\int\frac{\mathrm{d}^3p}{2p_0}\frac{\mathrm{d}^3\bar{p}}{2\bar{p}_0}\frac{\mathrm{d}^3k}{2k_0}\delta^4(Q-p-\bar{p}-k)\left[\sum|\mathcal{M}_{ij}|^2\right] \qquad (3.78)$$

These partonic cross sections have then to be folded with the quark and gluon luminosities to obtain the full cross section at the hadronic level

$$\sigma_{\rm LO} = \int\sum_{i,j}\frac{1}{1+\delta_{ij}}\Big(\mathcal{F}_i^p(x_1,\mu_F)\mathcal{F}_j^p(x_2,\mu_F)\hat{\sigma}^{ij}_{\rm LO}(x_1,x_2,\mu_F)+[1\leftrightarrow 2]\Big)\mathrm{d}x_1\mathrm{d}x_2 \qquad (3.79)$$

[28] Alternatively, one can use the simpler Feynman gauge for the summation over polarization, $\sum\epsilon_i^\mu\epsilon_i^\nu = -g^{\mu\nu}$, but two additional diagrams with ghosts replacing the gluons in the initial state have to be added.

where $\mathcal{F}_i^p$ are the distributions of the parton i in the proton defined at the factorization scale μ_F. The factor $1/(1+\delta_{ij})$ accounts for the identical gluons in the initial state.

The cross section for associated $t\bar{t}H$ and $b\bar{b}H$ production are shown for the Tevatron and LHC energies in Fig. 3.30. The MRST set of parton densities has been used and the renormalization and factorization scales have been identified with $\mu_R = \mu_F = m_Q + \frac{1}{2}M_H$ and $\frac{1}{4}M_H$ for the $t\bar{t}H$ and $b\bar{b}H$ cases, respectively. The pole masses of the top and bottom quarks have been fixed to $m_t = 178$ GeV and $m_b = 4.88$ GeV. As can be seen, the $p\bar{p} \to t\bar{t}H$ cross section at the Tevatron is of the order of 5 fb for small Higgs masses, $M_H \sim 120$ GeV, dropping to a level below 1 fb for $M_H \sim 180$ GeV, when the phase space becomes too narrow. At the LHC, the cross section is two orders of magnitude larger as a consequence of the higher energy, higher gluon luminosity and larger phase space. It varies however strongly with M_H, dropping by more than one order of magnitude when M_H varies from 120 to 250 GeV. The detection aspects at LHC [374–380] and Tevatron [381] will be discussed in §3.7.

Surprisingly, the $pp \to b\bar{b}H$ cross sections are slightly larger than the corresponding cross sections for $pp \to t\bar{t}H$ at both the Tevatron and the LHC, for small enough Higgs masses. This is mere consequence of the larger available phase space at the Tevatron and the participation of the low x gluons in the case of the LHC. The cross sections become comparable at moderate Higgs masses and, eventually, the $pp \to t\bar{t}H$ process dominates at higher Higgs masses, but the production rates become then too small.

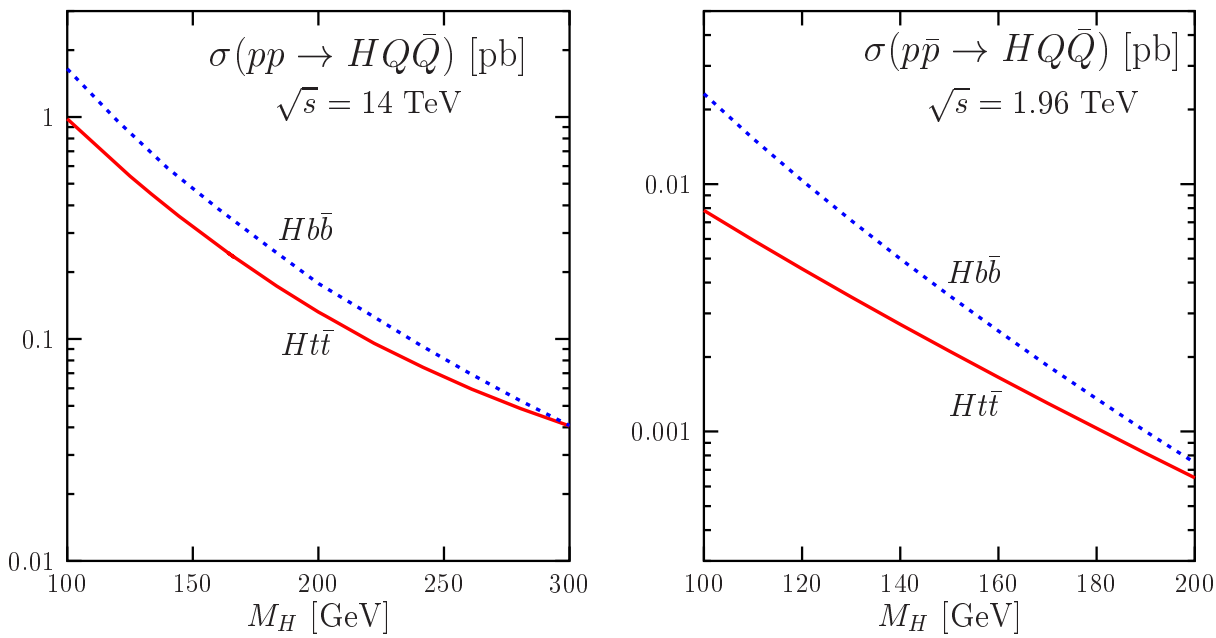

Figure 3.30: The $t\bar{t}H$ and $b\bar{b}H$ production cross sections at the LHC (left) and the Tevatron (right). The pole quark masses in the Yukawa couplings are set to $m_t = 178$ GeV and $m_b = 4.88$ GeV and the MRST PDFs are used. The renormalization and factorization scales have been set to $\mu_{R,F} = m_t + \frac{1}{2}M_H$ for $pp \to t\bar{t}H$ and $\mu_{R,F} = \frac{1}{2}m_b + \frac{1}{4}M_H$ for $pp \to b\bar{b}H$.

3.5.2 The ttH cross section at NLO

The calculation at NLO

As we have seen just before, it was already rather difficult to calculate the $pp \to Q\bar{Q}H$ cross section at LO. At NLO, the task becomes formidable. The computation of these NLO corrections, which was another *tour de force*, has been been completed only very recently, by two independent groups [287, 288]. The Feynman diagrams which contribute to the NLO QCD corrections can be divided into four gauge invariant subsets, some representative examples of which are presented in Fig. 3.31: *a*) virtual gluonic corrections to the $q\bar{q}g$ and ggg vertices as well as to the initial and final quark and gluon self–energies, *b*) vertex and box virtual corrections where the Higgs boson is emitted from the internal lines and where a final state gluon is emitted and splits into $Q\bar{Q}$ pairs, *c*) pentagonal $q\bar{q}$ and gg initiated diagrams where the Higgs boson is emitted from the heavy quark internal lines, and finally *d*) real corrections where an additional gluon is emitted in the final state in all possible ways, and which involve additional qg and $\bar{q}g$ scattering diagrams which do not occur at the tree–level.

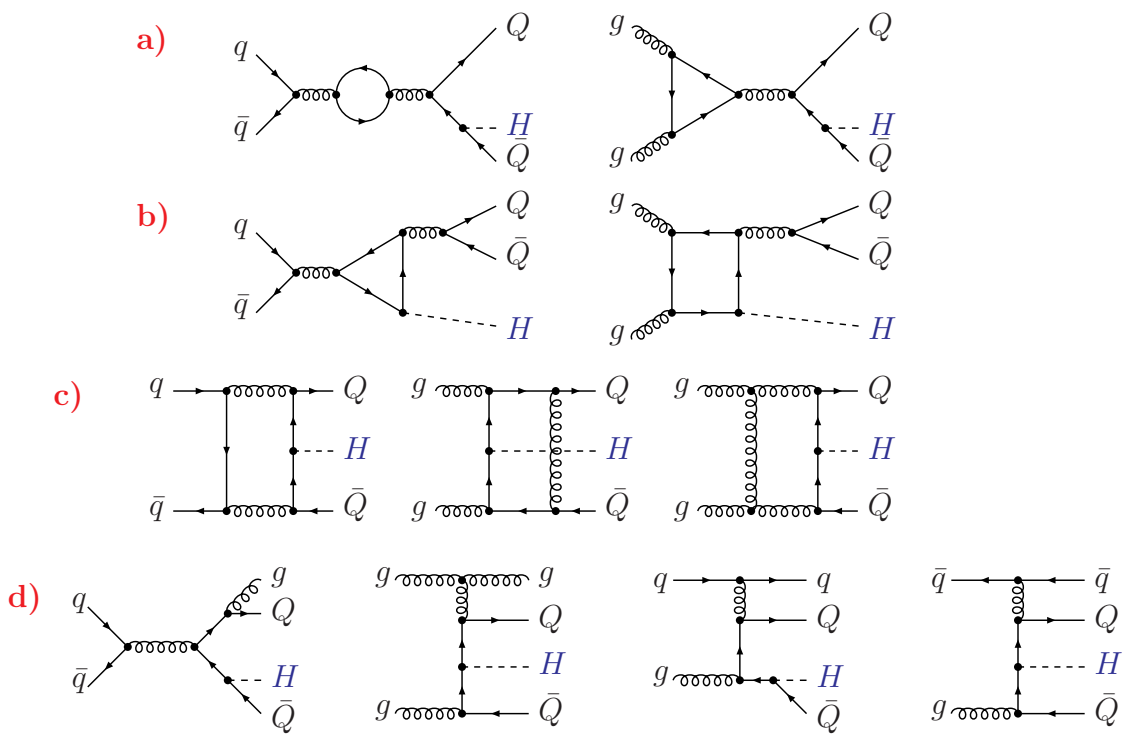

Figure 3.31: Representative Feynman diagrams for the NLO QCD corrections to $pp \to Q\bar{Q}H$.

Technically speaking, there are two main difficulties which arise when attempting to perform such a calculation. The first one is that the pentagonal one–loop 5–point functions [382] are rather difficult to evaluate in n dimensions since, not to mention the complicated tensorial structure which has to be reduced to known scalar integrals, they involve massive

particles and have ultraviolet, soft and collinear singularities which have to be calculated in the dimensional regularization scheme. The second major difficulty is the extraction of the soft and collinear singularities in the real part of the corrections, which involve 4 particles in the final state, with three of them being massive. This leads to severe numerical instabilities which have to be handled with great care [383]. Added to this, a large number of Feynman diagrams and the associated counterterms have to be evaluated.

Several methods have been devised to overcome these problems and a detailed account can be found in the original papers of Refs. [287, 288]. In both calculations, the renormalization has been performed in a mixed scheme, where the heavy quark mass is defined on–shell and the running of the $\overline{\rm MS}$ strong coupling constant includes only the light quarks and gluons with the heavy quarks decoupled. The factorization has been performed in the $\overline{\rm MS}$ scheme where the heavy quark is decoupled from the evolution of the parton densities. The two calculations have been compared against each other and, although the methods which have been used are different, a perfect agreement has been found. In the following, we simply summarize the numerical results which have been obtained in the case of $pp \to t\bar{t}H$.

Numerical results for $pp \to t\bar{t}H$

In Fig. 3.32, the LO and NLO cross sections for associated Higgs production with top quarks are presented in the case of the Tevatron with a c.m. energy $\sqrt{s} = 2$ TeV. The CTEQ4M (L) parton distribution functions at NLO (LO) have been used and the top quark mass and the strong coupling constants have been fixed to $m_t = 174$ GeV and $\alpha_s^{\rm NLO}(M_Z) = 0.116$. The left–hand side of the figure displays the LO and NLO cross sections as a function of the Higgs mass with the renormalization and factorization scales chosen to be $\mu_R = \mu_F = m_t$ and $2m_t$, while the right–hand side displays the variation of the cross sections with the renormalization and factorization scales for a Higgs boson with a mass $M_H = 120$ GeV.

One can see that over the entire Higgs mass range accessible at the Tevatron, the NLO corrections decrease the production rate. For $\mu_F = \mu_R = m_t$, the K–factor defined as the ratio of the NLO and LO cross sections consistently evaluated at their respective orders, is $K \sim 0.8$ and is nearly independent of the Higgs mass[29]. However, for a scale choice $\mu_R = \mu_F = 2m_t$, the NLO corrections are very small. This suggests a very strong dependence of the cross section on the scale choice and, indeed, as is illustrated in the right–hand side of Fig. 3.32 where the scales are varied from m_t to $\sim 3m_t$, while the NLO cross section is rather stable, the LO cross section changes by 60% in this range. Thus, the NLO corrections are mandatory to stabilize the prediction for the production cross section.

[29]This is one of the few examples of K–factors below unity. As discussed in Refs. [287, 289], the reason lies in the fact that at $\sqrt{s} = 2$ TeV, the $t\bar{t}H$ final state is produced in the threshold region, where gluon exchange between the top quarks gives rise to Coulomb singularities $\propto \alpha_s/\beta_t$. Since the $t\bar{t}H$ final state is in a color octet, these corrections are negative and decrease the Born cross section.

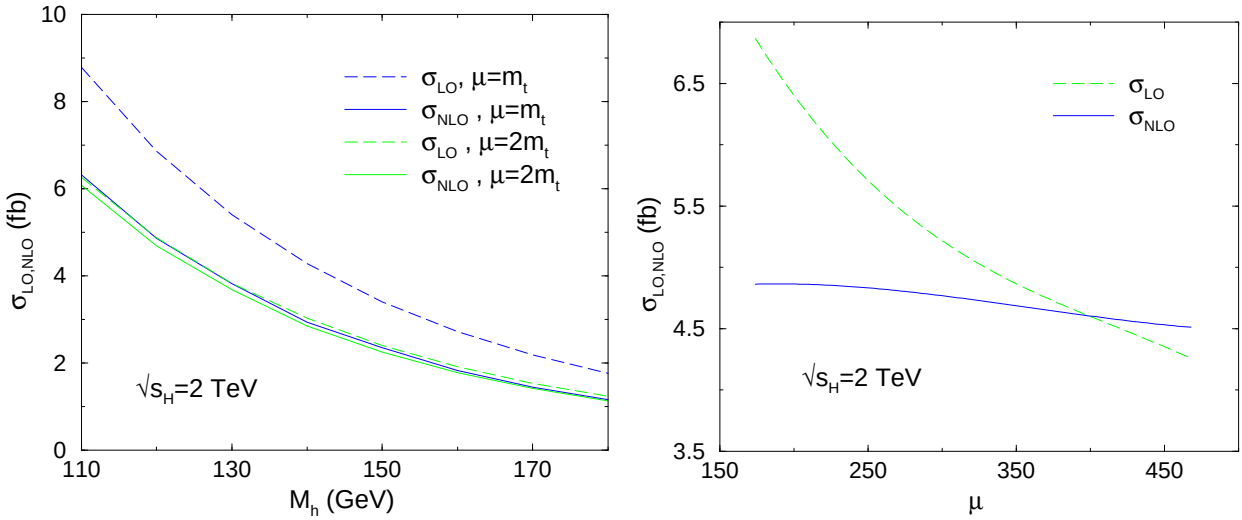

Figure 3.32: The $p\bar{p} \to t\bar{t}H + X$ production cross section at the Tevatron at both LO and NLO, as a function of the Higgs mass with two scale choices (left) and as a function of the scales $\mu = \mu_R = \mu_F$ for $M_H = 120$ GeV (right); from Ref. [289].

In the subsequent figures, Figs. 3.33–3.34, we present the LO and NLO results for the associated Higgs production with top quarks at the LHC, $pp \to t\bar{t}H + X$, as derived in Ref. [287]. Besides the total hadronic cross sections, the differential distributions in transverse momentum and rapidity of the Higgs boson have been discussed in this case. Here, the MRST sets of parton densities at LO and NLO have been adopted and the renormalization and factorization scales are set to $\mu_R = \mu_F = \mu_0 = \frac{1}{2}(2m_t + M_H)$ when they are not varied; the top–quark mass is also set to the old central value $m_t = 174$ GeV.

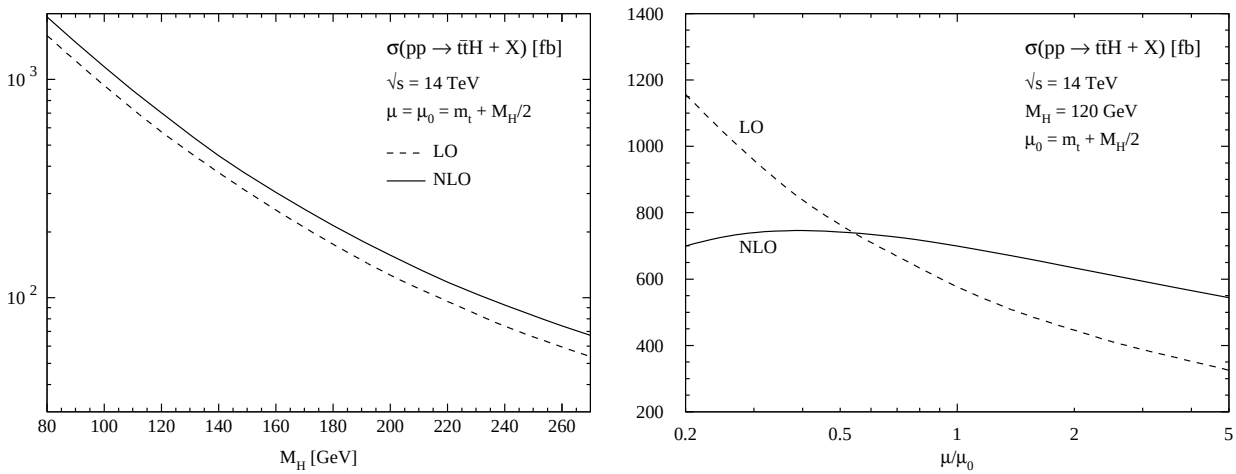

Figure 3.33: Total cross section for $pp \to t\bar{t}H + X$ at the LHC in LO and NLO as a function of M_H (left) and the variation with the scales for $M_H = 120$ GeV (right); from Ref. [287].

Because the cross section at the LHC is dominated by the gg fusion process, it receives positive NLO corrections for the central renormalization and factorization scale, $\mu_0 = m_t +$

$\frac{1}{2}M_H$, as shown in the left–hand side of Fig. 3.33. For this scale value, a factor $K \sim 1.2$ is obtained, increasing to $K \sim 1.4$ when the choice $\mu_F = \mu_R = 2\mu_0$ is made. As in the case of the Tevatron, these values are nearly independent of the Higgs boson mass in the displayed range. Again, and as is shown in the right–hand side of the figure, the NLO corrections significantly reduce the renormalization and factorization scale dependence and stabilize the theoretical prediction for the cross section at the LHC.

The scale dependence of the rapidity and transverse momentum distributions of the Higgs boson is also significantly reduced at NLO and the shape of the distributions is practically constant when the scales are varied in a reasonable range. The ratio of the normalized NLO and LO distributions in transverse momentum and rapidity, are shown in the inserts of, respectively, the left–hand and right–hand parts of Fig. 3.34 for $M_H = 120$ GeV. In the former case, the default scale was set to the transverse mass, $\mu^2 = p_{T,H}^2 + M_H^2$, which is a more natural choice for large transverse momenta. In this case, the NLO corrections are small for low values of the Higgs transverse momentum, $p_{T,H} \lesssim m_t$, but increase with increasing $p_{T,H}$ values, reaching $\sim 30\%$ at the boundary of phase space where the cross section is small. In the case of the normalized rapidity distribution, the NLO corrections are also very small in the central region but they become negative and of the order of 10% at the edge of phase space. A conclusion that one can draw from these figures, is that one cannot simply use a constant K–factor to describe these distributions.

Note that the transverse momentum and rapidity distributions of the top and antitop quarks have been also studied; they are barely affected by the NLO corrections once the scales have been properly chosen; see Ref. [287].

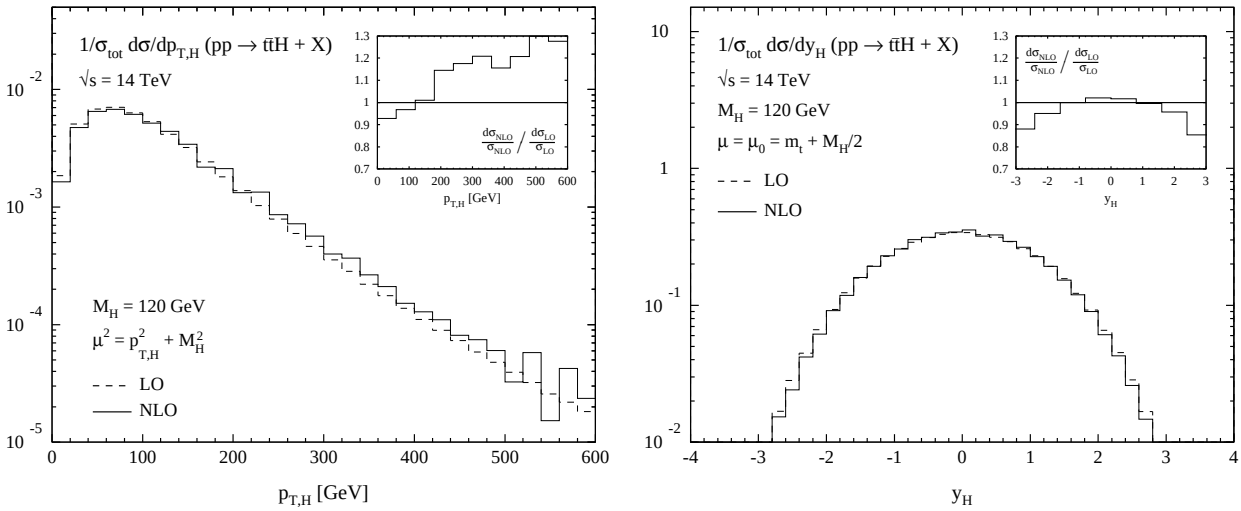

Figure 3.34: Normalized transverse momentum (left) and rapidity (right) distribution of the Higgs boson in the process $pp \to t\bar{t}H + X$ at the LHC in LO and NLO with M_H=120 GeV. The inserts to the figures show the ratio of the NLO to LO distributions; from Ref. [287].

The PDF uncertainties

Finally, let us discuss the PDF uncertainties in the prediction of the $pp \to Ht\bar{t}$ cross section, restricting ourselves to the case of the LHC. The central values and the uncertainty band limits are shown for the CTEQ, MRST and Alekhin parameterizations in Fig. 3.35 as a function of M_H, using the procedure outlined in §3.1.5. We also show in the insert, the spread uncertainties in the predictions when the cross sections are normalized to the values obtained using the CTEQ6M set. Since the NLO corrections have been calculated only recently and the presumably very complicated and slow programs are not yet publicly available, we simply use the program `HQQ` of Ref. [278] for the LO cross section with scales $\mu_F = \mu_R = 2m_t + M_H$ that we fold with the NLO PDFs. Although the overall normalization is different when including the NLO correction [one simply has to multiply by the K–factor which is approximately 1.4 in this case], this procedure should describe the relative effects of the different PDFs at NLO with a rather good approximation.

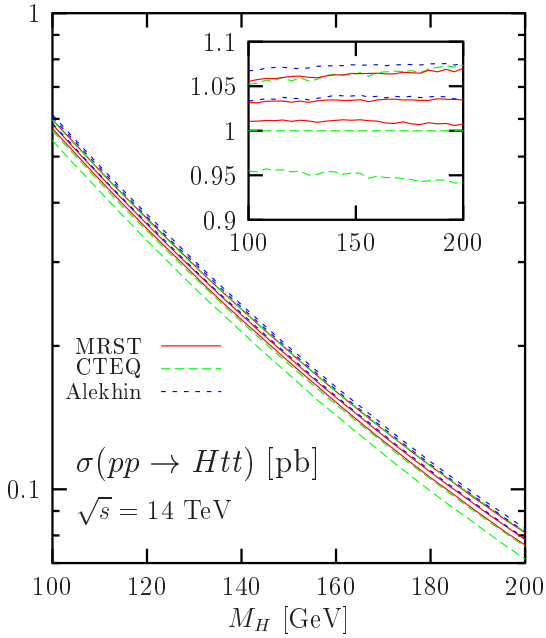

Figure 3.35: The CTEQ, MRST and Alekhin PDF uncertainty bands for the NLO cross section $pp \to t\bar{t}H$ at the LHC; the scales have been fixed to $\mu_F = \mu_R = 2m_t + M_H$. The insert shows the spread in the predictions compared to CTE6M; from Ref. [314].

As discussed above, the process is dominantly generated by gluon–gluon fusion at the LHC and, compared with the process $gg \to H$ discussed in §3.4 for a fixed Higgs mass, a larger Q^2 is needed for this final state and the initial gluons should therefore have higher x values. In addition, the quarks that are involved in the subprocess $q\bar{q} \to t\bar{t}H$, which is also contributing, are still in the intermediate regime because of the higher value [$x \sim 0.7$] at which the quark high–x regime starts. This explains why the uncertainty band increases smoothly from 5% to 7% when the M_H value increases from 100 to 200 GeV.

3.5.3 The case of the bbH process

As seen in §3.5.1, the production cross sections for the associated Higgs production with bottom quarks are not that small, despite of the tiny $Hb\bar{b}$ Yukawa coupling. However, the dominant $b\bar{b}b\bar{b}$ signal final state for a low mass Higgs boson decaying into $b\bar{b}$ pairs is rather complicated to be isolated experimentally and suffers from a huge QCD jet background. This channel is therefore not considered as a discovery channel for the SM Higgs boson at the Tevatron and the LHC. Nevertheless, in extensions of the SM, such as in minimal supersymmetric theories, the Higgs Yukawa coupling to bottom quarks can be strongly enhanced, leading to large $b\bar{b}H$ production rates which can exceed by far the cross sections in the $pp \to t\bar{t}H$ case, even for high mass Higgs bosons. This channel will be discussed in some detail in the second part of this review [24]. Here, we simply summarize the impact of the NLO corrections, restricting ourselves to the inclusive total rate generated via light quark annihilation and gg fusion, $q\bar{q}, gg \to b\bar{b}H$.

The calculation of the NLO correction to $b\bar{b}H$ production follows the same lines as what has been discussed previously for $pp \to t\bar{t}H$ and the results have been given in Refs. [290,291]. There is, however, a major difference between the two cases [384]: because of the small b–quark mass, the cross section $\sigma(gg \to b\bar{b}H)$ develops large logarithms[30], $\log(Q^2/m_b^2)$, with the scale Q being typically of the order of the factorization scale $Q \sim M_H \gg m_b$. This leads to large corrections, part of which can be absorbed by choosing a low value for the factorization and renormalization scales, $\mu_R = \mu_F \sim \frac{1}{4}(M_H + 2m_b)$ [384, 385].

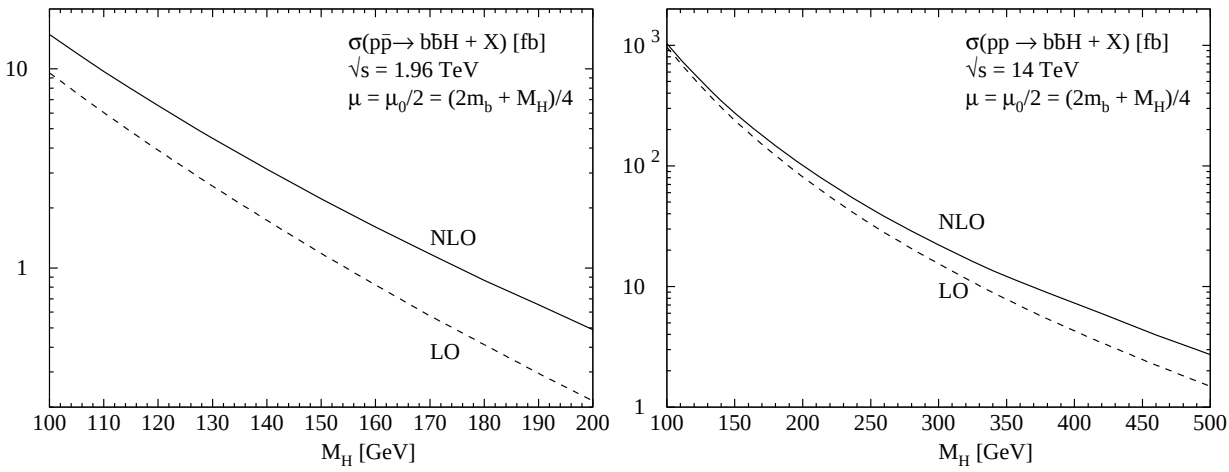

Figure 3.36: Total inclusive cross sections for $pp \to b\bar{b}H + X$ at the Tevatron (left) and the LHC (right) as a function of M_H with the factorization and renormalization scales set to $\mu_R = \mu_F \sim \frac{1}{4}(M_H + 2m_b)$. The running b–quark mass, with a starting pole value $m_b = 4.88$ GeV, has been used in the Higgs coupling and the CTEQ6 PDFs are adopted; from [290].

[30]The issue of resumming these large logarithms and stabilizing the scale dependence of the cross section using heavy quark distribution functions has been discussed in Ref. [385].

The NLO cross sections are shown at Tevatron and LHC energies in Fig. 3.36 as a function of the Higgs mass for this scale choice and compared to the LO cross sections. In both cases, the running b–quark mass at the scale of the Higgs mass, with the starting pole mass being $m_b = 4.9$ GeV, has been used for the Yukawa coupling. As can be seen, even with this scale choice, the NLO corrections are large, with K–factors ranging from 1.6 to 2.6 at the Tevatron and 1.1 to 1.8 at the LHC. The scale variation is still strong even at NLO and further work is needed to improve the theoretical prediction of the $b\bar{b}H$ production rate.

3.5.4 Associated Higgs production with a single top quark

Since the phase space for $t\bar{t}H$ production is too penalizing, in particular at the Tevatron, it has been suggested to consider the process where the Higgs boson is produced in association with a single top or antitop quark [386, 387]

$$pp/p\bar{p} \to tH + X \tag{3.80}$$

The expectation is that the cross section can be comparable to that of the $t\bar{t}H$ process, similarly to what occurs for top quark production in hadronic collisions where the rate for single top quark is not much smaller than that for top quark pair production, the ratio of the two being of the order of 1/3 [388]. There are three types of contributions to this production channel, as shown in Fig. 3.37 where a few generic Feynman diagrams are presented:

a) $q\bar{q}'$ annihilation with s–channel W boson exchange, which leads to the three–body final state involving a Higgs boson and a bt pair;

b) t–channel fusion of a light quark and a bottom parton from the proton sea which, through W exchange, leads to the qtH final state;

c) the scattering of gluons with again bottom partons from the proton sea and which lead to tWH final states.

In the language of gluon initiated production, the two last processes are in fact the higher–order mechanisms $gg \to bH + X$ with four final state particles but with one b–quark integrated out. Note that in all three channels, the Higgs boson can be radiated not only from the top quark lines but also from the W boson [as well as from the b–quark] lines.

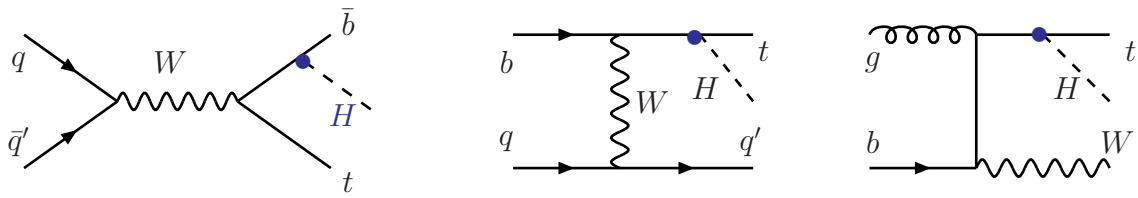

Figure 3.37: Generic Feynman diagrams for associated Higgs production with a single top quark in hadronic collisions: a) $q\bar{q}' \to \bar{b}tH$, b) $qb \to q'tH$ and c) $gb \to W^-tH$.

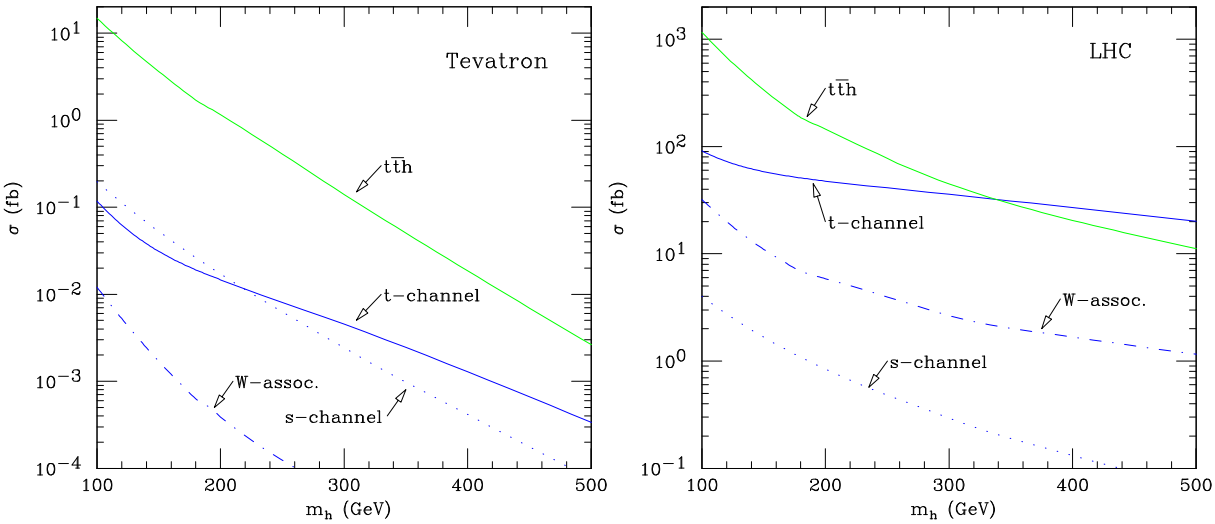

Figure 3.38: The cross sections for Higgs plus single top production at the Tevatron (left) and at the LHC (right), in the t–channel, s–channel and W–associated processes; for comparison the cross section for $t\bar{t}H$ is also shown. The CTEQ5L set of PDFs is used and the renormalization and factorization scales are set to M_H; from Ref. [387].

These processes have been revisited in Ref. [387] and the production cross sections are shown in Fig. 3.38 for the Tevatron (left) and LHC (right) as a function of the Higgs mass. The rates for the three channels are shown separately and compared with the $pp \to t\bar{t}H$ cross section. The renormalization and factorization scales are set to the Higgs mass and the CTEQ5 set of PDFs has been used. Unfortunately, and contrary to the $t\bar{t}$ case, the rates for associated Higgs production with a single top quark are in general much smaller than those of $t\bar{t}H$ production. At the Tevatron, all channels lead to cross sections that are two orders of magnitude smaller. At the LHC, this is also the case for the s–channel $q\bar{q}' \to \bar{b}tH$ and WtH associated production. However, for low Higgs masses, the t–channel $qb \to q'tH$ cross section is suppressed only by a factor of 10 compared to $t\bar{t}H$ production and for larger masses, $M_H \sim 300$ GeV, the two process have comparable but rather low rates.

Focusing on the latter channel, where for $M_H \lesssim 150$ GeV approximately 10^4 events can be collected at the LHC for $\mathcal{L} = 100$ fb^{-1} before cuts and efficiency losses are applied, the signals and the various backgrounds have been studied in Ref. [386] for a Higgs boson decaying into two photons and in Ref. [387] where the more copious $H \to b\bar{b}$ decays have been considered. The observation of a Higgs boson in the first channel is certainly not possible since the $\gamma\gamma$ branching ratio is of $\mathcal{O}(10^{-3})$. In the configuration where the Higgs boson decays into $b\bar{b}$ and the top quark into $Wb \to \ell\nu b$, the yield depends on the number of b–quarks that are to be tagged: for three b–tags, the background from $t\bar{t}j$ is overwhelming, while for four b–tags, several backgrounds with rates that are comparable to the signal are present. The conclusion of Ref. [387] is that a Higgs signal is unlikely to be observed in this channel, except in extensions of the SM where the production cross section can be enhanced.

3.6 The higher–order processes

3.6.1 Higgs boson pair production

In hadronic collisions, Higgs particles can be pair produced in three main processes[31]:

a) the gluon–gluon fusion mechanism which is mediated by loops of third generation heavy quarks that couple strongly to the Higgs boson [251, 252]

$$gg \to HH \tag{3.81}$$

b) double Higgs–strahlung from either a W or a Z boson [253, 254]

$$q\bar{q} \ \to V^* \ \to VHH \tag{3.82}$$

c) the WW/ZZ fusion processes which lead to two Higgs particles and two jets [254–256]

$$qq \ \to V^*V^*qq \ \to HHqq \tag{3.83}$$

The Feynman diagrams for these processes are shown in Fig. 3.39 and, as can be seen, one of them involves the trilinear Higgs boson coupling, $\lambda_{HHH} = 3M_H^2/v$, which can be thus probed in principle. The other diagrams involve the couplings of the Higgs boson to fermions and gauge bosons and are probed in the processes discussed in the previous sections.

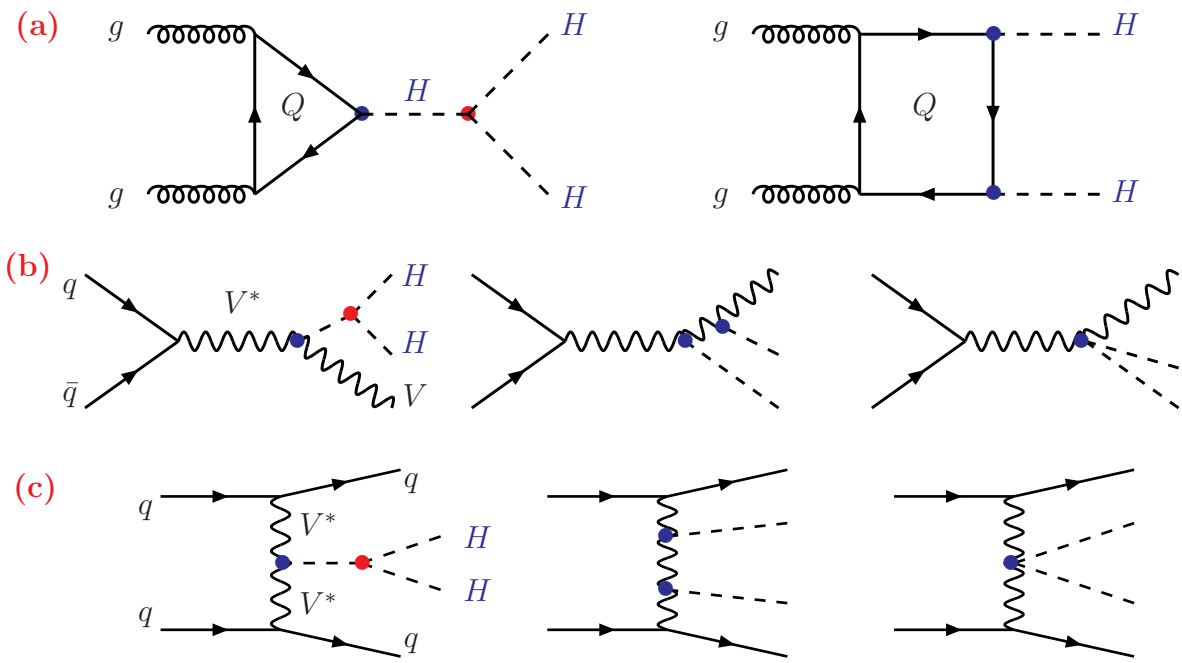

Figure 3.39: Feynman diagrams for Higgs pair production in hadronic collisions.

We briefly discuss these processes in this subsection, restricting ourselves to the case of the LHC where the phase space is not too penalizing.

[31] Triple Higgs production, which probes the quadrilinear Higgs coupling, has a too small cross section [389].

The gluon–gluon fusion mechanism

The large number of gluons in high–energy proton beams implies that the gluon–gluon fusion mechanism is the dominant process for Higgs boson pair production. As for single Higgs production in this mechanism, the coupling between gluons and Higgs bosons is mediated by heavy quark loops. In the SM, the top quark loop is dominating while the bottom quark loop gives a small but non–negligible contribution.

In terms of the trilinear Higgs coupling, $\lambda'_{HHH} = 3M_H^2/M_Z^2$ [note the change in the normalization], the partonic cross section at leading order is given by [252]

$$\hat{\sigma}_{\rm LO}(gg \to HH) = \int_{\hat{t}_-}^{\hat{t}_+} d\hat{t}\, \frac{G_\mu^2 \alpha_s^2(\mu_R)}{256(2\pi)^3} \left\{ \left| \frac{M_Z^2 \lambda'_{HHH}}{\hat{s} - M_H^2} F_T + F_B \right|^2 + |G_B|^2 \right\} \tag{3.84}$$

with the Mandelstam variables for the parton process given by

$$\hat{s} = Q^2 \;\; , \;\; \hat{t}/\hat{u} = -\frac{1}{2}\left[Q^2 - 2M_H^2 \mp Q^2 \beta_H \cos\theta\right] \tag{3.85}$$

where θ is the scattering angle in the partonic c.m. system with invariant mass Q and, as usual, $\beta = \sqrt{1 - 4M_H^2/Q^2}$. μ_R is the renormalization scale which, together with the factorization scale, will be identified to $\hat{s}$ and the integration limits correspond to $\cos\theta = \pm 1$ and $\hat{t}_\pm = -\frac{1}{2}\left[Q^2 - 2M_H^2 \mp Q^2\beta_H\right]$. The proton cross section is derived by folding the parton cross section $\hat{\sigma}(gg \to HH)$ with the gluon luminosity

$$\sigma(pp \to HH) = \int_{4M_H^2/s}^{1} d\tau \frac{d\mathcal{L}^{gg}}{d\tau} \hat{\sigma}(gg \to HH; \hat{s} = \tau s) \tag{3.86}$$

The dependence on the quark masses is contained in the triangle and box functions F_T, F_B and G_B. The expressions of these form factors with the exact dependence on the quark masses can be found in Refs. [251,252]. In the limit where the Higgs boson is much lighter or much heavier than the internal quark Q, the coefficients take a very simple form [252]

$$\begin{aligned} M_H \ll 4m_Q \qquad & F_T \simeq \frac{2}{3} \;, \quad F_B \simeq -\frac{2}{3} \;, \quad G_B \simeq 0 \\ M_H \gg 4m_Q \qquad & F_T \simeq -\frac{m_Q^2}{\hat{s}}\left[\log\frac{m_Q^2}{\hat{s}} + i\pi\right] \;, \; F_B \sim G_B \simeq 0 \end{aligned} \tag{3.87}$$

As one might have expected from single Higgs production, the QCD radiative corrections are particularly important for this production channel and must be included. They have been determined in the heavy quark limit $M_H^2 \ll 4m_Q^2$, where one can use the low energy theorem to determine the effective Hgg and $HHgg$ couplings in the triangle and box contributions, when the top quark is integrated out. One can then use these effective couplings to calculate the interaction of the light gluon and quark fields, as discussed previously. The K–factor was found to be $K \approx 1.9$ in the Higgs mass range between 100 and 200 GeV [390]. A K–factor of similar size is generally expected for larger Higgs masses and even beyond the top–quark threshold, as it was the case for the $gg \to H$ process.

The vector boson fusion and strahlung mechanisms

At high energies, on expects double Higgs production in the vector boson fusion channel to have a substantial cross section since the longitudinal vector bosons have couplings which grow with energy. The calculation of the full $2 \to 4$ process, $qq \to qqHH$, is rather complicated. However, one can use the equivalent longitudinal vector boson approximation in which one calculates the cross section for the $2 \to 2$ process

$$V_L V_L \to HH \tag{3.88}$$

Taking into account only the dominant longitudinal vector boson contribution, denoting by $\beta_{V,H}$ the V, H velocities in the c.m. frame, the production amplitude is given by

$$\begin{aligned} \mathcal{M}_{LL} &= \frac{G_\mu \hat{s}}{\sqrt{2}} \left\{ (1+\beta_V^2) \left[1+ \frac{M_Z^2 \lambda'_{HHH}}{(\hat{s}-M_H^2)} \right] \right. \\ &\left. + \frac{1}{\beta_V \beta_H} \left[\frac{(1-\beta_V^4)+(\beta_V-\beta_H \cos\theta)^2}{\cos\theta - x_V} - \frac{(1-\beta_V^4)+(\beta_V+\beta_H\cos\theta)^2}{\cos\theta + x_V} \right] \right\} \end{aligned} \tag{3.89}$$

with the variable x_V defined as $x_V = (1-2M_H^2/\hat{s})/(\beta_V\beta_H)$, θ the scattering angle in the VV c.m. frame and $\hat{s}^{1/2}$ the invariant energy of the VV pair.

Squaring the amplitude and integrating out the angular dependence, one obtains the cross section for the $V_L V_L \to HH$ subprocess,

$$\hat{\sigma}(V_L V_L \to HH) = \frac{G_\mu^2 M_V^4}{8\pi\hat{s}} \frac{\beta_H}{\beta_V (1-\beta_V^2)^2} \int_{-1}^{1} \mathrm{d}\cos\theta \, |\mathcal{M}_{LL}|^2 \tag{3.90}$$

which has then to be folded with the longitudinal vector boson luminosity spectra eq. (3.53) to obtain the $qq \to HHqq$ cross section, which again has to be convoluted with the parton densities to obtain the full hadronic cross section

$$\sigma(pp \to HHqq) = \int_{4M_H^2/s}^{1} d\tau \frac{d\mathcal{L}^{qq}}{d\tau} \, \hat{\sigma}(qq \to HHqq; \hat{s} = \tau s) \tag{3.91}$$

The result obtained in this way is expected to approximate the exact result within about a factor of two for low Higgs masses and very high energies [255, 256].

In the case of the double Higgs–strahlung mechanisms, $q\bar{q} \to HHV$, the production cross sections are expected to be rather small. This can be guessed by looking at the cross section for single Higgs–strahlung: for $M_H \sim 200$ GeV [which in terms of phase space would correspond to the production of two Higgs bosons with a mass of 100 GeV], it is of the order of 30 fb, and there will be still an additional suppression by the electroweak coupling factor in the case of double Higgs–strahlung. The analytical expressions will be given in the next section when this process will be discussed at e^+e^- colliders, where it is more relevant.

The cross sections at the LHC

The total cross sections for the pair production of Higgs bosons in the three processes are shown in Fig. 3.40 as a function of the Higgs mass in the range $M_Z \lesssim M_H \lesssim 2M_Z$. In the gg case, the full dependence on the quark mass has been taken into account and the $K \sim 1.9$ factor has been included. Note that the NLO QCD corrections to the double Higgs production in association with a vector boson and in the vector boson fusion channels, are the same as the respective processes for single Higgs production and will increase the cross sections by, respectively, $\sim 30\%$ and $\sim 10\%$; they have not been included.

As expected, gluon–gluon fusion dominates over the other mechanisms and has a cross section larger than 10 fb for this Higgs mass range. The WW/ZZ fusion mechanisms are the next important channels, but with cross sections which are one order of magnitude smaller; WW fusion dominates over ZZ fusion at a ratio $WW/ZZ \approx 2.3$. The cross sections for double Higgs–strahlung are relatively small as it follows from the scaling behavior of the cross sections which drop $\sim 1/\hat{s}$. The cross sections for Higgs–strahlung off W and Z bosons are combined in the figure and their their relative size is close to $W/Z \approx 1.6$.

The vertical arrows indicate the sensitivity of the production cross sections to the size of the trilinear Higgs coupling; they correspond to a modification of the coupling λ'_{HHH} by the rescaling coefficient $\kappa = \frac{1}{2} \to \frac{3}{2}$.

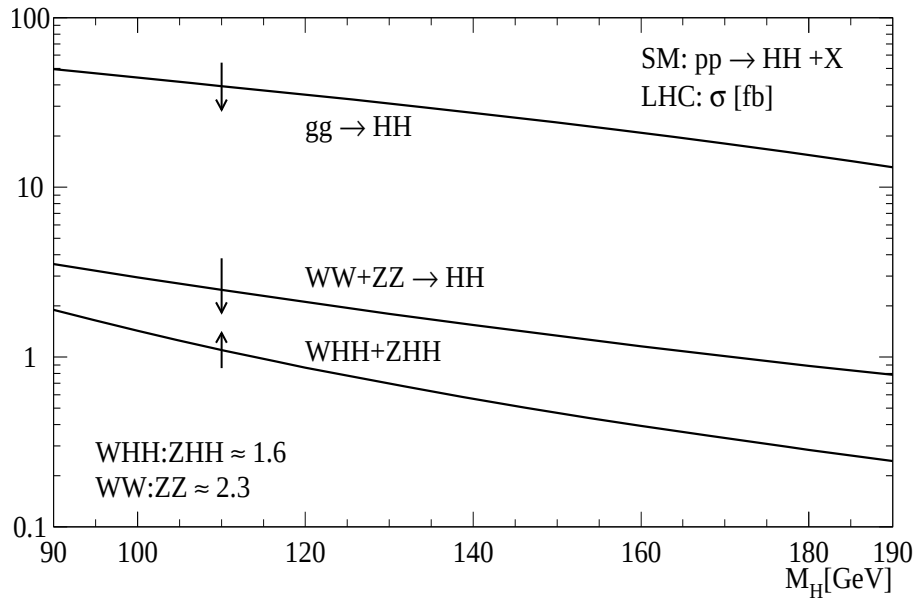

Figure 3.40: The cross sections for gluon fusion, $gg \to HH$, the WW/ZZ fusion $qq \to qqWW/ZZ \to HH$ and the double Higgs–strahlung $q\bar{q} \to WHH + ZHH$ in the SM as a function of M_H. The vertical arrows correspond to a variation of the trilinear Higgs coupling from $\frac{1}{2}$ to $\frac{3}{2}$ of the SM value, $\lambda'_{HHH} = 3M_H^2/M_Z^2$; from Ref. [254].

3.6.2 Higgs production in association with gauge bosons

Higgs production in association with gauge boson pairs

In high–energy collisions, the pair production of massive vector bosons $pp \to VV'$, with $V, V' = W, Z(\gamma)$, has a very large cross section. In view of these rates, it is tempting to consider the possibility of emitting an additional Higgs particle from one of the gauge boson lines [263, 264]

$$qq\,/\,q\bar{q} \;\to\; W^+W^-H\,,\,ZZH\,,\,W^\pm ZH \;\text{ and }\; qq\,/q\bar{q} \to \gamma ZH\;,\gamma W^\pm H \tag{3.92}$$

The hope is that the suppression by the additional electroweak coupling factor might be compensated by the initially large production rate for gauge bosons. Formally, these processes are of the same order, $\mathcal{O}(G_\mu^3)$, as Higgs production in the WW/ZZ fusion mechanisms and the suppression by the phase space should not be too drastic at high enough energies.

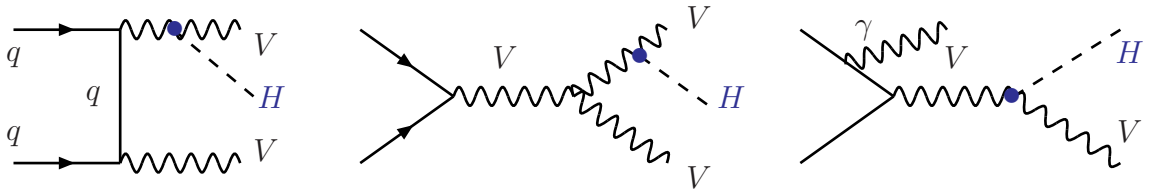

Figure 3.41: Diagrams for associated Higgs boson production with two gauge bosons.

As shown in Fig. 3.41, where some generic Feynman diagrams are displayed, the processes proceed through s–channel gauge boson and/or t–channel quark exchanges. Strictly speaking, the processes with additional final state photons which have enough large p_T to be observed, should be viewed as the ISR part of the electroweak corrections to the $q\bar{q} \to HV$ processes as discussed in §3.2. However, they are interesting since, besides the fact that the final state contains an additional photon which can be tagged, they can have larger rates compared to the parent processes which drop like $1/\hat{s}$ at high energies. The processes not involving photons are genuine higher–order processes, though at high energies they can also be viewed as a kind of "V bremsstrahlung" correction to the main mechanisms $q\bar{q} \to HV$.

The cross sections for these processes have been evaluated in Ref. [263] and updated recently [264] using `MadGraph` [391]. They are shown in Fig. 3.42 for the energy relevant at the LHC as a function of M_H. For the final states involving photons, the cuts $p_T^\gamma \geq 10$ GeV and $|\eta^\gamma| \leq 2.5$ have been applied. The CTEQ6 PDFs have been used and the scales were set at $\mu_R^2 = \mu_F^2 = \hat{s}$. The largest cross section is obtained for the $pp \to HWW$ process, as anticipated from the fact that the WW cross section is dominant at the LHC, being at the level of $\sigma(HWW) \sim 10$ fb for low mass Higgs values and decreases slowly to reach ~ 1 fb for $M_H \simeq 300$ GeV. Thus, it is larger than for double Higgs production in the strahlung and fusion processes. The cross sections for the other processes are a factor of 3 to 5 smaller but, except for $\sigma(HWZ)$, they are above the femtobarn level for $M_H \lesssim 160$ GeV.

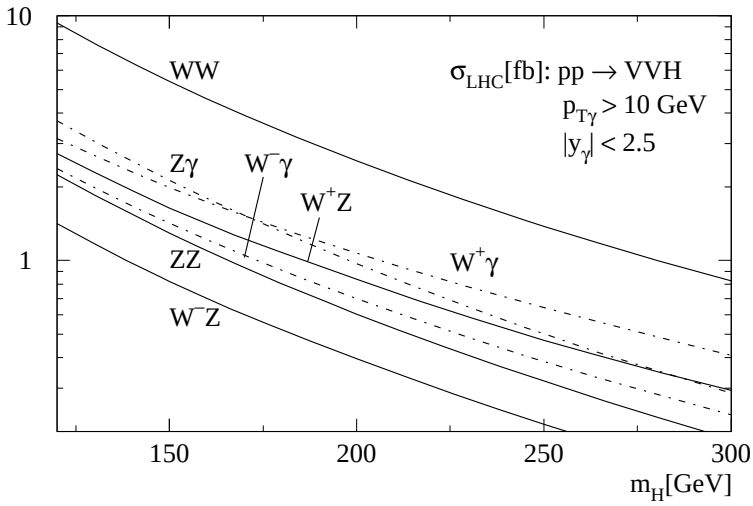

Figure 3.42: The total cross sections for the associated production of the Higgs boson with a pair of gauge bosons at the LHC, $pp \to HVV$, as a function of M_H; from Ref. [264].

In view of the smallness of the signal cross sections, these processes cannot of course be considered as Higgs discovery channels [in particular since the backgrounds from triple gauge boson production might be large]. However, once Higgs particles have been detected in the dominant detection channels, they could allow for additional tests and measurements, such as the determination of the HWW coupling from $pp \to HWW \to WWWW$ for instance.

Higgs production in association with a gauge boson and two jets

Associated Higgs production with a gauge boson and two quarks in hadronic collisions

$$qq \to HWqq \ , \ HZqq \ , \ H\gamma qq \tag{3.93}$$

originates from several sources, as shown in Fig. 3.43 where some Feynman diagrams are displayed, with the starting point being the fusion of the vector bosons producing a gauge or a Higgs boson. The production of $H\gamma qq$ final states occurs only through the $qq \to WWqq \to Hqq$ process, with the photon emitted from the quark or the internal W lines, which is part of the photonic corrections to the initial mechanism. Note that an additional source might come from the $pp \to HV$ process, with the emission of two jets in the final state: this also is part of the NNLO QCD corrections to Higgs–strahlung that we have already discussed.

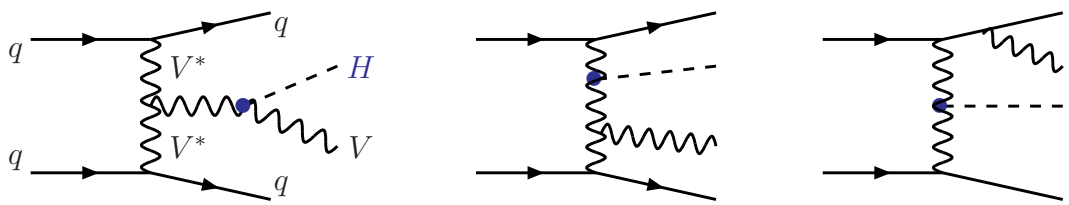

Figure 3.43: Feynman diagrams for associated $HVqq$ production in hadronic collisions.

The cross sections for these processes have been calculated sometime ago [265] both exactly and in the longitudinal W approximation [for the energy which was relevant for the late SSC] and the output was that the latter approximation gives results which are only about a factor of two different from the exact result. This is similar to Higgs pair production in the vector boson fusion channels $qq \to V^*V^* \to qqHH$, discussed previously. In fact, for $pp \to HZqq$, the analogy between the two processes is complete since the Z boson can be treated as a neutral Goldstone boson w_0, which has exactly the same coupling as the Higgs boson as can be seen from the effective potential eq. (1.58). The cross are not that small for such higher–order mechanisms: in the case of $pp \to HWqq$, they almost reach the level of 100 fb for Higgs masses in the low range [which is only one order of magnitude smaller than the Higgs–strahlung $pp \to HW$ cross section] and decrease only slowly with M_H.

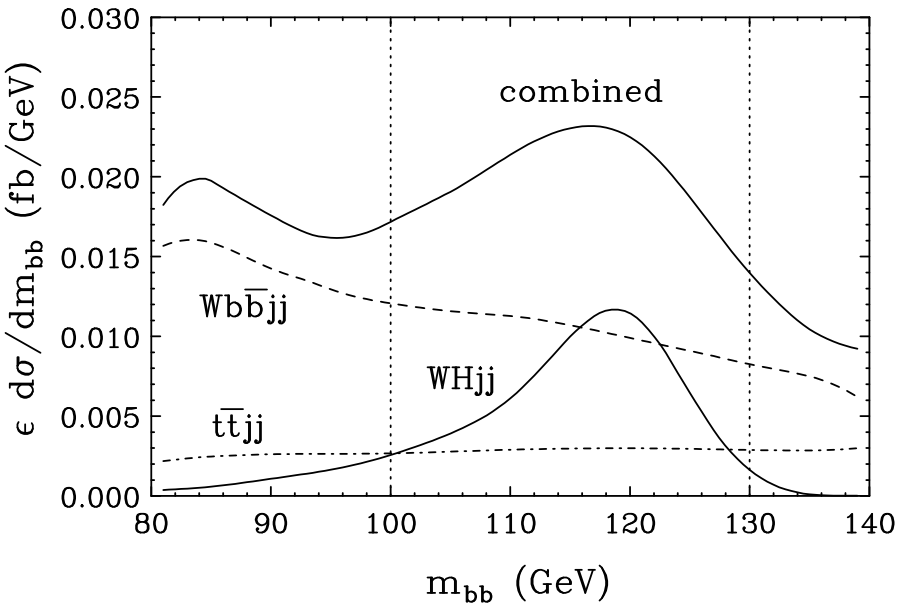

Figure 3.44: The $b\bar{b}$ invariant mass distribution of the $WHjj$ signal for $M_H = 120$ GeV and the $Wb\bar{b}jj, t\bar{t}jj$ backgrounds after cuts; the combined signal and backgrounds are also shown. The vertical dotted lines denote the mass bin used for calculating the statistical significance of the signal; from Ref. [266].

More recently, a detailed study of the signal for the $pp \to HWqq$ process has been performed at the LHC [266], in the channel where the Higgs decays into bottom quarks and the W boson leptonically. Applying cuts that are similar to those of the vector boson fusion process discussed in §3.3.3 and assuming reasonable efficiency for tagging the b quarks and resolution for the reconstruction of the $b\bar{b}$ invariant mass, the various backgrounds [in particular the $pp \to tt \to bbWW$ and the QCD $Wbbjj$ final states] can be reduced at a level comparable to the signal as shown in Fig. 3.44. This would allow for the extraction of the $Hb\bar{b}$ Yukawa coupling with a reasonable accuracy if a high luminosity is available.

3.6.3 More on higher–order processes

There are several other higher–order processes for Higgs production at hadron colliders, but they lead to extremely small cross sections at the LHC and, *a fortiori*, at the Tevatron. We briefly discuss some of them for completeness.

Higgs production in association with a photon

Higgs boson and photon final states in hadronic collisions [267] may originate from two main sources. An obvious possibility is the direct production from light quarks, $qq \to H\gamma$, where the Higgs boson is emitted from the quark lines. Because the Yukawa couplings are very tiny, the cross section are negligible. An exception might be the case of bottom quarks; however, besides the fact that the $Hb\bar{b}$ Yukawa coupling is still small, there is a suppression from the b density in the hadron. In fact, the cross section is comparable to the one for charm quark, the suppression of the Yukawa coupling m_c/m_b being partly compensated by the larger c–parton density and by the electric charge. For low Higgs masses, $M_H \sim 100$ GeV, the cross sections are at the femtobarn level at the LHC and one to two orders of magnitude smaller at the Tevatron. Since the dominant contribution is coming from $b\bar{b}$ initial state, this process is anyway equivalent to the processes $b\bar{b} \to H$ and $gg \to b\bar{b}H$ with two undetected b quarks, with the radiation of an ISR photon.

Another possibility to generate the Higgs plus photon final state is via loop diagrams in quark–antiquark annihilation [the corresponding process with initial state gluons, $gg \to H\gamma$, is forbidden by Furry's theorem similarly to the $H \to \gamma\gamma g$ decay discussed in §2.3]. There are triangular diagrams, when the $q\bar{q}$ state annihilates into a virtual photon or Z boson in the s–channel and which involve virtual top quarks and W bosons and box diagrams with W bosons and light quarks running in the loop. Since the process is of $\mathcal{O}(G_\mu^4)$ and because of the suppression by the loop factor, the cross sections are extremely small: at the LHC they are at the level of 0.1 fb and they are much lower at the Tevatron [267].

Loop induced Higgs pair production in $q\bar{q}$ annihilation

Similarly to the gg fusion process, $gg \to HH$, which provides the largest cross section for Higgs boson pairs at the LHC, one can produce pairs of Higgs particles in $q\bar{q}$ annihilation. Because the Higgs couplings to the light quarks are small and since CP conservation forbids a ZHH coupling at the tree–level, the entire contribution to this process originates from loop diagrams. In fact, as a result of chiral symmetry, only box diagrams involving quarks and massive gauge bosons, from which the Higgs particles are emitted, are present. The process is thus not sensitive to the trilinear Higgs coupling.

This calculation has been performed in Ref. [268] and, as one might have expected,

because of the lower luminosity for quarks than for gluons at high energies, the cross sections are much smaller than those of the $gg \to HH$ production process. At LHC energies the difference is at least one order of magnitude. At the Tevatron, the cross sections will be anyway very small because of the reduced phase space. The annihilation of $q\bar{q}$ states is, thus, not an important process for double Higgs boson production.

Higgs pair production with heavy quarks

Similarly to the double Higgs boson production in the WW/ZZ fusion processes, one might take advantage of the large Yukawa coupling to top quarks to produce two Higgs bosons emitted from the top quark lines in the process $gg/q\bar{q} \to t\bar{t}$. An interesting feature is that there is a contributing diagram where a Higgs boson is emitted from the top quark lines and then splits into two Higgs bosons. This process is therefore sensitive to the trilinear Higgs coupling and, despite of the suppression by the electroweak couplings, one might hope for a compensating enhancement of the cross section due to the presence of the Higgs boson exchange in the s–channel. The complete calculation for this four massive particle final state is rather complicated[32] and has been performed numerically in Ref. [270]. At the LHC, the cross section is at the level of 1 fb for $M_H \sim 120$ GeV and, thus, of the same order as VHH production and much smaller than $gg \to HH$ production. The large backgrounds make it impossible to extract any signal even with extremely high luminosities [270].

Rare decays of the top quark

The huge cross section of the process $gg/q\bar{q} \to t\bar{t}$ allows to produce 10^7 to 10^8 top quark pairs per year at the LHC. This large number of events could be used to look for very rare decays of this particle. If the Higgs boson is not too heavy, $M_H < m_t$, the decay $t \to cH$ can occur through loop diagrams. Starting from the flavor changing transition $t \to c$, which is mediated by loops involving W bosons and down–type [mainly bottom] quarks, one can attach a Higgs boson either to the external top quark line or to the internal W boson or b quark lines. However, because the decay is suppressed by three powers of the Fermi constant G_μ and by the GIM mechanism, the branching ratio is extremely small $\mathrm{BR}(t \to cH) \lesssim 10^{-13}$ for $M_H \gtrsim 100$ GeV [271]. In view of the experimental bound $M_H \gtrsim 115$ GeV, the parent decay process $t \to bWH$ [155, 272] is now kinematically closed.

[32] One can estimate the order of magnitude of the cross section, by naively treating the heavy top quarks as partons inside the hadron and considering at the partonic level the process of heavy top quark annihilation into two Higgs bosons, $t\bar{t} \to HH$. This calculation has been performed in Ref. [269] some time ago [at the time where the top quark was believed to have a mass of the order of 50 GeV and where the SSC was still expected to operate] and the output was that, even for hadronic c.m. energies of $\sqrt{s} = 40$ TeV, the "partonic" cross sections folded with luminosities which may be overestimated by a factor of ten, lead to a total rate which is at the level of the cross section for the longitudinal W boson fusion into two Higgs bosons.

3.6.4 Diffractive Higgs boson production

Diffractive processes in (anti)proton collisions are those in which color singlet objects are exchanged between the high energy initial protons, which allow them to be diffracted [273–275]. This can occur, for instance, when two gluons are exchanged in the t–channel by the initial protons: this neutralizes the color and allow the two protons to remain intact and continue their way. Higgs production occurs in the emission from the t–channel exchanged particles and, in the case of t–channel gluons, this occurs through the usual ggH vertex mediated by heavy quark loops. The signature is then two protons which are produced at very large rapidities and a centrally produced Higgs particle

$$p + p \to p + H + p \tag{3.94}$$

where the + sign means that there is a large rapidity gap between the particles. In addition, if one tags the initial hadrons [using the so–called roman pot detectors], these diffractive processes can be selected and result in a very clean signal [the backgrounds will be discussed later]: a Higgs boson in the central region, and nothing else.

There are many models for diffractive Higgs production in the literature, starting from the Bialas–Landshoff exclusive model [273]. They all involve a mixture of perturbative and non perturbative QCD physics which is not very well understood yet. In the context of Higgs physics, hard diffractive production in the central region are the most interesting ones. We briefly summarize the main features of some processes for a light Higgs boson decaying mainly into $b\bar{b}$ pairs, following Refs. [276,277] where a detailed account is given and to which we refer for earlier work. Figure 3.45, taken from Ref. [276], illustrates three processes for double diffractive Higgs production in hadronic collisions that one can partly discuss in the familiar terms of perturbative QCD. We use the terminology of this reference.

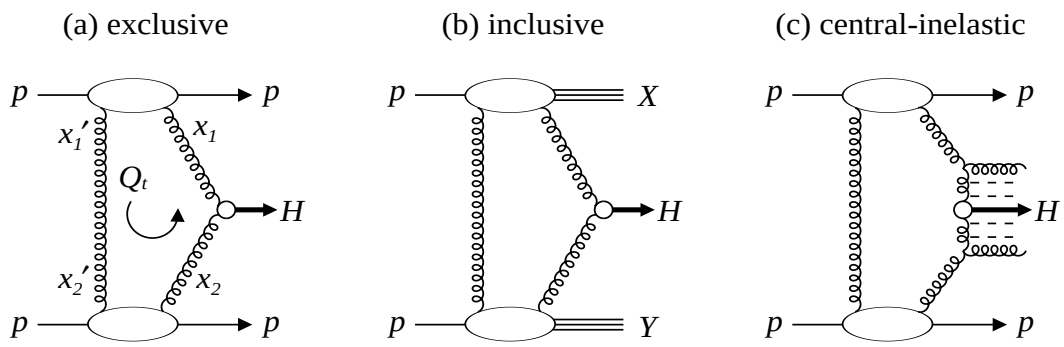

Figure 3.45: Examples of processes for double–diffractive Higgs production in pp collisions.

In the central exclusive double diffractive processes shown in Fig. 3.45a, the Higgs boson is produced alone and is separated from the outgoing hadrons by large rapidity gaps. If the latter are tagged, the Higgs mass can be determined either by measuring the missing

mass $M_{\rm inv}$ of the system or by reconstructing the $H \to b\bar{b}$ decays mass peak $M_{b\bar{b}}$; one can then match the two measurements, $M_{\rm inv} = M_{b\bar{b}} = M_H$ which provides a strong kinematical constraint. Moreover, an interesting feature is that in the production vertex, the polarization vectors of the gluons are correlated in a such way that with the resulting effective luminosity, only spin–zero particles with positive parity, i.e. with $J^{\rm PC} = 0^{++}$ quantum numbers, can be primarily produced [the cross section for CP–odd states is strongly suppressed]. On the other hand, the background from $gg \to b\bar{b}$ for instance is strongly suppressed, $\hat{\sigma}(gg \to b\bar{b}) \propto \alpha_s^2 m_b^2/\hat{s}$. The Higgs spin and parity quantum numbers can therefore be checked in this process [392] with only an ambiguity with 2^{++} states remaining. Unfortunately, the model predicts rather low Higgs production cross sections: for a Higgs boson with a mass $M_H \sim 120$ GeV, they are of the order of 0.2 fb at the Tevatron and 3 fb at the LHC; see Table 3.1. The uncertainty in the prediction is also large, a factor of 2 at the LHC for instance.

Model	Exclusive (a)	Inclusive (b)	Central inel. (c)
Tevatron	0.2	1	0.03
LHC	3	40	50

Table 3.1: Higgs boson production cross sections in fb at the Tevatron and the LHC for $M_H \sim 120$ GeV in the various diffractive models of Fig. 3.45; from Ref. [276].

In central inelastic production, Fig. 3.45c, there is an additional radiation accompanying the Higgs boson in the central region, but the latter is still separated from the final hadrons by large rapidity gaps[33]. This leads in general to a much larger Higgs production cross section at the LHC; see Tab. 3.1 [at the Tevatron all processes have too small cross sections to be useful]. However, the background from $gg \to b\bar{b}$ is also very large since there is no more the selection rule for spin–zero particle production and the signal to background ratio is then very low. In addition, one cannot use the missing mass technique to measure the Higgs mass [it has been suggested recently [394] to trigger on the remnants to improve the S/B ratio and to reconstruct the mass]. Nevertheless, besides the fact that these processes are actually the ones which have been experimentally observed, since the CDF dijet data indicate the presence of an additional soft hadronic radiation [395], they need to be considered, first because they are potential backgrounds to the exclusive process, and second because pseudoscalar Higgs bosons can be only produced in these mechanisms.

In inclusive production [according to the terminology of Ref. [276]], Fig. 3.45b, the previous discussion on the process of Fig. 3.45c also applies with the important exception that both incoming protons are allowed to dissociate. This process has not received much atten-

[33]In fact, in the terminology of Ref. [393] which is becoming the standard one, it is the process of Fig. 3.45c which is called the inclusive diffractive process.

tion in the literature as it has not the advantages of central exclusive diffraction. At the LHC, the production rates [276] are of the same order as in the previous case; Tab. 3.1.

As mentioned previously, the treatment of diffractive processes involves a mixture of perturbative and non–perturbative aspects of QCD. The rapidity gaps for instance may be associated with the exchange of an effective Pomeron which can be either a QCD Pomeron [which, at lowest order, is a gg state] or a phenomenological Pomeron fitted from e.g. the HERA data. The non perturbative aspect in exclusive diffraction arises when one attempts to calculate the survival probabilities S^2 of the rapidity gaps, when secondary particles are produced in the soft rescattering of the spectator partons and populate these gaps. This probability is not universal and depends on the initial energy and the considered final state. A recent estimate gives $S^2 \sim 0.02$ while diffractive deep–inelastic processes at HERA and diffractive dijet production at the Tevatron suggest, respectively, $S^2 \sim 1$ and ~ 0.1. Note that another probability for the gaps to be occupied arises from hard gluon radiation in $gg \to H$ for instance; the latter can be, however, calculated in perturbative QCD.

These non–perturbative aspects generate rather uncertain predictions of the various models and, until recently, the spread in the predictions ranging over several orders of magnitude. A critical comparison of the various predictions has been performed in Ref. [276], where it has been attempted to explain the origin of the large differences. The conclusion was that either different diffractive processes have been considered or important effects, such as higher–order QCD corrections, have been neglected. Many of the models, in particular those which predict large Higgs production rates, are already ruled out by Tevatron data on diffractive dijet production. Besides these theoretical issues, experimental problems such as the possibility of triggering on the events and the integration of the roman pot detectors within the machine, remain still to be solved; see Ref. [277] for instance.

Note that the expectation for the clean exclusive central Higgs production process can be checked at the LHC itself, since the main ingredients which are needed for the calculation of the Higgs signal cross section are involved in the calculation of dijet production with large rapidity gaps, $pp \to p + \text{dijet} + p$. Since the latter can be measured from the side bands, one can improve the prediction of the Higgs cross section. Other checks can be performed [275].

In summary, diffractive processes in hadronic collisions provide an additional means to produce the Higgs boson at the LHC. The double exclusive production process allows a good measurement of the Higgs mass and a check of the SM Higgs spin and parity quantum numbers [besides the selection which favors 0^{++} states, one can also use, for instance, the azimuthal asymmetry of the scattered protons], which are notoriously difficult to verify at hadron colliders, as will be discussed shortly. The production rates are, however, still uncertain and the experimental conditions not yet established. Many studies are being performed and the situation might become more clear in a near future.

3.7 Detecting and studying the Higgs boson

3.7.1 Summary of the production cross sections

The cross sections for Higgs boson production in the main channels, eqs. (3.1–3.4), are summarized in Fig. 3.46 at the Tevatron Run II with a c.m. energy $\sqrt{s} = 1.96$ TeV and in Fig. 3.47 for the LHC with $\sqrt{s} = 14$ TeV as functions of the Higgs boson mass, an update of Refs. [21, 396, 397]. They include the full NLO QCD corrections which have been discussed earlier. The MRST sets of parton densities [311] has been used for the cross sections. As inputs, we use the central values for the fermion and gauge boson masses given in eq. (2.1), in particular we use $m_t = 178$ GeV, while the strong coupling constant is chosen to be $\alpha_s(M_Z) = 0.119$ to match the value that is incorporated in the PDFs at NLO. Here also, we will denote sometimes by pp both pp and $p\bar{p}$ reactions and by $\mathcal{L}$ both $\mathcal{L}$ and $\int \mathcal{L} dt$.

The cross sections eqs. (3.1) to (3.4) have been calculated using, respectively, the NLO FORTRAN codes `V2HV, VV2H, HIGLU` and the LO code `HQQ` of Ref. [278] which are publicly available. A few remarks to explain how these cross sections have been obtained are in order:

– In the $gg \to H$ mechanism, we display the NLO cross sections which have been calculated for arbitrary quark masses, since the NNLO calculation is valid only in the heavy top quark limit [although it is expected to be a good approximation for the entire range if the Born amplitude contains the full m_t dependence]. However, we have set the renormalization and factorization scales at $\mu_R = \mu_F = \frac{1}{2} M_H$. As discussed previously, in this way the NLO (NNLO) correction increases (decreases) and the full result approaches the total cross section at NNLO. We have verified that the values that we obtain are in a very good agreement with the NNLO values given for $M_H \leq 300$ GeV in Ref. [303].

– In the case of the Higgs–strahlung processes, $pp \to HW$ and $pp \to HZ$, we incorporate the NLO and NNLO QCD corrections, including the $gg \to HZ$ component in the latter production process, as well as the electroweak radiative corrections [where we removed the kinks near the $2M_V$ thresholds]. For the PDFs, we will use the approximate densities which are included in the MRST2002 set and which approach very closely the exact result.

– For the $pp \to t\bar{t}H$ production process, the NLO corrections have become available only recently and the FORTRAN codes for calculating the cross sections at this order are not yet publicly available. We therefore use the LO program `HQQ` but we choose a scale for which the LO cross sections approach the NLO ones, i.e. $\mu_R = \mu_F \sim \frac{1}{2} M_H + m_t$. We then multiply the cross sections by constant K–factors of 1.2 and 0.8 for the LHC and the Tevatron, respectively, to approach the exact result. We have verified that, for $m_t = 174$ GeV, the obtained rates are in a very good agreement with the NLO ones given in Ref. [287].

– The cross section for the vector boson fusion process $pp \to Hqq$ has been calculated at NLO with the scales fixed to $\mu_R = \mu_F = Q_V$. No kinematical cut has been applied.

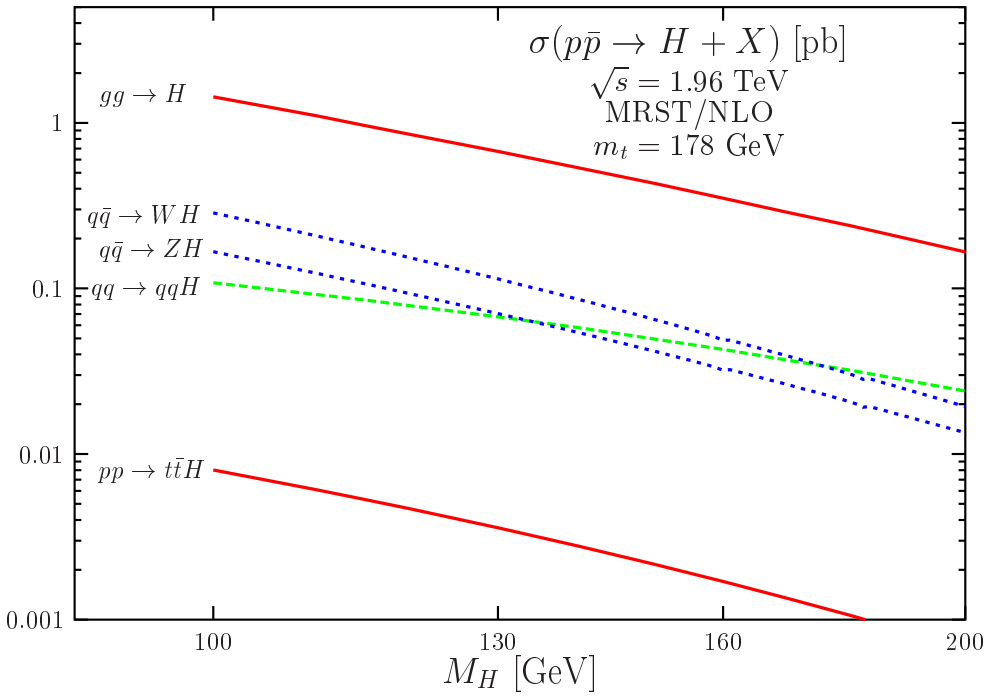

Figure 3.46: The Higgs boson production cross sections at the Tevatron in the dominant mechanisms as a function of M_H. They are (almost) at NLO with $m_t = 178$ GeV and the MRST set of PDFs has been used. The scales are as described in the text.

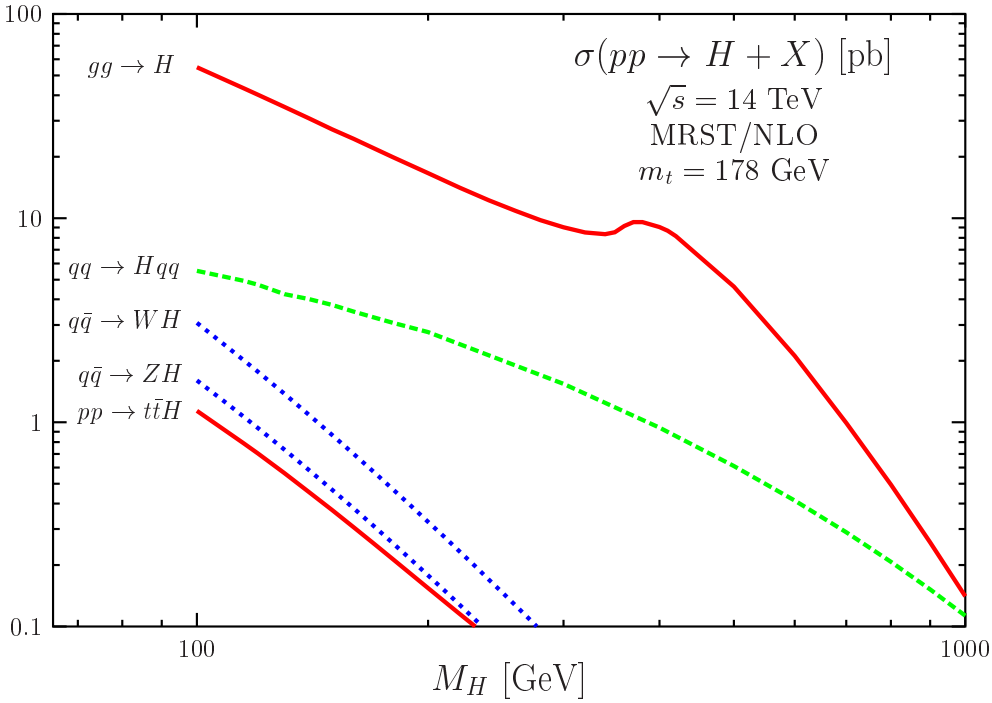

Figure 3.47: The same as Fig. 3.46 but for the LHC.

In Table 3.2, we display the numerical values of the cross sections for selected values of the Higgs mass that are relevant for the Tevatron and the LHC, as they might serve as useful inputs in other studies. The various SM input parameters are as discussed above.

M_H [GeV]	$\sigma(HW)$	$\sigma(HZ)$	$\sigma(Hqq)$	$\sigma(gg \to H)$	$\sigma(Ht\bar{t})$
115	0.178	0.107	0.085	0.96	0.0053
120	0.153	0.093	0.078	0.85	0.0047
130	0.114	0.070	0.067	0.67	0.036
140	0.086	0.054	0.058	0.54	0.0028
150	0.065	0.042	0.050	0.43	0.0022
160	0.048	0.032	0.043	0.35	0.0017
170	0.039	0.026	0.037	0.29	0.0013
180	0.030	0.020	0.032	0.24	0.0010
200	0.019	0.013	0.024	0.17	–

M_H [GeV]	$\sigma(HW)$	$\sigma(HZ)$	$\sigma(Hqq)$	$\sigma(gg \to H)$	$\sigma(Ht\bar{t})$
115	1.89	1.01	4.93	43.32	0.79
120	1.65	0.89	4.72	40.25	0.70
130	1.28	0.70	4.24	35.04	0.56
140	1.00	0.55	4.01	30.81	0.45
150	0.79	0.44	3.76	27.22	0.37
160	0.62	0.35	3.49	24.44	0.31
170	0.52	0.29	3.26	21.97	0.25
180	0.42	0.24	3.07	19.87	0.21
200	0.30	0.17	2.76	16.61	0.15
300	0.04	0.07	1.54	9.02	–
400	–	–	0.94	9.05	–
500	–	–	0.61	4.62	–
600	–	–	0.41	2.12	–
700	–	–	0.29	0.99	–
800	–	–	0.21	0.49	–
900	–	–	0.15	0.26	–
1000	–	–	0.11	0.14 ,	–

Table 3.2: Numerical values for SM Higgs production cross sections at the Tevatron (upper part) and the LHC (lower part) in picobarns for selected values of the Higgs mass. These values have been obtained as in Figs. 3.46–3.47 and as explained in the text.

As can be seen, in the interesting mass range favored by the electroweak precision data, $100 \lesssim M_H \lesssim 250$ GeV, the dominant production process of the SM Higgs boson at the LHC is by far the gluon–gluon fusion mechanism, the cross section being of the order a few tens of pb. In fact, this process dominates all the way up to Higgs masses of the order of 1 TeV, where the cross section is still sizable, $\sigma(gg \to H) \sim 0.1$ pb. It is followed by the WW/ZZ fusion process which has a cross section of a few pb in the interesting Higgs mass range above and which reaches the level of the gg fusion cross section for very large M_H values. The cross sections for the associated production with W/Z bosons or $t\bar{t}$ pairs are one to three orders of magnitude smaller than the gg cross section and these processes are only relevant in the mass range $M_H \lesssim 250$ GeV. For the luminosities expected at the LHC, a very large sample of Higgs particles can be thus collected before selection cuts are applied.

At the Tevatron, the most relevant production mechanism is the associated production with W/Z bosons [the $WH : ZH$ cross section ratio is approximately 1.5 for $M_H \lesssim 200$ GeV], where the cross section is slightly less than 250 fb for $M_H \sim 120$ GeV when both processes are summed, leading to 2.500 Higgs events for the maximal luminosity expected at the Tevatron, $\int \mathcal{L} = 10$ fb^{-1}; the cross section drops to the level of less than 30 fb for Higgs masses larger than 200 GeV. The WW/ZZ fusion cross sections are of the same order in the mass range $M_H \lesssim 100$–200 GeV, while the cross sections for associated production with $t\bar{t}$ pairs are rather low, being less than 10 fb already for $M_H \sim 115$ GeV. The gg fusion mechanism has the largest production cross section, reaching the picobarn level for low Higgs masses, but suffers from a very large QCD two–jet background as will be discussed later.

A huge effort, which already started in the late seventies, has been devoted to the search of suitable signals to detect the Higgs boson at hadron colliders and to suppress the various corresponding backgrounds, which are in general very large. It is an impossible task to present here a detailed account of the large number of theoretical and experimental studies which have been performed in this context. In the next subsection, we simply summarize the Higgs detection channels which are established since already some time, mostly relying on the report of the Higgs working group in the case of the Tevatron [218] [see [217] for earlier work] and in the case of the LHC[34], on the ATLAS Technical Design Report [228] and CMS Technical Proposal [229] with some updates made in Refs. [234–236] as well as on the joint theoretical and experimental studies which have been performed at the three Les Houches [238–240] and at the 2001 Snowmass [223] Workshops [where some of the references to the original work can be found]; see also Ref. [402]. Some of the important backgrounds will be briefly mentioned and a detailed account can be found in various reviews [45, 82, 403, 404]; see also Ref. [405]. For earlier work, we refer the reader to *The Higgs Hunter's Guide* where the pioneering analyses and a complete set of earlier references can be found.

[34]The analyses at the LHC that will be discussed here will be mostly based on Monte–Carlo [398, 399] simulations which take into account the parametrized [400, 401] or full detector response [228, 230].

3.7.2 Higgs signals and backgrounds at the Tevatron and the LHC

The $pp \to HW/HZ$ channel

It has been realized a long time ago [242,315] that the associated Higgs production with W/Z bosons, with the latter decaying into leptons $\ell = e^{\pm}, \mu^{\pm}$, is a potential channel for detecting the Higgs particle at high–energy hadron colliders [the LHC and the late SSC]. This has been confirmed later for the LHC in parton–level analyses in the case of the photonic Higgs boson decays [316,317]. Also more recently, it has been shown that this production channel is the most promising detection mode at the Tevatron Run II for a relatively light Higgs boson which decays dominantly into $b\bar{b}$ pairs [320,321].

In principle, the hadronic decays of the companion vector bosons cannot be used [unless the Higgs boson itself does not decay into hadrons] as they are overwhelmed by the huge irreducible QCD backgrounds. Since the branching fraction BR($W \to \ell\nu$) $\sim 20\%$ is larger than BR($Z \to \ell\ell$) $\sim 6\%$, and the cross section for $q\bar{q}' \to WH$ is a factor ~ 1.5 larger than for $q\bar{q} \to ZH$, the process $p\bar{p} \to HW \to H\ell\nu$ leads to five times more interesting events than the corresponding $p\bar{p} \to HZ \to H\ell\ell$ process. Both channels have to be summed, however, to increase the statistics. In addition, the neutrino decays of the Z boson which have a substantial rate, BR($Z \to \nu\bar{\nu}$) $\sim 18\%$, can also be considered. The final signals depend on the decay modes of the Higgs boson and, thus, on its mass and are summarized below.

• $\underline{H \to b\bar{b}}$: the dominant Higgs decay mode for $M_H \lesssim 135$ GeV, leads to the final states $\ell\nu b\bar{b}$, $\ell\ell b\bar{b}$ and $\nu\bar{\nu}b\bar{b}$ that exhibit distinctive signatures [isolated leptons and/or missing energy] which can be used at the Tevatron where the backgrounds are not too large. The latter mainly originate from the production of vector bosons plus two–jets, $p\bar{p} \to Vjj$ and in particular $Wb\bar{b}$ [406,407], vector boson pairs, $p\bar{p} \to VV$ [407–409], top quark pairs, $p\bar{p} \to t\bar{t}$ [410] and single top quarks $p\bar{p} \to t + X$ [388]. These processes are known at least to NLO in QCD. b–tagging as well as the reconstruction of the $b\bar{b}$ invariant mass peak are crucial to reject them. Results based on the the SHW simulation [411] which gives the average response of the upgraded CDF and DØ detectors in a simple way, show that these processes and, in particular, $p\bar{p} \to WH \to \ell\nu b\bar{b}$, are viable at the Tevatron [218]. In the case of the $\nu\bar{\nu}b\bar{b}$ channel, a significant $b\bar{b}$ background remains [which in Ref. [218] has been assumed to be equal to the sum of the remaining backgrounds]. The separation of the signal and backgrounds was optimized using neutral network techniques which lead to an appreciable increase of the signal significance [412,413]. The $WH \to \ell\nu b\bar{b}$ channel has been also discussed for the LHC [315,318] but due to the much larger QCD background, it is not considered alone as a clear discovery channel [228,235,414–416]. The significance of the signal is at the level of $\sim 3\sigma$ for $M_H = 120$ GeV with $\mathcal{L} = 30$ fb^{-1} [415] when the $Wb\bar{b}$ and $t\bar{t}$ backgrounds have been sufficiently suppressed. This significance can be, however, added to the one from $pp \to t\bar{t}H$ when it leads to the same final state as will be discussed later.

• $\underline{H \to WW^{(*)}}$: which becomes the dominant Higgs decay mode for $M_H \gtrsim 135$ GeV has also been considered both at the Tevatron and the LHC [319]. It receives irreducible backgrounds from triple vector boson production, $pp \to WW + W/Z$ [417], in addition to those from vector boson and $t\bar{t}$ pair production. Distinctive signatures are trilepton $\ell\ell\ell$ events, like sign dileptons and two jets $\ell^\pm\ell^\pm jj$ as well as a high–p_T lepton pair plus missing E_T. At the Tevatron, the small production cross section, the low luminosity as well as the small branching ratio $WWW \to 3\ell \sim 10^{-2}$, make that only a few trilepton events can be observed even for 30 fb^{-1} data; the $\ell^\pm\nu\ell^\pm\nu jj$ signal is only a factor of three larger. The rates are thus too small for this channel to be useful. The channel is more promising at the LHC, in particular for a Higgs boson in the mass range $M_H \sim 160$–180 GeV, where it decays almost 100% of the time into WW final states, and where the production cross section is still large. Detailed simulations have shown that a significance $S/\sqrt{B} \gtrsim 5$ can be obtained in the channel $pp \to HW \to \ell^\pm\nu\ell^\pm\nu jj$ or 3ℓ with a high luminosity $\mathcal{L} = 100$ fb^{-1} [418].

• $\underline{H \to ZZ^{(*)}}$: has a too small branching ratio for $M_H \lesssim 180$ GeV, when one of the Z bosons is virtual. Above the ZZ threshold, the HV production cross section is very small at the Tevatron. At the LHC, the cross section is still sizable and, once the leptonic branching fractions of the Z and W boson in HW production have been taken into account, a rate of ~ 2 fb can be obtained for $M_H \sim 200$ GeV before applying cuts. The few hundred $\ell\ell\ell\nu jj$ events which could be collected in the high luminosity regime might allow to detect the signal. To our knowledge, no simulation has been performed for this channel alone.

• $\underline{H \to \gamma\gamma}$: is a decay mode that is too rare to be useful at the Tevatron but it is the main detection channel at the LHC in the low Higgs mass range for this production process. In fact, it was the first channel in HV production which has been shown in parton–level analyses to be viable [316, 317]. The backgrounds are similar to those which affect the process $gg \to H \to \gamma\gamma(j)$ to be discussed later: the reducible ones are small [419] and the irreducible $\gamma\gamma\ell + \not{E}$ and $\gamma\gamma\ell\ell$ backgrounds can be suppressed by requiring high–p_T and well isolated photons and lepton(s). Early analyses have shown that this signal is indeed viable at the LHC for a Higgs boson in the low mass range [228, 229, 420] but the signal has a small significance and should be combined with the one from $pp \to t\bar{t}H \to \ell\gamma\gamma + X$ as will be seen shortly. A recent CMS simulation [421] has shown that in a one year of LHC at high–luminosity, a 5 (4) σ significance can be obtained for the signal if $M_H \lesssim 135$ (150) GeV.

• $\underline{H \to \tau\tau}$: has a branching ratio of only a few percent for $M_H \lesssim 135$ GeV and one cannot afford to let the associated gauge bosons to decay leptonically. The $pp \to ZH/WH \to jj\tau\tau$ channel has been considered in a parton level analysis [322] for the Tevatron with the result that a significant improvement of τ identification and a large luminosity might allow to detect the signal for low mass Higgs bosons if one can trigger on these events. No discussion of this channel has been made in the Tevatron study of Ref. [218] nor at the LHC, though.

The gluon–gluon fusion channel

This process, having the largest production cross section, has been considered for a long time as being the most efficient one in the search for the Higgs boson at the LHC. However, it appeared quite early that these searches cannot be made in the dominant hadronic $H \to b\bar{b}$ and $H \to WW/ZZ \to 4j$ decay channels because of the extremely large QCD jet backgrounds. The $H \to \tau^+\tau^-$ signature in the low Higgs mass range is also very difficult to extract at the LHC [and also at the Tevatron] because of these backgrounds. One has then to rely on rare Higgs decays which provide clean signatures involving photons and/or leptons for which the backgrounds are smaller but far from being negligible.

• $H \to \gamma\gamma$: has been proposed rather early [315,352] and is the "silver" detection channel for a Higgs boson with a mass below 150 GeV [422]. The reducible QCD background from jets faking photons is huge and a rejection factor of $\mathcal{O}(10^6)$ is needed to bring it down to the level of the irreducible one from direct $q\bar{q} \to \gamma\gamma + X$ production and the loop induced channel $gg \to \gamma\gamma + X$ which provides a 50% contribution. These have been studied in great detail [423] and the state–of–the–art higher–order results are contained in the program `DIPHOX` [424] which also includes the fragmentation effects. These backgrounds can, in principle, be determined by measuring the two–photon invariant mass distribution $\mathrm{d}\sigma/\mathrm{d}M_{\gamma\gamma}$ on both sides of the resonance peak. However, they need to be precisely calculated for the evaluation of the detection significance and when it comes to measurements of the Higgs properties [405]. A reconstruction efficiency of about 75% can be achieved for a single photon and for $M_H \sim 130$ GeV, the final signal to background ratio is of the order of 1/30 in a window of $M_{\gamma\gamma} \sim 2$ GeV. However, since the decay is rare, a large amount of luminosity needs to be collected. One could then use, in addition, the $pp \to Hj$ signal [372] as the $gg \to \gamma\gamma g$ background with a hard jet has been found to be much smaller. In fact, at low luminosities, the combination of all $H \to \gamma\gamma$ channels is required: not only the $pp \to \gamma\gamma$ and $pp \to \gamma\gamma j$ channels but also the channel $pp \to \gamma\gamma + \ell$ where the additional lepton comes from the decay of a W boson in the associated HW production process discussed previously or in $t\bar{t}H$ production with $t \to bW \to b\ell\nu$ as will be seen later.

• $H \to ZZ^{(*)}$: in the high mass region, $M_H > 2M_Z$, the decay $H \to ZZ \to 4\ell$ is the "gold–plated" mode [242, 315, 352, 353], allowing for Higgs detection up to masses of $\mathcal{O}(1\,\mathrm{TeV})$ [228, 425, 426]. The main background is due to continuum ZZ production which is known rather precisely [408, 409] but which can be also directly measured from the side bands of the resonance peak and interpolated to the signal region. For $M_H \gtrsim 600$ GeV, high enough luminosities are required since $\mathrm{BR}(H \to ZZ \to 4\ell) \sim 0.1\%$ is small and the total Higgs width becomes large. To increase the statistics, one can use in addition the $H \to ZZ \to \ell\ell\nu\nu$ decays [354] in which the signal appears as a Jacobian peak in the missing transverse energy spectrum. Additional backgrounds from Zj events [406], where the $\not{E}_T$

is due to neutrinos from semi–leptonic b decays for instance, need to be considered [427]. Allowing one of the Z bosons to be virtual, the discovery reach can be extended down to masses $M_H \sim 120$ GeV using $H \to ZZ^* \to 4\ell$ decays [428], except in the range $M_H \sim 2M_W$–$2M_Z$ where BR($H \to ZZ^*$) is too small. In this case, a very sharp peak can be observed in the 4ℓ invariant mass distribution. Here, additional backgrounds from $t\bar{t}$ [410] and $Zb\bar{b}$ [406] production contribute besides $ZZ^*, Z\gamma^*$ events.

• $\underline{H \to WW^{(*)}}$: leading to $\ell\ell\nu\nu$ final states turned out to be one of the most promising detection modes of a light Higgs boson at the LHC, i.e. from $M_H \sim 2M_Z$ down to $M_H \sim 120$ GeV [429, 430], and it is even a potential discovery mode at the Tevatron [358]. Indeed, BR($H \to WW$) is appreciable if not largely dominating in this mass range and the clean leptonic decays represent 4% of the initial WW sample. Since the Higgs mass cannot be reconstructed in this process, the signal should be observed from a clear excess of events above backgrounds which need, thus, to be known rather precisely. The most important source is due to W boson [408] and top quark [410] pair production. The latter can be removed with suitable cuts, while for the former one needs, in addition, to take advantage of the characteristic spin correlations in the $H \to WW^* \to \ell\nu\ell\nu$ decays [429, 431]: the azimuthal separation of the charged leptons, for instance, peaks at smaller values for the signal than for the WW background. A clear signal has been established at the LHC for Higgs masses down to $M_H \sim 120$ GeV if enough luminosity is collected [429, 430]. At higher Higgs masses, the additional channel $H \to WW \to \ell\nu jj$, eventually combined with $H \to ZZ \to \ell\ell jj$ and with the $H \to ZZ \to \ell\ell\nu\bar{\nu}$ channel discussed previously, would extend the discovery reach to masses up to 1 TeV at high luminosities, after reducing the enormous $t\bar{t}$ and W+jets backgrounds [432]. At the Tevatron, high p_T lepton pairs plus missing energy $\ell\ell\nu\bar{\nu}$ and like–sign dileptons plus jets $\ell^\pm\ell^\pm jj$ in $gg \to H \to WW^*$, when combined with similar events in $p\bar{p} \to HW/HZ$ associated production, would allow to detect the Higgs boson at the 3σ level for masses up to $M_H \sim 180$ GeV with 30 fb^{-1} data [358].

• $\underline{H \to \tau^+\tau^-}$: has been proposed long ago [258, 355] in associated $gg \to Hg$ production where the additional jet provides a significant transverse momentum to the $\tau^+\tau^-$ system. To our knowledge, the process has not been considered for the LHC in a realistic experimental simulation [at least not in positive terms]; see Ref. [433], however. The process has been discussed for the Tevatron [360] but, again, it needs a better identification of the τ–leptons and resolution on the missing E_T [218].

• $\underline{H \to \mu^+\mu^-}$: the signal in this very rare decay channel, BR($H \to \mu^+\mu^-$) $\sim 10^{-4}$ for $M_H \sim 115$–140 GeV, is rather clean but it needs a very large amount of luminosity: $\mathcal{L} = 300$ fb^{-1} is required for a 3σ signal in the Higgs mass range $M_H \sim 120$–140 GeV [356] [for lower masses one is still sensitive to the tail of the huge Drell–Yan $pp \to \gamma^*/Z \to \mu^+\mu^-$ background]. This process is, thus, more appropriate for the SLHC or VLHC.

• $\underline{H \to t\bar{t}}$: suffers from the huge $t\bar{t}$ continuum background which has to be evaluated in a large mass window as the Higgs total width is large. It has been shown in Refs. [434,435] that the surplus from Higgs events produces a dip–peak structure in the $gg \to t\bar{t}$ invariant mass spectrum which could have been observable at the LHC if the Higgs total width were smaller [as in extensions of the SM where the Higgs has reduced couplings to the vector bosons]. This is unfortunate as this process would allow to probe directly the $Ht\bar{t}$ couplings and to check, for instance, the presence of anomalous interactions and/or CP violation [436, 437].

The WW/ZZ fusion channel

This channel is not considered as being viable at the Tevatron. In the study of Ref. [218], it has been shown that even with a good resolution on the $b\bar{b}$ invariant mass, $\Delta m_{b\bar{b}} = \pm 10$ GeV, the signal to background ratio in the $p\bar{p} \to qqb\bar{b}$ channel is of $\mathcal{O}(10^{-3})$ within a 20 GeV $m_{b\bar{b}}$ bin. For cleaner decay modes of the Higgs boson, the $p\bar{p} \to Hqq$ production cross section is too small to be useful: for $\mathcal{L} \sim 10$ fb^{-1} for instance, only two $H \to \gamma\gamma$ events and four dileptons events from $H \to \tau^+\tau^-$ are expected before acceptance cuts are applied.

At the LHC, the cross section is two orders of magnitude larger and the double forward jet tagging as well as the central soft–jet vetoing [the latter still needs more studies to be more firmly established] discussed previously help to drastically suppress the various large backgrounds. Applying the specific vector boson fusion cuts discussed in §3.3.3, the signal cross section is still large, a few picobarns for Higgs masses in the range $M_H = 100$–200 GeV, while the signal to background ratio is of order one. In addition, these specific cuts allow to distinguish between this mechanism and the $gg \to H + 2j$ process as discussed in §3.4.4 [only $\sim 10\%$ of the latter is left after cuts]. Adding the fact that it is theoretically rather clean, since the K–factors, the renormalization and factorization scale dependence as well as the PDF uncertainties are rather small, this process will thus play a key role when it comes to extract the Higgs couplings to the SM particles at the LHC. For this purpose all possible decay channels of the Higgs boson must be considered.

• $\underline{H \to \tau^+\tau^-}$: is a promising channel for $M_H \sim 120$–140 GeV if enough luminosity, $\mathcal{L} \sim 30$ fb^{-1}, is available. This has been established first with parton level analyses [343] which were later confirmed by detector simulations [234, 438, 439]. In particular, for $M_H \sim 125$ GeV, a statistical significance of $2.3, 2.5$ and $\sim 4.5\sigma$ can be achieved in the channels $qqH \to qq\tau\tau \to qqee/\mu\mu + \not{E} + X$, $qqe\mu + \not{E} + X$ and $qq\ell h + \not{E} + X$, respectively, for the luminosity quoted above [438], leading to a combined significance of $\sim 6\sigma$. The $\tau^+\tau^-$ invariant mass can be determined at the level of 10% which would allow to measure the backgrounds [the major ones being QCD and electroweak Zjj production with $Z \to \tau^+\tau^-$, in addition to the usual VV and $t\bar{t}$ processes] from the side bands. τ–polarization effects [440] are useful to discriminate the decays $H \to \tau^+\tau^-$ from the Drell–Yan $\gamma^*, Z^* \to \tau^+\tau^-$ background.

• $\underline{H \to \gamma\gamma}$: as shown in a parton level analysis [342], this is a rather clean channel with backgrounds which can be measured directly from the data. However, since the decay is rare, the channel needs a high luminosity and eventually has to be combined with other production processes [such as the $gg \to H \to \gamma\gamma(j)$ and $pp \to WH \to \ell\gamma\gamma$ channel discussed previously] to allow for a significance that is larger than 5σ for masses below $M_H \lesssim 150$ GeV. For instance, in the CMS simulation performed in Ref. [441] and where only the irreducible $\gamma\gamma jj$ background has been included with an assumed two–photon invariant mass window of ± 3 GeV, it has been found that a statistical significance of 3–5σ can be obtained in the mass range $M_H = 115$–140 GeV with $\mathcal{L} = 30$ fb^{-1} data.

• $\underline{H \to WW^{(*)}}$: although feasible and competitive [344], this channel might prove to be rather difficult since one cannot reconstruct the Higgs mass peak and, thus, measure the background from the side bands. The most important backgrounds, $pp \to t\bar{t}+$ jets and $WWjj$ production, need therefore to be known precisely; QCD+EW $\tau\tau jj$ production [406] can be removed with suitable cuts. Recently, this mode has also been studied experimentally and the prospects are rather good [234,442,443]. In the ATLAS analysis of the $qqH \to qq\ell\nu\ell\nu$ channel [234], the signal [with the usual specific vector boson fusion cuts, the contributions of the $pp \to WH, ZH$ and $t\bar{t}H$ processes to this topology are small] and the $t\bar{t}$ plus zero, one and two–jet backgrounds [the other important background, $pp \to \gamma^*/Z + X$ with $Z \to \tau^+\tau^-$, can be rejected by requiring a high $\ell\ell\nu$ transverse mass] have been studied. It has been shown that a significance larger than 3σ can be obtained for a luminosity of $\mathcal{L} = 10$ fb^{-1} in both the $e\mu + X$ and $ee/\mu\mu + X$ channels in the Higgs mass range above $M_H \sim 130$ GeV, i.e. when BR$(H \to WW^*)$ is large enough. Combining these channels with the $\ell\nu jj$ mode [and with the standard $\gamma\gamma$ and ZZ^* channels], one then obtains a $\sim 5\sigma$ significance for the M_H and $\mathcal{L}$ values above [402]. In fact, the $pp \to qqH \to \ell\nu jj$ channel becomes very powerful at higher Higgs masses [234, 235, 443, 444]. With a slightly different optimization of the cuts than at low Higgs masses, one can arrive at a signal significance that is larger that 5σ in the entire mass range $M_H \sim 200$–800 GeV with a luminosity of $\mathcal{L} = 30$ fb^{-1} [444].

• $\underline{H \to ZZ}$: this channel has also been considered in experimental simulations [444, 445], but it cannot be used below the $M_H = 2M_Z$ threshold as the $H \to ZZ^*$ branching ratio is very small in view of the not so large production rate. In addition, since the rates in the $H \to ZZ \to 4\ell$ channel are also very tiny, on has to consider the final states $\ell\ell\nu\nu$ and $\ell\ell jj$. These processes receive large backgrounds, in particular from the process $Z + 4j$ in the second case where one has $S/B \sim 1/3$ at $M_H \sim 300$ GeV, after all cuts have been imposed. In the high Higgs mass range, these channels can be useful, but they need again very high luminosities. For instance, it has been shown in Ref. [444] that a significance of more than 5σ can be achieved for the $qqH \to \ell^+\ell^-\nu\nu jj$ signal with a luminosity of $\mathcal{L} = 30$ fb^{-1} in the Higgs mass window $M_H \sim 500$–800 GeV.

• $\underline{H \to \mu^+\mu^-}$: again, the signal in this channel is very clean but the branching ratio for the decay is too small. A large amount of luminosity, $\mathcal{L} = 0.5$–1 ab^{-1}, is required for a 3σ signal in the Higgs mass range below 140 GeV [346]. This signal should be combined with the $\mu^+\mu^-$ sample obtained from gluon–gluon fusion discussed previously.

• $\underline{H \to b\bar{b}}$: this channel suffers from a huge $4j$ QCD background which can possibly be measured using the side bands of the $b\bar{b}$ invariant mass; in addition, it has a major problem with overlapping events. A preliminary parton level analysis [347] shows that with reasonable assumptions but with a very large luminosity, $\mathcal{L} = 600$ fb^{-1}, one can obtain a signal to square–root background ratio of $S/\sqrt{B} \sim 3$ for a mass $M_H \sim 120$ GeV. However, it is not yet very clear if it possible to trigger efficiently on this channel [446].

The $pp \to t\bar{t}H$ channel

Finally, Higgs production in association with top quarks has a strongly decreasing cross section with increasing M_H which makes the process useful only in the low mass range, $M_H \lesssim 135$ GeV, when the $\gamma\gamma$ and $b\bar{b}$ Higgs decays are relatively important [see below, however]. In addition, one needs to have at least one of the W bosons from $t \to bW$ which decays leptonically, to trigger efficiently on the events and suppress the QCD backgrounds. Since the rates are rather low, a large luminosity is required, in particular at the Tevatron.

• $\underline{H \to b\bar{b}}$: associated Higgs production with $t\bar{t}$ pairs [377] is the only channel in which it has been firmly established that the Higgs decays into $b\bar{b}$ pair can be extracted from the backgrounds at the LHC [414]. A clear evidence of the $4b$ tagged jet and lepton signal above the $W+$ jets and $t\bar{t}+jj$ backgrounds [b–tagging is of course crucial here] can be obtained for $M_H \lesssim 130$ GeV if enough luminosity, $\mathcal{L} \gtrsim 100$ fb^{-1}, is collected [448]. A clear reconstruction of the $H \to b\bar{b}$ mass peak is difficult because of the combinatorial background from the signal itself and the reconstruction of the top quark decays might be needed. The fully hadronic final state $pp \to t\bar{t}H \to q\bar{q}q\bar{q}b\bar{b}b\bar{b}$ would double the number of $pp \to t\bar{t}H$ signal events [449] but one still needs a proper evaluation of the eight jet QCD background. At the Tevatron, the channel is more challenging as the production rate is very small but a signal might be visible if a very high enough luminosity is collected [218, 381].

• $\underline{H \to \gamma\gamma}$: the decay is too rare for the Tevatron, but it can be detected at the LHC when an additional lepton from the $t \to bW$ decay is present [375]. The process, again, gives a narrow mass peak which is visible for $M_H \lesssim 140$ GeV when the $pp \to t\bar{t}H$ production rate and the $H \to \gamma\gamma$ branching ratio are sizable enough [375]. With the additional charged lepton, the backgrounds are manageable [376] after suitable cuts [it can also be measured from the side bands], but the statistics have to be added to those obtained in the search of the $\gamma\gamma$ peak in the three other Higgs production channels $pp \to H \to \gamma\gamma, \gamma\gamma + j$, $pp \to qqH \to qq\gamma\gamma$ and $pp \to HW \to \gamma\gamma\ell\nu$ to obtain a significant signal at moderate luminosities.

• $\underline{H \to WW^{(*)}}$: with $\ell\ell\nu\nu$ final states, has been suggested recently to extend the reach of the $t\bar{t}H$ process to Higgs masses above ~ 140 GeV [379]. This mode receives very large $t\bar{t}Wjj$ and $t\bar{t}\ell\ell$ + jet backgrounds [and smaller ones from $t\bar{t}WW$ and $t\bar{t}t\bar{t}$ final states] which need to be accurately determined as the invariant Higgs mass peak cannot be reconstructed and one would have to rely on a counting of the signal versus the background events. It has been recently shown that a signal can be observed [450] but further investigations are needed to confirm that the backgrounds can be indeed reduced to a low level.

$\underline{H \to ZZ^*}$ has been discussed in Ref. [378] but it has too small rates for $M_H \lesssim 2M_Z$ if leptonic Z decays are selected; to our knowledge, no simulation for this channel is available.

• $\underline{H \to \tau\tau}$: this channel has also been discussed [380] in a parton–level analysis. It seems extremely challenging and, again, no detailed experimental simulation has been performed.

3.7.3 Discovery expectations at the Tevatron and the LHC

At the Tevatron, the required luminosity to discover or exclude a SM Higgs boson, combining all channels in the processes $p\bar{p} \to HV$ and $gg \to H$ discussed previously, and the results of both CDF and DØ experiments, is shown in Fig. 3.48 as a function of M_H [218]. With 10 fb^{-1} luminosity per experiment, a 3σ evidence for a Higgs boson can be achieved for $M_H \lesssim 125$ GeV and, in the absence of any signal, a 95% CL exclusion limit can be set up to Higgs masses of order 180 GeV. However, for discovery, only 30 fb^{-1} data per experiment will allow to observe a 5σ signal for $M_H \lesssim 130$ GeV, slightly above the LEP2 Higgs mass bound. Unfortunately, these large luminosities are not expected to be reached in Run II.

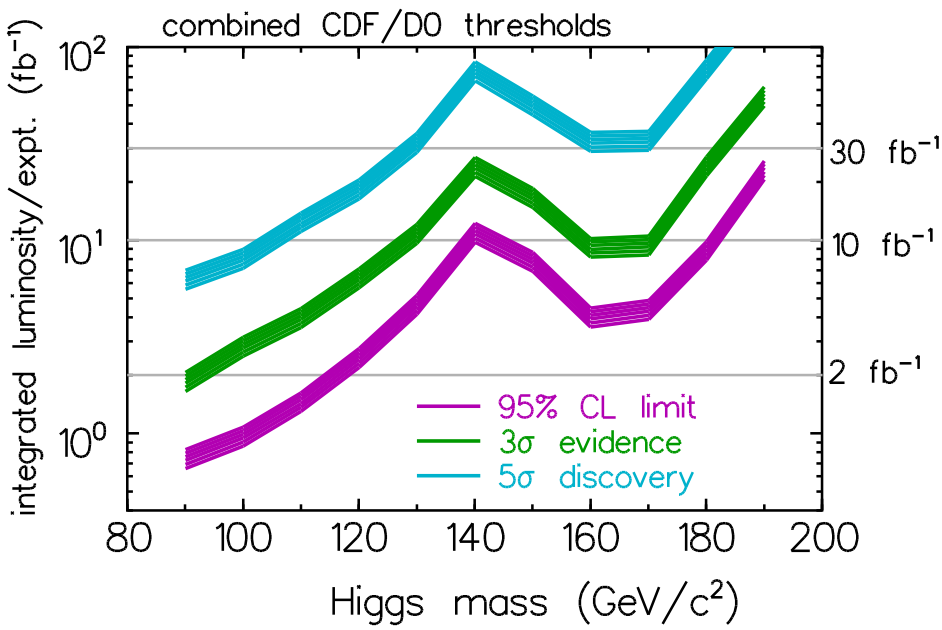

Figure 3.48: The integrated luminosity required per experiment at the Tevatron, to either exclude a SM Higgs boson at 95% CL or observe it at the 3σ or 5σ level; from Ref. [218].

At the LHC, the significance of the signals in the various Higgs production and decay channels are shown as a function of M_H in Figs. 3.49 and 3.50. The ATLAS plot in the left–hand side of Fig. 3.49 shows the significance for an integrated luminosity of $\mathcal{L} = 100$ fb^{-1} in the "standard" search channels where the vector boson fusion processes are not yet included. The detection in this case relies mostly on the $gg \to H$ production mechanism with the decays $H \to \gamma\gamma, WW^{(*)}$ and $ZZ^{(*)}$ [where one of the vector boson is allowed to decay hadronically in the high Higgs mass range], supplemented by the processes $pp \to t\bar{t}H$ with $H \to \gamma\gamma, b\bar{b}$ and $pp \to WH$ with $H \to \gamma\gamma$. As can be seen, the significance is above 10 in the entire Higgs mass range when the various channels are combined. The significance is the smallest in the low mass range, $M_H \lesssim 130$ GeV, when the $H \to VV^*$ decays are not yet dominant. This is exemplified in the right–hand side of the figure where the significance is shown in the mass range below $M_H = 200$ GeV but with the luminosity $\mathcal{L} = 30$ fb^{-1} which is expected at an earlier stage. The updated analysis now includes the vector boson fusion channels with the decays $H \to \tau\tau$ and $H \to WW^*$ which lead to a substantial increase of the total significance. Note that the K–factors, which would have significantly increased the signal for the $gg \to H$ process that is mostly used at high M_H, have unfortunately not been included [see the discussion below].

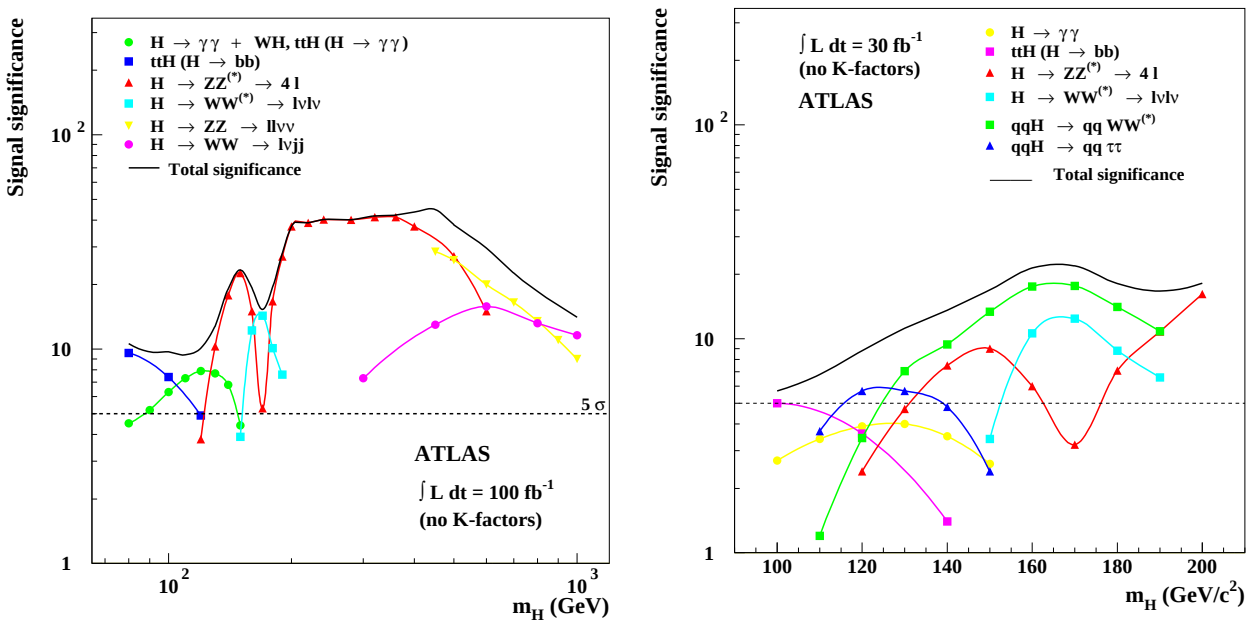

Figure 3.49: The significance for the SM Higgs boson discovery in various channels in ATLAS as a function of M_H. Left: the significance for 100 fb^{-1} data and with no vector boson fusion channel included and right: for 30 fb^{-1} data in the $M_H \leq 200$ GeV range with the $qq \to qqH$ channels included [234].

The CMS plot in Fig. 3.50 shows the integrated luminosity that is needed to achieve a 5σ discovery signal in the various detection channels. Here, the vector boson fusion process

with all relevant Higgs decays, $H \to \gamma\gamma, \tau\tau, WW^{(*)}, ZZ^{(*)}$, has been included [together with the K–factors for the $gg \to H$ process]. As can be seen, a minimal luminosity of 10 fb^{-1} is necessary to cover the low Higgs mass range down to $M_H \sim 115$ GeV and the high mass range up to $M_H \sim 800$ GeV when all channels are combined. One can see also that the vector boson fusion channels add value in the entire Higgs mass range. In particular, the $qq \to Hqq$ processes with $H \to WW, ZZ$ are also very useful in the high Higgs mass range.

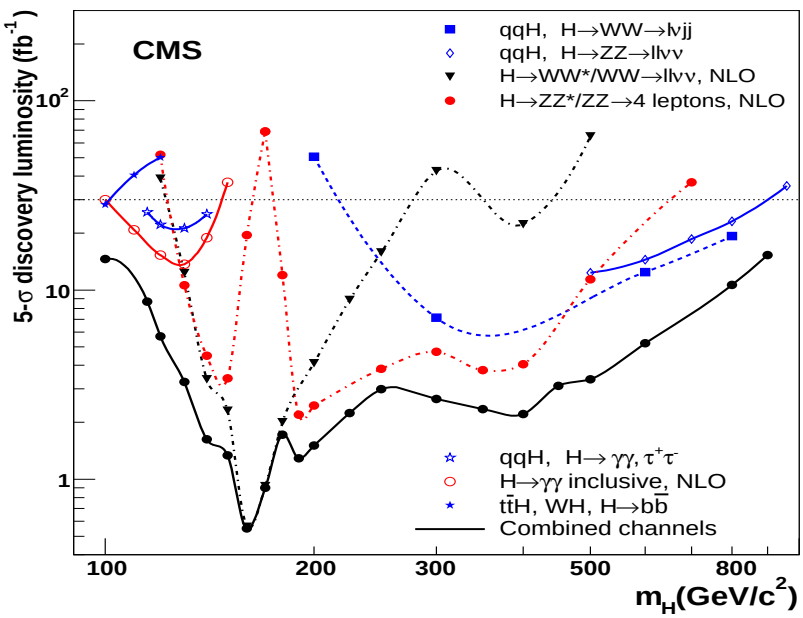

Figure 3.50: The required integrated luminosity that is needed to achieve a 5σ discovery signal in CMS using various detection channels as a function of M_H [235].

Thus, the SM Higgs boson in its entire mass range will be found at the LHC provided that a luminosity larger that $\int \mathcal{L} = 30$ fb^{-1} is collected and the performances of the detectors are as expected. For higher luminosities, this can be done in various and sometimes redundant channels, therefore strengthening the signal and providing great confidence that it is indeed a scalar Higgs boson which has been observed. However, at low luminosities, and in particular in the low Higgs mass range $M_H \lesssim 135$ GeV, several channels must be combined in order to establish a clear evidence for the Higgs particle. The interesting question which can be asked is thus: at which stage this integrated luminosity will be collected.

Before closing this section, let us make a digression about the K–factors. The inclusion of the higher–order radiative corrections to the Higgs production cross sections and distributions, which is theoretically indispensable to stabilize the scale dependence and to allow for precise predictions as it has been discussed at length in the previous sections, can be also very important in the experimental analyses. Indeed, not only they increase [in general] the size of the discovery signals and, thus, their significance, but they also can change the

kinematical properties of the processes under study, leading to different selection efficiencies and, thus, to a different number of collected events. This is particularly the case in the $gg \to H$ process where large K–factors appear and where the Higgs transverse momentum is generated at higher orders, when additional jets which balance this p_T are produced.

Of course, the K–factors can be included for the signal only if they are also available for the backgrounds and there are at least two situations in which this holds:

i) The signal appears as a narrow peak in an invariant mass distribution and, thus, the corresponding backgrounds can be precisely measured from the side bands and safely extrapolated to the signal region. This is the case of the important $H \to \gamma\gamma$ and $H \to ZZ^{(*)} \to 4\ell$ detection channels for instance.

ii) When estimates of signal significances are made before having the data or in the case where the invariant Higgs mass peak cannot be reconstructed and one would have to rely on a counting of the number of signal versus background events, the K factors can be included if the backgrounds are also known at the same level of accuracy as the signal. This is clearly the case for many background processes such as $\gamma\gamma, WW, ZZ$ and tt production which are known at least to NLO accuracy.

Furthermore, the K–factors should not only be implemented in the total normalization of the signal and backgrounds, but also in the various kinematical distributions when they are strongly affected by the higher–order corrections[35]. Ideally, this has to be performed at the level of Monte–Carlo event generators which are required in practice to obtain a realistic final state with fragmented particles and underlying events. This is not a trivial task and there are many ongoing discussions on this topic; see Ref. [404] as an example. Fortunately, besides the fact that NLO parton level Monte–Carlo programs start to appear [284,297,348], this can be performed in an effective way even in MC event generators [451,452]: differential effective K–factors can be defined for relevant kinematical variables and used to reweight individual events with reconstructed jets coming from a LO Monte–Carlo event generator[36].

[35]This is not always the case. In Ref. [451], the search sensitivity in the process $gg \to H \to ZZ \to 4\ell$ has been shown to depend mainly on the signal and background cross sections as well as on the detector performance and the selection cuts and not, for instance, on additional jet activity. A simple scaling of the signal and background rates with their respective K–factors leads, therefore, to reasonable results. It has been shown that in this particular case, one needs 30–35% less integrated luminosity to achieve a given signal significance when the K–factors are included.

[36]For instance, in Ref. [452], the channel $gg \to H \to WW \to \ell\nu\ell\nu$ has been considered and the higher–order QCD corrections have been taken into account by using this reweighting procedure, allowing to combine event rates obtained with the `PYTHIA` event generator with the most up–to–date theoretical predictions for the p_T spectra of the Higgs signal and the corresponding WW background. An experimental effective K–factor of ~ 2 has been obtained in the range $M_H = 140$–180 GeV, which is only about 15% smaller than the theoretical inclusive K–factor. This led to a considerable increase of the statistical significance of the Higgs discovery in this specific channel.

Thus, all K–factors [which have been determined after a very hard theoretical work] should ultimately be included in the experimental analyses as they allow a more accurate prediction of the discovery potential and often lead to a better cut optimization. Apparently, we are finally heading to this direction.

3.7.4 Determination of the Higgs properties at the LHC

Once a convincing signal for a Higgs boson has been established, the next step would be to determine its properties in all possible details and to establish that the particle is indeed the relic of the electroweak symmetry breaking mechanism and that it has the features that are predicted in the SM, that is: it is a spin–zero particle with $J^{\rm PC} = 0^{++}$ quantum numbers and that it couples to fermions and gauge boson proportionally to their masses. Ultimately, the scalar Higgs potential responsible for the symmetry breaking should be reconstructed by precisely measuring the trilinear and quartic Higgs self–couplings. At the LHC, several important measurements can be performed as is briefly summarized below.

The Higgs mass and total decay width

The Higgs mass can be measured with a very good accuracy [453]. In the range below $M_H \lesssim 400$ GeV where the total width is not too large, a relative precision of $\Delta M_H/M_H \sim 0.1\%$ can be achieved in the channel $H \to ZZ^{(*)} \to 4\ell^\pm$ if 300 fb^{-1} luminosity is collected by ATLAS and CMS. This is shown in Fig. 3.51 where the relative precision is displayed as a function of M_H and where the statistical and some systematical errors are included [454].

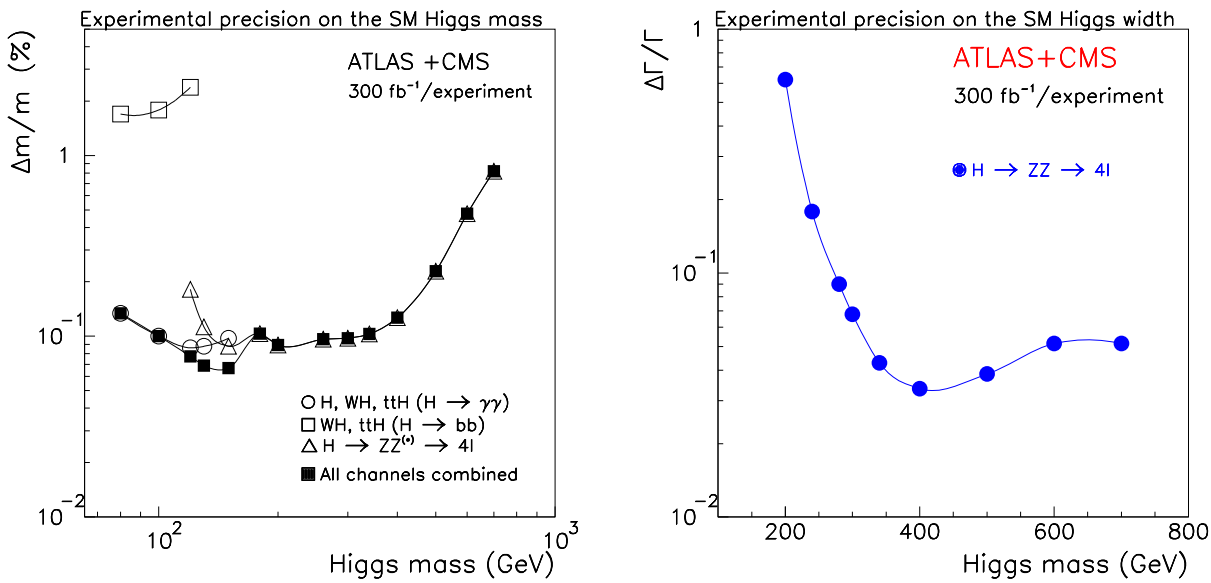

Figure 3.51: Expected errors on the measurement of the Higgs boson mass (left) and total decay width (right) at the LHC as a function of M_H, combining both ATLAS and CMS with a luminosity of 300 fb^{-1} per experiment; from Ref. [454].

In the low Higgs mass range, a slight improvement can be obtained by reconstructing the sharp $H \to \gamma\gamma$ peak. In the range $M_H \gtrsim 400$ GeV, the precision starts to deteriorate because of the smaller production rates which increase the statistical error. However a precision of the order of 1% can still be achieved for $M_H \sim 700$ GeV if theoretical errors, such as width effects, are not taken into account.

Using the same process, $H \to ZZ \to 4\ell^\pm$, the total decay width of the Higgs boson can be measured for masses above $M_H \gtrsim 200$ GeV when it is large enough to be resolved experimentally. While the precision is rather poor near this mass value, approximately 60%, it improves to reach the level of $\sim 5\%$ around $M_H \sim 400$ GeV and the precision stays almost constant up to a value $M_H \sim 700$ GeV [453]. This is shown in the right–hand side of Fig. 3.51 where the relative precision on Γ_H is displayed as a function of M_H with 300 fb^{-1} luminosity for the combined ATLAS and CMS experiments [454].

The Higgs spin and parity quantum numbers

As seen previously, if a high enough luminosity is collected at the LHC, a Higgs boson in the low mass range, $M_H \lesssim 135$ GeV, will be detected through its $H \to \gamma\gamma$ decay mode. This observation will immediately rule out the spin possibility $J = 1$ by Yang–Landau's theorem, and will fix the charge conjugation to be positive C= + [455]. This argument cannot be generalized to Higgs production in the gg fusion mechanism or to Higgs decays into gluons, $gg \leftrightarrow H$, since gluons cannot be reasonably distinguished from light quark jets.

For higher Higgs masses when the $\gamma\gamma$ decay becomes too rare, the observation of the Higgs boson in the decays $H \to WW^*, ZZ^*$ provides some information. Indeed, as discussed in §2.2, these decays are sensitive to the spin–zero nature of the Higgs boson, if one of the gauge bosons is virtual. The invariant mass (M_*) spectrum of the off–shell gauge boson in $H \to VV^*$, see eq. (2.32), is proportional to the velocity $d\Gamma/dM_* \sim \beta \sim \sqrt{(M_H - M_V)^2 - M_*^2}$, and therefore decreases steeply with M_* just below the kinematical threshold; see Fig. 2.12. This is characteristic of a spin–zero particle decaying into two vector bosons, and rules out all spin assignments except for two cases, $J^P = 1^+$ and 2^-. This is shown in the left–hand side of Fig. 3.52 where the threshold behavior of $d\Gamma/dM_*$ is displayed for the ~ 200 signal events which are expected for $M_H = 150$ GeV and $\mathcal{L} = 300$ fb^{-1} [histogram] and compared with the prediction for the SM Higgs and for two examples of spin 1 and 2 cases [174].

The spin–correlations, which are useful to discriminate between the signal $gg \to H \to WW^*$ and $pp \to WW$ background [429] for instance, can be used to determine the Higgs boson spin at the LHC. In practice, however, the complete final state must be reconstructed and one has to rely on the decays $H \to ZZ^* \to 4\ell$ which have rather low rates. The two remaining configurations $J = 1^+$ and 2^- which are not probed, as well as the CP–odd 0^- case, can be discriminated against the Higgs spin by looking at the angular distribution in the

decays $H \to VV^{(*)} \to 4f$ given in eq. (2.38), and experimentally observing a $\sin^2\theta_1 \sin^2\theta_3$ correlation and not observing the $(1+\cos^2\theta_{1,3})\sin^2\theta_{3,1}$ correlation [159, 174].

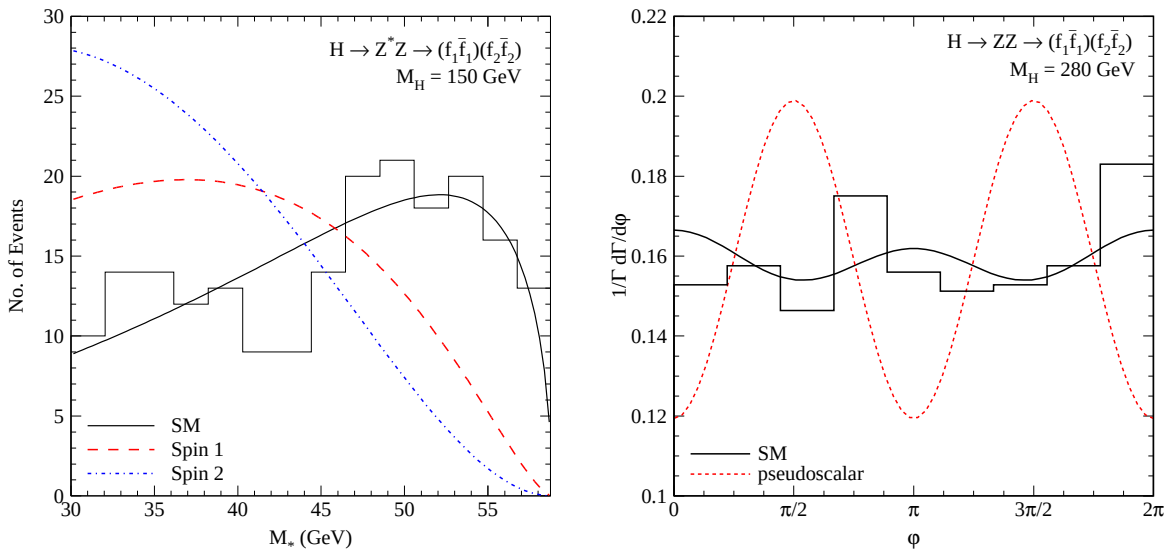

Figure 3.52: The threshold behavior of the differential distribution $d\Gamma/dM_*$ for the SM Higgs and two spin examples of $J=1$ and 2 for $M_H = 150$ GeV (left) and the azimuthal distributions $d\Gamma/d\phi$ for the SM and a pseudoscalar Higgs bosons for $M_H = 280$ GeV (right). The histograms have been obtained with $\int \mathcal{L}dt = 300\,\text{fb}^{-1}$ at the LHC, with efficiencies and cuts included according to an ATLAS simulation of Ref. [456]; from Ref. [174].

In fact, the angular correlations are also sensitive to the parity of the Higgs boson as seen in §2.2.4 and can discriminate between the CP–even SM Higgs case and the pseudoscalar Higgs case. In particular, the dependence on the azimuthal angle is very different, as it can be seen from eq. (2.38) and in Fig. 2.13. The same simulations as previously [174, 456] have been performed for $M_H = 280$ GeV and the distribution $d\Gamma/d\phi$ is shown in Fig. 3.52 as a function of the azimuthal angle for the 900 expected events at the LHC for this Higgs mass. A clear discrimination between the CP–even and CP–odd cases can be made in this case.

The Higgs CP properties and the structure of the HVV coupling can also be determined in the vector boson fusion process, $qq \to qqH$, by looking at the azimuthal dependence of the two outgoing forward tagging jets [457]. The analysis is independent of the Higgs mass and decay modes but might be difficult because of background problems [261, 458].

However, there is a theoretical caveat in this type of analyses [459]: if a Higgs boson is observed with substantial rates in channels where it couples to vector bosons, it is very likely that it is CP–even since the VV couplings of a pure CP–odd state are generated only through loop corrections. The decisive test of the CP properties should be therefore to verify that the SM Higgs boson is pure CP–even and rule out the small loop–induced CP–odd component. This becomes then a very high precision test which is very challenging at the LHC.

The couplings of the Higgs boson to fermions provide a more democratic probe of its CP nature since in this case, the CP–even and CP–odd components can have the same magnitude. One thus has to look at channels where the Higgs boson is produced and decays through these couplings. Discarding the possibility of $H \to b\bar{b}$ and $\tau^+\tau^-$ decays in the $gg \to H$ production channel, which have very large backgrounds, one has to rely on Higgs production in $pp \to t\bar{t}H$ with $H \to \gamma\gamma$ and eventually $b\bar{b}$. Techniques based on the different final states distributions in the production of a scalar or a pseudoscalar Higgs boson have been suggested in Refs. [460, 461] to discriminate between the two scenarios or a mixture. However these channels are rather difficult as we have seen previously. With very large luminosities $\mathcal{L} = 600$ fb^{-1} and for a rather light Higgs boson, $M_H \sim 100$ GeV, an equal mixture of CP–even and CP–odd couplings [with a total coupling squared equal to the SM one] can be probed at a few σ level [461]. But again, this method does not allow to check precisely the CP–even purity of the SM Higgs boson, at least in this particular channel. Central exclusive diffractive Higgs production [392, 462] might provide the solution; §3.6.4.

The measurement of the Higgs couplings at the LHC

The determination of the Higgs couplings to gauge bosons and fermions is possible at the LHC through the measurement of the cross sections times branching ratios, $\sigma \times$ BR, given by the event rate in the various search channels [222,463–466]; for earlier analyses see Ref. [227–229]. However, the accuracy in this determination is rather limited because of the small statistics that one obtains after applying the cuts that suppress the large backgrounds which are often plagued with uncertainties, and the various systematical errors such as the common uncertainty in the absolute luminosity. In addition, when one attempts to interpret the measurements, theoretical uncertainties from the limited precision on the parton densities and from the higher–order radiative corrections or scale dependence should be taken into account. Furthermore, the couplings which can be measured will critically depend on the Higgs boson mass. For instance, in the mass range above $M_H \sim 2M_W$, only the couplings to gauge bosons can be accessed directly and the $Ht\bar{t}$ coupling can be probed indirectly.

The cross sections times branching ratios which can be measured in various channels at the LHC are shown in Fig. 3.53 for Higgs masses below 200 GeV [463]. The gg fusion (solid lines), the expectations for weak boson fusion with a parton level analysis (dashed lines) and the associated $pp \to t\bar{t}H, H \to b\bar{b}$ (dotted lines) channels are for a luminosity of 200 fb^{-1}. The channels $pp \to t\bar{t}H \to t\bar{t}WW^*$ (red–dotted lines) assume a luminosity of 300 fb^{-1}. In this figure, as well as in the subsequent discussion, only the statistical errors are taken into account. A precision of the order of 10 to 20% can be achieved in some channels, while the vector boson fusion process, $pp \to Hqq \to WWqq$, leads to accuracies of the order of a few percent.

These $\sigma \times$ BR can be translated into Higgs partial widths in the various decay channels $\Gamma_X \equiv \Gamma(H \to XX)$ [464], which are proportional to the square of the Higgs couplings, g^2_{HXX}. However, in the case of the vector boson fusion mechanism, which has contributions from $ZZ \to H$ and $WW \to H$, the HZZ and HWW couplings cannot be disentangled. One then has to assume that they are related by SU(2) symmetry as is the case in the SM [an assumption which can be tested with a 20% accuracy in $gg \to H \to ZZ^*$ *versus* $gg \to H \to WW^*$ but for large enough M_H]. With this assumption, one can perform ratios of partial widths $\Gamma_{X_i}/\Gamma_{X_j}$, in which some common theoretical and experimental errors will cancel. This is shown in Fig. 3.54 (left) for a luminosity of 200 fb^{-1}, where the relative accuracy on the ratios of $\sigma \times$ BR of the production and decay channels discussed above can be formed. Again, measurements at the level of 10–20% can be made in some cases.

One can indirectly measure the total Higgs width Γ_H and thus derive the absolute values of the partial widths Γ_X by making additional assumptions besides g_{HWW}/g_{HZZ} universality: *i*) Γ_b/Γ_τ is SM–like [with an error of $\sim 10\%$ corresponding to the uncertainty on the b–quark mass] since both fermions have the same isospin and *ii*) the branching ratio for Higgs decays into unexpected channels is small [in the SM, this error is less than about 3% and corresponds to the missing BR$(H \to c\bar{c})$] so that $1 - \Gamma_{X_i}/\Gamma = \epsilon \ll 1$. The Higgs boson total width Γ_H can be then determined and the partial widths Γ_X as well.

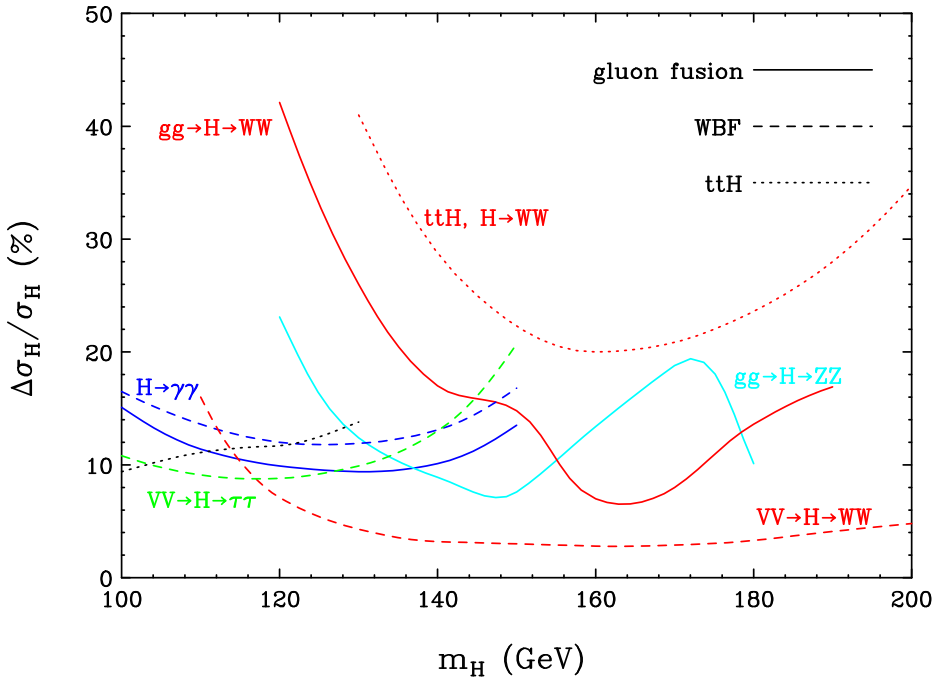

Figure 3.53: Expected relative errors on the determination of $\sigma \times$ BR *for various Higgs boson search channels at the LHC with 200–300 fb^{-1} data; from Ref. [463].*

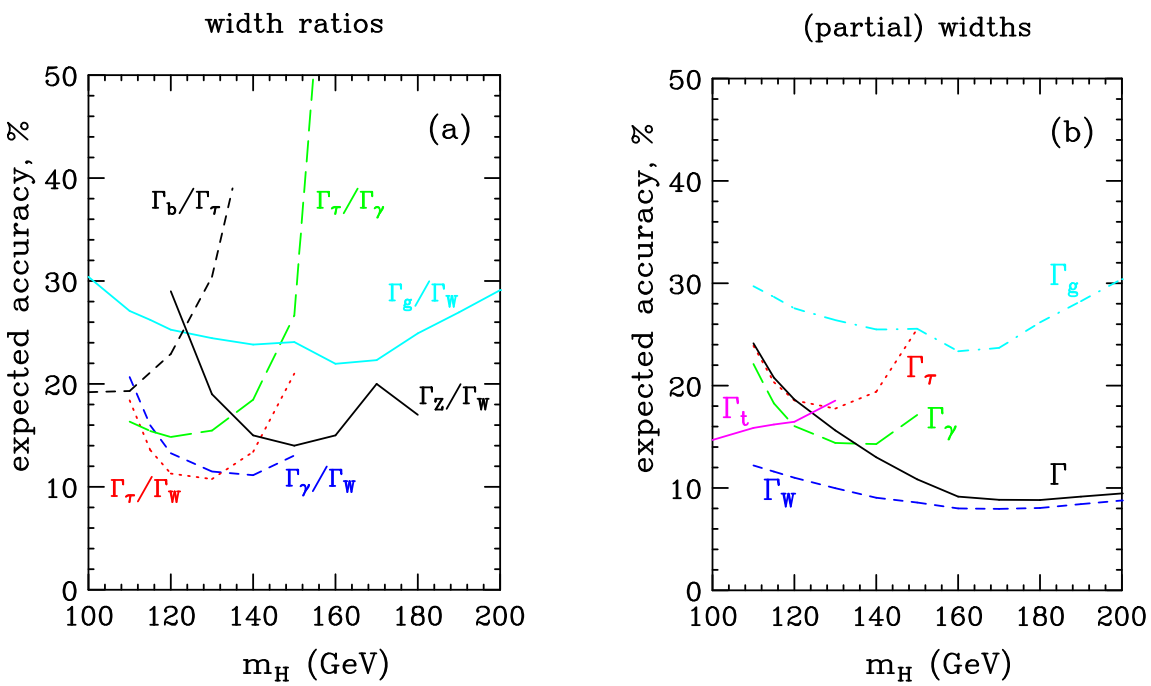

Figure 3.54: Relative accuracy expected at the LHC with a luminosity of 200 fb^{-1} for various ratios of Higgs boson partial widths (left) and the indirect determination of partial and total widths $\tilde{\Gamma}_i$ and Γ with the assumptions discussed in the text (right); from Ref. [464].

The expected accuracies are shown in the right–hand side of Fig. 3.54. They are at the level of 10 to 30% depending on the final states and on M_H, and translate to an accuracy on the couplings of the order of 5 to 15% [464]. Detailed experimental analyses accounting for the backgrounds and for the detector efficiencies, as well as further theoretical studies for the signal and backgrounds, have to be performed to confirm these values.

The Higgs self–coupling

The trilinear Higgs boson self–coupling λ_{HHH} is too difficult to be measured at the LHC because of the smallness of the $gg \to HH$ [and, *a fortiori*, the $VV \to HH$ and $qq \to HHV$] cross sections and the very large backgrounds [467–469]; see also Refs. [470] and [471] for an earlier and more recent analysis, respectively. A parton level analysis [468] has been recently performed in the channel $gg \to HH \to (W^+W^-)(W^+W^-) \to (jj\ell\nu)(jj\ell\nu)$ and $(jj\ell\nu)(\ell\ell\nu\nu)$ with same sign dileptons, including all the relevant backgrounds which, as one might have expected, are significantly large. At the LHC, the statistical significance of the signals, once most of the backgrounds are removed, is very small, even with an extremely high luminosity. However, it was found that the distribution of the invariant mass of the visible final state particles peaks at much higher values for the backgrounds than for the signal, independently of the value of the trilinear coupling; see the left–hand side of Fig. 3.55.

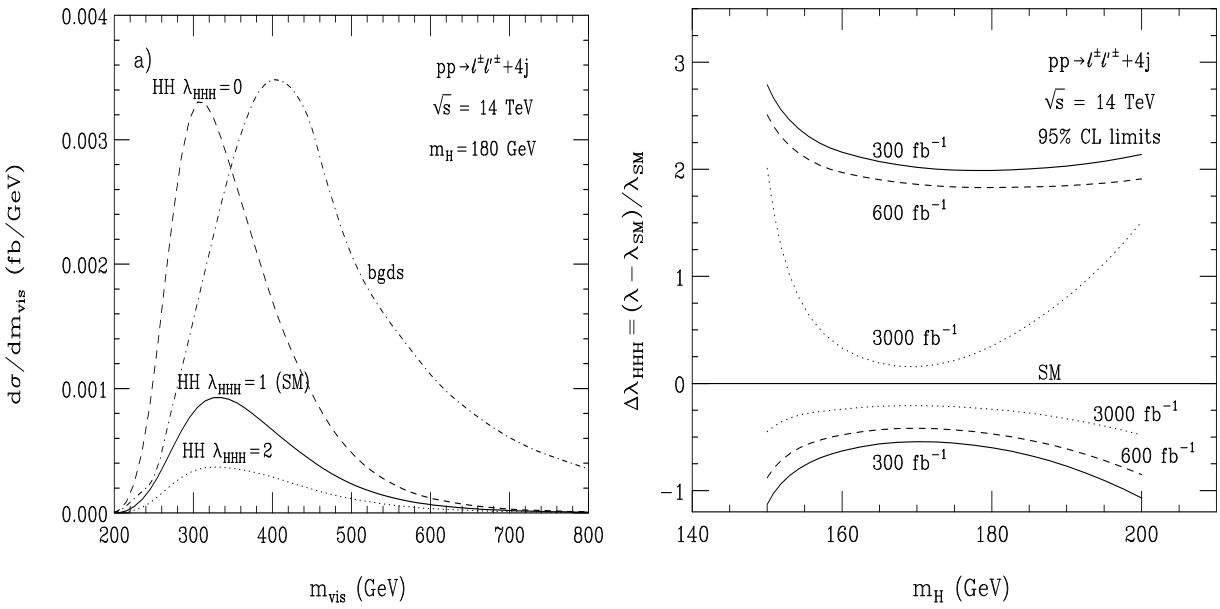

Figure 3.55: The visible mass distribution of the signal for $pp \to \ell^\pm\ell^\pm + 4j$ for $M_H = 180$ GeV at the LHC for various λ_{HHH} values and for the combined backgrounds (left). Limits achievable at 95% CL for $\Delta\lambda_{HHH} = (\lambda - \lambda_{SM})/\lambda_{SM}$ in $pp \to \ell^\pm\ell'^\pm + 4j$ at the LHC for various integrated luminosities (right); from Ref. [468].

This observation can be used to set limits on the Higgs self–coupling. For a luminosity of 300 fb^{-1} one can check a non–vanishing value of λ_{HHH} at the 95% CL if the Higgs boson mass happens to lie in the range 150–200 GeV. Much more luminosity would be needed to perform a decent measurement; see the right–hand side of Fig. 3.55. For lower Higgs masses, $M_H \lesssim 140$ GeV, one would have to rely on the dominant decays $HH \to 4b$ not to lose too much statistics, but in view of the formidable backgrounds, this process seems to be hopeless at the LHC. The channel $H \to b\bar{b}\tau\tau$ is only slightly easier [469].

3.7.5 Higher luminosities and higher energies

Some of the detection signals as well the measurements discussed previously would greatly benefit from an increase of the LHC luminosity. As mentioned in the beginning of this chapter, there are plans to achieve an instantaneous luminosity of $\mathcal{L} = 10^{35}\,\text{cm}^{-2}\text{s}^{-1}$ at $\sqrt{s} \simeq 14$ TeV, while keeping the present dipole and magnets. This would allow to collect 6 ab^{-1} for both the ATLAS and CMS experiments after three years of data tacking. This SLHC option will allow to probe rare production and decay processes of the Higgs particle. A brief summary of the interesting physics which can be performed at such a machine in the context of the SM Higgs boson is as follows [221, 222]:

– $H \to \mu^+\mu^-$: we have seen that with the present LHC design luminosity, this rare decay can be observed only at the 3σ level, even with 600 fb^{-1} of data. With 6 ab^{-1} data, the

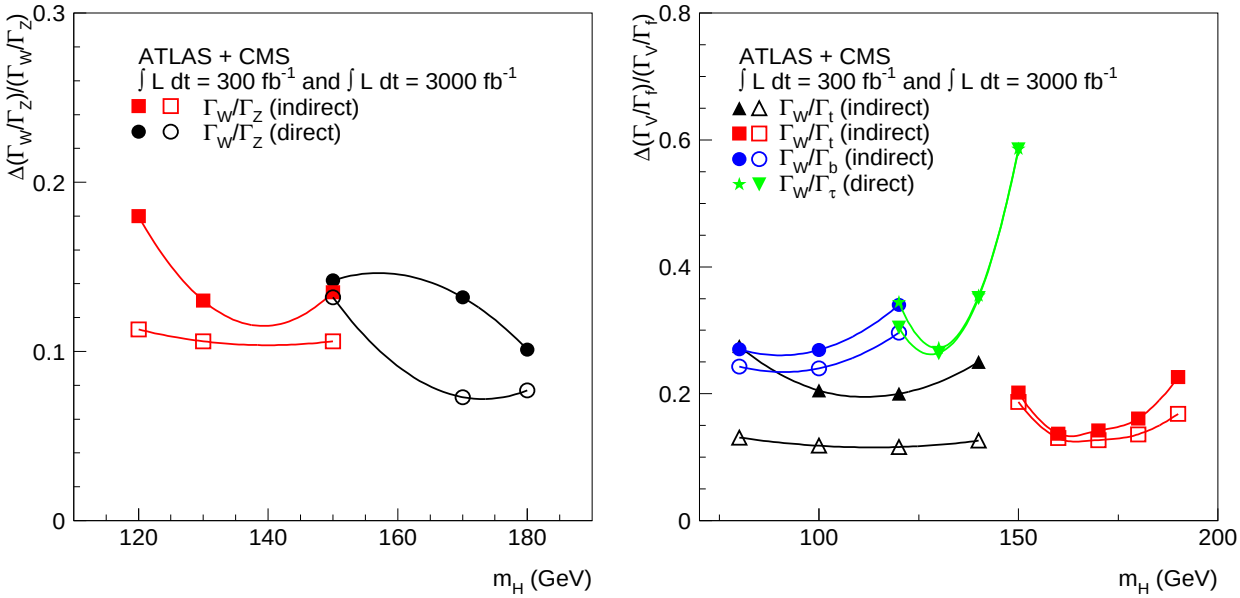

Figure 3.56: Expected uncertainties on the measured ratios of the Higgs boson widths to final states involving gauge bosons (left) and gauge bosons and fermions (right) as a function of the Higgs mass. The closed (open) symbols are for the two two experiments and 3000 (300) fb^{-1} data per experiment. Indirect measurements use the loop induced processes $gg \to H$ and $H \to \gamma\gamma$; from Ref. [221].

process can be observed at the $5\,\sigma$ level for M_H in the range 120 to 140 GeV and would allow the first measurement of the Higgs coupling to second generation fermions.

– $H \to Z\gamma$: this decay has not been mentioned in the previous discussion because it is too rare: if the Z boson decays leptonically, the branching fraction for this mode is about 2×10^{-4}. With 6 ab^{-1} data, the $gg \to H \to Z\gamma \to \ell\ell\gamma$ process can be observed at the $\sim 10\sigma$ level for a Higgs boson in the mass range $M_H = 120$–150 GeV and would provide complementary information to the $H \to \gamma\gamma$ decay channel.

– The measurement of the ratios of Higgs couplings discussed before is mostly statistics limited. Provided that detector performances are not significantly reduced in the high luminosity environment, these ratios of couplings can be probed at the level of 10% accuracy, and even below in some cases, if the the sample of 6 ab^{-1} data is collected. This is shown in Fig. 3.56 where the combined ATLAS+CMS accuracies in the direct [with tree–level processes] and indirect measurements [that is, involving the loop induced processes $gg \to H$ and $H \to \gamma\gamma$ which are indirectly sensitive to the Higgs couplings to the top quark, and in the case of $H \to \gamma\gamma$ also to the HWW coupling] are shown for a luminosity of 3 ab^{-1} per experiment and compared to what can be achieved with only 300 fb^{-1} data per experiment.

– The most important window that a sample of 6 ab^{-1} data could open would be the measurement of the Higgs self–coupling λ_{HHH}. As we have seen previously, this important

coupling cannot be probed with the presently planed luminosity. The same parton–level simulation mentioned previously [468] has shown that a signal for the process $gg \to HH \to WWWW \to \ell^\pm\ell^\pm\nu\nu jjjj$ can be observed with a 5.5 (3.8) significance for $M_H = 170\,(200)$ GeV with $\mathcal{L} = 6$ ab^{-1}, allowing to probe λ_{HHH}. As can be seen in Fig. 3.55, the trilinear coupling could be measured with a statistical error of about 25% in the Higgs mass window between 160 and 180 GeV in the channel $pp \to \ell^\pm\ell^\pm jj$ with 3 ab^{-1} data.

The precision on the various measurement discussed above can be improved by increasing the luminosity of the collider but, also, by raising the c.m. energy which leads to an increase of the Higgs boson production rates in most processes. This is explicitly shown in Fig. 3.57, where the cross sections for the various production processes for a single Higgs boson (upper curves) and for Higgs pairs (lower curves) are displayed as a function of $\sqrt{s}$ for a Higgs mass of 120 GeV. As can be seen, the $gg \to H$ cross section for instance increases by almost two orders of magnitude compared to the LHC when the energy of the collider is raised to $\sqrt{s} = 200$ TeV. The cross sections for Higgs pair production also tremendously increase and for the vector boson fusion processes, $pp \to HHqq$, they reach the level of 0.1 pb at c.m. energies of the order of $\sqrt{s} = 200$ TeV.

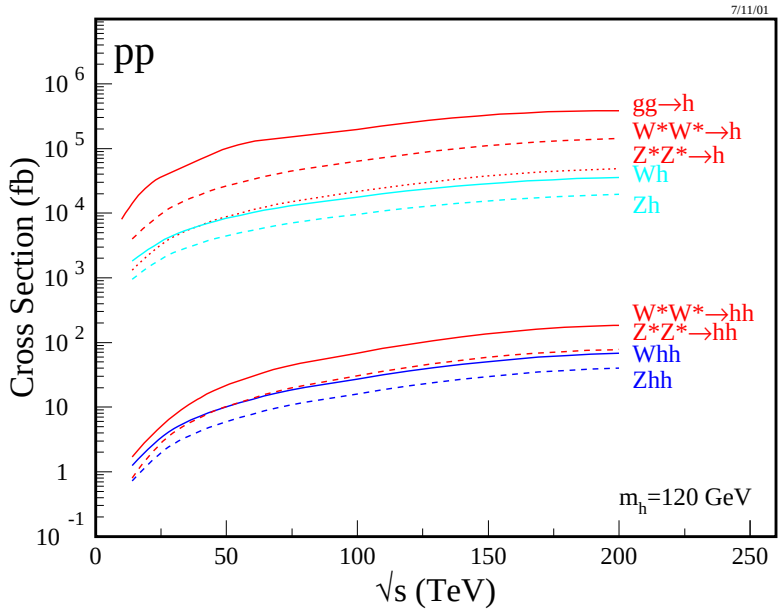

Figure 3.57: Total cross sections for single and double Higgs boson production in various processes as a function of $\sqrt{s}$ for pp collisions and $M_H = 120$ GeV; from Ref. [222].

One can then probe the rare decays of the Higgs boson and measure more precisely its couplings to fermions and gauge bosons and its self–coupling, in much the same way as it has been discussed for the SLHC. The accuracies in the determination of some couplings of the SM Higgs boson will for instance start to approach the few percent level.

In fact, with a luminosity of 100 fb^{-1}, a VLHC running at $\sqrt{s} = 50$ TeV will be comparable and in some cases superior to the SLHC. The potential of the two options has been discussed and compared in specific examples in Ref. [222] to which we refer for details. Note, however, that these accuracies cannot compete with those that can be achieved at high–energy e^+e^- linear colliders [which are expected to operate either before or at the same time] and to which we turn our attention now.

4 Higgs production at lepton colliders

4.1 Lepton colliders and the physics of the Higgs boson

4.1.1 Generalities about e^+e^- colliders

The e^+e^- collision [472] is a very simple reaction, with a well defined initial state and rather simple topologies in the final state. It has a favorable signal to background ratio, leading to a very clean experimental environment which allows to easily search for new phenomena and to perform very high–precision studies as has been shown at PEP/PETRA/TRISTAN and more recently at SLC and LEP. In particular, the high–precision studies of the properties of the Z boson at LEP1 and SLC, and the determination of the properties of the W boson at LEP2, have laid a very solid base for the Standard Model as was discussed in §1.

The physical processes in e^+e^- collisions are in general mediated by s–channel photon [for charged particles] and Z boson exchanges with cross sections which scale as the inverse of the center of mass energy squared, $\sigma \propto 1/s$, and t–channel gauge boson or electron/neutrino exchange, with cross sections which may rise like $\log(s)$. In these t–channel processes, only particles which couple directly to the electron are involved at lowest order. The s–channel exchange is the most interesting process when it takes place: it is democratic, in the sense that it gives approximately the same rates for weakly and strongly interacting matter particles, and for the production of known and new particles, when the energy is high enough.

However, in this channel, the rates are low at high energies and one needs to increase the luminosity to compensate for the $1/s$ drop of the interesting cross sections. At $\sqrt{s} \sim 1$ TeV, a luminosity $\mathcal{L} \sim 10^{34}$ cm^{-2} s^{-1} is required, which for a run time of 10^7s a year leads to an integrated luminosity of $\int \mathcal{L} \sim 100$ fb^{-1} per year, to produce 10^4 muon pairs as at PEP and PETRA. Such a luminosity is necessary to allow for thorough data analyses, including cuts on the event samples and allowing for acceptance losses in the detectors. At higher energies, the luminosity should be scaled as s to generate the same number of events.

Because of synchrotron radiation which rises as the fourth power of the c.m. energy in circular machines, e^+e^- colliders beyond LEP2 must be linear machines [473], a type of accelerator which has been pioneered by the SLC. Various reference designs of future high–energy e^+e^- colliders in the TeV range are being studied in Europe (TESLA [474] at DESY and CLIC [475] at CERN), the United States (NLC [476]) and in Japan (JLC [477]). Two technologies have been proposed for the next linear collider with center of mass energies up to $\sqrt{s} = 1$ TeV: one based on superconducting acceleration modules at moderate frequency, and another based on warm acceleration structures operating at high radio frequencies. A third and rather new approach is based on a two–beam scheme where high current and low energy beams create the acceleration field for the high–energy electron–positron beams. The technology for this collider, which could reach c.m. energies in the multi–TeV range after

presumably some halts at intermediate energies, is still to be proved.

To achieve the large luminosities which are targeted at these machines, many technological challenges need to be overcome. For instance, the beams have to be focused to extremely small dimensions near the interaction point and very high acceleration gradients are needed to reach center of mass energies in the TeV range. In the case of the TESLA machine, for which a Technical Design Report is already available, the main parameters of the beams are summarized in Table 4.1. In the case of the JLC and NLC machines, the designs have been worked out in detail and are documented in a zeroth order Technical Design Report. The two–beam acceleration scheme is being followed at CERN and it is hoped that before the end of this decade, the technical concept can be proved; this multi–TeV collider is thus expected to be a next generation machine.

Parameter	Label	Units	500 GeV	800 GeV	$\gamma\gamma$/500 GeV
Luminosity	$\mathcal{L}$	$10^{34}\text{cm}^{-2}\text{s}^{-1}$	3.4	5.8	0.6
Number of bunches	n_b		2820	4886	2820
Pulse train length	T_P	μs	950	860	950
Repetition rate	f_{rep}	Hz	5	5	
Acceleration gradient	E_{acc}	MV/m	23.4	35	23.4
Beamstrahlung	δ_E	%	3.2	4.3	–

Table 4.1: Main parameters of the TESLA Linear Collider for the energies $\sqrt{s} = 500$ and 800 GeV, with $\sqrt{s_{ee}} = 500$ GeV for the $\gamma\gamma$ option of the machine.

For details on the future machines and on the issues related to the foreseen and planned detectors, we refer the reader to Refs. [478, 479]. In the following, we briefly list a few important physics points about these future linear e^+e^- colliders [480–484]:

• One should have the possibility to adjust the c.m. energy of the colliders in order to make detailed studies and, for instance, to maximize the cross section for Higgs boson production in some particular channels or scan the threshold for W boson and top quark pair production, or for some newly produced particles.

• The requirement of a high–luminosity is achieved by squeezing the electrons and positrons into bunches of very small transverse size, leading to beamstrahlung which results into beam energy loss and the smearing of the initially sharp e^+e^- c.m. energy. Since the precise knowledge of the initial state energy is very important for precision studies [in particular in some channels where one would need missing mass techniques], beamstrahlung should be reduced to a very low level, as is already the case in narrow beam designs.

• The longitudinal polarization of the electron [and, to a lesser extent, positron] beam should be easy to obtain as has already been shown at the SLC. Degrees of polarization of the order of 80–90% and 40–50% for, respectively, the electron and positron beams are expected. The longitudinal polarization might be important when it comes to make very precise measurements of the properties of Higgs bosons and to suppress some large backgrounds [in particular from W bosons] to its production signals [485].

• By building a bypass for the transport of the electron and positron bunches, for instance, very high luminosities can also be obtained at energies in the range of 100 GeV. Operating on the Z boson resonance, 10^9 Z bosons can be produced, a sample which is two orders of magnitude larger than the one obtained at LEP1. This GigaZ machine, in particular since longitudinal polarization will be available, could significantly improve the precision tests of the SM which have been performed in the previous decade [486].

• Last but not least, the linear collider can run in three additional modes. First, one just needs to replace the positron bunches by electron bunches to have an e^-e^- collider. Then, by illuminating the initial lepton bunches by laser photons, one can convert the original collider into an $e\gamma$ or $\gamma\gamma$ collider, with a comparable total center of mass energy and luminosity as the initial lepton collider [487,488]. Higgs particles can be produced as s–channel resonance at $\gamma\gamma$ colliders [489, 491–493] and this mode will be very useful to address problems such as the Higgs boson couplings to photons and its CP properties. These options, will be also considered in this chapter.

Very recently, the International Technology Recommendation Panel has recommended [473] that the next linear e^+e^- machine, which should and hopefully will be a joint project, the International Linear Collider (ILC), is based on superconducting radio–frequency cavities. The machine should, in a first step, run at energies between $\sqrt{s} = 200$ and 500 GeV with an integrated luminosity of 500 fb^{-1} in the four first years, have the possibility of 80% polarized electron beams and two interaction regions with easy switching. In a second phase, the machine should run at an energy of $\sqrt{s} = 1$ TeV with an integrated luminosity of 1 ab^{-1} in four years. As options, the panel recommended that the machine should possibly run in the e^-e^- mode, have 50% positron polarization, the possiblity to operate near the M_Z and $2M_W$ thresholds, and the possibility to run in the $e\gamma$ and $\gamma\gamma$ modes.

In our study of the physics of the Higgs boson at e^+e^- linear colliders, we will assume for the numerical analyses three values for the c.m. energy, $\sqrt{s} = 0.5, 1$ and 3 TeV which will correspond to the two phases discussed above and to the subsequent CLIC phase, and an integrated luminosity $\mathcal{L} \sim 500$ fb^{-1}. We will also consider briefly the GigaZ option and in some detail the option of turning the machine into to a $\gamma\gamma$ collider, the particularities of which are summarized in the following subsection. Finally, future muon colliders will be discussed in the last section of this chapter.

4.1.2 The photon colliders

The Compton scattering of laser photons with energies ω_0 in the eV range with high–energy electrons, $E_e \sim \mathcal{O}(100\text{ GeV})$, leads to a tight bunch of back–scattered high–energy photons [487, 488]. The kinematics of the process is governed by the dimensionless parameter $x = 4\omega_0 E_e/m_e^2$. The fraction of energy carried by the back–scattered photon, $y = \omega/E_e$, is maximal for $y_{\max} = x/(1+x)$. The highest energy, compared to the e^- beam energy is therefore obtained for very large values of the parameter x. However, to prevent the creation of e^+e^- pairs in the annihilation of the laser and scattered photons, one demands that $x \lesssim x_0 = 4.83$. For this value, the photon collider can have as much as $\sim 80\%$ of the energy of the original e^+e^- collider. The scattering angle of the obtained photons is given by $\theta(y) \simeq m_e(1+x)/E_e \times \sqrt{y_{\max}/y - 1}$ and is of the order of a few micro–radians.

The energy spectrum of the back–scattered photon

$$f_c(y) = \sigma_c^{-1}\, \mathrm{d}\sigma_c(y)/\mathrm{d}y \tag{4.1}$$

depends on the product of the the mean helicity of the initial electron λ_e and on the degree of circular polarization of the laser photon P_γ with $-1 \leq 2\lambda_e P_\gamma \leq +1$. It is defined by the differential Compton cross section [488]

$$\frac{d\sigma_c}{dy} = \frac{\pi\alpha^2}{xm_e^2}[f_0 + 2\lambda_e P_\gamma f_1 + 2\lambda_e P_{\gamma'} f_2 + P_\gamma P_{\gamma'} f_3] \tag{4.2}$$

where the dependence on the polarization of the back–scattered photon $P_{\gamma'}$ has been retained. In terms of the variable $r = y/[x(1-y)]$, the functions f_i $(i = 0, .., 3)$ read

$$\begin{aligned} f_0 &= \frac{1}{1-y} + 1 - y - 4r(1-r)\ , \quad f_1 = xr(1-2r)(2-y) \\ f_2 &= xr\Big[1 + (1-y)(1-2r)^2\Big]\ , \quad f_3 = (1-2r)\Big[\frac{1}{1-y} + 1 - y\Big] \end{aligned} \tag{4.3}$$

When the polarization of the scattered photon is discarded, the integrated Compton cross section can be cast into the form

$$\begin{aligned} \sigma_c &= \sigma_c^{\rm np} + 2\lambda_e P_\gamma \sigma_c^{\rm p} \\ \sigma_c^{\rm np} &= \frac{\pi\alpha^2}{xm_e^2}\left[\frac{1}{2} + \frac{8}{x} - \frac{1}{2(1+x)^2} + \left(1 - \frac{4}{x} - \frac{8}{x^2}\right)\ln(x+1)\right] \\ \sigma_c^{\rm p} &= \frac{\pi\alpha^2}{xm_e^2}\left[-\frac{5}{2} + \frac{1}{x+1} - \frac{1}{2(x+1)^2} + \left(1 + \frac{2}{x}\right)\ln(x+1)\right] \end{aligned} \tag{4.4}$$

By selecting a given polarization of the initial e^- and laser beams, one can have different shapes for the energy distribution of the scattered photons: a flat distribution if the electron

and the laser have the same polarization, or an almost monochromatic distribution peaked at $y_{\max}$ if they have opposite polarization. The latter scenario if of course very interesting.

Because of the small scattering angle θ of the photons, the luminosity of the spectrum depends on the the conversion distance, i.e. the distance between the intersecting point of the laser and the electron beam and the interaction point, as well as on the size and shape of the electron beam. A geometrical factor $\rho = b\theta/a$ takes into account the non–zero conversion distance b and the radius a of the assumed round electron beam [typically, the sizes are $a \sim \mathcal{O}(10^2 \text{ nm})$ and $b \sim \mathcal{O}(1 \text{ cm})$]. If ρ is much larger than unity, only the photons with high energy can meet at the interaction point, while for $\rho \ll 1$, photons with various energies collide and give a rather broad spectrum.

When the Compton backscattered photons, that we will denote by γ_1 and γ_2, are taken as initial states, the cross section for the process $\gamma\gamma \to X$ with polarized photons reads

$$\mathrm{d}\hat{\sigma}_{\gamma\gamma} = \sum_{i,j=0}^{4} \xi_{1i}\xi_{2j}\, \mathrm{d}\hat{\sigma}_{ij} \tag{4.5}$$

in the ξ_{1i} and ξ_{2j} photon Stokes parameter basis, with zeroth components such that $\xi_{10} = \xi_{20} = 1$. The event rate $\mathrm{d}N$ can be then written as

$$\mathrm{d}N \;=\; \mathrm{d}\mathcal{L}\,\langle \mathrm{d}\hat{\sigma}_{\gamma\gamma}\rangle \;=\; \mathrm{d}\mathcal{L}\sum_{i,j=0}^{3} \langle \xi_{1i}\xi_{2j}\rangle\, \mathrm{d}\hat{\sigma}_{ij} \tag{4.6}$$

where $\mathrm{d}\mathcal{L}$ is the differential $\gamma\gamma$ luminosity and the average $\langle \xi_{1i}\xi_{2j}\rangle$ is along the interaction region [only the diagonal terms in the product are relevant in general].

For circularly polarized laser beams, one has for the average Stokes parameters

$$\langle \xi_{12}\xi_{22}\rangle = \xi_{12}\xi_{22}\ ,\ \langle \xi_{13}\xi_{23}\rangle = -\langle \xi_{11}\xi_{21}\rangle \ll 1 \tag{4.7}$$

so that the event rate can be written in terms of the luminosities corresponding to the $J_Z = 0$ and $J_Z = \pm 2$ scattering channels, as

$$\begin{aligned} \mathrm{d}N \;&=\; \mathrm{d}\mathcal{L}^{J_Z=0}\,\mathrm{d}\hat{\sigma}_{J_Z=0} \;+\; \mathrm{d}\mathcal{L}^{J_Z=\pm 2}\,\mathrm{d}\hat{\sigma}_{J_Z=\pm 2} \\ \mathrm{d}\mathcal{L}^{J_Z=0} = \frac{1}{2}\mathrm{d}\mathcal{L}\,(1+\langle \xi_{12}\xi_{22}\rangle)\ ,\ \mathrm{d}\mathcal{L}^{J_Z=\pm 2} &= \frac{1}{2}\mathrm{d}\mathcal{L}\,(1-\langle \xi_{12}\xi_{22}\rangle) \end{aligned} \tag{4.8}$$

With this polarization, a broad luminosity spectrum can be achieved by using electrons and laser photons with like–handed helicities and a small value, $\rho \sim 0.6$, which leads to low energetic backscattered photons in the interaction region. In contrast, a sharp spectrum peaking near $y_{\max}$ can be obtained using opposite–handed electrons and laser photons in a more restrictive interaction region $\rho \sim 3$; see Fig. 4.1 (left). The events in the $J_Z = 0\,(J_Z =$

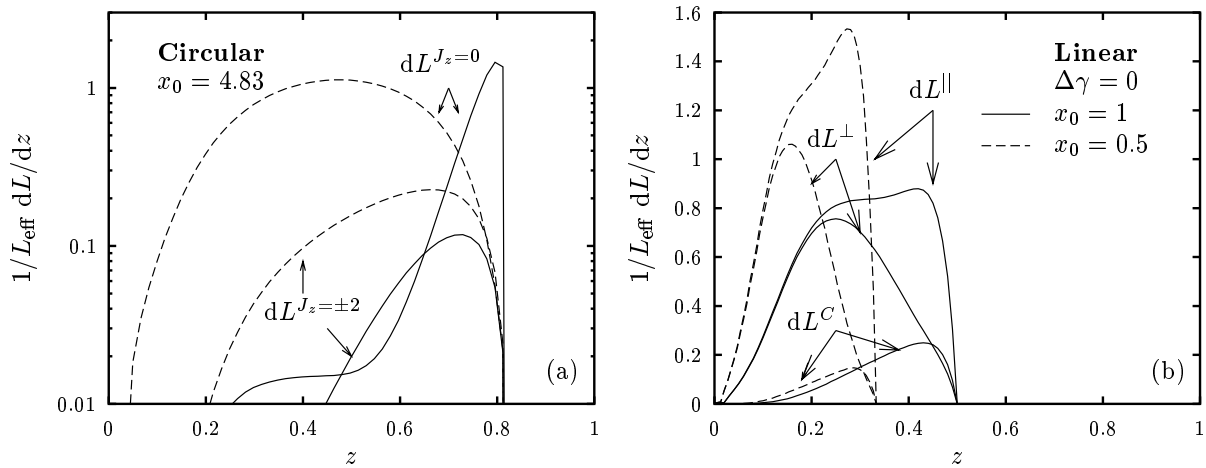

Figure 4.1: Normalized γ luminosities as functions of $z = \sqrt{s_{\gamma\gamma}}/\sqrt{s_{e^+e^-}}$ for left: circularly polarized lasers with $x_0 = 4.83$ and the solid (dashed) lines are for opposite-handed (like-handed) photons and electrons with $\rho = 3\,(0.6)$, and right: linearly polarized lasers with $\Delta\gamma = 0$, $\rho = 0.6$ and $x_0 = 1\,(0.5)$ for the solid (dashed) lines. The lasers are assumed to be completely polarized and the electrons 85% longitudinally polarized, and the configurations for both collider arms are the same; from Ref. [493].

± 2) channels can be enhanced (suppressed) by choosing the laser and electron beams so that $x_0 = 4.83$, which in addition, maximizes the collider energy.

For linearly polarized laser beams, neglecting $\rho \neq 0$ effects for simplicity, the average Stokes parameters are

$$\begin{aligned} \langle \xi_{12}\xi_{22}\rangle &\simeq \langle \xi_{12}\rangle\langle \xi_{22}\rangle = 4\lambda_{e^-}\lambda_{e^+}\, c_1 c_2 \\ \langle \xi_{13}\xi_{23} - \xi_{11}\xi_{21}\rangle &\simeq \langle \xi_{13}\rangle\langle \xi_{23}\rangle - \langle \xi_{11}\rangle\langle \xi_{21}\rangle = P_{1t}P_{2t}\,\ell_1\ell_2\,\cos 2(\Delta\gamma) \end{aligned} \tag{4.9}$$

where P_{ti} are the mean linear laser polarizations while c_i and ℓ_i are the induced circular and linear polarizations of the backscattered photons; $\Delta\gamma$ is the angle between the planes of maximal linear polarization of the two lasers. The circular polarizations c_i and linear polarizations ℓ_i are large for, respectively, high and low values of the parameter x, and both increase with y. The event rate in this case is given by

$$\mathrm{d}N = \mathrm{d}\mathcal{L}^{||}\,\mathrm{d}\hat{\sigma}_{||} + \mathrm{d}\mathcal{L}^{\perp}\,\mathrm{d}\hat{\sigma}_{\perp} + \frac{1}{2}\mathrm{d}\mathcal{L}^{C}\,\left(\mathrm{d}\hat{\sigma}_{J_Z=0} - \mathrm{d}\hat{\sigma}_{J_Z=2}\right) \tag{4.10}$$

$$\mathrm{d}\mathcal{L}^{||} = \frac{1}{2}\mathrm{d}\mathcal{L}\left(1 + \langle \xi_{13}\xi_{23} - \xi_{11}\xi_{21}\rangle\right),\ \mathrm{d}\mathcal{L}^{\perp} = \frac{1}{2}\mathrm{d}\mathcal{L}\left(1 - \langle \xi_{13}\xi_{23} - \xi_{11}\xi_{21}\rangle\right),\ \mathrm{d}\mathcal{L}^{C} = \mathrm{d}\mathcal{L}\,\langle \xi_{12}\xi_{22}\rangle$$

For this polarization, one has to make a compromise between having a good separation of the $||$ and $\perp$ components, which needs a small value of x, and having a high energy which needs a larger value since the available energy is proportional to $x/(x+1)$.

For more details on the main features of the $\gamma\gamma$ machines, such as energy, luminosity distributions, polarization, etc..., see the reviews given in Refs. [491–493].

4.1.3 Future muon colliders

The concept of $\mu^+\mu^-$ colliders, although introduced already in the late sixties [494], has been taken very seriously only in the last decade. A Muon Collider Collaboration (MCC) [495,496] has been formed in the US in the mid–nineties to complete the R&D that is required to determine whether a muon collider is technically feasible and, in the case of a positive answer, to propose a design for a First Muon Collider. In the late nineties, the European community joined the project and a study report on the feasibility of a muon collider at CERN has been produced [497]. A three–step scenario for a muon collider is presently foreseen [496, 497]:

– *i*) A first step would be an intense proton source for producing muons which will be then captured, cooled, accelerated and stored. In the storage ring, they then decay and they allow to produce high–intensity and high–quality neutrino beams which could be used to perform detailed studies of neutrino oscillations and neutrino–nucleon scattering, as well as some physics with stopped muons such as the measurement of the muon magnetic and electric dipole moments and the search for some rare μ decays.

– *ii*) The second step would be a $\mu^+\mu^-$ collider with a center of mass energy in the range $\sqrt{s} \sim$ 100–200 GeV. This collider could do the same physics as an e^+e^- collider and it will be a Higgs factory that would possibly allow to study in more detail the properties of the Higgs particles that have been produced at the LHC and at the ILC.

– *iii*) A final step would be then to operate the muon collider at the maximum possible c.m. energy and to probe the physics of the multi–TeV scale. For instance, energies up to $\sqrt{s} \sim 7$ TeV could be reached with the facilities that are available at CERN. However, with the present designs [and not to mention the very high luminosities which need to be achieved in this case], the radiation induced by the neutrinos is extremely high for c.m. energies in excess of a few TeV and poses a very serious problem. Major technological developments are therefore required to reach this high–energy step.

In this report, we will be interested only in the second phase of the muon collider, that is, the Higgs factories with c.m. energies $\sqrt{s} \lesssim 200$ GeV. Compared to an e^+e^- machine, the main advantages of a muon collider as far as Higgs physics is concerned [498–501], are principally due to the fact that the muon is much heavier than the electron, $m_\mu/m_e \sim 200$: the Higgs boson coupling to muons is much larger than the coupling to electrons, yielding significantly larger rates for s–channel Higgs production at muon colliders, $\mu^+\mu^- \to H$ [the production rate in this channel is of course negligible in e^+e^- collisions].

Another advantage of $\mu^+\mu^-$ colliders, compared to e^+e^- colliders, is the very precise knowledge of the beam energy spectrum which would allow for very high precision analyses of the mass, total width and peak cross section of the produced Higgs resonance. According to the analyses performed in Ref. [496,497], the energy can be tuned with a precision $\Delta E_{\rm b}/E_{\rm b} \sim$

$\times 10^{-6}$ [i.e. 100 keV for $\sqrt{s} = 100$ GeV] and values ten times smaller seem possible. The small amount of beamstrahlung [which, in e^+e^- collisions, induces an energy loss of a few percent that is difficult to measure very precisely] and bremsstrahlung [again due to the larger mass of the muon compared to the electron] could lead to a relative beam energy spread or resolution of the order of $R = \sigma_{E_\mathrm{b}}/E_\mathrm{b} \sim 10^{-3}$ down to $R = 3 \times 10^{-5}$ and which could be known with an accuracy of $\Delta\sigma_{E_\mathrm{b}}/E_\mathrm{b} \sim 0.5\%$. Such a small energy spread is very important when performing a scan around the very narrow Higgs resonance, $\Gamma_H \sim 2$ MeV for $M_H \sim 100$ GeV. In addition, since synchrotron radiation is also very small, one can still use the available circular machines. The energy calibration can be made by spin precession as the muons that are produced in the weak decays of pions are 100% polarized, leading to a natural longitudinal polarization of approximately 30% which, however, drops to the level of $\sim 20\%$ due to the handling before injection into the collider. The drawback, compared to e^+e^- machines, is that it is difficult to maximize this polarization without an important loss in luminosity and that a muon collider cannot be turned into a $\gamma\gamma$ or $\mu\gamma$ collider.

Nevertheless, the design of the machine is still at an early stage and many problems remain to be solved [496,497]. In addition, the delivered luminosity which can be achieved is still uncertain, and it depends strongly on the baseline parameters of the collider; Tab. 4.2. There is, for instance, a particularly strong dependence on the beam energy resolution. As can be seen from the table, at $\sqrt{s} = 100$ GeV, the estimates indicate that only $\mathcal{L} \sim 10^{31}\,(10^{32})\,\mathrm{cm}^{-2}\mathrm{s}^{-1}$ can be obtained for a resolution of $R = 0.003\%\,(0.1\%)$, leading to an integrated luminosity $\int \mathcal{L} = 0.1\,(1)\,\mathrm{fb}^{-1}$ per year. The luminosity, however can substantially be increased with energy reaching, for $R \sim 0.1\%$, values of the order of $\mathcal{L} \sim 10^{33}\,(10^{35})\,\mathrm{cm}^{-2}\mathrm{s}^{-1}$ for $\sqrt{s} \sim 0.4\,(3)$ TeV; see Table 4.2 and the details given in Refs. [496,497].

c.m. energy	3 TeV	400 GeV	100 GeV		
p power (MW)	4	4	4		
$1/\tau_\mu$ (Hz)	32	240	960		
μ/bunch	2×10^{12}	2×10^{12}	2×10^{12}		
circumference (m)	6000	1000	350		
$\langle B \rangle$ (T)	5.2	4.7	3		
$n_{\mathrm{turns}}^{\mathrm{effective}}$	785	700	450		
6-D $\epsilon_{6,N} \times 10^{-10}$ (πm^3)	1.7	1.7	1.7		
$R = \delta p/p$ (%)	0.16	0.14	0.12	0.001	0.003
RMS ϵ_T (π mm-rad)	0.05	0.05	0.085	0.0195	0.29
β^* and σ_z (cm)	0.3	2.6	4.1	9.4	14.1
σ_r (μm)	3.2	26	86	196	294
Luminosity (cm^{2}s^{-1})	7×10^{34}	10^{33}	1.2×10^{32}	2.2×10^{31}	10^{31}

Table 4.2: Possible parameter sets for a $\mu^+\mu^-$ Higgs factory at $\sqrt{s} = M_H = 100$ GeV as expected by the MCC [496]; higher energy machines are also shown for comparison.

4.1.4 Higgs production processes in lepton collisions

In e^+e^- collisions with center of mass energies beyond LEP2, the main production mechanisms for Higgs particles are the Higgs–strahlung process [32, 105, 111–113] and the WW fusion mechanism [112, 243–246, 502, 503], depicted in Fig. 4.2,

$$\text{Higgs} - \text{strahlung process}: \quad e^+e^- \longrightarrow (Z^*) \longrightarrow Z\,H \tag{4.11}$$

$$\text{WW fusion process}: \quad e^+e^- \longrightarrow \bar{\nu}\nu\,(W^*W^*) \longrightarrow \bar{\nu}\;\nu\,H \tag{4.12}$$

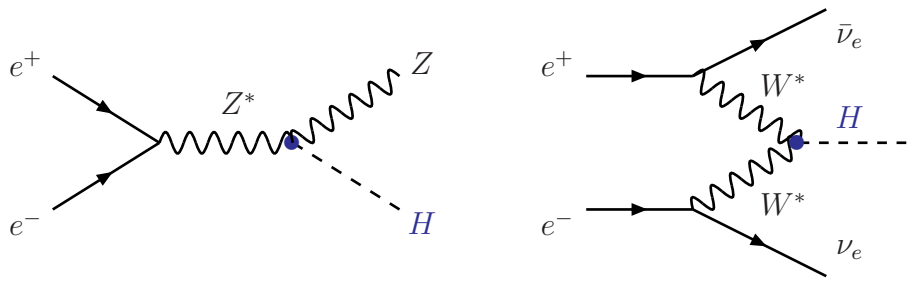

Figure 4.2: The dominant Higgs production mechanisms in high–energy e^+e^- collisions.

There are several other mechanisms in which Higgs bosons can be produced in e^+e^- collisions: the ZZ fusion process [243–245, 503, 504], the radiation off heavy top quarks [505, 506] and the double Higgs boson production process either in Higgs–strahlung or WW/ZZ fusion [255, 257, 263, 507, 508]

$$\text{ZZ fusion process}: \quad e^+e^- \longrightarrow e^+e^-(Z^*Z^*) \longrightarrow e^+e^-\,H \tag{4.13}$$

$$\text{radiation off heavy fermions}: \quad e^+e^- \longrightarrow (\gamma^*, Z^*) \longrightarrow f\bar{f}\,H \tag{4.14}$$

$$\text{double Higgs production}: \quad e^+e^- \longrightarrow ZHH\,,\ \ell\ell HH \tag{4.15}$$

These are, in principle, higher–order processes in the electroweak coupling with production cross sections much smaller than those of the Higgs–strahlung process and the WW fusion channel [for ZZ fusion, only at low energies]. However, with the high luminosity planned for future linear colliders, they can be detected and studied. These processes are extremely interesting since they allow for the determination of some of the fundamental properties of the Higgs particle, such as its self–coupling and its Yukawa coupling to top quarks.

There also other higher–order processes in which Higgs particles can be produced in e^+e^- collisions, but with even smaller production cross sections than those mentioned previously: associated production with a photon, $e^+e^- \to H + \gamma$ [509], loop induced Higgs pair production, $e^+e^- \to HH$ [510], associated production with vector bosons, $e^+e^- \to VV + H$ [511,512], and associated production with a gauge boson and two fermions, $e^+e^- \to VH + f\bar{f}$ [511]. Except possibly for the two latter processes, the cross sections are in general below the femtobarn level and, thus, too small for the processes to be detected at future machines, unless extremely high–luminosities are made available.

Higgs particles can be produced as s–channel resonances [489, 490] [among other possibilities which will be also discussed] in the $\gamma\gamma$ option of future e^+e^- linear colliders

$$\gamma\gamma \longrightarrow H \tag{4.16}$$

allowing the measurement of the important $H\gamma\gamma$ coupling. In the $e\gamma$ option, one can also produce the Higgs boson in the channel $e\gamma \to \nu_e W^- H$ [513].

Finally, on can also produce the Higgs boson as an s–channel resonance at future muon colliders [498, 514]

$$\mu^+\mu^- \longrightarrow H \tag{4.17}$$

In the following sections, we discuss the dominant production processes in some detail and summarize the main features of the subleading processes. We first focus on e^+e^- linear colliders in the e^+e^- option, and discuss in more details the physics potential at the first phase with center of mass energies around $\sqrt{s} \sim 500$ GeV [515, 516]; occasionally, we will comment on the benefits of raising the energy of the machine. The case of the $\gamma\gamma$ option of the machine, as well as the physics at future muon colliders will be postponed to, respectively, the previous–to–last and last sections.

Since e^+e^- colliders are known to be high–precision machines as demonstrated at LEP and SLC, the theoretical predictions have to be rather accurate and thus the radiative corrections to the Higgs production processes have to be taken into account. The one–loop electroweak and QCD radiative corrections to the most important production mechanisms have been completed only recently [517–529] and their main effects will be summarized.

In addition, the main motivation of future e^+e^- in the sub–TeV energy range is the detailed exploration of the electroweak symmetry breaking mechanism and the thorough study of the fundamental properties of the Higgs particle, in particular the spin and parity quantum numbers. At least in the main processes, we study the energy and the angular dependence of the cross sections as well as the angular correlations of the final decay products, and confront, whenever possible, the predictions for the $J^{\rm PC} = 0^{++}$ case of the SM Higgs particle to what would be expected if the Higgs were a pseudoscalar boson with $J^{\rm PC} = 0^{+-}$ spin–parity assignments. We also discuss the measurements of the Higgs mass and total decay width, the Higgs couplings to fermions and gauge bosons, and the Higgs self–coupling which allows for the reconstruction of part of the scalar potential that is responsible of the spontaneous breaking of the electroweak symmetry.

Some particular points relevant to this section have been already discussed in the context of hadron colliders or in the section on the decays of the Higgs particle. However, some important features will be rediscussed in the context of lepton colliders, to make the section more complete and self–contained.

4.2 The dominant production processes in e^+e^- collisions

4.2.1 The Higgs–strahlung mechanism

The production cross section

The production cross section for the Higgs strahlung process is given by

$$\sigma(e^+e^- \to ZH) = \frac{G_\mu^2 M_Z^4}{96\pi s}(\hat{v}_e^2 + \hat{a}_e^2)\ \lambda^{1/2} \frac{\lambda + 12M_Z^2/s}{(1 - M_Z^2/s)^2} \tag{4.18}$$

where, as usual, $\hat{a}_e = -1$ and $\hat{v}_e = -1 + 4s_W^2$ are the Z charges of the electron and $\lambda^{1/2}$ the usual two–particle phase–space function

$$\lambda = (1 - M_H^2/s - M_Z^2/s)^2 - 4M_H^2 M_Z^2/s^2 \tag{4.19}$$

The production cross section is shown in Fig. 4.3 as a function of the Higgs mass for the values of the c.m energy $\sqrt{s} = 0.5, 1$ and 3 TeV. At $\sqrt{s} = 500$ GeV, $\sigma(e^+e^- \to HZ) \sim 50$ fb for $M_H \sim 150$ GeV, leading to a total of ~ 25.000 Higgs particles that are created at an integrated luminosity of $\int \mathcal{L} = 500$ fb^{-1}, as expected for future machines. The cross section scales as the inverse of the c.m. energy, $\sigma \sim 1/s$ and, for moderate Higgs masses, it is larger for smaller c.m. energies. The maximum value of the cross section for a given M_H value is at $\sqrt{s} \sim M_Z + \sqrt{2}M_H$. An energy of the order of $\sqrt{s} \sim 800$ GeV is needed to cover the entire Higgs boson mass range allowed in the SM, $M_H \lesssim 700$ GeV.

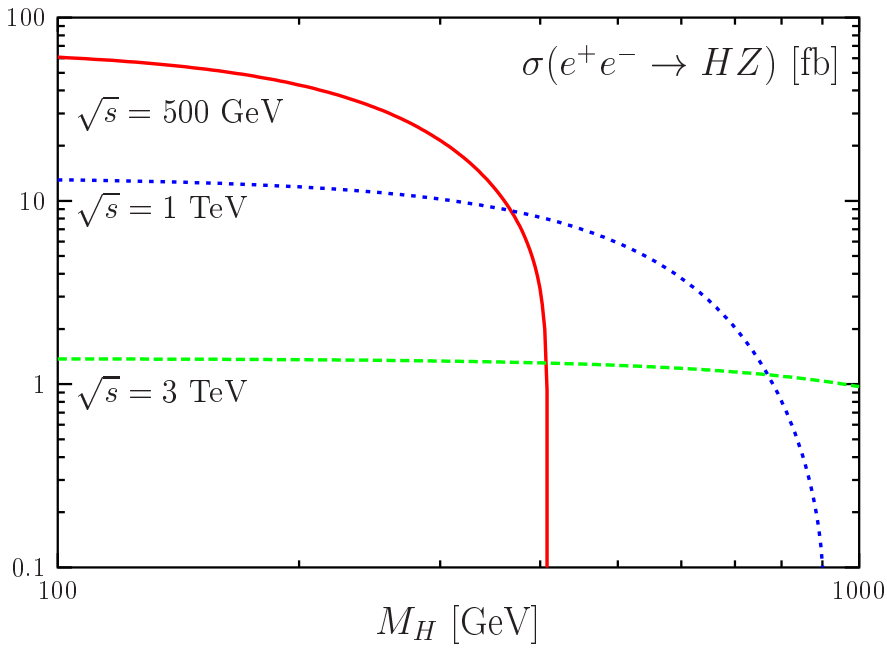

Figure 4.3: Higgs boson production cross sections in the Higgs–strahlung mechanism in e^+e^- collisions with c.m. energies $\sqrt{s} = 0.5, 1$ and 3 TeV as a function of M_H.

The energy dependence

The recoiling Z boson in the two–body reaction $e^+e^- \to ZH$ is mono–energetic, $E_Z = (s - M_H^2 + M_Z^2)/(2\sqrt{s})$, and the mass of the Higgs boson can be derived from the energy of the Z boson, $M_H^2 = s - 2\sqrt{s}E_Z + M_Z^2$, if the initial e^+ and e^- beam energies are sharp.

The excitation curve rises linearly with the phase–space factor $\lambda^{1/2}$, which is characteristic to the production of a scalar particle in association with a Z boson

$$\sigma(e^+e^- \to HZ) \sim \lambda^{1/2} \sim \sqrt{s - (M_H + M_Z)^2} \tag{4.20}$$

This behavior for the $J^{\rm PC} = 0^{++}$ SM Higgs boson can be compared with the case of a CP–odd Higgs boson A with $J^{\rm PC} = 0^{+-}$ quantum numbers and with couplings given in §2. The total production cross section for the process $e^+e^- \to ZA$ [159, 535]

$$\sigma(e^+e^- \to ZA) = \eta^2 \frac{G_\mu^2 M_Z^6}{48\pi M_A^4} (\hat{a}_e^2 + \hat{v}_e^2) \frac{\lambda^{3/2}}{(1 - M_Z^2/s)^2} \tag{4.21}$$

has a momentum dependence $\sim \lambda^{3/2}$ that is characteristically different from the ZH cross section near threshold. This is illustrated in Fig. 4.4, where the behavior near the production threshold for the assignments $J^{\rm PC} = 0^{++}$ and 0^{+-} is shown for a Higgs mass $M_H = 120$ GeV.

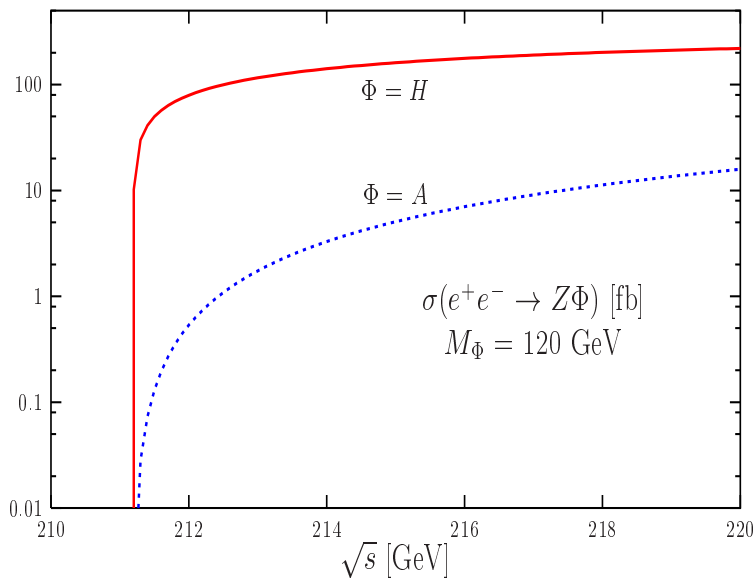

Figure 4.4: The $e^+e^- \to Z\Phi$ cross section energy dependence near the threshold for the two parity cases $\Phi = H$ and $\Phi = A$ [with $\eta = 1$] with $M_\Phi = 120$ GeV.

In fact, as discussed in Ref. [536], the linear threshold behavior of the SM Higgs boson rules out not only the quantum number $J^{\rm P} = 0^-$ but also $J^{\rm P} = 1^-, 2^+$ and higher spin $3^\pm, \cdots$, which rise with higher powers of λ too. The production of states with the two remaining spin–parity assignments $J^{\rm P} = 1^+, 2^+$ can be ruled out using the angular correlations as is discussed hereafter.

The angular distribution

The angular distribution of the Z/H bosons in the bremsstrahlung process is also sensitive to the spin of the Higgs particle [537]. The explicit form of the angular distribution, with θ being the scattering angle, is given by

$$\frac{\mathrm{d}\sigma(e^+e^- \to ZH)}{\mathrm{d}\cos\theta} \sim \lambda^2 \sin^2\theta + 8M_Z^2/s \overset{s\gg M_Z^2}{\longrightarrow} \frac{3}{4}\sin^2\theta \tag{4.22}$$

and approaches the spin–zero distribution asymptotically, $\propto \sin^2\theta$, in accordance with the equivalence theorem which requires that the production amplitude becomes equal to the amplitude where the Z boson is replaced by the neutral Goldstone boson w_0. Thus, for high energies, the Z boson is produced in a state of longitudinal polarization

$$\frac{\sigma_L}{\sigma_L + \sigma_T} = 1 - \frac{8M_Z^2}{12M_Z^2 + \lambda s} \tag{4.23}$$

Let us again confront the characteristics of a $J^{\rm PC} = 0^{++}$ state with those of a pseudoscalar Higgs boson A. In the process $e^+e^- \to ZA$, the angular distribution is given by

$$\frac{\mathrm{d}\sigma(e^+e^- \to ZA)}{\mathrm{d}\cos\theta} \sim 1 + \cos^2\theta \tag{4.24}$$

independent of the energy. The Z boson in the final state is purely transversally polarized, so that the cross section need not be $\sim \sin^2\theta$ in this case.

If the Higgs particle were a mixture Φ of scalar and pseudoscalar bosons, with a coupling to the virtual and real Z bosons given by

$$g_{ZZ\Phi} = g_{ZZH}\Big(g_{\mu\nu} + i\eta M_Z^{-2}\epsilon_{\mu\nu\rho\sigma}p_Z^\sigma p_Z^\rho\Big) \tag{4.25}$$

the angular distribution of $e^+e^- \to \Phi Z$ would read [$A_f = 2a_f v_f/(a_f^2 + a_f^2)$ as usual]

$$\frac{\mathrm{d}\sigma(e^+e^- \to Z\Phi)}{\mathrm{d}\cos\theta} \sim 1 + \frac{s\lambda^2}{8M_Z^2}\sin^2\theta + \eta A_e \frac{s\lambda}{M_Z^2}\cos\theta + \eta^2\frac{s^2\lambda^2}{M_Z^4}(1+\cos^2\theta) \tag{4.26}$$

The presence of the interference term proportional to η is a clear indication of CP–violation in the Higgs sector. One can thus define an observable [538], conveniently written as,

$$\langle O\rangle = 2\mathrm{Re}\Big(\frac{\mathcal{M}(e^+e^- \to ZH)\mathcal{M}^*(e^+e^- \to ZA)}{|\mathcal{M}(e^+e^- \to ZH)|^2}\Big) \propto \eta A_e \frac{s\lambda}{M_Z^2} \tag{4.27}$$

which quantifies the amount of this CP–violation.

The angular momentum structure specific to Higgs production can also directly be confronted experimentally with the one of the process $e^+e^- \to ZZ$ that is distinctly different. Mediated by electron exchange in the t–channel, the amplitude for this process is built–up by many partial waves, peaking in the forward/backward directions. The two angular distributions, together with the angular distribution for the CP–odd Higgs case, $e^+e^- \to AZ$, are compared with each other in Fig. 4.5 which demonstrates the specific character of the SM Higgs production process.

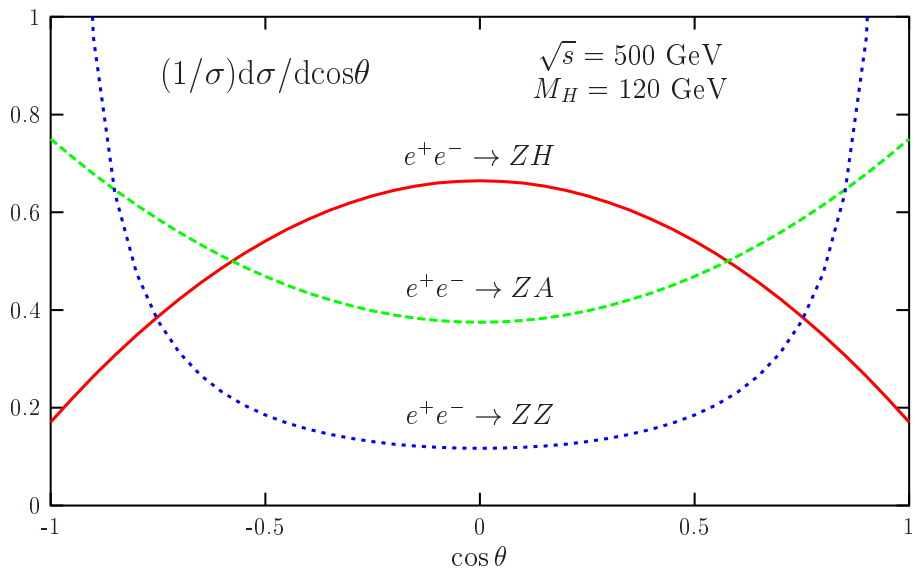

Figure 4.5: Angular distribution in the process $e^+e^- \to HZ$ for $\sqrt{s} = 500$ GeV and $M_H = 120$ GeV. The distributions for the CP–odd Higgs and $e^+e^- \to ZZ$ cases are also shown.

The angular correlations

The pattern for the Z boson polarization in the $e^+e^- \to HZ, HA$ and ZZ processes can be checked [159, 535]: while the distribution of the fermions in the $Z \to f\bar{f}$ rest frame with respect to the Z flight direction is given by $\sin^2\theta_*$ for longitudinally polarized Z bosons, it behaves as $(1 \pm \cos\theta_*)^2$ for transversally polarized states, after averaging over the azimuthal angles. The definition of the polar angles θ and θ_* is shown in Fig. 4.6; the azimuthal angle ϕ_* is the angle between the plane of the $f\bar{f}$ from Z decays and the Higgs decay products.

Including the azimuthal angles, the final angular correlations may be written for the process $e^+e^- \to ZH$ with $Z \to f\bar{f}$ as [159]

$$\begin{aligned}\frac{\mathrm{d}\sigma(e^+e^- \to ZH)}{\mathrm{d}c_\theta \mathrm{d}c_{\theta_*}\mathrm{d}\phi_*} \sim\ & s_\theta^2 s_{\theta_*}^2 - \frac{1}{2\gamma} s_{2\theta} s_{2\theta_*} c_{\phi_*} + \frac{1}{2\gamma^2}[(1+c_\theta^2)(1+c_{\theta_*}^2) + s_\theta^2 s_{\theta_*}^2 c_{2\phi_*}] \\ & -2A_e A_f \frac{1}{\gamma}\left[s_\theta s_{\theta_*} c_{\phi_*} - \frac{1}{\gamma} c_\theta c_{\theta_*}\right] \end{aligned} \tag{4.28}$$

where $s_\theta = \sin\theta$ *etc*, $A_f = 2v_f a_f/(v_f^2 + a_f^2)$ and $\gamma^2 = E^2/M_Z^2 = 1 + \lambda s/4M_Z^2$. As before, θ is the polar Z angle in the laboratory frame, θ_* the polar fermion angle in the Z rest frame and ϕ_* the corresponding azimuthal angle with respect to the $e^+e^- \to ZH$ production plane. After integrating out the polar angles θ and θ_*, one finds the familiar $\cos\phi_*$ and $\cos 2\phi_*$ dependence discussed in §2.2.4 associated with P–odd and even amplitudes, respectively

$$\frac{\mathrm{d}\sigma(e^+e^- \to ZH)}{\mathrm{d}\phi_*} \sim 1 + a_1 \cos\phi_* + a_2 \cos 2\phi_*$$

$$a_1 = -\frac{9\pi^2}{32} A_e A_f \frac{\gamma}{\gamma^2+2} \ , \qquad a_2 = \frac{1}{2}\frac{1}{\gamma^2+2} \tag{4.29}$$

The azimuthal angular dependence disappears for high energies $\sim 1/\gamma$ as a result of the dominating longitudinal polarization of the Z boson.

Note again the characteristic difference to the 0^{+-} case, $e^+e^- \to ZA \to f\bar{f}A$ [159, 175]

$$\frac{\mathrm{d}\sigma(e^+e^- \to ZA)}{\mathrm{d}c_\theta \mathrm{d}c_{\theta_*} \mathrm{d}\phi_*} \sim 1 + c_\theta^2 c_{\theta_*}^2 - \frac{1}{2} s_\theta^2 s_{\theta_*}^2 - \frac{1}{2} s_\theta^2 s_{\theta_*}^2 c_{2\phi_*} + 2A_e A_f c_\theta c_{\theta_*} \tag{4.30}$$

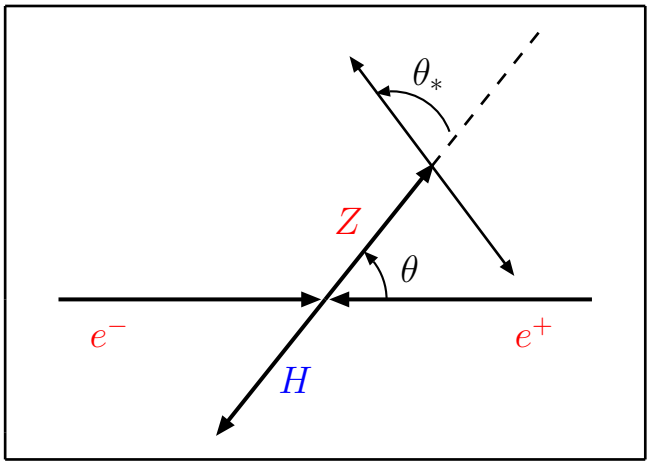

Figure 4.6: The definition of the polar angles θ, θ_* in the process $e^+e^- \to ZH \to Hf\bar{f}$.

This time, the azimuthal dependence is P–even and independent of the energy in contrast to the 0^{++} case; after integrating out the polar θ, θ_* angles, one obtains

$$\frac{\mathrm{d}\sigma(e^+e^- \to ZA)}{\mathrm{d}\phi_*} \sim 1 - \frac{1}{4}\cos 2\phi_* \tag{4.31}$$

The production of the two states with $J^{\mathrm{P}} = 1^+, 2^-$ quantum numbers, which also lead to a β behavior near the kinematical threshold as in the 0^+ case, can be ruled out using the angular correlations as they lead to $(1+c_\theta^2)s_{\theta_*}^2$ and $(1+c_{\theta_*}^2)s_\theta^2$ distributions which are absent in the SM Higgs case [174].

We can thus conclude that the angular analysis of the Higgs production in $e^+e^- \to Z^* \to ZH$ with $Z \to f\bar{f}$, together with the threshold behavior of the cross section, allows stringent tests of the $J^{\mathrm{PC}} = 0^{++}$ quantum numbers of the Higgs boson in the low and intermediate mass range. In the high mass range, $M_H \gtrsim 2M_W$, when the Higgs boson decays almost exclusively into two vector bosons, the Higgs spin–zero and parity can be checked not only in the production process $e^+e^- \to HZ$, but also in the decay processes $H \to VV \to 4f$ as discussed in §2.2.4. The full correlations between the final decay products $e^+e^- \to ZH \to ZVV \to 6f$ has not been yet worked out explicitly because of the rather complicated six fermion final state.

4.2.2 The WW fusion process

The production cross section

The WW fusion process [112, 243–246, 503] is most important for small values of the ratio $M_H/\sqrt{s}$, *i.e.* high energies where the cross section grows $\sim M_W^{-2}\log(s/M_H^2)$. The production cross section, discussed in §3.3 at hadron colliders, can be more conveniently written as

$$\sigma = \frac{G_\mu^3 M_V^4}{64\sqrt{2}\pi^3}\int_{\kappa_H}^1 \mathrm{d}x \int_x^1 \frac{\mathrm{d}y}{[1+(y-x)/\kappa_V]^2}\left[(\hat{v}_e^2+\hat{a}_e^2)^2 f(x,y) + 4\hat{v}_e^2\hat{a}_e^2 g(x,y)\right] \tag{4.32}$$

$$\begin{aligned} f(x,y) &= \left(\frac{2x}{y^3} - \frac{1+2x}{y^2} + \frac{2+x}{2y} - \frac{1}{2}\right)\left[\frac{z}{1+z} - \log(1+z)\right] + \frac{x}{y^3}\frac{z^2(1-y)}{1+z} \\ g(x,y) &= \left(-\frac{x}{y^2} + \frac{2+x}{2y} - \frac{1}{2}\right)\left[\frac{z}{1+z} - \log(1+z)\right] \end{aligned}$$

with $\kappa_H = M_H^2/s, \kappa_V = M_V^2/s, z = y(x-\kappa_H)/(\kappa_V x)$ and $\hat{v}, \hat{a}$ the electron couplings to the massive gauge bosons, $\hat{v}_e = \hat{a}_e = \sqrt{2}$ for the W boson. [Note that in the effective longitudinal W approximation, and as discussed in §3.3.5, one obtains a simple result for the cross section of this process, but which is twice larger than the exact result for small Higgs boson masses.].

The production cross section is shown in Fig. 4.7 as a function of M_H at c.m energies $\sqrt{s} = 0.5, 1$ and 3 TeV. For Higgs masses in the intermediate range, the cross section is comparable to the one of the Higgs–strahlung process at $\sqrt{s} = 500$ GeV, leading to ~ 25.000 events for the expected luminosity $\mathcal{L} = 500$ fb^{-1}, and is larger at higher energies.

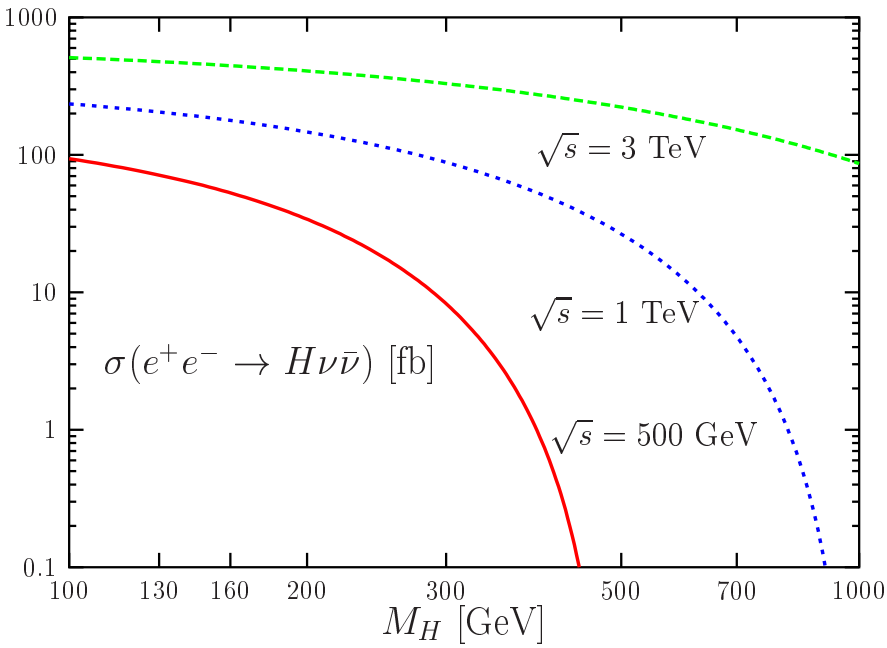

Figure 4.7: The Higgs production cross section in the WW fusion mechanism in e^+e^- collisions with c.m. energies $\sqrt{s} = 0.5, 1$ and 3 TeV as a function of M_H.

The full cross section with the interference with Higgs–strahlung

The overall cross section that will be observed experimentally for the process $e^+e^- \to H + \bar{\nu}\nu$ will not be due to the WW fusion process only, but part of it will come from the Higgs–strahlung process, $e^+e^- \to HZ$, with the Z boson decaying into the three types of neutrinos. A compact expression for the full cross section of the Higgs–strahlung and WW fusion mechanisms, including the interference terms, has been derived in the general case by choosing the energy E_H and the polar angle θ of the Higgs particle as the basic variables in the e^+e^- c.m. frame. Decomposing the total contribution into three parts, the contributions $3 \times g_S$ from Higgs–strahlung with Z decays into three types of neutrinos, g_W from WW fusion, and g_I from the interference term between fusion and Higgs–strahlung for $\bar{\nu}_e\nu_e$ final states, one has for energies $\sqrt{s}$ above the Z resonance [245, 246]

$$\frac{d\sigma(e^+e^- \to H\bar{\nu}\nu)}{dE_H\, d\cos\theta} = \frac{G_\mu^3 M_Z^8 p_H}{\sqrt{2}\,\pi^3 s}\,(3\,g_S + g_I + g_W) \tag{4.33}$$

$$\begin{aligned} g_S &= \frac{\hat{v}_e^2 + \hat{a}_e^2}{96}\,\frac{s s_\nu + s_1 s_2}{(s - M_Z^2)^2\,[(s_\nu - M_Z^2)^2 + M_Z^2\Gamma_Z^2]}\ , \quad g_W = \frac{c_W^8}{s_1 s_2 r}\,\mathcal{H}_+ \\ g_I &= \frac{(\hat{v}_e + \hat{a}_e)c_W^4}{8}\,\frac{s_\nu - M_Z^2}{(s - M_Z^2)\,[(s_\nu - M_Z^2)^2 + M_Z^2\Gamma_Z^2]}\,\mathcal{H}_I \end{aligned} \tag{4.34}$$

where all the abbreviated quantities have been defined in eq. (3.28), the factor $\mathcal{H}_+$ in eq. (3.27), while the factor $\mathcal{H}_I$ for the interference term is given by

$$\mathcal{H}_I = 2 - (h_1+1)\log\frac{h_1+1}{h_1-1} - (h_2+1)\log\frac{h_2+1}{h_2-1} + (h_1+1)(h_2+1)\frac{\ell}{\sqrt{r}} \tag{4.35}$$

To derive the total cross section $\sigma(e^+e^- \to H\bar{\nu}\nu)$, the differential cross section must be integrated over θ and E_H, with the boundary conditions given in eq. (3.29). The two main components and the total cross section for $e^+e^- \to H\bar{\nu}\nu$ are displayed in Fig. 4.8 as a function of the c.m. energy for $M_H = 115$ and 150 GeV. One can see that Higgs-strahlung is dominant a lower energies, WW fusion at higher energies, and the interference term is small except in the cross over regions.

At e^+e^- colliders, the initial $e^\pm$ beams can be polarized longitudinally. The Higgs–strahlung and WW fusion require opposite helicities of the e^- and e^+ beams. Denoting $\sigma_{U,L,R}$ the cross sections for unpolarized e^-/e^+, e_L^-/e_R^+ and e_R^-/e_L^+, respectively, one obtains [246]

$$\sigma_U \propto 3\,g_S + g_I + g_W\ , \quad \sigma_L \propto 6\,g_S + 4\,g_I + 4\,g_W\ , \quad \sigma_R \propto 6\,g_S \tag{4.36}$$

The cross section for WW fusion of Higgs particles increases by a factor four, compared with unpolarized beams, if left–handed electrons and right–handed positrons are used. By using right–handed electrons, the WW fusion mechanism is switched off. The interference term cannot be separated from the WW fusion cross section.

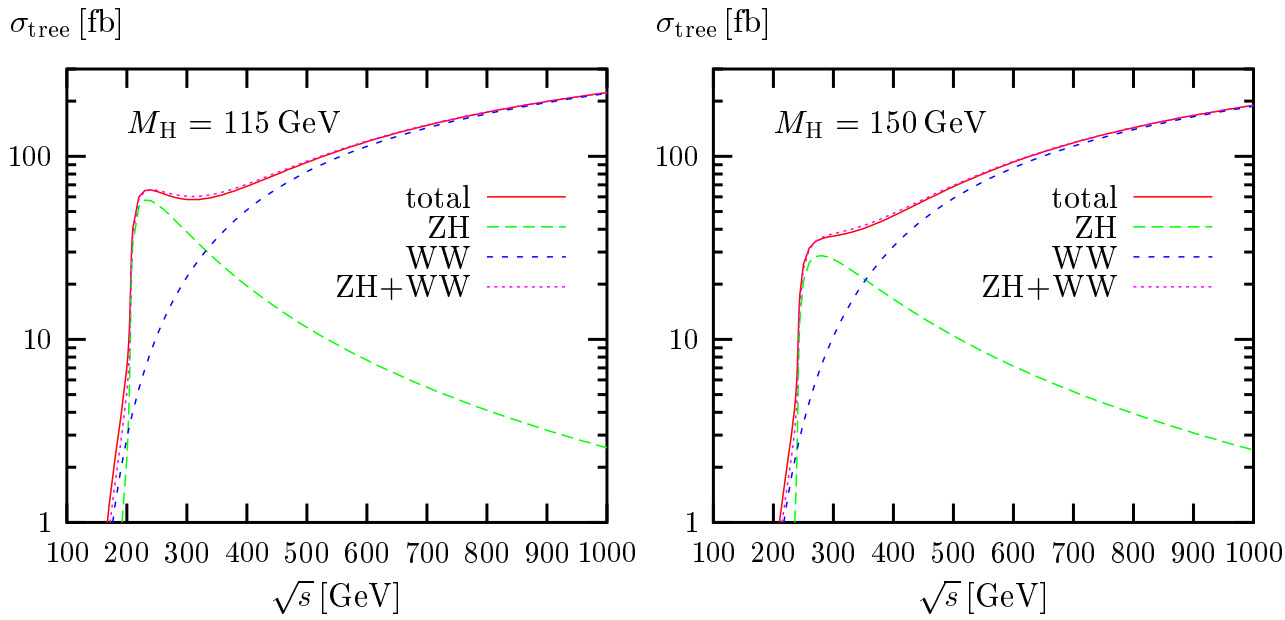

Figure 4.8: The production cross section for the process $e^+e^- \to H\bar{\nu}\nu$ as a function of $\sqrt{s}$ for $M_H = 115$ and 150 GeV. The three components, i.e. Higgs–strahlung, WW fusion, their sum, and the total cross section including the interference term, are shown; from Ref. [518].

4.2.3 The electroweak radiative corrections

To have a full control on the production cross sections of the Higgs–strahlung and WW fusion processes, in view of the high–precision tests which can be performed using them, the electroweak radiative corrections must be taken into account. These corrections, consisting of virtual and real corrections with the emission of an additional photon in the final or initial state (ISR), have been completed recently. Note, however, that at high–energy linear colliders, in addition to ISR, one has also to take into account the beam energy spread and beamstrahlung. The latter is machine dependent and will smear out the c.m. energy and the system moves along the beam axes; it must be thus suppressed as strongly as possible in order to allow for high–quality analyses which are often based on kinematical constraints derived from the precise knowledge of the initial beam energies.

The Higgs–strahlung process

At one–loop order, the radiative corrections to the Higgs–strahlung process consist of self–energy, vertex and box corrections to the tree–level amplitude and the emission of an additional photon in the initial state; Fig. 4.9. The corrections have been calculated some time ago [517] and reanalyzed recently in the context of the full $e^+e^- \to H\bar{\nu}\nu$ process [518–520]. Let us summarize the salient features of these corrections.

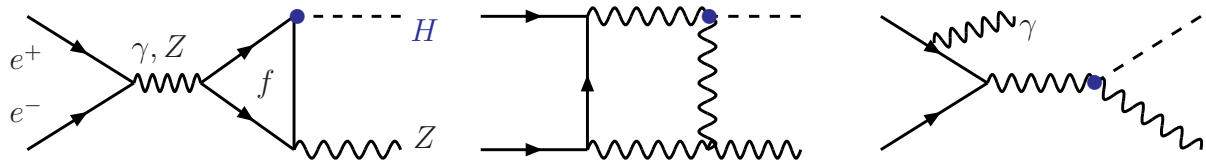

Figure 4.9: Generic diagrams for the $\mathcal{O}(\alpha)$ corrections to the process $e^+e^- \to HZ$.

The photonic corrections to the initial state, that is vertex and self–energy corrections with photon exchange as well as photon radiation (ISR) can be implemented using the structure function approach discussed in §1.2.1; see, eq. (1.103). The fermionic corrections which are contained in the running of the QED constant α for the light fermions, eq. (1.74), and the correction to the ρ parameter for the heavy top quark, eq. (1.106), can be incorporated by using the improved Born approximation (IBA): starting with the Born cross section defined in terms of the bare electromagnetic coupling $\alpha(0)$, one performs the substitution $\pi\alpha(0) \to \sqrt{2}G_F M_W^2(1 - M_W^2/M_Z^2)$ which absorbs the correction $\Delta r \simeq \Delta\alpha - 3\Delta\rho$. One has also to include the additional corrections to the HZZ vertex and in particular the heavy top contributions, δ^t_{HZZ} in eq. (2.77). The largest part of the weak correction is then absorbed into the couplings and the remaining corrections should be in principle rather small [518].

The overall correction to the tree–level $e^+e^- \to HZ$ amplitude, including an additional term that is logarithmic in the top quark mass, is given by [19]

$$K^t_{e^+e^-\to HZ} \simeq 1 + \frac{\alpha}{4\pi s_W^2}\frac{1}{g_i}\left[\frac{1}{8}\left(6\frac{c_W}{s_W} + g_i\right)\frac{m_t^2}{M_W^2} + \frac{3-2s_W^2}{3c_W s_W}\log\frac{m_t}{M_W}\right] \tag{4.37}$$

These factors correct in fact the amplitudes with left– and right–handed electrons with couplings $g_L = (2s_W^2 - 1)/(2s_W c_W)$ and $g_R = s_W/c_W$. At low and moderate energies, this approximation is rather good. However, at high energies, it turns out that this expression in the heavy–top quark limit does not reproduce exactly the full m_t dependent result, as a consequence of the presence of the box contributions which depend both on s and m_t.

The WW fusion process

Since already at the tree–level the WW–fusion mechanism is a three–body final state production process [which was thus not trivial to handle], the calculation of the one–loop radiative corrections is a real challenge. Indeed, not only one has to deal with the numerous diagrams involving self–energy, vertex and box corrections [due to the additional final state, the number of such diagrams is much larger than for a $2 \to 2$ process like Higgs–strahlung], one has to consider in addition one–loop corrections involving pentagonal diagrams which are extremely difficult to handle, and corrections with real photon emission, leading to four particles in the final state which are rather involved; see Fig. 4.10. To these complications,

one has to add the fact that to derive the full corrections to the $e^+e^- \to H\nu\bar{\nu}$ final state, both the WW fusion mechanism and the Higgs–strahlung process with $Z \to \nu\bar{\nu}$ have to be considered and added coherently.

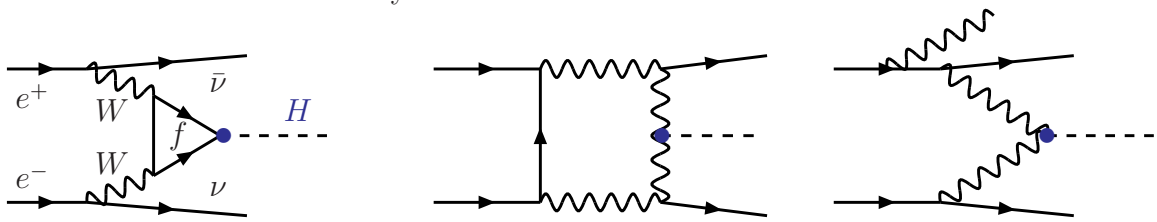

Figure 4.10: Generic diagrams for the $\mathcal{O}(\alpha)$ corrections to the WW fusion process.

The challenge of deriving these corrections has been met by three groups. In Ref. [519], the calculation was performed using `GRACE-LOOP` [530], an automatic calculation system. In Ref. [520], the results have been obtained as a `MAPLE` output using the program `DIANA` [531] without an explicit evaluation. In Ref. [518], the calculation has been performed in two independent ways, using the program `FeynArts` [532] to generate the Feynman graphs, and using `Mathematica` to express the amplitudes in terms of standard matrix elements or using the package `FormCalc` [533] based on `Form` [534]. We briefly summarize the main results of these calculations, mostly relying on Ref. [518].

The ISR corrections stemming from the radiation of a photon from the initial e^+e^- states and from the intermediate W bosons, can again be obtained in the structure function approach either at $\mathcal{O}(\alpha)$ or including higher–order corrections. The running of the electromagnetic constant due to the light fermion contributions [because the cross section is proportional to α^3, this leads to a $\sim 18\%$ change of the cross section] can be included using the IBA discussed previously. Finally, since the WW–fusion cross section gets its main contribution from small momenta W bosons, the loop corrections are mainly determined by the $\nu_e eW$ and HWW vertices at zero–momentum transfer. The correction to the $e\nu_e W$ vertex is well described by Δr and the HWW vertex correction is given by δ^t_{HWW} in eq. (2.77). It turns out that these corrections largely cancel the corresponding ones when G_μ is used in the tree–level expression of the amplitude and one obtains a small remaining piece [518]

$$K^t_{e^+e^-\to H\nu\bar{\nu}} = 1 - \frac{5\alpha}{16\pi s_W^2}\frac{m_t^2}{M_W^2} \tag{4.38}$$

which approximates the fermionic contribution to the amplitude quite well. To this correction, one has to add the bosonic contribution for which no simple approximation is possible.

Numerical results

The final output of the calculation is shown in Fig. 4.11, where the radiative corrections to the Higgs strahlung process [left figure] and the the WW fusion mechanism [right figure],

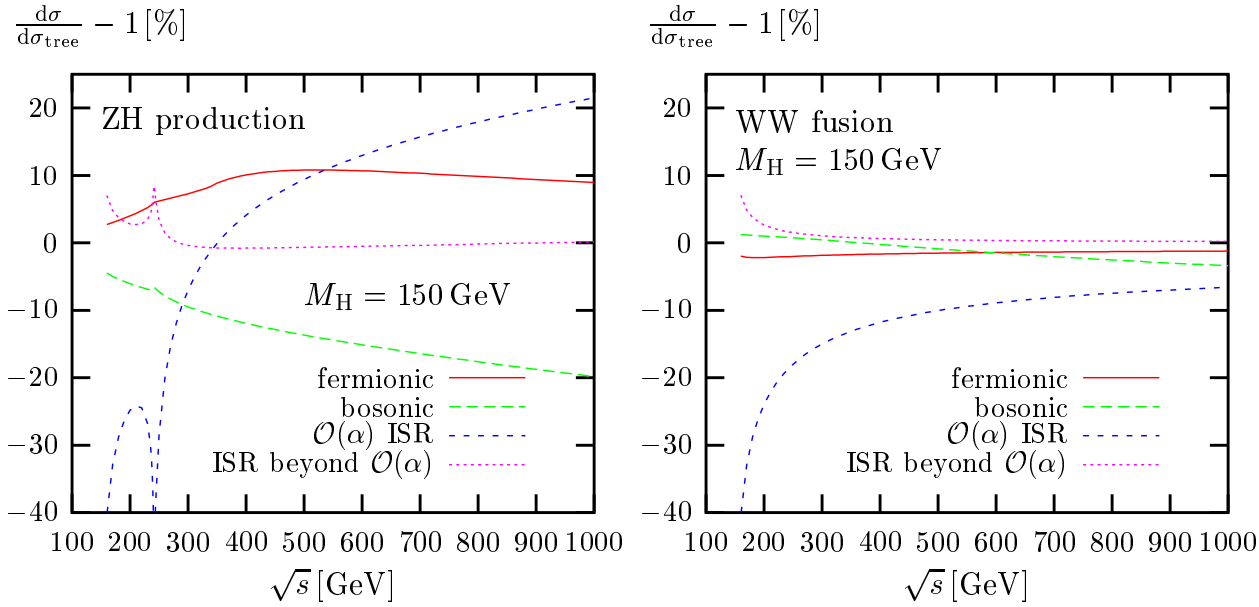

Figure 4.11: Relative electroweak corrections to the Higgs–strahlung $e^+e^- \to HZ$ and to WW fusion $e^+e^- \to H\nu\bar{\nu}$ processes resulting from ISR at $\mathcal{O}(\alpha)$ and beyond, fermion loops, and non–ISR bosonic corrections as a function of $\sqrt{s}$ for $M_H = 150$ GeV; from Ref. [518].

without the small interference terms, are shown as a function of $\sqrt{s}$ for $M_H = 150$ GeV. The various components, the fermionic contribution, the bosonic contribution, the initial state radiation at $\mathcal{O}(\alpha)$ and beyond, are displayed.

In the case of WW fusion, the ISR corrections, the bulk of which comes from $\mathcal{O}(\alpha)$ contributions, are negative for all energies as a consequence of the decrease of the effective c.m. energy which leads to a smaller cross section. The fermionic corrections are negative and small, being at the level of -2%, while the bosonic corrections range from $+1\%$ near the production threshold to -3% at high energy. For the Higgs strahlung process, at high enough energies $\sqrt{s} \gtrsim 500$ GeV, the fermionic contribution is positive and almost constant, $+10\%$, while the bosonic contribution is negative and large, increasing in absolute value with $\sqrt{s}$. The largest correction is due to the $\mathcal{O}(\alpha)$ ISR [the contribution of higher–orders is again very small], which increases the cross section by 20% for $\sqrt{s} = 1$ TeV.

Adding the channel where the neutrinos are coming from the Higgs–strahlung process and the small interference term, one obtains the total production cross section for the full $e^+e^- \to H\nu\bar{\nu}$ process. The relative corrections to the lowest order cross section for the various components are shown in Fig. 4.12 for $M_H = 115$ and 150 GeV as a function of $\sqrt{s}$. Below the threshold, the correction to the ZH channel are large and negative, reaching $\sim -20\%$, rise fastly near threshold, and at $\sqrt{s} = 1$ TeV reach the level of $\sim 20\,(10)\%$ for $M_H = 115\,(150)$ GeV. The corrections to the WW fusion channel rise also sharply at the threshold but reach quickly a plateau at a level of -10% beyond $\sqrt{s} = 500$ GeV. The

corrections to the complete process follow those of the WW component at high energy and those of the HZ process at low energies, a consequence of the relative magnitude of the two processes at tree–level. They are always negative, being of order -10% at $\sqrt{s} \gtrsim 350$ GeV.

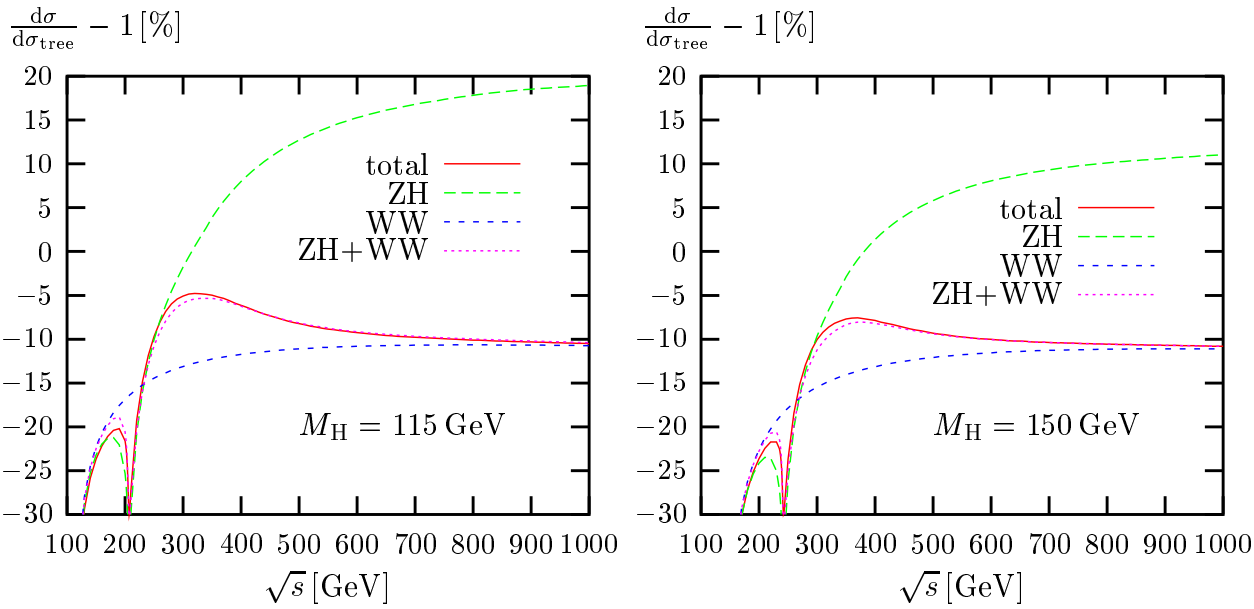

Figure 4.12: Relative corrections to the complete process $e^+e^- \to H\nu\bar{\nu}$ and the contributions of the various components as a function of $\sqrt{s}$ and for $M_H = 115$ and 150 GeV; from [518].

4.3 The subleading production processes in e^+e^- collisions

4.3.1 The ZZ fusion mechanism

The cross section for the ZZ fusion mechanism, $e^+e^- \to e^+e^-(Z^*Z^*) \to e^+e^-H$, Fig. 4.13, is given by the same expression in eq. (4.32) for the WW fusion mechanism with the vector boson $V = Z$ having the usual couplings to the electron $\hat{v}_e = -1 + 4s_W^2, \hat{a}_e = -1$. The total production cross section is about an order of magnitude smaller than the cross section for WW fusion, $\sigma(WW \to H)/\sigma(ZZ \to H) \sim 16c_W^2 \sim 9$, a mere consequence of the fact that the neutral current couplings are smaller than the charged current couplings. The lower rate, however, could be at least partly compensated by the clean signature of the e^+e^- final state. The cross section is shown in Fig. 4.14 as a function of M_H for the c.m. energies $\sqrt{s} = 0.5$, 1 and 3 TeV. It follows the same trend as the WW fusion cross section.

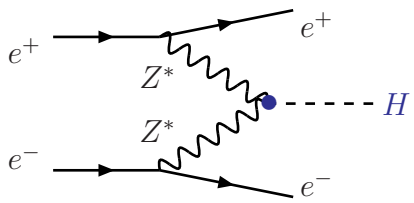

Figure 4.13: Higgs boson production in the ZZ fusion mechanism in e^+e^- collisions.

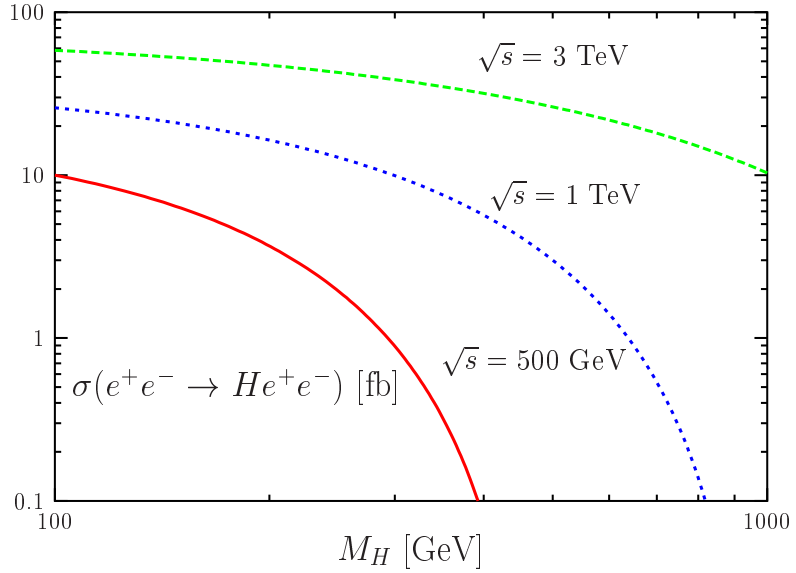

Figure 4.14: Higgs production cross sections in the ZZ fusion mechanism in e^+e^- collisions with c.m. energies $\sqrt{s} = 0.5, 1$ and 3 TeV as a function of M_H.

Similarly to the WW fusion case, the overall cross section for the process $e^+e^- \to H + e^+e^-$ receives contributions g_S from Higgs–strahlung with $Z \to e^+e^-$, $g_{Z_\pm}$ from ZZ fusion, and g_I from the interference term between fusion and Higgs–strahlung [504]

$$\frac{d\sigma(e^+e^- \to He^+e^-)}{dE_H\, d\cos\theta} = \frac{G_\mu^3 M_Z^8 p_H}{\sqrt{2}\,\pi^3 s}\,(g_S + g_I + g_{Z+} + g_{Z-}) \tag{4.39}$$

with

$$\begin{aligned}
g_S &= \frac{(\hat{v}_e^2 + \hat{a}_e^2)^2}{192}\,\frac{s s_e + s_1 s_2}{(s - M_Z^2)^2\,[(s_e - M_Z^2)^2 + M_Z^2\Gamma_Z^2]} \\
g_I &= \frac{(\hat{v}_e^2 + \hat{a}_e^2)^2 + 4\hat{v}_e^2\hat{a}_e^2}{64}\,\frac{s_e - M_Z^2}{(s - M_Z^2)\,[(s_e - M_Z^2)^2 + M_Z^2\Gamma_Z^2]}\mathcal{H}_I \\
g_{Z+} &= \frac{(\hat{v}_e^2 + \hat{a}_e^2)^2 + 4\hat{v}_e^2\hat{a}_e^2}{32\, s_1 s_2 r}\,\mathcal{H}_+\ ,\ g_{Z-} = \frac{(\hat{v}_e^2 - \hat{a}_e^2)^2}{32\, s_1 s_2 r}\,(1 - c_\chi)\mathcal{H}_-
\end{aligned} \tag{4.40}$$

where the same abbreviations as in the formulas for the W fusion case, with the appropriate replacements, $\nu \to e$ and $W \to Z$, have been used. Again, the three components and the total cross sections follow the same trend as in the case of the WW fusion process.

The calculation of the one–loop radiative corrections to this process follows the same lines as the one for the companion process $e^+e^- \to H\nu\bar{\nu}$, the only difference being that there are additional diagrams where photons are exchanged between the initial and final state electrons and positrons, and also between the final state e^+e^- pair. The corrections have been calculated using the `GRACE-LOOP` [530] system, and the result has recently appeared in Ref. [521]. They are summarized in Fig. 4.15 as a function of $\sqrt{s}$ for three Higgs mass values.

After subtracting the photonic corrections which decrease the cross section by about 5% for $\sqrt{s} \gtrsim 350$ GeV, as shown in the left–hand side of the figure, one obtains a rather small electroweak correction: when the tree–level cross section is expressed in terms of G_μ, the correction is $\mathcal{O}(-5\%)$ at $\sqrt{s} = 350$–500 GeV and varies very little with energy to reach -4% at 1 TeV, as can be seen in the right–hand side of Fig. 4.15. The correction is also almost independent of the Higgs mass in the chosen range, $M_H \sim 100$–200 GeV. The correction factor when α is used as input at the tree–level is also shown.

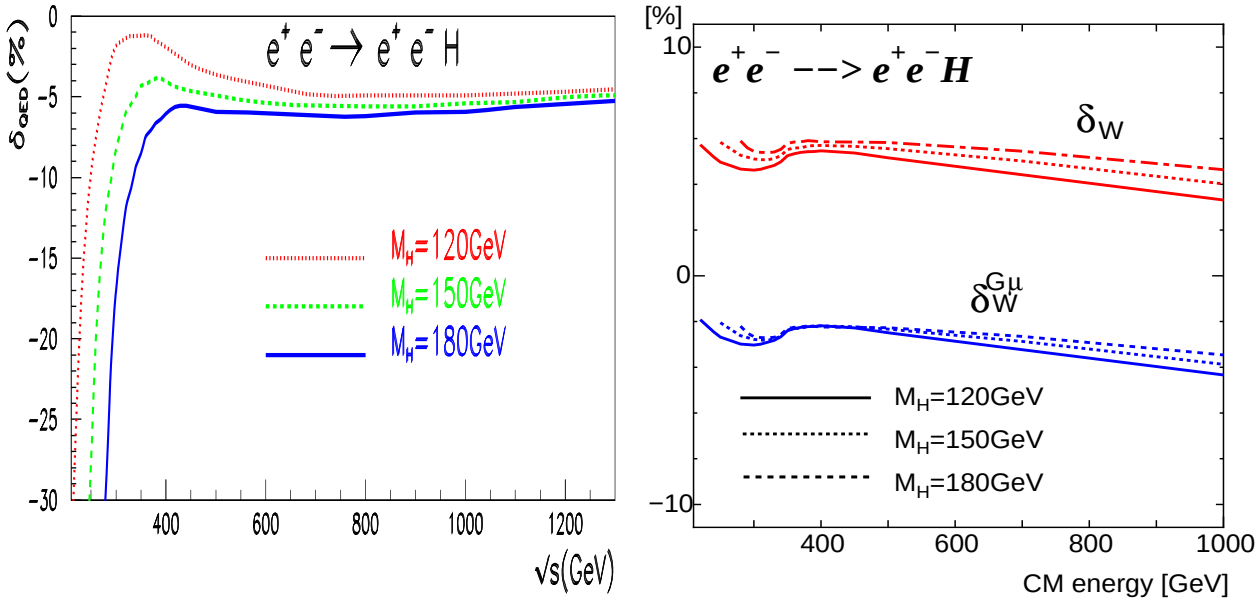

Figure 4.15: The photonic corrections (left) and the genuine electroweak radiative corrections in the G_μ and α schemes (right) for the process $e^+e^- \to He^+e^-$ as a function of the c.m. energy for $M_H = 120$, 150 and 180 GeV; from Ref. [521].

For the process $e^+e^- \to He^+e^-$, the pattern for the polarized and unpolarized cross sections is slightly more complicated than for the WW fusion process [504]

$$\begin{aligned} \sigma_U &\propto g_S + g_I + g_{Z+} + g_{Z-} \ , \ \sigma_{LL} = \sigma_{RR} \propto 2\, g_{Z-} \\ \sigma_{LR/RL} &\propto 2\frac{(\hat{v}_e \pm \hat{a}_e)^2}{(\hat{v}_e^2 + \hat{a}_e^2)} g_S + 2\frac{(\hat{v}_e \pm \hat{a}_e)^4}{(\hat{v}_e^2 + \hat{a}_e^2)^2 + 4\hat{v}_e^2\hat{a}_e^2}\,(g_I + g_{Z+}) \end{aligned}$$

Since $\hat{v}_e \sim -1 + 4s_W^2 \ll \hat{a}_e$, the difference between σ_{RL} and σ_{LR} is, however, strongly suppressed and one obtains $\sigma_{LR} \simeq \sigma_{LR} = 2(g_S + g_I + g_{Z_+})$.

Finally, let us note that in the e^-e^- option of future high–energy linear colliders, one can produce Higgs bosons in a similar channel [503]

$$e^-e^- \longrightarrow e^-e^-(Z^*Z^*) \longrightarrow e^-e^-H \tag{4.41}$$

The production cross section [up to some statistical factors due to the identical initial and final states] and the main features of the process are the same as those discussed above for the e^+e^- option of the machine.

4.3.2 Associated production with heavy fermion pairs

The process at the tree–level

In the SM, the associated production of Higgs bosons with a pair of heavy fermions, $e^+e^- \to Hf\bar{f}$ [505, 506], proceeds through two set of diagrams: those where the Higgs boson is radiated off the f and $\bar{f}$ lines, and a diagram where the Higgs boson is produced in association with a Z boson which then splits into an $f\bar{f}$ pair; Fig. 4.16.

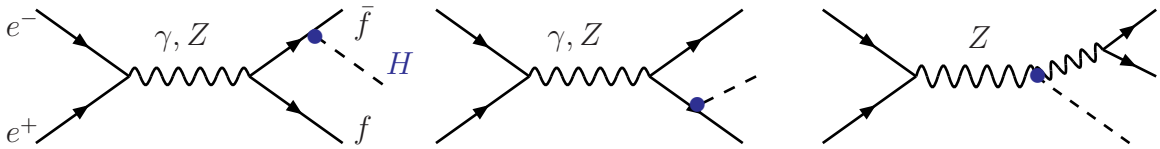

Figure 4.16: Diagrams for the associated production of Higgs bosons with a fermion pair.

Since the fermion and Higgs boson masses must be kept non–zero, the total cross section for these processes is quite involved. However, the Dalitz density, once the angular dependence is integrated out, can be written in a simple and compact form [506]

$$\frac{\mathrm{d}\sigma(e^+e^- \to f\bar{f}H)}{\mathrm{d}x_1\mathrm{d}x_2} = \frac{\bar{\alpha}^2 N_c}{12\pi s} \left\{ \left[Q_e^2 Q_f^2 + \frac{2Q_eQ_f v_e v_f}{1-z} + \frac{(v_e^2+a_e^2)(v_f^2+a_f^2)}{(1-z)^2} \right] G_1 \right. \\ \left. + \frac{v_e^2+a_e^2}{(1-z)^2} \left[a_f^2 \sum_{i=2}^{6} G_i + v_f^2(G_4+G_6) \right] + \frac{Q_eQ_f v_e v_f}{1-z} G_6 \right\} \tag{4.42}$$

with $\bar{\alpha} \equiv \alpha(s) \sim 1/128$, N_c the color factor and v_e, a_e the usual couplings of fermions to the Z boson, eq. (1.63). z is the scaled mass of the Z boson, $z = M_Z^2/s$, and we will use later on the scaled masses $f = m_f^2/s$ and $h = M_H^2/s$. $x_1 = 2E_f/\sqrt{s}$ and $x_2 = 2E_{\bar{f}}/\sqrt{s}$ are the reduced energies of the f and $\bar{f}$ states; we will also use the Higgs scaled energy, $x_H = 2E_H/\sqrt{s} = 2-x_1-x_2$, as well as the variables x_Z and x_{12} defined by $x_Z = x_H - 1 - h + z$ and $x_{12} = (1-x_1)(1-x_2)$. In terms of these variables and the $g_{Hff} = m_t/v$ and $g_{HZZ} = 2M_Z/v$ Higgs couplings, the coefficients G_i, with $i = 1$–6, are given by

$$\begin{aligned}
G_1 &= \frac{g_{Hff}^2}{x_{12}} \Big[x_H^2 - h\Big(\frac{x_H^2}{x_{12}} + 2(x_H - 1 - h)\Big) + 2f\Big(4(x_H - h) + \frac{x_H^2}{x_{12}}(4f - h + 2)\Big)\Big] \\
G_2 &= -2\frac{g_{Hff}^2}{x_{12}} \Big[x_{12}(1+x_H) - h(x_{12} + 2x_H + 8f - 2h) + 3fx_H\Big(\frac{x_H}{3} + 4 + \frac{x_H}{x_{12}}(4f - h)\Big)\Big] \\
G_3 &= 2\frac{g_{HZZ}^2}{x_Z^2} \Big[f(4h - x_H^2 - 12z) + \frac{f}{z}(4h - x_H^2)(x_H - 1 - h + z)\Big] \\
G_4 &= 2\frac{g_{HZZ}^2}{x_Z^2} z \Big[h + x_{12} + 2(1 - x_H) + 4f)\Big] \\
G_5 &= -\frac{g_{Hff}g_{HZZ}}{x_{12}x_Z} 4x_H \frac{m_f}{M_Z} \Big[(x_{12} - h)(x_H - 1 - h) + f(12z - 4h + x_H^2) - 3z\Big(h - 2\frac{x_{12}}{x_H}\Big)\Big] \\
G_6 &= -\frac{g_{Hff}g_{HZZ}}{x_{12}x_Z} 4z \frac{m_f}{M_Z} \Big[x_H(h - 4f - 2) - 2x_{12} + x_H^2\Big]
\end{aligned} \tag{4.43}$$

Integrating over the fermion energies, with the boundary conditions similar to that given in eq. (2.18), one obtains the total production cross section. In the case of $e^+e^- \to t\bar{t}H$, it is shown in Fig. 4.17 as a function of M_H for three c.m. energy values $\sqrt{s} = 0.5, 1$ and 3 TeV.

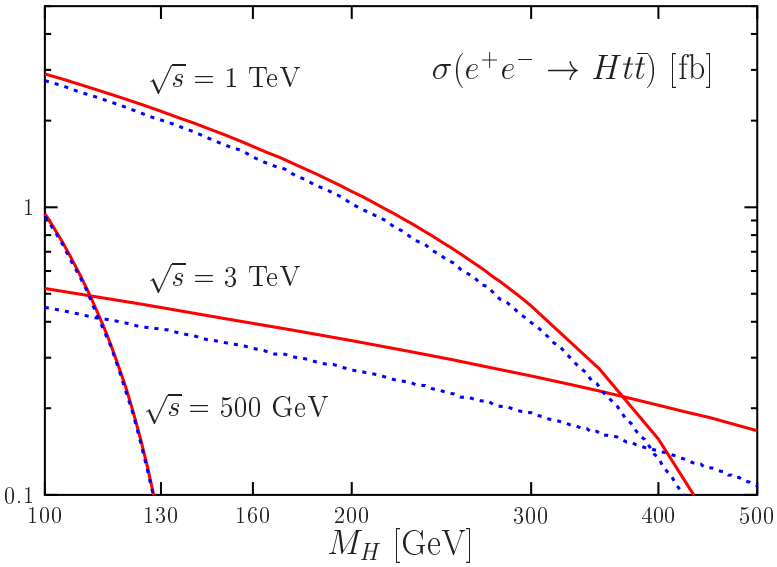

Figure 4.17: The cross section for the associated production of the Higgs boson with $t\bar{t}$ pairs in e^+e^- collisions with c.m. energies $\sqrt{s} = 0.5, 1$ and 3 TeV. The dotted lines are when only the contributions with the Higgs radiated off the top quark lines is taken into account.

While the cross section is in general small for the lowest c.m. energy $\sqrt{s} = 500$ GeV, it is more important at $\sqrt{s} = 1$ TeV as a result of the larger available phase–space. For $\sqrt{s} = 3$ TeV, it becomes again smaller as it scales like $1/s$. The cross section is at the level of a few to a fraction of a femtobarn, depending on the Higgs mass and the c.m. energy and therefore, this process requires high–luminosities. The $t\bar{t}H$ final state in this associated production mechanism is generated almost exclusively through Higgs–strahlung off top quarks. As shown in Fig. 4.17, the additional contributions from Higgs bosons emitted by the Z line are very small, amounting, for $\sqrt{s} \leq 1$ TeV, to only a few percent. In addition, since top quark pair production in e^+e^- collisions at high energy is known to be dominated by photon exchange, the bulk of the cross section is generated by the $e^+e^- \to \gamma^* \to t\bar{t}H$ subprocess. This process thus allows the determination of the important Yukawa coupling of the Higgs boson to top quarks in an almost unambiguous way.

The radiative corrections

The QCD corrections to the process $e^+e^- \to t\bar{t}H$, consist of the top vertex and self–energy corrections and the emission of an additional gluon in the final state, $e^+e^- \to t\bar{t}H + g$. The rather involved analytical expression of the cross section at NLO can be found in Refs. [522, 523]; see also Refs. [524, 525]. The corrections can be interpreted in an easy way and be given analytically in two kinematical regimes [522].

(i) In the case where the invariant $t\bar{t}$ mass is close to the threshold, the rescattering diagrams generated by the gluon exchange between the two quarks gives rise to a correction that is proportional to α_s/β_t, where β_t is the top quark velocity which vanishes at the threshold in the $t\bar{t}$ rest frame. The K–factor in this case is given by [522]

$$K^{\rm thresh}_{e^+e^-\to t\bar{t}H} = 1 + 64\alpha_s/(9\pi)\,\pi m_t\,\left[(\sqrt{s}-M_H^2)^2 - 4m_t^2\right]^{-1/2} \tag{4.44}$$

This pole is regularized by the vanishing phase–space at threshold in the leading order cross section, once it is integrated over the 3–body phase space.

(ii) At high energies, these rescattering corrections become less important. For the dominant component of the $e^+e^- \to t\bar{t}H$ process, i.e. Higgs radiation off top quarks, the correction can be crudely estimated in the limit $s \gg m_t^2 \gg M_H^2$: the radiation of a low mass Higgs boson can be separated from the top quark production process. The cross section can then be approximated by the product of the probability of producing top quark pairs [which at high energies, is given by the well–known factor $1+\alpha_s/\pi$] and the probability for the splitting processes $t \to t + H$ and $\bar{t} \to \bar{t}H$ [which at this order, gives a factor $-2\alpha_s$ for each state]. The net result will be then an NLO coefficient factor [522]

$$K^{\rm high-en.}_{e^+e^-\to t\bar{t}H} = 1 - 3\alpha_s/\pi \tag{4.45}$$

leading to a correction factor, $K \sim 0.9$ at high energies. The QCD correction factor is shown in Fig. 4.18 as a function of the c.m. energy for $M_H = 150$ GeV.

The electroweak corrections have been calculated only recently by two of the groups that evaluated the correction to the WW fusion process [524, 525]. The calculation's techniques are the same as those discussed previously. [There is a third calculation performed in Ref. [526] but the results differ from those of the two other calculations at large c.m. energies and at the threshold.] The results are also shown in Fig. 4.18 together with the QCD corrections, as a function of the c.m. energy and for $M_H = 150$ GeV.

As can be seen, the weak bosonic corrections are at the level of +10% close to the $2m_t + M_H$ threshold and drop rapidly with increasing energy to reach −20% at $\sqrt{s} = 1.5$ TeV. The fermionic corrections are approximately +10% over the entire energy range. The QED corrections, which include the full photonic and the higher–order ISR corrections are large and negative near threshold and rise with the energy to reach a few percent at $\sqrt{s} = 1.5$ TeV. At energies above $\sqrt{s} \sim 600$ GeV, the fermionic, weak bosonic and QED contributions partly cancel each other, leading to a total electroweak correction that is almost constant and of the order of −10%. This is of the same order as the QCD correction far enough from the production threshold. The total cross section at NLO, in which both the QCD and electroweak corrections are included, is thus 10 to 15% smaller than at tree–level for $\sqrt{s} \gtrsim 750$ GeV; see the right–hand side of Fig. 4.18.

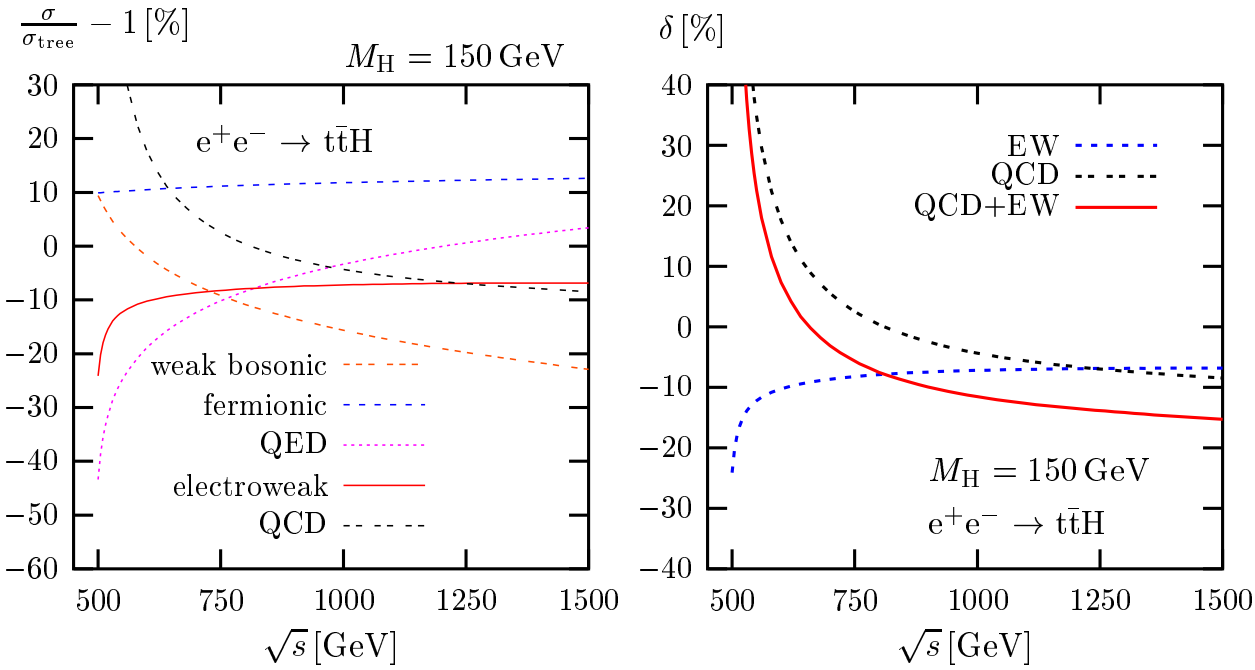

Figure 4.18: The QCD and the various components and the electroweak radiative corrections (left) and the total QCD and electroweak corrections (right) for the process $e^+e^- \to t\bar{t}H + X$ as a function of the c.m. energy for $M_H = 150$ GeV; from Ref. [524].

The pseudoscalar case and the Higgs CP properties

If the Higgs boson were of pseudoscalar nature, with couplings to fermions as given in eq. (2.5), the dominant contribution to the cross section of the process $e^+e^- \to f\bar{f}A$ would be also due to the Higgs radiation off the heavy fermion that are produced mainly through photon exchange. The expression of the Dalitz density $d\sigma(e^+e^- \to f\bar{f}A)/dx_1dx_2$ will be still as in eq. (4.43), with the coefficients G_1 and G_2 given by [here $a = M_A^2/s$] [506, 541]

$$
\begin{aligned}
G_1 &= \frac{g_{Aff}^2}{x_{12}}\Big[x_A^2 - a\Big(\frac{x_A^2}{x_{12}}(1+2f) + 2(x_A - 1 - a)\Big)\Big] \\
G_2 &= -2\frac{g_{Aff}^2}{x_{12}}\Big[x_{12}(1+x_A) - a(x_{12} - 4f + 2x_A - 2a) + f\frac{x_A^2}{x_{12}}(x_{12} - 3a)\Big]
\end{aligned}
\tag{4.46}
$$

while the contributions of G_3–G_6 can be neglected [note that, in two–Higgs doublet models, additional contributions to this process might come from other channels]. As can be seen, because the top quark is massive, the Dalitz density is different from the CP–even Higgs case by terms of $\mathcal{O}(m_t^2/s)$ which, for moderate c.m. energies, are not that small. This feature provides an additional means to discriminate between a scalar and a pseudoscalar Higgs boson and even, to probe CP violation in the $t\bar{t}$–Higgs couplings when both components are present; for a detailed discussion, see Ref. [543].

If one assumes general Higgs couplings to top quarks compared to the SM, $\mathcal{L}(Htt) = (a + ib\gamma_5)g_{Htt}$ [and also to the Z boson, $\mathcal{L}(HZZ) = cg_{HZZ}g_{\mu\nu}$, when the diagram $e^+e^- \to HZ^*$ with $Z^* \to t\bar{t}$ is included, since its contribution needs not to be small relative to the dominant ones in extensions of the SM], one would have a rather involved dependence of the $e^+e^- \to t\bar{t}H$ cross section on the phase space. The differential cross section can be written in a general form as $\mathrm{d}\sigma/\mathrm{d}\Phi = \sum_i d_i f_i(\Phi)$, where Φ is the final state phase–space configuration and d_i are combinations of the Higgs coupling parameters a, b, c [in the SM, only the combinations $d_i = a^2, ac$ and c^2 will be present with $a = c = 1$]. An optimal technique has been proposed in Ref. [543] for determining the coefficients d_i of the cross section by using appropriate weighting functions $w_i(\Phi)$ such that $\int \omega_i(d\sigma/d\Phi) = d_i$, with the additional requirement that the statistical error in the extraction of the coefficients is minimized.

4.3.3 Higgs boson pair production

To establish the Higgs mechanism experimentally, once the Higgs particle is discovered, the characteristic self–energy potential of the SM must be reconstructed. This task requires the measurement of the trilinear and quartic self–couplings of the Higgs boson, $\lambda_{HHH} = 3M_H^2/v$ and $\lambda_{HHHH} = 3M_H^2/v^2$. The trilinear Higgs coupling can be measured directly in pair production of Higgs particles in e^+e^- collisions and several mechanisms can be exploited. Higgs pairs can be produced through double Higgs–strahlung off Z bosons [257,507,508,544]

$$e^+e^- \to Z^* \longrightarrow ZHH \tag{4.47}$$

and vector boson [mostly W boson] fusion into two Higgs bosons [255,257,508]

$$e^+e^- \to V^*V^* \longrightarrow \ell\ell HH \tag{4.48}$$

The Feynman diagrams for the two processes are shown in Fig. 4.19 and, as can be seen, one of them involves the triple Higgs interaction. The other diagrams are generated by the gauge interactions familiar from single Higgs production in the dominant processes.

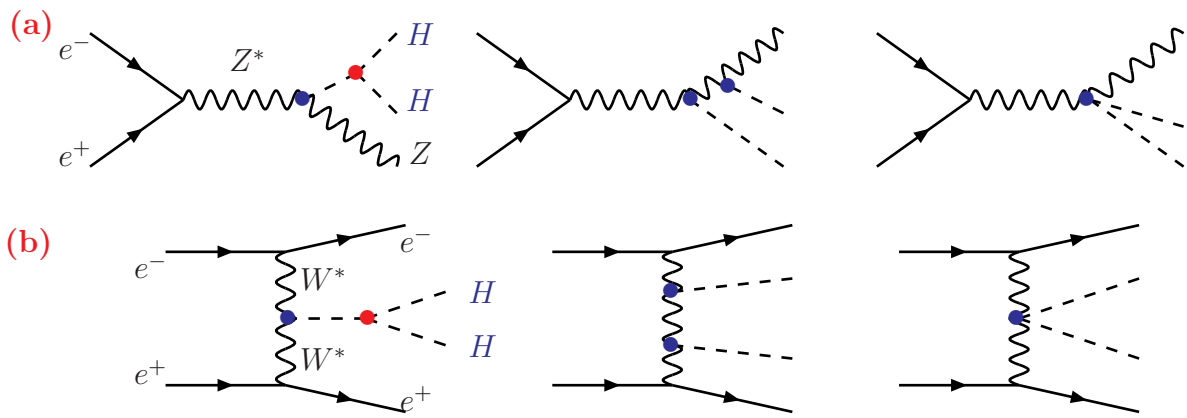

Figure 4.19: Higgs pair production in the bremsstrahlung and WW fusion processes.

The complete reconstruction of the SM Higgs potential requires the measurement of the quadrilinear coupling λ_{HHHH} which can be accessed directly only through the production of three Higgs bosons, $e^+e^- \to ZHHH$ and $e^+e^- \to \bar{\nu}_e\nu_e HHH$. However, these cross sections are reduced by two to three orders of magnitude compared to the corresponding double Higgs production channels, and are therefore too small to be observed at future e^+e^- colliders even with the large luminosities which are planned [see §4.3.4].

The double Higgs–strahlung

The differential cross section for the process of double Higgs-strahlung, $e^+e^- \to ZHH$, after the angular dependence is integrated out, can be cast into the form [508]

$$\frac{\mathrm{d}\sigma(e^+e^- \to ZHH)}{\mathrm{d}x_1\mathrm{d}x_2} = \frac{G_\mu^3 M_Z^6}{384\sqrt{2}\pi^3 s}\frac{(\hat{a}_e^2+\hat{v}_e^2)}{(1-\mu_Z)^2}\,\mathcal{Z} \tag{4.49}$$

where the electron–Z couplings are defined as usual, eq. (1.63). $x_{1,2} = 2E_{1,2}/\sqrt{s}$ are the scaled energies of the two Higgs particles, $x_3 = 2 - x_1 - x_2$ is the scaled energy of the Z boson, and we define $y_i = 1 - x_i$; the scaled masses are denoted by $\mu_i = M_i^2/s$. In terms of these variables, the coefficient $\mathcal{Z}$ may be written as

$$\begin{aligned}\mathcal{Z} &= \frac{1}{8}a^2 f_0 + \frac{1}{4\mu_Z(y_1+\mu_H-\mu_Z)}\left[\frac{f_1}{y_1+\mu_H-\mu_Z} + \frac{f_2}{y_2+\mu_H-\mu_Z} + 2\mu_Z\, a\, f_3\right] + \left\{y_1 \leftrightarrow y_2\right\} \\ &\text{with}\quad a = \frac{\lambda'_{HHH}}{y_3+\mu_Z-\mu_H} + \frac{2}{y_1+\mu_H-\mu_Z} + \frac{2}{y_2+\mu_H-\mu_Z} + \frac{1}{\mu_Z}\end{aligned} \tag{4.50}$$

The coefficients f_i are given by

$$\begin{aligned} f_0 &= \mu_Z[(y_1+y_2)^2 + 8\mu_Z] \\ f_1 &= (y_1-1)^2(\mu_Z-y_1)^2 - 4\mu_H y_1(y_1+y_1\mu_Z-4\mu_Z) + \mu_Z(\mu_Z-4\mu_H)(1-4\mu_H) - \mu_Z^2 \\ f_2 &= [\mu_Z(1+\mu_Z-y_1-y_2-8\mu_H) - (1+\mu_Z)y_1y_2](2+2\mu_Z-y_1-y_2) \\ &\quad + y_1y_2[y_1y_2+\mu_Z^2+1+4\mu_H(1+\mu_Z)] + 4\mu_H\mu_Z(1+\mu_Z+4\mu_H) + \mu_Z^2 \\ f_3 &= y_1(y_1-1)(\mu_Z-y_1) - y_2(y_1+1)(y_1+\mu_Z) + 2\mu_Z(\mu_Z+1-4\mu_H) \end{aligned} \tag{4.51}$$

The first term in the coefficient a includes the scaled trilinear coupling $\lambda'_{HHH} = 3M_H^2/M_Z^2$. The other terms are related to sequential Higgs–strahlung and the 4 gauge–Higgs boson coupling; the individual terms can easily be identified by examining the propagators.

The production cross section, which is a binomial in the self–coupling λ_{HHH}, is shown in Fig. 4.20 as a function of the Higgs mass for three c.m. energies $\sqrt{s} = 0.5, 1$ and 3 TeV. It is of the order of a fraction of a femtobarn when it is not too much suppressed by phase–space and, because it is mediated by s channel gauge boson exchange and scales like $1/s$, it is higher at lower energies for moderate Higgs masses. In addition, since the process is

mediated by Z–boson exchange, the cross section is doubled if oppositely polarized electron and positron beams are used. The cross section for the ZHH final state is rather sensitive to the λ_{HHH} coupling: for $\sqrt{s}=500$ GeV and $M_H=120$ GeV for instance, it varies by about 20% for a 50% variation of the trilinear coupling as shown in the figure.

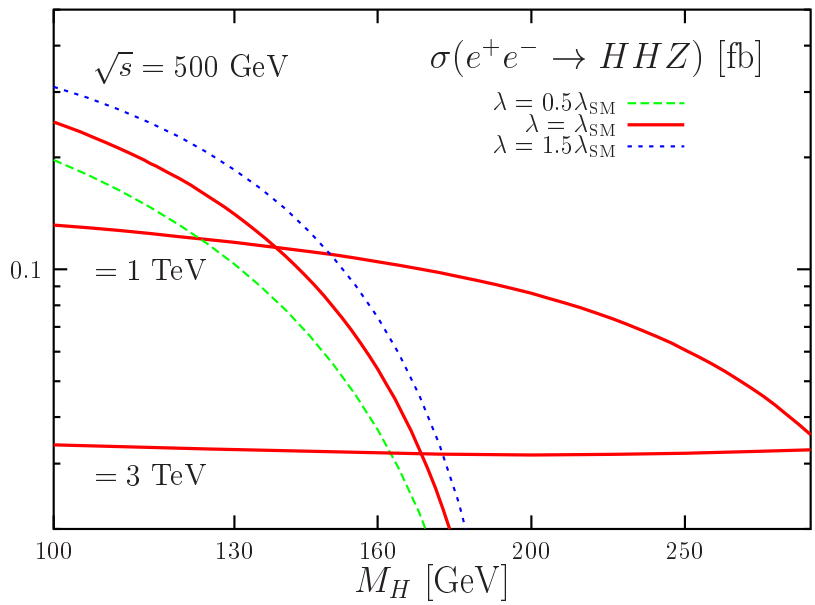

Figure 4.20: The cross section for double Higgs–strahlung in e^+e^- collisions, $e^+e^- \to HHZ$, at c.m. energies $\sqrt{s} = 0.5, 1$ and 3 TeV as a function of M_H. Shown for $\sqrt{s} = 500$ GeV are the effects of a variation of the trilinear coupling by 50% from its SM value.

The one–loop radiative corrections to the double Higgs–strahlung process are also very involved to calculate since, already at the tree–level, one has to deal with three massive particle in the final state and, thus, one has to consider pentagonal diagrams and four–body finals states at NLO. They have again been calculated recently by two independent groups [527,528], with results that agree reasonably, in particular at low energies. The QED corrections follow the same trend as what has been observed in the case of the $e^+e^- \to t\bar{t}H$ process for $M_H = 150$ GeV: they are very large and negative for c.m. energies near the production threshold, $\sim -40\%$ at $\sqrt{s} \sim 400$ GeV, and decrease in absolute value to reach the level of a few percent above $\sqrt{s} \sim 600$ GeV, $\sim +5\%$ at 1.5 TeV; see the left panel of Fig. 4.21. For the pure weak corrections, when calculated using α in the Born term, they are rather small not exceeding $\sim +5\%$ near the threshold and at moderate c.m. energies when the cross section is maximal; see the right panel of Fig. 4.21. At higher energies, the weak corrections turn negative and increase in size to reach $\sim -10\%$ at $\sqrt{s} = 1.5$ TeV. The weak corrections calculated in the IBA are also shown (dotted lines). As in the case of the $e^+e^- \to HZ$ parent process, this approximation fails to reproduce the magnitude of the weak corrections, especially at high energies. The approximate top quark mass correction to the Higgs self–coupling does also not reproduce the bulk of the weak correction.

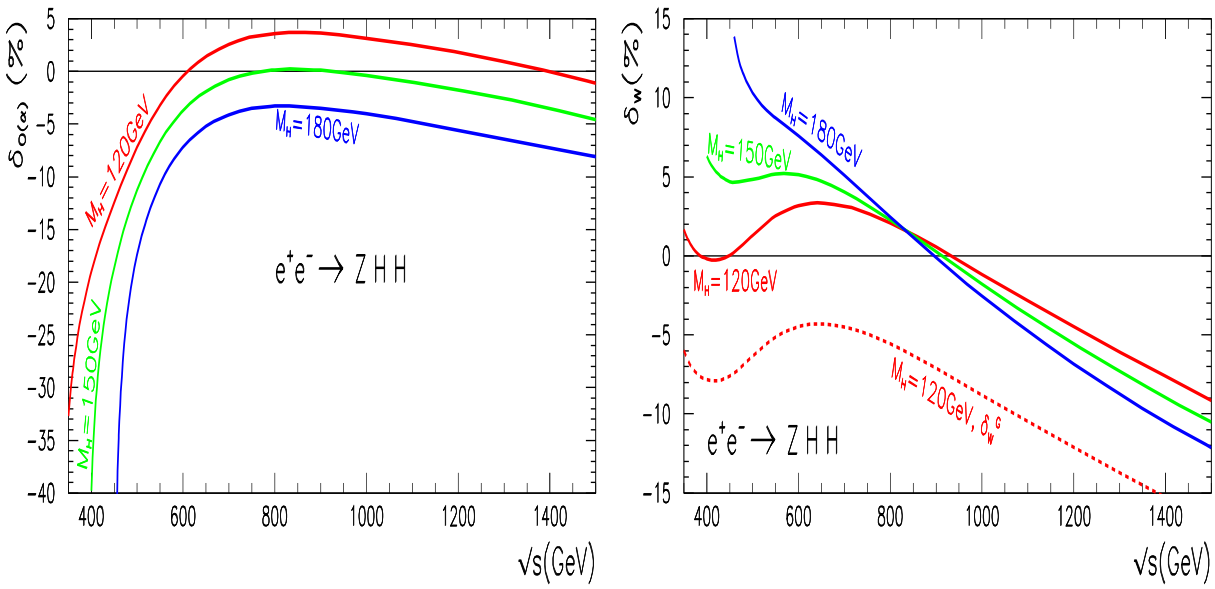

Figure 4.21: The full $\mathcal{O}(\alpha)$ relative correction (left panel) and the relative electroweak correction δ_W (right panel) as a function of the c.m. energy for $M_H = 120, 150, 180$ GeV; the genuine weak correction in the IBA is presented for $M_H = 120$ GeV (dotted line) [527].

Note that the correction to the invariant mass distribution of the Higgs pair, which can be a means to isolate the HHH vertex since the two Higgs bosons originate from the decay of an off–shell scalar particle [545], has also been calculated and found to be small.

The WW fusion process

At high energies, double Higgs boson production in the WW fusion channel, $e^+e^- \to \nu\bar{\nu}HH$ [255,257], provides the largest cross section for Higgs bosons in the intermediate mass range, in particular when the initial beams are polarized. [Again, the ZZ fusion channel has a cross section that is one order of magnitude smaller compared to WW fusion as a result of the smaller Z couplings to electrons]. The cross section for this four–particle final state is very involved but it can be roughly estimated in the equivalent W boson approximation, $WW \to HH$. Taking into account only the dominant longitudinal W contribution, denoting by $\beta_{W,H}$ the W, H boson velocities in the c.m. frame, we define the variable $x_W = (1 - 2M_H^2/\hat{s})/(\beta_W\beta_H)$ with $\hat{s}^{1/2}$ is the invariant energy of the WW pair. The amplitude $\mathcal{M}_{LL}$ has been given in eq. (3.90) when this process was discussed at hadron colliders and, integrating out the angular dependence, the corresponding total cross section reads [508, 545]

$$\begin{aligned}
\hat{\sigma}_{LL} &= \frac{G_F^2 M_W^4}{4\pi\hat{s}} \frac{\beta_H}{\beta_W(1-\beta_W^2)^2} \Bigg\{ (1+\beta_W^2)^2 \left[1 + \frac{\lambda'_{HHH}}{(\hat{s}-M_H^2)/M_Z^2} \right]^2 \\
&+ \frac{16}{(1+\beta_H^2)^2 - 4\beta_H^2\beta_W^2} \left[\beta_H^2(-\beta_H^2 x_W^2 + 4\beta_W\beta_H x_W - 4\beta_W^2) + (1+\beta_W^2-\beta_W^4)^2 \right] \\
&+ \frac{1}{\beta_W^2\beta_H^2} \left(\ell_W + \frac{2x_W}{x_W^2-1} \right) \left[\beta_H(\beta_H x_W - 4\beta_W)(1+\beta_W^2-\beta_W^4+3x_W^2\beta_H^2) \right.
\end{aligned}$$

$$+ \quad \beta_H^2 x_W(1-\beta_W^4+13\beta_W^2) - \frac{1}{x_W}(1+\beta_W^2-\beta_W^4)^2\Big] + \frac{2(1+\beta_W^2)}{\beta_W\beta_H}\left[1+\frac{\lambda_{HHH}}{(\hat{s}-M_H^2)/M_Z^2}\right]$$
$$\times \quad \left[\ell_W(1+\beta_W^2-\beta_W^4-2\beta_W\beta_H x_W+\beta_H^2 x_W^2)+2\beta_H(x_W\beta_H-2\beta_W)\right]\Big\} \tag{4.52}$$

with $\ell_W = \log[(x_W-1)/(x_W+1)]$. After folding the cross section of the subprocess with the longitudinal W_L spectra given in eq. (3.51), one obtains the total e^+e^- cross section in the effective W_LW_L approximation, which exceeds the exact value of the $e^+e^- \to \nu\bar{\nu}HH$ cross section by about a factor 2 to 5 depending on the collider energy and the Higgs mass.

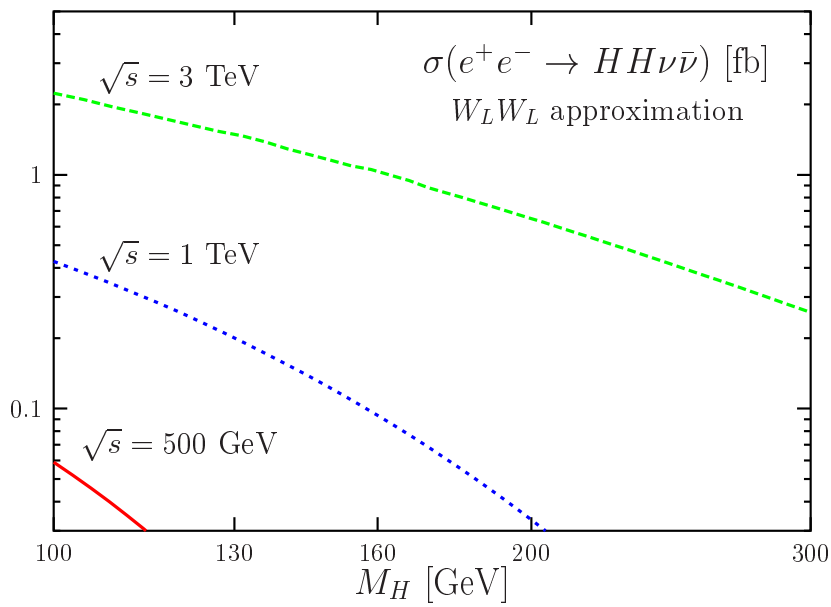

Figure 4.22: The cross section for the $W_LW_L \to HH$ process in e^+e^- collisions with at c.m. energies $\sqrt{s} = 0.5, 1$ and 3 TeV as a function of M_H.

The cross section is shown in Fig. 4.22 as a function of M_H for $\sqrt{s} = 0.5, 1$ and 3 TeV. As expected, the fusion cross sections increase with rising energy. Again, there is a significant variation of the cross section with a variation of λ_{HHH}. The transverse components of the W bosons give rather small contributions through $W_TW_T \to HH$ for large Higgs masses. Note that the $\mathcal{O}(\alpha)$ corrections have been also calculated using `GRACE-LOOP` and a preliminary result has appeared in Ref. [521]; the corrections are of $\mathcal{O}(10\%)$.

4.3.4 Other subleading processes in e^+e^- collisions

Finally, there are other subdominant higher–order Higgs production processes: the associated production with a photon, the loop induced as well as some tree–level higher–order double Higgs production, the associated Higgs production with gauge boson pairs and the associated production with two fermions and a gauge boson. We briefly summarize the main features of these processes for completeness.

Higgs production in association with two gauge bosons

Similarly to what one observes at hadron colliders, in high–energy e^+e^- collisions, W pair production, $e^+e^- \to W^+W^-$, has a very large cross section. This is also the case of $e^+e^- \to ZZ$ and $Z\gamma$ production[37], which are mediated by t–channel electron exchange. It is thus tempting to take advantage of these large production rates and consider the emission of an additional Higgs particle from one of the gauge boson lines

$$e^+e^- \to W^+W^-H \ , \ ZZH \ , \ Z\gamma H \tag{4.53}$$

as shown in Fig. 4.23. The hope is that the suppression by the additional electroweak factor might be compensated by the initially large production rates.

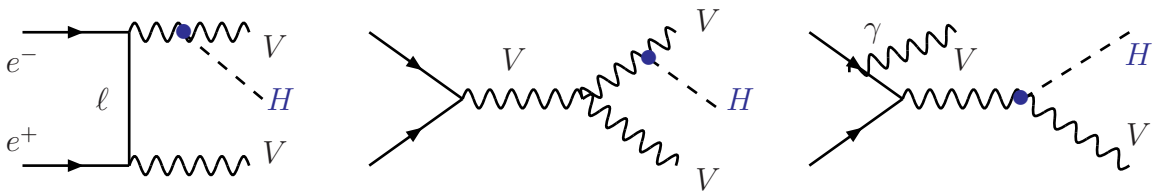

Figure 4.23: Diagrams for associated Higgs boson production with two gauge bosons.

This turns out to be quite true [264, 511, 512]: at least for the process $e^+e^- \to Z\gamma H$ [where one has to apply a cut on the transverse momentum $p_T \gtrsim 5$ GeV of the photon] and for the $e^+e^- \to W^+W^-H$ mechanism, the cross sections are quite sizable. At $\sqrt{s} = 800$ GeV and for $M_H \sim 100$–200 GeV, they are at the level of a few fb as shown in Fig. 4.24. With the expected luminosity $\mathcal{L} = 500$ fb^{-1}, they could lead to more than 1000 events which are rather clean. For masses $M_H \sim 300$ GeV, they are still at the level of 1 fb, which is only one order of magnitude smaller than the Higgs–strahlung process at these values of M_H and $\sqrt{s}$. Again, as one might have expected, the production rate for the $e^+e^- \to ZZH$ process is an order of magnitude smaller than that of the $e^+e^- \to WWH$ process. Note that the cross sections for these processes do not become larger at higher energies.

Once the Higgs particle has been detected in the main channels, these processes could be useful: in conjunction with the dominant Higgs–strahlung and WW fusion processes, they would allow to test the quartic couplings involving Higgs and gauge bosons and, for instance, to probe directly the HZW^+W^- and $H\gamma W^+W^-$ couplings and even, potentially, C–violating $HZZZ$ and $H\gamma ZZ$ couplings which are absent in the SM.

[37] As noted before, the process with the additional final state photon should be viewed as part of the radiative corrections to the Higgs–strahlung process [the same remark holds for the process $e^+e^- \to \nu_e\bar{\nu}_e H\gamma$ to be discussed later, which is part of the QED correction to the WW fusion mechanism]. However, this process can be discussed on its own since here the photon is required to be detected and the $e^+e^- \to HZ\gamma$ process can have a comparable rate than the parent process which scales as $1/s$ at high energies, as the ISR photon will decrease the effective c.m. energy.

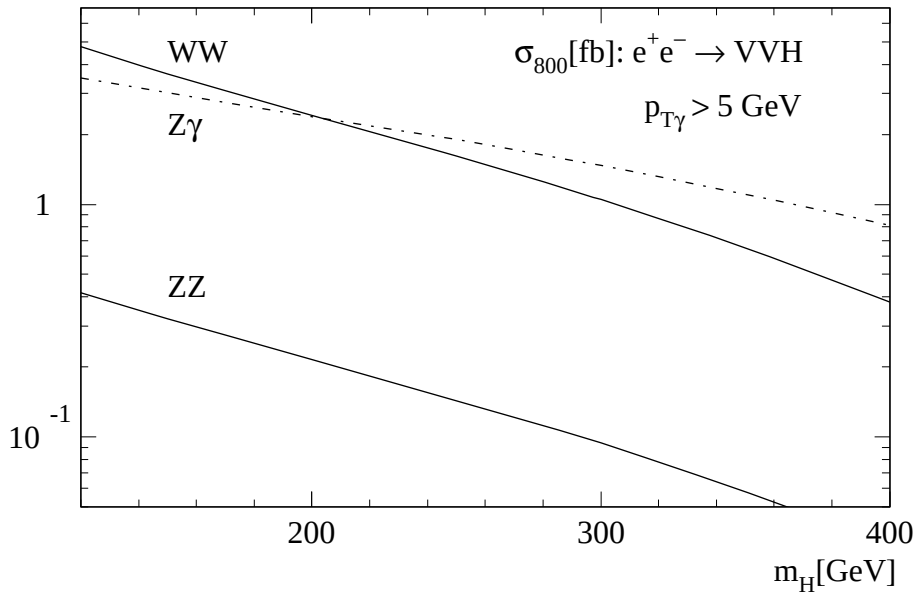

Figure 4.24: The cross sections for the associated production of the Higgs boson with a pair of gauge bosons, $e^+e^- \to HVV$, as a function of M_H at $\sqrt{s} = 800$ GeV; from [264].

Higgs production in association with a gauge boson and two leptons

Also as in the case of the LHC, Higgs bosons can be produced in association with a gauge boson and two leptons in the fusion processes [264, 511]

$$e^+e^- \to \nu_e e^\pm W^\mp H \ , \ \nu_e\bar{\nu}_e\gamma H \ , \ \nu_e\bar{\nu}_e ZH \tag{4.54}$$

with some generic Feynman diagrams shown in Fig. 4.25.

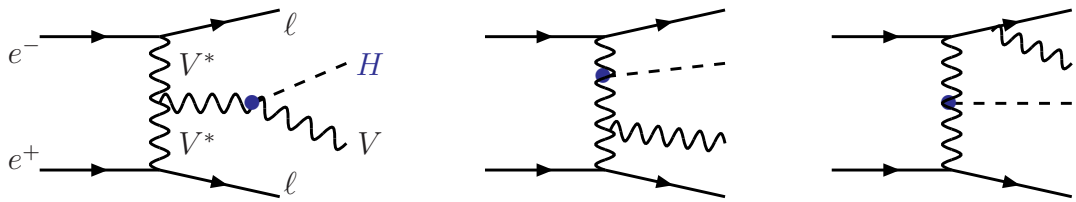

Figure 4.25: Feynman diagrams for the associated production of a Higgs boson with a gauge boson and two leptons in e^+e^- collisions.

Since, as previously discussed, the parent fusion processes $e^+e^- \to H\ell\ell$ have rather large production cross sections at high energies, one might hope again that the emission of an additional gauge boson will still lead to a reasonable event rate, similarly to the case of double Higgs boson production in the vector boson fusion channels $e^+e^- \to HH\ell\ell$ discussed in the preceding section. These processes have been considered in Ref. [511] and are being

updated [264]. The cross sections for $e^+e^- \to \nu\bar{\nu}ZH$ and $e^+e^- \to \nu eWH$ are shown in Fig. 4.26 as a function of the c.m. energy for $M_H = 160$ GeV. As can be seen, they follow the general trend of vector boson fusions mechanisms and increase with energy and/or lower Higgs masses. They are quite sizable since, for $e^+e^- \to \nu_e e^\pm W^\mp H$, the cross section reaches almost the level of 10 fb at $\sqrt{s} \sim 1$ TeV for $M_H \sim 120$ GeV. The cross section is a factor of ~ 5 smaller in the case of the $e^+e^- \to \nu_e\bar{\nu}_e ZH$ mechanism and is even smaller in the case of the $e^+e^- \to e^+e^- ZH$ process for which is not shown.

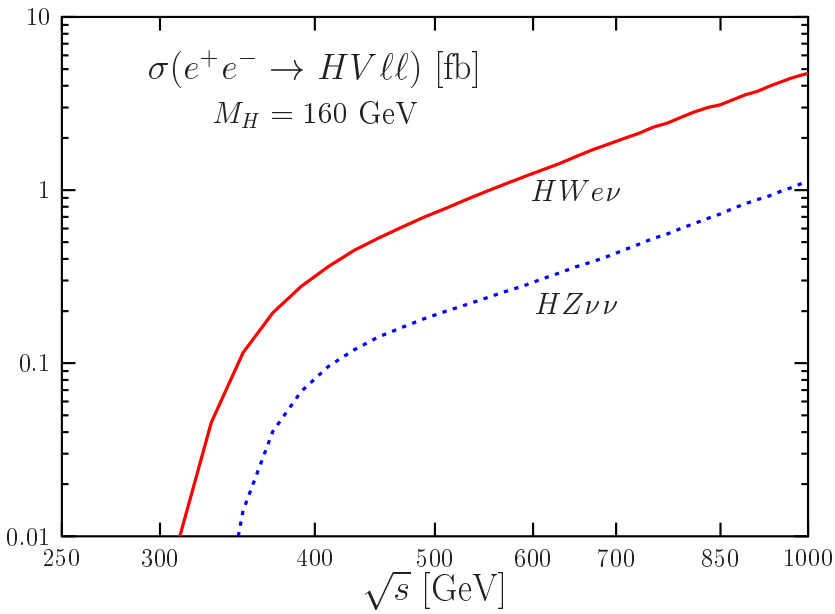

Figure 4.26: The cross sections for associated production of the Higgs boson with a gauge boson and two leptons, $e^+e^- \to HV\ell\ell$, as a function of $\sqrt{s}$ for $M_H = 160$ GeV. They have been obtained using the program `WHIZARD` *[546].*

Higgs production in association with a photon

In the SM, the process where a Higgs boson is produced in association with a photon, $e^+e^- \to H\gamma$ [509], proceeds through s–channel $\gamma^*\gamma H$ and $Z^*\gamma H$ vertex diagrams, but additional t–channel vertex and box diagrams involving W/neutrino and Z/electron exchange also occur; Fig. 4.27. The s–channel contributions involve the same form factors as the effective couplings for the $H \to Z\gamma, \gamma\gamma$ decays discussed in S2.3, but with one of the two photons and the Z boson being virtual, with an effective mass $M_{Z^*} = \sqrt{s}$.

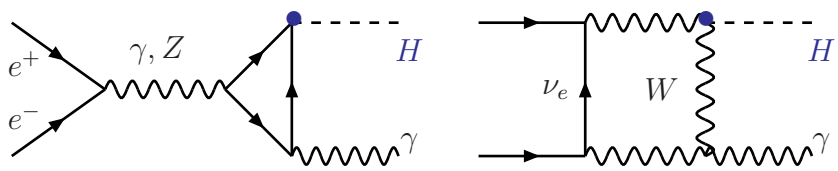

Figure 4.27: Diagrams for associated Higgs production with a photon in e^+e^- collisions.

Since it is a higher–order process in the electroweak coupling, the cross section is rather small, $\sigma(e^+e^- \to H\gamma) \sim 0.05$ fb for $M_H \sim 100$–200 GeV at $\sqrt{s} = 500$ GeV. However, since the photon is mono–chromatic, the signal is very clean allowing for a reasonable hope to isolate these events if enough luminosity is collected a future high–energy colliders. Note that the longitudinal polarization of both electron and positron beams will increase the cross sections by about a factor of 4 compared to the unpolarized case. This process would then allow for an alternative way to probe the induced $H\gamma\gamma$ and $HZ\gamma$ couplings and, potentially, to probe the heavy particles involved in the loops.

Loop induced double Higgs production

Due to CP invariance, the ZHH coupling is absent in the SM and the process $e^+e^- \to Z \to HH$ does not occur at tree–level but only through loop contributions [510]. Because of orbital momentum conservation, the amplitudes for the vertex diagrams with s–channel γ and Z bosons giving rise to two H bosons vanish [only the contribution of the longitudinal component of the Z boson survives but it is proportional to the electron mass and is thus negligible]. In addition, because of chiral symmetry for $m_e = 0$, the diagrams involving the He^+e^- vertices give zero contributions. The contribution of vertices involving the $HHVV$ interaction give also contributions that are proportional to m_e or m_{ν_e}. Therefore, in the SM, the process $e^+e^- \to HH$ can be generated only through box diagrams involving W/neutrino and Z/electron virtual states, Fig. 4.28.

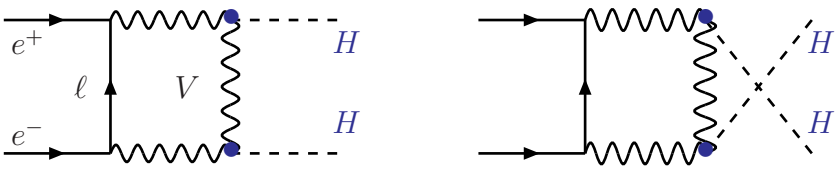

Figure 4.28: Feynman diagrams for loop induced Higgs pair production.

Again, because of the additional electroweak factor, the production cross sections are rather small. Except when approaching the $M_H = 2M_W$ threshold, where there is a small increase, the cross section is practically constant and amounts to ~ 0.2 fb at $\sqrt{s} = 500$ GeV for $M_H \sim 100$–200 GeV. With left–handed polarization of the electron beam, the cross section is increased by a factor of two, while for left–handed electrons and right–handed positrons, it increases by a factor of four; these simple factors are due to the fact that, as usual the contribution of the box with W exchange is much larger than that with the Z exchange. With a very high luminosity, one might hope that the final state can be isolated. A deviation from the SM expectation would signal a breakdown of CP–invariance or the existence of new particles contributing to the loop diagrams.

Higher order tree–level multi Higgs production

Finally, there are also higher–order processes for double Higgs production which occur at the tree–level. Besides the ZZ fusion process $e^+e^- \to HHe^+e^-$ which, as mentioned previously, has a cross section that is one order of magnitude smaller than that of the WW fusion process [for $M_H \sim 100$ GeV, the $e^+e^- \to e^+e^-HH$ cross section barely reaches the level of ~ 0.1 fb even at very high energies, $\sqrt{s} \sim 2$ TeV], one has the following reactions with $V = W, Z$ and $\ell = e, \nu_e$:

$$\begin{aligned} \text{associated double Higgs production with two gauge bosons} \quad &: \quad e^+e^- \longrightarrow VVHH \\ \text{associated double Higgs production with t}\bar{\text{t}}\text{ pairs} \quad &: \quad e^+e^- \longrightarrow t\bar{t}HH \end{aligned} \tag{4.55}$$

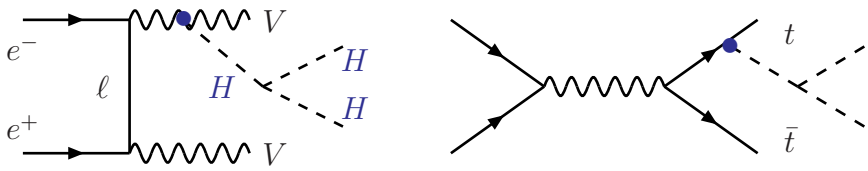

Figure 4.29: Higher order double Higgs production processes at the tree–level.

Some Feynman diagrams for these reactions [those which involve the trilinear Higgs interaction] are displayed in Fig. 4.29. The production cross sections for these processes have been calculated in Refs. [547] using the package `CompHEP` [548] for the automatic evaluation of the full set of amplitudes and, as expected, they are very small. The $e^+e^- \to WWHH$ cross section is at the level of 0.03 fb at $\sqrt{s} \sim 700$ GeV even for a Higgs mass as low as $M_H \sim 65$ GeV, while the rate for $e^+e^- \to ZZHH$ is again one order of magnitude smaller. In the case of the $e^+e^- \to t\bar{t}HH$ process [547, 549], the cross section is at the level of 6 (15) ab at a c.m. energy $\sqrt{s} = 0.8\,(1.6)$ TeV for $M_H \sim 130$ GeV and $m_t = 175$ GeV. Thus, about 10 of such events could be produced if very high luminosities, $\mathcal{L} \sim 1$ ab^{-1}, can be collected at these energies.

In the case of triple Higgs production processes, which would allow for the determination of the quartic Higgs coupling, the cross section are unfortunately too small as mentioned earlier. In the $e^+e^- \to ZHHH$ process [508, 547], for instance, the signal amplitude squared involving the four–Higgs coupling [as well as the irreducible Higgs–strahlung amplitudes] is suppressed by a factor $[\lambda^2_{HHHH}/16\pi^2]/[\lambda^2_{HHH}/M_Z^2] \sim 10^{-3}$ relative to $e^+e^- \to ZHH$, not to mention the phase–space suppression due to the additional final–state heavy particle. The cross sections are below the atobarn level: $\sigma(HHHZ) \sim 0.44$ ab for $M_H \sim 110$ GeV and $\sqrt{s} \sim 1$ TeV and are not very sensitive to a variation of the self–coupling: $\sigma(HHHZ) \sim 0.41\,(0.46)$ ab when λ_{HHHH} is altered by a factor $\frac{1}{2}\,(\frac{3}{2})$ [508]. The fusion process $e^+e^- \to HHH\nu\bar{\nu}$ has also a very small cross section, $\sigma(HHH\nu\bar{\nu}) \sim 0.4$ ab at $\sqrt{s} = 3$ TeV [550].

4.4 Higgs studies in e^+e^- collisions

In this section, we summarize the precision tests of the SM Higgs sector which can be performed at an e^+e^- machine operating in the 350–1000 GeV energy range. We also briefly discuss the additional precision studies which can be made by moving to higher energies at CLIC and by revisiting the physics at the Z resonance in the GigaZ option. We will almost exclusively rely on the detailed studies which have been performed for the TESLA Technical Design Report [480, 486] and on the very recent analyses of the CLIC Physics working group [484], since they involve realistic simulations of the experimental environments[38]. We refer to these two reports for more details and for more references on the original work. We will also mention some updated analyses which appeared during the Linear Collider Workshops held in Amsterdam [557] and Paris [558]. Complementary material can be found in the reports of the American Linear Collider working group [482] and of the JLC working group [483], as well as in the detailed reviews given in Refs. [515, 559].

4.4.1 Higgs boson signals

As discussed in the previous sections, the main production mechanisms for SM Higgs particles are the Higgs–strahlung process $e^+e^- \to ZH$ and the WW fusion process $e^+e^- \to \bar{\nu}_e\nu_e H$. Subleading production channels are the ZZ fusion mechanism, $e^+e^- \to e^+e^-H$, the associated production with top quarks $e^+e^- \to t\bar{t}H$ and double Higgs production in the strahlung $e^+e^- \to HHZ$ and fusion $e^+e^- \to \bar{\nu}\nu HH$ processes which, despite the small production rates, are very useful when it comes to the study of the Higgs properties. The other production processes, although some of them have substantial cross sections such as $e^+e^- \to HW^+W^-$ and $\nu_e e^\pm W^\mp H$, will not [at least in the context of the SM] provide any additional information and we will ignore them in the following discussion.

The cross sections have been given previously, but we summarize them again in Fig. 4.30 for four c.m. energies $\sqrt{s} = 350$ GeV, 500 GeV, 1 TeV and 3 TeV, as functions of the Higgs mass. They have been obtained with the FORTRAN code `HPROD` [560]. We should mention that these cross sections do not include the radiative corrections which have been discussed in this chapter [except that we work in the IBA which absorbs some of the electroweak corrections], and no photon ISR nor beamstrahlung effects have been taken into account. However, since these corrections and effects are rather small, except in peculiar regions of the phase space [such as for $e^+e^- \to t\bar{t}H$ near threshold and $e^+e^- \to HZ$ at $\sqrt{s} \gg M_H$], these numbers approach the exact results to better than 5 to 10% depending on the process, and this approximation is sufficient for most of the purposes that one can have before the

[38]For the TESLA analyses in particular, the backgrounds, the beamstrahlung and detector response have been taken into account, generally using programs such as `CompHEP` [548] or `WHiZard` [546] in addition to the usual Monte-Carlo generators [398, 551, 552], `Circe` [553] and `SIMDET` [554] or `BRAHMS` [555]; see Ref. [556].

experiments actually start. In Table 4.3, we display the numerical values of the cross sections for selected values of the Higgs mass at the two different energies $\sqrt{s} = 500$ GeV and 1 TeV.

M_H (GeV)	$\sigma(HZ)$	$\sigma(H\nu_e\bar{\nu}_e)$	$\sigma(He^+e^-)$	$\sigma(Ht\bar{t})$	$\sigma(HHZ)$	$\sigma(HH\nu\bar{\nu})$
115	58.67	81.98	8.77	0.36	0.19	0.03
120	57.91	78.30	8.38	0.23	0.18	0.02
130	56.31	71.28	7.64	0.07	0.14	0.01
140	54.61	64.71	6.95	–	0.11	–
150	52.83	58.58	6.30	–	0.08	–
160	50.96	52.88	5.69	–	0.05	–
170	49.03	47.60	5.13	–	0.03	–
180	47.03	42.71	4.60	–	0.02	–
200	42.88	34.03	3.67	–	–	–
300	21.38	8.26	0.89	–	–	–
400	3.24	0.73	0.07	–	–	–

M_H (GeV)	$\sigma(HZ)$	$\sigma(H\nu_e\bar{\nu}_e)$	$\sigma(He^+e^-)$	$\sigma(Ht\bar{t})$	$\sigma(HHZ)$	$\sigma(HH\nu\bar{\nu})$
115	12.90	219.54	24.26	2.50	0.12	0.30
120	12.86	214.58	23.73	2.38	0.12	0.27
130	12.76	204.92	22.70	2.16	0.12	0.21
140	12.66	195.60	21.70	1.96	0.11	0.16
150	12.55	186.63	20.73	1.79	0.11	0.12
160	12.44	178.01	19.80	1.63	0.10	0.10
170	12.32	169.72	18.90	1.49	0.10	0.07
180	12.19	161.76	18.03	1.36	0.10	0.06
200	11.92	146.78	16.40	1.14	0.09	0.03
300	10.22	88.19	9.93	0.45	0.03	–
400	8.13	50.32	5.68	0.16	–	–
500	5.89	26.55	3.00	0.04		–
600	3.78	12.41	1.40	–	–	–
700	2.03	4.75	0.53	–	–	–
800	0.81	1.24	0.14	–	–	–

Table 4.3: Numerical values for SM Higgs production cross sections [in fb] in e^+e^- collisions at two center of mass energies $\sqrt{s} = 500$ GeV (top) and $\sqrt{s} = 1$ TeV (bottom) for selected values of the Higgs boson mass. These numbers have been obtained with the program HPROD *[560] and no radiative correction nor beamstrahlung is included.*

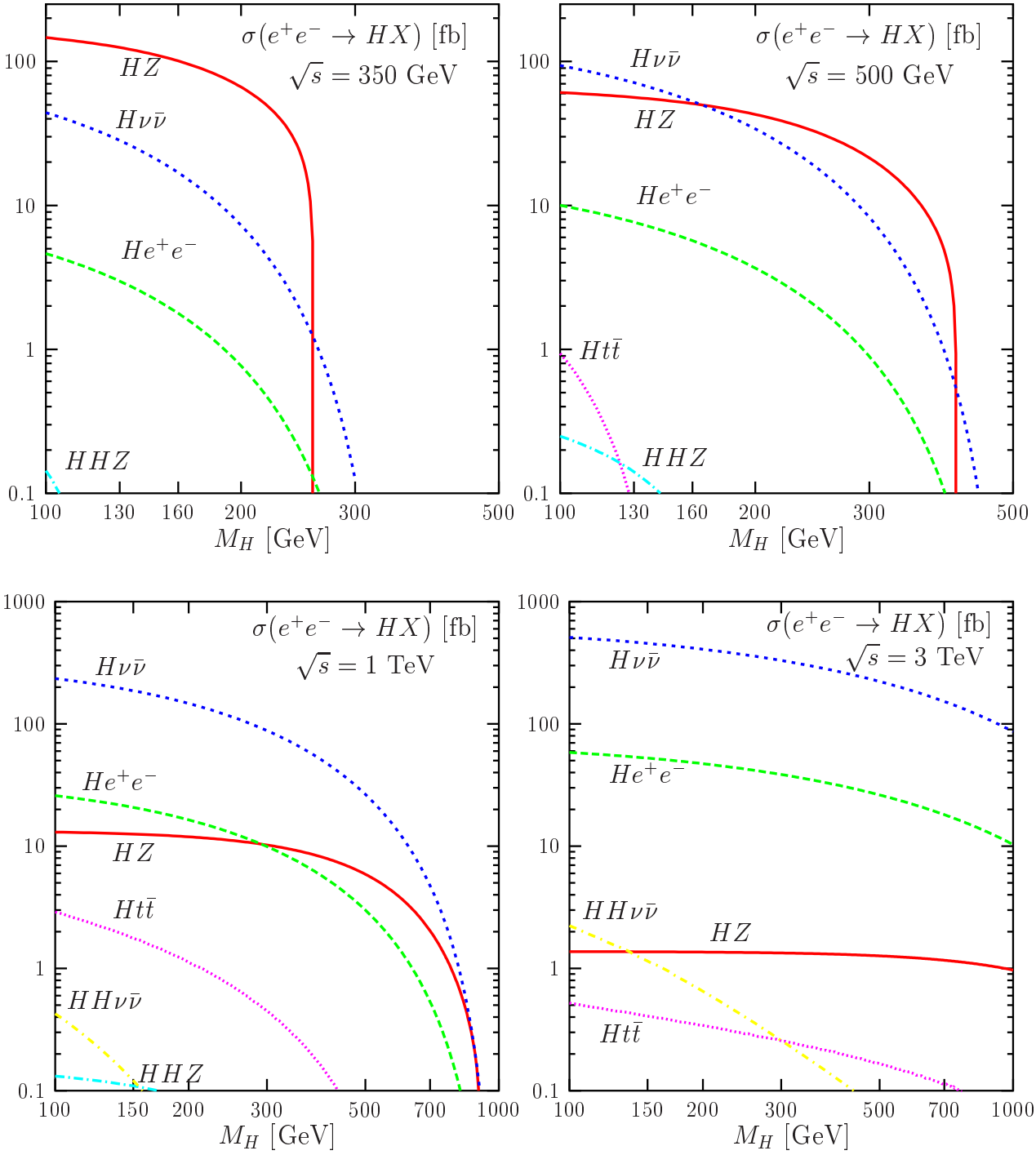

Figure 4.30: Production cross sections of the SM Higgs boson in e^+e^- collisions in the dominant and subdominant processes as a function of the Higgs mass for four center of mass energies, $\sqrt{s} = 350$ GeV, 500 GeV, 1 TeV and 3 TeV. Radiative corrections, initial state radiation and beamstrahlung effects are not included. The cross sections have been obtained with the program `HPROD` *[560].*

As previously mentioned, the Higgs–strahlung cross section scales as $1/s$ and therefore dominates at low energies, while the one of WW fusion mechanism rises like $\log(s/M_H^2)$ and becomes more important at high energies. At $\sqrt{s} \sim 500$ GeV, the two processes have approximately the same cross sections, $\mathcal{O}(50$ fb) for the interesting Higgs mass range 115 GeV $\lesssim M_H \lesssim$ 200 GeV. With an integrated luminosity $\mathcal{L} \sim 500$ fb^{-1}, as expected at the TESLA machine for instance, approximately 30.000 and 40.000 events can be collected in, respectively, the HZ and $\nu\bar{\nu}H$ channels for $M_H \sim 120$ GeV. This sample is more than enough to observe the Higgs particle and to study its properties in great detail.

In the Higgs–strahlung process, the recoiling Z boson, which can be tagged through its clean $\ell^+\ell^-$ decays, with $\ell = e$ or μ, but also through decays into quarks which have a much larger statistics, is mono–energetic and the Higgs mass can be derived from the energy of the Z boson since the initial $e^\pm$ beam energies are sharp when the effect of beamstrahlung is strongly suppressed. Therefore, it will be easy to separate the signal from the backgrounds [561, 562]. In the low mass range, $M_H \lesssim 140$ GeV, the process leads to $b\bar{b}q\bar{q}$ and $b\bar{b}\ell\ell$ final states, with the b–quarks being efficiently tagged by means of micro–vertex detectors. In the mass range where the decay $H \to WW^*$ is dominant, the Higgs boson can be reconstructed by looking at the $\ell\ell+4$–jet or 6–jet final states, and using the kinematical constraints on the fermion invariant masses which peak at M_W and M_H, the backgrounds are efficiently suppressed. Also the $\ell\ell q\bar{q}\ell\nu$ and $q\bar{q}q\bar{q}\ell\nu$ channels are easily accessible.

It has been shown in detailed simulations [480] that only a few fb^{-1} data are needed to obtain a 5σ signal for a Higgs boson with a mass $M_H \lesssim 150$ GeV at a 500 GeV collider, even if it decays invisibly [as could happen in some extensions of the SM]. In fact, for such small masses, it is better to move to lower energies where the Higgs–strahlung cross section is larger. Fig. 4.31 shows the reconstructed Higgs mass peaks in the strahlung process at $\sqrt{s} = 350$ GeV with a luminosity $\mathcal{L} = 500$ fb^{-1} for $M_H = 120$ GeV in the decay $H \to q\bar{q}$ and for $M_H = 150$ GeV in the decay $H \to WW^*$. At this energy and integrated luminosity, Higgs masses up to $M_H \sim 260$ GeV can be probed in this channel.

M_H (GeV)	350 GeV	500 GeV	1000 GeV
120	4670	2020	377
180	2960	1650	365
250	230	1110	333
Max M_H	258	407	730

Table 4.4: Expected number of signal events for 500 fb^{-1} for the Higgs-strahlung channel with dilepton final states $e^+e^- \to ZH \to \ell^+\ell^-X$, at different $\sqrt{s}$ and M_H values. The last line is for the maximum M_H value yielding more than 50 signal events in this final state. The numbers for $\sqrt{s}$=1 TeV do not include the selection cuts and ISR corrections of [480].

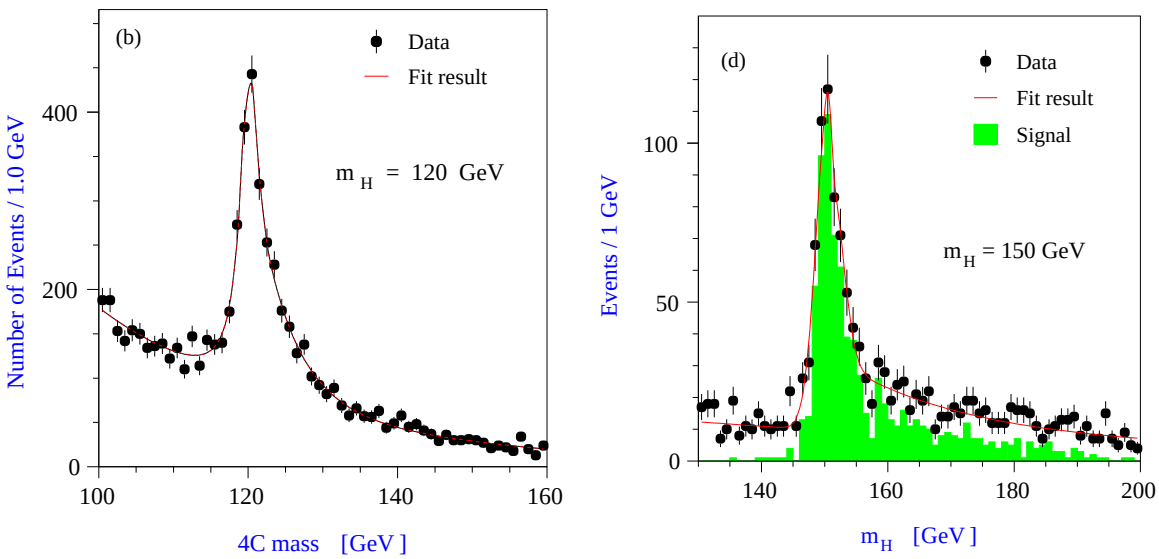

Figure 4.31: The Higgs mass peak reconstructed in different channels with constrained fits for two values of M_H, an integrated luminosity of 500 fb^{-1} and $\sqrt{s} = 350$ GeV in $HZ \to q\bar{q}\ell^+\ell^-$ at $M_H = 120$ GeV (left) and $HZ \to W^+W^-\ell^+\ell^-$ at $M_H = 150$ GeV (right); from Ref. [480].

Moving to higher energies, Higgs bosons with masses up to $M_H \sim 400$ GeV can be discovered in the strahlung process at an energy of 500 GeV and with a luminosity of 500 fb^{-1}. For even higher masses, one needs to increase the c.m. energy of the collider and, as a rule of thumb, Higgs masses up to $\sim 80\%$ $\sqrt{s}$ can be probed. This means that a 1 TeV collider can probe the entire SM Higgs mass range, $M_H \lesssim 700$ GeV. Table 4.4 shows the maximal Higgs mass values which can be reached at various c.m. energies by requiring at least 50 signal events in the process $e^+e^- \to HZ \to H\ell\ell$.

The WW fusion mechanism offers a complementary production channel. In the low Higgs mass range where the decay $H \to b\bar{b}$ is dominant, flavor tagging plays an important role to suppress the 2–jet plus missing energy background. The $e^+e^- \to H\bar{\nu}\nu \to b\bar{b}\bar{\nu}\nu$ final state can be separated from the corresponding one in the Higgs–strahlung process $e^+e^- \to HZ \to b\bar{b}\bar{\nu}\nu$ [563] by exploiting their different characteristics in the $\nu\bar{\nu}$ invariant mass which are measurable through the missing mass distribution; see Fig. 4.32. The polarization of the electron and positron beams, which allow to switch on and off the WW fusion contribution, can be very useful to control the systematic uncertainties.

For larger Higgs boson masses, when the decays $H \to WW^{(*)}, ZZ^{(*)}$ are dominant, the main backgrounds are $WW(Z)$ and $ZZ(Z)$ production which have large cross sections at high energies and eventually $t\bar{t}$, but again, they can be suppressed using kinematical constraints from the reconstruction of the Higgs mass peak. For even higher masses, when the Higgs boson decays into $t\bar{t}$ final states, the $e^+e^- \to t\bar{t}$ and $t\bar{t}e^+e^-$ backgrounds can be reduced to a manageable level by exploiting the characteristics of the $\nu\bar{\nu}b\bar{b}WW$ signature.

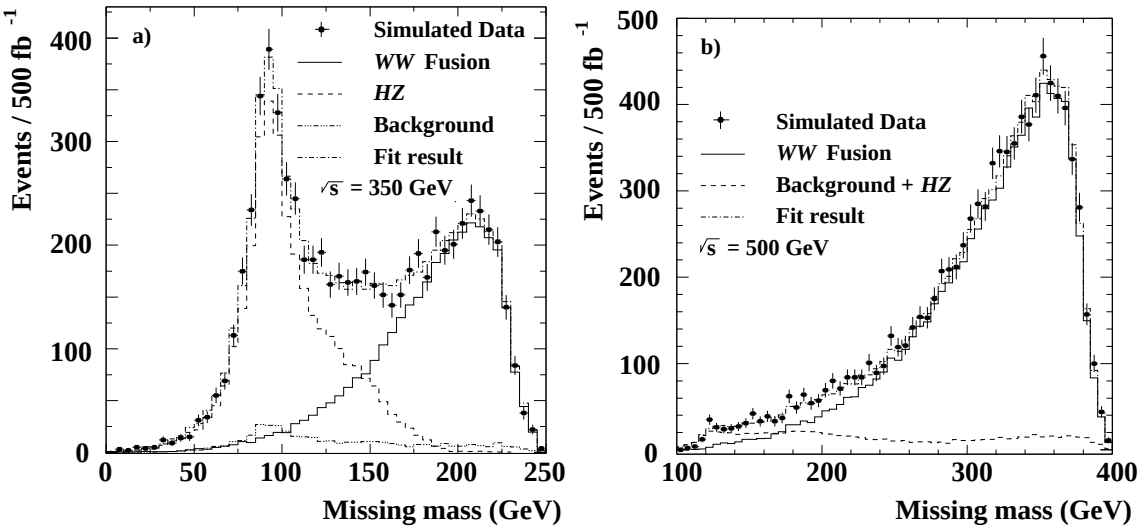

Figure. 4.32: The missing mass distribution in the $\nu\bar{\nu}b\bar{b}$ final state at $\sqrt{s} = 350$ GeV (left) and 500 GeV (right) for $M_H = 120$ GeV in WW fusion, Higgs–strahlung and the interference, as well as for the background. The WW fusion contribution is measured from a fit to the shape of this distribution; from Ref. [480].

Turning to the subleading processes, we have seen that the ZZ fusion mechanism has a cross section that is one order of magnitude smaller than WW fusion, a result of the smaller neutral couplings compared to the charged current couplings. However, the full final state can be reconstructed in this case. At c.m. energies above 1 TeV, the cross section exceeds the one of the Higgs strahlung process so that $e^+e^- \to He^+e^-$ can be used instead for model independent searches by tagging the e^+e^- pair and reconstructing the missing mass [558].

The associated production with top quarks has a very small cross section at $\sqrt{s} = 500$ GeV due to the phase space suppression but at $\sqrt{s} = 800$ GeV it can reach the level of a few femtobarn. For $M_H \lesssim 140$ GeV, the spectacular final state signal, $W^+W^-b\bar{b}b\bar{b}$, has large backgrounds which can be suppressed by tagging the b–quarks and reconstructing the Higgs mass. The statistics are nevertheless very small and one has to resort to a neural network analysis to isolate the signal from the remaining backgrounds. For higher Higgs masses, the final state $Ht\bar{t} \to 4Wb\bar{b}$ has also large backgrounds, which are nevertheless manageable using again a neutral network.

The cross section for the double Higgs production in the strahlung process is at the level of $\sim \frac{1}{2}$ fb for a light Higgs at $\sqrt{s} = 500$ GeV and is smaller at higher energies. The large backgrounds from four and six fermion events can be suppressed for $M_H \lesssim 140$ GeV by using the characteristic signal of four b–quarks and a Z boson, reconstructed in both leptonic an hadronic final to increase the statistics, and using b–tagging. For higher Higgs masses, the dominant final state is $Z + 4W$. In contrast, the cross section for the $e^+e^- \to \nu_e\bar{\nu}_e HH$ is extremely small at $\sqrt{s} = 500$ GeV but reaches the fb level at $\sqrt{s} = 3$ TeV.

4.4.2 Precision measurements for a light Higgs boson

Once the Higgs boson is found, it will be of great importance to explore all its fundamental properties. This can be done at great details in the clean environment of e^+e^- linear colliders: the Higgs boson mass, its spin and parity quantum numbers and its couplings to fermions, massive and massless gauge bosons as well as its trilinear self–couplings can be measured with very good accuracies. The measurements would allow to probe in all its facets the electroweak symmetry breaking mechanism.

The Higgs boson mass

Many of the properties of the SM Higgs boson can be determined in a model independent way by exploiting the recoil mass technique in the strahlung process, $e^+e^- \to HZ$. The measurement of the recoil e^+e^- or $\mu^+\mu^-$ mass in $e^+e^- \to ZH \to H\ell\ell$, allows a very good determination of the Higgs mass [564, 565]. At $\sqrt{s} = 350$ GeV and with a luminosity of $\mathcal{L} = 500$ fb^{-1}, a precision of $\Delta M_H \sim 70$ MeV can be reached for a Higgs mass of $M_H \sim 120$ GeV. The precision can be increased to $\Delta M_H \sim 40$ MeV by using in addition the hadronic decays of the Z boson which have more statistics [565]. Accuracies of the order of $\Delta M_H \sim 80$ MeV can also be reached for M_H values between 150 and 180 GeV when the Higgs boson decays mostly into gauge bosons [see Ref. [566], however]. The reconstructed Higgs mass peak is shown in Fig. 4.33 at a 350 GeV collider in the two channels $HZ \to b\bar{b}q\bar{q}$ for $M_H = 120$ GeV and $HZ \to W^+W^-q\bar{q}$ for $M_H = 150$ GeV. The obtained accuracy on M_H is a factor of two better than the one which could be obtained at the LHC.

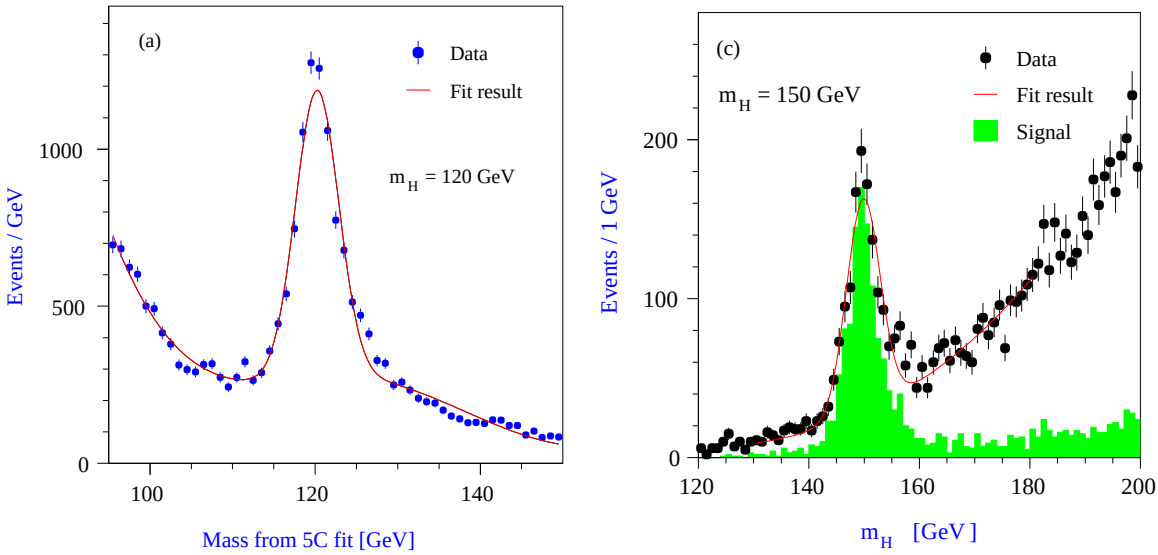

Figure 4.33: The Higgs mass peak reconstructed in different channels with constrained fits for two values of M_H, an integrated luminosity of 500 fb^{-1} and $\sqrt{s} = 350$ GeV in $HZ \to b\bar{b}q\bar{q}$ at $M_H = 120$ GeV (left) and $HZ \to W^+W^-q\bar{q}$ at $M_H = 150$ GeV (right); from Ref. [480].

The Higgs spin and parity

The determination of the $J^{\rm P} = 0^+$ quantum number of the SM Higgs boson can also be performed in the strahlung process. As discussed in §4.2.1, the measurement of the rise of the cross section near threshold, $\sigma(e^+e^- \to HZ) \propto \lambda^{1/2}$, rules out $J^{\rm P} = 0^-, 1^-, 2^+$ and higher spin $3^\pm, \cdots$, which rise with higher powers of the velocity $\lambda^{1/2}$. A threshold scan with a luminosity of 20 fb^{-1} at three center of mass energies is sufficient to distinguish the various behaviors; Fig. 4.34. The production of states with the two remaining $J^{\rm P} = 1^+, 2^-$ quantum numbers can be ruled out using the angular correlations of the final state $e^+e^- \to HZ \to 4f$.

The angular distribution of the Z/H bosons in the Higgs–strahlung process is also sensitive to the spin–zero of the Higgs particle: at high–energies, the Z is longitudinally polarized and the distribution follows the $\sim \sin^2\theta$ law which unambiguously characterizes the production of a $J^P = 0^+$ particle, since in the case of a pseudoscalar Higgs boson, the angular distribution would behave as $1 + \cos^2\theta$. Assuming that the Higgs particle is a mixed CP–even and CP–odd state with η parameterizing the mixture, the angular distribution given by eq. (4.26) can be checked experimentally. This is shown in the right–hand side of Fig. 4.34, where one can see that the parameter η can be measured to a precision of 3–4 percent, which is the typical size of electroweak radiative corrections which, in CP–conserving models, could generate the CP–odd component of the $ZZ\Phi$ coupling. Note that the Higgs $J^{\rm PC}$ quantum numbers can also be checked by looking at correlations in the production $e^+e^- \to HZ \to 4f$ or in the decay $H \to WW^*, ZZ^* \to 4f$ processes, just as in the LHC case but with more accuracy at the LC since one can use the larger hadronic modes of the W and Z bosons.

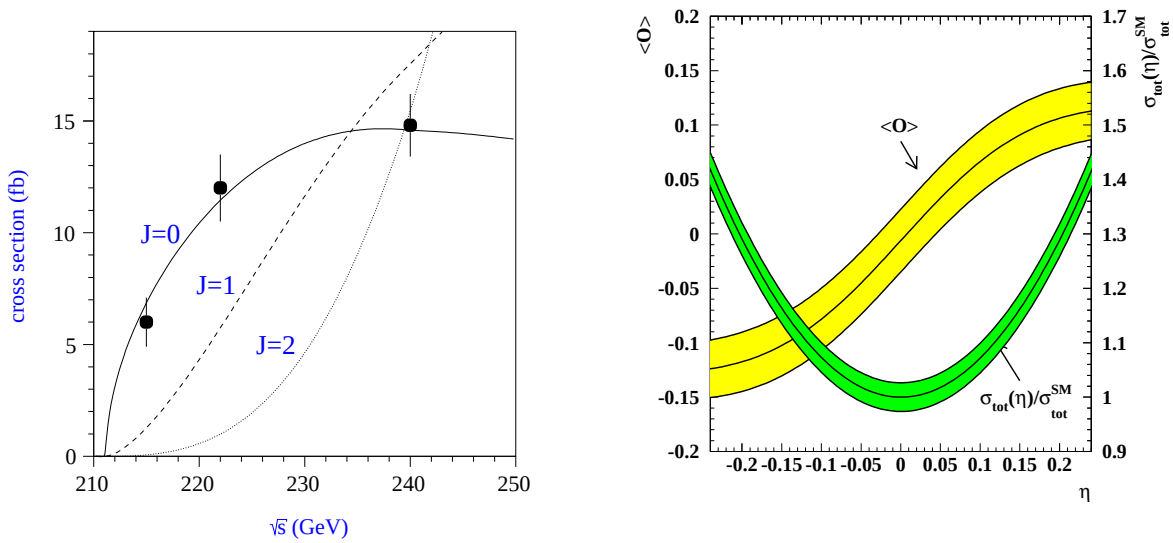

Figure 4.34: The $e^+e^- \to ZH$ cross section energy dependence near threshold for $M_H = 120$ GeV for spin $0^+, 1^-$ and 2^+ bosons [567] (left). The dependence of $\sigma(e^+e^- \to HZ)$ and the observable $\langle O \rangle$ defined in eq. (4.27) on the parameter η with the shaded bands showing the 1σ uncertainties at $\sqrt{s} = 350$ GeV and 500 fb^{-1} [568] (right).

The CP nature of the Higgs boson would be best tested in the couplings to fermions, where the scalar and pseudoscalar components might have comparable size. Such tests can be performed in the decay channel $H \to \tau^+\tau^-$ for $M_H \lesssim 140$ GeV by studying the spin correlations between the final decay products of the two τ leptons [158, 160]. The acoplanarity angle between the decay planes of the two ρ mesons produced from τ^+ and τ^-, which can be reconstructed in the Higgs rest frame using the τ lifetime information, is a very sensitive probe, allowing a discrimination between a CP–even and CP–odd state at the 95% CL for $M_H = 120$ GeV at the usual energy and luminosity [167]; using the additional information from the τ impact parameter significantly improves this determination.

If the observed Higgs boson is a mixture of CP–even and CP–odd states, with a coupling $g_{\Phi\tau\tau} = g_{H\tau\tau}(\cos\phi + i\sin\phi\gamma_5)$ with $\phi = 0$ in the SM Higgs case, the angular distributions in the $\tau^\pm \to \rho^\pm\nu$ decays allow to measure the mixing angle with an accuracy of $\Delta\phi \sim 6°$. This is shown in Fig. 4.35, which displays the distribution of the acoplanarity angle φ^* between the decay planes of the ρ^+ and ρ^- in the rest frame of the pair, for several values of the mixing angle ϕ, as a result of a simulation for $\sqrt{s} = 350$ GeV and $\mathcal{L} = 1$ ab^{-1}.

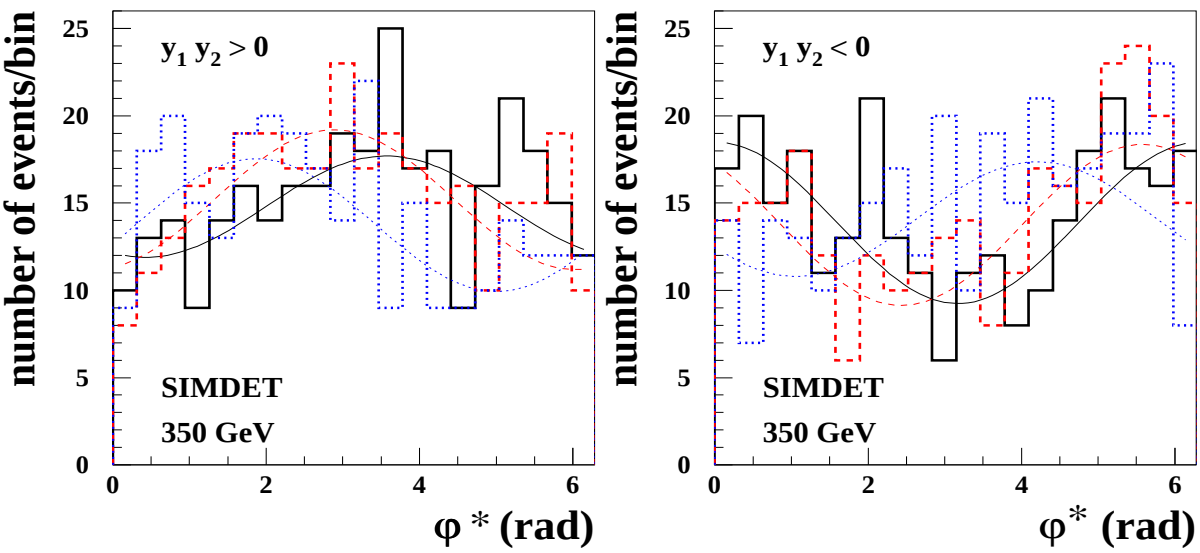

Figure 4.35: Distribution of the reconstructed acoplanarity angle φ^* for $\phi = 0$ (full histogram), $\phi = \pi/8$ (dashed) and $\phi = \pi/4$ (dotted) for $y_1y_2 > 0$ (left) and $y_1y_2 < 0$ (right) with $y_{1,2} = (E_{\pi^\pm} - E_{\pi^0})/(E_{\pi^\pm} + E_{\pi^0})$; the lines indicate the results of the fits; from [557].

For heavier Higgs bosons, when the $H \to \tau^+\tau^-$ becomes too small, these studies cannot be performed anymore. A promising channel would be the decay $H \to t\bar{t}$ for $M_H > 2m_t$, but no realistic simulation of the potential of this channel has been performed. Finally, and as discussed in §4.3.2, the differential cross section in associated production with top quarks, $e^+e^- \to t\bar{t}H$, is sensitive to the CP nature of the Higgs boson, though no analysis has been performed to verify at which extent this information can be experimentally extracted.

The Higgs couplings to gauge bosons

The fundamental prediction that the Higgs couplings to ZZ/WW bosons are proportional to the masses of these particles can be easily verified experimentally since these couplings can be directly determined by measuring the production cross sections in the bremsstrahlung and the fusion processes. $\sigma(e^+e^- \to HZ \to H\ell^+\ell^-)$ can be measured by analyzing the recoil mass against the Z boson and provides a determination of the g_{HZZ} couplings independently of the decay modes of the Higgs boson. Adding the two lepton channels, one obtains a statistical accuracy of less than 3% at $\sqrt{s} \sim 350$ GeV and with $\int \mathcal{L} = 500$ fb^{-1} [564].

The coupling g_{HWW} for $M_H \lesssim 2M_W$ can determined from the measurement of the total cross section of the process $e^+e^- \to W^*W^*\nu\bar{\nu} \to H\nu\bar{\nu}$ which, as discussed previously, can be efficiently separated from the $e^+e^- \to HZ \to H\nu\bar{\nu}$ channel and from the backgrounds, see Fig. 4.32. A precision of also less than 3% can be achieved for $M_H = 120$ GeV, but at a slightly higher energy, $\sqrt{s} \sim 500$ GeV, where the production rate is larger [569]. The precision becomes worse for increasing Higgs mass as a result of the falling cross section.

The accuracies which can be achieved are shown in Tab. 4.5 for three Higgs masses and the precision on the Higgs couplings is half of these errors, since the cross sections scale as g^2_{HVV}. Thus, a measurement of the Higgs couplings to gauge bosons can be performed at the statistical level of 1 to 2% and would allow to probe the quantum corrections.

Channel	$M_H = 120$ GeV	$M_H = 140$ GeV	$M_H = 160$ GeV
$\sigma(e^+e^- \to HZ)$	2.5%	2.7%	3.0 %
$\sigma(e^+e^- \to H\nu\bar{\nu})$	2.8%	3.7%	13 %

Table 4.5: Relative precision in the determination of the SM Higgs cross sections for 120 GeV $\leq M_H \leq$ 160 GeV with $\mathcal{L} = 500$ fb^{-1} at $\sqrt{s} = 350$ and 500 GeV; from Ref. [480].

The Higgs decay branching ratios

The measurement of the branching ratios of the Higgs boson [570–580] is of utmost importance. For Higgs masses below $M_H \lesssim 150$ GeV a large variety of branching ratios can be measured at the linear collider, since the $b\bar{b}, c\bar{c}$ and gg final states can be very efficiently disentangled by means of vertex detectors [581]. The $b\bar{b}, c\bar{c}$ and $\tau^+\tau^-$ fractions allow to measure the relative couplings of the Higgs boson to these fermions and to check the prediction of the Higgs mechanism that they are indeed proportional to fermion masses. In particular, BR$(H \to \tau^+\tau^-) \sim m_\tau^2/3\bar{m}_b^2$ allows such a test in a rather clean way. The gluonic branching ratio is indirectly sensitive to the $t\bar{t}H$ Yukawa coupling and would probe the existence of new strongly interacting particles that couple to the Higgs and which are too heavy to be produced directly. The branching ratio of the loop induced $\gamma\gamma$ and $Z\gamma$ Higgs decays are also very sensitive to new heavy particles and their measurement is thus very important. The

branching ratio of the Higgs decays into W bosons starts to be significant for $M_H \gtrsim 120$ GeV and allows to measure again the HWW coupling in an independent way. In the mass range 120 GeV $\lesssim M_H \lesssim 180$ GeV, the $H \to ZZ^*$ fraction is too small to be precisely measured, but for higher masses it is accessible and allows an additional determination of the HZZ coupling.

There are two methods to measure the Higgs branching ratios: first by measuring the event rate in the Higgs–strahlung process for a given final state configuration and then dividing by the total cross section which is measured from the recoil mass, and second, by selecting a sample of unbiased events in the $e^+e^- \to HZ$ recoil mass peak and determining the fraction of events corresponding to a given final state decay. The first case, which is called the indirect method, has been used to study the Higgs branching ratios for the TESLA TDR [480,572] while the second one, called the direct method, appeared only recently [573]. Both methods give rather similar results but, since they are almost independent, these results may be combined to provide a significant improvement of the expected accuracies.

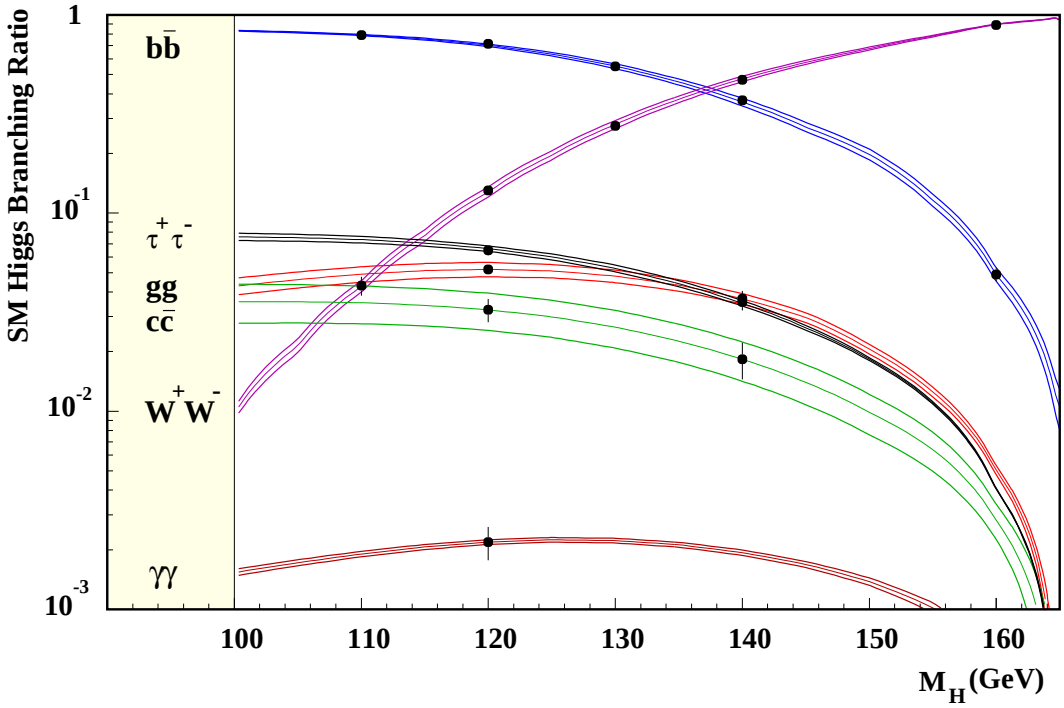

Figure 4.36: The theoretical predictions [with the bands due to the uncertainties in the measurement of the quark masses and α_s] and the experimental accuracy [the points with error bars] for the SM Higgs branching ratios at $\sqrt{s} = 350$ GeV with 500 fb^{-1}; from Ref. [480].

The expected accuracies on the Higgs branching fractions are shown in Fig. 4.36 and in Table 4.6 [the low–energy (LE) numbers at the left] mostly at $\sqrt{s} = 350$ GeV and with 500 fb^{-1} integrated luminosity for $M_H \leq 160$ GeV. The $b\bar{b}, c\bar{c}, \tau^+\tau^-, gg$ and WW branching ratios of the Higgs boson can be measured with a very good accuracy. For the mass value

M_H = 120 GeV and using the indirect method, one obtains an accuracy of, respectively, 2.4%, 8.3%, 5%, 5.5% and 5.1%. When combined with the direct method measurements labeled LE(D), the errors decrease quite significantly. The uncertainties in the measurements become larger when approaching the WW threshold: at $M_H \sim 160$ GeV, only the $b\bar{b}, WW$ and ZZ fractions are accessible, with still a poor accuracy in the latter case. For $M_H \sim 200$ GeV, a higher energy $\sqrt{s} = 500$ GeV is needed to compensate for the falling cross section, and the precision is good only for the WW and ZZ channels. For the $H \to b\bar{b}$ decays, an energy of 800 GeV and 1 ab^{-1} data are required to reach the quoted precision of 17%.

M_H [GeV]	120			140		160		200	
Decay mode	Relative Precision (%)								
	LE	LE(D)	HE	LE	HE	LE	HE	LE	HE
$b\bar{b}$	2.4	1.5	1.6	2.6	1.8	6.5	2.0	17.	9.0
$c\bar{c}$	8.3	5.8	–	19.	–				
$\tau\tau$	5.0	4.1	–	8.0	–				
gg	5.5	3.6	2.3	14.0	3.5	–	14.6		
WW	5.1	2.7	2.0	2.5	1.8	2.1	1.0	3.5	2.5
ZZ						16.9	–	9.9	–
$\gamma\gamma$	23	21.	5.4	–	6.2	–	24		
$Z\gamma$				27.	–				
$\mu\mu$	30		–						

Table 4.6: Summary of expected precisions on Higgs boson branching ratios from existing studies within the ECFA/DESY workshops (LE) [557] obtained for 500 fb^{-1} at $\sqrt{s} = 350$ GeV, except for $M_H = 200$ GeV where BR(WW) and BR(ZZ) are measured at $\sqrt{s} = 500$ GeV and BR(bb) which uses 1 ab^{-1} at 800 GeV, as in the case of BR($\mu\mu$). LE stands for the measurement with the indirect method, while LE(D) is for the combined measurements of the direct and indirect methods [573]. HE is the combination of the measurements from the direct method with the NLC results obtained for 1 ab^{-1} at $\sqrt{s} = 1$ TeV [574].

In the low Higgs mass range, even the rare decays into $\gamma\gamma$ and $Z\gamma$ final states can be measured with an accuracy of approximately 5 to 20% [574, 575, 577]. The very rare decay into muon pairs is also measurable, though with a rather poor accuracy, by going to high energies and taking advantage of the enhanced production rates in $e^+e^- \to H\nu\bar{\nu}$ [578]. A luminosity of 1 ab^{-1} is necessary to probe all these rare decay modes of the Higgs boson.

Finally, invisible Higgs decays can also be probed with a very good accuracy, thanks to the missing mass technique. One can also look directly for the characteristic signature of missing energy and momentum. Recent studies show that in the range 120 GeV $\lesssim M_H \lesssim$ 160 GeV, an accuracy of $\sim 10\%$ can be obtained on a invisible decay with a branching ratio of 5% and a 5σ signal can be seen for a branching ratio as low as 2% [580].

Moving to higher energies, $\sqrt{s} = 1$ TeV, the larger rate for the WW fusion process helps improving the accuracy on the main decay branching ratios and even search for rare decays [as it was the case for $H \to \mu^+\mu^-$]. In the right–hand side of Table 4.6, the HE numbers stand for measurements performed at this energy and with 1 ab^{-1} data, when combined with the respective measurements at low energies [574]. As can be seen the accuracy on some decay branching ratios, in particular BR($H \to b\bar{b}, \gamma\gamma$), can be significantly improved.

The Higgs total decay width

The total decay width of the Higgs boson, for $M_H \gtrsim 200$ GeV, is large enough to be accessible directly from the reconstruction of the Higgs boson lineshape. For smaller Higgs masses, the total decay is less than 1 GeV and it cannot be resolved experimentally. However, it can be determined indirectly by exploiting the relation between the total and partial decay widths for some given final states. For instance, in the decay $H \to WW^*$, the total decay width is given by $\Gamma_H = \Gamma(H \to WW^*)/\text{BR}(H \to WW^*)$. One can then combine the direct measurement of the $H \to WW^*$ branching ratio discussed above and use the information on the HWW coupling from the WW fusion cross section to determine the partial decay width $\Gamma(H \to WW^*)$. Alternatively, on can exploit the measurement of the HZZ coupling from the production cross section of the Higgs–strahlung process, since the mass reach is higher than in WW fusion, and assume SU(2) invariance to relate the two couplings, $g_{HWW}/g_{HZZ} = 1/\cos\theta_W$. The accuracy on the total decay width measurement follows then from that of the WW branching ratio and the g_{HWW} coupling.

Channel	$M_H = 120$ GeV	$M_H = 140$ GeV	$M_H = 160$ GeV
g_{HWW} from $\sigma(e^+e^- \to H\nu\nu)$	6.1%	4.5%	13.4 %
g_{HWW} from $\sigma(e^+e^- \to HZ)$	5.6%	3.7%	3.6 %
BR(WW) at $\sqrt{s} = 1$ TeV	3.4%	3.6%	2.0 %

Table 4.7: Relative precision in the determination of the SM Higgs decay width with $\int \mathcal{L} = 500$ fb^{-1} at $\sqrt{s} = 350$ GeV using the two methods described in the text [480]. The last line shows the improvement which can be obtained when combining these results with those which can be extracted from measurements at $\sqrt{s} \sim 1$ TeV with $\int \mathcal{L} = 1$ ab^{-1} [574].

As shown in Tab. 4.7, in the range 120 GeV $\lesssim M_H \lesssim$ 160 GeV, an accuracy ranging from 4% to 13% can be achieved on Γ_H if the HWW coupling is measured in the fusion process. This accuracy greatly improves for higher M_H values by assuming SU(2) universality which allows to use the HWW coupling as derived from the strahlung process. If in addition a measurement of BR($H \to WW$) is performed at higher energies and combined with the previous values, the accuracy on the total Higgs width will greatly improve for high masses.

Note that the same technique would allow to extract the total Higgs decay width using

the $\gamma\gamma$ decays of the Higgs boson together with the cross section from $\gamma\gamma \to H \to b\bar{b}$ as measured at a photon collider. This is particularly true since the measurement of BR($\gamma\gamma$) at $\sqrt{s} \sim 1$ TeV is rather precise, allowing the total width to be determined with an accuracy of $\sim 5\%$ with this method for $M_H = 120$–140 GeV independently of the WW measurement.

The Higgs Yukawa coupling to top quarks

The Higgs Yukawa coupling to top quarks, which is the largest coupling in the electroweak SM, is directly accessible in the process where the Higgs is radiated off the top quarks, $e^+e^- \to t\bar{t}H$, since the contribution from the diagram where the Higgs boson is radiated from the Z line, $e^+e^- \to HZ \to Ht\bar{t}$, is very small; Fig. 4.17. Because of the limited phase space, this measurement can only be performed at high energies $\sqrt{s} \gtrsim 500$ GeV. For $M_H \lesssim 140$ GeV, the Yukawa coupling can be measured in the channel $WWb\bar{b}b\bar{b}$ with the W bosons decaying both leptonically and hadronically to increase the statistics; b–tagging is essential in this mass range [582, 583]. For higher Higgs masses, $M_H \gtrsim 140$ GeV, the channels with $b\bar{b} + 4W$ have to be considered, with again, at least two W bosons decaying hadronically, leading to 2 leptons plus 6 jets and one lepton plus 8 jets, respectively. The complexity of the final states and the small statistics requires a neural network analysis [582].

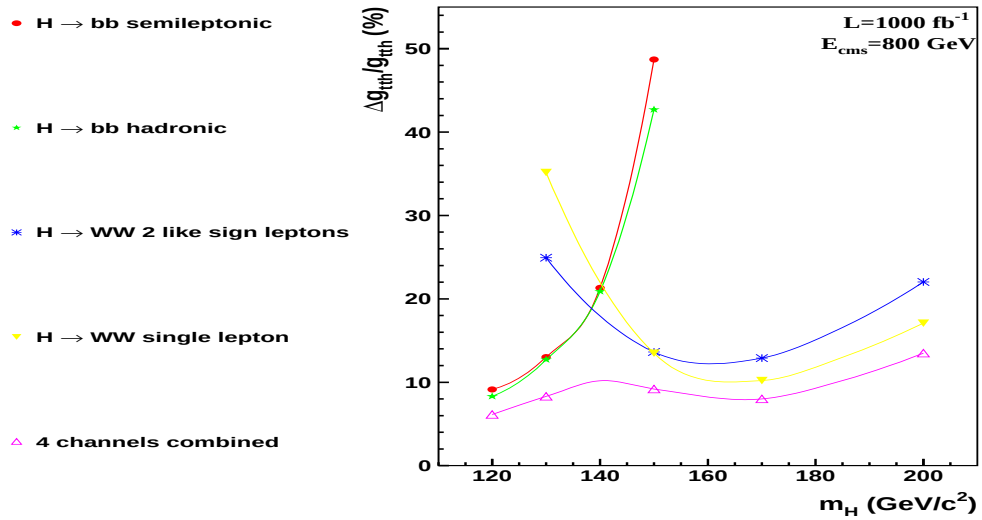

Figure 4.37: Expected accuracies for the measurement of the $Ht\bar{t}$ coupling as a function of M_H in the process $e^+e^- \to t\bar{t}H$ for $\sqrt{s} = 800$ GeV and 1 ab^{-1} in various decay channels. A 5% systematical error is assumed on the normalization of the background; from Ref. [582].

The expected accuracies on the $Ht\bar{t}$ Yukawa coupling are shown in Fig. 4.37 from Ref. [582] as a function of the Higgs mass, for $\sqrt{s} = 800$ GeV and a luminosity of 1 ab^{-1}. Assuming a 5% systematical uncertainty on the normalization of the background, accuracies on the $Ht\bar{t}$ Yukawa coupling of the order of 5% can be achieved for Higgs masses in the low range. A 10% measurement is possible up to Higgs masses of the order of 200 GeV.

For large masses, $M_H \gtrsim 350$ GeV, the $Ht\bar{t}$ coupling can be derived by measuring the $H \to t\bar{t}$ branching ratio with the Higgs boson produced in the strahlung and WW fusion processes [584, 585]. A detailed simulation, performed for the TESLA TDR in the latter channel, shows that once the $t\bar{t}$ and $e^+e^-t\bar{t}$ backgrounds are removed by requiring four light jets and two b quarks in the final state in addition to the missing energy, an accuracy of the order of 5% (12%) for a Higgs mass of 400 (500) GeV can be achieved on the top quark Yukawa coupling, again at $\sqrt{s} = 800$ GeV and with $\mathcal{L} \sim 1$ ab^{-1} data [586].

The trilinear Higgs coupling

The measurement of the trilinear Higgs self–coupling, which is the first non–trivial probe of the Higgs potential and, probably, the most decisive test of the electroweak symmetry breaking mechanism, is possible in the double Higgs–strahlung process. For Higgs masses in the range 120 GeV $\lesssim M_H \lesssim$ 140 GeV, one has to rely on the $b\bar{b}$ decays and the cross section in the $e^+e^- \to HHZ \to \bar{b}b\bar{b}b + \ell^+\ell^-$ or $q\bar{q}$ channels is rather small, see Fig. 4.20, while the four and six fermion background are comparatively very large.

The excellent b–tagging efficiencies and the energy flow which can be achieved at future linear colliders makes it possible to overcome the formidable challenge of suppressing the backgrounds, while retaining a significant portion of the signal. Accuracies of about 20% can be obtained on the measurement of the $e^+e^- \to HHZ$ cross section in the mass range below 140 GeV; see the left–hand side of Fig. 4.38. Neural network analyses allow to improve the accuracy of the measurement from 17% to 13% at a Higgs mass $M_H = 120$ GeV and to obtain a 6σ significance for the signal [587]; see also Ref. [588].

Since the sensitivity of the process $e^+e^- \to HHZ$ to the trilinear Higgs coupling is diluted by the additional contributions originating from diagrams where the Higgs boson is emitted from the Z boson lines, only an accuracy of $\Delta\lambda_{HHH} \sim 22\%$ can be obtained for $M_H = 120$ GeV at an energy of $\sqrt{s} \sim 500$ GeV with an integrated luminosity of $\mathcal{L} \sim 1$ ab^{-1}. The accuracy becomes worse for higher Higgs masses. In particular, for $M_H \gtrsim 140$ GeV, the $H \to WW^*$ decays must be used, leading to the even more complicated $4W{+}2f$ final state topologies. No experimental analysis of this topology has been attempted yet.

Also in this case, one can proceed to higher energy and take advantage of the WW fusion process $e^+e^- \to HH\nu\bar{\nu}$ [589, 590] which has a larger cross section, in particular with longitudinally polarized $e^\pm$ beams. The estimated sensitivity of the trilinear Higgs couplings to $\sqrt{s}$ is shown in the right–hand side of Fig. 4.38 for $M_H = 120$ and 150 GeV with polarized electron beams and no efficiency loss [589]. It is dominated by Higgs–strahlung at low energy and WW fusion for $\sqrt{s} \gtrsim 700$ GeV. A recent simulation at $\sqrt{s} = 1$ TeV which combines both the $e^+e^- \to HHZ$ and $e^+e^- \to HH\nu\bar{\nu}$ processes with $HH \to 4b$ final states, assuming a 80% e^-_L polarization and a luminosity of 1 ab^{-1}, shows that an accuracy of $\Delta\lambda_{HHH}/\lambda_{HHH} \sim 12\%$

may be achieved if the trilinear coupling is SM–like [589]. The relative phase of the coupling and its sign, may be also measured from the interference terms [558, 589].

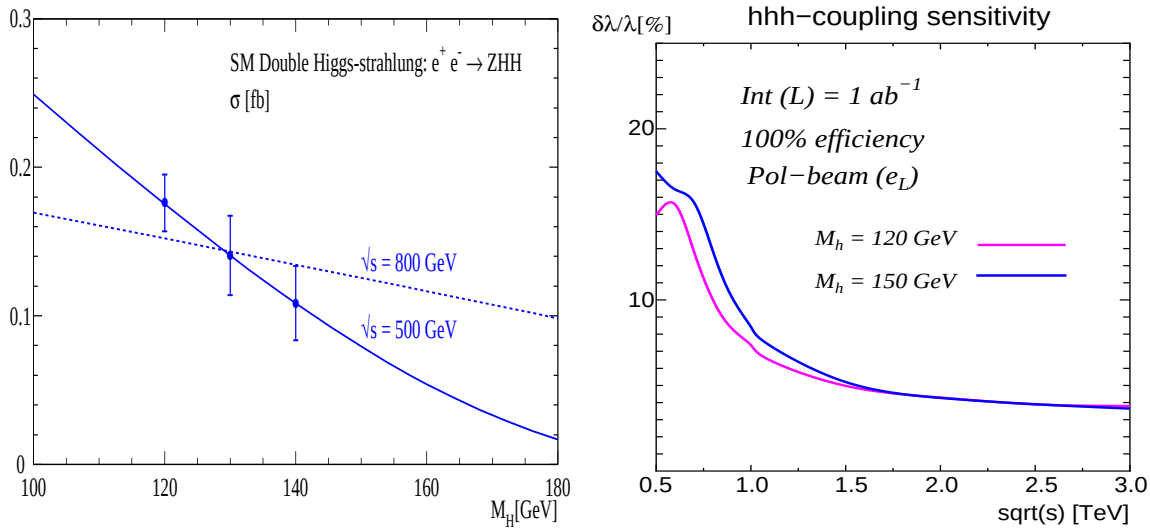

Figure 4.38: The accuracy in the determination of $\sigma(e^+e^- \to HHZ)$ for several Higgs masses at $\sqrt{s} = 500$ GeV with $\mathcal{L} = 1$ ab^{-1} (left) [587] and the sensitivity of λ_{HHH} to the c.m. energy for $\mathcal{L} = 1$ ab^{-1}, $P_L(e^-) = 100\%$ and without efficiency corrections (right) [589].

Expectations for a heavier Higgs boson

Finally, let us make a few remarks about a Higgs boson that is heavier than $2M_Z$, which has been recently discussed in Ref. [591]. In this case, all decay channels other than $H \to WW, ZZ$ are not accessible experimentally. The only exceptions are the $b\bar{b}$ decays for masses $M_H \lesssim 200$ GeV and the $t\bar{t}$ decays for $M_H \gtrsim 350$ GeV. However, the Higgs boson mass and its total decay width, as well as the production cross sections which provide the couplings to gauge bosons, can be obtained from the lineshape. Typical accuracies on these parameters are shown in Table 4.8 at a c.m. energy of 500 GeV with 500 fb^{-1}. The accuracies of the WW and ZZ branching are also shown for the same energy and luminosity [other decay channels have not been discussed yet]. Thus, relatively precise measurements can also be performed for heavier Higgs particles.

M_H(GeV)	$\Delta\sigma$(%)	ΔM_H(%)	$\Delta\Gamma_H$ (%)	ΔBR(WW) (%)	ΔBR(ZZ) (%)
200	3.6	0.11	34	3.5	9.9
240	3.8	0.17	27	5.0	10.8
280	4.4	0.24	23	7.7	16.2
320	6.3	0.36	26	8.6	17.3

Table 4.8: Expected precision on heavier Higgs lineshape parameters with 500 b^{-1} at $\sqrt{s} =$ 500 GeV [557] and on the WW/ZZ branching ratios with 1 ab^{-1} at $\sqrt{s} = 1$ TeV [574].

4.4.3 Combined measurements and the determination of the couplings

Once the Higgs production cross sections and the various decay branching ratios have been measured, one can derive the Higgs boson couplings to fermions and gauge bosons. This is a crucial test for the experimental verification that the Higgs mechanism is responsible for the generation of the masses of the particles. Since some of the couplings can be determined in different ways, while other determinations are partially correlated, a global fit to the various observables is highly desirable to extract the Higgs couplings in a model independent way. Such a fit would optimize the collected information and takes properly into account all the experimental correlations between the various measurements.

A dedicated program called HFITTER [592], based on HDECAY [214] for the calculation of the Higgs decay branching ratios, has been developed for this purpose. It uses as inputs the production cross sections $\sigma(e^+e^- \to HZ)$, $\sigma(e^+e^- \to H\nu\bar{\nu})$ and $\sigma(e^+e^- \to t\bar{t}H)$, and the branching ratios into $WW, \gamma\gamma, b\bar{b}, c\bar{c}, \tau^+\tau^-$ and gg. It uses the full covariance matrix for the correlated measurements, and the non–correlated measurement of the Higgs self–coupling from $\sigma(e^+e^- \to HHZ)$ can be added. The results for the accuracies on the Higgs couplings to fermions, gauge bosons and the self–coupling are displayed in Table 4.9 for $M_H = 120$ GeV and 140 GeV at a c.m. energy of 500 GeV with a luminosity of 500 fb^{-1} [except again for the measurement of g_{Htt} which has been performed at $\sqrt{s} = 800$ GeV with a luminosity of 1 ab^{-1}; the same luminosity is also used for the measurement of λ_{HHH}]. For completeness, we also display the errors on the Higgs boson mass, its total decay width and its CP–even component [ΔCP represents the relative deviation from the 0^{++} case], which have been measured at $\sqrt{s} = 350$ GeV with the same luminosity $\mathcal{L} = 500$ fb^{-1}.

As can be seen, an e^+e^- linear collider in the energy range $\sqrt{s} = 350$–800 GeV and a high integrated luminosity, $\mathcal{L} \sim 500$ fb^{-1}, is a very high precision machine in the context of Higgs physics. This precision would allow the determination of the complete profile of the SM Higgs boson, in particular if its mass is smaller than ~ 140 GeV. It would also allow to distinguish the SM Higgs particle from a scalar particle occurring in some of its extensions, with a very high level of confidence.

Thus, very precise measurements can be performed at the next linear collider allowing the detailed exploration of the electroweak symmetry breaking mechanism and the determination of the fundamental properties of the Higgs boson in the SM. We have seen in the previous section on hadron colliders that while the SM Higgs boson will undoubtedly be produced at the LHC, the detailed study of its properties will be a difficult task in the rather hostile hadronic environment. Due to the limited signal statistics for some channels, the large backgrounds and various systematic uncertainties, the LHC can provide only some ratios of Higgs couplings [as well as the Higgs mass and the total decay width for $M_H \gtrsim 200$ GeV, which can be measured rather well]. The measurement of the various absolute couplings can

Quantity	$M_H = 120$ GeV	$M_H = 140$ GeV
ΔM_H	$\pm$ 0.00033	$\pm$ 0.0005
Γ_H	$\pm$ 0.061	$\pm$ 0.045
ΔCP	$\pm$ 0.038	–
λ_{HHH}	$\pm$ 0.22	$\pm$ 0.30
g_{HWW}	$\pm$ 0.012	$\pm$ 0.020
g_{HZZ}	$\pm$ 0.012	$\pm$ 0.013
g_{Htt}	$\pm$ 0.030	$\pm$ 0.061
g_{Hbb}	$\pm$ 0.022	$\pm$ 0.022
g_{Hcc}	$\pm$ 0.037	$\pm$ 0.102
$g_{H\tau\tau}$	$\pm$ 0.033	$\pm$ 0.048

Table 4.9: Relative accuracy on Higgs couplings obtained from a global fit. An integrated luminosity of 500 fb^{-1} at $\sqrt{s} = 500$ GeV is assumed except for the measurement of $g_{Htt}(\lambda_{HHH})$, which assumes 1000 fb^{-1} at $\sqrt{s} = 800$ (500) GeV in addition. On top of the table we display the accuracies on the Higgs mass, the total width and its CP–component as obtained at $\sqrt{s} = 350$ GeV with 500 fb^{-1}.

be performed only at an e^+e^- collider. There is therefore a clear complementarity between the LHC and the linear collider Higgs physics programs.

From the previous discussions, one can single out two physics points for which e^+e^- colliders have some weakness: the determination of the total width is rather poor [without the $\gamma\gamma$ option] for low mass Higgs bosons and the CP–quantum numbers cannot be determined in a very convincing way for $M_H \gtrsim 140$ GeV when the $H \to \tau^+\tau^-$ decay mode becomes too rare. Unambiguous tests of the CP properties of the Higgs boson can be performed at photon colliders in the loop induced process $\gamma\gamma \to H$ or at muon colliders in the process $\mu^+\mu^- \to H$, if suitable polarization of the initial beams is available. The measurement of Γ_H can benefit from the precise determination of the Higgs photonic width at $\gamma\gamma$ colliders. However, it is at the muon collider that extremely good accuracies on Γ_H can be obtained by simply performing a threshold scan around the Higgs resonance produced in $\mu^+\mu^- \to H$. These topics will be addressed in detail in the next section. Before that, we first briefly summarize the benefits of raising and lowering the energy of the e^+e^- collider.

4.4.4 Measurements at higher and lower energies

Measurements at CLIC

Some of the previously discussed measurements can significantly benefit from an increase of statistics. This can be obtained not only by increasing the luminosity, but also by raising the energy. Indeed, at the c.m. energies relevant for CLIC, $\sqrt{s} \sim 3$ TeV, the cross section for the WW fusion process becomes extremely large. If the luminosity is also scaled with s, a sample of more than one million Higgs particles can be collected for $\mathcal{L} = 3$ ab^{-1}. Some of the previous measurements could thus be performed with more accuracy and new ones could be made possible. Examples of such measurements at CLIC are as follows [484]:

i) With $\mathcal{L} = 3$ ab^{-1} at a c.m. energy of 3 TeV, 400 $H \to \mu^+\mu^-$ events can be collected for $M_H = 120$ GeV. This sample would allow the measurement of the Higgs couplings to muons to better than 5% [the precision drops to 10% for $M_H = 150$ GeV due to the smaller branching ratio]. The dimuon signal can be isolated from the important $WW, WW\nu\bar{\nu}, ZZ\nu\bar{\nu}$ backgrounds with a statistical significance which is rather large; see the left–hand side of Fig. 4.39. This would be the first precise measurement of the Higgs couplings to second generation fermions since, as seen previously, although the $Hc\bar{c}$ coupling can be determined with the same accuracy, the associated theoretical uncertainties are rather large.

ii) The $H \to b\bar{b}$ branching ratio becomes very small in the intermediate and high Higgs mass ranges, and at $\sqrt{s} = 500$ GeV, it cannot be determined to better than 10% for $M_H \sim 200$ GeV. At $\sqrt{s} = 3$ TeV, the signal to background ratio is very favorable at these masses, as shown in the right–hand side of Fig. 4.39, and the rather large number of events to be collected at CLIC would allow a measurement of the $Hb\bar{b}$ coupling with an accuracy of 5% for Higgs masses up to about $M_H = 250$ GeV.

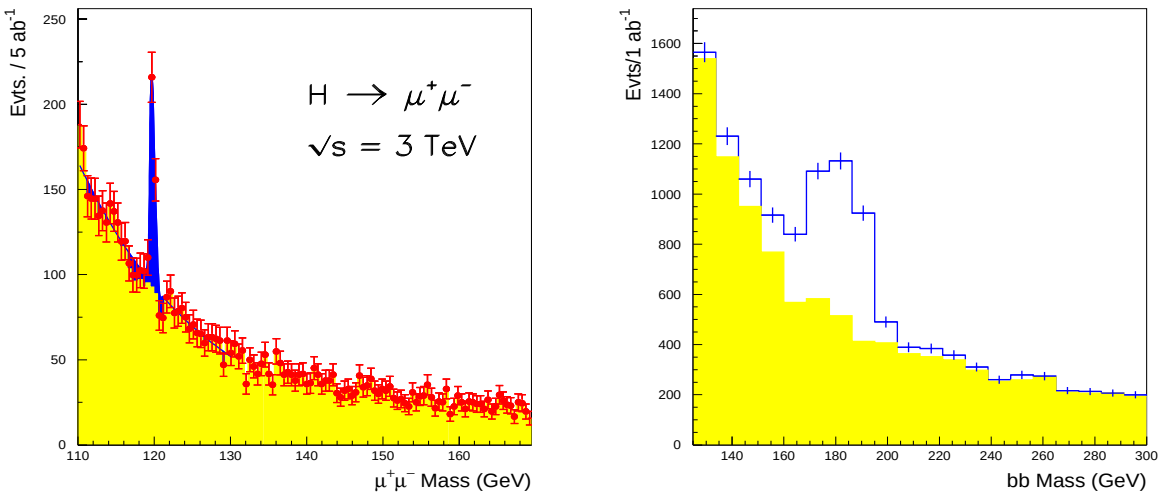

Figure 4.39: The reconstructed signals for $e^+e^- \to \nu\bar{\nu}H \to \nu\bar{\nu}\mu^+\mu^-$ for $M_H = 120$ GeV (left) and $e^+e^- \to \nu\bar{\nu}H \to \nu\bar{\nu}b\bar{b}$ for $M_H = 200$ GeV (right) at CLIC with $\sqrt{s}$=3 TeV [550].

iii) The trilinear Higgs coupling can be measured in the WW fusion process, $e^+e^- \to \nu\bar{\nu}HH$, for which the cross section reaches the level of a few fb at energies around 3 TeV. A relative accuracy of $\sim 10\%$ can be obtained on this coupling for Higgs masses up to 250 GeV. Contrary to what occurs in the process $e^+e^- \to HHZ$, the interference between the diagram involving the self–Higgs coupling and the others, is negative. The sensitivity to λ_{HHH} can be enhanced by studying the angle θ^* of the $H^* \to HH$ system in its rest frame: because of the scalar nature of the Higgs boson, the $\cos\theta^*$ distribution is flat for $H^* \to HH$ while it is peaked in the forward direction for the other diagrams [545]; see the left–hand side of Fig. 4.40. From a fit of the distribution one can perform a very nice determination of the λ_{HHH} coupling as shown in the right–hand side of Fig. 4.40. Note that the quadrilinear Higgs couplings remains elusive, even at c.m. energies of 5 TeV.

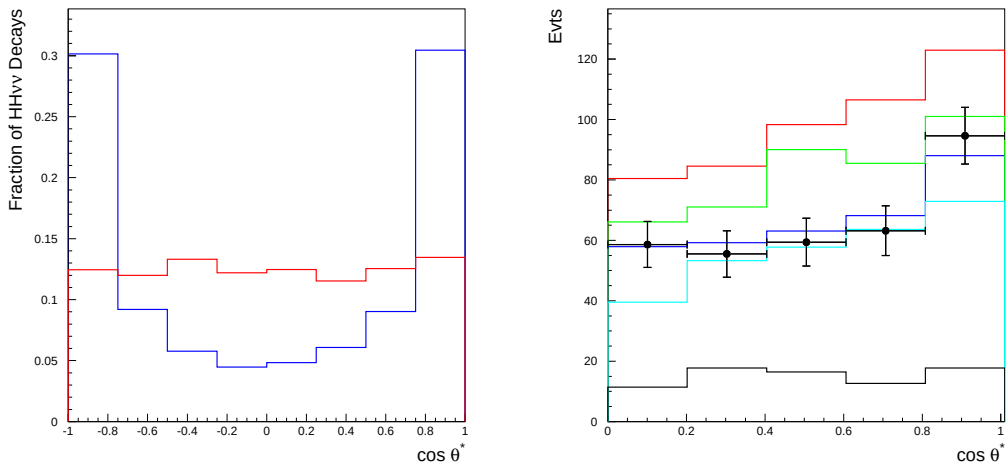

Figure 4.40: The $\cos\theta^*$ distribution in the process $e^+e^- \to HH\nu\bar{\nu}$ due to the diagram containing the triple Higgs vertex (red/light grey) and other diagrams (blue/dark grey) for $M_H = 120$ GeV at $\sqrt{s}$=3 TeV (left) and the reconstructed $|\cos\theta^*|$ distribution for $\lambda_{HHH}/\lambda_{HHH}^{\rm SM}$ =1.25,1.0,0.75 and 0.5 from bottom to top, with the points with error bars showing the expectation for 5 ab^{-1} of data (right); from Ref. [550].

The higher energy of the collider can also be very useful in the case where the Higgs boson is very heavy. For $M_H \sim 700$ GeV and beyond, the cross sections in the Higgs–strahlung and WW fusion processes are small at $\sqrt{s} \sim 1$ TeV [see Fig. 4.30] and do not allow to perform detailed studies. At CLIC energies, $\sqrt{s} = 3$ TeV, one has $\sigma(e^+e^- \to H\nu\bar{\nu}) \sim 150$ fb which allows for a reasonable sample of Higgs particles to be studied. In addition, the cross section for the ZZ fusion process is large enough, $\sigma(e^+e^- \to He^+e^-) \sim 20$ fb for $M_H \sim 700$ GeV, to allow for model independent Higgs searches in much the same way as in the Higgs–strahlung process at low energies, since the forward electron and positron can be tagged, and the mass recoiling against them can be reconstructed. The high energy available at CLIC will also be important to investigate in detail a possible strongly interacting Higgs sector scenario, as will be discussed in another part of this review.

The GigaZ and MegaW options

The high luminosities available at the next generation of e^+e^- colliders would allow to collect more than 10^9 Z bosons in one year by running at energies close to the resonance. The same luminosity would allow to collect more than 10^6 W boson pairs near the WW threshold. These samples are two orders of magnitude larger than those obtained at LEP1 and LEP2 and can be used to significantly improve the high–precision tests of the SM which have been performed in the last decade [486].

At GigaZ, using the possibility of polarizing the electron/positron beams, one can measure the longitudinal left–right asymmetry $A_{LR} = 2a_e v_e/(a_e^2 + v_e^2) \sim 2(1 - 4\sin^2\theta_{\rm eff}^{\rm lep})$ with a very high statistical accuracy in hadronic and leptonic Z decays. Using the Blondel scheme [593], the asymmetry can be obtained from the cross sections when the polarization of both the electron and positron beams $P_{e^\pm}$ are used in the various combinations, $\sigma = \sigma_{\rm unpol}[1 - P_{e^+}P_{e^-} + A_{LR}(P_{e^+} - P_{e^-})]$, leading to a systematical error of about 10^{-4}. This corresponds to a measurement of the electroweak mixing angle with a precision

$$\Delta \sin^2\theta_{\rm eff}^{\rm lep} \simeq 1.3 \times 10^{-5} \tag{4.56}$$

which is one order of magnitude more accurate than the presently measured value, $\sin^2\theta_{\rm eff}^{\rm lep} = 0.2324 \pm 0.00012$. The measurement of the total and partial Z decay widths and the various polarization and/or forward–backward asymmetries can be significantly improved. In particular, the measurement of the ratio of leptonic to hadronic Z decay widths with an expected accuracy of $\Delta R_\ell/R_\ell \sim 0.05\%$, would allow a clean measurement of the strong coupling constant to better than $\Delta\alpha_s \simeq 0.001$.

On the other hand, one can perform a scan around the WW threshold, where the cross section for W pair production rises quickly, $\sigma(e^+e^- \to W^+W^-) \sim \beta$, allowing an accurate measurement of the W boson mass. With an integrated luminosity of only $\mathcal{L} \simeq 100$ fb^{-1} at $\sqrt{s} \sim 2M_W$ and a 6 point scan, the mass can be measured with an accuracy

$$\Delta M_W \simeq 6 \text{ MeV} \tag{4.57}$$

which is six times better than the present measurement, $M_W = 80.449 \pm 0.034$ GeV, and almost three times the precision which can be reached at the LHC and at the LC.

Since the top quark mass, which leads to the major part of the theoretical uncertainties in the present high–precision observables, will be measured with an accuracy of $\Delta m_t \simeq 200$ MeV at the LC and that α_s will be known more precisely at this time, $\Delta\alpha_s \simeq 0.001$, the only dangerous source of errors from SM inputs will be the hadronic uncertainty in $\Delta\alpha$. One might hope that with the low energy e^+e^- experiments which will be performed in the future, the error will reduce to $\Delta\alpha^{\rm had} \simeq 5 \times 10^{-5}$. Taking into account also the error $\Delta M_Z \simeq 2$ MeV

on the Z boson mass, which at this level of precision induces an error on $\sin^2\theta_{\rm eff}^{\rm lep}$ which is of the same size as the experimental error, the future total theoretical uncertainties on the two observables from the various sources are estimated to be [594]

$$\Delta \sin^2\theta_{\rm eff}^{\rm lep} \simeq \pm 3 \times 10^{-5} \ , \ \Delta M_W \simeq \pm 3 \text{ MeV} \tag{4.58}$$

The very small experimental and theoretical errors on these two parameters will allow to test the SM on much more solid grounds than in the past and to isolate the effects of the Higgs boson in the electroweak radiative corrections with an incredible accuracy. This is exemplified in the left–hand side of Fig. 4.41 where the expected accuracy in the determination of the Higgs mass at GigaZ/MegaW in the plane M_H–m_t, together with the allowed bands for $\sin^2\theta_{\rm eff}^{\rm lep}$ and M_W, are shown. The central values of the various input parameters and the Higgs mass, as well as the area labeled "now", are for the measurements which were available in the year 2000. One can simply notice the vast improvement which can be made at the GigaZ/MegaW option, where one can indirectly measure the Higgs boson mass with a precision of $\Delta M_H/M_H \sim 7\%$ [594]. One can also use the direct measurement of the Higgs boson mass at the LC (and LHC) with $\Delta M_H \simeq 50$ MeV, to predict the value of $\sin^2\theta_{\rm eff}^{\rm lep}$ and M_W and to check the consistency of the SM, as shown in the right–hand side of Fig. 4.41. Because of the high–precision which can be reached at GigaZ/MegaW, the improvement compared to the present situation and even after LHC/LC is again spectacular.

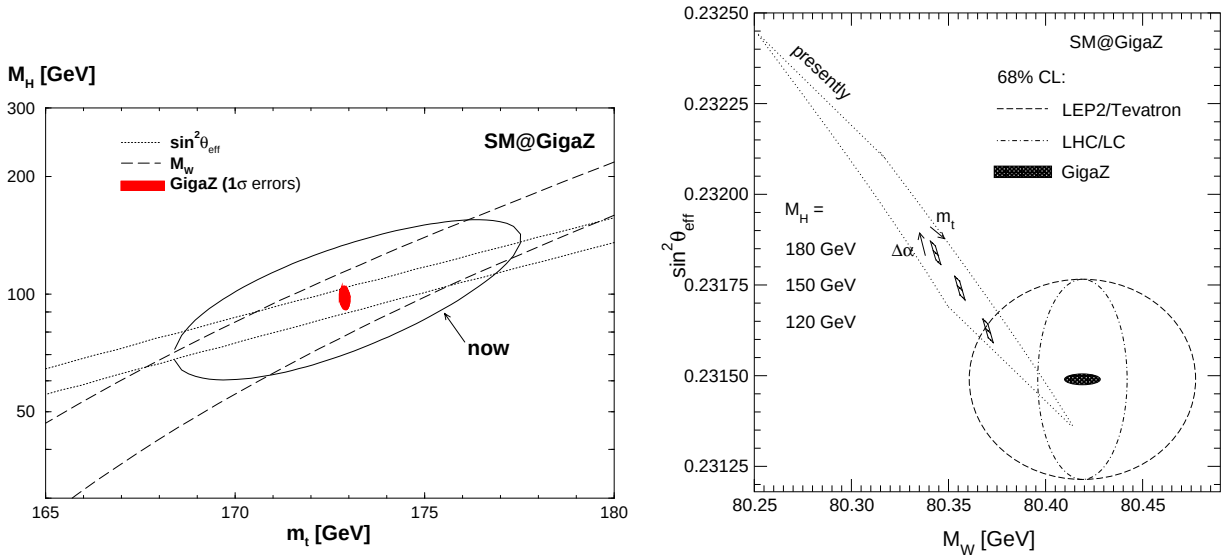

Figure 4.41: The allowed region in the M_H–m_t plane after the precision measurements at GigaZ/MegaW compared to the situation in the year 2000 (left) and the theoretical predictions for $\sin^2\theta_{\rm eff}^{\rm lep}$ and M_W for three M_H values compared to the experimental measurements at LEP2/Tevatron, LHC/LC and after GigaZ/MegaW. The various theoretical and experimental uncertainties are as discussed in the text; from Ref. [594].

4.5 Higgs production in $\gamma\gamma$ collisions

As discussed in §4.1.2, future high–energy e^+e^- linear colliders can be made to run in the $e\gamma$ or $\gamma\gamma$ modes by using Compton back scattering of laser light off the high–energy electron beams [487, 488]. These colliders will have practically the same energy, up to $\sim 80\%$, as the original e^+e^- collider and a luminosity that is somewhat smaller. One of the best motivations for turning to the $\gamma\gamma$ mode of the linear collider is undoubtedly the study of the properties of the Higgs boson, which can be produced as a resonance in the s–channel [489–492]. In this context, two main features which are difficult to study in the e^+e^- mode can be investigated at such colliders: first, the precise measurement of the $H\gamma\gamma$ coupling [595–599] and second, the determination of the CP–properties of the Higgs boson [160, 599–604]. Several other studies can also be made, such as the measurement of the Higgs boson self–coupling and its Yukawa coupling to top quarks, although these studies can be already performed in e^+e^- collisions [and, in general, in a much cleaner way].

4.5.1 Higgs boson production as an s–channel resonance

The production cross section for the process $\gamma\gamma \to X$ with initial state polarized photons, can be written in the helicity basis as

$$\mathrm{d}\hat{\sigma}_{\gamma\gamma} = \sum_{i,j,k,l=\pm} \rho^1_{ik}\, \rho^2_{jl} M_{ij} M^*_{kl}\, \mathrm{d}\Gamma \tag{4.59}$$

where M_{ij} are the invariant scattering amplitudes with photon helicities $i, j = \pm 1$ and $\mathrm{d}\Gamma$ the phase space element divided by the incoming flux. Comparing to the cross section written in the Stokes parameter basis, the elements of the photon polarization density matrix are such that $\rho^i_{\pm\pm} = \frac{1}{2}(1 \pm \xi_{i2}), \rho^i_{+-} = \rho^{i*}_{-+} = -\frac{1}{2}(\xi_{i3} - i\xi_{i1})$. The unpolarized cross section is

$$\begin{aligned} \mathrm{d}\hat{\sigma} &= \mathrm{d}\hat{\sigma}_{00} = \frac{1}{4}\mathrm{d}\Gamma \left(|M_{++}|^2 + |M_{--}|^2 + |M_{+-}|^2 + |M_{-+}|^2\right) \\ &= \frac{1}{2}(\mathrm{d}\hat{\sigma}_{J_Z=0} + \mathrm{d}\hat{\sigma}_{J_Z=\pm 2}) = \frac{1}{2}(\mathrm{d}\hat{\sigma}_{||} + \mathrm{d}\hat{\sigma}_{\perp}) \end{aligned} \tag{4.60}$$

where $\mathrm{d}\hat{\sigma}_{J_Z=0}\,(\mathrm{d}\hat{\sigma}_{J_Z=\pm 2})$ are the cross sections for photons with total helicity $0\,(\pm 2)$ and $\mathrm{d}\hat{\sigma}_{||}\,(\mathrm{d}\hat{\sigma}_{\perp})$ is for parallel (orthogonal) linear photon polarizations.

In the case of a spin–zero particle, the production occurs through the $J_Z = 0$ channel. In terms of the Higgs total decay width Γ_H, the width into two photons $\Gamma(H \to \gamma\gamma)$ and into a given final state, $\Gamma(H \to X)$, the cross section for the subprocess $\gamma\gamma \to H$ is given by

$$\hat{\sigma}(W) = 8\pi \frac{\Gamma(H \to \gamma\gamma)\Gamma(H \to X)}{(W^2 - M_H^2)^2 + M_H^2 \Gamma_H^2}\,(1 + \lambda_1\lambda_2) \tag{4.61}$$

where W is the invariant mass of the $\gamma\gamma$ system. Using the same photon helicities $\lambda_1\lambda_2 = 1$ projects out the $J_Z = 0$ component and therefore maximizes the Higgs cross section.

For masses below $M_H \sim 2M_Z$, the Higgs boson is very narrow with a total decay width $\Gamma_H \lesssim 1\,\text{GeV}$ and, therefore, the detector resolution should be taken into account. When the Higgs width can be neglected, a rather simple way to obtain the effective signal cross section is to introduce a Gaussian smearing of the $\gamma\gamma$ invariant mass W [490]

$$N_{\text{eff}} = \mathcal{L}_{\text{eff}} \frac{\mathrm{d}\sigma^{\text{eff}}}{\mathrm{d}W}(W) = \int_{M_X}^{y_m\sqrt{s_{e^+e^-}}} \mathrm{d}W' \frac{1}{\sqrt{2\pi}\delta} \exp\left(-\frac{(W'-W)^2}{2\delta^2}\right) \frac{\mathrm{d}\mathcal{L}}{\mathrm{d}W'} \langle\hat{\sigma}(W')\rangle \quad (4.62)$$

and select events within bins of invariant masses $M_H \pm \Delta$, where the Higgs mass is assumed to be precisely known already. In the previous expression, $\mathcal{L}_{\text{eff}}$ and $y_m\sqrt{s_{e^+e^-}}$ are the effective luminosity and the maximum energy of the $\gamma\gamma$ collider and δ is one sigma of the detector resolution for W. The cross section for the signal process $\gamma\gamma \to H \to X$ can be written as [for $\Gamma_H \ll M_H$, $\Gamma_H M_H[(W^2 - M_H^2)^2 + M_H^2\Gamma_H^2]^{-1} \simeq \frac{\pi}{2M_H}\delta(W - M_H)$]

$$\hat{\sigma}_{\text{signal}}(W) = 4\pi^2 \frac{\Gamma(H\to\gamma\gamma)\text{BR}(H\to X)}{M_H^2}(1+\lambda_1\lambda_2)\delta(W-M_H) \quad (4.63)$$

Inserting this expression in eq. (4.62), and selecting the events in the bin $M_H \pm \Delta$, one has

$$\mathcal{L}_{\text{eff}}\ \sigma^{\text{eff}}_{\text{signal}}(M_H) = R(\Delta/\delta)\ \frac{\mathrm{d}\mathcal{L}}{\mathrm{dW}}^{J_Z=0}\Big|_{W=M_H} 4\pi^2 \frac{\Gamma(H\to\gamma\gamma)\text{BR}(H\to X)}{M_H^2} \quad (4.64)$$

with $R(\Delta/\delta)$ being the Gaussian error function giving the fraction of signal events contained in the bin $M_H \pm \Delta$ [for instance, for $\Delta = 2\delta$ one has $R \simeq 0.95$].

The effective background, $\gamma\gamma \to X$, for an effective invariant mass of the two–photon system $W = M_H$ can be approximated by

$$N^{\text{eff}}_{\text{bckg}}(W) \simeq 2\Delta \frac{\mathrm{d}\mathcal{L}}{\mathrm{d}W} \langle \mathrm{d}\hat{\sigma}_{\text{bckg}}(W)\rangle \quad (4.65)$$

if one assumes a smooth enough distribution of two–photon invariant masses weighted with luminosity distributions.

To have a large effective cross section for the Higgs boson signal, the $\gamma\gamma$ energy must be tuned at the peak, $0.8\sqrt{s}_{e^+e^-} \sim M_H$ for a perfect spectrum, while the luminosity with circularly polarized laser photon and electron beams are chosen so that they have opposite handedness with $x = 4.83$. The $J_Z = 0$ events containing the signal are then enhanced, while the $J_Z = \pm 2$ events are suppressed [488, 605].

The measurement of the $\Gamma(H \to \gamma\gamma) \times \text{BR}(H \to X)$ rate and, thus, the $H\gamma\gamma$ coupling squared if the branching ratio is known, will follow from eq. (4.64) if the effective luminosity and the Higgs mass are specified, and from the signal and background rates. The statistical error in the decay width times branching ratio determination is

$$\Delta(\Gamma\times\text{BR})/(\Gamma\times\text{BR}) = (\mathcal{L}_{\text{eff}})^{-1} S^{-1}\sqrt{S+B} \quad (4.66)$$

Low mass Higgs boson

In the low mass range, $M_H \lesssim 130$ GeV, the Higgs boson will mainly decay into $b\bar{b}$ final states, $H \to b\bar{b}$, and the main source of background is the continuum production of b– and c–quark pairs [606], including gluon radiation which leads to fake two–jet events [607]. The total cross section for heavy quark production, $\gamma\gamma \to q\bar{q}$, with a polar cut in the center of mass of the two–photon system $|\cos\theta| < c$ is given, at the tree–level, by

$$\begin{aligned}
\hat{\sigma}_{J_Z=0}(W) &= \frac{12\pi\alpha^2 Q_q^4}{W^2}\frac{8m_q^2}{W^2}\left(1-\frac{2m_q^2}{W^2}\right)\left[\frac{1}{2}\log\frac{1+c\beta}{1-c\beta}+\frac{c\beta}{1-c^2\beta^2}\right] \\
\hat{\sigma}_{J_Z=2}(W) &= \frac{12\pi\alpha^2 Q_q^4}{W^2}\left[\frac{1}{2}(5-\beta^4)\log\frac{1+c\beta}{1-c\beta}-c\beta\left(2+\frac{(1-\beta^2)(3-\beta^2)}{1-c^2\beta^2}\right)\right] \quad (4.67)
\end{aligned}$$

with the quark velocity $\beta = \sqrt{1-4m_q^2/W^2}$ and electric charge Q_q. One can choose $c = 0.7$ which helps to eliminate many background events which are peaked in the forward and backward directions, with only a moderate loss of the signal events. In addition, as can be seen, the contribution of the $J_Z = 0$ channel is proportional to m_q^2/W^2 and is therefore strongly suppressed [606]. Choosing the configuration where $\lambda_1\lambda_2 = 1$ helps to suppress the two–jet background, while it maximizes the signal cross section; see e.g. Refs. [488, 605].

The background cross sections receive important QCD radiative corrections [607, 608], which are particularly large for the $J_Z = 0$ component to which additional continuum $q\bar{q}g$ final states contribute [one can select slim two–jet final state configurations to suppress this gluon radiation contribution to the $J_Z = 0$ amplitude], and also non–negligible electroweak corrections [609]. The radiative corrections to the signal cross section discussed in §2.3.1, and the corrections to the interference between the signal and background cross sections [610] have to be taken into account. In addition, one has to consider low energy $\gamma\gamma \to$ hadrons processes which contribute to the overlaying events [611]. The overlaying events are peaked in the forward and backward directions and can be suppressed by the angular cut. b–tagging is of course mandatory and one can take advantage of the fact that the Higgs boson is produced almost at rest so that the total longitudinal momentum of the visible particles is smaller than the total visible energy.

A full simulation, which uses a realistic spectrum for the photon collider and includes the overlaying $\gamma\gamma \to$ hadrons events, as well as a realistic b–tagging, has been recently performed [596]. The signal and backgrounds events have been generated with all the relevant higher–order corrections and including the fragmentation into hadrons, and the expected response of the detector has been taken into account. Cuts such as those discussed above have been applied and the output is shown in Fig. 4.42 where the energy of the original collider, $\sqrt{s_{ee}} = 210$ GeV leading to a yearly luminosity of $\mathcal{L}_{\gamma\gamma} = 410$ fb^{-1}, has been optimized for the production of a Higgs boson with a mass $M_H = 120$ GeV.

The left–hand side of the figure displays the reconstructed invariant mass distribution of the selected $b\bar{b}$ events, when it is corrected to take into account the effect of the undetected neutrinos. The Higgs boson signal as well as the $b\bar{b}(g)$ and $c\bar{c}(g)$ backgrounds including the overlaying events are displayed for $M_H = 120$ GeV at the luminosity of 410 fb^{-1}. The most precise measurement of the $H \to \gamma\gamma$ width is obtained in the mass window 110–150 GeV which is indicated. With the assumed luminosity, about 7000 signal events are reconstructed with about 9000 background events surviving the cuts, leading to a signal over background ratio of order one. Therefore, a statistical accuracy of 1.8% can be achieved on the measurement of $\Gamma(H \to \gamma\gamma) \times \mathrm{BR}(H \to b\bar{b})$. The right–hand side of the figure shows the accuracy of the measurement of $\Gamma(H \to \gamma\gamma) \times \mathrm{BR}(H \to b\bar{b})$ for various Higgs mass values, with and without the inclusion of the overlaying events (OE). Again, this is the result of a full simulation where the energy of the initial collider has been optimized to produce a Higgs boson with a mass $M_H = 130, 140, 150$ and 160 GeV. A precision of 2–7% can be obtained in the entire Higgs mass range $M_H = 120$–160 GeV.

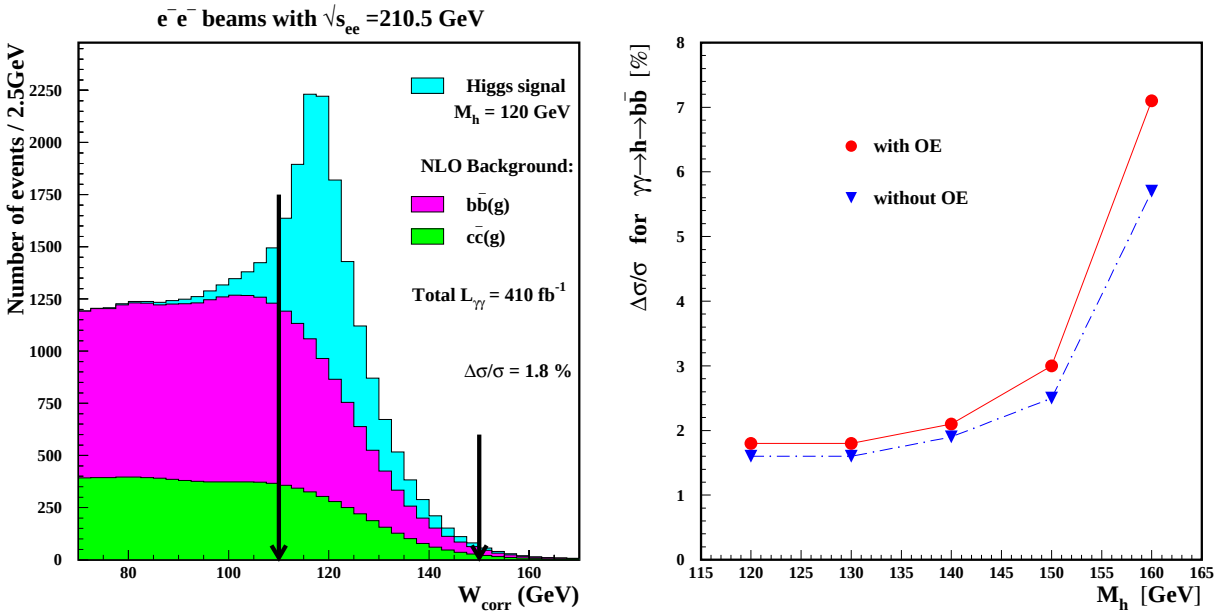

Figure 4.42: The reconstructed invariant mass distribution of the $b\bar{b}$ signal and the $b\bar{b}(g)$ and $c\bar{c}(g)$ backgrounds for $M_H = 120$ GeV at the luminosity of 410 fb^{-1} (left) and the accuracy of the measurement of the cross section $\sigma(\gamma\gamma \to H \to b\bar{b})$ for various Higgs mass values, with and without the inclusion of the overlaying events (right); from Ref. [596].

From the measurement of the branching ratio of the Higgs decays into bottom quarks which, as seen previously, can be made with an accuracy of 1.5% for $M_H = 120$ GeV [see Table 4.6], the partial decay width $\Gamma(H \to \gamma\gamma)$ can be extracted with a precision of 2.3%. With a precise measurement of the $H \to \gamma\gamma$ branching ratio in the e^+e^- mode of the collider, one can determine the Higgs total width with an accuracy of the order of 10%.

Heavier Higgs bosons

For masses larger than $M_H \sim 140$ GeV, the Higgs boson decays predominantly into massive gauge bosons, $H \to WW$ and $H \to ZZ$, the branching ratios being $\sim 2/3$ and $1/3$, respectively, for the charged and neutral decays for M_H above the ZZ threshold. The total Higgs decay width becomes significant, being of the order of $\Gamma_H \sim 1.5\,(8)$ GeV for $M_H = 200\,(300)$ GeV, and cannot be neglected anymore. However, the total production cross section of such heavy Higgs particles is of the same order as the one discussed previously, once the energy of the $\gamma\gamma$ collider is tuned to the Higgs boson mass.

The backgrounds for the production of such a Higgs boson at $\gamma\gamma$ colliders are vector boson production, $\gamma\gamma \to W^+W^-$ and $\gamma\gamma \to ZZ$. The former process occurs at the tree–level and has an extremely large cross section, $\sigma(\gamma\gamma \to W^+W^-) \sim \mathcal{O}(10^2$ pb) in both the $J_Z = 0$ and $J_Z = \pm 2$ channels [612,613]. This background cannot therefore be very efficiently suppressed by selecting only the $J_Z = 0$ channel in which the Higgs boson is produced. The only region where the signal and backgrounds have similar rates is for $M_H \sim 170$ GeV, where the Higgs boson decays almost 100% of the time into WW bosons, while the background cross sections are not yet too large since they increase with higher photon c.m. energy [598].

In the case of ZZ boson final states, the background is generated only at the one–loop level [597] since the Z boson is neutrally charged and does not couple directly to photons. It is therefore much less dangerous than the WW background: for c.m. energies of the order of $\sqrt{s}_{\gamma\gamma} \sim 200 - 300$ GeV, the cross section is at the level $\sigma(\gamma\gamma \to ZZ) \sim \mathcal{O}(10^2$ fb) in the $J_Z = 0$ channel. Therefore, for $M_H \gtrsim 180$ GeV where the ZZ Higgs branching ratio becomes significant, the cross section is dominated by the Higgs boson contribution.

For photons colliding with a total angular momentum $J_Z = 0$, the interference between the signal $\gamma\gamma \to H \to VV$ and the background $\gamma\gamma \to VV$ must be taken into account. For WW final states, the interference is very large: for $M_H \gtrsim 200$ GeV, this term is negative and is larger than the resonant contribution from the Higgs boson, leading to a decrease of the total WW cross section. For ZZ production, the interference term is rather small, although it has visible effects, resulting for instance in an asymmetric Higgs resonance. Thus, in addition to the extraction of the $H\gamma\gamma$ couplings as in the $H \to b\bar{b}$ case discussed before, these processes could in principle allow for the determination of the phase of the $H\gamma\gamma$ amplitude via a measurement of the interference term which is sensitive to it.

A detailed simulation has been also performed in these two channels [599] and the analysis follows the same lines as what has been previously discussed in the case of $\gamma\gamma \to H \to b\bar{b}$. The cuts have been optimized to select the final states $H \to WW \to q\bar{q}q\bar{q}$ and $H \to ZZ \to q\bar{q}\ell\ell$. The center of mass energy of the original electron collider has been tuned to optimize Higgs production: for $\sqrt{s_{ee}} = 305\,(500)$ GeV, which is the optimal choice for $M_H = 200\,(350)$ GeV, a luminosity of about 600 (1000) fb^{-1} can be collected in a photon collider such as the

one discussed for TESLA. Once the distributions of the reconstructed invariant masses for $\gamma\gamma \to WW$ and ZZ are obtained experimentally, one can fit the simulated mass distributions with the width $\Gamma_{\gamma\gamma}$ and the phase $\phi_{\gamma\gamma}$ as being the only free parameters.

The output is shown in Fig. 4.43 where the statistical accuracies expected for the $\Gamma_{\gamma\gamma}$ width and the $\phi_{\gamma\gamma}$ phase are displayed for four examples of Higgs masses $M_H = 200, 250, 300$ and 350 GeV. The solid thick light (yellow) line shows for comparison the prediction in a specific two–Higgs doublet model (2HDM). As can be seen for low Higgs masses, $M_H \sim 200$ GeV, the width can be measured with a precision $\Delta\Gamma_{\gamma\gamma} \simeq 3\%$ which is similar to the accuracy obtained in the case of $H \to b\bar{b}$. For this Higgs mass value, the phase can be measured with an accuracy of $\Delta\phi_{\gamma\gamma} \sim 35$ mrad. For higher Higgs masses, the uncertainties increase and for $M_H = 350$ GeV, they are a factor of three larger. Note that the phase is mainly constrained by the WW process as expected, while the width is more accurately measured in the channel $ZZ \to q\bar{q}\ell\ell$ as the background is smaller. Thus, it is only the combination of the two processes which allow to determine both parameters.

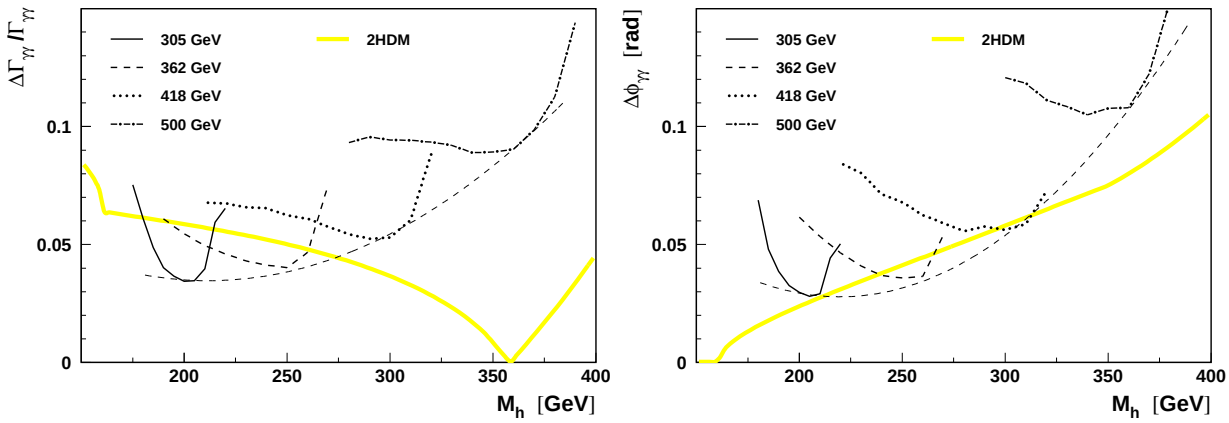

Figure 4.43: Expected statistical errors in the determination of the Higgs width $\Gamma_{\gamma\gamma}$ (left) and phase $\phi_{\gamma\gamma}$ (right) at a photon collider, from the simultaneous fit to the observed W^+W^- and ZZ mass spectra. The yellow (thick light) band shows the prediction in a 2HDM [599].

For even heavier Higgs bosons, $M_H \gtrsim 350$ GeV, the $H \to t\bar{t}$ decays can be in principle exploited. However, the branching fraction is not very large, $\mathrm{BR}(H \to t\bar{t}) \sim 15\%$ for $M_H \simeq 400$ GeV, and becomes even smaller for higher masses. The main background process $\gamma\gamma \to t\bar{t}$ has a much larger cross section [which is still given by eq. (4.67)] compared to b–quark production, first because of the larger charge $Q_t = +2/3$ with the cross section being proportional to Q_q^4, and second, because the $J_Z = 0$ contribution is not suppressed since the top quark mass is of the same order as the effective $\gamma\gamma$ energy. Furthermore, the total width of the Higgs boson becomes too large, $\Gamma_H \sim 30$ GeV for the previous mass value, and the particle is not a narrow resonance anymore; because of this large Γ_H value, one has to

integrate the continuum background over a rather large bin.

For all these reasons, the process $\gamma\gamma \to H \to t\bar{t}$ is expected to be a rather difficult channel to exploit. However, it can provide some valuable information on the CP properties of the produced Higgs particle [601–604], a subject to which we turn our attention now.

4.5.2 Measuring the CP–properties of the Higgs boson

Measurements using photon polarization

The general amplitude for the production of a spin–zero Higgs particle in two–photon collisions, $\gamma\gamma \to H$, cand be written in terms of the CP–even and CP–odd components of the $H\gamma\gamma$ coupling which are proportional to, respectively, $(\epsilon_1 \cdot \epsilon_2)$ and $(\epsilon_1 \times \epsilon_2)$, as

$$M_{\lambda_1\lambda_2} = (\epsilon_1 \cdot \epsilon_2)\mathcal{C}_+ + (\epsilon_1 \times \epsilon_2)\mathcal{C}_- \tag{4.68}$$

where $\mathcal{C}_+ (\mathcal{C}_-)$ are the CP–even (odd) contributions to the amplitude. Four independent functions describe the process out of the 16 helicity amplitudes present in the general case

$$\begin{aligned}
\mathrm{d}\hat{\sigma}_{00} + \mathrm{d}\hat{\sigma}_{22} &= \frac{1}{2}\mathrm{d}\Gamma \left(|M_{++}|^2 + |M_{--}|^2\right) = |\mathcal{C}_+|^2 + |\mathcal{C}_-|^2 \\
\mathrm{d}\hat{\sigma}_{20} + \mathrm{d}\hat{\sigma}_{02} &= \frac{1}{2}\mathrm{d}\Gamma \left(|M_{++}|^2 - |M_{--}|^2\right) = -2\mathrm{Im}\left(\mathcal{C}_+\mathcal{C}_-^*\right) \\
\mathrm{d}\hat{\sigma}_{31} + \mathrm{d}\hat{\sigma}_{13} &= \mathrm{d}\Gamma\, \mathrm{Im}\left(M_{++}M_{--}^*\right) = -2\mathrm{Re}\left(\mathcal{C}_+\mathcal{C}_-^*\right) \\
\mathrm{d}\hat{\sigma}_{33} + \mathrm{d}\hat{\sigma}_{11} &= \mathrm{d}\Gamma \left(M_{++}M_{--}^*\right) = |\mathcal{C}_+|^2 - |\mathcal{C}_-|^2
\end{aligned} \tag{4.69}$$

One can then define the asymmetries [600]

$$\begin{aligned}
\mathcal{A}_1 &= \frac{|M_{++}|^2 - |M_{--}|^2}{|M_{++}|^2 + |M_{--}|^2} = -\frac{2\mathrm{Im}(\mathcal{C}_+\mathcal{C}_-^*)}{|\mathcal{C}_+|^2 + |\mathcal{C}_-|^2} \\
\mathcal{A}_2 &= \frac{2\mathrm{Im}(M_{++}M_{--}^*)}{|M_{++}|^2 + |M_{--}|^2} = -\frac{2\mathrm{Re}(\mathcal{C}_+\mathcal{C}_-^*)}{|\mathcal{C}_+|^2 + |\mathcal{C}_-|^2} \\
\mathcal{A}_3 &= \frac{2\mathrm{Re}(M_{++}M_{--}^*)}{|M_{++}|^2 + |M_{--}|^2} = \frac{|\mathcal{C}_+|^2 - |\mathcal{C}_-^*|^2}{|\mathcal{C}_+|^2 + |\mathcal{C}_-|^2}
\end{aligned} \tag{4.70}$$

and write the event rate as $\mathrm{d}N = \mathrm{d}\mathcal{L}^{J_Z=0}\mathrm{d}\hat{\sigma}$ with

$$\mathrm{d}\mathcal{L}^{J_Z=0} = \mathrm{d}\mathcal{L}\Big[1 + \langle\xi_{12}\xi_{22}\rangle + \langle\xi_{12} + \xi_{22}\rangle\mathcal{A}_1 + \langle\xi_{13}\xi_{21} + \xi_{11}\xi_{23}\rangle\mathcal{A}_2 + \langle\xi_{13}\xi_{23} - \xi_{11}\xi_{21}\rangle\mathcal{A}_3\Big] \tag{4.71}$$

with the unpolarized cross section given by

$$\mathrm{d}\hat{\sigma}_0 = \frac{1}{4}\mathrm{d}\Gamma \left(|M_{++}|^2 + |M_{--}|^2\right) \tag{4.72}$$

If $\mathcal{A}_1$ and $\mathcal{A}_2$ are both non–zero, then, CP is violated since the Higgs boson is a mixture of CP–even and CP–odd states. One can thus, by analyzing the spins of the final photons,

probe CP–violation. If the Higgs boson is a definite CP–eigenstate, that is, a pure scalar or pseudoscalar particle, one has $\mathcal{A}_1 = \mathcal{A}_2 = 0$ and $\mathcal{A}_3 = \eta_{\rm C}$ with $\eta_{\rm CP} = 1\,(-1)$ for a CP–even (CP–odd) Higgs particle. The luminosity written above simplifies then to

$$\mathrm{d}\mathcal{L}^{J_Z=0} \;=\; \mathrm{d}\mathcal{L}\left[1 + \langle\xi_{12}\xi_{22}\rangle + \eta_{\rm CP}\langle\xi_{13}\xi_{23} - \xi_{11}\xi_{21}\rangle\right] \tag{4.73}$$

In fact, if CP is conserved, one has $M_{++} = \eta_{\rm CP} M_{--}$ leading to the relation between cross sections with parallel and orthogonal linear polarizations for the photons, $\mathrm{d}\hat{\sigma}_{||} - \mathrm{d}\hat{\sigma}_{\perp} = \eta_{\rm CP}\cdot(\mathrm{d}\hat{\sigma}_{||} + \mathrm{d}\hat{\sigma}_{\perp})$. This means that only photons with parallel (orthogonal) linear polarizations couple to scalars (pseudoscalars). Note that only if the lasers are linearly polarized that it is possible to distinguish between the two CP quantum numbers since the relevant average for the Stokes parameters, $\langle\xi_{13}\xi_{23} - \xi_{11}\xi_{21}\rangle$, is negligible for circularly polarized lasers.

In practice, the asymmetry $\mathcal{A}_3$ is determined by making two runs and measuring the difference of the event rates for lasers with parallel polarization, $\Delta\gamma = 0$, and lasers with perpendicular polarization, $\Delta\gamma = \frac{\pi}{2}$ [600]

$$\langle\mathcal{A}_3\rangle = \frac{\sigma^{\rm eff}(\Delta\gamma = 0) - \sigma^{\rm eff}(\Delta\gamma = \frac{\pi}{2})}{\sigma^{\rm eff}(\Delta\gamma = 0) + \sigma^{\rm eff}(\Delta\gamma = \frac{\pi}{2})} \tag{4.74}$$

where the contamination from the background is taken into account $\sigma^{\rm eff} = \sigma^{\rm eff}_{\rm signal} + \sigma^{\rm eff}_{\rm bckg}$. In terms of the electron and laser beam polarization, the asymmetry is given by

$$\langle\mathcal{A}_3\rangle \simeq \frac{\eta_{\rm CP}\,\sigma_{\rm signal}\,P_{1t}P_{2t}\langle\ell_1\ell_2\rangle}{\frac{1}{2}(1 + 4\lambda_{e^-}\lambda_{e^+}\langle c_1c_2\rangle)(2\hat{\sigma}^{\rm signal} + \hat{\sigma}_0^{\rm bckg}) + \frac{1}{2}(1 - 4\lambda_{e^-}\lambda_{e^+}\langle c_1c_2\rangle)\hat{\sigma}_2^{\rm bckg}} \tag{4.75}$$

where the effects for $\rho \neq 0$ have been ignored for simplicity [there is also a generally small contribution to the background in the numerator from the component $\hat{\sigma}_{||}^{\rm bckg} - \hat{\sigma}_{\perp}^{\rm bckg} \propto m_q^4/W^4$]. As can be seen, a very important role is played by the linear laser polarization P_{it}, the average of the induced linear polarizations of the photons [the asymmetry is directly proportional to the product] and by the longitudinal polarizations of the electron beams and the induced circular polarization of the photons.

The statistical significance of the signal is given by

$$N_{\rm SD}(\mathcal{A}_3) = \frac{|\sigma^{\rm eff}(\Delta\gamma = 0) - \sigma^{\rm eff}(\Delta\gamma = \frac{\pi}{2})|}{\sqrt{\sigma^{\rm eff}(\Delta\gamma = 0) + \sigma^{\rm eff}(\Delta\gamma = \frac{\pi}{2})}} \times \sqrt{\mathcal{L}^{\rm eff}} \tag{4.76}$$

With the machine parameters, polarization and luminosity discussed above, a measurement at the level of 10% can be made, allowing the distinction between the two CP possibilities for the Higgs particle; see Ref. [600] for an analysis where a realistic luminosity spectra and photon polarizations are taken into account.

Measurements using angular distributions

Another way to test the CP nature of the produced Higgs particle is to study the angular distributions in its decays. For a relatively heavy Higgs boson, $M_H \gtrsim 2M_Z$, this can be done in the final state $H \to WW, ZZ \to 4f$ in which, as discussed in §2.2.4, the angular correlations between the final state fermions are very different in the case of scalar and pseudoscalar Higgs particles. For instance, the azimuthal dependence on the angle $\Delta\phi$ between the decay planes of the two vector bosons is characteristically different in the 0^{++} and 0^{+-} cases [159, 174]. Another different observable is the correlation

$$\zeta_{VV} = \frac{\sin^2\theta_1 \ \sin^2\theta_3}{(1+\cos^2\theta_1)\ (1+\cos^2\theta_3)} \tag{4.77}$$

where θ_1 and θ_3 are the polar angles of the two fermions from the $V \to f\bar{f}$ decays defined in Fig. 2.11 and which corresponds to the ratio of the angular distributions expected for the decay of a scalar and a pseudoscalar particle in the limit $M_H \gg M_V$.

A detailed simulation in the decay channels $H \to ZZ \to \ell\ell jj$ and $H \to WW \to 4j$ has been performed [599] along the same lines as for the measurement of the amplitudes of the HVV couplings and their phases discussed earlier. The output of this analysis is shown in Fig. 4.44 for the example of a Higgs boson with a mass $M_H = 200$ GeV, produced in the $\gamma\gamma$ mode of an e^+e^- collider with initial energy of $\sqrt{s_{e^+e^-}} = 305$ GeV and decaying into $ZZ \to \ell\ell jj$ final states. The figure shows the number of expected events for a scalar and pseudoscalar Higgs boson and for the non–resonant SM background, for a variation of the reconstructed azimuthal angle $\Delta\phi_{ZZ}$ (left) and the correlation ζ_{ZZ} (right). The points with error bars indicate the statistical precision of the measurements after a one year running of the photon collider with a luminosity of 600 fb^{-1}.

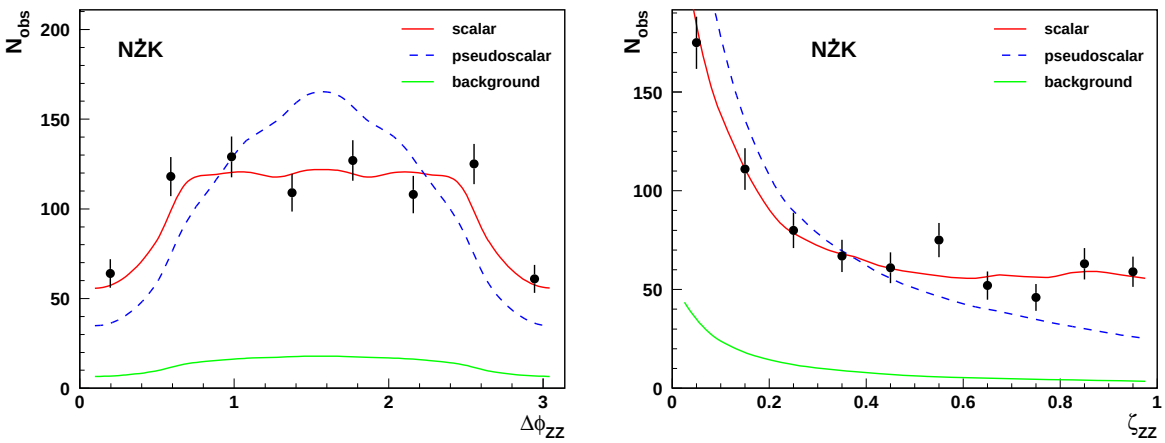

Figure 4.44: The measurement of the azimuthal angle $\Delta\phi_{ZZ}$ and the correlation ζ_{ZZ} in the process $\gamma\gamma \to H \to ZZ \to \ell\ell jj$ for $M_H = 200$ GeV at a photon collider; from [599].

If the HVV coupling, including CP–violation, is parameterized as $g_{HVV} = \lambda \cos\Phi$ with $\lambda = 1$ and $\Phi = 0$ in the SM, from a combined fit of the $H \to WW/ZZ \to 4f$ events which includes a free variation of the two photon width and phase one can measure the absolute magnitude of the coupling with a precision $\Delta\lambda/\lambda = 2\%$ and the CP–violating phase with a precision $\Delta\Phi = 50$ mrad, in the entire Higgs mass range $M_H = 200$–350 GeV [599].

Similar tests can be performed in the decay $H \to t\bar{t}$ for a heavier Higgs particle, $M_H > 350$ GeV. In particular, the interference pattern of the resonant and the continuum amplitudes for the $\gamma\gamma \to t\bar{t}$ process allows to check the parity of the Higgs boson and the presence of CP–violation, by using circularly polarized colliding photons [602]. Indeed, from the $t\bar{t}$ decay angular distribution one can built four convoluted observables $\Sigma_{1..4}$

$$\Sigma_i(\sqrt{s}_{\gamma\gamma}) = \int \mathrm{d}\sqrt{s}_{\gamma\gamma} \sum_{\lambda_1,\ \lambda_2} \left(\frac{1}{\mathcal{L}} \frac{\mathrm{d}\mathcal{L}^{\lambda_1\lambda_2}}{\mathrm{d}\sqrt{s}_{\gamma\gamma}} \right) \left(\frac{3\beta}{32\pi s_{\gamma\gamma}} \int S^i_{\lambda_1\lambda_2}(\theta, \sqrt{s}_{\gamma\gamma}) \mathrm{d}\cos\theta \right) \tag{4.78}$$

with θ being the polar angle of the t momentum in the $\gamma\gamma$ c.m. frame and the first bracket corresponding to the normalized luminosity distribution for each of the photon $\lambda_1\lambda_2$ helicity combinations. The functions $S^i_{\lambda_1\lambda_2}$ contain the information on the $\gamma\gamma \to t\bar{t}$ helicity amplitudes

$$S^1_{\lambda_1\lambda_2} = \left|M^{RR}_{\lambda_1\lambda_2}\right|^2 \ , \ S^2_{\lambda_1\lambda_2} = \left|M^{LL}_{\lambda_1\lambda_2}\right|^2 \ , \ S^{3(4)}_{\lambda_1\lambda_2} = 2\mathrm{Re(Im)}\left[M^{RR}_{\lambda_1\lambda_2} M^{LL*}_{\lambda_1\lambda_2}\right] \tag{4.79}$$

Writing the $\gamma\gamma \to t\bar{t}$ amplitudes as sums of the resonant and non–resonant contributions

$$M^{\sigma\sigma}_{\lambda\lambda} = [M_t]^{\sigma\sigma}_{\lambda\lambda} + \left(\frac{\sqrt{s}_{\gamma\gamma}}{M_H}\right)^3 r_H \cdot i \left[1 + \exp\left(2i \tan^{-1} \frac{s^2_{\gamma\gamma} - M^2_H}{M_H \Gamma_H}\right)\right] \tag{4.80}$$

the phase of the resonance amplitude is shifted by r_H which is essentially the phase of the $\gamma\gamma H$ coupling when neglecting the phase in the $t\bar{t}H$ vertex. In the left–hand side of Fig. 4.45, the four observables $\Sigma_{1..4}$ for the production of scalar H and pseudoscalar A bosons with $M_{H,A} = 400$ GeV, are shown for two values of the $\gamma\gamma H/A$ phase, $\arg(r_{H,A}) = 0$ and $\frac{\pi}{4}$, and one can see that the difference is significant enough to be measured experimentally.

Another possibility to probe the Higgs CP–quantum numbers in $\gamma\gamma \to t\bar{t}$ production is to look at the net polarization of the $t/\bar{t}$ quarks either with circularly polarized [603] or linearly polarized photons [601]. In the latter case, the top polarization has been analyzed through the decay lepton energy and angular distributions in the decay $t \to b\ell\nu$. The full differential distribution of the decay lepton has been written and, in terms of the initial state e^+e^- polarizations $\lambda_{e^+e^-} = \pm 1$ and final charge of the decay lepton $e_{\ell^\pm} = \pm 1$, one can obtain four cross sections $\sigma(\pm,\pm)$ from which one can construct six asymmetries that are sensitive to the Higgs coupling [601]

$$\mathcal{A}_{1/4} = \frac{\sigma(+,\pm) - \sigma(-,-)}{\sigma(+,\pm) + \sigma(-,-)} \ , \ \mathcal{A}_{2/3} = \frac{\sigma(+,\mp) - \sigma(-,+)}{\sigma(+,\mp) + \sigma(-,+)} \ , \ \mathcal{A}_{5/6} = \frac{\sigma(\pm,+) - \sigma(\pm,-)}{\sigma(\pm,+) + \sigma(\pm,-)} \tag{4.81}$$

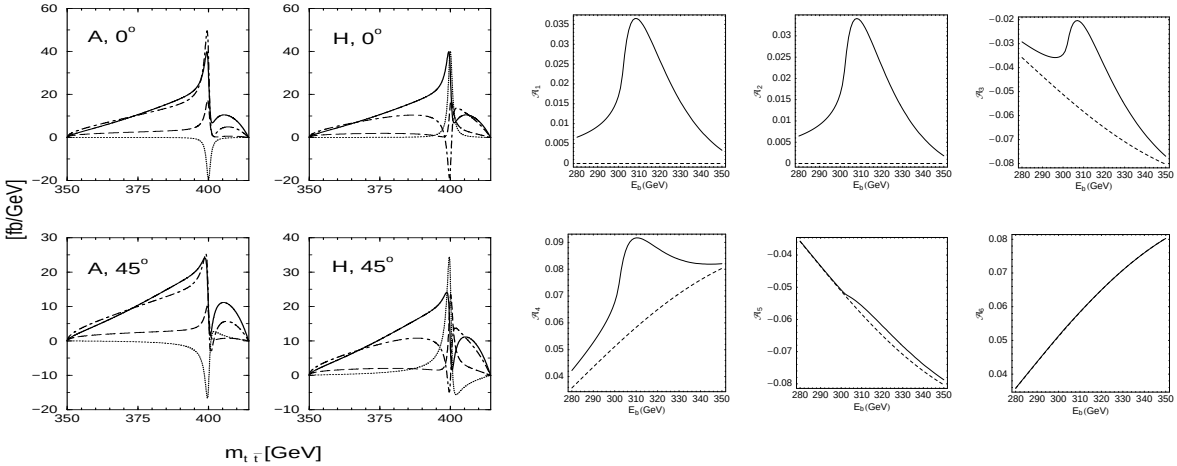

Figure 4.45: Left: The observables Σ_1 (solid), Σ_2 (dashed), Σ_3 (dot–dashed) and Σ_4 (dotted) for the production of H and A bosons for $\arg(r_{H,A}) = 0$ and $\frac{\pi}{4}$ with $x = 4.8$, $P_L = -1.0$ and $P_e = 0.9$; from Ref. [602]. Right: The asymmetries $\mathcal{A}_{1..6}$ as a function of the e^- beam energy for continuum $\gamma\gamma \to t\bar{t}$ production (dotted line) and when the resonant contribution with $M_{H,A} = 500$ GeV is included (solid lines); from Ref. [601].

$\mathcal{A}_{5/6}$ are charge asymmetries for a given polarization and vanish for zero–angle, which is not the case for the purely CP–violating $\mathcal{A}_{1/2}$ asymmetries; $\mathcal{A}_{3/4}$ are the polarization asymmetries for a given lepton charge. Note that the charge asymmetries do not vanish in the case of the SM where only the non–resonant amplitude is taken into account. The sensitivity of the six asymmetries to the $\gamma\gamma H/A$ coupling and to its possible CP–violating component is exhibited in the right–hand side of Fig. 4.45 for a specific point with $M_{H,A} = 500$ GeV and a $\gamma\gamma H/A$ vertex which has both real and imaginary parts, as a function of the electron beam energy. As can be seen, the asymmetries can be large and in most cases different from the asymmetries of the continuum $\gamma\gamma \to t\bar{t}$ production.

Finally, for $M_H \lesssim 140$ GeV, one can also study the CP–nature of the Higgs boson by looking at the polarization of the τ leptons produced in $\gamma\gamma \to H \to \tau^+\tau^-$. One can again construct polarization asymmetries which probe both the $H\gamma\gamma$ and $H\tau\tau$ couplings [614]

4.5.3 Other Higgs production mechanisms

Other processes than Higgs boson production as s–channel resonances have been discussed in the context of $\gamma\gamma$ colliders: Higgs pair production via loop diagrams [615,616], production in association with vector bosons [545, 617, 618] and associated Higgs production with top quarks [619]. At $e\gamma$ colliders, the Higgs boson can also be produced in the reaction $e\gamma \to \nu_e W^+ H$ [622,623]. In this section, we briefly summarize the main features of these processes, concentrating only on the magnitude of the cross sections of the subprocesses [i.e. without folding with the photon luminosity spectra].

Higgs pair production: $\gamma\gamma \to HH$

The pair production of Higgs bosons in $\gamma\gamma$ collisions is induced by loops of top quarks and W bosons where two sets of diagrams are involved: (i) s–channel vertex diagrams where the intermediate Higgs particle splits into two and which involves the trilinear Higgs coupling λ_{HHH}; the contributions of these diagrams are essentially the same as those discussed for $\gamma\gamma \to H$, except that here the Higgs particle is virtual, and (ii) box diagrams involving top quarks and W bosons, as well as vertex and self–energy diagrams which do not involve the trilinear Higgs coupling but the quartic Higgs–gauge boson interaction.

The cross section has been calculated in Ref. [615] in the SM case; see also Ref. [616]. At small energies, $\sqrt{s}_{\gamma\gamma} \sim 500$ GeV, it is dominated by the top quark contribution. For photons having the same helicities, it is at the level of ~ 0.5 fb for $M_H \sim 100$ GeV, decreases very slowly with M_H and falls–off rapidly when approaching the $\sqrt{s}_{\gamma\gamma} = 2M_H$ threshold. At higher energies, $\sqrt{s}_{\gamma\gamma} \gtrsim 1$ TeV, the cross section is dominated by the W boson loop contribution which, contrary to the case of single Higgs boson, interferes constructively with the top quark contribution for large enough M_H. While the cross section is smaller than at 500 GeV for low M_H, it increases with M_H almost up to the kinematical boundary, where it reaches values of the order 1 (10) fb at $\sqrt{s}_{\gamma\gamma} \sim 1\,(2)$ TeV. This is mainly due to the large triple and quartic Higgs couplings to the Goldstone or W_L bosons which grow as M_H^2.

For opposite photon helicities, the cross section has the same magnitude as in the same–helicity case for $M_H \sim 100$ GeV, but because in this case it is dominated by the contributions of transverse W bosons it falls off more rapidly with increasing M_H values even for high center of mass energies. At $\sqrt{s} = 2$ TeV, there is bump for a very heavy Higgs boson.

The sensitivity of the production cross section to the trilinear Higgs coupling λ_{HHH} depends on the relative weight of the diagram with the exchange of the Higgs boson in the s–channel and the other diagrams [616]. For very heavy Higgs bosons, $M_H \sim 500-800$ GeV, the cross section is very sensitive to the coupling λ_{HHH}, in particular near the $\sqrt{s}_{\gamma\gamma} = 2M_H$ threshold where it is maximal: for $M_H \sim 700$ GeV, removing the trilinear coupling leads to an increase of the cross section [which is unfortunately rather small, being less than 1 fb] by about 60%. For smaller M_H values, the sensitivity is much weaker since the cross section at high energies [where it is sizable] is dominated by the box contributions which do not involve λ_{HHH}, while at low energies the rates are too small. Note finally, that a change of the trilinear Higgs coupling does not affect the angular distribution of the Higgs pair production process.

Thus, at very high energies and for rather heavy Higgs bosons, on can possibly probe the trilinear Higgs coupling in the process $\gamma\gamma \to HH$. This is complementary to the e^+e^- case where the coupling can be best probed for low Higgs boson masses. However, to assess to which extent the coupling can be measured, more detailed analyses are needed.

Higgs production in association with top quarks: $\gamma\gamma \to t\bar{t}H$

The process $\gamma\gamma \to t\bar{t}H$ offers an additional opportunity to probe the Yukawa coupling of the Higgs boson to top quarks [619, 620]. Contrary to the similar process in the e^+e^- case, where the Higgs boson can be radiated not only from the top quark lines but also from the Z line in the Higgs strahlung like process $e^+e^- \to HZ^* \to Ht\bar{t}$ [although the contribution of the latter is very tiny as discussed earlier], in associated $Ht\bar{t}$ production in photon–photon collisions, the Higgs boson is only radiated from the top quark lines and the cross section is directly proportional to the $Ht\bar{t}$ Yukawa coupling.

As in the case of e^+e^- collisions, the cross section for $t\bar{t}H$ production is rather small at $\sqrt{s}_{\gamma\gamma} \sim 500$ GeV, because of the limited phase space. It increases with energy and for $M_H \sim 100$ GeV it reaches the level of $\sigma(\gamma\gamma \to t\bar{t}H) = \mathcal{O}(1 \text{ fb})$ at $\sqrt{s}_{\gamma\gamma} \sim 1$ TeV, where it begins to flatten [this is opposite to the e^+e^- case, where $\sigma \propto 1/s$]. The cross section drops rapidly with increasing M_H and at a c.m. energy of 1 TeV it is one order of magnitude smaller for $M_H \sim 200$ GeV than for $M_H \sim 100$ GeV.

The $\gamma\gamma \to t\bar{t}H$ process can be used as a means to determine the CP properties of the Higgs boson and to distinguish between scalar and pseudoscalar particles and to probe CP–violation. In addition, associated Higgs production with lighter fermions, such as τ–leptons and b–quarks, which have larger cross sections in extensions of the SM where the Higgs couplings to down–type fermions are enhanced, has been discussed [621].

Higgs production in association with gauge bosons

As mentioned previously, the $\gamma\gamma \to W^+W^-$ production cross section is enormous, being at the level of $\mathcal{O}(100 \text{ pb})$ for c.m. energies around $\sqrt{s}_{\gamma\gamma} \sim 300 - 500$ GeV [612], and one could attach one or even two additional Higgs bosons to the W lines, while still having sizable rates [617]. For a Higgs boson with a mass $M_H \sim 100$ GeV, the cross section for $\gamma\gamma \to W^+W^-H$ is about 20 fb for $\sqrt{s}_{\gamma\gamma} = 500$ GeV and, therefore, it is at level of the cross section for the Higgs–strahlung process in e^+e^- collisions with the same c.m. energy. The cross section quickly rises with energy, to reach the level of 400 fb for $\sqrt{s}_{\gamma\gamma} = 2$ TeV, i.e. almost two orders of magnitude larger than the Higgs–strahlung cross section which drops like $1/s$, and of the same order as the dominant production mechanism, $e^+e^- \to H\nu\bar{\nu}$. Compared to the processes for associated Higgs production with gauge bosons in e^+e^- collisions discussed previously, $\sigma(\gamma\gamma \to W^+W^-H)$ is a factor of three larger than any of the $e^+e^- \to HVV$ processes. Note however, that this process does not provide any additional information that could not be obtained in the e^+e^- option of the machine.

A channel that is, in principle, more interesting is when two Higgs particles are produced in association with the W boson pair. Indeed, similarly to the WW fusion mechanism

$WW \to HH$, this process is sensitive to the trilinear Higgs boson coupling since the Higgs particle produced in $\gamma\gamma \to WWH$ can split into two Higgs bosons. Unfortunately, the rates are too small to be useful even with very high luminosities [545]: for $\gamma\gamma$ energies of the order of 1 TeV, $\sigma(\gamma\gamma \to W^+W^-HH) \sim 0.02$ fb for $M_H \sim 100$ GeV, and barely reaches 0.2 fb at $\sqrt{s}_{\gamma\gamma} \sim 2$ TeV. Finally, note that the Higgs bosons can be also produced in association with a Z boson in the loop induced process $\gamma\gamma \to HZ$ [618] where, in particular, virtual top quarks and W bosons contribute. The cross section are, however, rather small: for $\sqrt{s}_{\gamma\gamma} = 500$ GeV and $M_H \sim 100$ GeV, they are at the level of 0.1 fb.

Higgs production in $e\gamma$ collisions

Finally, let us close this discussion on Higgs physics at the photonic mode of future e^+e^- linear colliders by considering the other possible option, the $e\gamma$ mode, that can be obtained by converting only one of the electron beams into a very energetic back–scattered photon. Higgs bosons can be produced in $e\gamma$ collisions through bremsstrahlung off the W lines, $e^-\gamma \to \nu_e W^- H$ [622, 623]; the relevant diagrams are shown in Fig. 4.46.

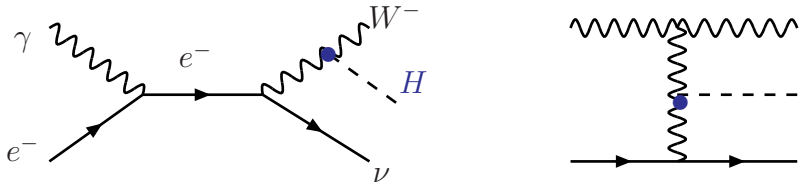

Figure 4.46: Diagrams for Higgs boson production in $e\gamma$ collisions.

For a low mass Higgs boson, $M_H \sim 100$ GeV, the cross section for the subprocess [again without folding with the photon spectrum] is at the level of ~ 40 fb for $\sqrt{s}_{e\gamma} = 500$ GeV and increases monotonically to reach values of the order of 100 (300) fb for $\sqrt{s}_{e\gamma} = 1\,(2)$ TeV; i.e. the rates are comparable to those of the WW fusion in e^+e^- collisions at high energies. While the variation of the cross section with the Higgs mass is rather pronounced at low energies [$\sigma(e\gamma \to \nu_e WH)$ drops by a factor of two when increasing M_H from 100 to 150 GeV, as a result of phase space reduction], it is very mild at higher energies. When convoluting the cross sections with the back–scattered photon flux, they are reduced by about 50% at $\sqrt{s_{e\gamma}} = 500$ GeV and slightly less at higher energies [623].

The large Higgs production rates in this process could allow to perform an independent determination of the HWW couplings [which can be made already in the $e^+e^- \to H\nu\bar{\nu}$ production and $H \to WW$ decay process if the Higgs is not too heavy] and to probe anomalous contributions. However, the environment of the collision should be well under control to match the accuracy which can be achieved in the clean e^+e^- mode of the linear collider.

4.6 Higgs production at muon colliders

The ability of a future $\mu^+\mu^-$ collider to investigate the Higgs sector of the SM and its extensions has been discussed in numerous papers; see for instance the detailed reviews of Refs. [496–501]. In this section, we simply summarize the main studies which have been performed in this context, concentrating on the benefits of such a collider compared to e^+e^- linear colliders for determining the properties of the Higgs particle.

4.6.1 Higgs production in the s–channel

Resonant Higgs production at the tree–level

In $\mu^+\mu^-$ collisions, the resonance production cross section for a Higgs boson decaying into a final state X is given, in terms of the partial decay widths, by

$$\sigma_H(\sqrt{s}) = \frac{4\pi\Gamma(H\to\mu^+\mu^-)\Gamma(H\to X)}{(s-M_H^2)^2+M_H^2\Gamma_H^2} \tag{4.82}$$

In practice, however, on has to include the Gaussian center of mass energy spread $\sigma_{\sqrt{s}}$. Assuming a central c.m. energy value $\sqrt{s}$, one obtains after convolution [514]

$$\overline{\sigma}_H(\sqrt{s}) = \frac{1}{2\pi\sigma_{\sqrt{s}}}\int \sigma_H(\sqrt{\hat{s}})\,\exp\left(\frac{-\left(\sqrt{\hat{s}}-\sqrt{s}\right)^2}{2\sigma^2_{\sqrt{s}}}\right)\,\mathrm{d}\sqrt{\hat{s}} \tag{4.83}$$

which, when the energy is tuned to the Higgs boson mass value, gives

$$\overline{\sigma}_H(\sqrt{s}\simeq M_H) = \frac{4\pi}{M_H^2}\frac{\mathrm{BR}(H\to\mu^+\mu^-)\mathrm{BR}(H\to X)}{\left[1+\frac{8}{\pi}\left(\sigma_{\sqrt{s}}/\Gamma_H\right)^2\right]^{1/2}} \tag{4.84}$$

If the energy spread is much smaller than the Higgs boson total decay width, the effective cross section is simply given by

$$\sigma_{\sqrt{s}} \ll \Gamma_H \;:\quad \overline{\sigma}_H \simeq \frac{4\pi}{M_H^2}\,\mathrm{BR}(H\to\mu^+\mu^-)\mathrm{BR}(H\to X) \tag{4.85}$$

while in the opposite case, the effective cross section reads

$$\sigma_{\sqrt{s}} \gg \Gamma_H \;:\quad \overline{\sigma}_H \simeq \frac{4\pi^2}{M_H^2}\Gamma(H\to\mu^+\mu^-)\mathrm{BR}(H\to X)\times\frac{1}{2\sqrt{2\pi}\sigma_{\sqrt{s}}} \tag{4.86}$$

One needs therefore a very small resolution to maximize the Higgs boson production rate.

Recalling that there is a trade between the luminosity delivered by the machine and the energy resolution R of the muon beams, §4.1.3, the production rate can be maximized by choosing R such that the energy spread $\sigma_{\sqrt{s}}$ is slightly smaller than the Higgs boson total

decay width, $\sigma_{\sqrt{s}} \lesssim \Gamma_H$, which in the SM corresponds to $R = 0.003\%$ for $M_H \lesssim 120$ GeV. The energy spread can be then more conveniently written as [498]

$$\sigma_{\sqrt{s}} = 0.002\,\text{GeV}\left(\frac{R}{0.003\%}\right)\left(\frac{\sqrt{s}}{100\,\text{GeV}}\right) \tag{4.87}$$

For Higgs bosons in the low mass range, $M_H \lesssim 130$ GeV, a small resolution $R = 0.003\%$ would be more advantageous. In the intermediate Higgs mass range, 130 GeV $\lesssim M_H \lesssim$ 160 GeV, the Higgs boson is broad enough and one can use a resolution $R = 0.01\%$ without too much loss of production rates. In such a case, the cross sections are functions of the Higgs branching fractions and Higgs masses and practically do not depend on R; this is even more true for Higgs bosons in the high mass range, $M_H \gtrsim 180$ GeV. [See Table 2.1, for the Higgs total width and branching ratios for selected values of M_H.]

$\mu^+\mu^- \to b\bar{b}$ and the radiative corrections

For a light Higgs boson, $M_H \lesssim 140$ GeV, the dominant decay is $H \to b\bar{b}$ and one has to consider the full process $\mu^+\mu^- \to b\bar{b}$ which receives contributions from the resonant $\mu^+\mu^- \to H \to b\bar{b}$ channel and continuum $\mu^+\mu^- \to \gamma, Z \to b\bar{b}$ production; Fig. 4.47a. The latter is mediated by gauge boson s–channel exchange and would act as a background.

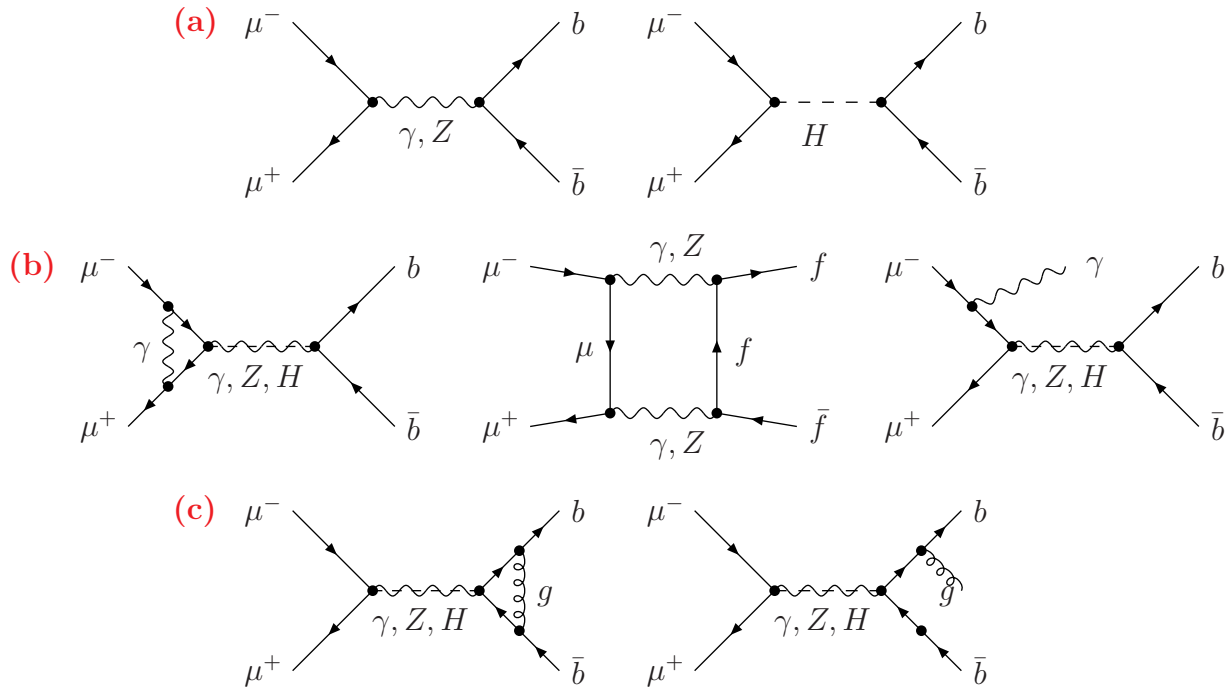

Figure 4.47: Lowest-order diagrams for $\mu^-\mu^+ \to b\bar{b}$ including the continuum and resonant channels (a) as well as the photonic QED (b) and the final state QCD corrections (c).

The photonic corrections which include the gauge invariant subset of initial and final state virtual corrections and box diagrams involving at least one photon as well a initial and final state photon radiation, Fig. 4.47b, and the QCD corrections to the final state with virtual gluon exchange and gluon emission, Fig. 4.47c, have been calculated in Ref. [624] with a careful treatment of both the Z and Higgs boson resonances. In the case where no energy resolution is included, the results are shown in Fig. 4.48 for the production of SM Higgs bosons with masses $M_H = 115$ GeV and 150 GeV. The tree–level couplings have been expressed in terms of G_μ to encapsulate the leading electroweak correction and the running b–quark mass has been used in the $Hb\bar{b}$ coupling to absorb the bulk of the QCD corrections.

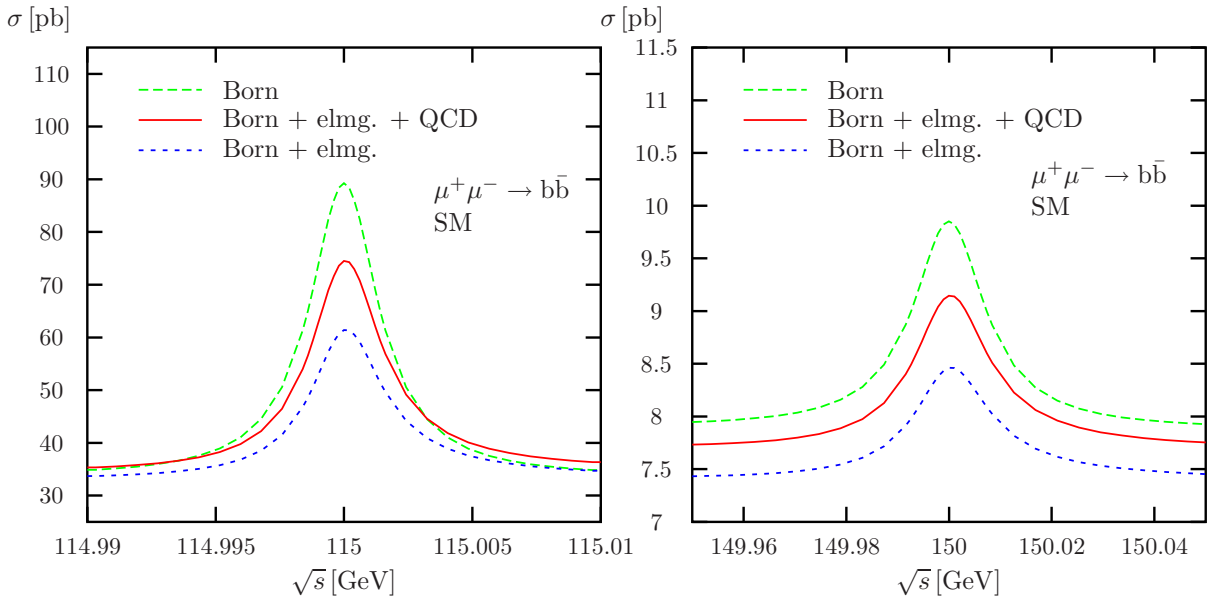

Figure 4.48: The effective cross section for Higgs production in $\mu^+\mu^- \to b\bar{b}$ for $M_H = 115$ and 150 GeV. Shown are the Born cross sections and the cross section with electromagnetic and QCD corrections. No energy resolution has been assumed; from Ref. [624].

For the photonic corrections, the large ISR corrections from the radiative return to the Z resonance can be suppressed by requiring that the invariant mass of the hadronic final state, thus including gluon radiation, should not exceed 10 GeV compared to the Higgs mass, $M_{\rm had} > \sqrt{s} - 10$ GeV. [For continuum production, the main difference between e^+e^- and $\mu^+\mu^-$ collisions is due to the different leading logarithmic photonic corrections, $\log(s/m_\ell^2)$, which lead to ISR effects that are roughly a factor of two smaller in $\mu^+\mu^-$ than in e^+e^- collisions.] With this cut, the photonic corrections which are still dominated by $\mathcal{O}(\alpha)$ ISR turn negative and of order $-5\,(10)\%$ for $M_H = 115\,(150)$ GeV for the continuum production and $\sim -50\%$ for the resonant production, leading to a reduction of the resonance peak compared to the continuum background. The QCD corrections are positive and, as they are larger for the Higgs mediated channel [$\sim 20\%$ as discussed in §2.1.2] compared to $b\bar{b}$ continuum production [$\sim \frac{\alpha_s}{\pi} \sim 4\%$], they tend to enhance the resonance peak.

When including a beam energy resolution $R = 0.003\%$, the relative impact of the radiative correction stays the same. However, the signal peaks are suppressed, in particular for small Higgs masses. For instance, the ratio is $\sigma_{\sqrt{s}}/\Gamma_H \sim 0.7$ at $M_H = 115$ GeV, compared to $\sigma_{\sqrt{s}}/\Gamma_H \sim 0.2$ at $M_H = 150$ GeV, as can be seen in Fig. 4.49.

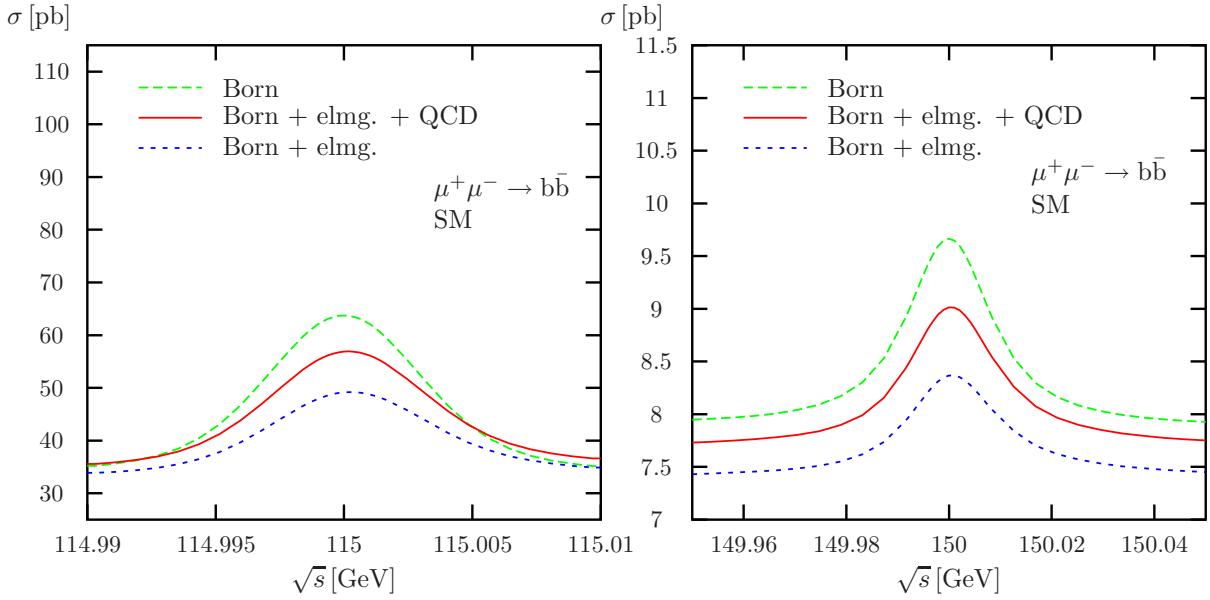

Figure 4.49: Same as in Fig. 4.48, but with an energy resolution $R = 0.003\%$; from [624].

Signals and backgrounds in $\mu^+\mu^- \to H \to b\bar{b}, WW, ZZ$

In the main Higgs decay channels, $H \to b\bar{b}, WW, ZZ$, the cross sections for the signals and the corresponding SM backgrounds are shown in the left–hand side of Fig. 4.50 as a function of the Higgs mass in the range $M_H = 80$–160 GeV for an energy resolution $R = 0.003\%$. In the right–hand side of the figure, the luminosity that is required to observe the signal at the 5σ level is displayed for the same energy resolution. Various cuts have been applied to reject part of the background [b–tagging, cuts to remove gauge bosons in the forward and backward directions] and are discussed in Ref. [498] from which we borrowed the figure.

As can be seen, the $\mu^+\mu^- \to H \to b\bar{b}$ signal rate is rather large for $M_H \lesssim 140$ GeV, leading to $\mathcal{O}(10^4)$ events for a luminosity of $\mathcal{L} = 1$ fb^{-1}. The backgrounds from direct $\mu^+\mu^- \to \gamma, Z^* \to b\bar{b}$ production[39] [the light quark–jet background can be removed with b–tagging] is much larger than the signal for a Higgs boson in the mass range $M_H \lesssim 115$ GeV which is ruled out by the LEP2 negative searches [in particular, for $M_H \sim 90$ GeV a huge background from the resonant production $\mu^+\mu^- \to Z \to b\bar{b}$ is present], and is of comparable size as the signal in the mass range 115 GeV $\lesssim M_H \lesssim$ 135 GeV. For larger masses, the signal event drop dramatically because of the decrease of the $H \to b\bar{b}$ branching ratio.

[39] Since the background is practically constant in the window $M_H \pm \sigma_{\sqrt{s}}$, one can measure it below and above the resonance and eventually, subtract it if enough luminosity is available

In the case of gauge boson production, $\mu^+\mu^- \to WW^*$ and ZZ^*, the event rates are much smaller than those of the $b\bar{b}$ final states in the low Higgs mass range, as a result of the tiny branching ratios. For larger masses, $M_H \sim 140$ GeV, the WW and $b\bar{b}$ cross sections become comparable but the absolute rates are rather small; for $M_H \gtrsim 160$ GeV, the cross sections are below the femtobarn level. The backgrounds from continuum $\mu^+\mu^- \to WW^*, ZZ^*$ production [once cuts have been applied to remove for instance the forward and backward events which are rare in the signal where the Higgs boson is centrally produced] do not exceed the signal cross sections for $M_H \lesssim 150$ GeV. For higher Higgs masses, $M_H \gtrsim 160$ GeV, when the production of two real gauge bosons opens up kinematically, the backgrounds become much larger than the resonant signal.

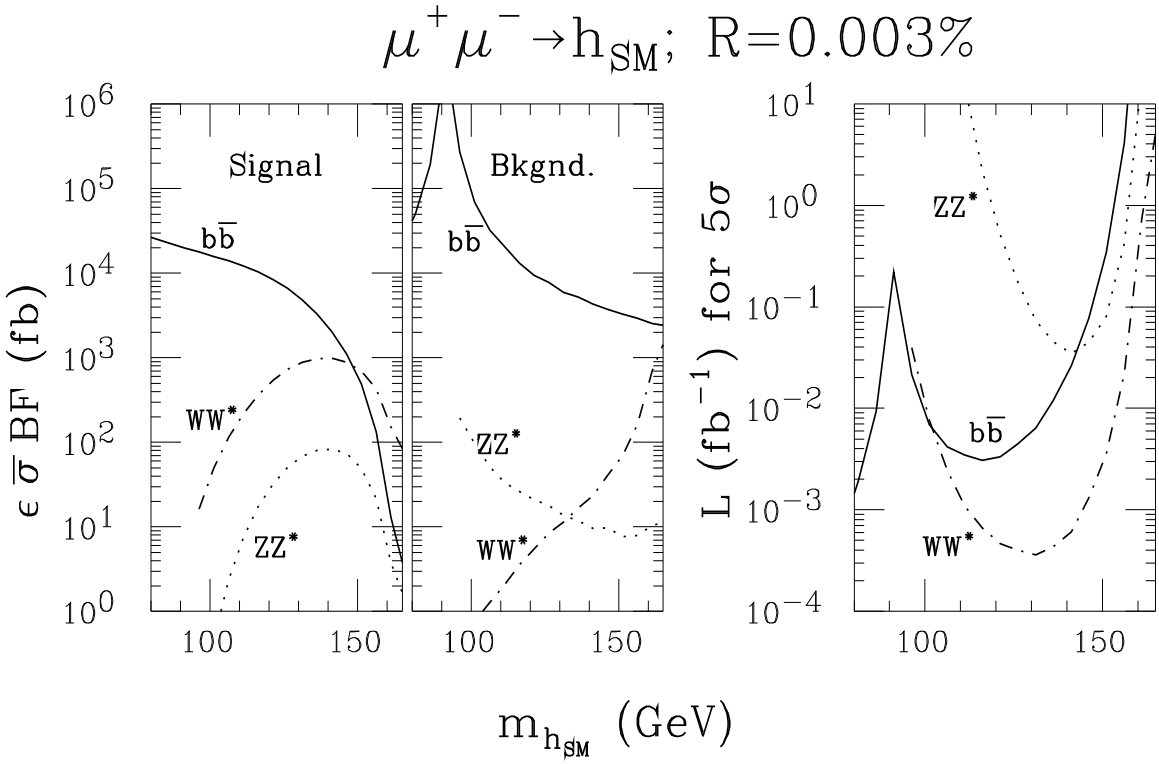

Figure 4.50: The cross sections for the processes $\mu^+\mu^- \to b\bar{b}, WW, ZZ$ for signals and backgrounds as a function of M_H for $R = 0.003\%$ (left) and the luminosity required for a 5σ observation of the $\mu^+\mu^- \to H \to b\bar{b}, WW, ZZ$ signals (right); from Ref. [498].

For a SM Higgs boson with a mass $M_H \gtrsim 2M_W$, s–channel production in $\mu^+\mu^-$ colliders will, anyway, not be very useful since the total width becomes large and the $H \to \mu^+\mu^-$ decay branching fraction drops drastically. However, there are extensions of the SM in which Higgs bosons can have relatively large masses but suppressed total widths [this is the case of e.g. pseudoscalar Higgs bosons which do not couple to massive gauge bosons at tree–level]. In this case, the production rates are not very suppressed and muon colliders can be valuable tools in determining their properties as will be discussed in another part of this review.

4.6.2 Determination of the properties of a light Higgs boson

In the SM, for Higgs bosons in the mass range $M_H \lesssim 160$ GeV, important measurements can be performed at the muon collider in the channels $\mu^+\mu^- \to H \to b\bar{b}, WW^*, ZZ^*$, which have sizable production rates as shown previously, as well as in the channel $\mu^+\mu^- \to H \to \tau^+\tau^-$. The Higgs mass, its total decay width and the cross section for the various final states, which are sensitive to the branching fractions and thus the Higgs couplings, can be determined.

The Higgs mass can be measured by a straightforward scan in the vicinity of $\sqrt{s} = M_H$. The approximate values of M_H would be already known from measurements at e^+e^- and hadron colliders, or being measured at the muon collider by producing first the Higgs boson in the Higgs–strahlung channel, $\mu^+\mu^- \to HZ$. The detection of the signal peak for a Higgs mass $M_H = 110$ GeV has been performed e.g. in Ref. [625] and the output is summarized in Fig. 4.51 which has been obtained with 10 pb^{-1} data, assuming that the beam energy spread is very small. The Monte Carlo generator `PYTHIA` has been used to generate the $\mu^+\mu^- \to H \to b\bar{b}$ signal and the $\mu^+\mu^- \to q\bar{q}(\gamma)$ background events and a crude estimate of detector effects [using a typical LEP detector] has been made. It has been assumed that 80% efficiency for b–quark tagging can be achieved as expected at the LC for instance. For such a Higgs mass, one is close the Z boson resonance and the backgrounds are rather large; they become smaller when one moves to higher Higgs masses, but the Higgs branching ratio BR($H \to b\bar{b}$) becomes then smaller. In another analysis presented in Ref. [626] but which takes into account the energy spread, it has been shown that a precision of the order of $\Delta M_H \sim 0.1$ MeV for $M_H \simeq 115$ GeV can be achieved with ~ 30 data points with a luminosity $\mathcal{L} = 1.25$ pb^{-1} per point and a resolution $R = 0.003\%$.

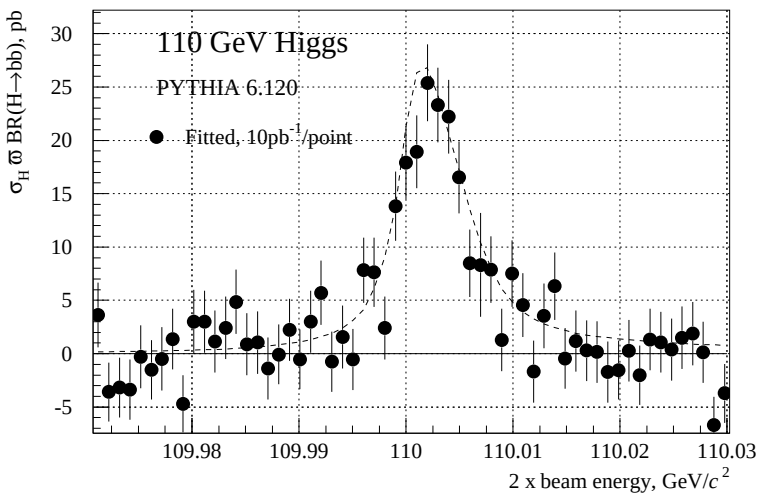

Figure 4.51: The $\mu^+\mu^- \to b\bar{b}$ production cross section as a function of the beam energy for $M_H = 110$ GeV; the points corresponding to 10 pb^{-1} data are superimposed and no beam energy spread is taken into account; from Ref. [625].

Since both the Higgs mass M_H and its total width Γ_H enter the cross section value at the same time, and if one refrains from making any theoretical assumption on the partial decay widths, a model–independent determination of Γ_H is required. This determination can be made [498, 627] by noting that if one adjusts the normalization of the theoretical curve of Γ_H at $\sqrt{s} = M_H$ in such a way that it agrees with the experimental curve, then the wings of the theoretical curve are increased (decreased) if Γ_H is larger (smaller). With precise measurements at a central energy value $\sqrt{s}$ and at the wings, one can measure Γ_H through the ratio of the cross sections at the central peak and on the wings, in which the partial decay widths cancel out. This method, with a dedicated three point scan near the threshold, allows to measure M_H at the same time with a precision that is expected to be better than the rough scan discussed above, with the same integrated luminosity.

However, for a light Higgs boson which might be very narrow, one could achieve a very small beam energy resolution, $\sigma_{\sqrt{s}} \ll \Gamma_H$, only at a cost of a low luminosity. In this case, it has been advocated to operate the collider at the Higgs peak with two different resolutions, $\sigma^{\rm min}_{\sqrt{s}} \ll \Gamma_H$ and $\sigma^{\rm max}_{\sqrt{s}} \gg \Gamma_H$ and determine the total width from the ratios of the peak cross sections [627]. Using eqs. (4.85)–(4.86), one obtains

$$\overline{\sigma}_H(\sigma^{\rm min}_{\sqrt{s}})/\overline{\sigma}_H(\sigma^{\rm max}_{\sqrt{s}}) = [2\sqrt{2}\sigma^{\rm min}_{\sqrt{s}}]/[\sqrt{\pi}\Gamma_H] \tag{4.88}$$

Figure 4.52a, shows the results of a Monte-Carlo simulation [501] for the determination of the total decay width of the Higgs boson as a function of its mass in the range between 100 and 160 GeV. Also shown in the figure are the spread in the c.m. energy for a resolution of $R = 0.003\%$ (solid circles) and the spread that is obtained if the resolution R is varied in such a way that the beam energy spread is always 40% of the Higgs total decay width (open squares). Here, one assumes that any value of the resolution R can be obtained and that the luminosity scales as $R^{2/3}$; this procedure helps to optimize the Higgs production rate and, hence, the statistical error on the production cross section.

Figure 4.52b displays the factor which reduces the peak cross section when the Gaussian distribution with a width $\sigma_{\sqrt{s}}$ is included. This signal reduction factor is given by

$$S_R = \eta\, A e^{A^2} \left(\sqrt{\pi} - 2 \int_0^A e^{-t^2} {\rm d}t \right) \ , \quad A = \frac{1}{2\sqrt{2}} \frac{\Gamma_H}{\sigma_{\sqrt{s}}} \tag{4.89}$$

where η is factor which takes into account the effects of ISR. With a fixed resolution, $R = 0.003\%$ (filled circles), the signal cross section is reduced by approximately a factor of two for low Higgs masses, $M_H \lesssim 130$ GeV, while for masses close to $M_H \sim 160$ GeV, the Higgs total width becomes large enough and there is no reduction. For an optimally varying R value (open squares), the peak cross section is reduced by a constant factor $S_R \simeq 0.8$.

The peak cross sections for the processes $\mu^+\mu^- \to b\bar{b}$ and $\mu^+\mu^- \to WW^{(*)}$ are shown in Fig. 4.52c as a function of M_H under the same conditions as above with an integrated

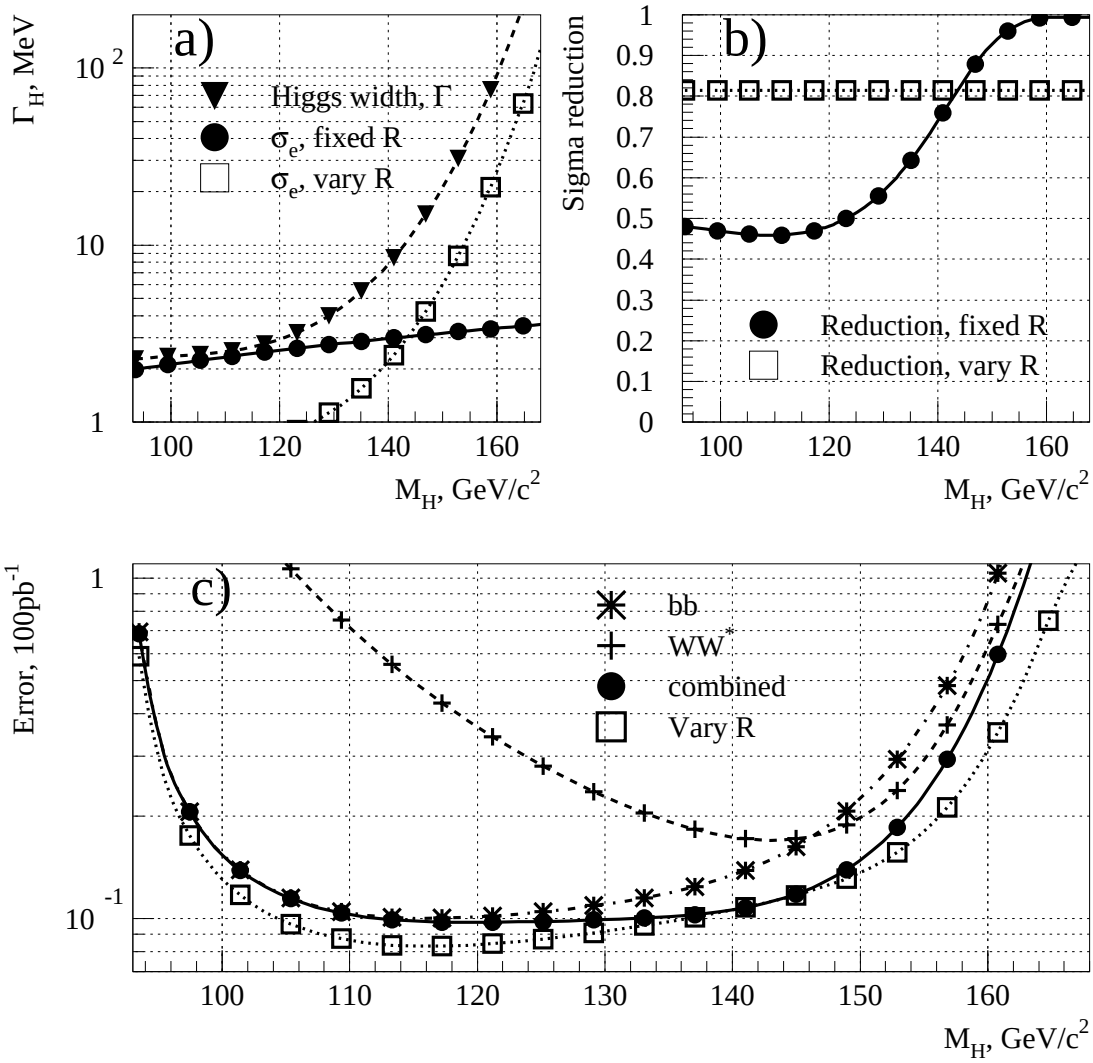

Figure 4.52: a): The width of the SM Higgs boson as a function of its mass (triangles), also shown are the effects of a fixed c.m. energy spread for $R = 0.003\%$ (filled circles) and an optimal varying energy spread (open squares). b) The cross section suppression factor due to the width of the beams if $R = 0.003\%$ (filled circles) and for the optimal varying R (open squares). c): The fractional error with which the Higgs cross section can be measured in the $b\bar{b}$ (stars) and WW^* (crosses) decay modes using 100 pb^{-1} data with $R = 0.003\%$; the solid circles show the accuracy with which the peak cross sections can be extracted if the SM branching ratios are assumed and the open squares show the errors obtained in the same running period by optimizing R. From Ref. [501].

luminosity of $\mathcal{L} = 100$ pb^{-1}. While the simulation of $b\bar{b}$ decays is as described previously, the efficiency in the channel $H \to WW^*$ is based on a LEP2–type detector with the conservative assumption that the spin information is not used to further reduce the non–resonant WW background. As can be seen, the $b\bar{b}$ cross section can be measured with a statistical accuracy of about 10%, while a 20% accuracy can be achieved on the WW^* cross section for $M_H =$

130–150 GeV. The accuracy will improve by a factor of two if the luminosity is increased to $\mathcal{L} = 400$ pb^{-1}, which corresponds to four years of running, thereby approaching those which can be achieved at the LC. The accuracy on the production cross section for the ZZ final state is expected to be worse as BR($H \to ZZ^*$) is very small in this mass range.

Once the Higgs mass, total decay width and peak cross sections have been determined, one can measure the partial decay width into muons $\Gamma(H \to \mu^+\mu^-)$ and the final state branching ratios BR($H \to X$). From the cross section eq. (4.86), they appear as the product

$$B(X) = \Gamma(H \to \mu^+\mu^-) \times \mathrm{BR}(H \to X) \tag{4.90}$$

These measurements can be then combined with other precision measurements performed at the LHC and/or at e^+e^- colliders to determine the couplings of the Higgs boson in a model independent way. For instance, the Higgs partial decay width into muons, if the measurements at the linear collider discussed in the previous section are available, can be determined through [499]

$$\Gamma(H \to \mu^+\mu^-) \;=\; \frac{B(X)}{\mathrm{BR}(H \to X)_{\mathrm{LC}}} \tag{4.91}$$

with $b\bar{b}$ and WW^* final states for instance, where the branching ratios in the denominator can be measured precisely at the LC in the low Higgs mass range, or make use of the total decay width measured at muon colliders, via

$$\Gamma(H \to \mu^+\mu^-) \;=\; \frac{B(X) \times \Gamma_H}{\Gamma(H \to X)|_{\mathrm{LC}}} \tag{4.92}$$

for the WW^* and eventually ZZ^* final states where the partial widths can be measured at the LC for large enough Higgs boson masses. The combination of all measurements allow a very precise test of the Higgs couplings to fermions and gauge bosons and, in particular, a precise determination of the Higgs couplings to second generation fermions.

4.6.3 Study of the CP properties of the Higgs boson

Measurements in the decay $H \to \tau^+\tau^-$

A very interesting process to study at muon colliders is $\mu^+\mu^- \to \tau^+\tau^-$ [628, 629]. The process proceeds through s–channel photon and Z boson exchanges as well as via s–channel Higgs boson exchange. In the former channels, the production is similar to what occurs in e^+e^- collisions and, as discussed in §1.2, the process has characteristic forward–backward and left–right asymmetries. Assuming that the $\mu^\pm$ beams have longitudinal polarizations $P_\pm$ and using eqs. (1.92,1.97,1.99) for the cross section and asymmetries, one can write the differential cross section for $\mu^+\mu^- \to \gamma, Z^* \to \tau^+\tau^-$ as

$$\frac{\mathrm{d}\sigma_{\gamma,Z}}{\mathrm{d}\cos\theta} = \frac{4\pi\alpha^2}{3s} \times \frac{3}{8}\sigma_U \left[(1+\cos^2\theta) + \frac{8}{3}\cos\theta A_{FB}^{\mathrm{eff}}\right] \tag{4.93}$$

where $A_{FB}^{\rm eff}$ has the usual component A_{FB}^{τ} already discussed, but also a component which includes the information on the longitudinal polarization and $A_{LR,FB}^{\tau}$ in eq. (1.99)

$$A_{FB}^{\rm eff} = \frac{A_{FB}^{\tau} + P_{\rm eff} A_{LR,FB}^{\tau}}{1 + P_{\rm eff} A_{LR}^{\tau}} \quad , \quad P_{\rm eff} = \frac{P_+ - P_-}{1 - P_+ P_-} \tag{4.94}$$

The angular distribution has a clear forward–backward asymmetry: it vanishes for $\theta = \frac{\pi}{2}$ and is large and positive for $\theta = 0$. For $\sqrt{s} = 120$ GeV one has $A_{FB} \sim 0.7$ and $A_{LR} = 0.15$ [628].

In the Higgs boson exchange channel, the differential cross section is flat and is simply given, in terms of the effective cross section with $\sqrt{s} = M_H$, by

$$\frac{{\rm d}\sigma}{{\rm d}\cos\theta} = \frac{1}{2}\overline{\sigma}_H \left(1 + P_+ P_-\right) \tag{4.95}$$

Considering this channel as the signal and the γ, Z exchange channel as the background, the enhancement of the signal cross section compared to the background is given by

$$\frac{S}{B} \sim \frac{1 + P_+ P_-}{1 - P_+ P_- + (P_+ - P_-) A_{LR}^{\tau}} \tag{4.96}$$

One can therefore use the polarization of the initial beams and the forward–backward asymmetries to enhance the signal–to–background ratio.

One can also distinguish the signal from the background by using the final state polarization of the τ leptons which are very different. We will briefly discuss this point, following Ref. [628] and recalling the discussion of §2.1.4 on $H \to \tau^+\tau^-$ decays. In the two–body decays of the τ lepton, $\tau^- \to \pi^-\nu_\tau, \rho^-\nu_\tau$, *etc.*., defining θ_i as the angle between the momenta of the τ lepton and the charged final particle, B as the branching ratio of the decay and $P_\tau = \pm 1$ as the τ lepton helicity, the normalized differential decay rate in the τ rest frame is simply

$$\frac{1}{\Gamma}\frac{{\rm d}\Gamma_i}{{\rm d}c_{\theta_i}} = \frac{B_i}{2}(1 + r_i P_\tau \cos\theta_i) \tag{4.97}$$

with $r_i = 1$ for decays into pions and $r_i = -(m_\tau^2 - 2m_i^2)/(m_\tau^2 + 2m_i^2) \simeq 0.45$ for $i = \rho$. In the signal, $\mu^+\mu^- \to H \to \tau^+\tau^-$, the τ^- and τ^+ helicities are correlated as $P_{\tau^-} = P_{\tau^+} = \pm 1$, and the spin correlated differential cross section with polarized $P_\pm$ beams reads

$$\frac{{\rm d}\sigma_H}{{\rm d}c_{\theta_i}{\rm d}c_{\theta_j}} = (1 + P_- P_+)\, \sigma_H \, \frac{B_i B_j}{4} \left[a_i a_j + b_i b_j c_{\theta_i} c_{\theta_j}\right] \tag{4.98}$$

reaching a maximum (minimum) for $c_{\theta_i} = c_{\theta_j} (c_{\theta_i} = -c_{\theta_j}) = \pm 1$, with the significance of the peaks depending on the magnitude of r_i. In the case of the decay $\tau^- \to \rho^-\nu_\tau$, distinctive peaks in the distribution can be seen for $c_{\theta_{\rho^-}} = c_{\theta_{\rho^+}} = \pm 1$ and $P_+ = P_- = 25\%$ [628].

In contrast, in the standard channel $\mu^+\mu^- \to \gamma, Z^* \to \tau^+\tau^-$, the τ leptons are produced with helicities $P_{\tau^-} = -P_{\tau^+} = \pm 1$ and the number of left–handed and right–handed τ leptons are different because of the polarization left–right asymmetry. The spin correlated differential distribution in this case is

$$\begin{aligned} \frac{\mathrm{d}\sigma_{\gamma,Z}}{\mathrm{d}c_{\theta_i}\mathrm{d}c_{\theta_j}} &= (1 - P_- P_+)\sigma_{\gamma,Z}\,(1 + P_{\rm eff} A_{LR}) \\ &\times \frac{1}{4} B_i B_j \left[(a_i a_j - b_i b_j c_{\theta_i} c_{\theta_j}) + (a_i b_j c_{\theta_j} - a_j b_i c_{\theta_i}) A_{LR}^{\rm eff}\right] \end{aligned} \tag{4.99}$$

with

$$A_{LR}^{\rm eff} = \frac{A_{FB,LR}^{\tau} + P_{\rm eff} A_{FB}^{\tau}}{1 + P_{\rm eff} A_{LR}^{\tau}} \tag{4.100}$$

Again, for the decay $\tau^- \to \rho^- \nu_\tau$, the peaks in the distribution for $\cos\theta_{\rho^-} = -\cos\theta_{\rho^+} = \pm 1$ can be seen for $P_+ = P_- = 25\%$ [628]. The peaks occur in opposite regions compared to the Higgs signal and the spin correlation in the signal is symmetric, while it is not the case in the background as a consequence of the presence of the term $A_{LR}^{\rm eff}$ in eq. (4.99).

Summing both $\rho\nu$ and $\tau\nu$ final states and using $R = 0.0005\%$, $P_\pm = 25\%$ and $\mathcal{L} = 1$ fb^{-1}, one obtains the statistical error $\epsilon = \sqrt{S+B}/S$ on the cross section measurement which determines to which extent the $H\tau^+\tau^-$ coupling can be measured. For $M_H = 110\,(130)$ GeV, one has $\epsilon \simeq 20\%$ (30%) showing that one can observe the resonant $\mu^+\mu^- \to H \to \tau^+\tau^-$ process above the continuum background and therefore possibly measure the $H\tau^+\tau^-$ coupling and check the Higgs boson spin.

Note that because of depolarization effects, this type of analysis cannot be performed in the decays $H \to b\bar{b}$, while for $H \to t\bar{t}$ the rates are too small, the Higgs resonance being very broad as discussed earlier. On the other hand, the CP quantum numbers of a relatively heavier Higgs boson, $M_H \gtrsim 140$ GeV, can be studied in the decays $H \to VV^* \to 4f$ by looking at angular distributions and correlations as discussed in detail in §2.2.4.

CP Measurements with transverse polarization

It is expected that muon colliders will have a natural transverse polarization of the order of 20% for both the μ^+ and μ^- beams. This polarization, if maximized, could also provide an unambiguous test of the CP quantum numbers of the Higgs boson [163, 173, 630], similarly to the case of $\gamma\gamma$ colliders previously discussed. Indeed, if one considers a scalar particle with couplings to muons which have both CP–even and CP–odd components, $\mathcal{L}(H\mu\mu) \propto H\bar{\mu}(a + ib\gamma_5)\mu$, and assumes that the muon beams are 100% transversally polarized, with ϕ being the angle between the μ^+ and μ^- transverse polarizations, the production cross section of the Higgs boson in the s–channel reads

$$\sigma(\mu^+\mu^- \to H) \propto 1 - \frac{a^2 - b^2}{a^2 + b^2}\cos\phi + \frac{2ab}{a^2 + b^2}\sin\phi \tag{4.101}$$

If the Higgs boson is a mixture of CP–even and CP–odd states, both the a_+ and a_- components are non–zero and the asymmetry

$$\mathcal{A}_1 = \frac{\sigma(\phi = \frac{\pi}{2}) - \sigma(\phi = -\frac{\pi}{2})}{\sigma(\phi = \frac{\pi}{2}) + \sigma(\phi = -\frac{\pi}{2})} = \frac{2ab}{a^2 + b^2} \tag{4.102}$$

is large if a and b have the same magnitude. A non–zero value of this asymmetry would indicate a clear violation of CP symmetry. For a pure CP–eigenstate, one of the coefficients a or b is zero and the asymmetry

$$\mathcal{A}_2 = \frac{\sigma(\phi = \pi) - \sigma(\phi = 0)}{\sigma(\phi = \pi) + \sigma(\phi = 0)} = \frac{a^2 - b^2}{a^2 + b^2} \tag{4.103}$$

is either equal to $+1$ or -1, if the Higgs boson is, respectively a CP–even or a CP–odd state. In the ideal world, this is an unambiguous test of the CP nature of the Higgs boson. However, the transverse polarization will most probably not be maximal and background events will alter the signal and dilute the asymmetries. Thorough studies, including the machine and background aspects must be performed to quantify the extent to which the Higgs boson CP–properties can be measured; see Ref. [173] for such an attempt.

References

[1] S. Glashow, Nucl. Phys. 22 (1961) 579; S. Weinberg, Phys. Rev. Lett. 19 (1967) 1264; A. Salam, in "Elementary Particle Theory", ed. N. Svartholm, Almqvist and Wiksells, Stockholm (1969) p. 367.

[2] M. Gell-Mann, Phys. Lett. 8 (1964) 214; G. Zweig, CERN-Report 8182/TH401 (1964); H. Fritzsch, M. Gell-Mann and H. Leutwyler, Phys. Lett. B47 (1973) 365; D. Gross and F. Wilczek, Phys. Rev. Lett. 30 (1973) 1343; H.D. Politzer, Phys. Rev. Lett. 30 (1973) 1346; G. 't Hooft, Marseille Conference on Yang–Mills fields (1972).

[3] P.A.M. Dirac, Proc. Roy. Soc. Lond. A114 (1927) 243; P. Jordan and W. Pauli, Z. Phys. 47 (1928) 151; W. Heisenberg and W. Pauli, Z. Phys. 56 (1929) 1; S. Tomonaga, Progr. Theor. Phys. 1 (1946) 27; J. Schwinger, Phys. Rev. 73 (1948) 416; R. Feynman, Phys. Rev. 76 (1949) 749.

[4] E. Fermi, Nuovo Cim. 11 (1934) 1; *ibid.* Z. Phys. 88 (1934) 161; R. Feynman and M. Gell-Mann, Phys. Rev. 109 (1958) 193.

[5] G. 't Hooft, Nucl. Phys. B33 (1971) 173; *ibid.* Nucl. Phys. B35 (1971) 167; G. 't Hooft and M. Veltman, Nucl. Phys. B44 (1972) 189.

[6] P.W. Higgs, Phys. Rev. Lett. 13 (1964) 508; *ibid.* Phys. Rev. 145 (1966) 1156; F. Englert and R. Brout, Phys. Rev. Lett. 13 (1964) 321; G.S. Guralnik, C.R. Hagen and T. Kibble, Phys. Rev. Lett. 13 (1965) 585; T. Kibble, Phys. Rev. 155 (1967) 1554.

[7] Ch. Llewellyn Smith, Phys. Lett. 46B (1973) 233; J.S. Bell, Nucl. Phys. B60 (1973) 427; J.M. Cornwall, M.D. Levin and G. Tiktopoulos, Phys. Rev. Lett. 30 (1973) 1268; *ibid.* Phys. Rev. D10 (1974) 1145 and (E) *ibid.* D11 (1975) 972.

[8] The LEP Collaborations (ALEPH, DELPHI, L3 and OPAL), the LEP Electroweak Working Group and the SLD Heavy Flavour Group, *A combination of preliminary Electroweak measurements and constraints on the Standard Model*, hep-ex/0412015; `http://lepewwg.web.cern.ch/LEPEWWG`.

[9] Particle Data Group, K. Hagiwara *et al.*, Phys. Rev. D66 (2002) 010001; S. Eidelman *et al.*, Phys. Let. B592 (2004) 1.

[10] The LEP Collaboration (ALEPH, DELPHI, L3 and OPAL), Phys. Lett. B565 (2003) 61.

[11] F.J. Hasert *et al.* (Gargamelle Collaboration), Phys. Lett. B46 (1973) 121; *ibid.* Phys. Lett. B46 (1973) 138; T. Eichten *et al.* (Gargamelle Collaboration), Phys. Lett. B46 (1973) 274.

[12] G. Arnison *et al.* (UA1 Collaboration), Phys. Lett. B122 (1983) 103; M. Banner *et al.* (UA2 Collaboration), Phys. Lett. B122 (1983) 476; G. Arnison *et al.* (UA1 Collaboration), Phys. Lett. B126 (1983) 398; P. Bagnaia *et al.* (UA2 Collaboration), Phys. Lett. B129 (1983) 130.

[13] J. Gunion, H. Haber, G. Kane, and S. Dawson, *The Higgs Hunter's Guide*, Addison–Wesley, Reading (USA), 1990.

[14] F. Abe *et al.* (CDF Collaboration), Phys. Rev. Lett. 74 (1995) 2626; S. Abachi *et al.* (D0 Collaboration), Phys. Rev. Lett. 74 (1995) 2632.

[15] The CDF and DØ collaborations and the Tevatron Electroweak Working Group, hep-ex/0404010.

[16] See for instance: I. Aitchison and A. Hey, *Gauge Theories in Particle Physics*, Adam Hilger, Bristol (UK), 1982; C. Quigg, *Gauge Theories of the Strong, Weak, and Electromagnetic Interactions*, Benjamin-Cummings, Reading (USA), 1983; T.P. Cheng and L.F. Li, *Gauge theory of Elementary Particle Physics*, Oxford Sciences Publications, Clarendon Press, Oxford, 1984; F. Halzen and A.D. Martin, *Quarks and Leptons: an introductory course in modern Particle Physics*, Wiley, New York (USA), 1984; C. Itzykson and J.B. Zuber, *Quantum Field Theory*, Mac Graw Hill Book Co (Singapore), 1985; D. Bailin and A. Love, *Introduction to Gauge Field Theory*, Adam Hilger, Bristol (UK), 1986; M.E. Peskin and D.V. Schroeder, *An introduction to Quantum Field Theory*, Addison-Wesley, Reading (USA) 1995.

[17] See for instance: E. Abers and B. Lee, Phys. Rep. 9 (1973) 1; M.A.B. Beg and A. Sirlin, Phys. Rept. 88 (1982) 1; C. Quigg, *Introduction to gauge theories of the strong, weak and electromagnetic interactions*, Lectures given at "NATO Advanced Study Inst.: Techniques and Concepts of High Energy Physics", St. Croix, U.S. Virgin Islands, July 1980, published in Virgin Islands Inst.1980:143; R.N. Cahn, Rept. Prog. Phys. 52 (1989) 389; M.E. Peskin, *Theory of precision electroweak mesurements*, Lectures given at "17th SLAC Summer Inst.: Physics at the 100 GeV Mass Scale", Stanford, July 1989, published in SLAC Summer Inst.1989:71-126; F.M. Renard, *Standardissimo*, published in Annales Phys. (France) 17 (1992) 301; G. Altarelli, *The standard electroweak theory and its experimental tests*, Lectures given at "32nd Internationale Universitatswochen fur Kern- und Teilchenphysik", Schladming, Austria, Feb–Mar

1993, Published in Schladming School 1993:323-382; P. Langacker, *Tests of the Standard Model and searches for New Physics*, in "Precision tests of the standard electroweak model", P. Langacker (ed.), hep-ph/9412361; S.F. Novaes, *Standard Model: an introduction*, Proceedings of the "10th Jorge Andre Swieca Summer School: Particle and Fields", Sao Paulo, Brazil, February 1999, hep-ph/0001283; H. Spiesberger, M. Spira and P.M. Zerwas, *The Standard Model: Physical basis and scattering experiments*, published in "Scattering", P. Sabatier (ed), Academic Press, London, 2000, hep-ph/0011255; A. Pich, *The Standard Model of Electroweak Interactions*, Lectures given at the "2004 European School of High–Energy Physics", Sant Feliu de Guixol (Spain), June 2004, hep-ph/0502002.

[18] See for instance: W.J. Stirling, *Higgs Phenomenology*, Lectures given at "42nd Scottish Universities Summer School in Physics: High Energy Phenomenology", St. Andrews (Scotland), August 1993, published in Scottish Summer School 1993:0225-270; M.E. Peskin, *Beyond the Standard Model*, Lectures given at the European School of High-Energy Physics, Carry-le-Rouet (France), September 1996, hep-ph/9705479; S. Dawson, *Introduction to Electroweak Symmetry Breaking*, Lectures given at "ICTP Summer School in High-Energy Physics and Cosmology", Trieste (Italy), 29 Jun - 17 Jul 1998, hep-ph/9901280; M. Spira and P.M. Zerwas, *Electroweak symmetry breaking and Higgs Physics*, Lectures given at "36th Internationale Universitatswochen fuer Kernphysik und Teilchenphysik: Computing Particle Properties", Schladming, Austria, March 1997, hep-ph/9803257; C. Quigg, *Electroweak Symmetry breaking and the Higgs sector*, presented at "27th International Meeting on Fundamental Physics", Sierra Nevada, Granada (Spain), February 1999, Acta Phys. Polon. B30 (1999) 2145, hep-ph/9905369.

[19] B.A. Kniehl, Phys. Rep. 240 (1994) 211.

[20] A. Djouadi, Int. J. Mod. Phys. A10 (1995) 1.

[21] M. Spira, Fortschr. Phys. 46 (1998) 203.

[22] M. Steinhauser, Phys. Rept. 364 (2002) 247.

[23] M. Carena and H.E. Haber, Prog. Part. Nucl. Phys. 50 (2003) 63.

[24] A. Djouadi, *The Anatomy of Electro–Weak Symmetry Breaking, II: The Higgs bosons in the minimal Supersymmetric Model*; hep-ph/0503173.

[25] A. Djouadi, *The Anatomy of Electro–Weak Symmetry Breaking, III: The Higgs sector in models beyond the SM and MSSM benchmarks*, in preparation.

[26] C.N. Yang and R. Mills, Phys. Rev. 96 (1954) 191.

[27] S.L. Adler and W.A. Bardeen, Phys. Rev. 182 (1969) 1517; R. Jackiw, Lectures on "Current Algebra and its Applications", Princeton University Press, 1972.

[28] C. Bouchiat, J. Iliopoulos and Ph. Meyer, Phys. Lett. 38B (1972) 519.

[29] Y. Nambu, Phys. Rev. Lett. 4 (1960) 380; Y. Nambu and G. Jona–Lasinio, Phys. Rev. 122 (1961) 345; *ibid.* Phys. Rev. 124 (1961) 246; J. Goldstone, Nuov. Cim. 19 (1961) 154; J. Goldstone, A. Salam and S. Weinberg, Phys. Rev. 127 (1962) 965.

[30] K. Fujikawa, B.W. Lee and A. Sanda, Phys. Rev. D6 (1972) 2923; Y.P. Yao, Phys. Rev. D7 (1973) 1647; G. 't Hooft in Ref. [5].

[31] M. Chanowitz and M. Gaillard, Phys. Lett. 142B (1984) 85; *ibid.* Nucl. Phys. B261 (1985) 379.

[32] B.W. Lee, C. Quigg and H.B. Thacker, Phys. Rev. D16 (1977) 1519.

[33] C. E. Vayonakis, Lett. Nuovo Cimento 17 (1976) 383; H. Weldon, Phys. Lett. 146B (184) 59; G. J. Gounaris, R. Kögerler and H. Neufeld, Phys. Rev. D34 (1986) 3257; Y.P. Yao and C.P. Yuan, Phys. Rev. D38 (1988) 2237; W. Marciano, G. Valencia and S. Willenbrock, Phys. Rev. D40 (1989) 1725; J. Bagger and C. Schmidt, Phys. Rev. D41 (1990) 264; H. Veltman, Phys. Rev. D41 (1990) 2294.

[34] N. Cabibbo, Phys. Rev. Lett. 10 (1963) 531; M. Kobayashi and T. Maskawa, Prog. Theor. Phys. 49 (1973) 652.

[35] S. Glashow, J. Illiopoulos and L. Maiani, Phys. Rev. D2 (1970) 1285.

[36] D. Ross and M. Veltman, Nucl. Phys. B95 (1975) 135.

[37] T. Appelquist and J. Carazzone, Phys. Rev. D11 (1975) 2856.

[38] G. Källén and A. Sabry, K. Dan. Vidensk. Selsk. Mat.-Fys. Medd. 29 (1955) No. 17; M. Steinhauser, Phys. Lett. B429 (1998) 158.

[39] M. Davier and A. Köcker, Phys. Lett. B419 (1998) 419; J. Erler, Phys. Rev. D59 (1999) 054008; F. Jegerlehner, hep-ph/0308117; K. Hagiwara, A. Martin, D. Nomura and T. Teubner, Phys. Rev. D69 (2004) 093003.

[40] H. Burkhardt and B. Pietrzyk, Phys. Lett. B513 (2001) 46.

[41] R.E. Behrends, R.J. Finkelstein and A. Sirlin, Phys. Rev. 101 (1956) 866; T. Kinoshita and A. Sirlin, Phys. Rev. 113 (1959) 1652; T. van Ritbergen and R. Stuart, Phys. Rev. Lett. 82 (1999) 488.

[42] For reviews, see e.g.: G. Altarelli, *A QCD Primer*, Lectures given at "2001 European School of High-Energy Physics", Beatenberg (Switzerland), Aug–Sep 2001, hep-ph/0204179; S. Bethke, J. Phys. G26 (2000) R27; *ibid.* Nucl. Phys. Proc. Suppl. 121 (2003); I. Hinchliffe in Ref. [9].

[43] O. Tarasov, A. Vladimirov and A. Zharkov, Phys. Lett. B93 (1980) 429; S.A. Larin and J.A.M. Vermaseren, Phys. Lett. B303 (1993) 334.

[44] M. Jeżabek and J. H. Kühn, Nucl. Phys. B314 (1989) 1; *ibid.* Nucl. Phys. B320 (1989) 20; *ibid.* Phys. Rev. D48 (1993) 1910 ; A. Czarnecki, Phys. Lett. B252 (1990) 467; C.S. Li, R.J. Oakes and T.C. Yuan, Phys. Rev. D43 (1991) 3759; A. Denner and T. Sack, Nucl. Phys. B358 (1991) 46; G. Eilam, R. Mendel, R. Migneron and A. Soni, Phys. Rev. Lett. 66 (1991) 3105; T. Kuruma, Z. Phys. C57 (1993) 551; A. Czarnecki and K. Melnikov, Nucl. Phys. B544 (1999) 520; K. G. Chetyrkin, R. Harlander, T. Seidensticker and M. Steinhauser, Phys. Rev. D60 (1999) 114015.

[45] For a detailed review on the top quark see, for instance, M. Beneke, I. Efthymiopoulos, M.L. Mangano and J. Womersley (conv) *et al.*, *Top Quark Physics* in the Report of the "1999 CERN Workshop on SM Physics at the LHC", Report CERN-TH/2000-100, hep-ph/0003033.

[46] For theoretically oriented reviews on the top quark properties, see: J.H. Kuhn, hep-ph/9707321; S. Dawson, hep-ph/0303191.

[47] S. Narison, *Light and heavy quark masses, flavor breaking of chiral condensates, meson weak leptonic decay constants in QCD*, hep-ph/0202200.

[48] N. Gray, D.J. Broadhurst, W. Grafe and K. Schilcher, Z. Phys. C48 (1990) 673; K.G. Chetyrkin and M. Steinhauser, Phys. Rev. Lett. 83 (1999) 4001; *ibid.* Nucl. Phys. B573 (2000) 617; K. Melnikov and T. van Ritbergen, Phys. Lett. B482 (2000) 99.

[49] S.G. Gorishny, A.L. Kataev, S.A. Larin and L.R. Surguladze, Mod. Phys. Lett. A5 (1990) 2703; *ibid.* Phys. Rev. D43 (1991) 1633.

[50] K.G. Chetyrkin, Phys. Lett. B404 (1997) 161; J.A.M. Vermaseren, S.A. Larin and T. van Ritbergen, Phys. Lett. B405 (1997) 327.

[51] The LEP2 WW Working Group (U. Parzefall *et al.*), Note LEPEWWG/TGC/2003–01; see the web site: `http://lepewwg.web.cern.ch/LEPEWWG/tgc`.

[52] The CDF and DØ collaborations, Phys. Rev. D70 (2004) 092008.

[53] *Z Physics at LEP1*, CERN Report 89–08 (1989), eds. G. Altarelli, R. Kleiss and C. Verzegnassi; see this reference for earlier work.

[54] *Reports of the Working Group on Precision Calculations for the Z Resonance*, CERN Report 95–03 (1995), eds. D. Bardin, W. Hollik and G. Passarino.

[55] *Physics at LEP2*, CERN Report 96–01, eds. G. Altarelli, T. Sjöstrand and F. Zwirner.

[56] For a more recent account of high–precision measurements, see the review of W. Hollik, *SM Theory*, plenary talk given at the XXIX ICHEP, Vancouver, Canada, July 1998, hep-ph/9811313.

[57] M. Böhm and W. Hollik (conv.) *et al.*, *Forward–Backward Asymmetries* in Ref. [53], Part 1, p. 203; J. Kühn and P.M. Zerwas (conv.) *et al.*, *Heavy Flavors at LEP* in Ref. [53], Part 1, p. 269.

[58] K.G. Chetyrkin, J.H. Kühn and A. Kwiatkowski, *QCD corrections to the e^+e^- cross-section and the Z boson decay rate*, Phys. Rept. 277 (1996) 189 and in Ref. [54], p. 175.

[59] F. Berends (conv.) *et al.*, *The Z lineshape* in Ref. [53], Part 1, p. 81.

[60] M. Consoli, W. Hollik and F. Jegerlehner, *Electroweak radiative corrections for Z physics* in Ref. [53], Part 1, p.7; G. Burgers, F. Jegerlehner, B. Kniehl and J. Kühn, *Δr or the relation between the electroweak couplings and the weak boson masses* in Ref. [53], Part 1, p.55.

[61] M. Veltman, Nucl. Phys. B123 (1977) 89; M.S. Chanowitz, M.A. Furman and I. Hinchliffe, Phys. Lett. B78 (1978) 285.

[62] A. Djouadi and C. Verzegnassi, Phys. Lett. B195 (1987) 265; A. Djouadi, Nuovo Cim. A100 (1988) 357; B. Kniehl, Nucl. Phys. B347 (1990) 86; F. Halzen and B. Kniehl, Nucl. Phys. B353 (1991) 567; A. Djouadi and P. Gambino, Phys. Rev. D49 (1994) 3499.

[63] L. Avdeev, J. Fleischer, S.M. Mikhailov and O. Tarasov, Phys. Lett. B336 (1994) 560 and (E) *ibid.* B349 (1995) 597; K.G. Chetyrkin, J.H. Kühn and M. Steinhauser, Phys. Lett. B351 (1995) 331.

[64] J.J. van der Bij and F. Hoogeveen, Nucl. Phys. B283 (1987) 477.

[65] R. Barbieri, M. Beccaria, P. Ciafaloni, G. Curci and A. Vicere, Phys. Lett. B288 (1992) 95; *ibid.* Nucl. Phys. B409 (1993) 105; J. Fleischer, F. Jegerlehner and O.V. Tarasov, Phys. Lett. B319 (1993) 249.

[66] G. Degrassi, P. Gambino and A. Vicini, Phys. Lett. B383 (1996) 219; G. Degrassi, P. Gambino and A. Sirlin, Phys. Lett. B394 (1997) 188; A. Freitas, W. Hollik, W. Walter and G. Weiglein, Phys. Lett. B495 (2000) 338; *ibid.* Nucl. Phys. B632 (2002) 189; M. Awramik and M. Czakon, Phys. Lett. B568 (2003) 48; M. Awramik, M. Czakon, A. Freitas and G. Weiglein, Phys. Rev. D69 (2004) 053006.

[67] G. Degrassi and P. Gambino, Nucl. Phys. B567 (2000) 3.

[68] M. Awramik, M. Czakon, A. Freitas and G. Weiglein, Phys. Rev. Lett. 93 (2004) 201805.

[69] J. van der Bij, K. Chetyrkin, M. Faisst, G. Jikia and T. Seindensticker, Phys. Lett. B498 (2001) 156; M. Faisst, J.H. Kühn, T. Seindensticker and O. Veretin, Nucl. Phys. B665 (2003) 649.

[70] M. Veltman, Acta. Phys. Pol. B8 (1977) 475.

[71] T. Appelquist and C. Bernard, Phys. Rev. D22 (1980) 200; A. Longhitano, Nucl. Phys. B188 (1981) 118; M. Einhorn and J. Wudka, Phys. Rev. D39 (1989) 2758.

[72] J.J. van der Bij and M. Veltman, Nucl. Phys. B231 (1985) 205.

[73] R. Boughezal, J.B. Tausk and J.J. van der Bij, hep-ph/0410216.

[74] J. Jersak, E. Laermann and P.M. Zerwas Phys. Rev. D25 (1982) 1218 and (E) *ibid.* D36 (1987) 310; A. Djouadi, J. Kühn and P.M. Zerwas, Z. Phys. C46 (1990) 411; A. Djouadi, B. Lampe and P.M. Zerwas, Z. Phys. C67 (1995) 123; A.B. Arbuzov, D.Yu. Bardin and A. Leike, Mod. Phys. Lett. A7 (1992) 2029 and (E) *ibid.* A9 (1994) 1515.

[75] A.A. Akhundov, D.Yu. Bardin and T. Riemann, Nucl. Phys. B276 1 (1986) 1; W. Beenakker and W. Hollik, Z. Physik C40 (1988) 141; J. Bernabeu, A. Pich and A. Santamaria, Phys. Lett. B200 (1988) 569; B.W. Lynn and R.G. Stuart, Phys. Lett. B252 (1990) 676.

[76] F. Boudjema, A. Djouadi and C. Verzegnassi, Phys. Lett. B238 (1990) 423; A. Blondel, A. Djouadi and C. Verzegnassi, Phys. Lett. B293 (1992) 253; A. Djouadi, G. Girardi, C. Verzegnassi, W. Hollik and F.M. Renard, Nucl. Phys. B349 (1991) 48.

[77] A. Denner, W. Hollik and B. Lampe, Z. Phys. C60 (1993) 193.

[78] O.P. Sushkov, V.V. Flambaum and V.V. Khriplovich, Sov. J. Nucl. Phys. 20 (1975) 537; W. Alles, C. Boyer and A. Buras, Nucl. Phys. B119 (1977) 125.

[79] M. Lemoine and M. Veltman, Nucl. Phys. B164 (1980) 445; R. Phillipe, Phys. Rev. D26 (1982) 1588; M. Bohm, A. Denner, T. Sack, W. Beenakker, F. Behrends and H. Kuifj, Nucl. Phys. B304 (1988) 463; J. Fleisher, F. Jegerlehner and M. Zralek, Z. Phys. C42 (1989) 409; W. Beenakker, K. Kolodziej and T. Sack, Phys. Lett. B258 (1991) 469; J. Fleisher, F. Jegerlehner and K. Kolodziej, Phys. Rev. D47 (1993) 830.

[80] For a review of weak boson production in e^+e^- collisions including radiative corrections, see: W. Beenakker and A. Denner, Int. J. Mod. Phys. A9 (1994) 4837.

[81] For a recent review, see e.g. U. Baur, *Measuring the W boson mass at hadron colliders*, published in "Zeuthen 2003, Electroweak precision data and the Higgs mass", p. 47, hep-ph/0304266.

[82] For a detailed discussion of electroweak SM processes at the LHC, including weak boson production, see: R. Haywood, P. Hobson, W. Hollik and Z. Kunszt (conv.) *et al.*, Report of the Electroweak Working Group at "1999 CERN Workshop on SM Physics at the LHC", hep-ph/0003275.

[83] S.D. Drell and T.M. Yan, Phys. Rev. Lett. 25 (1970) 316.

[84] G. Altarelli, R.K. Ellis and G. Martinelli, Nuc. Phys. B157 (1979) 461; J. Kubar–André and F. Paige, Phys. Rev. D19 (1979) 221.

[85] R. Hamberg, W.L. van Neerven and T. Matsuura, Nucl. Phys. B359 (1991) 343 and (E) *ibid.* B644 (2002) 403.

[86] A. Sirlin, Phys. Rev. D22 (1980) 971; W. Marciano and A. Sirlin, Phys. Rev. D22 (1980) 2695; *ibid.* Phys. Rev. D29 (1984) 945; A. Sirlin and W. Marciano, Nucl. Phys. B189 (1981) 442.

[87] W. Marciano, Phys. Rev. D20 (1979) 274; W. Marciano and A. Sirlin, Phys. Rev. Lett. 46 (1981) 163; W. Marciano, S. Sarantakos and A. Sirlin, Nucl. Phys. B217 (1983) 84.

[88] M. Awramik and M. Czakon, Phys. Rev. Lett. 89 (2002) 241801; A. Onishchenko and O. Veretin, Phys. Lett. B551 (2003) 111.

[89] K. Gaemers and G. Gounaris, Z. Phys. C1 (1979) 259; K. Hagiwara, K. Hikasa, R. D. Peccei and D. Zeppenfeld, Nucl. Phys. B282 (1987) 253.

[90] G. Gounaris, J.-L. Kneur and D. Zeppenfeld (conv.) *et al.*, *Triple Gauge Boson Couplings* in Ref. [55], p. 525.

[91] W. Hollik, Fortsch. Phys. 38 (1990) 165.

[92] M. Peskin and T. Takeuchi, Phys. Rev. Lett. 65 (1990) 964; *ibid.* Phys. Rev. D46 (1992) 381.

[93] G. Altarelli and R. Barbieri, Phys. Lett. B253 (1991) 161; G. Altarelli, R. Barbieri and F. Caravaglios, Nucl. Phys. B405 (1993) 3.

[94] C.S. Wood *et al.*, Science 275 (1997) 1759; S.C. Bennett and C.E. Wieman, Phys. Rev. Lett. 82 (1999) 2484; M. Kuchiev and V. Flambaum, Phys. Rev. Lett. 89 (2002) 283002.

[95] G.P. Zeller *et al.*, Phys. Rev. Lett. 88 (2002) 091802.

[96] For a review, see P. Gambino, Int. J. Mod. Phys. A19 (2004) 808.

[97] Very recently, new $\mathcal{O}(\alpha)$ photon bremsstrahlung corrections have been calculated and shown to remove the NuTeV discrepancy if included; M. Gluck, P. Jimenez–Delgado and E. Reya, hep-ph/0503103.

[98] For a review, see M. Chanowitz, published in "Zeuthen 2003, Electroweak precision data and the Higgs mass", p. 15-24, hep-ph/0304199.

[99] C.J.C. Burges and H. J. Schnitzer, Nucl. Phys. B228 (1983) 464; C.N. Leung, S.T. Love and S. Rao, Z. Phys. C31 (1986) 433: W. Buchmuller and D. Wyler, Nucl. Phys. B268 (1986) 621; K. Hagiwara, S. Ishihara, R. Szalapski and D. Zeppenfeld, Phys. Lett. B283 (1992) 353; *ibid.* Phys. Rev. D48 (1993) 2182.

[100] K. Whisnant, J. M. Yang, B.-L. Young and X. Zhang, Phys. Rev. D56 (1997) 467; G.J. Gounaris, D.T. Papadamou and F. M. Renard, Z. Phys. C76 (1997) 333; J.M. Yang and B.-L Young, Phys. Rev. D56 (1997) 5907; G. Gounaris and G. Tsirigoti, Phys. Rev. D56 (1997) 3030.

[101] See for instance, R. Barbieri and A. Strumia Phys. Lett. B462 (1999) 144; L. Hall and C. Kolda, Phys. Lett. B459 (1999) 213.

[102] M. Peskin and J. Wells, Phys. Rev. D64 (2001) 093003.

[103] For Z' physics as well as production and study at future colliders, see for instance: J.L. Hewett and T.G. Rizzo, Phys. Rept. 183 (1989) 193; A. Djouadi *et al.*, Z. Phys.

C56 (1992) 289; A. Leike, Phys. Rept. 317 (1999) 143; M. Dittmar *et al.*, Phys. Lett. B583 (2004) 111.

[104] P.J. Franzini and P. Taxil (conv.) *et al.*, *Higgs at LEP1* in Ref. [53], Part II, p. 59; E.W.N. Glover, J.J. van der Bij (conv.) *et al.*, *Rare Z Decays* in Ref. [53], Part II, p. 1.

[105] J.D. Bjorken, Proc. 1976 SLAC Summer Inst. Part. Phys., SLAC report 198 (1977) 1.

[106] F.A. Behrends and R. Kleiss, Nucl. Phys. B260 (1985) 32.

[107] R.N. Cahn, M.S. Chanowitz and N. Fleishon, Phys. Lett. 82B (1979) 113.

[108] L. Bergstrom and G. Hulth, Nucl. Phys. B259 (1985) 137.

[109] ALEPH Collaboration (D. Buskulic *et al.*), Phys. Lett. B384 (1996) 427; DELPHI Collaboration (P. Abreu *et al.*), Nucl. Phys. B421 (1994) 3; L3 Collaboration (M. Acciarri *et al.*), Phys. Lett. B385 (1996) 454; OPAL Collaboration (G. Alexander *et al.*), Z. Phys. C73 (1997) 189.

[110] J.F. Grivaz, Rapporteur talk given at "International Europhysics Conference on High Energy Physics" (HEP 95), Brussels, 1995; Particle Data Group (R. M. Barnett *et al.*), Phys. Rev. D54 (1996) 1.

[111] J. Ellis, M.K. Gaillard, and D.V. Nanopoulos, Nucl. Phys. B106 (1976) 292.

[112] D.R.T. Jones and S.T. Petcov, Phys. Lett. B84 (1979) 440.

[113] B.L. Joffe and V.A. Khoze, Sov. J. Part. Phys. 9 (1978) 50; E. Ma and Y. Okada, Phys. Rev. D20 (1979) 1052; J. Finjord, Physica Scripta 21 (1980) 143.

[114] M. Carena and P.M. Zerwas (conv.) *et al.*, *Higgs Physics at LEP2* in Ref. [55], Part I, p. 351, hep-ph/9602250.

[115] The LEP Collaborations (ALEPH, DELPHI, L3 and OPAL), hep-ex/0107032.

[116] The LEP Collaborations (ALEPH, DELPHI, L3 and OPAL), hep-ex/0107034.

[117] D.A. Dicus and S. Mathur, Phys. Rev. D7 (1973) 3111; B. Lee, C. Quigg and H. Thacker, Phys. Rev. Lett. 38 (1977) 883; H.A. Weldon, Phys. Rev. D30 (1984) 1547; M. Chanowitz, M. Golden and H. Georgi, Phys. Rev. Lett. 57 (1986) 2344; *ibid.* Phys. Rev. D36 (1987) 1490.

[118] M. S. Chanowitz, *Strong WW scattering at the end of the 90's: Theory and experimental prospects*, pulished in Zuoz 1998, "Hidden symmetries and Higgs phenomena", p. 81, hep-ph/9812215.

[119] M. Lüscher and P. Weisz, Phys. Lett. B212 (1988) 472; *ibid.* Nucl. Phys. B318 (1989) 705.

[120] A. Arhrib, *Unitarity constraints on scalar parameters of the standard and two Higgs doublets models*, hep-ph/0012353.

[121] W. Marciano and S. Willenbrock, Phys. Rev. D37 (1988) 2509; S. Dawson and S. Willenbrock, Phys. Rev. Lett. 62 (1989) 1232.

[122] L. Durand, B. A. Kniehl and K. Riesselmann, Phys. Rev. D51 (1995) 5007; A. Ghinculov, Nucl. Phys. B455 (1995) 21; A. Frink, B. Kniehl, D. Kreimer and K. Riesselmann, Phys. Rev. D54 (1996) 4548; T. Binoth, A. Ghinculov and J.J. van der Bij, Phys. Rev. D57 (1998) 1487.

[123] A. Ghinculov, Phys. Lett. B337 (1994) 137 and (E) *ibid* B346 (1995) 426; A. Frink, B. Kniehl and K. Riesselmann, Phys. Rev. Lett. 72 (1994) 2534 and (E) *ibid.* 74 (1995) 1699; V. Borodulin and G. Jikia, Phys. Lett. B391 (1997) 434.

[124] S. Dawson and S. Willenbrock, Phys. Rev. D40 (1989) 2880.

[125] L. Durand, P. Maher and K. Riesselmann, Phys. Rev. D48 (1993) 1084; K. Riesselmann, Phys. Rev. D53 (1996) 6226; U. Nierste and K. Riesselmann, Phys. Rev. D53 (1996) 6638.

[126] K. Riesselmann and S. Willenbrock, Phys. Rev. D55 (1997) 311.

[127] T. Cheng, E. Eichten and L. Li, Phys. Rev. D9 (1974) 2259; B. Pendleton and G. Ross, Phys. Lett. B98 (1981) 291; C. Hill, Phys. Rev. D24 (1981) 691; J. Bagger, S. Dimopoulos and E. Masso, Nucl. Phys. B253 (1985) 397; M. Beg, C. Panagiotakopoulos and A. Sirlin, Phys. Rev. Lett. 52 (1984) 883; M. Duncan, R. Philippe and M. Sher, Phys. Lett. B153 (1985) 165; K. Babu and E. Ma, Phys. Rev. Lett. 55 (1985) 3005.

[128] K.G. Wilson and J. Kogut, Phys. Rept. 12 (1974) 75.

[129] N. Cabibbo, L. Maiani, G. Parisi and R. Petronzio, Nucl. Phys. B158 (1979) 295; R. Dashen and H. Neuberger, Phys. Rev. Lett. 50 (1983) 1897; D. Callaway, Nucl. Phys. B233 (1984) 189; P. Hasenfratz and J. Nager, Z. Phys. C37 (1988) 477; J. Kuti, L. Lin, and Y. Shen, Phys. Rev. Lett. 61 (1988) 678; R. Chivukula and E. Simmons, Phys. Lett. B388 (1996) 788.

[130] A. Hasenfratz, *Quantum Fields on the Computer*, Ed. M. Creutz, World Scientific, Singapore, 1992, p. 125; M. Gõckeler, H. Kastrup, T. Neuhaus and F. Zimmermann, Nucl. Phys. B405 (1993) 555.

[131] M. Lindner, M. Sher and H.W. Zaglauer, Phys. Lett. 228B (1989) 139; M. Sher, Phys. Lett. B317 (1993) 159; *ibid.* Phys. Lett. B331 (1994) 448; G. Altarelli and I. Isidori, Phys. Lett. B337 (1994) 141; J.A. Casas, J.R. Espinosa and M. Quiros, Phys. Lett. B342 (1995) 171; J. Espinosa and M. Quiros, Phys. Lett. B353 (1995) 257.

[132] M. Sher, Phys. Rept. 179 (1989) 273.

[133] G. Isidori, G. Ridolfi and A. Strumia, Nucl. Phys. B609 (2001) 387.

[134] G. Anderson, Phys. Lett. B243 (1990) 265; P. Arnold and S. Vokos, Phys. Rev. D44 (1991) 3620; J.R. Espinosa and M. Quiros, Phys. Lett. B353 (1995) 257.

[135] M. Lindner, Z. Phys. C31 (1986) 295; B. Grzadowski and M. Lindner, Phys. Lett. B178 (1986) 81.

[136] T. Hambye and K. Riesselmann, Phys. Rev. D55 (1997) 7255.

[137] M. Veltman, Acta Phys. Polon. B12 (1981) 437.

[138] M. Einhorn and D. Jones, Phys. Rev. D46 (1992) 5206.

[139] I. Jack and D.R.T. Jones, Nucl. Phys. B342 (1990) 127; R. Decker and J. Pestieau, Mod. Phys. Lett. A4 (1989) 2733; M. Capdequi-Peyranère, J. Montero and G. Moultaka, Phys. Lett. B260 (1991) 138; P. Osland and T. Wu, Phys. Lett. B291 (1992) 315; M. Chaichian, R. Gonzalez-Felipe and K. Huitu, Phys. Lett. B363 (1995) 101; A. Andrianov and N. Romanenko, Phys. Lett. B343 (1995) 295.

[140] C.F. Kolda and H. Murayama, JHEP 0007 (2000) 035.

[141] J.A. Casas, J.R. Espinosa and I. Hidalgo, JHEP 0411 (2004) 057.

[142] K. Hagiwara, R. Szalapski and D. Zeppenfeld, Phys. Lett. B318 (1993) 155; J.M. Hernandez, M.A. Perez and J.J. Toscano, Phys. Rev. D51 (1995) 2044.

[143] G.J. Gounaris and F. M. Renard, Phys. Rev. D59 (1999) 113015.

[144] J. Romao and S. Andringa, Eur. Phys. J. C7 (1999) 631.

[145] L. Resnick, M.K. Sundaresan and P.J.S. Watson, Phys. Rev. D8 (1973) 172.

[146] J.F. Gunion and H.E. Haber, Nucl. Phys. B272 (1986) 1.

[147] T. Arens, U. Gieseler and L.M. Sehgal, Phys. Lett. B339 (1994) 127.

[148] E. Braaten and J.P. Leveille, Phys. Rev. D22 (1980) 715; N. Sakai, Phys. Rev. D22 (1980) 2220; T. Inami and T. Kubota, Nucl. Phys. B179 (1981) 171; S.G. Gorishny, A.L. Kataev and S.A. Larin, Sov. J. Nucl. Phys. 40 (1984) 329.

[149] M. Drees and K. Hikasa, Phys. Rev. D41 (1990) 1547; *ibid.* Phys. Lett. B240 (1990) 455 and (E) *ibid.* B262 (1991) 497.

[150] K.G. Chetyrkin, Phys. Lett. B390 (1997) 309; K.G. Chetyrkin and M. Steinhauser, Phys. Lett. B408 (1997) 320.

[151] K.G. Chetyrkin and A. Kwiatkowski, Nucl. Phys. B461 (1996) 3; S.A. Larin, T. van Ritbergen and J.A.M. Vermaseren, Phys. Lett. B362 (1995) 134.

[152] A. Djouadi and P. Gambino, Phys. Rev. D51 (1995) 218.

[153] K. Melnikov, Phys. Rev. D53 (1996) 5020.

[154] R. Harlander and M. Steinhauser, Phys. Rev. D56 (1997) 3980.

[155] R. Decker, M. Nowakowski and A. Pilaftsis, Z. Phys. C57 (1993) 339; *ibid.* Mod. Phys. Lett. A6 (1991) 3491 and (E) *ibid.* A7 (1992) 819.

[156] A. Djouadi, J. Kalinowski and P.M. Zerwas, Z. Phys. C70 (1996) 435.

[157] S. Moretti and W. Stirling, Phys. Lett. B347 (1995) 291 and (E) *ibid.* B366 (1996) 451.

[158] J. R. Dell'Aquila and C.A. Nelson, Nucl. Phys. B320 (1989) 61; *ibid.* Nucl. Phys. B320 (1989) 86; C.A. Nelson, Phys. Rev. D41 (1990) 2805; S. Weinberg, Phys. Rev. D42 (1990) 860; B.K. Bullock, K. Hagiwara and A.D. Martin, Phys. Lett. B273 (1991) 501; S. Barr and A. Zee, Phys. Rev. Lett. 65 (1990) 21; J. Gunion and R. Vega, Phys. Lett. B251 (1990) 157; D. Chang, W.Y. Keung and T.C. Yuan, Phys. Lett. B251 (1990) 608; *ibid.* Phys. Rev. D43 (1991) R14; R. Leigh, S. Paban and R. Xu, Nucl. Phys. B352 (1991) 45; A. Skjold and P. Osland, Phys. Lett. B311 (1993) 261; W. Bernreuther and P. Overmann, Z. Phys. C61 (1994) 599; *ibid.* Z. Phys. C72 (1996) 461; X.G. He, J.P. Ma and B. McKellar, Phys. Rev. D49 (1994) 4548; *ibid.* Mod. Phys. Lett. A9 (1994) 205; W.N. Cottingham and I.B. Whittingham, Phys. Rev. D52 (1995) 539.

[159] V. Barger, K. Cheung, A. Djouadi, B. Kniehl and P. Zerwas, Phys. Rev. D49 (1994) 79.

[160] M. Kramer, J.H. Kuhn, M.L. Stong and P.M. Zerwas, Z. Phys. C64 (1994) 21.

[161] D. Chang, W.Y. Keung and I. Phillips, Phys. Rev. D48 (1993) 3225.

[162] H. Pois, T. Weiler and T.C. Yuan, Phys. Rev. D47 (1993) 3886; D. Chang and W.Y. Keung, Phys. Lett. B305 (1993) 261.

[163] B. Grzadkowski and J.F. Gunion, Phys. Lett. B350 (1995) 218.

[164] J.H. Kuhn and F. Wagner, Nucl. Phys. B236 (1984) 16.

[165] W. Bernreuther, A. Brandenburg and M. Flesch, Phys. Rev. D56 (1997) 90.

[166] Z. Was and M. Worek, Acta Phys. Polon. B33 (2002) 1875; M. Worek, Acta Phys. Polon. B34 (2003) 4549; G.R. Bower, T. Pierzchala, Z. Was and M. Worek, Phys. Lett. B543 (2002) 227.

[167] K. Desch, Z. Was and M. Worek, Eur. Phys. J. C29 (2003) 491; K. Desch, A. Imhof, Z. Was and M. Worek, Phys. Lett. B579 (2004) 157.

[168] G. Pocsik and T. Torma, Z. Phys. C6 (1980) 1; T.G. Rizzo, Phys. Rev. D22 (1980) 722; W.-Y. Keung and W.J. Marciano, Phys. Rev. D30 (1984) 248.

[169] D.A. Dicus, S. Willenbrock, T. Imbo, W.K. Keung and T. Rizzo, Phys. Rev. D34 (1986) 2157; T.G. Rizzo, Phys. Rev. D31 (1985) 2366; P. Langacker and J. Liu, Phys. Rev. D46 (1992) 5069.

[170] A. Grau, G. Panchieri and R.J.N. Phillips, Phys. Lett. B251 (1990) 293.

[171] R.N. Cahn, Rep. Prog. Phys. 52 (1989) 389; B. Kniehl, Phys. Lett. B244 (1990) 537; E. Gross, B. Kniehl and G. Wolf, Z. Phys. C63 (1994) 417 and (E) *ibid.* C66 (1995) 321; D.J. Summers, Phys. Rev. D53 (1996) 6374.

[172] J.R. Dell'Aquila and C.A. Nelson, Phys. Rev. D33 (1986) 80; M. Duncan, G. Kane and W. Repko, Nucl. Phys. B272 (1986) 517; C.A. Nelson, Phys. Rev. D37 (1988) 1220; D. Chang, W.Y. Keung and I. Phillips, Phys. Lett. B305 (1993) 261; B. Grzadkowski, Phys. Lett. B305 (1993) 384; A. Soni and R.M. Xu, Phys. Rev. D48 (1993) 5259; T. Arens and L.M. Sehgal, Z. Phys. C66 (1995) 89.

[173] B. Grzadkowski, J.F. Gunion and J. Pliszka, Nucl. Phys. B583 (2000) 49.

[174] S. Choi, D. Miller, M. Muhlleitner and P. Zerwas, Phys. Lett. B553 (2003) 61.

[175] A. Djouadi and B. Kniehl, *Correlations in Higgs production and decay as a probe of CP-violation in the scalar sector*, published in Proceedings of Workshop on "e^+e^- Collisions", Report DESY–93–123C.

[176] A.I. Vaĭnshteĭn, M.B. Voloshin, V.I. Zakharov and M.A. Shifman, Sov. J. Nucl. Phys. 30 (1979) 711.

[177] L. Okun, *Leptons and Quarks*, Ed. North Holland, Amsterdam, 1982.

[178] M. Gavela, G. Girardi, C. Malleville and P. Sorba, Nucl. Phys. B193 (1981) 257.

[179] H. Zheng and D. Wu, Phys. Rev. D42 (1990) 3760; A. Djouadi, M. Spira, J. van der Bij and P.M. Zerwas, Phys. Lett. B257 (1991) 187; S. Dawson and R.P. Kauffman, Phys. Rev. D47 (1993) 1264; K. Melnikov and O. Yakovlev, Phys. Lett. B312 (1993) 179; A. Djouadi, M. Spira and P.M. Zerwas, Phys. Lett. B311 (1993) 255; M. Inoue, R. Najima, T. Oka and J. Saito, Mod. Phys. Lett. A9 (1994) 1189; J. Fleischer and O.V. Tarasov, Z. Phys. C64 (1994) 413.

[180] M. Spira, A. Djouadi, D. Graudenz and P.M. Zerwas, Nucl. Phys. B453 (1995) 17.

[181] J. Fleischer, O.V. Tarasov and V.O. Tarasov, Phys. Lett. B584 (2004) 294.

[182] K. Melnikov, M. Spira and O. Yakovlev, Z. Phys. C64 (1994) 401.

[183] M. Spira, A. Djouadi and P.M. Zerwas, Phys. Lett. B276 (1992) 350.

[184] F. Wilczek, Phys. Rev. Lett. 39 (1977) 1304; J. Ellis, M. Gaillard, D. Nanopoulos and C. Sachrajda, Phys. Lett. 83B (1979) 339; T. Rizzo, Phys. Rev. D22 (1980) 178.

[185] H. Georgi, S. Glashow, M. Machacek and D. Nanopoulos, Phys. Rev. Lett. 40 (1978) 692.

[186] T. Inami, T. Kubota and Y. Okada, Z. Phys. C18 (1983) 69.

[187] A. Djouadi, M. Spira and P.M. Zerwas, Phys. Lett. B264 (1991) 440.

[188] M. Spira, A. Djouadi, D. Graudenz and P.M. Zerwas, Phys. Lett. B318 (1993) 347.

[189] S. Dawson and R.P. Kauffman, Phys. Rev. D49 (1994) 2298.

[190] A. Djouadi, M. Spira and P.M. Zerwas, Z. Phys. C70 (1996) 427.

[191] M.S. Chanowitz, M.A. Furman and I. Hinchliffe, Phys. Lett. 78B (1978) 285; Nucl. Phys. B153 (1979) 402; J. Fleischer and F. Jegerlehner, Phys. Rev. D23 (1981) 2001; F. Jegerlehner, in "Workshop on Radiative Corrections in $SU(2)_L \times U(1)$", Trieste, Italy, June 1983, Eds. B.W. Lynn and J.F. Wheater (World Scientific, Singapore, 1984), p. 237; Z. Hioki, Phys. Lett. B224 (1989) 417 and (E) *ibid.* B228 (1989) 560.

[192] B.A. Kniehl, Nucl. Phys. B376 (1992) 3; D.Yu. Bardin, B.M. Vilenskiĭ and P.Kh. Khristova, Sov. J. Nucl. Phys. 53 (1991) 152; A. Dabelstein and W. Hollik, Z. Phys. C53 (1992) 507.

[193] S. Dawson and S. Willenbrock, Phys. Lett. B211 (1988) 200; B.A. Kniehl, Nucl. Phys. B352 (1991) 1; *ibid.* Nucl. Phys. B357 (1991) 439; D.Yu. Bardin, B.M. Vilenskiĭ and P.Kh. Khristova, preprint JINR-P2-91-140.

[194] B.A. Kniehl and A. Sirlin, Phys. Lett. B318 (1993) 367; B.A. Kniehl, Phys. Rev. D50 (1994) 3314.

[195] A. Djouadi and P. Gambino, Phys. Rev. D49 (1994) 4705.

[196] B.A. Kniehl and M. Spira, Nucl. Phys. B432 (1994) 39; A. Kwiatkowski and M. Steinhauser, Phys. Lett. B338 (1994) 66 and (E) B342 (1995) 455.

[197] B.A. Kniehl and M. Spira, Nucl. Phys. B443 (1995) 37; B.A. Kniehl, Phys. Rev. D53 (1996) 6477.

[198] B.A. Kniehl and M. Steinhauser, Nucl. Phys. B454 (1995) 485; *ibid.* Phys. Lett. B365 (1996) 297.

[199] K.G. Chetyrkin, B.A. Kniehl and M. Steinhauser, Phys. Rev. Lett. 78 (1997) 594; *ibid.* Nucl. Phys. B490 (1997) 19.

[200] A. Djouadi, P. Gambino and B. Kniehl, Nucl. Phys. B523 (1998) 17.

[201] A. Djouadi and P. Gambino, Phys. Rev. Lett. 73 (1994) 2528.

[202] F. Fugel, B. Kniehl and M. Steinhauser, Nucl. Phys. B702 (2004) 333.

[203] U. Aglietti, R. Bonciani, G. Degrassi and A. Vicini, Phys. Lett. B595 (2004) 432.

[204] G. Degrassi and F. Maltoni, Phys. Lett. B600 (2004) 255.

[205] M. Steinhauser, in Proceedings of the Ringberg Workshop on "The Higgs Puzzle", hep-ph/9612395.

[206] K.G. Chetyrkin, B.A. Kniehl and M. Steinhauser, Phys. Rev. Lett. 79 (1997) 353; *ibid.* Nucl. Phys. B510 (1998) 61.

[207] A.L Kataev, JETP Lett. 66 (1997) 327; A. L. Kataev and V. Kim, hep-ph/93042428.

[208] M. Steinhauser, Phys. Rev. D59 (1999) 054005.

[209] J.K. Korner, K. Melnikov and O. Yakovlev, Phys. Rev. D53 (1996) 3737.

[210] M.A. Shifman, A.I. Vaĭnshteĭn and V.I. Zakharov, Phys. Lett. 78B (1978) 443; A.I. Vaĭnshteĭn, V.I. Zakharov and M.A. Shifman, Sov. Phys. Usp. 23 (1980) 429; M.B. Voloshin, Sov. J. Nucl. Phys. 44 (1986) 478.

[211] B. Kniehl and M. Spira, Z. Phys. C69 (1995) 77; W. Kilian, Z. Phys. C69 (1995) 89.

[212] S. L. Adler, J. C. Collins and A. Duncan, Phys. Rev. D15 (1977) 1712.

[213] O. Tarasov, Preprint JINR P2-82-900 (1982), unpublished.

[214] A. Djouadi, J. Kalinowski and M. Spira, Comput. Phys. Commun. 108 (1998) 56.

[215] P. Garbincius, Talk given at the 2004 Moriond Conference on electroweak interactions, hep-ph/0406013.

[216] The web site of the *Collider Run II Integrated Luminosity* at the address: `http://www.fnal.gov/pub/now/tevlum.html`.

[217] U. Heintz, S. Kuhlmann and S. Willenbrock, in *Future Electroweak Physics at the Fermilab Tevatron*, Report of the TeV2000 Study Group, edited by D. Amidei and R. Brock, Fermilab-PUB-96-082 (April 1996), pp. 120-156; W. M. Yao, in *New Direction for High Energy Physics*, proceedings of the 1996 DPF/DPB Summer Study on High Energy Physics, June 25-July 12, 1996, Snowmass, Colorado, edited by D. G. Cassel, L. Trindele Gennari, and R. H. Siemann, pp. 619-621; D. Amidei *et al.*, *The TEV33 Committee Report*, February, 1996; J. Womersly, DØ Note 003227, April, 1997.

[218] M. Carena J. Conway, H. Haber and J. Hobbs (conv.) *et al.*, Report of the Higgs Working Group for "RUN II at the Tevatron", hep-ph/0010338.

[219] See the review talk given by J. Engelen in Ref. [220].

[220] Proceedings of the Conference "Physics at LHC" in Vienna, 13–17 July 2004; see the web site: `wwwhephy.oeaw.ac.at/phlhc04/`.

[221] F. Gianotti, M. Mangano et T. Virdee (conv.) *et al.*, *Physics Potential and experimental Challenges of the LHC Luminosity Upgrade*, hep-ph/0204087.

[222] U. Baur *et al.*, Report of the Working Group *Physics at future colliders*, in APS/DPF/DPB Snowmmass study in Ref. [223], hep-ph/0201227.

[223] Proceedings of the APS/DPF/DPP Summer Study on the Future of Particle Physics, Snowmass 2001, Colorado; see the web site `http://snowmass2001.org/`.

[224] Proceedings of the LaThuile Workshop on Physics at Future Accelerators, La Thuile 1987, Yerllow Report CERN–87–07, 2 Volumes.

[225] VLHC Design Study Group, *Design Study for a Staged Very Large Hadron Collider*, FERMILAB-TM-2149, June 2001.

[226] S. Peggs, The Hadron Colliders Working Group Report in the 2001 Snowmass of Ref. [223].

[227] ATLAS Collaboration, *Technical Proposal*, CERN/LHCC/94-43.

[228] ATLAS Collaboration, *Detector and Physics Performance Technical Design Report*, Vols. 1 and 2, CERN–LHCC–99–14 and CERN–LHCC–99–15.

[229] CMS Collaboration, *Technical Proposal*, CERN–LHCC–94–38.

[230] CMS Collaboration, *ECAL Project Technical Design Report*, CERN/LHCC/97-33 and *The compact muon solenoid: the muon Technical Design Report*, CERN/LHCC/97-32.

[231] See the talks given by M. Nesssi (ATLAS) and A. Ball (CMS) in Ref. [220].

[232] Proceedings of the Large Hadron Collider Workshop, Aachen 1990, CERN Report 90–10, G. Jarlskog and D. Rein (eds.).

[233] D. Froidevaux, Z. Kunszt and J. Stirling [conv.] *et al.*, Report of the SM Higgs Working Group in the proceedings of Ref. [232], Vol. II; see also the Rapporteurs talks by G. Altarelli and D. Denegri, *ibid.*, Vol. I.

[234] S. Asai *et al.* (ATLAS Collaboration), Eur. Phys. J. C32S2 (2004) 19.

[235] S. Abdullin *et al.* (CMS Collaboration), CMS Note 2003/33.

[236] G. Branson *et al.* (CMS and ATLAS Collaborations), Eur. Phys. J. direct C4 (2002) N1.

[237] P. Sphicas, talk at the conference "Physics at LHC" in Ref. [220]; D. Froidevaux, talk given at the final meeting of the European Network "Physics at Colliders", Montpellier, 26–27 September 2004.

[238] A. Djouadi, R. Kinnunen, E. Richter-Was, H.U. Martyn (conv.) *et al.*, Report of the Higgs Working Group, Proceedings of the Les Houches Workshop on "Physics at TeV Colliders", 1999, hep-ph/0002258.

[239] D. Cavalli, A. Djouadi, K. Jakobs, A. Nikitenko, M. Spira, C.E.M. Wagner, W.-M. Yao (conv.) *et al.*, Report of the Higgs Working Group, Proceedings of the Les Houches Workshop on "Physics at TeV Colliders", 2001, hep-ph/0203056.

[240] K.A. Assamagan, M. Narain, A. Nikitenko, M. Spira, D. Zeppenfeld (conv.) *et al.*, Report of the Higgs Working Group, Proceedings of the Les Houches Workshop on "Physics at TeV Colliders", 2003, hep-ph/0406152.

[241] S.L. Glashow, D. Nanopoulos and A. Yildiz, Phys. Rev. D18 (1978) 1724; J. Finjord, G. Girardi and P. Sorba, Phys. Lett. B89 (1979) 99.

[242] E. Eichten, I. Hinchliffe, K. Lane and C. Quigg, Rev. Mod. Phys. 56 (1984) 579.

[243] R.N. Cahn and S. Dawson, Phys. Lett. 136B (1984) 196 and (E) *ibid.* B138 (1984) 464.

[244] D. Dicus and S. Willenbrock, Phys. Rev. D32 (1985) 1642.

[245] G. Altarelli, B. Mele and F. Pitolli, Nucl. Phys. B287 (1987) 205.

[246] W. Kilian, M. Kramer and P.M. Zerwas, Phys. Lett. B373 (1996) 135.

[247] R. Raitio and W.W. Wada, Phys. Rev. D19 (1979) 941; Z. Kunszt, Nucl. Phys. B247 (1984) 339; A.S. Bagdasaryan *et al.*, Sov. J. Nucl. Phys. 46 (1987) 315.

[248] J. Ng and P. Zakarauskas, Phys. Rev. D29 (1984) 876.

[249] R.M. Barnett, H.E. Haber and D.E. Soper, Nucl. Phys. B306 (1988) 697; F.I. Olness and W.-K. Tung, Nucl. Phys. B308 (1988) 813.

[250] D.A. Dicus and S. Willenbrock, Phys. Rev. D39 (1989) 751.

[251] E.N. Glover and J. van der Bij, Nucl. Phys. B309 (1988) 282; D.A. Dicus, C. Kao and S. Willenbrock, Phys. Lett. B203 (1988) 457; G. Jikia, Nucl. Phys. B412 (1994) 57.

[252] T. Plehn, M. Spira and P.M. Zerwas, Nucl. Phys. B479 (1996) 46.

[253] V. Barger, T. Han and R. Phillips, Phys. Rev. D38 (1988) 2766.

[254] A. Djouadi, W. Kilian, M. Mühlleitner and P. Zerwas, Eur. Phys. J. C10 (1999) 45.

[255] W. Y. Keung, Mod. Phys. Lett. A2 (1987) 765; O. Eboli, G. Marques, S. Novaes and A. Natale, Phys. Lett. B197 (1987) 269; D. Dicus, K. Kallianpur and S. Willenbrock, Phys. Lett. B200 (1988) 187; K. Kallianpur, Phys. Lett. B215 (1988) 392; A. Dobrovolskaya and V. Novikov, Z. Phys. C52 (1991) 427.

[256] A. Abbasabadi, W. Repko, D. Dicus and R. Vega, Phys. Rev. D38 (1988) 2770.

[257] V. Barger and T. Han, Mod. Phys. Lett. A5 (1990) 667.

[258] R.K. Ellis, I. Hinchliffe, M. Soldate and J.J. van der Bij, Nucl. Phys. B297 (1988) 221.

[259] U. Baur and E. W. Glover, Nucl. Phys. B339 (1990) 38; C. Kao, Phys. Lett. B328 (1994) 420.

[260] S. Dawson and R. Kauffman, Phys. Rev. Lett. 68 (1992) 2273; R.P. Kauffman, S.V. Desai and D. Risal, Phys. Rev. D55 (1997) 4005 and Phys. Rev. D59 (1999) 057504.

[261] V. Del Duca, W. Kilgore, C. Oleari, C. Schmidt and D. Zeppenfeld, Phys. Rev. Lett. 87 (2001) 122001; *ibid.* Nucl. Phys. B616 (2001) 307.

[262] V. Del Duca, A. Frizzo and F. Maltoni, JHEP 0405 (2004) 064.

[263] K. Cheung, Phys. Rev. D49 (1994) 6224.

[264] A. Djouadi, W. Kilian and T. Plehn, in preparation.

[265] A. Abassabadi, W. Repko, D. Dicus and R. Vega, Phys. Lett. B213 (1988) 386.

[266] D. Rainwater, Phys. Lett. B503 (2001) 320.

[267] A. Abassabadi, D. Bowser–Cho, D. Dicus and W. Repko, Phys. Rev. D58 (1998) 057301; *ibid.* Phys. Rev. D57 (1998) 550.

[268] D. Dicus, Z. Phys. C39 (1988) 583.

[269] K.J. Kallianpur, Phys. Lett. B215 (1988) 392.

[270] C.G. Papadopoulos in Ref. [221].

[271] B. Mele, S. Petrarca and A. Soddu, Phys. Lett. B435 (1998) 401; G. Eilam, J.L. Hewett and A. Soni, Phys. Rev. D44 (1991) 1473 and (E) *ibid.* D59 (1999) 039901.

[272] G. Mahlon and S. Parke, Phys. Lett. B347 (1995) 394.

[273] A. Bialas and P.V. Landshoff, Phys. Lett. B256 (1991) 540.

[274] M. Boonekamp, R. Peschanksi and C. Royon, Phys. Rev. Lett. 87 (2001) 251806; *ibid.* Nucl. Phys. B669 (2003) 277; B.E. Cox, J.R. Forshaw and B. Heinemann, Phys. Lett. B540 (2002) 263; R. Enberg, G. Ingelman, A. Kissavos and N. Timneanu, Phys. Rev. Lett. 89 (2002) 081801; J.-R. Cudell and O.F. Hernandez, Nucl. Phys. B471 (1996) 471; E.M. Levin, hep-ph/9912402.

[275] V.A. Khoze, A.D. Martin and M.G. Ryskin, Eur. Phys. J. C23 (2002) 311; A. De Roeck *et al.*, Eur. Phys. J. C25 (2002) 391; A.B. Kaidalov, V.A. Khoze, A.D. Martin and M.G. Ryskin, Eur. Phys. J. C31 (2003) 387; *ibid.* Eur. Phys. J. C33 (2004) 261.

[276] V.A. Khoze, A.D Martin and M.G. Ryskin, Eur. Phys. J. C26 (2002) 229.

[277] A. De Roeck and V.A. Khoze in Ref. [240].

[278] The NLO Fortran codes for HV, Hqq and $gg \to H$ production and the LO Fortran code for $Q\bar{Q}H$ production, have been written by M. Spira and can be found at `http://people.web.psi.ch/spira/`. See also M. Spira, hep-ph/9510347 for the users manual of the program `HIGLU`.

[279] T. Han and S. Willenbrock, Phys. Lett. B273 (1990) 167.

[280] H. Baer, B. Bailey and J. Owens, Phys. Rev. D47 (1993) 2730; J. Ohnemus and W. Stirling, Phys. Rev. D47 (1993) 2722; S. Mrenna and C.P. Yuan, Phys. Lett. B416 (1998) 200.

[281] A. Djouadi and M. Spira, Phys. Rev. D62 (2000) 014004.

[282] T. Han, G. Valencia and S. Willenbrock, Phys. Rev. Lett. 69 (1992) 3274.

[283] T. Figy, C. Oleari and D. Zeppenfeld, Phys. Rev. D68 (2003) 073005.

[284] E. L. Berger and J. Campbell, Phys. Rev. D70 (2004) 073011.

[285] S. Dawson, Nucl. Phys. B359 (1991) 283.

[286] D. Graudenz, M. Spira and P. M. Zerwas, Phys. Rev. Lett. 70 (1993) 1372; M. Spira, Ph. D. Thesis, RWTH Aachen, 1992.

[287] W. Beenakker, S. Dittmaier, M. Krämer, B. Plümper, M. Spira and P.M. Zerwas, Phys. Rev. Lett. 87 (2001) 201805; *ibid.* Nucl. Phys. B653 (2003) 151.

[288] S. Dawson, L.H. Orr, L. Reina and D. Wackeroth, Phys. Rev. D67 (2003) 071503; S. Dawson, C. Jackson, L.H. Orr, L. Reina and D. Wackeroth, Phys. Rev. D68 (2003) 034022.

[289] L. Reina and S. Dawson, Phys. Rev. Lett. 87 (2001) 201804; L. Reina, S. Dawson and D. Wackeroth, Phys. Rev. D65 (2002) 053017.

[290] S. Dittmaier, M. Krämer and M. Spira, Phys. Rev. D70 (2004) 074010.

[291] S. Dawson, C. Jackson, L. Reina and D. Wackeroth, Phys. Rev. D69 (2004) 074027.

[292] I. Hinchliffe and S.F. Novaes, Phys. Rev. D38 (1988) 3475; S. Catani, E. D'Emilio and L. Trentadue, Phys. Lett. B211 (1988) 335; R. P. Kauffman, Phys. Rev. D44 (1991) 1415 and D45 (1992) 1512; C.P. Yuan, Phys. Lett. B283 (1992) 395; C. Balazs and C. P. Yuan, Phys. Lett. B478 (2000) 192; C. Balazs, J. Huston and I. Puljak, Phys. Rev. D63 (2001) 014021.

[293] C.R. Schmidt, Phys. Lett. B413 (1997) 391; D. de Florian, M. Grazzini and Z. Kunszt, Phys. Rev. Lett. 82 (1999) 5209; D. de Florian and M. Grazzini, Phys. Rev. Lett. 85 (2000) 4678 and Nucl. Phys. B616 (2001) 247; S. Catani, D. de Florian and M. Grazzini, Nucl. Phys. B596 (2001) 299; V. Ravindran, J. Smith and W.L. Van Neerven, Nucl. Phys. B634 (2002) 247; E. L. Berger and J. W. Qiu, Phys. Rev. D67 (2003) 034026; A. Kulesza, G. Sterman and W. Vogelsang, Phys. Rev. D69 (2004) 014012.

[294] C. J. Glosser and C. R. Schmidt, JHEP 0212 (2002) 016.

[295] G. Bozzi, S. Catani, D. de Florian and M. Grazzini, Phys. Lett. B564 (2003) 65.

[296] C. Anastasiou, L. Dixon and K. Melnikov, Nucl. Phys. Proc. Suppl. 116 (2003) 193.

[297] C. Anastasiou, K. Melnikov and F. Petriello, hep-ph/0501130.

[298] V. Ravindran, J. Smith and W.L. Van Neerven, Nucl. Phys. B634 (2002) 247; *ibid.* Mod. Phys. Lett. A18 (2003) 1721; C. Anastasiou, K. Melnikov and F. Petriello, hep-ph/0409088.

[299] O. Brein, A. Djouadi and R. Harlander, Phys. Lett. B579 (2004) 149.

[300] R. Harlander and W. Kilgore, Phys. Rev. Lett. 88 (2002) 201801.

[301] C. Anastasiou and K. Melnikov, Nucl. Phys. B646 (2002) 220.

[302] V. Ravindran, J. Smith and W. L. van Neerven, Nucl. Phys. B665 (2003) 325.

[303] S. Catani, D. de Florian, M. Grazzini and P. Nason, JHEP 0307 (2003) 028.

[304] G. Altarelli and G. Parisi, Nucl. Phys. B126 (1977) 298.

[305] S.A. Larin, T. van Ritbergen and J.A.M. Vermaseren, Nucl. Phys. B427 (1994) 41 and B492 (1997) 338; A. Rétey and J.A.M. Vermaseren, Nucl. Phys. B604 (2001) 281.

[306] A.D. Martin, R.G. Roberts, W.J. Stirling and R.S. Thorne, Phys. Lett. B531 (2002) 216.

[307] S. Moch, J.A.M. Vermaseren and A. Vogt, Nucl. Phys. B688 (2004) 101; *ibid.* Nucl. Phys. B691 (2004) 129.

[308] R.S. Thorne *et al.* (MRST Collaboration), hep-ph/0407311.

[309] V. Gribov and L. Lipatov, Sov. J. Nucl. Phys.15 (1972) 438; Y. Dokshitzer, Sov. Phys. JETP 46 (1977) 641.

[310] J. Pumplin, D.R. Stump, J. Huston, H.L. Lai, P. Nadolsky and W.K. Tung, (CTEQ Collaboration), JHEP 0207 (2002) 012.

[311] A.D. Martin, R.G. Roberts, W.J. Stirling and R.S. Thorne (MRST Collaboration), Eur. Phys. J. C28 (2003) 455.

[312] S. Alekhin, Phys. Rev. D63 (2001) 094022 and Phys. Rev. D68 (2003) 014002.

[313] W.T. Giele, S.A. Keller and D.A. Kosower, hep-ph/0104052; M. Botje, J. Phys. G28 (2002) 779.

[314] A. Djouadi and S. Ferrag, Phys. Lett. B586 (2004) 345.

[315] J. Gunion, P. Kalyniak, M. Soldate and P. Galison, Phys. Rev. D34 (1986) 101.

[316] R. Kleiss, Z. Kunszt and W.J. Stirling, Phys. Lett. B253 (1991) 269.

[317] Z. Kunszt, Z. Trocsanyi and W.J. Stirling, Phys. Lett. B271 (1991) 247; J.F. Gunion and L.H. Orr, Phys. Rev. D46 (1992) 2052; J. Ohnemus and W.J. Stirling, Phys. Rev. D47 (1993) 336.

[318] J. Gunion, P. Kalyniak, M. Soldate and P. Galison, Phys. Rev. Lett. 54 (1985) 1226; P. Agrawal and S.D. Ellis, Phys. Lett. B229 (1989) 145; P. Agrawal, D. Bowser-Chao and K. Cheung, Phys. Rev. D51 (1995) 6114.

[319] H. Baer and J.D. Wells, Phys. Rev. D57 (1998) 4446; W. Loinaz and J.D. Wells, Phys. Lett. B445 (1998) 178.

[320] A. Stange, W.J. Marciano and S. Willenbrock, Phys. Rev. D49 (1994) 1354 and D50 (1994) 4491.

[321] J. Gunion and T. Han, Phys. Rev. D51 (1995) 1051.

[322] S. Mrenna and G. L. Kane, hep-ph/9406337.

[323] U. Baur, T. Han, N. Kauer, R. Sobey and D. Zeppenfeld, Phys. Rev. D56 (1997) 140.

[324] J.F. Gunion, G. Kane *et al.*, published in Snowmass Summer Study 1990, pp. 0059-81.

[325] W. Furmanski and R. Petronzio, Z. Phys. C11 (1982) 293.

[326] W.H. Furry, Phys. Rev. 51 (1937) 125.

[327] D.A. Dicus and S.S.D. Willenbrock, Phys. Rev. D34 (1986) 148.

[328] K. Hikasa, Phys. Rev. D29 (1984) 1939; R. Gonsalves, C. Hung and J. Pawlowski, Phys. Rev. D46 (1992) 4930; P. Rijken and W. van Neerven, Phys. Rev. D52 (1995) 149.

[329] V. Barger *et al.*, Phys. Rev. Lett. 57 (1986) 1672; D. Dicus and C. Kao, Phys. Rev. D38 (1988) 1008 and (E) *ibid.* D42 (1990) 2412.

[330] B. Kniehl, Phys. Rev. D42 (1990) 2253.

[331] M.L. Ciccolini, S. Dittmaier and M. Krämer, Phys. Rev. D68 (2003) 073003

[332] J. Kripfganz and H. Perlt, Z. Phys. C41 (1988) 319; H. Spiesberger, Phys. Rev. D52 (1995) 4936.

[333] W.J. Stirling, talk given at the Workshop "Electroweak Radiative Corrections to Hadronic Observables at TeV Energies", Durham, UK, September 2003. In a toy model, it has been shown that these effects amount to $\mathcal{O}(1\%)$, see: M. Roth and S. Weizierl, Phys. Lett. B590 (2004) 190. Recently, the QED effects have been included in the MRST set of PDFs and the fit remains essentially unchanged; see A.D. Martin, R.G. Roberts, W.J. Stirling and R.S. Thorne, Eur. Phys. J. C39 (2005) 155.

[334] O. Brein, M.L. Ciccolini, S. Dittmaier, A. Djouadi, M. Krämer and R. Harlander, hep-ph/0402003 and in Ref. [240].

[335] M. Dittmar, F. Pauss and D. Zürcher, Phys. Rev. D56 (1997) 7284.

[336] R.N. Cahn, S.D. Ellis, R. Kleiss and W.J. Stirling, Phys. Rev. D35 (1987) 1626; V. Barger, T. Han and R. Phillips, Phys. Rev. D37 (1988) 2005 and D36 (1987) 295; R. Kleiss and J. Stirling, Phys. Lett. 200B (1988) 193; V. Barger *et al.*, Phys. Rev. D42 (1990) 3052; *ibid.* Phys. Rev. D44 (1991) 1426; *ibid.* Phys. Rev. D46 (1992) 2028; D. Froideveaux, in Ref. [232] Vol II, p. 444; M. H. Seymour, *ibid.*, p. 557; U. Baur and E.W.N. Glover, Phys. Lett. B252 (1990) 683.

[337] D. Dicus, J. Gunion and R. Vega, Phys. Lett. B258 (1991) 475; D. Dicus, J. Gunion, L. Orr and R. Vega, Nucl. Phys. B377 (1991) 31.

[338] V. Barger, R. Phillips and D. Zeppenfeld, Phys. Lett. B346 (1995) 106.

[339] Y.L. Dokshitzer, S.I. Troian and V.A. Khoze, Sov. J. Nucl. Phys. 46 (1987) 712; J.F. Gunion, G. Kane, C.P. Yuan, H. Sadrozinski, A. Seiden and A. Weinstein, Phys. Rev. D40 (1989) 2223; J.D. Bjorken, Int. J. Mod. Phys. A7 (1992) 4189; *ibid.* Phys. Rev. D47 (1993) 101; K. Iordanidis and D. Zeppenfeld, Phys. Rev. D57 (1998) 3072.

[340] D. Zeppenfeld, *Collider Physics*, Lectures given at TASI98, hep-ph/9902307.

[341] D. Rainwater, Ph.D Thesis, hep-ph/9908378.

[342] D. Rainwater and D. Zeppenfeld, JHEP 9712 (1997) 005.

[343] D. Rainwater, D. Zeppenfeld and K. Hagiwara, Phys. Rev. D59 (1999) 014037; T. Plehn, D. Rainwater and D. Zeppenfeld, Phys. Rev. D61 (2000) 093005 and Phy. Lett. B454 (1999) 297.

[344] D. Rainwater and D. Zeppenfeld, Phys. Rev. D60 (1999) 113004 and (E) *ibid.* D61 (1999) 099901; N. Kauer, T. Plehn, D. Rainwater and D. Zeppenfeld, Phys. Lett. B503 (2001) 113.

[345] For an early analysis of this channel, see: R. Kleiss and J. Stirling, Phys. Lett. 200B (1988) 193.

[346] T. Plehn and D. Rainwater, Phys. Lett. B520 (2001) 108.

[347] M.L. Mangano, M. Moretti, F. Piccinini, R. Pitau and A.D. Polosa, Phys. Lett. B556 (2003) 50.

[348] J. Campbell and K. Ellis, "MCFM - Monte Carlo for FeMtobarn processes", see the web site `http://mcfm.fnal.gov/`.

[349] G. Kane, W. Repko and W. Rolnick, Phys. Lett. B148 (1984) 367; R. Cahn, Nucl. Phys. B255 (1985) 341; J. Gunion, J. Kalinowski and A. Tofighi-Niaki, Phys. Rev. Lett. 57 (1986) 2351; J. Gunion and A. Tofighi–Niaki, Phys. Rev. D36 (1987) 2671; M. Bento and C.H. Llewellyn Smith, Nucl. Phys. B289 (1987) 36.

[350] C. von Weizsäcker, Z. Phys. 88 (1934) 612; E. Williams, Phys. Rev. 45 (1934) 729; S. Brodsky, T. Kinoshita and H. Terezawa, Phys. Rev. D4 (1971) 1532.

[351] S. Dawson, Nucl. Phys. B249 (1985) 42; J. Lindfors, Z. Phys. C28 (1985) 427; P. Johnson, F. Olness and W.K. Tung, Phys. Rev. D36 (1987) 291; R. Godbole and S. Rindani, Phys. Lett. 190B (1987) 192; *ibid.* Z. Phys. C36 (1987) 295; I. Kuss and H. Spiesberger, Phys. Rev. D53 (1996) 6078.

[352] J. Gunion, G. Kane and J. Wudka, Nucl. Phys. B299 (1988) 231.

[353] J. Stirling, R. Kleiss and S.D. Ellis, Phys. Lett. 163B (1985) 261; J. Gunion, Z. Kunst and M. Soldate, Phys. Lett. 163B (1985) 389; J. Gunion and M. Soldate, Phys. Rev. D34 (1986) 826; E. Glover, J. Ohnemus and S. Willenbrock, Phys. Rev. D37 (1988) 3193; V. Barger, G. Bhattachrya, T. Han and B. Kniehl, Phys. Rev. D43 (1991) 779.

[354] R. Cahn and M. Chanowitz, Phys. Rev. Lett. 56 (1986) 1327.

[355] M. Chaichian, I. Liede, J. Lindfors and D.P. Roy, Phys. Lett. B198 (1987) 416; D. Atwood *et al.*, Proceedings of the "1987 Berkeley Workshop", Eds. R. Donaldson and M. Gilchrisese, World Scin., 1988, p. 20.

[356] T. Han and B. McElrath, Phys. Lett. B528 (2002) 81.

[357] For a discussion of the $\mu^+\mu^-$ channel in extensions of the SM, see: V. Barger and C. Kao, Phys. Lett. B424 (1998) 69; S. Dawson, D. Dicus and C. Kao, Phys. Lett. B545 (2002) 132; E. Boos, A. Djouadi and A. Nikitenko, Phys. Lett. B578 (2004) 384.

[358] T. Han and R.-J. Zhang, Phys. Rev. Lett. 82 (1999) 25; T. Han, A.S. Turcot and R.-J. Zhang, Phys. Rev. D59 (1999) 093001.

[359] For an earlier study of the $H \to WW^*$ channel and for higher Tevatron energies, see Ref. [321].

[360] A. Belyaev, T. Han and R. Rosenfeld, JHEP 0307 (2003) 021.

[361] M. Krämer, E. Laenen and M. Spira, Nucl. Phys. B511 (1998) 523.

[362] P.A. Baikov and V.A. Smirnov, Phys. Lett. B477 (2000) 367.

[363] R. Harlander, Phys. Lett. B492 (2000) 74.

[364] See also for earlier work, R. Harlander and M. Steinhauser, Prog. Part. Nucl. Phys. 43 (1999) 167.

[365] R. Harlander and W. Kilgore, Phys. Rev. D64 (2001) 013015.

[366] S. Catani, D. de Florian and M. Grazzini, JHEP 05 (2001) 025.

[367] S. Catani, D. de Florian and M. Grazzini, JHEP 0201 (2002) 015.

[368] R. Harlander and W. Kilgore, hep-ph/0211380.

[369] J.C. Collins, D.E. Soper and G. Sterman, in *Perturbative Quantum Chromodynamics*, ed. A.H. Mueller, World Scientific, Singapore, 1989.

[370] G. Sterman, Nucl. Phys. B281 (1987) 310; S. Catani and L. Trentadue, Nucl. Phys. B327 (1989) 323.

[371] G. Parisi and R. Petronzio, Nucl. Phys. B154 (1979) 427; G. Curci, M. Greco and Y. Srivastava, Nucl. Phys. B159 (1979) 451; J. Kodaira and L. Trentadue, Phys. Lett. B112 (1982) 66; J. C. Collins and D. E. Soper, Nucl. Phys. B193 (1981) 381; Y. L. Dokshitzer, D. Diakonov and S. I. Troian, Phys. Rept. 58 (1980) 269; J. C. Collins, D. E. Soper and G. Sterman, Nucl. Phys. B250 (1985) 199.

[372] S. Abdullin, M. Dubinin, V. Ilyin, D. Kovalenko, V. Savrin and N. Stepanov, Phys. Lett. B431 (1998) 410.

[373] V. Del Ducca, talk given at the "International Workshop on QCD", Conversano (Italy), June 2003, hep-ph/0312184.

[374] J. Gunion, H. Haber, F. Paige, W.-K. Tung and S. Willenbrock, Nucl. Phys. B294 (1987) 621.

[375] W.J. Marciano and F.E. Paige, Phys. Rev. Lett. 66 (1991) 2433; J.F. Gunion, Phys. Lett. B261 (1991) 510.

[376] A. Ballestrero and E. Maina, Phys. Lett. B268 (1991) 437; D.J. Summers, Phys. Lett. B306 (1993) 129; E. Richter-Was, Z. Phys. C61 (1994) 323; H.Y. Zhou and Y.P. Kuang, Phys. Rev. D47 (1993) 3680; *ibid.* Phys. Rev. D53 (1996) 4095; M. Dubinin, V. Ilyn and V. Savrin, hep-ph/9712335.

[377] J. Dai, J.F. Gunion and R. Vega, Phys. Rev. Lett. 71 (1993) 2699.

[378] A. Ballestrero and E. Maina, Phys. Lett. B287 (1992) 231.

[379] F. Maltoni, D. Rainwater and S. Willenbrock, Phys. Rev. D 66 (2002) 034022.

[380] A. Belyaev and L. Reina, JHEP 0208 (2002) 041.

[381] J. Goldstein, C.S. Hill, J. Incandela, S.J. Parke, D. Rainwater and D. Stuart, Phys. Rev. Lett. 86 (2001) 1694.

[382] D. B. Melrose, Nuovo Cim. 40 (1965) 181; W. L. van Neerven and J. A. Vermaseren, Phys. Lett. B137 (1984) 241.

[383] S. Catani, S. Dittmaier, M. Seymour and Z. Trócsányi, Nucl. Phys. B627 (2002) 189.

[384] D. Dicus, T. Stelzer, Z. Sullivan and S. Willenbrock, Phys. Rev. D59 (1999) 094016; C. Balazs, H.–J. He and C.P. Yuan, Phys. Rev. D60 (1999) 114001; M. Spira, plenary talk at SUSY02, hep-ph/0211145; T. Plehn, Phys. Rev. D67 (2003) 014018; E. Boos and T. Plehn, Phys. Rev. D69 (2004) 094005.

[385] J. Campbell, R. K. Ellis, F. Maltoni and S. Willenbrock, Phys. Rev. D67 (2003) 095002; R. Harlander and W. Kilgore, Phys. Rev. D68 (2003) 013001; F. Maltoni, Z. Sullivan and S. Willenbrock Phys. Rev. D67 (2003) 093005; J. Campbell *et al.* in Ref. [240].

[386] J. L. Diaz-Cruz and O. A. Sampayo, Phys. Lett. B276 (1992) 211; W. J. Stirling and D. J. Summers, Phys. Lett. B283 (1992) 411; A. Ballestrero and E. Maina, Phys. Lett. B299 (1993) 312; G. Bordes and B. van Eijk, Phys. Lett. B299 (1993) 315.

[387] F. Maltoni, K. Paul, T. Stelzer and S. Willenbrock, Phys. Rev. D64 (2001) 094023.

[388] S. S. Willenbrock and D. A. Dicus, Phys. Rev. D34 (1986) 155; C. P. Yuan, Phys. Rev. D41 (1990) 42; R. K. Ellis and S. Parke, Phys. Rev. D46 (1992) 3785; S. Cortese and R. Petronzio, Phys. Lett. B253 (1991) 494; T. Stelzer and S. Willenbrock, Phys. Lett. B357 (1995) 125; A. P. Heinson, A. S. Belyaev and E. E. Boos, Phys. Rev. D56 (1997) 3114; T. Stelzer, Z. Sullivan and S. Willenbrock, Phys. Rev. D58 (1998) 094021.

[389] G. Cynolter, E. Lendvai and G. Pocsik, Acta Phys. Polon. B31 (2000) 1749.

[390] S. Dawson, S. Dittmaier and M. Spira, Phys. Rev. D58 (1998) 115012.

[391] T. Stelzer and W.F. Long, Comput. Phys. Commun. 81 (1994) 357; F. Maltoni and T. Stelzer, JHEP 0302 (2003) 027.

[392] V.A. Khoze, A.D. Martin and M.G. Ryskin, Eur. Phys. J C23 (2002) 311; *ibid.* Eur. Phys. J. C34 (2004) 327; B.E. Cow *et al.*, Phys. Rev. D68 (2003) 075004.

[393] M. Boonekamp, R. Peschanksi and C. Royon, Phys. Lett. B599 (2004) 236. Note that, in this reference, a detailed Monte Carlo analysis of the signal, backgrounds and detector effects has been performed for the double exclusive diffraction process and it is shown that a ratio $S/B \sim 1$ can be achieved for $M_H = 120$ GeV and a missing mass resolution of 1 GeV.

[394] M. Boonekamp, R. Peschanksi, A. de Roeck and C. Royon, Phys. Lett. B550 (2002) 93.

[395] T. Affolder *et al.* (CDF Collaboration), Phys. Rev. Lett. 84 (2000) 5043.

[396] Z. Kunszt and J. Stirling in Ref. [232]; Z. Kunszt, S. Moretti and W.J. Stirling, Z. Phys. C74 (1997) 479.

[397] M. Spira, hep-ph/9711394 and hep-ph/9810289; A. Djouadi, Pramana 60 (2003) 215 [hep-ph/0205248], Pramana 62 (2004) 191 [hep-ph/0303097] and plenary talk given at the conference "Physics at the LHC" in Ref. [220], hep-ph/0412238.

[398] T. Sjöstrand, `PYTHIA`, Comp. Phys. Comm. 82 (1994) 74.

[399] G. Corcella *et al.*, `HERWIG`, JHEP 01 (2001) 010; hep-ph/0011363, hep-ph/0107071, hep-ph/0201201, hep-ph/0210213.

[400] E. Richter-Was, D. Froidevaux and L. Poggioli, `ATLFAST2.0`: *a fast simulation package for ATLAS*, ATLAS Note ATL-PHYS-98-131.

[401] S. Abdullin, A. Khanov and N. Stepanov, CMS Note-1994/180; for the *CMS Simulation Package*, see `http://cmsdoc.cern.ch/cmsim/cmsim.html`.

[402] After completing this work, we received the paper, *Higgs bosons searches at hadron colliders* by V. Büsher and K. Jakobs (to appear in Mod. Phys. Lett. A), where the recent experimental analyses of the various channels for Higgs detection at the Tevatron and the LHC have been reviewed and where complementary material can be found. We thank Karl Jakobs for pointing this review to us.

[403] S. Catani, M. Dittmar, D. Soper, W.J. Stirling and S. Tapprogge [conv.] *et al.*, Report of the QCD Working Group at the Workshop "Standard Model physics (and more) at the LHC", CERN Geneva 1999, hep-ph/0005025

[404] See e.g. the proceedings of the SM/QCD working groups at the three Les Houches Workshops: S. Catani *et al.*, hep-ph/0005114; W. Giele *et al.*, hep-ph/0204316; M. Dobbs *et al.*, hep-ph/0403045 and hep-ph/0403100.

[405] D. Rainwater, M. Spira and D. Zeppenfeld in Ref. [240].

[406] R.K. Ellis and S. Veseli, Phys. Rev. D60 (1999) 011501; *ibid.* Nucl. Phys. B511 (1998) 649; J.M. Campbell and R.K. Ellis, Phys. Rev. D62 (2000) 114012; *ibid.* Phys. Rev. D65 (2002) 113007.

[407] F. Berends, H. Kuijf, B. Tausk and W. Giele, Nucl. Phys. B357 (1991) 32; W. Giele, E. Glover and D. Kosower, Nucl. Phys. B403 (1993) 633; C. Balazs and C.-P. Yuan, Phys. Rev. D56 (1997) 5558.

[408] J. Smith, D. Thomas and W.L. van Neerven, Z. Phys. C44 (1989) 267; B. Mele, P. Nason and G. Ridolfi, Nucl. Phys. B357 (1991) 409; S. Frixione, P. Nason and G. Ridolfi, Nucl. Phys. B383 (1992) 3; J. Ohnemus and J.F. Owens, Phys. Rev. D43

(1991) 3626; J. Ohnemus, Phys. Rev. D44 (1991) 1403; *ibid.* Phys. Rev. D44 (1991) 3477; *ibid.* Phys. Rev. D47 (1992) 940; S. Frixione, Nucl. Phys. B410 (1993) 280; U. Baur, T. Han and J. Ohnemus, Phys. Rev. D48 (1993) 5140; *ibid.* Phys. Rev. D51 (1995) 3381; *ibid.* Phys. Rev. D48 (1996) 1098; *ibid.* Phys. Rev. D57 (1998) 2823; L.J. Dixon, Z. Kunszt and A. Signer, Phys. Rev. D60 (1999) 114037.

[409] E. Glover and J. van der Bij, Nucl. Phys. B321 (1989) 561 and Phys. Lett. B219 (1991) 488; E. Richter-Was, Z. Phys. C64 (1994) 227; C. Zecher, T. Matsuura and J.J. van der Bij, Z. Phys. C64 (1994) 219; D. Kominis and V. Koulovassilopoulos, Phys. Rev. D52 (1995) 2737; C. Balazs and C.-P. Yuan, Phys. Rev. D59 (1999) 114007; K.L. Adamson, D. de Florian and A. Signer, Phys. Rev. D65 (2002) 094041.

[410] S. Dawson, P. Nason and R.K. Ellis, Nucl. Phys. B303 (1988) 607; *ibid.* Nucl. Phys. B327 (1989) 49; W. Beennakker, H. Kuijf, W. van Neerven and J. Smith, Phys. Rev. D40 (1989) 54. For later developments, see the review of S. Frixione, M. Mangano, P. Nason and G. Ridolfi, hep-ph/9702287. See also, N. Kauer and D. Zeppenfeld, Phys. Rev. D65 (2002) 014021.

[411] See the site: `http://www.physics.rutgers.edu/~jconway/soft/shw/shw.html`.

[412] P. Bhat, R. Gilmartin and H. Prosper, Phys. Rev. D62 (2000) 074022.

[413] For an updated analysis, see: E. Boos *et al.* in Ref. [240].

[414] D. Froidevaux and E. Richter-Was, Z. Phys. C67 (1995) 213.

[415] E. Richter-Was, Acta. Phys. Polon. B31 (2000) 1931 and ATL-PHYS-2000-023.

[416] B.P. Kersevan and E. Richter-Was, Eur. Phys. J. C25 (2002) 379; V. Drollinger, T. Muller and D. Denegri, CMS–Note–2002/006; V. Drollinger, PhD Thesis, University of Karlsruhe, 2001.

[417] M. Golden and S. Sharpe, Nucl. Phys. B261 (1985) 217; V. Barger and T. Han, Phys. Lett. B212 (1988) 117.

[418] V. Cavasinni and D. Costanzo, ATL-PHYS-2000-013; K. Jakobs, ATL–PHYS–2000–008.

[419] M. Dubinin *et al.*, CMS-NOTE-1997-101.

[420] M. Dzelalija, Z. Antunovic, D. Denegri and R. Kinnunen, CMS-TN 96-091; G. Eynard, *Etude de la production associée du boson de Higgs* $WH, t\bar{t}H$ *avec* $H \to \gamma\gamma$ *avec le detecteur ATLAS*, PhD thesis (1997) LAPP–Annecy.

[421] O. Ravat and M. Lethuillier in Ref. [240].

[422] L. Fayard and G. Unal, EAGLE internal note PHYS-NO-NO-001 (1992); C. Seez, CMS-TN/94-289 (1994); D. Froidevaux, F. Gianotti and E. Richter Was, ATLAS Note PHYS-NO-064 (1995); F. Gianotti and I. Vichou, ATLAS Note PHYS-NO-078 (1996); V. Tisserand, Ph.D. Thesis (1997) LAL 97-01; K. Lassila–Perini, PhD Thesis (1998) ETH no. 12961; M. Wielers, ATL-PHYS-2002-004.

[423] E.L. Berger, E. Braaten and R.D. Field, Nucl. Phys. B239 (1984) 52; P. Aurenche, A. Douiri, R. Baier, M. Fontannaz and D. Schiff, Z. Phys. C29 (1985) 459; L. Ametller, E. Gava, N. Paver and D. Treleani, Phys. Rev. D32 (1985) 1699; D.A. Dicus and S.S.D. Willenbrock, Phys. Rev. D37 (1988) 1801; B. Bailey, J.F. Owens and J. Ohnemus, Phys. Rev. D46 (1992) 2018; B. Bailey and J.F. Owens, Phys. Rev. D47 (1993) 2735; Z. Bern, L. Dixon and D.A. Kosower, Phys. Rev. Lett. 70 (1993) 2677; C. Balazs, E.L. Berger, S. Mrenna and C.-P. Yuan, Phys. Rev. D57 (1998) 6934; D. de Florian and Z. Kunszt, Phys. Lett. B460 (1999) 184; C. Balazs, P. Nadolsky, C. Schmidt and C.-P. Yuan, Phys. Lett. B489 (2000) 157; T. Binoth, J.P. Guillet, E. Pilon and M. Werlen, Phys. Rev. D63 (2001) 114016; T. Binoth, arXiv:hep-ph/0005194; Z. Bern, A. De Freitas and L.J. Dixon, JHEP0109 (2001) 037; C. Anastasiou, E.W.N. Glover and M.E. Tejeda-Yeomans, Nucl. Phys. B629 (2002) 255; Z. Bern, L.J. Dixon and C. Schmidt, Phys. Rev. D66 (2002) 074018.

[424] T. Binoth, J.P. Guillet, E. Pilon and M. Werlen, Eur. Phys. J. C16 (2000) 311.

[425] J.-C. Chollet *et al.*, ATLAS note PHYS-NO-17 (1992); L. Poggioli, ATLAS Note PHYS-NO-066 (1995); D. Denegri, R. Kinnunen and G. Roullet, CMS-TN/93-101 (1993); I. Iashvili R. Kinnunen, A. Nikitenko and D. Denegri, CMS TN/95-076; D. Bomestar *et al.*, Note CMS TN-1995/018; C. Charlot, A. Nikitenko and I. Puljak, CMS TN/95-101; G. Martinez, E. Gross, G. Mikenberg and L. Zivkovic, ATLAS Note ATL-PHYS-2003-001 (2003).

[426] For recent studies using the new software, see the talks of S. Hassani, T. Lagouri and M. Sani, at the Conference "Physics at LHC" in Ref. [220].

[427] G. Zuckerman *et al.*, ATLAS Internal Note PHYS-NO-007 (1992). M. Bosman and M. Nessi, ATLAS Note PHYS-NO-050 (1994); N. Stepanov, CMS-TN/93-87 (1993).

[428] Ph. Mine, S. Moreau and I. Puljak, CMS Note 1999/071; I. Puljak, Ph.D Thesis, Ecole Polytechnique, 2000.

[429] M. Dittmar and H. Dreiner, Phys. Rev. D55 (1997) 167; M. Dittmar, hep-ex/9901009.

[430] D. Green *et al.*, J. Phys. G26 (2000) 1751; K. Jakobs and Th. Trefzger, ATLAS Note ATL–PHYS–2003–024.

[431] M.J. Duncan, Phys. Lett. 179B (1986) 393; A. Abbasabadi and W.W. Repko, Nucl. Phys. B292 (1987) 461; T. Matsuura and J. van der Bij, Z. Phys. C51 (1991) 259; M.J. Duncan and M.H. Reno, Phys. Rev. D56 (1997) 3129.

[432] S. Zmushko *et al.*, ATLAS Internal Note PHYS-NO-008 (1992); S. Abdullin and N. Stepanov, CMS-TN/94-178 (1994).

[433] E. Richter-Was and T. Szymocha, ATL-PHYS-2004-012; S. Mrenna, talk given at the GDR–Supersymétrie, Lyon 2002.

[434] D. Dicus, A. Stange and S. Willenbrock, Phys. Lett. B333 (1994) 126.

[435] For an early discussion, see K. Gaemers and F. Hoogeveen, Phys. Lett. 146B (1984) 347.

[436] G. Kane, G.A. Ladinsky and C.P. Yuan, Phys. Rev. D45 (1991) 124; C. Schmidt and M. Peskin, Phys. Rev. Lett. 69 (1992) 410; W. Bernreuther and A. Brandenburg, Phys. Lett. B314 (1993) 104; A. Pilaftsis and M. Nowakowski, Int. J. Mod. Phys. A9 (1994) 1097; W. Bernreuther, M. Flesch and P. Haberl, Phys. Rev. D58 (1998) 114031; W. Khater and P. Osland, Nucl. Phys. B661 (2003) 209.

[437] For a review of CP–violation in the top quark sector and a complete set of references, see: D. Atwood, S. Bar-Shalom, G. Eilam and A. Soni, Phys. Rept. 347 (2001) 1.

[438] G. Azuelos *et al.* in Ref. [239].

[439] M. Klute, ATLAS Note ATL-PHYS-2002-018 (2002); G. Azuelos and R. Mazini, ATL–PHYS–2003-004.

[440] R. Decker, S. Jadach, M. Jezabek, J.H. Kühn and Z. Was, Comp. Phys. Comm. 76 (1993) 361; *ibid.* 70 (1992) 69; *ibid.* 64 (1991) 275.

[441] M. Dubinin, CMS–NOTE–2001/022. For an ATLAS analysis, see: K. Cranmer, B. Mellado, W. Quayle and S.L. Wu, ATLAS Note ATL-PHYS-2003-036 (2003) and hep-ph/0401088.

[442] C. Buttar, K. Jakobs and R. Harper, ATL-PHYS-2002-033; N. Akchurin *et al.*, CMS–NOTE–2002/016; K. Cranmer, B. Mellado, W. Quayle and S.L. Wu, ATLAS Notes ATL-PHYS-2003-007 and ATL-PHYS-2003-008. A study has been performed for CMS in N. Akchurin *et al.*, CMS–NOTE–2002/016.

[443] M. Dittmar, Pramana 55 (2000) 151; M. Dittmar and S. Nicollerat, CMS–Note 2001/036.

[444] H.D. Yildiz, M. Zeyrek and R. Kinnunen, CMS–NOTE–2001/050; H.D. Yildiz, PhD Thesis (2002) Ankara.

[445] K. Cranmer, B. Mellado, W. Quayle and S.L. Wu, Note ATL–PHYS–2004-005 and in Ref. [240]; Michael Dührssen, PhD Thesis.

[446] K. Jacobs, private communications to the authors. We thank Tilman Plehn for pointing this feature to us and for other discussions on the vector boson fusion process.

[447] A. Belyaev, L. Reina, M. Sapinski and V. Drolinger, in Ref. [46].

[448] E. Richter-Was and M. Sapinski, Acta. Phys. Polon. B30 (1999) 1001; V. Drollinger, T. Muller and D. Denegri, CMS-Note-2002/054 and hep-ph/0111312; J. Cammin and M. Schumacher, ATL-PHYS-2000-013; D. Green, K. Maeshima, R. Vidal, W. Wu and S. Kunori, CMS–NOTE-2001/039.

[449] D. Benedetti and L. Fano, CMS–NOTE–2002/044.

[450] J. Leveque, J.B. de Vivie, V. Kostiokhine and A. Rozanov, ATL–PHYS-2002–019.

[451] K. Cranmer, B. Mellado, W. Quayle and S. L. Wu, hep-ph/0307242.

[452] G. Davatz, G. Dissertori, M. Dittmar, M. Grazzini and F. Pauss, JHEP 0405 (2004) 009.

[453] V. Drollinger and A. Sopczak, Eur. Phys. J. direct C3 (2001) N1; M. Hohfeld, ATLAS Note ATL–Phys–2001–004.

[454] F. Gianotti and M. Pepe–Altarelli, Nucl. Phys. Proc. Suppl. 89 (2000) 177.

[455] L. Landau, Dokl. Akad. Nauk. Ser. Fiz. 60 (1948) 207; C.N. Yang, Phys. Rev. 77 (1950) 242; N. Kroll and W. Wada, Phys. Rev. 98 (1955) 1355; R. Plano, A. Prodell, N. Samios, M. Schwartz and J. Steinberger, Phys. Rev. Lett. 3 (1959) 525.

[456] C. Buszello, I. Fleck, P. Marquard and J. van der Bij, Eur. Phys. J. C32 (2004) 209.

[457] T. Plehn, D. Rainwater and D. Zeppenfeld, Phys. Rev. Lett. 88 (2002) 051801.

[458] K. Odagiri, JHEP 0303 (2003) 009.

[459] J.F. Gunion, L. Poggioli, R. van Kooten, C. Kao and P. Rowson [conv.] *et al.*, *Higgs boson discovery and properties*, Proceedings of the 1996 DPF/DPB Snowmass study, hep-ph/9703330.

[460] J.F. Gunion and X.G. He, Phys. Rev. Lett. 76 (1996) 4468; J.F. Gunion and J. Pliska, Phys. Lett. B444 (1998) 136.

[461] B. Field, Phys. Rev. D66 (2002) 114007.

[462] J.R. Ellis, J.S. Lee and A. Pilaftsis, hep-ph/0502251.

[463] D. Zeppenfeld, R. Kinnunen, A. Nikitenko and E. Richter-Was, Phys. Rev. D62 (2000) 013009 and in Ref. [238].

[464] M. Dührssen, S. Heinemeyer, H. Logan, D. Rainwater, G. Weiglein and D. Zeppenfeld, Phys. Rev. D70 (2004) 113009 and in Ref. [240],

[465] M. Dührssen, ATLAS Note PHYS-2003-030 and talk given in Ref. [220].

[466] J. Conway *et al.*, *The precision Higgs working group of Snowmass 2001* in Ref. [223], hep-ph/0203206.

[467] U. Baur, T. Plehn and D. L. Rainwater, Phys. Rev. D69 (2004) 053004.

[468] U. Baur, T. Plehn and D. L. Rainwater, Phys. Rev. Lett. 89 (2002) 151801; *ibid.* Phys. Rev. D67 (2003) 033003.

[469] U. Baur, T. Plehn and D. L. Rainwater, Phys. Rev. D68 (2003) 033011.

[470] R. Lafaye, D.J. Miller, M. Muhlleitner and S. Moretti, hep-ph/0002238 and in Ref. [239].

[471] M. Moretti, M. Moretti, F. Piccinini, R. Pitau and A. Polosa, hep-ph/0410334.

[472] F.M. Renard, *Basics of electron-positron collisions*, Ed. Frontiéres, Gif–sur–Yvette, France, 1981; P.M. Zerwas, *Physics with an e^+e^- Linear Collider at High Luminosity* in: *Particle Physics: Ideas and Recent Developments*, J.J. Aubert *et al.* (eds.), Kluwer Academic Publishers, Amsterdam, 1999.

[473] See the web site: `http://www.interactions.org/linearcollider/`.

[474] J. Andruszkow *et al.*, TESLA Technical Design Report, Part II, *The Accelerator*, DESY 2001-011, ECFA 2001-209, Eds. R. Brinkmann, K. Flöttmann, J. Rossbach, P. Schmüser, N. Walker and H. Weise.

[475] R.W. Assmann *et al.*,"*A 3-TeV e^+e^- linear collider based on CLIC technology*", Report CERN-2000-008, Ed. G. Guignard.

[476] *Zeroth Order Design Report for the Next Linear Collider*, SLAC Report 474, 1996; *2001 Report on the Next Linear Collider*, Fermilab-Conf-01-075-E.

[477] N. Akasaka *et al.*, *JLC Design Study Group*, KEK-Report 97-1, 1997.

[478] For recent reviews on machine and detector physics, see the Proceedings of the *Linear Collider International Workshop*, Paris, April 2004.

[479] For a dicussion of the basic parameters of the next Linear Collider, see the work of the Parameter ICFA SubCommittee, R. Heuer (chair.) *et al.* at the web site: `http://www.fnal.gov/directorate/icfa/`.

[480] J.A. Aguilar-Saavedra *et al.*, *TESLA Technical Design Report*, Part III, *Physics at an e^+e^- Linear Collider*, Eds. R.D. Heuer, D. Miller, F. Richard and P.Zerwas, hep-ph/0106315.

[481] The LC notes on the ECFA–DESY Workshops used for the TESLA report and after can be found at: `http://www.desy.de/lcnotes`.

[482] T. Abe et al, *Linear Collider Physics Resource Book for Snowmass 2001*, hep-ex/0106055-58.

[483] K. Abe et al, *Particle Physics Experiments at JLC*, hep-ph/0109166.

[484] M. Battaglia, A. de Roeck, J. Ellis and D. Schulte (eds), *Physics at the CLIC multi–TeV Linear Collider*, CERN Report CERN–2004–005 (june 2004), hep-ph/0412251.

[485] See e.g. G. Moortgat–Pick *et al.*, hep-ph/0210212; G. Moortgat–Pick, hep-ph/0210212 and hep-ph/0410118.

[486] See section 5.1 of Ref. [480].

[487] I. Ginzburg, G. Kotkin, V. Serbo and V. Telnov, Pizma ZhETF 34 (1981) 514 and JETP Lett. 34 (1982) 491; I. Ginzburg, G. Kotkin, V. Serbo and V. Telnov, Nucl. Instr. Meth. 205 (1983) 47; V. Telnov, Nucl. Instr. Meth. A472 (2001) 43.

[488] I. Ginzburg, G. Kotkin, S. Panfil, V. Serbo and V. Telnov, Nucl. Instr. Meth. A219 (1984) 5.

[489] J.F. Gunion and H.E. Haber, Proceddings of the 1990 Snowmass Study, p. 206; T. Barklow, *ibid.* p. 440; J.F. Gunion and H.E. Haber, Phys. Rev. D48 (1993) 5109; S. Brodsky and P.M. Zerwas, Nucl Instrum. Meth. A355 (1995) 19; M. Baillargeon, G. Bélanger and F. Boudjema, Phys. Rev. D51 (1995) 4712; A. Djouadi, V. Driesen, W. Hollik and J.I. Illana, Eur. Phys. J. C1 (1998) 149; M. Melles, W.J. Stirling and V.A. Khoze, Phys. Rev. D61 (2000) 054015; S. Soldner-Rembold and G. Jikia, Nucl Instrum. Meth. A472 (2001) 133.

[490] D. L. Borden, D. A. Bauer and D. O. Caldwell, Phys. Rev. D48 (1993) 4018.

[491] B. Badelek *et al.*, *The Photon Collider at TESLA*, hep-ph/0108012; A. de Roeck, hep-ph/0311138; E. Boos et al, Nucl Instrum. Meth. A472 (2001) 100; D. Asner et al, hep-ph/0308103.

[492] M.M. Velasco *et al.*, *Photon–Photon and Electron-Photon Colliders with energies below a TeV*, Snowmass 2001 Study, hep-ex/0111055; D. Asner, J. Gronberg and J.F. Gunion, Phys. Rev. D67 (2003) 035009.

[493] J. Illana, hep-ph/9912467.

[494] G.I. Budker, Proceedings of the "7th Conference on High Energy Accelerators", Yerevan, 1969 and extract from AIP Conf. Proc. 352 (1996) 4; A.N. Skrinsky, Proceedings of the "Intgernational Seminar od Prospects in High Eneregy Physics", Morges, 1971 and extract from AIP Conf. Proc. 352 (1996) 6; G.I. Budker and A.N. Skrinsky, Sov. Phys. Usp. 21 (1978) 277; D. Cline and D. Neuffer, extracts from AIP Conf. Proc. 68 (1980) 846 and AIP Conf. Proc. 352 (1996) 10.

[495] The Working Group on $\mu^+\mu^-$ *Collider Feasability Study*, Reports BNL–52503, FNAL Conf–96/092 and LBNL–389446 (1996); Proceedings of the Workshop on "Physics at the First Muon Collider and at the front end of the Muon Collider", eds. S. Geer and R. Raja, 6-9 Nov 1997, Batavia, Illinois, USA (AIP Conf. Proc. 435). See also the web site of the Neutrino factory and Muon Collider Collaboration: `http://www.cap.bnl.gov/mumu`.

[496] C.M. Ankenbrandt *et al.*, Phys. Rev. ST Accel. Beams 2 (1999) 081001.

[497] B. Autin, A. Blondel and J. Ellis (conv.) *et al.*, Proceedings of the Workshop "Prospective Study of Muon Storage Rings at CERN", CERN Report 99–02 (1999).

[498] V. Barger, M. S. Berger, J. F. Gunion and T. Han, Phys. Rept. 286 (1997) 1.

[499] J.F. Gunion, hep-ph/9707379.

[500] V. D. Barger, M. Berger, J. F. Gunion and T. Han, in Proc. of the APS/DPF/DPB 2001 Snowmass Study, hep-ph/0110340; J. Gunion, hep-ph/9802258.

[501] C. Blöchinger *et al.*, Proceedings of the CERN Workshop "Physics Opportunities at $\mu^+\mu^-$ Higgs Factories", hep-ph/0202199.

[502] S. Dawson and J.L. Rosner, Phys. Lett. B148 (1984) 497.

[503] K. Hikasa, Phys. Lett. 164B (1985) 385 and (E) *ibid.* 195B (1987) 623.

[504] W. Kilian, M. Kramer and P.M. Zerwas, hep-ph/9605437.

[505] K. Gaemers and G. Gounaris, Phys. Lett. B77 (1978) 379.

[506] A. Djouadi, J. Kalinowski and P. M. Zerwas, Mod. Phys. Lett. A7 (1992) 1765; *ibid.* Z. Phys. C54 (1992) 255.

[507] G. Gounaris, D. Schildknecht and F.M. Renard. Phys. Lett. B83 (1979) 191; E.W.N. Glover and A.D. Martin, Phys. Lett. B226 (1989) 393.

[508] A. Djouadi, W. Kilian, M.M. Muhlleitner and P.M. Zerwas, Eur. Phys. J. C10 (1999) 27; *ibid.* hep-ph/0001169.

[509] A. Barroso, J. Pulido and J.C. Romao, Nucl. Phys. B267 (1986) 509; A. Abbasabadi, D. Bowser-Chao, D.A. Dicus and W. Repko, Phys. Rev. D52 (1995) 3919; A. Djouadi, V. Driesen, W. Hollik and J. Rosiek. Nucl. Phys. B491 (1997) 68.

[510] K. Gaemers and F. Hoogeveen, Z. Phys. C26 (1984) 249; A. Djouadi, V. Driesen and C. Junger, Phys. Rev. D54 (1996) 759.

[511] V. Barger, T. Han and A. Stange, Phys. Rev. D42 (1990) 777.

[512] M. Baillargeon, F. Boudjema, F. Cuypers, E. Gabrielli and B. Mele, Nucl. Phys. B424 (1994) 343.

[513] E. Boos *et al.*, Phys. Lett. B273 (1991) 173; K. Hagiwara, I. Watanabe and P. M. Zerwas, Phys. Lett. 278B (1992) 187.

[514] V. D. Barger, M. S. Berger, J. F. Gunion and T. Han, Phys. Rev. Lett. 75 (1995) 1462.

[515] For earlier reviews on e^+e^- physics, see for instance: S. Dawson and M. Oreglia, hep-ph/0403015; J. Gunion, H. Haber and R. Van Kooten, hep-ph/0301023; P. Derwent *et al.*, hep-ex/0107044; J. Bagger *et al.*, hep-ex/0007022; E. Accomando, Phys. Rept. 299 (1998) 1; P.M. Zerwas, Acta Phys. Polon. B30 (1999) 1871; H. Murayama and M. Peskin, Ann. Rev. Nucl. Part. Sci. 46 (1996) 533; P.M. Zerwas *et al.*, hep-ph/9605437.

[516] P.M. Zerwas *et al.*, Proceddings of the ECFA–DESY Workshops e^+e^- *collisions at TeV energies: The physics Potential*, DESY-92-123A-B (1991), DESY-92-123C (1993) and DESY-96-123D (1996).

[517] J. Fleischer and F. Jegerlehner, Nucl. Phys. B216 (1983) 469; B. Kniehl, Z. Phys. C55 (92) 605; A. Denner, J. Küblbeck, R. Mertig and M. Böhm, Z. Phys. C56 (92) 261.

[518] A. Denner, S. Dittmaier, M. Roth and M. M. Weber, Nucl. Phys. B660 (2003) 289.

[519] G. Bélanger, F. Boudjema, J. Fujimoto, T. Ishikawa, T. Kaneko, K. Kato and Y. Shimizu, Phys. Lett. B559 (2003) 252.

[520] F. Jegerlehner and O. Tarasov, Nucl. Phys. Proc. Suppl. 116 (2003) 83.

[521] F. Boudjema, J. Fujimoto, T. Ishikawa, T. Kaneko, K. Kato, Y. Kurihara, Y. Shimizu and Y. Yasui, Phys. Lett. B600 (2004) 65.

[522] S. Dittmaier, M. Krämer, Y. Liao, M. Spira and P.M. Zerwas, Phys. Lett. B478 (2000) 247; *ibid.* Phys. Lett. B441 (1998) 383.

[523] S. Zhu, hep-ph/0212273; for the correction to the dominant channel see also S. Dawson and L. Reina, Phys. Rev. D57 (1998) 5851; *ibid.* Phys. Rev. D59 (1999) 054012.

[524] G. Bélanger, F. Boudjema, J. Fujimoto, T. Ishikawa, T. Kaneko, K. Kato, Y. Shimizu and Y. Yasui, Phys. Lett. B571 (2003) 163.

[525] A. Denner, S. Dittmaier, M. Roth and M.M. Weber, Phys. Lett. B575 (2003) 290.

[526] Y. You, W.G. Ma, H. Chen, R.Y Zhang, Y.B. Sun and H.S. Hou, Phys. Lett. B571 (2003) 85.

[527] G. Bélanger, F. Boudjema, J. Fujimoto, T. Ishikawa, T. Kaneko, Y. Kurihara, K. Kato and Y. Shimizu, Phys. Lett. B576 (2003) 152.

[528] T.Y. Zhang, W.G. Ma, H. Chen, Y.B. Sun and H.S. Hou, Phys. Lett. B578 (2004) 349.

[529] F. Boudjema *et al.* as reported by Y. Yasue in the talk given at the ECFA Workshop on e^+e^- colliders, Durham, Sept. 2004.

[530] J. Fujimoto, T. Ishikawa, Y. Shimizu, K. Kato, N. Nakazawa and T. Kaneko, Acta Phys. Polon. B28 (1997) 945; F. Yuasa *et al.*, Prog. Theor. Phys. Suppl. 138 (2000) 18; G. Bélanger *et al.*, hep-ph/0308080.

[531] M. Tentyukov and J. Fleischer, Comput. Phys. Commun. 132 (2000) 124.

[532] J. Kublbeck, M. Bohm and A. Denner, Comput. Phys. Commun. 60 (1990) 165 and Comput. Phys. Commun. 64 (1991) 345; T. Hahn, Comput. Phys. Commun. 140 (2001) 418.

[533] T. Hahn and M. Perez-Victoria, Comput. Phys. Commun. 118 (1999) 153.

[534] J.A.M. Vermaseren, math-ph/0010025.

[535] K. Hagiwara and M.L. Stong. Z. Phys. C62 (1994) 99; B. Grzadkowski and J. Wudka, Phys. Lett. B364 (1995) 49; G. Gounaris, J. Layssac and F.M. Renard, Z. Phys. C65 (1995) 245; A. Skjold and P. Osland, Nucl. Phys. B453 (1995) 3; J.P. Ma and B. McKellar, Phys. Rev. D52 (1995) 22; G. Gounaris, F.M. Renard and N. Vlachos, Nucl. Phys. B459 (1996) 51; W. Kilian, M. Krämer, and P. Zerwas, Phys. Lett. B381 (1996) 243; G. Mahlon and S.J. Parke, Phys. Rev. D58 (1998) 054015; T. Han and J. Jiang, Phys. Rev. D63 (2001) 096007; M.T. Dova and S. Ferrari, Phys. Lett. B605 (2005) 376.

[536] D.J. Miller, S.Y. Choi, B. Eberle, M. Muhlleitner and P. Zerwas, Phys. Lett. B505 (2001) 149.

[537] R.L. Kelly and T. Shimuda, Phys. Rev. D23 (1981) 1940; R.M. Godbole and P. Roy, Phys. Rev. Lett. 50 (1983) 717; P. Kalyniak, J.N. Ng and P. Zakarauskas, Phys. Rev. D29 (1984) 502; J.C. Romão and A. Barroso, Phys. Lett. B185 (1987) 195; Z. Kunszt and J. Stirling, Phys. Lett. B242 (1990) 507; N. Brown, Z. Phys. C49 (1991) 657; V. Barger and K. Whisnant, Phys. Rev. D43 (1991) 1443.

[538] K. Hagiwara, S. Ishihara, J. Kamoshita and B. Kniehl, Eur. Phys. J. C14 (2000) 457.

[539] A. Chalov, A. Likhoded and R. Rosenfeld, J. Phys. G29 (2003) 337; V. Braguta, A. Chalov, A. Likhoded and R. Rosenfeld, Phys. Rev. Lett. 90 (2003) 241801.

[540] V. Barger, J. Beacom, K. Cheung and T. Han, Phys. Rev. D50 (1994) 6704; F. Cuypers, hep-ph/9512201 and published in Iwate Linear Colliders 1995:707-716; P. Minkowski, published in eConf C960625:LTH099,1996; C.A. Boe, O.M. Ogreid, P. Osland and J.Z. Zhang, Eur. Phys. J. C9 (1999) 413.

[541] A. Djouadi, P.M. Zerwas and J. Zunft, Phys. Lett. B259 (1991) 175.

[542] S. Bar-Shalom, D. Atwood, G. Eilam, R.R. Mendel and A. Soni, Phys. Rev. D53 (1996) 1162; S. Moretti, Phys. Lett. B452 (1999) 338; D. Chang and W.-Y. Keung, Phys. Rev. D48 (1993) 3225; S. Moretti, Phys. Lett. B452 (1999) 338; B. Grzadkowski, J. F. Gunion and J. Kalinowski, Phys. Rev. D60 (1999) 075011. H. Baer, S. Dawson

and L. Reina, Phys. Rev. D61 (2000) 013002; T. Han, T. Huang, Z.-H. Lin, J.-X. Wang and X. Zhang, Phys. Rev. D61 (2000) 015006; C.S. Huang and S.H. Zhu, Phys. Rev. D65 (2002) 077702.

[543] B. Grzadkowski, J.F. Gunion and X. He, Phys. Rev. Lett. 77 (1996) 5172; J.F. Gunion and X. He, hep-ph/9703330.

[544] A. Djouadi, H.E. Haber and P.M. Zerwas, Phys. Lett. B375 (1996) 203; P. Osland and P.N. Pandita, Phys. Rev. D59 (1999) 055013; D.J. Miller and S. Moretti, Eur. Phys. J. C13 (2000) 459; V. Barger at al., Phys. Rev. D67 (2003) 115001.

[545] F. Boudjema and E. Chopin, Z. Phys. C73 (1996) 85.

[546] W. Kilian, `WHiZard`, LC-TOOL-2001-039; M. Moretti, T. Ohl and J. Reuter, hep-ph/0102195.

[547] V.A. Ilyin, A.E. Pukhov, Y. Kurihara, Y. Shimizu and T. Kaneko, Phys. Rev. D54 6717 (1996).

[548] A. Pukhov *et al.*, `CompHEP`, hep-ph/9908288.

[549] A. Gutierrez-Rodriguez, M.A. Hernandez-Ruiz and O.A. Sampayo, hep-ph/0302120.

[550] M. Battaglia, E. Boos and W.M. Yao, hep-ph/0111276 and in Ref. [484].

[551] S. Moretti, "`HERWIG`: *an event generator for* e^+e^- *Linear Colliders*, hep-ph/0209209, LC-TOOL-2002-009.

[552] P. Janot, `HZHA` in Physics at LEP2, CERN 96-01, Vol.2, 309.

[553] T. Ohl, `CIRCE`, Comput. Phys. Commun. 101 (1997) 269.

[554] M. Pohl and H.J. Schreiber, `SIMDET`, LC-DET-2002-005.

[555] T. Behnke *et al.*, `BRAHMS`, LC-TOOL-2001-005.

[556] For a comparion of various event generators and of different fast detector simulation programs, see M. Ronan, *Multi-Jet Higgsstrahlung Analysis*, LC-PHSM-2003-048 (2003) in Ref. [481].

[557] K. Desch *et al.*, Report of the Higgs Working Group for the *Extended ECFA–DESY Study*, Amsterdam 2003, hep-ph/0311092.

[558] See for instance the summary talks of of the Higgs WG session given by S. Kanemura, hep-ph/0410133 and T. Barklow, hep-ph/0411221, at the "International Linear Collider Workshop", Paris, April 2004.

[559] G. Weiglein *et al.* (LHC–LC Study Group), hep-ph/0410364.

[560] A. Djouadi, `http://www.cern.ch/djouadi/programs.html`.

[561] For discussions of backgrounds, see for instance: P. Grosse–Wiesmann, D. Haidt and H.J. Schreiber, Report DESY 92–123A in Ref. [516]; P. Janot, Waikoloa Linear Collid 1993:0192-217; E. Boos, M. Sachwitz, H.J. Schreiber and S. Shichanin, Z. Phys. C64 (1994) 391; *ibid.* Z. Phys. C67 (1995) 613; G. Montagna, O. Nicrosini and F. Piccinini, Phys. Lett. B348 (1995) 496; S. Moretti, Phys. Rev. D52 (1995) 6316; *ibid.* Z. Phys. C71 (1996) 267; D. Apostolakis, P. Ditsas and S. Katsanevas, Z. Phys. C76 (1997) 201.

[562] V. Barger, K. Cheung, B. Kniehl, R. Phillips, Phys. Rev. D46 (1992) 3725; A. Ballestrero, E. Maina and S. Moretti, Phys. Lett. B333 (1994) 434 and Phys. Lett. B335 (1994) 460; S. Moretti, Phys. Rev. D52 (1995) 6316.

[563] R. van Kooten, talk at LCWS, Baltimore, March 2001; see also the PhD Thesis of N. Meyer.

[564] P. Garcia-Abia and W. Lohmann, Eur. Phys. J. direct C2 (2000) 2.

[565] P. Garcia-Abia, W. Lohmann and A. Resperaza, LC-PHSM-2000-62 in Ref. [481].

[566] Recently, an analysis has shown that in the Higgs mass mesurement using the recoil mass technique, systematical errors from the beam energy scale and differential luminosity distributions lead to an additional combined uncertainty of 30 MeV for $M_H = 120$ GeV; see A. Resperaza in Ref. [558].

[567] M. Dova, P. Garcia-Abia and W. Lohmann, LC-PHSM-2001-054.

[568] M. Schumacher, LC-PHSM-2001-003.

[569] K. Desch and N. Meyer, Eur. Phys. J. C35 (2004) 171 and LC-PHSM-2001-025.

[570] M. Hildreth, Preprint SLAC-PUB 6036; M.D. Hildreth, T.L. Barklow and D.L. Burke, Phys. Rev. D49 (1994) 3441; I. Nakamura and K. Kawagoe, Phys. Rev. D54 (1996) 3634; J. Kamoshita, Y. Okada and M. Tanaka, Phys. Lett. B391 (1997) 124; G. Borisov and F. Richard, hep-ph/9905413; Marco Battaglia, hep-ph/9910271; E. Boos, V. Ilyin, A. Pukhov, M. Sachwitz and H.J. Schreiber, Eur. Phys. J. direct C2 (2000) 5.

[571] C.T. Potter, J. E. Brau and M. Iwasaki, eConf C010630 (2001) P118 and Ref. [223].

[572] Using an improved version of the TESLA detector simulation program `SIMDET`, it has been shown that the charm tagging capabilities have been overestimated in the analyses performed for the TESLA TDR and the precision on the the $b\bar{b}, c\bar{c}$ and gg are thus worse than those presented in Ref. [480]; see T. Kuhl in Ref. [558].

[573] J.-C. Brient, Note ECFA - LC Workshop, LC-PHSM-2002-03.

[574] T. Barklow, hep-ph/0312268 and in Ref. [240].

[575] E. Boos, J.C. Brient, D.W. Reid, H.J. Schreibe and R. Shanidze, Eur. Phys. J. C19 (2001) 455 and Note LC-PHSM-2000-053.

[576] J. Gunion and P.C. Martin, Phys. Rev. Lett. 78 (1997) 4541.

[577] M. Dubinin, H.J. Schreiber and A. Vologdin, LC-PHSM-2003-004.

[578] M. Battaglia and A. de Roeck, hep-ph/0111307.

[579] M. Battaglia, hep-ph/0211461.

[580] M. Schumacher, LC-PHSM-2003-096.

[581] Most of the analyses with the tagging of heavy quarks use a realistic neural network algorithm based on D.J. Jackson, *A topological vertex reconstruction algorithm for hadronic jets*, Nucl. Instrum. Meth. A388 (1997) 247.

[582] A. Gay, presentation at the ECFA/DESY Workshop, Amsterdam 2003 LC–Note 2004 and in Ref. [557].

[583] A. Juste and G. Merino, hep-ph/9910301; M. Martinez and R. Miquel, Eur. Phys. J. C27 (2003) 49; K. Desch and M. Schmucher in Ref. [559]; S. Dawson, A. Juste, L. Reina and D. Wackeroth in Ref. [559].

[584] K. Hagiwara, H. Murayama and I. Watanabe, Nucl. Phys. B367 (1991) 257.

[585] For studies of the $H \to t\bar{t}$ decay, see also, S. Bar-Shalom, D. Atwood and A. Soni, Phys. Lett. B419 (1998) 340; B. Grzadkowski and J. Pliszka, Phys. Rev. D60 (1999) 115018.

[586] J. Alcaraz and E.R. Morales, hep-ph/0012109.

[587] C. Castanier, P. Gay, P. Lutz et J. Orloff, LC-PHSM-2000-061 and hep-ph/0101028.

[588] U. Baur, T. Plehn and D. Rainwater in Ref. [559].

[589] Y. Yasui *et al.*, in LCWS Fermilab (2001) hep-ph/0211047.

[590] For recent related studies, see S. Kanemura *et al.*, Phys. Lett. B558 (2003) 157, hep-ph/0209326 and hep-ph/0410048.

[591] N. Meyer, LC-PHSM-2003-066 and hep-ph/0308142.

[592] K. Desch and M. Battaglia, LC-PHSM-2001-053.

[593] A. Blondel, Phys. Lett. B202 (1988) 145; K. Mönig, LC-PHSM-2000-059.

[594] J. Erler, S. Heinemeyer, W. Hollik, G. Weiglein and P.M. Zerwas, Phys. Lett. B486 (2000) 125.

[595] I. Watanabe *et al.* in Ref. [483]; T. Ohgaki, T. Takahashi, I. Watanabe and T. Tauchi, Phys. Rev. D56 (1997) 1723 and Int. J. Mod. Phys. A13 (1998) 2411; S. Soldner-Rembold and G. Jikia, Nucl. Phys. Proc. Suppl. 82 (2000) 373; M. Melles, hep-ph/9906467 and hep-ph/0008125; P. Niezurawski, A.F. Zarnecki and M. Krawczyk, Acta Phys. Polon. B34 (2003) 177; A. Rosca and K. Mönig, LC-PHSM-2003-084.

[596] P. Niezurawski, A.F. Zarnecki and M. Krawczyk, hep-ph/0307183 and LC-PHSM-2003-086.

[597] G. Jikia, Phys. Lett. B298 (1993) 224; *ibid.* Nucl. Phys. B405 (1993) 24; M.S. Berger, Phys. Rev. D48 (1993) 5121; D.A. Dicus and C. Kao, Phys. Rev. D49 (1994) 1265; G. Gounaris, J. Layssac, P. Porfyriadis and F.M. Renard, Eur. Phys. J. C13 (2000) 79.

[598] D. Morris, T. Truong and D. Zappala, Phys. Lett. B323 (1994) 421; I. Ginzburg and I. Ivanov. Phys. Lett. B408 (1997) 325; E. Boos *et al.*, Phys. Lett. B427 (1998) 189.

[599] P. Niezurawski, A.F. Zarnecki and M. Krawczyk, hep-ph/0307175 and LC-PHSM-2003-088; *ibid.* JHEP 0211 (2002) 034.

[600] B. Grzadkowski and J.F. Gunion, Phys. Lett. B294 (1992) 361; J.F. Gunion and J.G. Kelly, Phys. Lett. B333 (1994) 110.

[601] R. Godbole, S. Rindani and R. Singh, Phys. Rev. D67 (2003) 095009.

[602] E. Asakawa and K. Hagiwara, Eur. Phys. J. C31 (2003) 351; E. Asakawa, hep-ph/0409083.

[603] E. Asagawa, J. Kamoshita, A. Sugamoto and I. Watanabe, Eur. Phys. J. C14 (2000) 335; E. Asagawa, S.Y. Choi, K. Hagiwara and J.S. Lee, Phys. Rev. D62 (2000) 115005.

[604] For a recent work and for earlier references, see: B. Grzadkowski, Z. Hioki and K. Ohkuma, Nucl. Phys. B689 (2004) 108.

[605] J. Kuhn, E. Mirkes and J. Steegborn, Z. Phys. C57 (1993) 615.

[606] T. Barklow in Proceddings of the 1990 Snowmass Study, Ref. [489]; K. Ispirian *et al.*, Sov. J. Nucl. Phys. 11 (1970) 712.

[607] M. Drees *et al.*, Phys. Lett. B306 (1993) 371; D. Borden *et al.*, Phys. Rev. D50 (1994) 4499; B. Kamal, Z. Merebashvili and A.P. Contogouris, Phys. Rev. D51 (1995) 4808; G. Jikia and A. Tkabaldze, Phys. Rev. D54 (1996) 2030.

[608] V.S. Fadin, V.A. Khoze and A.D. Martin, Phys. Rev. D56 (1997) 484; M. Melles, W.J. Stirling. Eur. Phys. J. C9 (1999) 101; *ibid.* Nucl. Phys. B564 (1999) 325; M. Melles, W.J. Stirling and V.A. Khoze. Phys. Rev. D61 (2000) 54015.

[609] A. Denner, S. Dittmaier and M. Strobel, Phys. Rev. D51 (1996) 44.

[610] M. Mühlleitner, M. Krämer, M. Spira and P. Zerwas, Phys. Lett. B508 (2001) 31.

[611] See for instance, M. Drees and R. Godbole, Z. Phys. C59 (1993) 591.

[612] For reviews of the various processses in $\gamma\gamma$ collisions, see: M. Baillargeon, G. Bélanger and F. Boudjema, *Electroweak physics issues at a high–energy $\gamma\gamma$ collider*, hep-ph/9405359.

[613] K. Cheung, Nucl. Phys. B403 (1993) 19; G. Jikia, Nucl. Phys. B494 (1997) 19.

[614] R. Godbole, S. Kraml and R. Singh, hep-ph/0409199.

[615] G. Jikia, Nucl. Phys. B412 (1994) 57.

[616] R. Belusveic and G. Jikia, Phys. Rev. D70 (2004) 073017.

[617] M. Baillargeon and F. Boudjema, Phys. Lett. B317 (1993) 371.

[618] O. Eboli, M.C. Gonzalez-Garcia and S. Novaes, Phys. Rev. D50 (1994) 3546; G. Gounaris, P. Porfyriadis and F.M. Renard, Eur. Phys. J. C20 (2001) 659.

[619] K. Cheung, Phys. Rev. D47 (1993) 3750.

[620] For additional discussions of this process, see: J.Y Guo, Y. Liao and Y.P. Kuang, Phys. Rev. D62 (2000) 035007; H. Chen *et al.*, Nucl. Phys. B683 (2004) 196.

[621] J.Y. Guo, Y. Liao and Y.P. Kuang, Phys. Rev. D62 (2000) 035007; Y.J. Zhou *et al.*, Phys. Rev. D68 (2003) 0903004.

[622] K. Hagiwara, I. Watanabe and P. M. Zerwas, Phys. Lett. B278 (1992) 187; E. Boos *et al.*, Phys. Lett. B273 (1991) 173; K. Cheung, Phys. Rev. D48 (1993) 1035.

[623] E. Boos, A. Pukhov, M. Sachwitz and H.J. Schreiber, Z. Phys. C75 (1997) 237.

[624] S. Dittmaier and A. Kaiser, Phys. Rev. D65 (2002) 113003.

[625] W. Murray, hep-ph/0104268 and in Ref. [497].

[626] P. Janot in Ref. [497].

[627] R. Casalbuoni, A. Deandrea, S. De Curtis, D. Dominici, R. Gatto and J. F. Gunion, Phys. Rev. Lett. 83 (1999); R. Casalbuoni *et al.*, JHEP 9908 (1999) 011.

[628] V. Barger, T. Han and C.G. Zhou, Phys. Lett. B480 (2000) 140.

[629] B. Kamal, W.J. Marciano and Z. Parsa, hep-ph/9712270.

[630] D. Atwood and A. Soni, Phys. Rev. D52 (1995) 6271; S. Y. Choi and J. S. Lee, Phys. Rev. D61 (2000) 111702; E. Asakawa, S. Y. Choi and J. S. Lee, Phys. Rev. D63 (2001) 015012.